Elson Longo · Felipe de Almeida La Porta
Editors

Recent Advances in Complex Functional Materials

From Design to Application

Springer

Recent Advances in Complex Functional Materials

Elson Longo • Felipe de Almeida La Porta
Editors

Recent Advances in Complex Functional Materials

From Design to Application

Springer

Editors
Elson Longo
Chemistry Department
Universidade Estadual Paulista
Araraquara, São Paulo, Brazil

Felipe de Almeida La Porta
Chemistry Department
Universidade Tecnológica Federal do Paraná
Londrina, Paraná, Brazil

ISBN 978-3-319-53897-6 ISBN 978-3-319-53898-3 (eBook)
DOI 10.1007/978-3-319-53898-3

Library of Congress Control Number: 2017938787

Printed on acid-free paper

This Springer imprint is published by Springer Nature
The registered company is Springer International Publishing AG
The registered company address is: Gewerbestrasse 11, 6330 Cham, Switzerland

Preface

Our book not only covers many interesting and important issues of the current research in the field of complex functional materials (e.g., metal oxides, semiconductors, porous materials, carbon-based materials as well as polymeric materials and devices) but also includes important fabrication methods, materials properties, and their potential applications in the several fields of nanotechnology. Hence, there are enormous benefits to a deeper understanding of the physical and chemical behavior of complex functional materials at the nanoscale.

In order to achieve this goal, crystalline materials are treated in greater wealth of detail than the amorphous as well as the partially crystalline materials, mainly due to the various physical and chemical behaviors related to the structural and electronic order-disorder effects (i.e., at the short-, medium-, and long range) to understand novel complex functional materials, which in principle, is as an important parameter to a rational control of their physical and chemical properties at the nanoscale. Analyzing the importance of structural and electronic defects and their effects on the materials properties, this point of view has a still very unexplored origin, which allows us to explore even more the capacity we have always had to transform great challenges into new opportunities from a modern viewpoint of physics, chemistry, and materials engineering. In this context, this book is very interesting for all scientific community.

With scientific developments in the last century, new and important advances have been observed in recent years, in turn, opening a wide range of the technological applications and thus generating infinite possibilities, producing ever more refined knowledge for the future. Hence, we explore new approaches to understand the physical and chemical properties of emergent complex functional materials, revealing a close relationship between their structures and properties at the molecular level. In particular, this book is subdivided into three fundamental parts. The primary focus of this book is the ability to synthesize materials with a controlled chemical composition, a crystallographic structure, and a well-defined morphology. Also more importantly, different strategies of the analysis and characterization are discussed in detail, being an important tool for students and researchers to develop research involving a modern and attractive logic in the different fields of

knowledge. Special attention is also given to the interplay of theory, simulation, and experimental results, to interconnect theoretical knowledge and experimental approaches, which can reveal new scientific and technological directions in several fields, expanding the versatility to yield a variety of new complex materials with desirable applications and functions.

Some of the challenges and opportunities in this field are also discussed, targeting the development of new emergent complex functional materials with tailored properties to solve problems related to renewable energy, health, and environmental sustainability. A more fundamental understanding of the physical and chemical properties of new emergent complex functional materials is essential to achieve more substantial progress in some technological fields. We believe this book can, in principle, offer new possibilities for acquiring fundamental and innovative knowledge that can accelerate the process of discovering new complex materials with completely new and interesting properties for a wide variety of applications in emerging technologies.

In short, we hope that this book will serve as a facilitating tool for learning. This book was written with the help of experts in various fields of knowledge. Without their help, this book would not have been completed. With this goal in mind, the editors invited acknowledged specialists to contribute chapters covering a broad range of disciplines. Good reading!

Araraquara, São Paulo, Brazil — Elson Longo
Londrina, Paraná, Brazil — Felipe de Almeida La Porta

Contents

Part I
Advances in the Processing of Complex Functional Materials

Chapter 1
Multifunctional Complex Oxide Processing

Maria A. Zaghete, Leinig A. Perazolli, Gisane Gasparotto, Glauco M. M.M. Lustosa, Glenda Biasotto, Guilhermina F. Teixeira, Natalia Jacomaci, Rafael A. C. Amoresi, and Silvia L. Fernandes

Among the complex functional materials, such as semiconductors, metals, and polymers, ceramics are a most likely class of materials with the widest variety of functions for desired technological application, such as capacitors, power transducers, gas and biological sensors, and electrooptical and electro-chromic devices. In crystalline materials of type ABX_3, the properties are due to some intrinsic characteristics as there is no center of symmetry, crystalline anisotropy, spontaneous and reversible-oriented dipoles, degree of order-disorder, bandgap energy, and the presence of intrinsic or promoted defects by former or modifier lattice; these are some decisive points in the characteristics of these compounds. Considering this broad range of intrinsic and extrinsic parameters that determine the functionality and efficiency of this class of complex and multifunctional materials, the processing procedure is a crucial step. The different syntheses routes that provide to get control of composition, crystal structure, morphology, and size as well as type and location of defects allow obtaining complex compounds with synergy between properties for many applications. The goal of this chapter is to present different processing routes and discuss what are the most appropriate depending on the desired applications. In this chapter, the processing of the complex oxide perovskite type as titanates, niobates, tungstates; semiconductors such as (Zn-Nb-Co-Cr)-SnO_2 and Au-ZnO modified systems will be presented. The materials which will be discussed here present a potential applications as piezoelectrics, photoluminescent, photocatalyst, sensors, oxide electrodes, varistor, and solar cells devices.

M.A. Zaghete (✉) • L.A. Perazolli • G. Gasparotto • G.M.M.M. Lustosa • G. Biasotto
G.F. Teixeira • N. Jacomaci • R.A.C. Amoresi • S.L. Fernandes
Center for Development of Functional Materials, Interdisciplinar Laboratory of Electrochemistry and Ceramics, Chemistry Institute of UNESP/Araraquara, R. Prof. Francisco Degni, no 55, Bairro Quitandinha, CEP 14800-060, Araraquara, SP, Brazil
e-mail: zaghete@iq.unesp.br

E. Longo, F.A. La Porta (eds.), *Recent Advances in Complex Functional Materials*,
DOI 10.1007/978-3-319-53898-3_1

1 Introduction

The increasing technological advancement of our modern society stimulates the development of materials with multiple applications. These multifunctional materials are, by their nature, capable of combining a wide range of characteristics aiding in the discovery of new applications for materials that are already known to be applicable to a single property.

As a direct result of their electrical, sensing, and optical properties, complex ceramic oxides have been largely employed in the composition of devices with a high efficiency and specificity. Among the many multifunctional oxides with perovskite-type crystal structures (ABX_3), wurtzite and rutile, to mention only a few, are found to allow the existence of essentially differentiated electric properties including ferroelectricity, piezoelectricity, semiconductivity, and sensitivity besides optical properties derived from photoexcitation. In addition to these properties, we can also highlight the emergence of photonic and photoelectronic properties which is attributed to the synergism of the varied range of properties. Among the prominent complex oxides that merit mentioning include those used as photoluminescent devices, oxide electrodes, sensors, varistors, photocatalytic systems, and power converters. The efficiency of these materials is directly related to their chemical composition and processing mechanism. Depending on the desired application, such materials are processed in the form of bulk, thin films, or nanostructures with well-controlled morphologies. The control of the parameters like chemical composition, size and shape of the particles, the crystalline structure, thickness, roughness, and structural features such as textureness, epitaxy, or preferential growth (as in the case of films) likewise the thermal treatment are decisively crucial steps in the production of materials with predetermined properties. The concept of multifunctionality stated here bears its relevance when it comes to obtaining singular combinations of properties from the same semiconducting oxide which are, by and large, unattainable with traditional materials. This modulation may be widely reached by varying the processing mechanism right from the obtaining of the precursor material to the final thermal treatment and the device assembly.

SnO_2, for instance, is known to be an intrinsic multifunctional semiconducting oxide of type n; in other words, it exhibits oxygen vacancies in its crystal structure [100]. In its pure form, this oxide exhibits a non-densifying behavior during sintering process, where one can only observe the formation of necks in the particles in addition to a further growth of grain with a decrease in the surface area. Essentially, these characteristics are of great importance for obtaining high-density varistors or gas sensors and photocatalyst that require a large surface area. The final step will depend on the methodology adopted and the characteristics of the dopants added during the modulation of the desired material.

In piezoelectric materials, the application of a mechanical force changes the relative positions of the atoms in the crystal structure resulting in direct-mode charges which reflect a change in potential or electric current, thus converting mechanical energy into electrical energy (direct piezoelectric effect). The opposite

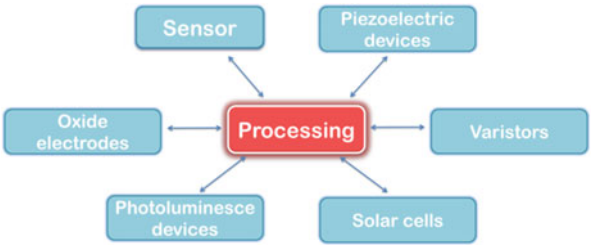

Fig. 1.1 Properties related to the material processing

effect is, in other words, the mechanical deformation of the material stemming from the difference in potential applied to the material, being the inverse piezoelectric effect. As a result of these properties, piezoelectric materials are used in dynamic applications involving mechanical impacts. They are also employed in sonars, ultrasonic transducers, and actuators, among others. Nowadays, a line of research that is being extensively studied in the area of piezoelectric materials is the use of these materials in energy storage nanodevices, well known as energy harvest devices, an alternative to conventional batteries [98].

The development of anisotropic materials has undoubtedly enabled us to improve already known properties and to obtain new devices with multiple functions. A number of researchers have been channeling their efforts in obtaining particles grown in one dimension (1D) focusing their attention on the control of the size and shape of the particles as the key to optimizing the use of existing materials in new applications.

Materials with the piezoelectric property are directly influenced by this control once piezoelectricity is a volume property with a vectorial character; thus, when such materials are grown using 1D morphology as in the case of zinc oxide (ZnO), they are found capable of storing implemented energy [77]. In the same light, niobium-based compounds also exhibit an enhanced piezoelectric property when they are grown in one dimension ($NaNbO_3$) and known to be widely applied in piezoelectric nanogenerators. Apart from the piezoelectric property, other features including sensing, luminescence, and photocatalysis can also be strongly influenced by the anisotropy. Based on these concepts, the main objective of this chapter is to deepen our understanding on the influence of the processing methods regarding the properties and the applications of multifunctional complex oxides (Fig. 1.1). We will discuss some compounds of great technological interest such as the oxides of the perovskite family, semiconductors, and conductors.

2 Processing of Perovskite-Type Multifunctional Oxides

Perovskite-type structures exhibit the general formula ABX_3 stoichiometry where site A is generally an alkaline metal or rare earth, for example, the Ca^{+2}, Sr^{+2}, and La^{+3}; site B is commonly occupied by transition metals such as Ti^{+4}, Zr^{+4},

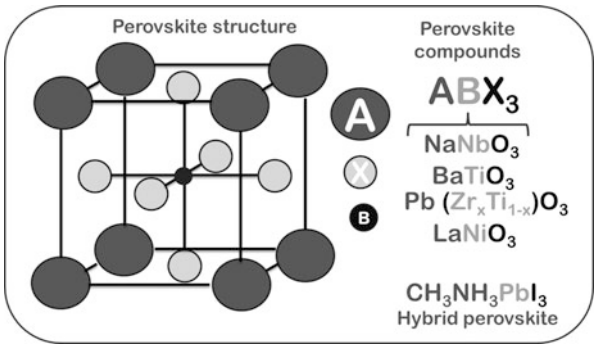

Fig. 1.2 Representation of perovskite structure (ABX_3) along with the different compounds of this class covered in this chapter

Ni^{+3}; and X are anions found at the center of the unit cell phases. When the perovskites are in the form of oxides, these anions are oxygen and through them originate a dense packing forming octahedral [BX_6] clusters bonded through the vertices while the cations A are coordinated by 12 X anions which form the cuboctahedral [AX_{12}] clusters in the typical structure. The large interest in studying the compounds pertaining to this structure class is driven by the wide range of well-defined properties they exhibit besides the flexibility by which almost all the elements of the periodic table are accounted for. Despite being a polymorphic material, the perovskites generally exhibit cubic structure and as such have dielectric behavior; nevertheless, the ideal cube is uncommon as distortions are often seen in the lattice, thereby reducing the symmetry and paving the way for the presence of properties characteristic of multifunctional materials [58]. Figure 1.2 depicts the perovskite structure along with the compounds of this structure which will be covered in this chapter.

The device operating temperature is a relevant factor indeed as it determines the phase transitions of the perovskite structure. Let us take, for instance, sodium niobate ($NaNbO_3$), a multifunctional oxide widely employed because of the following phase transitions it possesses: for temperatures below −100 °C, the oxide exhibits rhombohedral ferroelectric phase and antiferroelectric phase with an orthorhombic structure at the interval between −100 °C and 640 °C and a paraelectric cubic structure from 640 °C onward [22, 87]. Lead zirconate titanate (PZT) exhibits better values as regards to its piezoelectric properties when its stoichiometric composition promotes the coexistence between the tetragonal and rhombohedral phases known as the region of morphotropic phase transition, $Pb(Zr_{0.52}Ti_{0.48})O_3$, MPT [127].

Besides the operating temperature, another factor that determines the emergence of new physical and chemical properties in complex oxides is the presence of doping elements in the structure which can act either as formers or modifiers of the crystal lattice, i.e., introducing more or less defects in the structure that can, in principle, improve their performance in a variety of technological applications as well as aiding in the emergence of new properties. In $CaTiO_3$-based (calcium titanate) materials, the substitution of Ca^{2+} or Ti^{4+} cations leads to novel and interesting applications for this well-known material as reported in the study conducted by

Oliveira et al. [94], which showed that doping $CaTiO_3$ with Cu^{2+} cations causes distortions in the perovskite structure, and these distortions are responsible for the control of crucial physical and chemical properties for the development of $Ca_{1-x}Cu_xTiO_4$-based devices.

The perovskite family comprises the class of perovskite halides and the subclasses with organic components apart from the inorganic oxides. This occurs when you substitute oxygen atoms from the X position with elements such as chlorine, bromine, or iodine, forming the perovskite halides and maintaining a total electrical neutrality. Besides the substitution of the ions in X, the versatility of this structure allows the substitution of the other elements of its general formula like those of sites A in place of organic structures giving rise to the organic-inorganic hybrid compounds (Fig. 1.2) through which the plans of the organic and inorganic components alternate in batteries in a molecular scale. In particular, the organic groups occupying the A position are normally alkyl chain groups or mere aromatic rings. This subclass in the perovskite family exhibits attractive light absorption properties to application in photovoltaic devices. Multiple applications are therefore possible for perovskite structures. The efficient performance of these devices is, however, intrinsically associated with its obtaining process; in view of that, we will try to shed light on some relevant concepts below regarding the preparation of these materials.

2.1 Piezoelectric and Photoluminescent Materials

Within the research and development of complex materials capable of tapping and storing, energy from the environment known as nanogenerators of energy has been drawing an increasingly wider attention in recent times. The functioning of these materials, in part, is based on the concept of piezoelectricity by which the mechanical energy to be converted into electricity is obtained from the environment including energy tapped from the air in circulation, the movement of the escalator and car tires, people walking, heart beats, and blood flow. Conventional piezoelectric materials in form of bulk have a high piezoelectric coefficient, yet they lack flexibility and often need to operate in their resonance frequency which tends to diminish their efficiency when it comes to tapping mechanical energy from the small amplitude and low frequency. Thus, complex materials in form of bulk present lower piezoelectric efficiency compared to those grown in unidimensional structures – 1D [6].

Hydrothermal synthesis is the most efficient mechanism employed in obtaining materials with perovskite-type structure with a variety of well-defined morphologies. The advantage of this way of processing is that it eliminates the steps involving calcination and grinding which are generally used in other synthesis methods such as the polymeric precursor, sol-gel, coprecipitation, solid-state reaction, and combustion. In additional, when using the hydrothermal synthesis renders the processing relatively faster and less costly as lower temperature and lesser time are

used in obtaining the highly crystalline compounds. Another fact worth considering is that the particle crystallization directly in the reagent solution regulates the rate of nucleation/crystallization/growth resulting in the control of the crystal size and morphology while contributing additionally toward diminishing the level of aggregation, which are relevant factors impossible to be controlled via traditional synthesis methods [108, 109].

Through hydrothermal synthesis, Jung et al. obtained piezoelectric materials based on $NaNbO_3$ with different morphologies (nanoneedles and nanocubes). By varying the synthesis time between 1 and 4 h with a fixed temperature of 150 °C, they observed that the increase in synthesis time favored the formation of $NaNbO_3$ in cubic form whereas shorter synthesis periods formed nanoneedles of $Na_2Nb_2O_6.H_2O$ which were converted to $NaNbO_3$ after thermal treatment maintaining the nanoneedle morphology. The possibility of producing nanoneedles at relatively low temperature and the easy control of their piezoelectric domain through the electric field are factors that contribute toward the application of this compound in nanogenerators of energy [60].

Barium titanate ($BaTiO_3$) ferroelectric nanoneedles grown vertically on fluorine-doped tin oxide (FTO)-coated glass substrate were obtained for the first time by the Koka et al. where they applied the processing in two steps: first, a precursor layer of TiO_2 nanoneedles was grown through acidic hydrothermal reaction; after that the nanoneedles were subsequently placed into a solution containing Ba^{2+} cations and were then converted into $BaTiO_3$ nanoneedles through a second hydrothermal treatment performed by varying the synthesis time and temperature. After the hydrothermal treatment, the $BaTiO_3$ nanoneedles were treated at 600 °C aiming at removing alkaline residues and enabling the material to be applied in the desired devices [64].

Hence, the use of a driving agent of growth (template) in the reaction medium contributes toward the anisotropic growth of particles yielding a product with low surface energy, as well as with well-defined morphologies. Wang et al. [135] investigated the hydrothermal growth mechanism of PZT nanoneedles using polyvinyl alcohol (PVA) as a template. Following 6 h of synthesis at 200 °C, they obtained monocrystalline PZT with needlelike morphology associated with particles-agglomerates. Furthermore, it was also possible to observe that the individual 1D structure of PZT exhibited monodomains with a polarization vector along the anisotropic axis of the needlelike structures [135]. Guided by the same objective, Xu et al. [139] used polyacrylic acid (PAA) as growth template for the synthesis of PZT nanoneedles. It is believed that anisotropic surface tensions are generated during PZT growth where the asymmetric morphology is induced by the particles connected to the polymeric surface that limit the growth of some crystal planes through the reduction of the surface tension in aqueous solution leading to the growth of needlelike PZT structures [139].

A variation of the hydrothermal synthesis that has gained an importance notorious in recent years, in particular, consists mainly in the use of the microwave heating during the hydrothermal treatment. Thus, the microwave-assisted hydrothermal synthesis (MAHS) as it is widely called offers an innovative strategy for a superior

control in the new complex material synthesis. In general, the rotational energy released by the solvent molecules or by the ions during the microwave heating makes the synthesis temperature to be rapidly reached favoring the formation of the particles at a much shorter time [12]. For example, the use of microwaves as heating source in the hydrothermal process contributed meaningfully toward obtaining the $NaNb_2O_6.H_2O$ fibers within 30 min of synthesis. As similarly reported by Joung [60], after the thermal treatment, the metastable structure of $NaNb_2O_6.H_2O$ is converted to $NaNbO_3$ without the occurrence of alteration in the 1D morphology. By increasing the synthesis time to 1 h, the cubic structures of $NaNbO_3$ are obtained in different sizes [128]. When $NaNbO_3$ fibers or cubes were immersed in polymeric matrix forming flexible piezoelectric compounds, we noticed the anisotropic effect of the $NaNbO_3$ particles which was reflected by the greater value of the piezoelectric coefficient and the remaining polarization of the compounds constituted of fibers compared to those compounds containing cubes, maintaining all the other processing parameters constant [126].

Compounds related to the perovskite family, containing the clusters TiO_6 or NbO_6, including $Pb(Zr_{1-x}Ti_x)O_3$, $NaNbO_3$, $BaTiO_3$ among others can also present photoluminescent emission which occurs as a result of the electronic transition between the valence band (VB) and the conduction band (CB). Aiming at explaining photoluminescence in perovskite materials, a model known as the broadband model was proposed [21]. This model is embedded inferentially on the understanding that there are intermediate energy states between VB and CB bands associated with structural or punctual defects generated in the material during processing. Such defects may be either at shallow or deep levels, where shallow defects promote emission around the violet and blue region, while deep defects are seen to promote emission in the yellow and red region [118]. The emission around the green region may, on the other hand, be related to surface defects [75]. One of the characteristics of a multifunctional material lies in its ability to combine properties synergically, for instance, the combination of piezoelectricity with photoluminescence leading to the formation of the so-called piezophotonic devices [136].

$NaNbO_3$ in the form of powder or film exhibits photoluminescent emission around the region corresponding to the blue color of the electromagnetic spectrum (around 450 nm). However, one can observe that the emission intensity is directly related to the particle morphology, and as can be noticed when $NaNbO_3$ presents a cubic-like morphology, the photoluminescent emission is found to be more intense relative to the emission exhibited by the material in the fiber form. Taking the aforementioned considerations into account with respect to defects and emission, we propose the rapid crystallization of the particles using the microwave as that enables the structure of $NaNbO_3$ to be more organized in the fibers than in cubes [128]. The scheme related to the obtaining of $NaNbO_3$ particles and the photoluminescent emission of the material is shown in Fig. 1.3.

When we consider the processing of PZT microtubes, the photoluminescent emission in relation to the increase in synthesis time is also associated with the structural order-disorder and the surface defects that arise during the synthesis. Furthermore, we also ought to consider that the emission bands located around

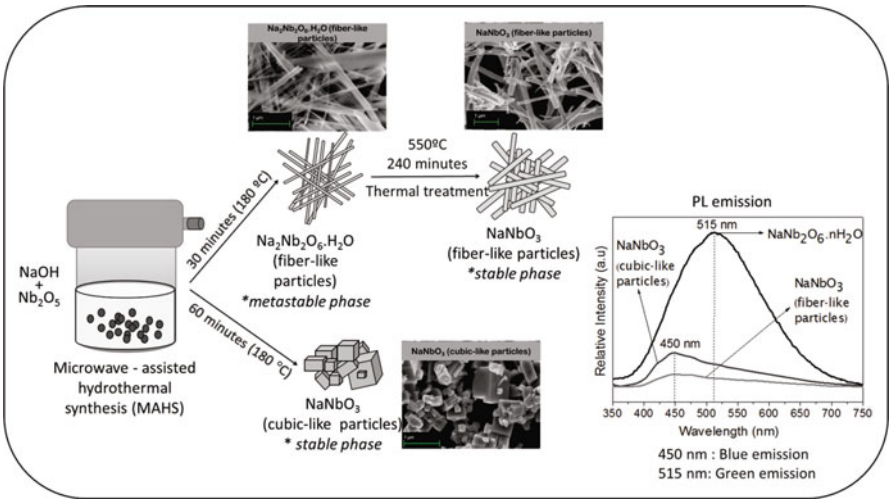

Fig. 1.3 Scheme for obtaining $NaNbO_3$ particles and photoluminescent emission of the material with different morphologies

600 nm are composed of three components, namely, blue, green, and red. The surface defects generated as a result of the particle dissolution-recrystallization process promote the increase in emission around the blue-green region, while a reduction in emission is seen around the yellow region [129]. In the case of the photoluminescent emission, the use of a growth driver not only modifies PZT morphology but also leads to the appearance of photoluminescent emission bands at different wavelengths as a function of the synthesis time. For the PZT obtained following 2, 4, and 8 h of synthesis, the bands were found to be at 550 nm. The 8 h of synthesis time was seen to present the highest photoluminescent emission with the biggest emission contribution coming from the green-yellow region. For the PZT obtained after 12 h of synthesis, the band is seen displaced to 480 nm, and the product obtained presented the lowest photoluminescent emission [127].

Similar to $NaNbO_3$ and PZT, the photoluminescent property of the $BaTiO_3$ is also attributed to the structural order-disorder involving various states in the prohibited band. Moreira et al. [91] obtained photoluminescent particles of $BaTiO_3$ through microwave-assisted hydrothermal synthesis where they found the emission bands of the products obtained located between 556 and 567 nm. In their study, the increase in synthesis time was also found to promote the reduction of the emission component around the green region, while an increase in emission was observed around the yellow region [91]. Nonetheless, when we consider the photoluminescence behavior of $BaTiO_3$ films, we notice the presence of photoluminescent emission around the UV and visible regions with the increase in emission related to the increase in the film thickness [85]. Several reports can be found in the literature with respect to piezoelectric and photoluminescent materials obtained by different synthesis

methods. The abovementioned methods are few examples that clearly demonstrate the influence of processing over the oxide properties when these oxides present perovskite structure with piezoelectric and photoluminescent features.

2.2 Hybrid Perovskite Used in Solar Devices: $CH_3NH_3PbI_3$

As previously stated, perovskite structure is endowed with huge versatility. To enable its usage in solar devices, organic cations such as methylammonium, $CH_3NH_3^+$, are incorporated in sites A, Pb^{2+} cations in sites B, and iodide anions, I^{1-}, in X leading to the formation of the structure $CH_3NH_3PbI_3$, (MAPbI), as illustrated in Fig. 1.2.

Organic-inorganic hybrid perovskites are particularly interesting owing largely to their incomparable optical and electronic properties [61]. The organic part is responsible for the high light absorption of these materials besides aiding in defining the degree of interaction between the components while the inorganic part is where the electronic properties are originated. Thus, these perovskites have become an object of intense interest with studies being undertaken to better understand their application in solar cells, devices that absorb sunlight and are capable of transforming it into electrical energy [96]. Notwithstanding their wide range of benefits, perovskites can be easily prepared through chemical processes, enabling them to be used in large scale as a result of the low cost and low temperature required.

$CH_3NH_3PbI_3$ is a perovskite which, unlike most inorganic oxides, is processed at low temperature. These materials can be synthesized by a variety of the physical or chemical methods. Physical methods such as the mechanical mixture of the precursors PbI_2 and CH_3NH_3I give rise to crystalline powders with tetragonal structure [7]. This is attributed to the fact that the process is conducted at room temperature. When processed using temperature, the material exhibits a cube-like structure. The temperatures related to phase transition occur as demonstrated in the following scheme:

$$\gamma - CH_3NH_3PbI_3 \overset{162.2\ K}{\rightarrow} \beta - CH_3NH_3PbI_3 \overset{327.4\ K}{\rightarrow} \alpha - CH_3NH_3PbI_3 \quad (1.1)$$

Besides obtaining $CH_3NH_3PbI_3$ powders through the mechanical mixture of the precursors, these materials can be processed in the form of films. There are two methods most used for the formation of these films: solvent engineering and sequential deposition [18].

The solvent engineering method entails basically four steps: The first step involves the preparation of the $CH_3NH_3PbI_3$ solution in an organic solvent, generally using dimethylformamide (DMF), dimethyl sulfoxide (DMSO), or butyrolactone (GBL), which is added onto the glass substrate with FTO electrode. The second step involves the acceleration of the substrate via spin coating up to the rotation velocity desired for the formation of $CH_3NH_3PbI_3$ film. At the third step, an

anti-solvent (does not dissolve the perovskite but it is miscible with DMSO, DMF, or GBL) is dripped over the film, while the substrate is kept rotating. The fourth step involves the formation of the intermediate phase complex followed by the thermal treatment at 100 °C/10 min for the formation of the perovskite crystalline phase [57]. Jeon et al. carried out a systemic study on perovskite formation using the solvent engineering method where they concluded that delaying or anticipating the addition of the anti-solvent by seconds interferes in the film formation, thus rendering this technique less reproductive [57].

In order to remove the solvent and eliminate the pores present in the film at the end of the last step, the best thermal treatment time is approximately 1 h; for lesser periods like 30 min, the film presents small pores which tend to undermine its properties. Treatment time periods superior to 1 h also tend to promote the evaporation of methylammonium iodide cations leading to the decomposition of the perovskite and giving rise to lead iodide (PbI_2) as a secondary phase. Upon treatment, the resulting films from this intermediate layer begin to appear dark and brilliant indicating the formation of the crystalline phase of $CH_3NH_3PbI_3$. Without subjecting the film to the treatment with the anti-solvent chlorobenzene, the film is found not to be totally converted, thus compromising the recoating of the substrate.

The concentration of the starting solution is among the relevant parameters that exert influence over the thickness of $CH_3NH_3PbI_3$ films. Normally, concentration solutions of 45% mass/volume are used [37, 84] as high concentrated solutions often generate films with particles due to the difficultly to dissolve high amounts of PbI_2. By contrast, more diluted solutions give rise to thinner films lacking good final properties. When a precursor solution of $CH_3NH_3PbI_3$ with 45% (mass/volume) is employed, films with the thickness of ∼300 nm are produced, which are ideal for use in solar cell devices. Nonetheless, when the solution concentration is increased, the film thickness increased. For instance, when the solution concentration reaches 55%, films with the thickness of around 470 nm are obtained.

For the development of efficient solar cells, in particular, the active layer responsible for light absorption ought to be sufficiently thick to ensure the absorption of the highest possible quantity of incident light. However, the elevated absorption coefficient of $CH_3NH_3PbI_3$ allows the use of thinner films with thickness ranging from 350–500 nm which often lead to a good absorption. Yet when thicker films of say 500 nm are employed, a much greater amount of light is absorbed resulting in a better performance of the solar cells. This explains the reason why the processing of a material is largely dependent on the desired properties.

The second methodology that will be discussed here is the sequential deposition methodology. Sequential deposition is the most widely employed for the processing of $CH_3NH_3PbI_3$; the processing involves the deposition of the PbI_2 solution on the substrate by spin coating, followed by the film exposure to CH_3NH_3I solution aiming at converting all the lead iodide in the $CH_3NH_3PbI_3$ phase [18, 38]. In this method, the reaction of the perovskite formation occurs rapidly from the surface of the PbI_2 film to the inner regions resulting in an incomplete coating of the substrate, lack of roughness control, and incomplete conversion of PbI_2 into $CH_3NH_3PbI_3$. However, the grains formed here are bigger, thereby favoring the charge transfer

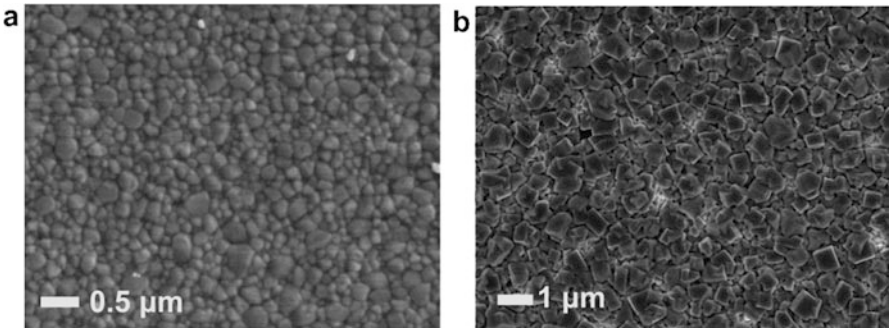

Fig. 1.4 Scanning electron microscopy images of $CH_3NH_3PbI_3$ deposited by (**a**) solvent engineering and (**b**) sequential deposition

processes within the $CH_3NH_3PbI_3$ film. In addition to that, the sequential deposition method is easy to execute besides having a high rate of reproducibility (Fig. 1.4).

$CH_3NH_3PbI_3$ has a wide range of well-defined optical and electronic properties which render it an excellent candidate as a light absorber in solar cells. The optical properties are mainly derived from its large absorption interval ranging from 350 to 800 nm, having an optical bandgap (E_g) determined by diffuse reflectance spectroscopy measurements of $E_g = 1{,}5$ eV, while the VB energy determined by ultraviolet photoelectron spectroscopy measurements is $E_{VB} = -5.43$ eV at vacuum [62, 115]. Hence, the conduction band position can be estimated to be $E_{CB} = -3.93$ eV. It is noteworthy that the bandgap of these materials can be easily modified through changes in the conditions of processing, which implies a direct alteration in the device properties such as the values of open-circuit voltage. For example, the sequential deposition method leads to the development of materials that form solar cells with a lower open-circuit voltage compared to those formed by perovskite processed via the solvent engineering mechanism. Clearly, the performance of the solar devices is inherently related to the processing mechanism of the materials that constitute the cells, while the small changes in the synthesis parameters are found to directly affect the rate of solar energy conversion.

2.3 Oxide Electrodes

Perovskite oxide thin films are being employed as bottom electrodes acting as a support medium for the growth of the multifunctional oxides and are mainly applied in nonvolatile ferroelectric memory devices, the reason being that oxide electrodes minimize the degradation of ferroelectric properties and preventing fatigue. Oxide electrode films are mainly characterized by a metallic behavior, and their use is attributed to the electric conductivity as well as the structural characteristics compatible with most of the ferroelectric oxides. In this sense, it is worth pointing out that the efficiency of an electrode is related to conductivity and mainly to its

Table 1.1 Structural parameters of some oxide electrodes

Materials	Crystalline structure	Lattice constant (nm)	Reference
LSCO	Pseudocubic	0.383	[26]
YBCO	Orthorhombic	0.382	[92]
SRO	Pseudocubic	0.393	[142]
LNO	Cubic	0.385	[116] [105]
LNO	Rhombohedral	0.545	[42]

surface characteristics which are, in effect, the basis for the growth of the functional film. This is because the surface along with the structural parameters of the oxide electrode is responsible for the control of textureness, domain orientation, interface stress reduction, and the growth of the grains with regular size and shapes [3, 151]. Among the most widely used oxide electrodes, we can highlight the following: $La_{0,5}Sr_{0,5}CoO_3$ (LSCO) [107], $YBa_2Cu_3O_{7-x}$ (YBCO) [106], $SrRuO_3$ (SRO) [142], and e $LaNiO_3$ (LNO). The similarity between the crystalline structure of the bottom electrode and the ferroelectric film which is to be deposited is a crucial factor for the good performance of the set to be assembled (*functional* device or a mere device): substrate/oxide electrode film/functional film.

Table 1.1 shows the structural parameters of the most employed oxide electrodes. Among these electrodes, LNO and SRO draw a wider attention owing to the fact that they exhibit simple stoichiometry, and lattice parameters similar to those of the most common ferroelectric electrodes though ruthenium precursors are much more costly compared to nickel making the use of LNO electrodes economically more feasible. With regard to the metallic behavior of lanthanum nickelate, there are two aspects that may well explain this feature: The first aspect refers to the strong covalent interaction between the 3*d*-2*p* orbital states of the Ni-O bond – where the Ni^{3+} cation has a low-spin configuration of the orbitals *d* ($3d^7$: $t_{2g}{}^6 e_g{}^1$). [104]. As a result, the CB (σ^*) formation can be observed through the orbital-free electron e_g. The second aspect is related to the crystalline structure of the nickelate family where all the compounds are seen to present an orthorhombic phase with the exception of LNO which does not exhibit an orthorhombic phase in the ABX_3 stoichiometric form, rather depicting a rhombohedral/trigonal structure [45]. LNO obtained in thin film exhibits a pseudocubic perovskite structure distorted to rhombohedral within which the metallic phase is obtained for the totally stoichiometric material (ABX_3). When oxygen deficiencies are present in $LaNiO_{3-\gamma}$ ($\gamma \geq 0.25$), interferences occur between the oxygen p bands and the nickel d bands leading to an isolating behavior [102]. The hybridization of *d* orbital states of Ni, the crystalline structure, and stoichiometry contribute toward explaining the metallic behavior of the material, and they demonstrated that the electrical behavior is regulated by electronic conductivity.

LNO thin films which are employed as electrodes can be obtained either via physical deposition or by chemical solution deposition (CSD). In the former method, the deposition is done through an equipment (such as RF magnetron sputtering, pulsed laser deposition (PLD), among others) using the LNO as the

target, which is properly evaporated and where crystallization takes place in situ. Via CSD method, the film is easily obtained with a good-quality crystalline and at low cost by a chemical route highly controlled. The solution containing the precursors is prepared by a method that allows the formation of homogeneous and dense films when deposited over the substrate following by the crystallization process. With that in mind, the methods that fit this purpose are the sol-gel and the polymeric precursor methods (PPM). The solution containing the metal precursors needs to be stable and to have suitably ionic concentration and viscosity so as to generate a dense textured film devoid of roughness and cracks. With the suitable solution, the film electrode deposition is performed. At this step, a wide range of parameters can be controlled including the film thickness through the spinning velocity and a number of deposited layers. At the crystallization step, time, temperature, and the atmosphere of the thermal treatment should all be essentially controlled. With regard to the first step of processing, Yang et al. [144] assessed the influence of the variation of LNO electrode solution concentration from 0.1 to 0.3 mol in the properties of PZT ferroelectric films. They observed that the lower the concentration employed toward the preparation of the inferior electrode, in particular, the better were the ferroelectric behaviors of the PZT films as prepared, based on the remaining polarization as well as the dielectric constant of the device. This is as a result of the fact that the ionic concentration controls the structural evolution of the film electrode. In other words, the lower concentration leads to a better structural crystallization, greater densification, and smoother surface. These conditions contributed largely toward the site nucleation for the PZT film growth oriented on the plane (100); the growth oriented toward this direction enables us to obtain better ferroelectric properties of the device.

Wang et al. [134] studied the behavior of LNO film electrodes obtained by the sol-gel and deposited over the substrates of SiO_2, crystallizing them at 650 °C and varying the pyrolysis temperature between 300 and 420 °C. They correlated the results to the preferential orientation factor (100) and arrived at the conclusion that the pyrolysis at 360 °C promoted an oriented growth of the film electrode. Nonetheless, the thermochemical decomposition of the oxide electrode is a parameter that depends on the precursors used in the solution as demonstrated by Wang et al. [134] who reported having complexed metal acetate with acetic acid and deionized water. Analytically speaking, if the precursor solution of the film contains sulfate, carbonates, hydroxides, and nitrates, considering that each of these elements has a decomposition temperature, the pyrolysis temperature tends to change, and in this case, thermogravimetric analysis becomes essential once it provides us with the useful information to define the process temperature. Figure 1.5 illustrates the difference in thermal decomposition between two LNO solutions, one of them obtained by the sol-gel method (Fig. 1.5a) which is quite similar to the process used by Wang et al. [134], while Fig. 1.5b illustrates the thermal decomposition of the solution obtained via the PPM.

LNO sol-gel solution contains nickel acetate, lanthanum nitrate, and 2-metoxyethanol; we can observe that in temperatures above 200 °C, there is an exothermic peak related to the decomposition of nitrate and ammonium, while

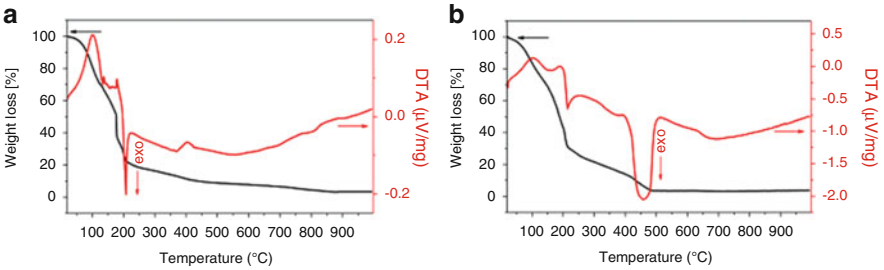

Fig. 1.5 Thermogravimetric analysis in synthetic air atmosphere for LNO precursor solutions prepared. (**a**) Sol-gel and (**b**) PPM

the mass loss of the metal complex occurs at 370 °C, quite close to the condition observed by Wang et al. [134]. Figure 1.5b shows the bands to decomposition of polyester at 210 °C, as well as the carboxyl decomposition and crystallization of LNO at 450 °C. Thus, we may conclude that the best pyrolysis condition and the structural aspects of the film electrode all depend on the solution composition. After the pyrolysis, the temperature is raised aiming at crystallizing the oxide electrode.

This step exerts a direct influence on the network parameters, the volume of the unit cell, and the surface roughness. Hsiao and Qi [54] reported obtaining LNO film electrodes by the sol-gel method with approximately 60 nm of thickness, where they observed that lower resistivity was related to lower values of cell volume and of the network constant. The control of these structural parameters was effected through the alterations of the crystallization process of the electrode (Fig. 1.6a), relating the temperature and atmosphere of sintering to the structural parameters [54]. The sintering atmosphere, besides inducing significant changes in the unit cell, is also responsible for controls on the morphology, roughness surface, and porosity. As observed in Fig. 1.6b, the material sintered in the presence of air, where it exhibited roughness of 12.3 nm, average grain size of 52.8 nm, and resistivity of 1.2×10^{-2} Ω.cm [3]. Figure 1.6c illustrates the film sintered in the presence of O_2, leading to average grain size of 50.4 nm, roughness of approximately half (6.1 nm), and resistivity of one order of magnitude inferior to the film obtained in the air. In this sense, it is worth pointing out that the presence of oxygen leads to structural alterations at short range in the crystalline network with lower volume of unit cell [54], besides engendering morphological alterations with a surface seen to be atomically smoother compared to the film sintered in the presence of air, resulting in alterations in the electronic behavior of the electrode.

Other parameters shown in Table 1.2 are equally relevant to the processing of the film electrodes; among such parameters include the variation of thickness and the choice of substrate. Generally, the difference in terms of resistivity shown in the table is intimately associated with the mismatching of the film network in relation to the substrate. In the case of A as described in Table 1.2, lower thickness results higher electrode resistivity; this occurs because the films are deposited on Si substrates (100) which have a network parameter ($a = 5.40$) different from that

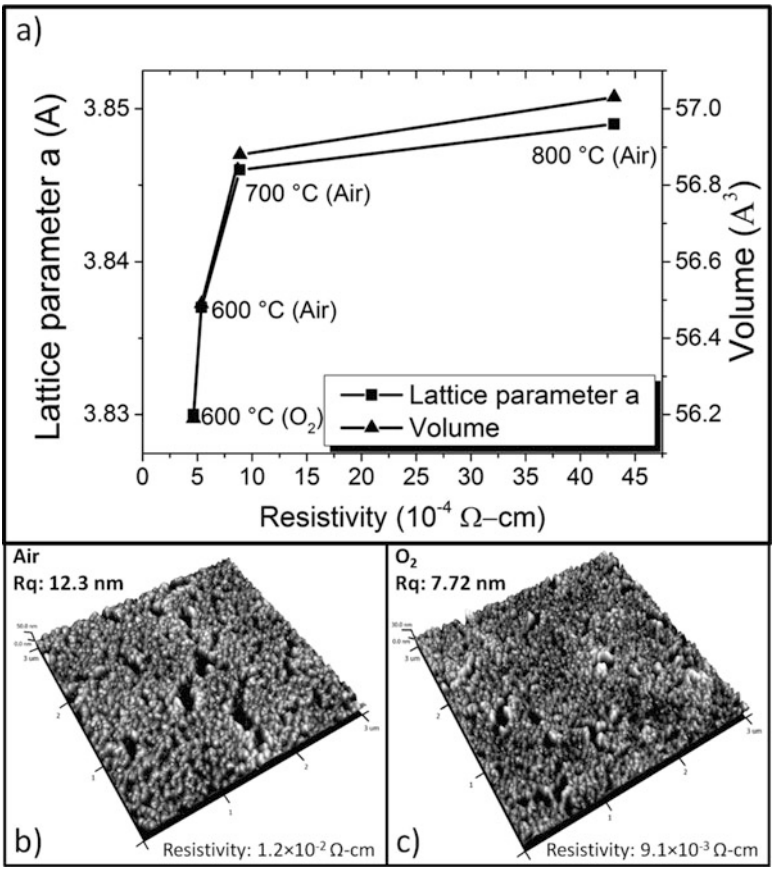

Fig. 1.6 (**a**) Resistivity, measured at room temperature, of LNO/Si films as a function of the network parameters and sintering conditions [54], (**b**) [2] and (**c**) LNO/Si films, sintered at 700 °C in the air and using O_2, respectively

of LNO, rising the tension at the interface [134]. This tension deepens when the film thickness decreases resulting in lower crystalline orientation and reducing the electrode conductivity. Similarly, the variations in the substrate network parameter among quartz, Si, and monocrystalline $SrTiO_3$ are shown in topic B (Table 1.2); the films with the same thickness exhibit different resistivities due to the substrate network parameters that interfere with the growth of the films. The film grown on the substrate with structural parameters much closer to the LNO phase exhibits a more ordered arrangement contributing in a better way toward the conductivity as noted in the case of the $SrTiO_3$ monocrystalline substrate [71]. At topic C with similar thickness and varying the monocrystalline substrate plane notices that the substrate orientation causes structural distortions in the electrode film growth. The film grown on the $SrLaAlO_4$ substrate (001) exhibits metallic behavior, while the one that grown

Table 1.2 Variation of thickness and substrates in the processing of LNO

	Electrode/substrate	Temperature (°C)	Thickness (nm)	Resistivity (Ω-cm)	Reference
A	LNO/Si	650	20	$\sim 1.0 \cdot 10^{-2}$	[134]
	LNO/Si	650	120	$\sim 1.0 \cdot 10^{-3}$	[134]
	LNO/Si	650	200	$\sim 8.0 \cdot 10^{-4}$	[134]
B	LNO/Quartz	700	250	$\sim 1.3 \cdot 10^{-3}$	[71]
	LNO/Si	700	250	$\sim 7.0 \cdot 10^{-4}$	[71]
	LNO/$SrTiO_3$	700	250	$\sim 3.0 \cdot 10^{-4}$	[71]
C	LNO/$SrLaAlO_4$ (001)	700	100	Metallic behavior	[102]
	LNO/$SrLaAlO_4$ (100)	700	100	Isolating behavior	[102]

on the plane substrate (100) shows an isolating character. This fact is attributed to the change in the degree of orientation of the film growth (100), resulting in a weak texturing, thereby leading to high degrees of disorder and consequently to the isolating behavior of the material [102].

3 Processing of Semiconducting-Type Multifunctional Oxides

There has been a growing interest, in recent times, in inorganic compound materials having semiconducting electrical properties; some of these materials that deserve mentioning include SnO_2, TiO_2, ZnO, and Fe_2O_3 oxides employed in applications such as gas sensors, varistors, and electrodes [29, 32, 63, 72, 138]. The n-type semiconductors in particular which mainly include SnO_2 and ZnO are known to be applied in a wide range of devices, as demonstrated throughout this topic. Each application essentially requires specific structural features with well-defined properties (electrical, optical, or magnetic), as well as a high efficiency and reproducibility, features that vary according to the type of processing mechanism employed in the production. Some semiconducting oxides are considered multifunctional, take SnO_2, for example, which can be applied as varistor [1, 80], gas sensors [121], solar cells [10], and supercapacitors [132].

Tin dioxide (SnO_2) exhibits chemical, thermal, and mechanical stability with a tetragonal structure of the rutile type. When pure, the oxide is considered an intrinsic semiconductor of type n, having a wide bandgap of 3.6 eV and electrical conductivity as a result of the excess of electrons and structural defects. Lattice modifying or forming metals introduced as dopants act as modifying elements of the crystalline and electronic lattice allowing the bandgap alteration while aiding in controlling, improving, and creating new properties that can be applied in diverse technological areas, such as the protection against corrosion [49], sensors [28], biosensors [67], varistors [79], solar cells [10], photocatalysts [150], etc. During the sintering process, it is worth noting that conductivity can be promoted in SnO_2

by increasing the defects including oxygen vacancies, electrons, or holes mobility caused by the presence of dopants aiming at accepting or donating electrons to the ceramic matrix [70]. The introduction of interstitial ion-generating dopants leads to the formation of defects, such as the Frenkel and Schottky types, which generate vacancy formation in the grain boundary region of the sintered and dense SnO_2, while the barrier characteristics define the varistor property of SnO_2 [5, 17, 70]. The potential barrier is formed by the intrinsic defects such as the tin vacancy and the oxygen vacancy (V_{Sn}'', V_O'') as well as by extrinsic defects created by the dopants. The positive defects are loaded with a charge density in both sides of the grain boundary and form a depletion layer of length ω. The negative interface is formed during the thermal treatment process, and it is composed of the negative defects with charge density of the surface states at the grain boundary interfaces [5, 43]. The possibility of modulation of this potential barrier [80], mainly during the process, allows SnO_2 to be used in a wide range of applications. Considering that the device resistivity is directly related to the height of the potential barrier and, hence, can be controlled by modulating the barrier through the use of dopants, the device resistivity is also modulated.

With regard to ZnO, an equally relevant multifunctional material with applications in varistors, sensors, transparent electrodes, catalysts, piezoelectric materials, and solar cells [68, 90], its bandgap energy is 3.37 eV, with excitation binding energy of 60 meV at room temperature [95]. ZnO crystalline structure comes in three forms: cubic, hexagonal, and wurtzite. The latter shape is considered more stable at room temperature as a result of its possession of the ions Zn^{2+} and O^{2-} tetrahedral coordination with the crystalline lattice parameters $a = 0.325$ nm and $c = 0.521$ nm [30, 39]. The multifunctionality of the oxide is associated with the different structures, and the presence of polar surfaces such as (0001) Zn_{2p} and (0001) O_2 through which the interaction of the charges with polar surfaces leads to the growth of several types of nanostructures, including nanobelts, nanosprings, nanorings, nanohelices, etc. [83]. A further characteristic of ZnO structure is the absence of symmetry center, which as a consequence leads to piezoelectric effects. Here, it should be noted that polarity is a surface effect, while piezoelectricity is a volume effect [140].

The excellent physical and chemical properties and the versatility by which ZnO can be synthesized through several methods with different morphologies and high stability render it attractive for a wide range of applications such as heterostructure-based sensors [68, 69, 90] and varistors – which is undoubtedly the most widely known owing to the excellent performance. However, for sensing application requiring an elevated surface area, which in other words can be understood as a porous morphology with small particle size, there is the need to control the processing parameters such as grain growth and the densification of the system. Some aspects of the processing of tin and zinc oxides with the use of different synthesis methodologies as well as the addition of different modifiers will be covered here stating and highlighting the properties involved.

3.1 Processing of Tin Oxide

Tin oxide processing can be carried out via several routes including oxide mixture, hydrothermal synthesis, carbothermic reduction, PPM, sol-gel, and so forth. As is well-known, the method of processing has a strong impact on its properties and, hence, ought to be chosen taking into account the application desired [10]. On the other hand, the oxide doping is additionally a relevant factor when it comes to the alteration of electrical properties and in other applications such as varistors. Aguilar-Martínez et al. [1] prepared SnO_2 doped with fix concentrations of Cr^{3+} and Sb^{5+} ions while varying the concentration of Co^{4+} ions using the oxide mixture method in a planetary mill, followed by the grinding of the powder and thermal treatment. They noted that the concentration of Co^{4+} ions exerts an influential role over the grain size and the ceramic density altering the electrical properties of the material. A similar report published by Lustosa et al. [80] was aimed at studying the varistor properties using an alternative mechanism of processing SnO_2, where nanoparticles doped with Zn^{2+} and Nb^{5+} were deposited on Si/Pt substrate by the electrophoresis method – EPD and the film subjected to sintering using the microwave oven. Following the sintering, the deposition of Cr^{3+} ions was carried out via electrophoresis aiming at modifying the grain boundary barrier while promoting the nonohmic behavior of the electrical property tension x current. The diffusion of the chromium ions across the grain boundary was promoted by the thermal treatment in a microwave oven at a temperature 50C less than the one applied in sintering.

By analyzing the characteristics and the behavior of the SnO_2-ZnO-Nb_2O_5-Cr_2O_3 system, we can say that this processing mechanism generates a ceramic with a homogeneous composition, spherical particles with uniform size, and distribution which can be applied to a varistor with low voltage. The addition of bivalent metals like cobalt [89], zinc [51], and copper [40] has the goal of improving densification once these cations act as electron acceptors and substitute the tin ions in the crystalline lattice creating oxygen vacancy defects, which favor mass diffusion in the lattice, while promoting densification as in line with Eq. 1.2:

$$MO \overset{SnO_2}{\rightarrow} M'_{Sn} + V_O^{\bullet\bullet} + O_O^X \tag{1.2}$$

The defects of the type M'_{Sn} found around the grain boundary region capture electrons released by other modifying agents and create a potential barrier around this region.

Electrical conductivity of the varistor system can be enhanced through the addition of pentavalent ions such as Sb_2O_5 [86], Nb_2O_5 [16], and V_2O_5 [41] which act as donors of electrons when added to the SnO_2 crystalline lattice leading to the concentration of electrons and tin vacancies as evident in Eq. 1.3.

$$2M_2O_5 \overset{SnO_2}{\rightarrow} M'_{Sn} + 2V''''_{Sn} + 10O_O^X \tag{1.3}$$

Aiming at improving the varistor properties of the system, trivalent cations such as chromium [5], ytterbium [103], and samarium [9] which play the role of electron acceptors when added to the SnO_2 lattice given the fact that when they are segregated at the grain boundary region, they increase the values of the potential barrier as well as the resistivity since they imprison the electron acceptor species at the grain boundary region, as depicted in Eq. 1.4.

$$M_2O_3 \overset{SnO_2}{\rightarrow} 2M'_{Sn} + 2V'_O \ + 2O_O + \frac{1}{2}O_2 \tag{1.4}$$

These days, the processing technology of ceramic materials is aimed at developing feasible low cost methods of processing at industrial scale. For the production of bulk, films, or nanostructures of high performance and reproducibility, we can mention the techniques of chemical synthesis such as coprecipitation, sol-gel, combustion, lyophilization, and the PPM [73, 119, 124], which involves the complexation of metallic ions by carboxylic acid followed by the polyesterification using a polyalcohol. The immobilization of the metal on organic matrix reduces the segregation of the metals during the polymeric combustion and crystallization of the compounds ensuring their compositional homogeneity. The versatility of the method allows one to obtain powders and films with a relatively good control of the chemical composition and the oxide crystallization at temperatures ranging from 400 to 700 °C and has a great potential in the preparation of thin films via deposition techniques including spinning or dip coating. The PPM allows one to prepare nanoparticles of oxide systems and can be used to make deposition of thick films via physical methods as, for example, the technique of electrophoresis (EPD) considered quite efficient as a result of its ease to scale up and to controlling the thickness, compactness, and the geometric shape of the film [14].

The films deposited by EPD were obtained through the suspension of nanometric particles prepared by PPM, which were showed in Fig. 1.7. Silicon-platinum (Si/Pt) substrate used for the deposition of the particles was adjusted on the negative electrode and immersed in an aliquot of 20 mL of an ethyl suspension containing 14 mg of particles, where a tension of 2 kV was applied for 10 min, with an indication of a current of approximately 2.0 mA. After the film deposition it was then subjected to sintering in a microwave oven and the homogeneity of the substrate recoating, and the film thickness and morphology were evaluated by SEM and can be found illustrated in Fig. 1.8.

The deposition by electrophoresis requires the particle to have a surface charge for it to be directed by the current toward the supporting film electrode [14, 19, 137]. The nonpolar organic solvents which are more viscous favor the particle stability and minimize the heating through the current passage and the electrochemical attack on the electrodes [50, 130, 149].

Considering that the electrical property of the semiconductors, in part, is related to the defects that form the potential barrier at the grain boundary region, the sintering process of these materials stands to be primarily vital as it is at this stage that control is exercised over the homogeneity of the microstructure, the diffusion

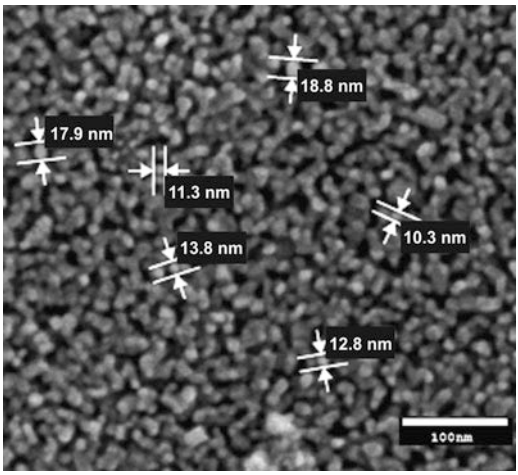

Fig. 1.7 SEM of (Zn,Nb)-SnO_2 nanoparticles selected for deposition via EPD (By authors)

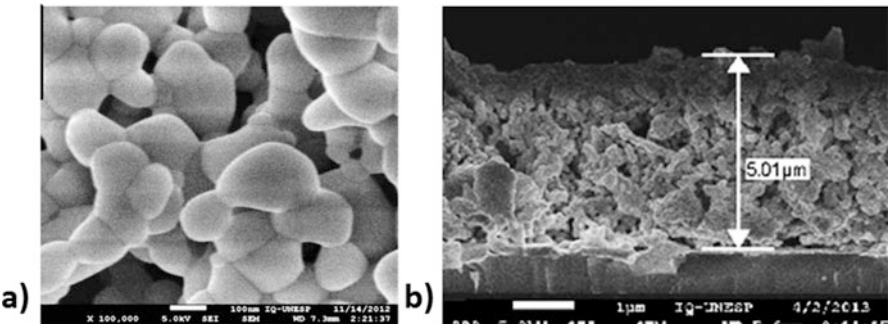

Fig. 1.8 SEM of the film deposited using 2 kV/10 min, sintered at 1000 °C/40 min in microwave oven (**a**) surface, (**b**) cross-sectional view (Reproduced from Lustosa et al. [81])

of the dopants, the densification (if desired), and the grain size. Furthermore, it is during sintering that the formation of the grain boundaries and potential barriers occurs [101, 114]. The use of microwave heating for the thermal treatment of the ceramic oxides is an alternative to conventional sintering once the heating takes place uniformly and instantaneously in the entire material mass which by so doing promotes the grain diffusion and avoids the irregular growth of the grains, thereby enabling the control of the formation of the potential barrier [88, 113].

From Fig. 1.8, it can be observed that the film formed has a homogeneous thickness of around 5 μm when sintered at 1000 °C/40 min, exhibiting porosity though with grain boundaries for the generation of the potential barrier. After sintering, the film was recoated with Cr^{3+} ions using EPD (2 kV/5 min) and thermally treated in microwave oven aiming at promoting the diffusion of the Cr^{3+} ions at the grain boundaries while generating the potential barrier. The SEM and EDS analyses show that the use of a higher temperature of thermal treatment leads to a bigger diffusion of Cr^{3+} (Fig. 1.9a, b). The influence of chromium diffusion

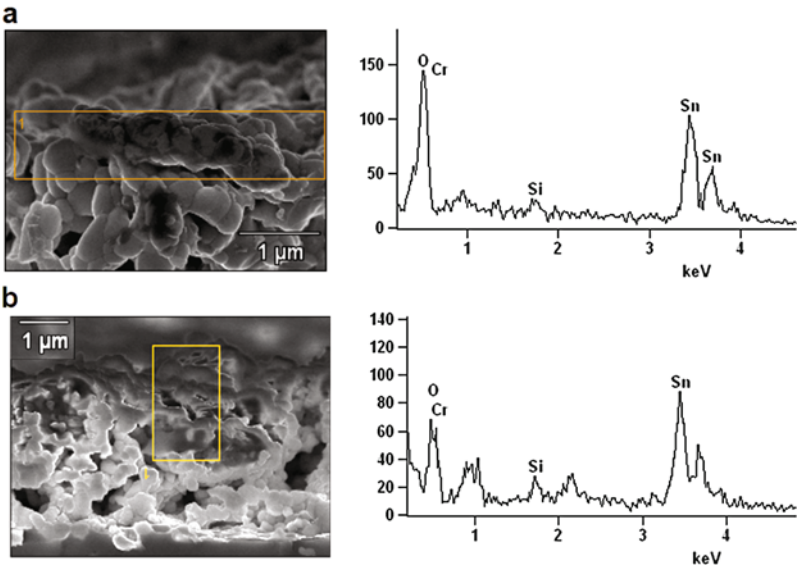

Fig. 1.9 EDS analysis of the cross-section of the films treated thermally. (**a**) 900 °C/15 min, (**b**) 1000 °C/15 min following Cr^{3+} ions deposition (Reproduced from Lustosa et al. [80])

at the grain boundaries of the films was assessed through the measurements of a nonlinear coefficient (α), rupture tension (E_R).

The films treated at 1000 °C for 10 and 15 min present α values superior to 10. A further observation worth mentioning is the low leakage current which is a desired characteristic when it comes to the preparation of varistors once this represents a huge current capturing at the grain boundary. Following the obtainment of electrical results with parameter values similar to the films in Table 1.3, we can say that the process involving the obtainment of films with varistor characteristics through the particle deposition method via electrophoresis and diffusion of Cr^{3+} cations at the grain boundary region has a reproducibility in the electrical characteristics. For the purpose of analyzing the electronic conduction at the grain boundary region, the films obtained were also subjected to the measurements of tension vs current as a function of temperature in atmospheric air. To carry out this analysis, the samples were placed in a furnace produced by Microtube, with a temperature controller of the brand Flyever, model FE50RP. The measurements were carried out at room temperature within the range of 50–300 °C, with the electrical analysis done at intervals of 50 °C, and stabilization of the temperature in 20 min (Tables 1.4 and 1.5).

The addition of Cr^{3+} ions in the films was found to increase the values of the potential barrier height. These same values are found to be higher given an increase in the thermal treatment time. The values are in line with those obtained for the decline in leakage current shown in Table 1.3; a higher value of the potential barrier height present at the grain boundary leads to a greater difficulty in the passage of the

Table 1.3 Values calculated for nonlinear coefficient (α), rupture tension (E_R), rupture voltage (V_R), and leakage current (I_F) for films sintered at 1000 °C/40 min, treated at 1000 °C for 10 or 15 min in order to promote diffusion of Cr^{3+}

Thermal treatment after Cr^{3+} deposition	α	E_R (kV/cm)	V_R (Volts)	I_F (A)
1000 °C/10 min 1000 °C/10 min	10.510.8	141 157	70.4 78.5	$6.2 \times 10^{-6}1.6 \times 10^{-6}$
1000 °C/15 min 1000 °C/15 min	13.811.5	151 120	75.5 60.4	$8.5 \times 10^{-6}2.8 \times 10^{-6}$

Table 1.4 Values corresponding to height (ϕ_b) and width (ω) of the potential barrier for films without and with Cr^{3+} deposition, both thermally treated at 900 °C after Cr^{3+} deposition [83]

Time of thermal treatment	ϕ_b (eV)	Ω (V)
Without Cr^{3+}deposition	0.34	0.36
5 min 10 min 15 min	0.51 0.56 0.64	0.37 0.14 0.09

Table 1.5 Values corresponding to height (ϕ_b) and width (ω) of the potential barrier for the films treated thermally at 1000 °C after Cr^{3+} deposition [83]

Time of thermal treatment	ϕ_b (eV)	Ω (V)
5 min 10 min 15 min	0.47 0.56 0.61	0.25 0.21 0.08

Table 1.6 Verification of reproducibility to height (ϕ_b) and width (ω) of Schottky-type potential barrier

With Cr^{3+} deposition-thermal treatment	ϕ_b (eV)	*ω (V)*
1000 °C/10 min 1000 °C/10 min	0.58 0.60	0.20 0.22
1000 °C/15 min 1000 °C/15 min	0.68 0.60	0.11 0.09

electrons. Accompanied by the increase in ϕ_b, the values of ω were seen to decline implying that the addition of Cr^{3+} causes the bottlenecking of the potential barrier given an increase in density of the imprisoned states at the grain boundary.

The films from Table 1.3 used to verify the reproducibility of the remaining electrical characteristics of the films which presented the best values of α were also characterized electrically as a function of temperature where they presented similar values as shown in Table 1.6, thus confirming the reproducibility of the property.

The electronic resistivity ($\boldsymbol{\rho}$) exhibited at the sample grain boundary was evaluated with an analysis of the low current linear region (0–1 mA/cm^2) of the graphs I and V of the samples subjected to characterization as a function of temperature (Fig. 1.10). The material resistivity was determined through the angular coefficient of the straight line obtained by linear regression at the ohmic region. Upon carrying out the analysis of the linear region for the varistor curves of the SnO_2 films at varying temperatures, the resistivity values were determined afterward.

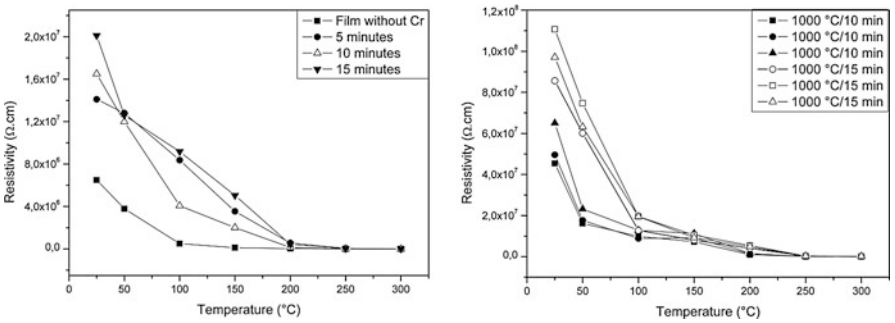

Fig. 1.10 Resistivity measurements (ρ) of SnO_2 films modified with ZnO and Nb_2O_5 as a function of the analysis temperatures. Films sintered at 1000 °C/40 min and treated thermally at (**a**) 900 °C and (**b**) 1000 °C at varying degrees following Cr^{3+} deposition (Reproduced from Lustosa et al. [80])

The curves of Fig. 1.10 show the reduction of the material resistivity with the occurrence of a significant variation between 25 and 100 °C. The films treated with greater time and temperature exhibit higher resistivity. From 150 °C onward, the materials exhibit curves with similar values of low resistivity (lower than 1×10^7 Ω.cm). Based on the data presented so far, we observe the relation between resistivity and the values presented corresponding to α in analysis at room temperature. The films obtained in the verification of reproducibility of the electrical characteristics also show similarity in the values of ρ.

As a result of the processing mechanism, the same oxide system can be applied in different areas. The system with 20 mg of powder in 20 mL of alcoholic suspension were used to obtain films by electrophoresis, aiming at the application in varistors; SnO_2 particles were deposited on Si/Pt substrate using 2 kV/40 s, while alumina substrate with interdigital silver-palladium electrodes applied at 2 kV/1 min was used for the study of the sensor activity. The sintering process of the varistor film was developed at 900 °C/30 min in a microwave oven (Fig. 1.11), since the formation of the liquid phase occurs at 1000 °C, followed by the deposition of chromium ions on the surface of the sample by EPD and treated at 900 °C/15 min aiming at the diffusion of chromium at the grain boundaries so as to increase the resistivity in this region through the induction of defects and the formation of the potential barrier. The sensor film was in turn sintered at 500 °C/10 min in a microwave oven without subjecting it to recoating with chromium ions as there was no interest in elevating the resistivity or in obtaining a dense material.

The processing can also exert control over characteristics such as grain size and the film density that influences the nonlinear coefficient (α), for example, tin oxide film doped with 1% mol of cobalt and 0.05% mol of niobium with 78 μm of thickness (Fig. 1.11) exhibited α of 7.2 and rupture voltage of 205 Volts and leakage current of 2.44×10^{-7} A, when sintered at ambient atmosphere. When sintered at O_2 atmosphere, a (Co,Nb)-SnO_2 film is obtained with low porosity and bigger grain

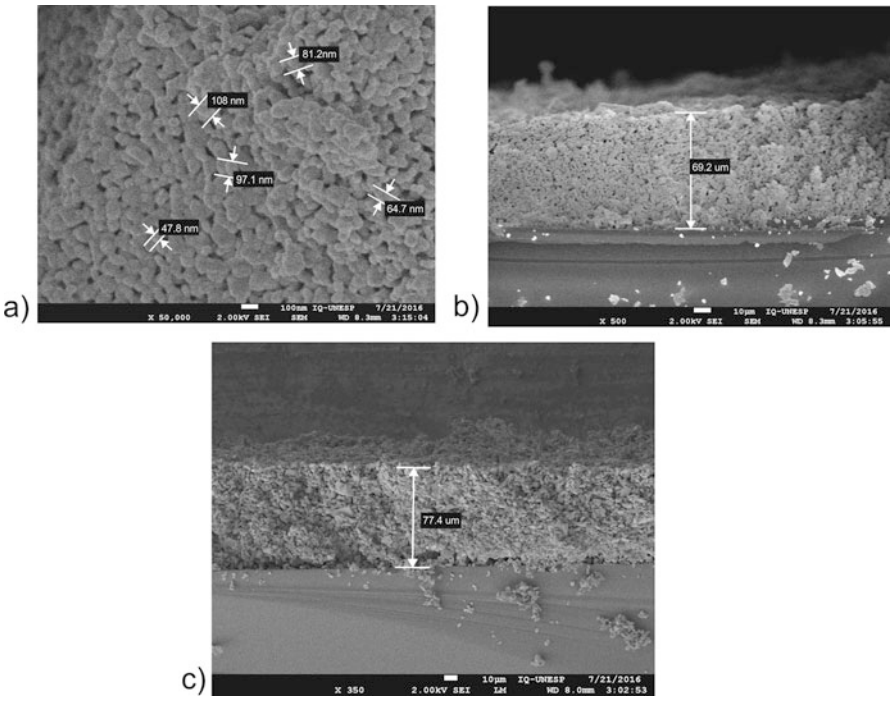

Fig. 1.11 Views of (**a**) surface, (**b**) cross-section of (Co,Nb)-SnO_2 films deposited at 2 kV for 30 s, (**c**) cross-section of the sample deposited at 2 kV for 40 s. Samples sintered in microwave oven at 900 °C/30 min with O_2 atmosphere

size presenting a nonlinear coefficient α of 15.1, a rupture voltage of 250 Volts, and leakage current of 1.14×10^{-8} A.

The film prepared for sensor analysis (self-heating system) presented a response of 1.81 when exposed to 100 ppm of carbon monoxide gas. In this film, the application of O_2 is not regarded necessary once it would diminish the pores, thereby reducing the surface area for contact/adsorption of gas on the semiconductor surface. Figure 1.12 illustrates the result of the tension vs current analysis (Fig. 1.12a) for the varistor film and (Fig. 1.12b) shows the electrical response of the sensing activity for the carbon monoxide gas (CO) at the concentrations of 10, 20, 40, and 100 ppm using the self-heating system.

SnO_2 can be used in the harvesting of energy when it is associated with reduced graphene oxide (RGO). In this case, MAHS is used for the production of the hybrid SnO_2-RGO; the outcome is a material with efficiency in the transport of electrons capable of being used in solar cells. Tin oxide nanocompounds/graphene (SnO_2/G) obtained via the moist chemical route has dielectric properties with application in capacitors [132]. The morphology and the state of oxidation of tin oxide can also be altered through processing by controlling the atmosphere and temperature as reported by Suman et al. [125]. In their work, they employed carbothermal

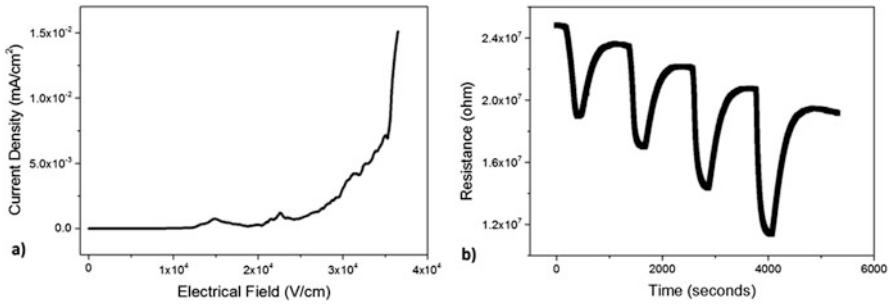

Fig. 1.12 Electrical response for (**a**) SnO_2-based varistor film and (**b**) SnO_2-based sensor films after characterization

reduction method where they obtained nanoribbons of (SnO_2), Sn^{4+}; (SnO) Sn^{2+} and Sn_3O_4, and Sn^{2+}/Sn^{3+} resulting in distinct sensing activities for each type of oxide obtained [121].

3.2 Zinc Oxide Processing

Considering that the processing of ZnO for use in varistors is well defined and has been vastly reported in the literature [82], we will try to cover the alternative possibilities of processing for sensors that require a high surface reactivity in this topic. In this sense, a large number of the chemical methods are indicated in order to obtain porous or nanostructured films.

The morphological characteristics such as porosity, particle size, roughness, and density are all crucial parameters that can easily be controlled in the chemical synthesis procedure [13]. Processes such as sol-gel, metal-organic decomposition, and PPM [76, 99] can all be employed. The PPM is efficient to obtaining films because it is possible to adjust the concentration and viscosity of the solution [27, 36] enabling one to obtain homogeneous, dense, textured films provided monocrystalline substrates are used. However, in this processing, the thermal decomposition and the crystallization of the polymeric precursor containing a huge volume of organic material require a ratio of low heating to avoid cracks and/or structural defects.

Another relevant factor has to do with the choice of substrate once the difference between the coefficient of thermal expansion of the film and the substrate can also give rise to the development of cracks and the detachment of the film [93]. Thus, obtaining homogeneous films devoid of cracks and low surface roughness is inherently related to the choice of the substrate, viscosity, and ionic concentration of the solutions, film-substrate adhesion, the speed of deposition, thermodecomposition, and thermal treatment atmosphere. All these parameters are associated with its properties and applications in diverse devices. Some careful tips on the processing

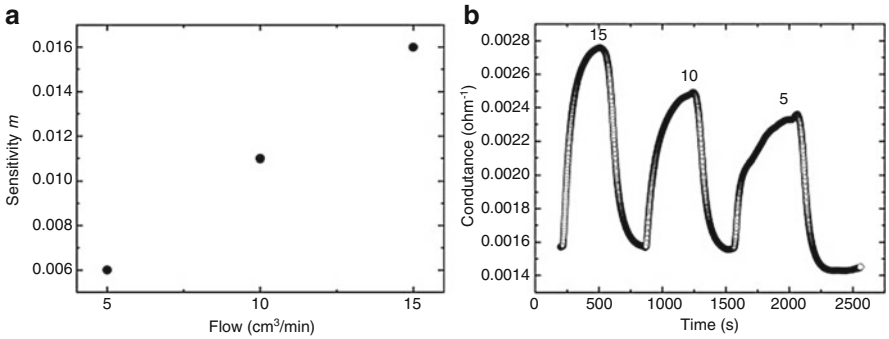

Fig. 1.13 Changes in the sensor response of ZnO thin film annealed at 600 °C for 2 h. (**a**) Sensitivity as a function of gas flow and (**b**) conductance as a function of time (Reproduced from Biasotto et al. [11])

using a PPM solution merit a thorough discussion. One needs to begin with the dissolution of dehydrated zinc acetate in water then followed by its addition to an aqueous solution of citric acid. Ethylene glycol should be added to the solution after the homogenization of these components, and all the procedure should occur under shaking at a temperature of 90 °C. Upon the adjustment of viscosity (∼20 cP), the solution is deposited on the alumina substrate with interdigital electrodes by spin coating at 5000 rpm for 30 s, after which the film is treated thermally at 600 °C for 2 h, obtaining a porous and crystalline ZnO film [11]. The material sensitivity to the gas is attributed to the change in conductivity of the semiconductor through the adsorption and desorption process of gas on its surface contributing toward the removal or transfer of electrons. The gas detection is converted into electric signals which can be measured in the form of variation of the semiconductor oxide resistance, for instance [49]. The sensing characterization was performed at 300 °C applying tension d.c. of 20 V and measuring the variations in the electrical resistance during the exposition to CO gas flow of 5, 10, and 15 cm^3/min, with a high-voltage source (Keithley, model 237) [11]. Figure 1.13 shows the sensor measuring; the ZnO sensor exhibits greater sensitivity to 15cm^3/min flow at 300 °C (see Fig. 1.13b). These results confirm the application of this method in the development of a nanostructured ZnO thin film for detection of CO above 15 cm^3/min.

Figure 1.14 shows the scanning electron microscopy image of the surface and the cross-sectional image of ZnO film obtained by the method described above. The study of the morphology revealed a random orientation of the grains with a nanometric size which is considered essential for its application as a gas sensor.

When speaking of sensor applications, we cannot forget to highlight the relevance of nanostructures among them including nanorods (1D) applied in sensors and in energy harvesting devices. The 1D nanostructures have been synthesized using a vast range of techniques, such as chemical methods [97], physical vapor deposition [52, 122, 146], metal-organic chemical vapor deposition (MOCVD) [53, 138, 141], molecular beam epitaxy (MBE) [46] pulsed-laser deposition [112], and sputtering

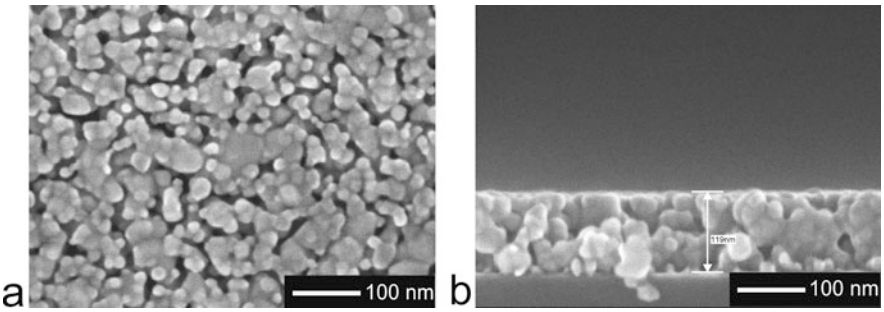

Fig. 1.14 Micrographs obtained by scanning electron microscopy of high resolution of ZnO film deposited by spin coating (**a**) surface, (**b**) cross-section (Reproduced from Biasotto et al. [10])

[125] among others. Based on the synthesis methods such as MOCVD and MBE, ZnO nanowires with high quality are generated though at an elevated costs making them less employed. The chemical methods have become widely attractive for the fact that they involve low cost. Under these methods, the growth occurs at low temperature, and they are known to be compatible with flexible organic substrates without requiring the use of metal as catalysts besides being able to be integrated with silicon technology [148]. Furthermore, there is a range of parameters that can be significantly altered so as to efficiently control their size, morphology, as well as the property of the final product [34, 147].

A number of studies have pointed out that the growth of highly oriented ZnO nanorods can be carried out on a substrate with a layer of preexisting cores in the form of nanoparticles or ZnO films [47]; the features of this layer determine the morphology of the nanostructures that will grow and which can take the shape of rods, tubes, and flowers [2]. The catalyst layer is essential of primary importance, as its thickness along with the size and morphology of the grains determines the size and the aligning of the nanorods. As such, the bigger the thickness of the nucleation layer, the smaller the size and the more aligned the nanorods are toward the axis [44]. The ratio length/diameter of the nanorods is also influenced by the growth time of the structures [123]. For sensing application, the chemical bath deposition (CBD) method can be used for the process involving the growth of the nanorods over the seed layer. This method is characterized by the formation of nanorods using a precursor solution of zinc nitrate (0.03 mol.L^{-1}) and KOH (0.03 mol.L^{-1}) at 90 °C/1 h, where the growth mechanism entails the phenomenon crystallization – dissolution – recrystallization [30]. In these conditions, perpendicular nanorods are found to grow on the substrate plane at the c axis. Another stage of the processing involves improving the sensitivity of the nanostructures through the surface chemical functionalization of the ZnO nanorods with gold nanoparticles (AuNPs) (Fig. 1.15). The sensing activity of H_2 gas was evaluated using pure and functionalized nanorods, as shown in Fig. 1.16, measured at temperature 300 °C. The results indicate that the AuNPs present greater sensitivity compared to pure ZnO nanorods. This is related to the interaction between the catalytic activity of AuNPs and the oxygen species (O^-, O_2^- and O^{-2}) as a result of the spillover

effect [55, 59, 66]. Gold, on the other hand, functions as electrons well raising the concentration of spatial charge on the surface, resulting in the depletion of the electrons close to the interface [120, 143].

Another processing mechanism employed for the growth of nanorods and which deserves mentioning is the hydrothermal method. This method is known to aid in obtaining materials with high degree of purity, crystallinity, and control of morphology and particle size [112, 125] by adjusting a few parameters such as solvent, temperature, pH, and catalysts [148]. Besides that, growth-driving agents like hexamethylenetetramine (HMTA) [14, 134] which by virtue of being a nonionic cyclic tertiary amine acts as weak base fixing itself on the nonpolar side facets facilitating the anisotropic growth on the pathway [0001] [8].

In this process, for the fact that it is an amphoteric oxide with an isoelectric point at 9.5 [147], ZnO is formed from the salt hydrolysis of zinc in a basic strong or weak solution. The widely employed alkaline compounds, in this case, include KOH and NaOH, with KOH being much more utilized as a result of the greater atomic radius of K^+, which makes incorporation into the interstices of ZnO crystalline structure difficult [34, 74, 133]. The high base concentration in the medium promotes the dissolution of zinc hydroxide leading to the formation of $Zn(OH)_4{}^{-2}$ ions, followed by the occurrence of dehydration reaction of the tetrahydroxozincate $[Zn(OH)_4{}^{-2}]$ ion and to the formation of ZnO during the growth of phase [140]. The reactions are as follows:

$$Zn^{2+} + 2OH^- \leftrightarrow Zn(OH)_2 \tag{1.5}$$

$$Zn(OH)_2 + 2OH^- \leftrightarrow [Zn(OH)_4]^{2-} \tag{1.6}$$

$$[Zn(OH)_4]^{2-} \leftrightarrow ZnO_2^{2-} + 2H_2O \tag{1.7}$$

$$ZnO_2^{2-} + H_2O \leftrightarrow ZnO + 2OH^- \tag{1.8}$$

$$ZnO + OH^- \leftrightarrow ZnOOH^- \tag{1.9}$$

As a consequence, this mechanism is strongly driven by the ZnO surface. It should be noted that defects formed during the growth of these materials can vary

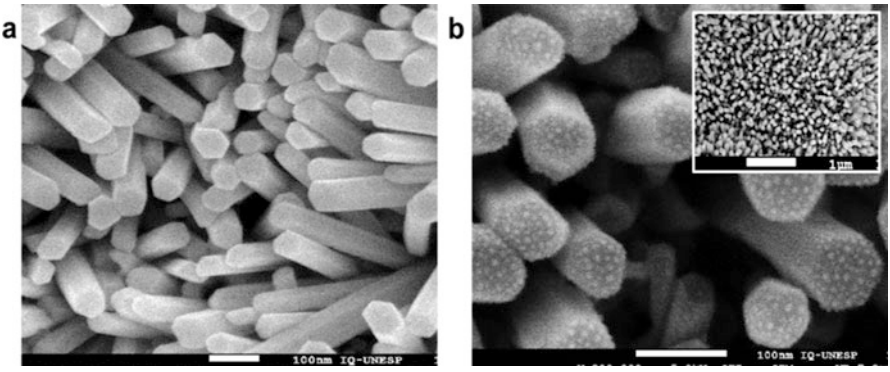

Fig. 1.15 Nanorods of pure and functionalized ZnO, obtained by chemical bath at 90 °C/ 1 h

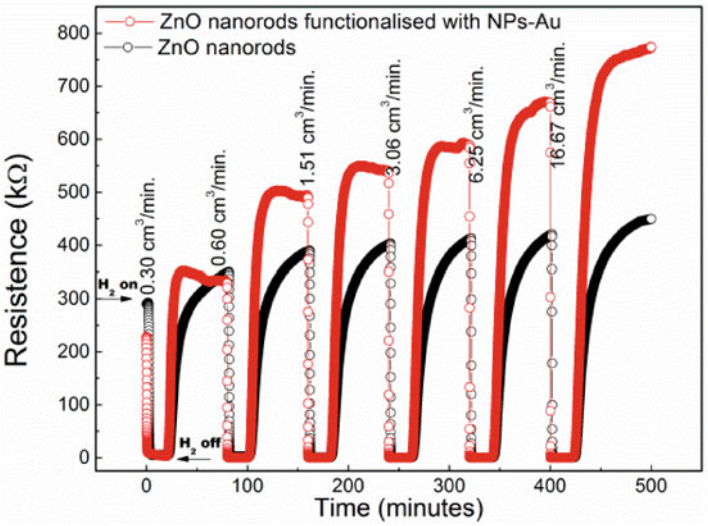

Fig. 1.16 Variation of electrical resistance as a function of time during expositions using H_2 gas flow of 0.30, 0.60, 1.51, 3.06, 6.25, and 16.67 cm^3/min

considerably depending on the processing method used. These defects, especially at the surface, have played a key role in the sensor behavior. Based on these considerations, ZnO materials have a surface with oxygen vacancies (i.e., V_O^x, $V_O^{\bullet}$, and $V_O^{\bullet\bullet}$) that functions as donor and/or acceptor of states [25]; this, in effect, allows the adsorption of oxygen on the surface or at the grain boundary extracting electron from the semiconductor and fostering the increase in resistivity [35]. In that sense, the conductivity of the semiconducting oxides depends on the oxygen partial pressure (P_{O2}); hence, type n tends to reduce the conductivity given an increase in P_{O2}, and the opposite can be observed in type-p oxides [65, 111]. Based on the fact that several technological applications, including sensors, biosensors, varistors, and so on, strongly depend on electronic and structural properties, which have their origin in the microstructure, we can say that the processing mechanism is fundamental to obtaining and development of novel multifunctional devices.

4 Complex Oxides and Interfaces

A significant advantage in the development of novel multifunctional materials was the processing heterostructured materials forming an interface area which provides the synergistic effect device. The science of heterogeneous interfaces covers some primordial theoretical aspects about the structure, force of cohesion, mechanics, and thermodynamics of the solid interface which are seen to play a direct influential role over the following phenomena: excitation, emission, and electronic mobility. Among these aspects, we need to highlight the strong dependence observed between

the lattice parameters and the crystalline symmetry of both solids [47]. The control of the material interface synthesis with neighboring lattice parameters is characterized by the stacking of layers known as the epitaxial growth oriented toward the matrix structure. The electronic transport properties are favorable in continuous interfaces, which is formed by similar symmetry and lattice parameters [78]. When incompatible crystalline structures form the interface, it is possible to observe the occurrence of a translational symmetry breaking and rotation of charges that cause polarization and accumulation of electrons near the interface provoking changes in the electronic configuration that determine the physicochemical properties of the complex materials. The formation of a crystal follows the stacking of successive monolayers under a preferential orientation, when this growth is influenced by factors such as lattice incompatibility, symmetry, roughness, kinetic parameters of nucleation, and growth including reagent concentration, temperature, rate of heating, and surface energy, these factors may cause a disordered stacking of layers without preferential orientation and consequently without a long-range order. In these cases, the heterostructures exhibit a peculiar microstructure around the crystalline-amorphous interface region with great quantity of structural defects like oxygen vacancies which increase conductivity at the interface region [24]. One of the much complex structures that is being widely studied among the complex oxides is silver tungstate Ag_2WO_4. The structure of this oxide is characterized by symmetrical dependence and spontaneous polarization property [4] besides presenting polymorphism in three crystalline structures including α-orthorhombic, β-hexagonal, and γ-cubic, where the α phase is considered the most stable at room temperature. The kinetics of nucleation and growth in homogeneous solutions can be adjusted through the cation and anion concentrations of the starting salts, while the particle size is influenced by the concentration of reagents, pH, temperature, and method of synthesis [20]. Notwithstanding the fact that all the phases of this complex oxide are highly known, the α-orthorhombic phase is by far the most studied and synthesized through the microwave hydrothermal method. Here, the synthesis temperatures can be varied; in addition to that, driving and restricting agents of growth can also be employed [31, 110]. This can give rise to a complex structure formed by octahedral clusters of WO_6 and AgO_y ($y = 2, 4, 6$ and 7) which exhibit spectral patterns of vibration along with structural and electronic order-disorder effects, which are key elements for understanding its applications. These crystals exhibit a broadband photoluminescent emission with low emission intensity located around the blue-green region, which is characteristic of the complex mechanism of electronic transfer among the ordered-disordered octahedral, tetrahedral, and deltahedral clusters in the crystalline structure [20].

When the microcrystals of α-Ag_2WO_4 are irradiated with electron beam under ultrahigh vacuum by scanning electron microscope over the surface of α-Ag_2WO_4, the crystal lattice, which is formed by internal clusters of WO_6, AgO_6, and AgO_7 and recoated with external AgO_4 and angular AgO_2 clusters, suffers a distortion which is diffused throughout of bulk materials modified by the electronic configuration of these polar clusters. Such amorphization gives rise to a reaction of disproportionation, forming metallic silver as it is illustrated in Fig. 1.17.

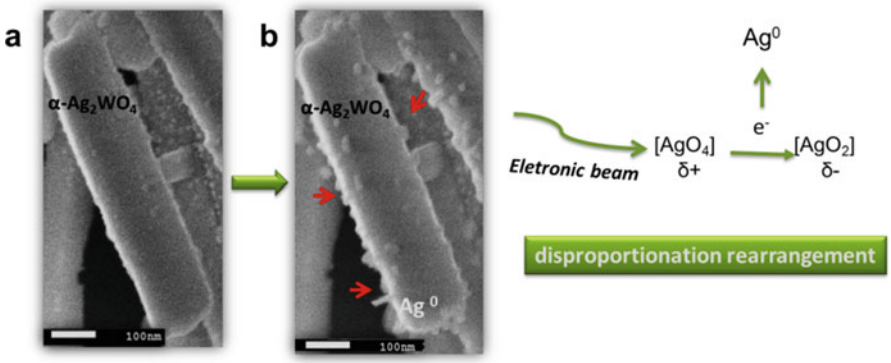

Fig. 1.17 Scheme showing the formation of metallic silver filaments on α-Ag_2WO_4

The inducing of the growth of silver filaments through the electron beam forms a metal/semiconductor interface α-Ag_2WO_4, thus enabling its application as a multifunctional device [79].

The formation of heterostructures of α-Ag_2WO_4 is emerging with the goal of prompting synergic effects related to multifunctional applications along with those structures obtained by the nanocomposite system Ag_2WO_4@ZnO@Fe_3O_4, processed via the hydrothermal method. While ZnO exhibits electric conductivity and photoreactivity, Fe_3O_4 has magnetic properties and high absorption of visible light which when associated with the Ag_2WO_4 result in an alignment of bands that reduces the electronic recombination besides presenting hysteresis curves which could act to facilitate the magnetic separation of the compound [117]. At this point, it is worth pointing out that the nanocomposite crystallinity increases because of disoriented growth of the α-Ag_2WO_4 phase once both crystalline structures exhibit lattice incompatibility and crystalline symmetry.

Another polymorphous complex oxide quite similar to the α-Ag_2WO_4 is silver molybdate (β-Ag_2MO_4), which exhibits the phases α-tetragonal and β-cubic, with the cubic phase (spinel-like) being characterized by high thermal stability and photocatalytic activity around the visible light region. The formation of the interface between the orthorhombic phase of α-Ag_2WO_4 and the cubic phase of β-Ag_2MO_4 causes a medium-range disorder in the material which is characterized by polyhedral distortions, and/or oxygen vacancies create deeper energy levels in the prohibited band and explain the increase observed in intensity and the dislocation of bands to greater wavelengths [33]. It is extremely important to choose the range of pH and temperature of these materials once they exhibit solubility products that vary as a function of pH and temperature. In that sense, when carrying out the core recoating synthesis, there could be an occurrence of a total or partial dissolution of the initial structure forming suboxide nonstoichiometric phases of their oxides (for instance, W_5O_{14} and Mo_8O_{23}) or doped phase with modified of the crystal lattice, similar to what happens in the synthesis of α-Ag_2WO_4/β-Ag_2MO_4, whose initial synthesis of α-Ag_2WO_4 takes place at pH 7 while the recoating occurs at pH 4, leading to the dissolution of part of the microcrystals and coprecipitation in its hexagonal shape

β-Ag_2WO_4 [33, 56]. Through the method of coprecipitation followed by MAHS, it is possible to obtain heterostructures of silver molybdate tungstate $Ag_2W_{1-x}Mo_xO_4$ ($x = 0.0$ and 0.50). By using accelerated electron beam under ultrahigh vacuum, metallic silver filaments (Ag) are grown on the crystals of $Ag_2W_{1-x}Mo_xO_4$. With the formation of the heterostructures, intermediate levels of energy are created in the bandgap, decreasing the energy between the VB and CB of material while increasing the photoluminescent intensity of the material ($\lambda_{emission} = 455$ nm) [31]. Santana et al. reported obtaining silver tungstate microcrystals (Ag_2WO_4) and silver molybdate (Ag_2MoO_4) used as core-shell compound precursors of α-Ag_2WO_4/β-Ag_2MoO_4 and β-Ag_2MoO_4/β-Ag_2WO_4. The formation of the interface between α-Ag_2WO_4 and β-Ag_2MoO_4 was made from MAHS at temperature of 140 °C and pH 7. Already, the formation of the interface between β-Ag_2WO_4 and β-Ag_2MoO_4 was employed the co-precipitation method at temperature 70 °C in pH 4. In this case, the temperature, pH and method of synthesis, determine the kinetics growth and formation of core-shell structure between stable (α) and metastable (β) phases, which promoted the interaction between the octahedral of WO_6 and tetrahedral of MoO_4 in which it affects the photoluminescent property of the material [33].

Apart from the tungstates and molybdates, there are studies about heterostructures based on vanadates via the synthesis using EPD followed by calcination. Ye et al. reported obtaining p-n heterostructures of the bismuth and bismuth vanadate oxides (Bi_2O_3/$BiVO_4$) for the application in photoelectrochemical cells (PEC). To obtain the heterostructures, first, nanobelts of bismuth (Bi) were grown via EPD on FTO substrate. The nanobelts were placed into a solution of NH_4VO_3 for 6 h after which thermal treatment was conducted at 500 °C in atmospheric air, transforming the metallic Bi in Bi_2O_3/$BiVO_4$ [145]. In a related study, Chen et al. reported obtaining Bi_2O_3/$BiVO_4$ compounds in a one-step synthesis aiming at studying their photocatalytic properties. To this end, via the solvothermal method, they applied a mixture of water and ethylene glycol, NH_4VO_3, $Bi(NO_3)_3.5H_2O$ as a source of bismuth and L-lysine as *template*. The compounds were found to present a superior photocatalytic activity compared to that of Bi_2O_3 and $BiVO_4$ [23].

5 Conclusion

In summary, this chapter has reported the importance of processing way to improve the physical and chemical properties of new multifunctional complex oxides, making them of large interest for a huge variety of technological applications. As it was described, several methods are used to synthesize complex oxides (e.g., sol-gel, PPM, chemical bath, hydrothermal synthesis, oxide mixing, and coprecipitation method) and to prepare films (e.g., chemical bath, electrophoresis, and spin coating). Microwave irradiation can be used both in synthesis and sintering process and hence could, in principle, offer new possibilities to solve some key problems in material science. By microwave-assisted hydrothermal synthesis, as seen in this chapter, it is possible to obtain perovskite oxides with piezoelectric and photoluminescent features, beside that heterostructured oxides. The sintering process using microwave

irradiation is a fundamental step to developing new and more efficient materials, as, for example, for varistors and gas sensor applications. The growth of orientated ZnO nanorods may be done on substrates with previous nucleation layers. After the growth, the surface functionalization using gold nanoparticles improves the sensor response of ZnO nanorods. To ensure the best performance of oxide electrodes, the crystallinity, microstructural organization, and smooth surface are parameters that need to be controlled during the processing. About solar cells, a small change in the synthesis parameters can affect the solar energy conversion. The study of interface features is an important way to understand in-depth the novel properties of heterostructured oxides, based on work synergistically.

Acknowledgments The authors would like to thank the Brazilian research agencies CAPES, CNPq, and FAPESP-CEPID/CDMF 2013/07296-2 for granting the financial support for the research group.

References

1. Aguilar-Martínez JA, Zambrano-Robledo P, Garcá-Villarreal S, Hernández MB, Rodríguez E, Falcon-Franco L (2016) Effect of high content of Co_3O_4 on the structure, morphology, and electrical properties of (Cr,Sb)-doped SnO_2 varistors. Ceram Int 42:7576–7582
2. Ahsanulhaq Q, Umar A, Hahn YB (2007) Growth of aligned ZnO nanorods and nanopencils on ZnO/Si in aqueous solution: growth mechanism and structural and optical properties. Nanotechnology 18:115603–115610
3. Amoresi RAC, Felix AA, Lustosa GMMM et al (2016) Role of morphological characteristics on the conductive behavior of $LaNiO_3$ thin films. Ceram Int 42:16242–16247
4. Andrés J, Gracia L, Gonzalez-Navarrete P et al (2014) Structural and electronic analysis of the atomic scale nucleation of Ag on α-Ag_2WO_4 induced by electron irradiation. Sci Rep 4:5391
5. Bacelar WK, Bueno PR, Leite ER et al (2006) How Cr_2O_3 influences the microstructure and nonohmic features of the $SnO_2(Co_x,Mn_{1-x})O$-based varistor system. J Eur Ceram Soc 26:1221–1229
6. Bai S, Xu Q, Gu L et al (2012) Single crystalline lead zirconate titanate (PZT) nano/microwire based self-powered UV sensor. Nano Energy 1:789–795
7. Baikie T, Fang Y, Kadro JM et al (2013) Synthesis and crystal chemistry of the hybrid perovskite (CH3NH3)PbI3 for solid-state sensitised solar cell applications. J Mater Chem A 1:5628–5641
8. Baruah S, Dutta J (2009) Hydrothermal growth of ZnO nanostructures. Sci Tech Adv Mater 10:1468–6996
9. Bastami H, Taheri-Nassaj E (2012) Effect of Sm_2O_3 on the microstructure and electrical properties of SnO_2-based varistors. Ceram Int 38:265–270
10. Batmunkh M, Dadkhah M, Shearer CJ, Biggs MJ, Shapter JG (2016) Incorporation of graphene into SnO_2 photoanodes for dye-sensitized solar cells. Appl Surf Sci 387:690–697
11. Biasotto G, Ranieri MGA, Foschini CR et al (2014) Gas sensor applications of zinc oxide thin film grown by the polymeric precursor method. Ceram Int 40:14991–14996.
12. Bilecka I, Niederberger M (2010) Microwave chemistry for inorganic nanomaterials synthesis. Nanoscale 2:1358–1374
13. Birkefeld LD, Azad AM, Akbar SA (1992) Carbon monoxide and hydrogen detection by anatase modification of titanium dioxide. J Am Ceram Soc 75:2964–2968

14. Boccaccini AR, Roether JA, Thomas BJC, Chaves MSPE, Shaffer ES, Minay EJ (2006) The electrophoretic deposition of inorganic nanoscaled materials. J Ceram Soc Jpn 114:1–14
15. Boyle DS, Govender K, O'brien P (2002) Novel low temperature solution deposition of perpendicularly orientated rods of ZnO: substrate effects and evidence of the importance of counter-ions in the control of crystallite growth. Chem Commun 1:80–81
16. Brankovic G, Brankovic Z, Davolos MR et al (2004) Influence of the common varistor dopants (CoO, Cr_2O_3 and Nb_2O_5) on the structural properties of SnO_2 ceramics. Mater Charact 52:243–251
17. Bueno PR, Oliveira MM, Santos MRC, Longo E, Tebcherani SM, Varela JA (2000) Varistores à base de SnO_2: estado da arte e perspectivas. Ceramica 46:124–130
18. Burschka J, Pellet N, Moon S-J et al (2013) Sequential deposition as a route to high-performance perovskite-sensitized solar cells. Nature 499:316–319
19. Caproni E, Muccillo R (2012) Application of the electrophoretic deposition technique for obtaining yttria-stabilized zirconia tubes. Ceramica 58:131–136
20. Cavalcante LS, Almeida MAP, Avansi WJ et al (2012) Cluster coordination and photoluminescence properties of α-Ag_2WO_4 microcrystals. Inorg Chem 51:10675–10687
21. Cavalcante LS, Sczancoski JC, Longo VM et al (2008) Intense violet-blue photoluminescence in BaZrO3 powders: a theoretical and experimental investigation of structural order-disorder. Opt Commun 281:3715–3720
22. Chaiyo N, Muanghlua R, Niemcharoen S et al (2011) Solution combustion synthesis and characterization of lead-free piezoelectric sodium niobate ($NaNbO_3$) powders. J Alloys Compd 509:2445–2449
23. Chen L, Zhang Q, Huang R et al (2012) Porous peanut-like Bi_2O_3–$BiVO_4$ composites with heterojunctions: one-step synthesis and their photocatalytic properties. Dalton Trans 41:9513–9518
24. Chen Y, Pryds N, Kleibeuker E et al (2011) Metallic and insulating interfaces of amorphous $SrTiO_3$ – based oxide heterostructures. Nano Lett 11:3774–3778
25. Chen YJ, Nie L, Xue XY et al (2006) Linear ethanol sensing of SnO_2 nanorods with extremely high sensitivity. Appl Phys Lett 88:083105/1–083105/3
26. Cheung JT, Morgan PED, Lowndes DH et al (1993) Structural and electrical properties of $La_{0.5}Sr_{0.5}CoO_3$ epitaxial films. Appl Phys Lett 62:2045–2047
27. Cho SG, Johnson RA (1990) Condrate thermal decomposition of (Sr,Ti) organic precursor during the Pechini process. J Mater Sci 25:4738–4744
28. Choi JY, Oh TS (2012) CO sensitivity of La_2O_3-doped SnO_2 thick film gas sensor. Thin Solid Films 547:230–234
29. Chu SY, Yan TM, Chen SL (2000) Analysis of ZnO varistors prepared by the sol-gel method. Ceram Int 26:733–737
30. Chua SJ, Tay CB, Tang J (2013) ZnO nanostructures and thin films grown in aqueous solution: growth, defects and doping. In: Feng ZC (ed) Handbook of zinc oxide and related materials. Taylor & Francis, Boca Raton, pp 107–140
31. da Silva LF, Catto AC, Avansi WJ et al (2014) A novel ozone gas sensor based on one-dimensional (1D) α-Ag2WO4 nanostructures. Nanoscale 6:4058–4062
32. Dai Y, Zhang Y, Li QK (2002) Synthesis and optical properties of tetrapod- like zinc oxide nanorods. Chem Phys Lett 358:83–86
33. de Santana YVB, Gomes JEC, Matos L et al (2014) Silver molybdate and silver tungstate nanocomposites with enhanced photoluminescence. Nanomater Nanotechnol 4:22–32
34. Demianets LN, Kostomarov DV, Kuz'mina IP, Pushko SV (2002) Mechanism of growth of ZnO single crystals from hydrothermal alkali solutions. Crystallogr Reports 47:S86–S98
35. Devi GS, Subrahmanyam VB, Gadkari SC et al (2006) NH_3 gas sensing properties of nanocrystalline ZnO based thick films. Anal Chim Acta 568:41–46
36. Eror NG (1990) Polymeric precursors synthesis and processing of electronic material syntheses BaO–TiO_2 system. J Mater Sci 25:1169–1183
37. Fernandes SL, Bregadiolli BA, Véron AC et al (2016) Hysteresis dependence on $CH_3NH_3PbI_3$ deposition method in perovskite solar cells. Proc SPIE 9936:99360B

38. Fernandes SL, Véron AC, Neto NFA et al (2016) Nb_2O_5 hole blocking layer for hysteresis-free perovskite solar cells. Mater Lett 181:103–107
39. Fu YQ, Luo JK, Du XY et al (2010) Recent developments on ZnO films for acoustic wave based bio-sensing and microfluidic applications: a review. Sensors Actuators B Chem 143:606–619
40. Gaponov AV, Glot AB (2010) Electrical properties of SnO_2 based varistor ceramics with CuO addition. J Mater Sci Mater Electron 21:331–337
41. Gaponov AV, Glot AB, Ivon AI et al (2007) Varistor and humidity-sensitive properties of SnO_2-Co_3O_4-Nb_2O_5-Cr_2O_3 ceramics with V_2O_5 addition. Mater Sci Eng B 459:76–84
42. García-Munoz JL, Rodríguez-Carvajal J (1992) Neutron-diffraction study of $RNiO_3$ (R = La,Pr,Nd,Sm): electronically induced structural changes across the metal-insulator transition. Phys Rev B 46:4414–4425
43. Gasparotto G, Perazolli LA, Jacomaci N, Ruiz M, Zaghete MA et al (2012) SnO dense ceramic microwave sintered with low resistivity. Mater Sci Appl 3:272–280
44. Ghayour H, Rezaie HR, Mirdamadi S et al (2011) The effect of seed layer thickness on alignment and morphology of ZnO nanorods. Vacuum 86:101–105
45. Goodenough JB, Zhou JS (2007) Orbital ordering in orthorhombic perovskites. J Mater Chem 17:2394–2405
46. Govender K, Boyle DS, Kenway PB, O'Brien P (2004) Understanding the factors that govern the deposition and morphology of thin films of ZnO from aqueous solution. J Mater Chem 14:2575–2591
47. Greene LE, Law M, Tan DH et al (2005) General route to vertical ZnO nanowire arrays using textured ZnO seeds. Nano Lett 2005(5):1231–1236
48. Gurlo A, Bârsan N, Weimar U (2006) Gas sensors based on semiconducting metal oxides. In: Fierro JLG (ed) Metal oxides: chemistry and applications, vol 22. Taylor & Francis, Boca Raton, pp 683–738
49. Gurrola MP, Gutiérrez J, Rivas S et al (2014) Evaluation of the corrosion of Sb-doped SnO_2 supports for electrolysis systems. Int J Hydrog Energy 39:16763–16770
50. Harbach F, Nienburg H (1998) Homogeneous functional ceramic components through electrophoretic deposition from stable colloidal suspensions I. Basic concepts and application to zirconia. J Eur Ceram Soc 18:675–683
51. He J, Peng Z, Fu Z, Wang C, Fu X (2012) Effect of ZnO doping on microstructural and electrical properties of SnO_2–Ta_2O_5 based varistors. J Alloys Compd 528:79–83
52. Heo YW, Varadarajan V, Kaufman M et al (2002) Site-specific growth of Zno nanorods using catalysis-driven molecular-beam epitaxy. Appl Phys Lett 81:3046–3048
53. Hong J-I, Bae J, Wang ZL, Snyder RL (2009) Room-temperature, texture-controlled growth of ZnO thin films and their application for growing aligned ZnO nanowire arrays. Nanotechnology 20:85609
54. Hsiao CL, Qi X (2013) Substrate-dependant chemical stability and conductivity of $LaNiO_{3-x}$ thin films. Thin Solid Films 529:356–359
55. Im J, Singh J, Soares JW, Steeves DM, Whitten JE (2011) Synthesis and optical properties of dithiol-linked ZnO/gold nanoparticle composites. J Phys Chem C 115:10518–10523
56. Jensen JB, Buch JSR (1980) Solubility of silver tungstate in aqueous solutions at different ionic strengths and temperatures. Thermodynamic quantities of Ag_2WO_4. Acta Chem Scand A 34:99–107
57. Jeon NJ, Noh JH, Kim YC et al (2014) Solvent engineering for high-performance inorganic-organic hybrid perovskite solar cells. Nat Mater 13:1–7
58. Johnsson M, Lemmens P (2007) Crystallography and chemistry of perovskites. John Wiley Sons, Ltd, New York, p 11
59. Joshi RK, Hu Q, Alvi F, Joshi N, Kumar A (2009) Au decorated zinc oxide nanowires for CO sensing. J Phys Chem C 113:16199–16202
60. Jung JH, Lee M, Hong II J et al (2011) Lead-free $NaNbO_3$ nanowires for a high output piezoelectric nanogenerator. ACS Nano 5:10041–10046

61. Kazim S, Nazeeruddin MK, Grätzel M, Ahmad S (2014) Perovskite as light harvester: a game changer in photovoltaics. Angew Chemie Int Ed 53:2812–2824
62. Kim H-S, Lee C-R, Im J-H et al (2012) Lead iodide perovskite sensitized all-solid-state submicron thin film mesoscopic solar cell with efficiency exceeding 9%. Sci Rep 2:591–598
63. Kofstad P (1972) Nonstoichiometry, diffusion, and electrical conductivity in binary metal oxides. Wiley, NewYork, 394 p
64. Koka A, Zhou Z, Sodano HA (2014) Vertically aligned $BaTiO_3$ nanowire arrays for energy harvesting. Energy Environ Sci 7:288–296. doi:10.1039/c3ee42540a
65. Koplin T, Siemons M, Valentin C et al (2006) Workflow for high through put screening of gas sensing materials. Sensors 6:298–307
66. Kung MC, Davis RJ, Kung HH (2007) Understanding Au-catalyzed low-temperature CO oxidation. J Phys Chem C 11:11767–11775
67. Lavanya N, Radhakrishnan S, Sekas C (2012) Fabrication of hydrogen peroxide biosensor based on Ni doped SnO_2 nanoparticles. Biosens Bioelectron 36:41–47
68. Lavrov RI, Ivon AI, Chernenko IM (2004) Comparative characteristics of silver and copper electrodes on ZnO varistor ceramics. J Eur Ceram Soc 24:2591–2595
69. Lee JB, Lee HJ, Seo SH et al (2001) Characterization of undoped and Cu-doped ZnO films for surface acoustic wave applications. Thin Solid Films 398-399:641–646
70. Leite DR, Cilense M et al (2010) The effect of TiO_2 on the microstructural and electrical properties of low voltage varistor based on $(Sn,Ti)O_2$ ceramics. Phys Status Solidi A 207:457–446
71. Li AD, Ge CZ, Wu D et al (1997) Conductive metallic $LaNiO_3$ films from metallo-organic precursors. Thin Solid Films 298:165–169
72. Lin Y, Zhang Z, Yuan F (1999) Characterisation of ZnO-based varistors prepared from nanometre precursor or powders. Adv Mater Opt Electron 9:205–209
73. Lisboa Filho PN, Zenatti A et al (2002) Magnetic behavior at low temperatures of Ti oxide polycrystalline samples. J Sol Gel Sci Techn 24:241–245
74. Liu B, Zeng HC (2004) Room temperature solution synthesis of monodispersed single-crystalline ZnO nanorods and derived hierarchical nanostructures. Langmuir 20:4196–4204
75. Liu D, Lv Y, Zhang M et al (2014) Defect-related photoluminescence and photocatalytic properties of porous ZnO nanosheets. J Mater Chem (A Mater Energy Sustain) 2:15377–15388
76. Liu M, Wang D (1995) Synthesis of $La_{1z}Sr_zCo_{1y}Fe_yO_{3y}$ on dense or porous substrates using the polymeric precursors method. J Mater Res 10:3210–3214
77. Lizandara-Pueyo C, Siroky S, Wagner MR et al (2011) Shape anisotropy influencing functional properties: trigonal prismatic ZnO nanoparticles as an example. Adv Funct Mater 21:295–304
78. Löher T, Tomm Y, Pettenkofer C, Jaegermann W (1994) Van der Waals epitaxy of three-dimensional CdS on the two-dimensional layered substrate MoTe2(0001). Appl Phys Lett 65:555–557
79. Longo E, Cavalcante LS, Volanti DP et al (2013) Direct in situ observation of the electron-driven synthesis of Ag filaments on α-Ag_2WO_4 crystals. Sci Rep 3:1676–1679
80. Lustosa GMMM, Costa JPC, Perazolli LA, Stojanovic BD, Zaghete MA (2016) Potential barrier of (Zn, Nb) SnO_2-films induced by microwave thermal diffusion of Cr^{3+} for low-voltage varistor. J Am Ceram Soc 99:152–157
81. Lustosa GMMM, Costa JPC et al (2015) Electrophoretic deposition of (Zn, Nb)SnO_2-films varistor superficially modified with Cr^{3+}. J Eur Ceram Soc 35:2083–2089
82. Ma S, Xu Z, Chu R, Hao J et al (2014) Influence of Cr_2O_3 on ZnO-Bi_2O_3-MnO_2-based varistor ceramics. Ceram Int 40:10149–10152
83. Mahadeva SK, Kim J (2011) Conductometric glucose biosensor made with cellulose and tin oxide hybrid nanocomposite. Sensors Actuators B Chem 157:177–182
84. Makha M, Fernandes SL, Jenatsch S, et al (2016) A transparent, solvent-free laminated top electrode for perovskite solar cells. doi: 10.1080/14686996.2016.1176512

85. Maneeshya LV, Anitha VS, Thomas PV, Joy K (2015) Thickness dependence of structural, optical and luminescence properties of $BaTiO_3$ thin films prepared by RF magnetron sputtering. J Mater Sci Mater Electron 26:2947–2954
86. Mazali IO, Las WC, Cilense M (2003) The effect of preparation meted and Sb content on SnO_2-CuO sintering. J Mater Sci 38:3325–3330
87. Megaw HD (1974) The seven phases of sodium niobate. Ferroelectrics 7:87–89
88. Menezes RR, Souto PM, Kiminami GA (2007) Sinterização de cerâmicas em microondas. Parte I: aspectos fundamentais. Ceramica 53:1–10
89. Metz R, Koumeir D, Morel J et al (2008) Electrical barriers formation at the grain boundaries of Co-doped SnO_2 varistor ceramics. J Eur Ceram Soc 28:829–835
90. Minami T, Suzuki S, Miyata T (2001) Transparent conducting impurity-co-doped ZnO: Al thin films prepared by magnetron sputtering. Thin Solid Films 3981:53–58
91. Moreira ML, Mambrini GP, Volanti DP et al (2008) Hydrothermal microwave: a new route to obtain photoluminescent crystalline $BaTiO_3$ nanoparticles. Chem Mater 20:5381–5387
92. Nozik YZ, Kuklina ES, Schuster G et al (1991) Neutron diffraction study of HTSC ceramics $YBa_2Cu_3O_{6.9}$. Kristallografiya 36:217–218
93. Okuyama M, Hamakawa H (1985) Preparation and basic properties of $PbTiO_3$ ferroelectric thin films and their device applications. Ferroelectrics 63:243–247
94. Oliveira LH, De Moura AP, La Porta FA et al (2016) Influence of Cu-doping on the structural and optical properties of $CaTiO_3$ powders. Mater Res Bull 81:1–9
95. Ozgur U, Alivov YI, Liu C et al (2005) A comprehensive review of ZnO materials and devices. J Appl Phys 98:041301/1–041301/103
96. Park N-G (2014) Perovskite solar cells: an emerging photovoltaic technology. Mater Today (Oxford, UK) 18:65–72
97. Park WI, Kim DH, Jung SW, Yi GC (2002) Metalorganic vapor-phase epitaxial growth of vertically well-aligned ZnO nanorods. Appl Phys Lett 80:4232–4234
98. Patel I (2011) Ceramic based intelligent piezoelectric energy harvesting device. In: Sikalidis C (ed) Advances in ceramics – electric and magnetic ceramics, bioceramics, ceramics and environment. InTech, Rijeka, pp 133–155
99. Pechini MP (1967) Method of preparing lead and alkaline earth titanates and niobates and coating method using the same to forma capacitor. US Pat. 3,330697
100. Perazolli LA, Gasparotto Gisane, Jaomaci N et al (2012) SnO_2 dense ceramic microwave sintered with low resistivity. Mater Sci Appl 3:272–280
101. Pereira GJ, Gouvêa D (2003) Densificação rápida de cerâmicas de SnO_2. Ceramica 49:116–119
102. Pontes DSL, Pontes FM, Pereira-da-Silva MA et al (2013) Structural and electrical properties of $LaNiO_3$ thin films grown on (100) and (001) oriented $SrLaAlO_4$ substrates by chemical solution deposition method. Ceram Int 39:8025–8034
103. Qi P, Wang JF, Su WB, Cheng HC, Zang GZ et al (2005) (Yb,Co,Nb)-doped SnO_2 varistors ceramics. Mater Sci Eng B 119:94–98
104. Rajeev KP, Shivashankar GV, Raychaudhuri AK (1991) Low-temperature electronic properties of a normal conducting perovskite oxide ($LaNiO_3$). Solid State Commun 79:591–595
105. Rakshit S, Gopalakrishnan PS (1994) Oxygen nonstoichiometry and its effect on the structure of $LaNiO_3$. J Solid State Chem 110:28–31
106. Ramesh R, Chan WK, Wilkens B (1992) Fatigue and retention in ferroelectric Y-Ba-Cu-O/Pb-Zr-Ti-O/Y-Ba-Cu-O heterostructures. Appl Phys Lett 31:1537–1539
107. Ramesh R, Gilchrist H, Sands T et al (1993) Ferroelectric La-Sr-Co-O/Pb-Zr-Ti-O/La-Sr-Co-O heterostructures on silicone via template growth. Appl Phys Lett 63:3592–3594
108. Riman RE, Suchanek WL (2006) Hydrothermal synthesis of advanced ceramic powders. 11th Int Ceram Congr 45:184–193
109. Riman RE, Suchanek WL, Lencka MM (2002) Hydrothermal crystallization of ceramics. Ann Chim Sci des Mater 27:15–36

110. Roca RA, Sczancoski JC, Nogueira IC et al (2015) Facet-dependent photocatalytic and antibacterial properties in α-Ag2WO4 crystals: combining experimental data and theoretical insights. Cat Sci Technol 5:4091–4107
111. Saluja A, Pan J, Kerr L et al (2008) Gas sensing properties of porous ZnO nano-platelet films. Mater Res Soc Symp Proc 1035:1557/PROC–1035-L11-07
112. Santos MRC, Sousa VC, Oliveira MM et al (2005) Recent research developments in SnO_2-based varistors. Mater Chem Phys 90:1–9
113. Santos MRC, Sousa VC, Oliveiras MM et al (2001) Cerâmicas eletrônicas à base de SnO_2 e TiO_2. Ceramica 47:136–143
114. Santos PA, Maruchin S, Menegoto GF, Zara AJ, Pianaro SA (2006) The sintering time influence on the electrical and microstructural characteristics of SnO_2 varistor. Mater Lett 60:1554–1557
115. Schulz P, Edri E, Kirmayer S et al (2014) Interface energetics in organo-metal halide perovskite-based photovoltaic cells. Energy Environ Sci 7:1377–1381
116. Seim H, Molsa H, Nieminen M et al (1997) Deposition of $LaNiO_3$ thin films in an atomic layer epitaxy reactor. J Mater Chem 7:449–454
117. Shen J, Lu Y, Liu J-K, Yang X-H (2016) Design and preparation of easily recycled Ag_2WO_4@ZnO@Fe_3O_4 ternary nanocomposites and their highly efficient degradation of antibiotics. J Mater Sci 51:7793–7802
118. Silva Junior E, La Porta FA, Liu MS et al (2015) A relationship between structural and electronic order-disorder effects and optical properties in crystalline TiO_2 nanomaterials. Dalton Trans 44:3159–3175
119. Stojanovic BD, Mitic V, Pejovic V, Vijatovic MM, Zaghete MA (2007) Screen printed PLZT thick films prepared from nanopowders. J Eur Ceram Soc 27:4359–4362
120. Subramanian V, Wolf EE, Kamat PV (2003) Green emission to probe photoinduced charging events in ZnO-Au nanoparticles. Charge distribution and fermi-level equilibration. J Phys Chem B 107:7479–7485
121. Suman PH, Felix AA, Tuller HL, Varela JA, Orlandi MO (2015) Comparative gas sensor response of SnO_2, SnO and Sn_3O_4 nanobelts to NO_2 and potential interference. Sensors Actuators B Chem 208:122–127
122. Sun Y, Fuge GM, Ashfold MNR (2004) Growth of aligned ZnO nanorod arrays by catalyst-free pulsed laser deposition methods. Chem Phys Lett 396:21–26
123. Tak Y, Yong K (2005) Controlled growth of well-aligned ZnO nanorod array using a novel solution method. J. Phys. Chem. B. 109:19263–19269
124. Tang FQ, Uchikoshi T, Sakka Y (2002) Electrophoretic deposition behavior of aqueous nanosized zinc oxide suspensions. J Am Ceram Soc 85:2161–2165
125. Tao Y, Fu M, Zhao A et al (2010) The effect of seed layer on morphology of ZnO nanorod arrays grown by hydrothermal method. J Alloys Compd 489:99–102
126. Teixeira GF, Ciola RA, Sakamoto WK, Zaghete MA (2015) Perovskite-based mesostructures and related composites-influence exerted by morphology and interface. In: Barranco AP (ed) Ferroelectric materials-synthesis and characterization. InTech, Rijeka, pp 59–83
127. Teixeira GF, Gasparotto G, Paris EC et al (2012) Photoluminescence properties of PZT 52/48 synthesized by microwave hydrothermal method using PVA with template. J Lumin 132: 46–50
128. Teixeira GF, Wright TR, Manfroi DC et al (2015) Photoluminescence in $NaNbO_3$ particles and films. Mater Lett 139:443–446
129. Teixeira GF, Zaghete MA, Gasparotto G et al (2012) Photoluminescence properties and synthesis of a PZT mesostructure obtained by the microwave-assisted hydrothermal method. J Alloys Compd 512:124–127
130. Van der Biest OO, Vandeperre LJ (1999) Electrophoretic deposition of materials. Annu Rev Mater Sci 29:327–352
131. Vayssieres L (2003) Growth of arrayed nanorods and nanowires of ZnO from aqueous solutions. Adv Mater 15:464–466

132. Vermurugan V, Srinivasarao U, Ramachandran R, Saranya M, Grace AN (2016) Synthesis of tin oxide/graphene (SnO_2/G) nanocomposite and its electrochemical properties for supercapacitor applications. Mater Res Bull 84:145–151
133. Viswanatha R, Amenitsch H, Sarma DD (2007) Growth kinetics of ZnO nanocrystals: a few surprises. J Am Chem Soc 129:4470–4475
134. Wang GS, Zhao Q, Meng XJ et al (2005) Preparation of highly (100)-oriented $LaNiO_3$ nanocrystalline films by metalorganic chemical liquid deposition. J Cryst Growth 277:450–456
135. Wang J, Durussel A, Sandu CS et al (2012) Mechanism of hydrothermal growth of ferroelectric PZT nanowires. J Cryst Growth 347:1–6
136. Wang ZL (2010) Piezopotential gated nanowire devices: piezotronics and piezo-phototronics. Nano Today 5:540–552
137. Will J, Hrushka MKM, Gubbler L, Gauckler LJ (2001) Electrophoretic deposition of zirconia and porous anodic substrates. J Am Ceram Soc 84:328–332
138. Wu R, Xie C, Xia H et al (2000) The thermal physical formation of ZnO nanoparticles and their morphology. J Cryst Growth 217:274–280
139. Xu G, Ren Z, Du P et al (2005) Polymer-assisted hydrothermal synthesis of single-crystalline tetragonal perovskite $PbZr_{0.52}Ti_{0.48}O_3$ nanowires. Adv Mater 17:907–910
140. Xu S, Wang LZ (2011) One-dimensional ZnO nanostructures: solution growth and functional properties. Nano Res 4:1013–1098
141. Xu S, Wei Y, Kirkham M et al (2008) Patterned growth of vertically aligned ZnO nanowire arrays on inorganic substrates at low temperature without catalyst. J Am Chem Soc 130:14958–14959
142. Yang D, Tang X, Wei R et al (2016) Epitaxial growth of $SrRuO_3$ thin films with different orientation by chemical solution deposition. J Alloys Compd 682:154–159
143. Yang TT, Chen WT, Hsu YJ, Wei KH, Lin TY, Lin TW (2010) Interfacial charge carrier dynamics in core-shell Au-CdS nanocrystals. J Phys Chem C 114:11414–11420
144. Yang X, Cheng J, Yu S et al (2008) Effect of $LaNiO_3$ sol concentration on the structure and dielectric properties of $Pb(Zr_{0.53}Ti_{0.47})O_3$ thin films grown on $LaNiO_3$-coated Si substrates. J Cryst Growth 310:3466–3469
145. Ye K-H, Yu X, Qiu Z et al (2015) Facile synthesis of bismuth oxide/bismuth vanadate heterostructures for efficient photoelectrochemical cells. RSC Adv 5:34152–34156
146. Yuan H, Zhang Y (2004) Preparation of well-aligned ZnO whiskers on glass substrate by atmospheric MOCVD. J Cryst Growth 263:119–124
147. Zang J, Li CM, Cui X et al (2007) Tailoring zinc oxide nanowires for high performance amperometric glucose sensor. Electroanalysis 19:1008–1014
148. Zhang Y, Chung J, Lee J et al (2011) Synthesis of ZnO nanospheres with uniform nanopores by a hydrothermal process. J Phys Chem Solids 72:1548–1553
149. Zhitomirsky I, Petric A (2001) The electrodeposition of ceramic and organoceramic films for fuel cells. J Miner Met Mater Soc 53:48–50
150. Zhou H, Li Z et al (2016) The enhanced gas-sensing and photocatalytic performance of hollow and hollow core-shell SnO2 based nanofibers induced by the Kirkendall effect. Ceram Int 42:1817–1826
151. Zhu Z, Zhang X, Guo JQ et al (2016) The domain configurations of $(Na_{0.85}K_{0.15})_{0.5}Bi_{0.5}TiO_3$ thin film with different bottom electrodes. Appl Surf Sci 367:59–63

Chapter 2
Carbothermal Reduction Synthesis: An Alternative Approach to Obtain Single-Crystalline Metal Oxide Nanostructures

M. O. Orlandi, P. H. Suman, R. A. Silva, and E. P. S. Arlindo

1 Introduction

In recent years, researchers in nanoscience and nanotechnology fields have focused on the development of new devices with optimized performance. Nanoscale materials, especially the single-crystalline ones, have attracted special attention as result of their size-dependent properties, which make them interesting candidates to be used as building blocks for the next generation of nanoelectronic/optoelectronic devices [1–3]. It is well known that material properties depend strongly on the processing parameters. Thereby, manufacturing materials in nanoscale with well-defined characteristics such as size, morphology, crystallinity, and chemical compositions have become a big challenge for technological applications [4–6].

Different approaches have been widely used to synthesize a variety of single-crystalline metal oxide nanostructures [7–9]. However, among these methods, the carbothermal reduction process emerges to be an interesting route, mainly due to its simplicity as well as its low cost and good quality of obtained materials [10]. This method is typically a chemical vapor deposition (CVD) process, in which a carbon source (e.g., carbon black, carbon nanotubes, graphite, etc.) is used as a reducing agent for increasing the vapor pressure of desired precursor. In this way, by controlling parameters like temperature, time, and the atmosphere of synthesis, single-crystalline nano- and microstructures can be grown in temperatures lower than the ones typically used in a conventional thermal evaporation route [10, 11].

M.O. Orlandi (✉) • P.H. Suman • R.A. Silva
Department of Physical-Chemistry, São Paulo State University, Araraquara, SP, 14800-900, Brazil
e-mail: orlandi@iq.unesp.br

E.P.S. Arlindo
Instituto de Ciências Exatas e da Terra, Federal University of Mato Grosso, Barra do Garças, MT, 78600-000, Brazil

E. Longo, F.A. La Porta (eds.), *Recent Advances in Complex Functional Materials*,
DOI 10.1007/978-3-319-53898-3_2

Based on the carbothermal reduction method, our group has synthesized several single-crystalline structures, such as tin oxide nanobelts in different oxidation states (SnO_2, SnO, and Sn_3O_4) and SnO micro-disks [10–12] as well as indium tin oxide (ITO) nanowires [13] and zinc oxide (ZnO) tetrapods [14]. These materials present high potential to be used in gas sensor application or transparent and conductive composite thin films [15, 16]. Other materials like carbides and phosphates have also been produced by using this method [17, 18].

Overall, controlling the synthesis of materials in nanoscale as well as understanding its growth mechanism is essential to produce materials in large scale. In this direction, the carbothermal reduction synthesis presents great potential to be used as a straightforward approach to producing single-crystalline nanomaterials for high-performance applications.

2 Principles of Carbothermal Reduction Process

Carbon is one of the most important chemical elements on Earth, and life is based on it. Besides, chemistry has a specific field focused on carbon study, which is the organic chemistry. So, carbon can be the main actor in many types of research, but it can also aim the research in materials science, working as a coadjutant actor. This is the base of carbothermal reduction method, in which the carbon is used to assist in the synthesis process.

The carbothermal reduction process is a versatile method, and it is based on the Ellingham diagram, as presented in Fig. 2.1. The Ellingham diagram is a plot of Gibbs free energy versus temperature and reactions appears like straight lines due to the following equation:

$$\Delta G = \Delta H – T\ \Delta S \tag{2.1}$$

in which ΔG is the change in the Gibbs free energy, ΔH is the enthalpy of formation, ΔS is the entropy variation, and T is the temperature. It is known that the free energy of an element decreases when it becomes an oxide, so the ΔG axis presents negative values in Fig. 2.1. The intercept is related to the enthalpy of formation, meaning the reaction is a spontaneous process. Besides, increasing the temperature the entropy of material decreases ($\Delta S < 0$), so straight lines with positive slope are expected.

Materials with small enthalpy of formation are at the top of the diagram, while materials with high enthalpy of formation are located at the bottom of it. So, it is expected that a material positioned at the bottom of Ellingham diagram can reduce a material located at the top of the diagram. However, instead of using one oxide to reduce another one, it is easier to use carbon. It is observed that the reaction $2C + O_2 \rightarrow 2CO$ has a negative slope, because 2 moles of solid carbon reacts with 1 mol of oxygen to generate 2 moles of CO, becoming more disordered.

In this way, it is possible to use carbon to reduce most of the oxides, since the temperature used is higher than the crossing point between the oxide reaction line and the abovementioned carbon reaction line. Using the Sn-O system as an example,

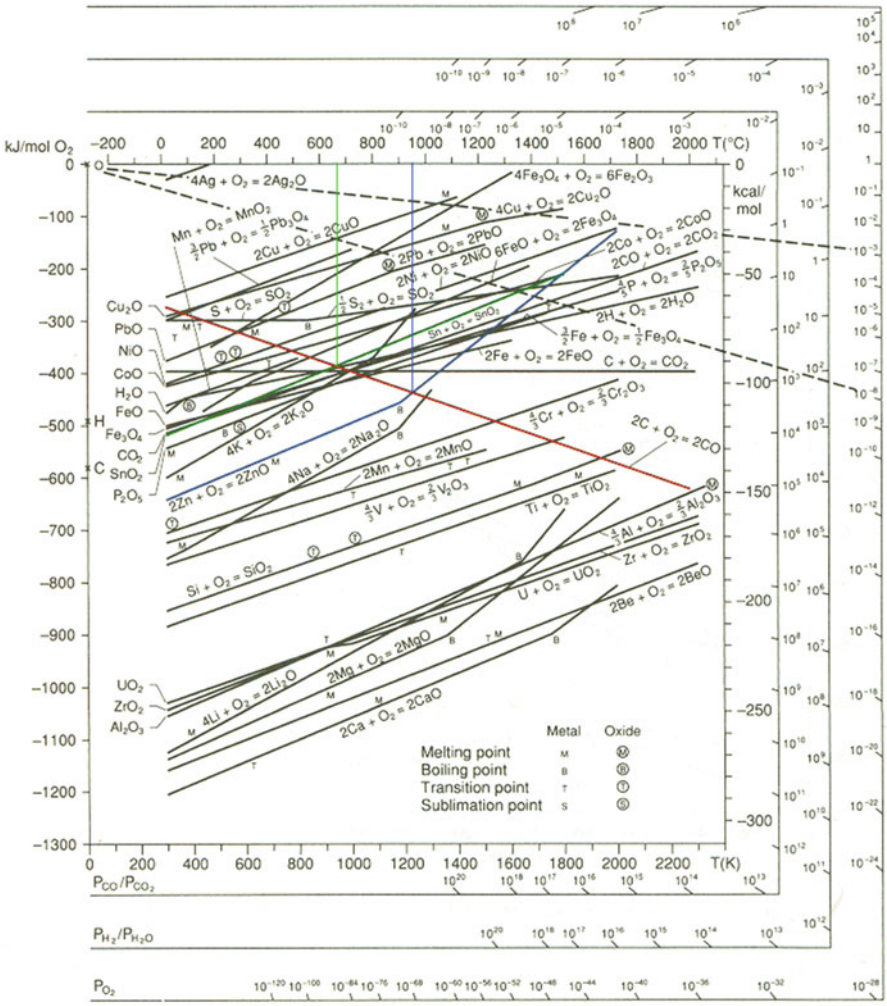

Fig. 2.1 The Ellingham diagram for several elements. The crossing points related to the formation of tin oxide and zinc oxide are indicated

Ellingham diagram shows that the crossing point between the $Sn + O_2 \rightarrow SnO_2$ and the $2C + O_2 \rightarrow 2CO$ reactions is around 680 °C, meaning that temperatures higher than it are enough to reduce the SnO_2. In fact, previous results showed that it is possible to synthesize SnO nanobelts at 900 °C [10]. Moreover, results also show that reducing an oxide increases its vapor pressure for most of oxides [19]. For instance, the SnO_2 vapor pressure at 1,250 °C is 3.6×10^{-5} Pa, while at the same temperature, the vapor pressure of SnO is 234.4 Pa [20], which is a large difference. In fact, results indicate that the vapor pressure of SnO_2 is enough to produce single-crystalline materials at temperatures higher than 1,350 °C [20, 21].

It means that the carbothermal reduction method enables to obtain nanocrystals of tin oxide at temperatures much lower than using direct evaporation, implying saving both costs and time of synthesis.

To perform the carbothermal reduction synthesis, in principle, any carbon source can be used, but the most common is the carbon black, although we also observed the growth of materials using graphite, carbon nanotubes, or even sugar. However, it is important to keep in mind that carbon black is a generic material used mainly as pigment, and there is variety of it, changing the particle size, morphology, and the conductivity. Up to now, there is no study about the efficiency of synthesis using different carbon sources.

Once the reaction between the carbon and the oxide is of fundamental importance for the synthesis process, the atmosphere must be carefully controlled, and oxygen leaks have to be avoided since it can react with carbon and jeopardize all this process.

Although studying the Ellingham diagram is a good starting point to have success in the synthesis of new complex materials, no rare a careful and dedicated work to find the best synthesis conditions is necessary.

Lieber et al. [22, 23] used the carbothermal reduction method to produce one-dimensional (1D) single-crystalline MgO nanorods with an average diameter of 20 nm. A detailed characterization showed rods grew in the [001] direction and were used to produce a composite in order to obtain high-temperature superconductors based on copper oxide. Guo et al. [24] reported beaded nanochains of silicon carbide obtained using carbothermal reduction method and its use to reinforce (0.5 wt%) epoxy-based composites. The mechanical tests showed an improvement of 32% in the tensile strength, which was attributed to the unique morphology obtained for the SiC material. Lead sulfide (PbS), which is an interesting material for nonlinear optical devices, was also prepared by carbothermal reduction process, resulting in PbS nanowires and nanobelts, both growing in the [110] direction.

Then, the carbothermal reduction process is an interesting method to use when it is desired to obtain single-crystalline 1D materials. Besides, it is very common that the grown materials are free of defects. Since 1D materials are the best ones to study electrical transport at the nanoscale, the carbothermal synthesis provides an excellent alternative to produce these complex materials.

Below we report a short introduction about the most common growth processes from the vapor phase, which are vapor-liquid-solid (VLS) and vapor-solid (VS), and after that we present the main results obtained by our group using the carbothermal reduction process, especially growing single-crystalline 1D materials.

3 Growth Mechanisms from Vapor Phase

Structures produced from vapor phase can follow basically two main growth mechanisms: vapor-liquid-solid (VLS) or vapor-solid (VS) [25, 26]. Other mechanisms were reported, but all of them are related in some way to the VS or VLS methods. A typical VLS growth mechanism starts with the adsorption of gaseous species in

a liquid metallic droplet. When the droplets become supersaturated by the vapor, the nucleation occurs followed by the growth of a solid from the droplet. The liquid droplet limits the lateral growth of material, which is important when 1D materials with controlled dimensions are desired [27, 28]. Besides, it is possible to have more control about the growth position by depositing catalyst droplets on specific sites on a substrate.

In contrast, in the VS method, 1D structures are generated only by changing the physical state of a starting material, usually by sublimation. It can occur in two different ways, called direct and indirect evaporation. In the indirect method, it is necessary for some chemical reaction to obtain the desired material. It occurs, for instance, when Mg vapor reacts with oxygen to provide MgO nanorods [23]. For the direct method, no chemical reaction is necessary, and it can occur to SiC, for example. In the VS process, no liquid particles are present during the growth of the structures, which allows to produce materials without any contamination by the metallic droplet. However, for the same reason, it is not possible to control accurately the structure dimensions and the position of the grown material.

4 Multiple Stoichiometries of Tin Oxide Nano- and Microstructures

Tin dioxide (SnO_2) is one of the most studied semiconducting materials, and due to its interesting physical and chemical properties, it has been used in several technological applications, such as sensors, fuel cells, and optical and electronic devices [29–32]. Pan, Dai, and Wang reported, for the first time, the synthesis of single-crystalline SnO_2 nanobelts by a simple thermal evaporation of oxide powders at high temperatures [33]. Since then, SnO_2 nanostructures including nanowires, nanotubes, and nanorods have been produced using several methods [34–36]. Moreover, other stoichiometries of tin oxide (e.g., SnO and Sn_3O_4) have also attracted a great attention in recent years [12, 15, 16].

Nano- and microstructures in different oxidation states of tin oxide (SnO_2, SnO, and Sn_3O_4) were synthesized by carbothermal reduction method from a mixture of SnO_2 powder (Sigma-Aldrich, 99.9% purity) and carbon black (Union Carbide, >99% purity) in the molar ratio of 1.5:1 (SnO_2:C). In a typical synthesis process, 1 g of this mixture was put into an alumina boat, which was introduced in the hot zone of a furnace tube with a sealing system at tube extremities, where both the temperature and the synthesis atmosphere are carefully controlled. The same starting material was used to perform synthesis runs at 1135 °C for 75 min but, using two different synthesis atmospheres, one inert and other oxidizing. To prepare SnO micro-disks and nanobelts, an inert synthesis atmosphere was established by a nitrogen gas flow of 80 sccm, whereas both SnO_2 and Sn_3O_4 nanobelts were synthesized in a controlled oxidizing synthesis atmosphere by using a nitrogen gas flow of 150 sccm and an oxygen gas flow of 0.5 sccm, which was introduced in the counterflow of

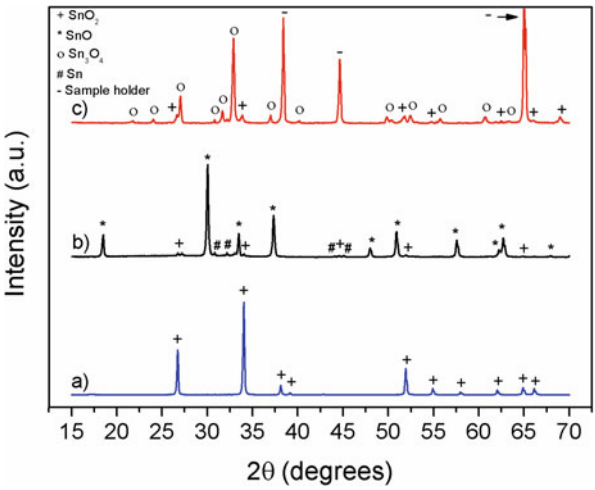

Fig. 2.2 XRD pattern of the (**a**) *white*, (**b**) *dark*, and (**c**) *yellow* woollike materials collected after the synthesis by carbothermal reduction method (Figure from Ref. [16] with permission from Elsevier)

nitrogen gas when the temperature reached 900 °C. Optimized parameters used to prepare all of these materials are described in detail in our previous reports [10, 12].

After both syntheses, woollike materials with different colors were collected in different regions from the inner walls of the alumina tube. In an inert synthesis atmosphere, a dark material was removed from the tube region where the temperature was about 350 °C. On the other hand, when an oxidizing synthesis atmosphere was established, both white and yellow materials were obtained where the temperature was about 500 °C and 700 °C, respectively.

Figure 2.2 shows the XRD spectra of the materials obtained after the synthesis by carbothermal reduction method. The XRD pattern of the white material (Fig. 2.2a) shows it is composed only by materials in the tetragonal structure of cassiterite SnO_2 phase (card JCPDS #41-1445), with evident preferential growth in the [101] direction. Figure 2.2b reveals that the dark material consists of three phases: SnO (card JCPDS #6-395), SnO_2 (card JCPDS #41-1445), and Sn° (card JCPDS #4-673). However, from the relative intensities of the peaks, it is clear that the SnO phase is the largest one, with minor contributions from SnO_2 and Sn° phases. It was found from Fig. 2.2c that the yellow material is constituted mainly of material's growth in the triclinic structure of the Sn_3O_4 (card JCPDS #16-0737) and a small amount in the tetragonal structure of cassiterite SnO_2 phase (card JCPDS #41-1445), as reported in the literature [2, 37]. The peaks marked with "-" ($2\theta = 38.4°$, 44.7° and 65.0°) are related to the aluminum sample holder. Based on the results obtained by XRD, it is notable that by controlling the synthesis atmosphere, structures in different stoichiometries of tin oxide can be produced.

Figure 2.3 shows the FE-SEM images of the SnO_2 materials collected after the synthesis. A low-magnification image (Fig. 2.3a) reveals that this material consists of 1D nanostructures with micrometers or even millimeters in length and rectangular cross-section, which are called nanobelts (Fig. 2.3b–c). Besides, it was observed that these structures present homogenous width along the length and have a smooth

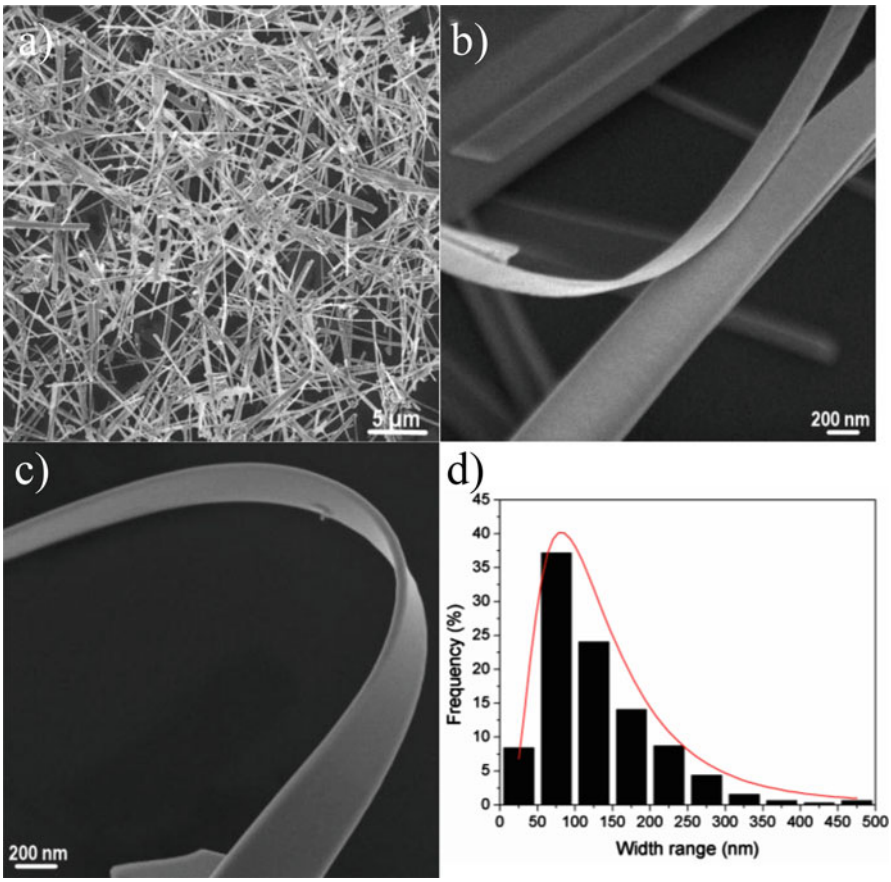

Fig. 2.3 FE-SEM images showing (**a**) a general view of the 1D SnO_2 structures and (**b**, **c**) the rectangular cross-section of the nanobelts. (**d**) Width distribution histogram of the nanobelts

surface. Figure 2.3d shows the histogram of the width distribution of the SnO_2 nanobelts presenting a single-modal width distribution with a maximum frequency between 50 and 100 nm and approximately 70% of the nanobelts smaller than 150 nm in width.

The proposed growth mechanism of SnO_2 nanobelts is the vapor-solid (VS) process [33, 38], since no metallic particles were observed at belts extremities. This process occurs due to the reduction of the SnO_2 power by the carbon black forming SnO and CO vapors inside the tube, according to the reaction showed in Eq. 2.2. The products of this reaction are transported to a lower temperature region by the N_2 gas flow and react with the O_2 inserted in the counterflow, forming the SnO_2 nanobelts and CO_2 gas (Eqs. 2.3 and 2.4).

$$SnO_{2(s)} + C_{(s)} \rightarrow SnO_{(g)} + CO_{(g)} \quad (2.2)$$

$$SnO_{(g)} + 1/2\ O_{2(g)} \rightarrow SnO_{2(s)} \quad (2.3)$$

$$CO_{(g)} + 1/2\ O_{2(g)} \rightarrow CO_{2(g)} \quad (2.4)$$

Figure 2.4 shows FE-SEM images of the SnO material grown using inert synthesis atmosphere. It was found that this material is composed of both micro-disks and nanobelts. Due to the size difference between these structures, it was possible to separate them by sedimentation. The diameter of the disks ranging from 500 nm up to several microns and their surface can be flat and smooth (Fig. 2.4a) or in steps with a sphere in the top (Fig. 2.4b), as also reported by Dai et al. and Orlandi et al. [11, 39]. Figure 2.4c indicated that the nanobelts are also flat and homogeneous along their length; most of them presenting metallic tin particles at their tips (Fig. 2.4d). The presence of these particles is related to their growth mechanism, which occurs by a self-catalytic VLS method [8, 11, 25]. It also is possible to observe from Fig. 2.4e that some SnO nanobelts present dendrites perpendicular to the growth axis of the belt. The dendrites are very thin and generally present a metallic sphere at its extremity. The width distribution histogram of the SnO nanobelts shown in Fig. 2.4f reveals the maximum width frequency to be between 20 and 30 nm and approximately 90% of the nanobelts smaller than 50 nm in width.

Since the presence of metallic spheres in one end of the SnO nanobelts was observed, it is proposed that the growth mechanism of these structures occurs by VLS [11, 25]. The VLS growth mechanism involves the presence of catalyst particles, and once they were formed during the synthesis, the SnO nanobelts grow by a self-catalytic VLS process. After the reduction of the SnO_2 power by the carbon black, only vapor of SnO and CO is formed inside the tube according to the Eq. 2.2. Since no oxygen is considered to be in the synthesis atmosphere, the SnO vapor can react with CO and produce metallic tin in the liquid phase (Eq. 2.5) and CO_2. The Sn° particles act as active sites for adsorption of SnO vapor molecules, and after they become supersaturated with SnO vapor, the first solid core of SnO is obtained. Thus, while the metallic drop remains in the liquid form and enough SnO vapor is present, the growth of the nanobelt will occur in a direction oriented by the core [11].

$$SnO_{(g)} + CO_{(g)} \rightarrow Sn^{0}{}_{(l)} + CO_{2(g)} \quad (2.5)$$

FE-SEM images of the Sn_3O_4 materials collected after the synthesis are shown in Fig. 2.5. In general, these structures present the same characteristics of the SnO_2 and SnO nanobelts, i.e., they are 1D nanostructures with dozens of micrometers in length and rectangular cross-section (Fig. 2.5a). These structures exhibit homogeneous width along the length, but a detailed characterization performed by high-resolution FE-SEM reveals that Sn_3O_4 nanobelts present a layered surface (Fig. 2.5b). The layered characteristic is related to their growth mechanisms, and it is similar to the model proposed by Ma et al. for layered SnO_2 nanobelts [40]. Figure 2.5c shows

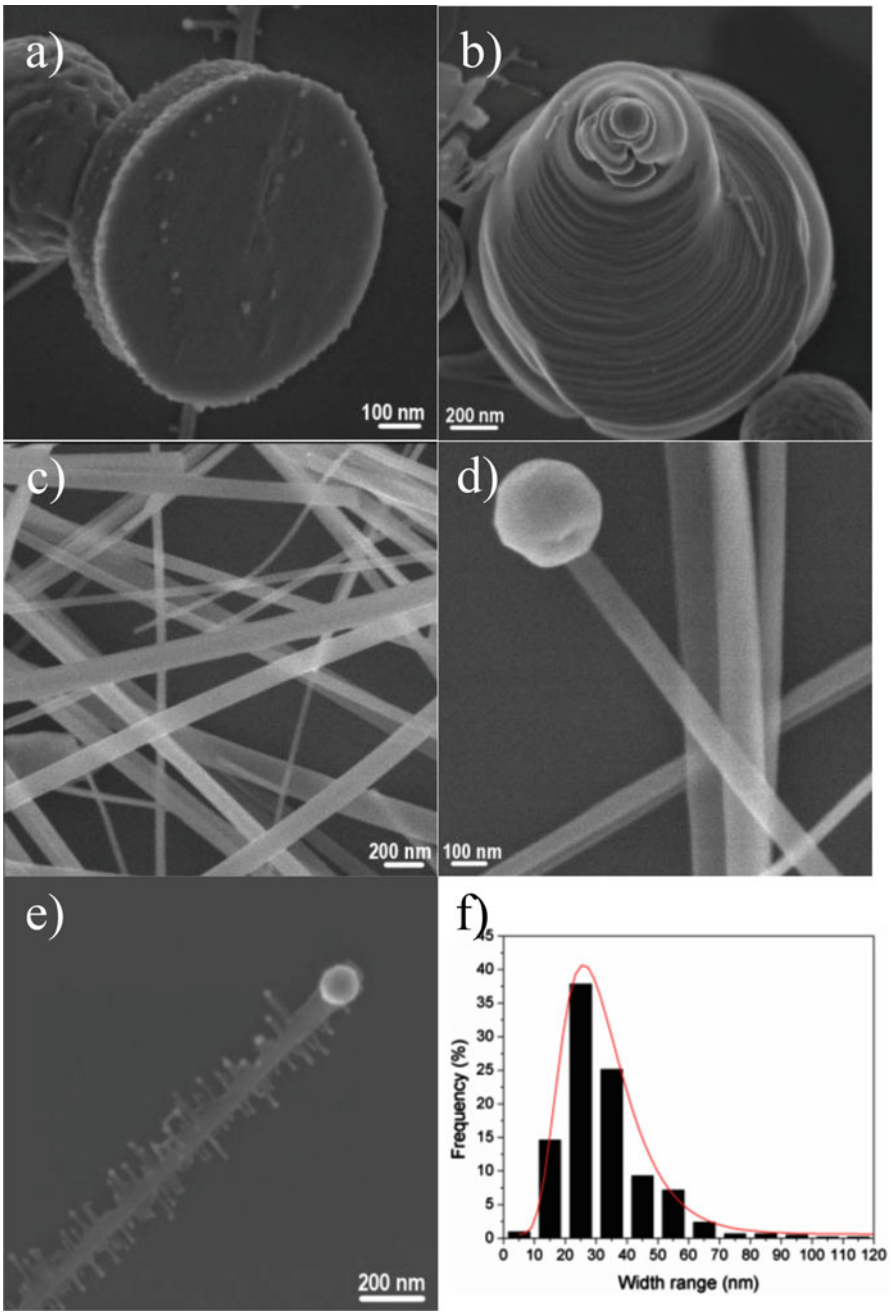

Fig. 2.4 FE-SEM images of SnO disks with (**a**) flat and (**b**) in-step surface. FE-SEM images showing (**c**) a general view of the SnO nanobelts, (**d**) their smooth surface, and (**e**) one nanobelt with dendrites in their structures. (**f**) Width distribution histogram of the belts

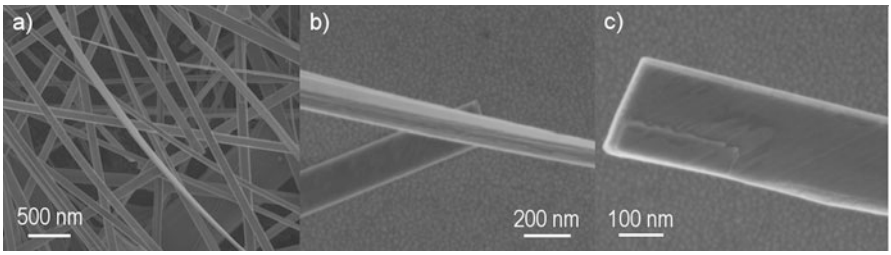

Fig. 2.5 (**a**) General view of the structures present in the Sn_3O_4 material. (**b**) High-resolution FE-SEM image showing the layered character of nanobelts. In (**c**) the initial stage of growth of a new layer on the surface of a nanobelt is showed

the initial growth stage of a new Sn_3O_4 layer. The Sn_3O_4 nanobelts present single-modal width distribution with a maximum frequency at the range of 80–120 nm.

Since no metallic particles were observed at Sn_3O_4 nanobelt extremities, it was proposed that they grow by a VS process according to Eqs. 2.2 and 2.6. After the reduction of the SnO_2 powder by the carbon black (Eq. 2.2), some SnO vapor molecules will react with the oxygen introduced in the counterflow (Eq. 2.6) in order to grow structures in an intermediate phase of tin oxide (Sn_3O_4). Despite the fact that SnO_2 and Sn_3O_4 nanobelts grow in the same synthesis, the Sn_3O_4 nanobelts are formed in a region closest to the center of the tube, i.e., in a region of lower oxygen concentration, which explains this material to grow in a more reduced state of tin oxide.

$$3SnO_{(g)} + 1/2\ O_{2(g)} \rightarrow Sn_3O_{4(s)} \tag{2.6}$$

All synthesized structures were also characterized by TEM. Figure 2.6a shows a low-magnification TEM image of SnO_2 nanobelt, confirming the homogeneous width along the length. Figure 2.6b presents the selected area electron diffraction (SAED) pattern of the nanobelt showing the single-crystalline character of each belt. The SAED pattern confirms that nanobelts grow in the SnO_2 cassiterite phase. An HRTEM image of the SnO_2 nanobelts is presented in Fig. 2.6c, and the indexed interplanar distance showed are 0.26 ± 0.01 nm and 0.33 ± 0.01 nm, which correspond to the (101) and (110) planes of the SnO_2 tetragonal structure, respectively. This means that belts grow preferentially in the [101] direction, which agrees with the XRD results.

Figure 2.7a shows a low-magnification TEM image of a flat-surface disk with an octagon shape. An HRTEM image of the disk is presented in Fig. 2.7b, and the interplanar distance indexed is 0.27 ± 0.01 nm, related to the (110) planes of the tetragonal structure of SnO (JCPDS card #6-395). The inset in Fig. 2.7b presents the SAED pattern confirming that disks are single-crystalline materials. All of the spots in the SAED pattern can be indexed by the litharge structure of SnO (tetragonal), confirming the HRTEM results. The SnO disks presented the so-called Giant Chemoresistance Response (GCR) when used as a sensor for NO_2 gas.

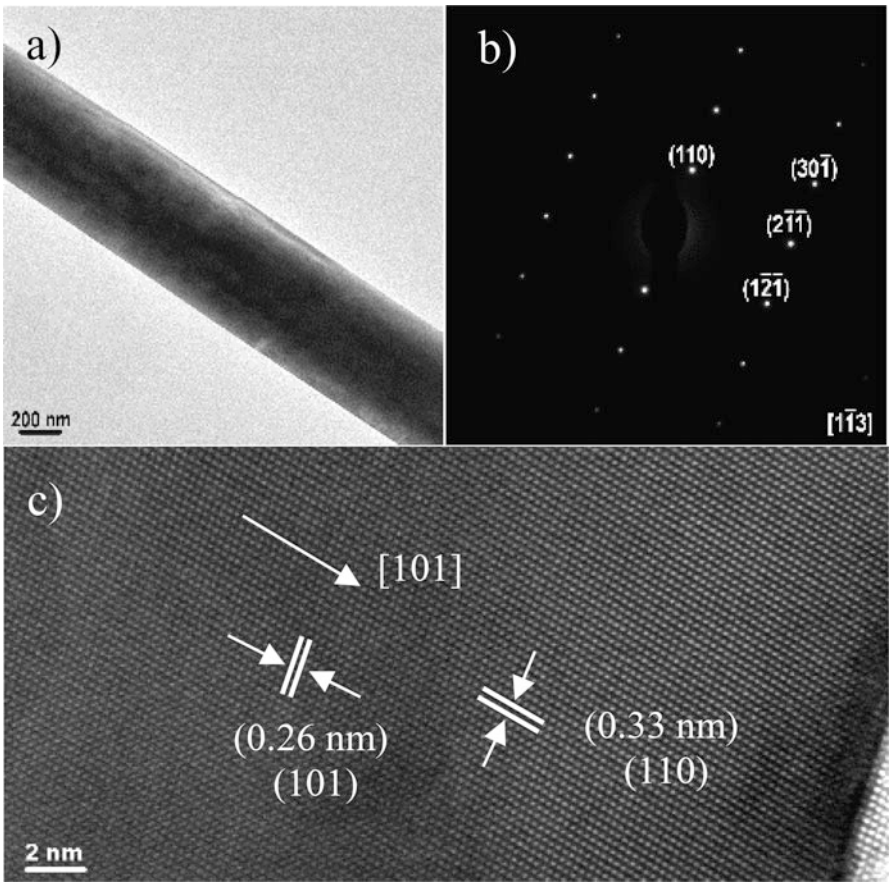

Fig. 2.6 (**a**) Low-mag TEM image of a SnO_2 nanobelt, (**b**) SAED pattern, and (**c**) HRTEM image of the belt

Figure 2.8 shows a low-magnification TEM image of typical SnO nanobelts. The corresponding EDS spectrum of the smaller nanobelt and of the nanoparticle is shown in Fig. 2.8a–c, respectively. From EDS results, it was found that the nanobelt was composed of tin oxide, while the nanoparticles consisted basically of metallic tin. Besides, the nanobelts presented a Sn concentration of 49 ± 3 (% atomic) and of 51 ± 3 (% atomic) for O, which is close to SnO stoichiometry. A SnO nanobelt with a metallic drop at one extremity is shown in Fig. 2.8d, which also presents the SAED pattern of this belt (inset). The SAED shows that the nanobelt is a single crystal and it can be indexed by the orthorhombic structure of SnO (JCPDS #13-0111). The HRTEM image of the SnO nanobelt presented in Fig. 2.8e confirms that the nanobelts are single crystalline. Additionally, the obtained interplanar distance of 0.37 nm is related to the [110] planes of the orthorhombic structure of the SnO which arises from a normal growth direction by about 8°, meaning that the SnO nanobelts grow in the [110] direction.

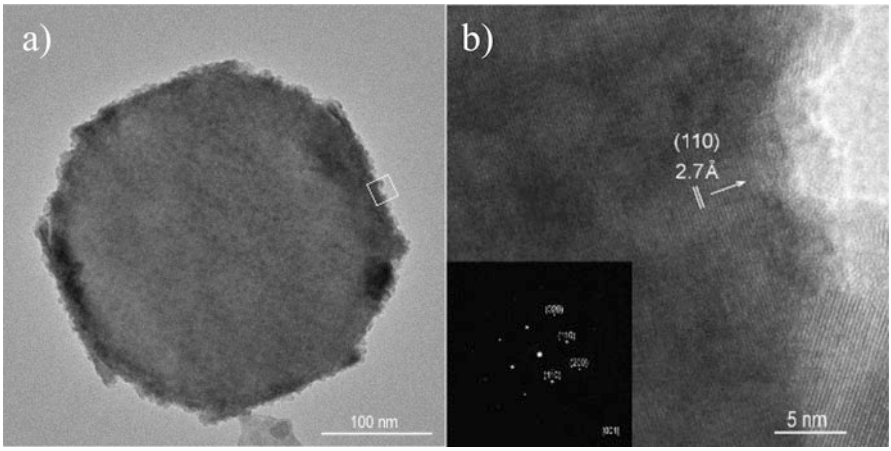

Fig. 2.7 (**a**) Low-mag TEM image of a typical faceted disk and (**b**) HRTEM image of the white square area selected in (**a**). The inset in (**b**) is the SAED pattern of the disk (Figure from Ref. [15] with permission from Elsevier)

Figure 2.9a presents a low-magnification TEM image of a Sn_3O_4 nanobelt. The color contrast is related to the mass difference along the belt, which is an evidence of the layered character of these structures (darker part of the belts represents the thicker regions). The chemical analysis performed by EDS characterization confirms that the nanobelts are composed only by Sn and O atoms, as shown in Fig. 2.9b (the carbon and copper peaks of EDS spectrum are due to the carbon-coated copper grids used in the analysis). SAED pattern (Fig. 2.9c) reveals that the nanobelts are single-crystalline structures and each layer is supposed to serve as a substrate for a layer-by-layer growth. A HRTEM image of the belt is shown in Fig. 2.9d. The indexed interplanar distance of 3.7 ± 0.1 Å is related to [−101] and [101] planes, while the 2.9 ± 0.1 Å interplanar distance is related to the [200] plane.

Tin oxide is one of the most studied materials for sensor application, so the ability to synthesize tin oxide with different oxidation states can enable in obtaining more sensitive and selective sensors. We have studied the sensor response of all tin oxide materials reported above, and results show that SnO and Sn_3O_4 materials can present better response than SnO_2. This opens new applications of nonstoichiometric tin oxide materials, and they also must be applied in other areas, such as solar cells and electronic devices.

5 Obtaining ZnO Nanostructures

The carbothermal reduction process is one of the most used methods for the growth of ZnO nanostructures with different morphologies. Along with the CVD method, it has demonstrated the possibility of obtaining a wide variety of crystal morphologies

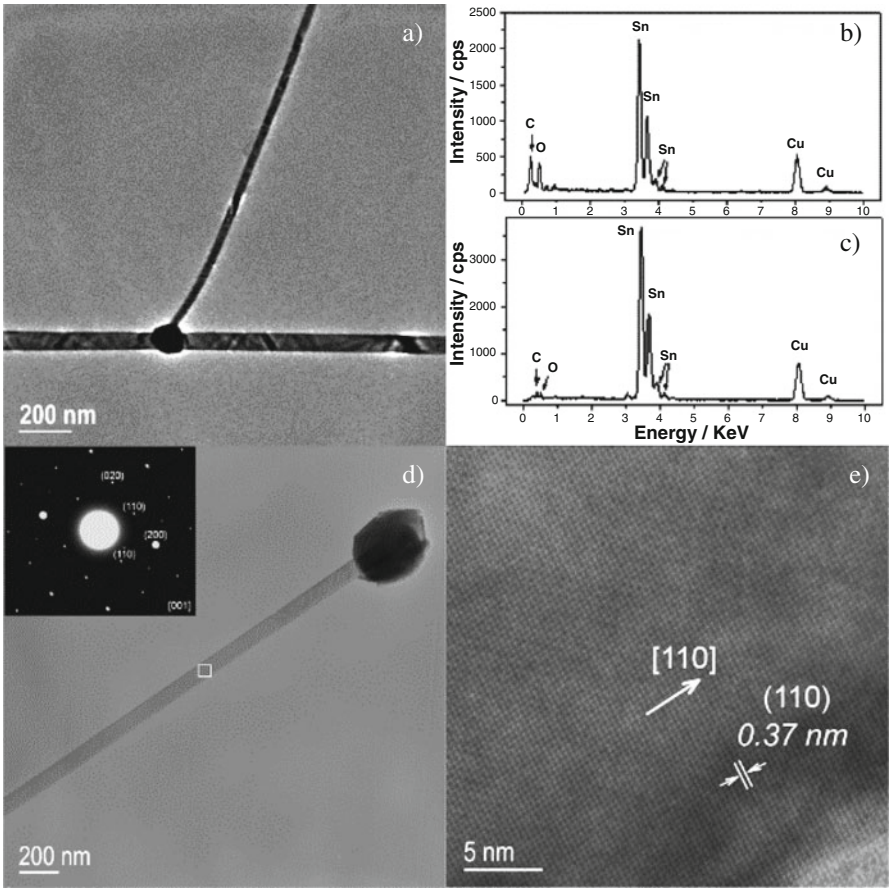

Fig. 2.8 (**a**) Low-magnification TEM image of VLS nanobelts. (**b**) EDS spectrum of the nanobelt of Fig. 2.4a. (**c**) EDS spectrum of a metallic tin nanoparticle. (**d**) Low-magnification TEM image of other VLS nanobelt. The inset shows the SAED of the belt. (**e**) HRTEM image of the SnO VLS nanobelt marked in (**d**) (Figure from Ref. [11] with permission from American Chemical Society)

with excellent properties for applications in several technological areas [41, 42]. The reduction of ZnO to Zn vapor by using carbon occurs at temperatures above 900 °C (as indicated by the Ellingham diagram), and different structures can be grown in lower temperatures with or without the presence of oxygen gas in the synthesis atmosphere. There is a great interest in the growth of ZnO nanostructures at low temperatures, since it would increase the kind of substrates for the oriented growth reducing the effects of high temperature, such as the diffusion of elements from the substrates to the nanostructures. This avoids the need for more elaborate processes including the use of buffer layer as reported by Duclère et al. [43], which used cerium oxide (CeO_2) layer to obtain epitaxial growth of ZnO thin films by pulsed laser deposition technique on sapphire substrates. The diffusion of aluminum

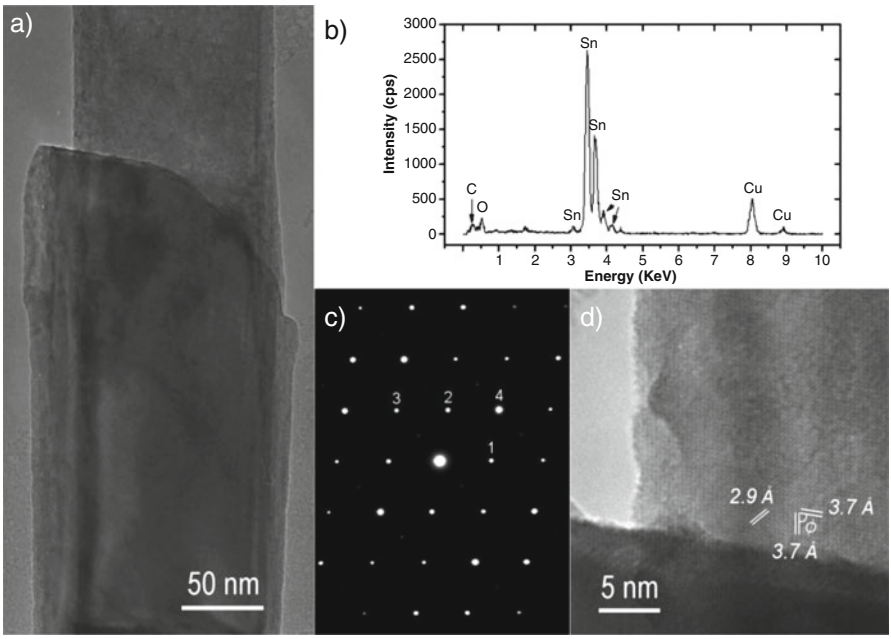

Fig. 2.9 (**a**) Bright-field TEM image of a layered nanobelt. (**b**) EDS spectrum of the thin layer of belt. (**c**) SAED pattern. The points 1, 2, 3, and 4 are related to the planes (−101), (101), (200), and (002), respectively. (**d**) HRTEM image of the belt

from the sapphire (Al_2O_3) may be unfavorable to the production of epitaxial ZnO at temperatures around 900 °C, leading to the formation of the $ZnAl_2O_4$ layer located at the interface between ZnO and sapphire [44].

Lim et al. [45] studied the formation of zinc oxide using graphite and three types of carbon black as carbon sources, whose surface areas were 3.5 m^2/g for graphite and 70, 236 and 1,440 m^2/g for carbon black materials. The study was conducted at 800 °C for 30 min under airflow. Results suggested that the reduction of ZnO to Zn vapor is strongly linked to the surface area of the carbon source, since increasing its surface area increases the formation of zinc silicate islands until complete formation of a zinc silicate layer. Finally, using the carbon black with larger surface area, ZnO nanorods were grown over zinc silicate layer (Figure 2.10). Authors associated the formation of zinc silicate, followed by the growth of ZnO nanorods, due to the increased formation of the Zn vapor phase.

Hence, the proposed mechanism of ZnO reduction is associated with (i) carbon vaporization via carbon dioxide to form carbon monoxide, (ii) the carbon monoxide diffusion for surface of ZnO, (iii) reduction of ZnO by carbon monoxide forming Zn vapor, and (iv) diffusion of Zn vapor and the carbon dioxide returning to the first stage.

The ZnO reduction kinetics in the presence of carbon can be improved by using additives such as Fe_2O_3, mills scale, and $CaCO_3$ [46]. Usually, additives are used to generate a percentage of Zn from the ZnO powder. The increased reaction rate

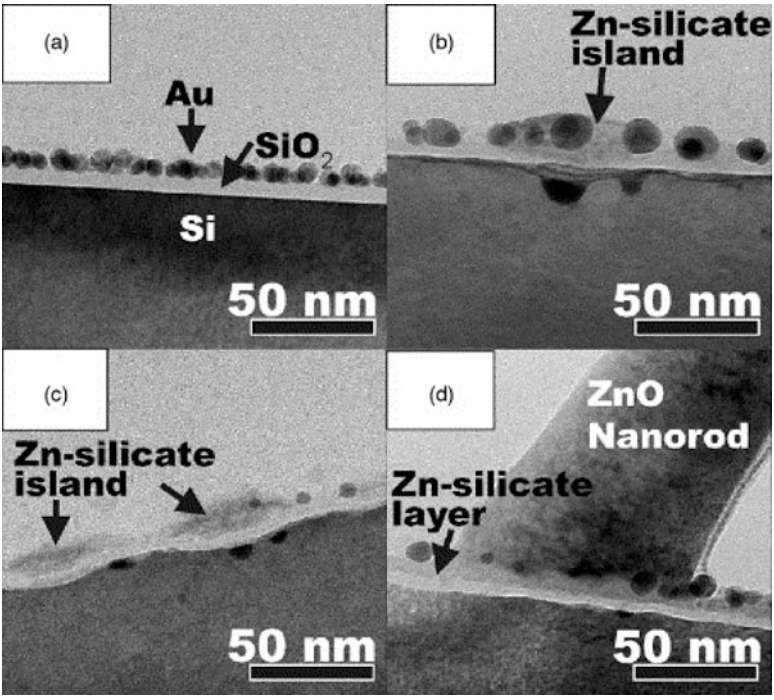

Fig. 2.10 Cross-sectional TEM micrographs of samples fabricated by using (**a**) graphite (3.5 m^2/g), (**b**) *carbon black* (70 m^2/g), (**c**) *carbon black* (236 m^2/g), and (**d**) *carbon black* (1440 m^2/g) carbon source (Figure from Ref. [45] with permission from Elsevier)

by using additives to the mixture of ZnO and carbon may be related to the easy production of CO and CO_2 gases by reaction of these additives with solid carbon, and, therefore, the Boudouard reaction is promoted on the carbon surface, which results in a rapid reduction rate. Figure 2.11 compares the reduction rate curves with various additives in certain weight percentages of ZnO at 1323 K. From this, the spherical shrinking core model (SCM) is well diffused to calculate and compare the energy response in the absence and presence of additives and has proven to be useful to describe the kinetics of the reaction.

Carbothermic reduction processes using microwave radiation has been employed in order to reduce energy costs and promote improvements in reduction rates [47, 48]. The method consists of heating a mixture of ZnO and a reducing agent rich in carbon with the incidence of microwave radiation. In the processing of ceramic materials, the energy of microwaves interacts with the matter at the molecular level, and material heating depends on the dielectric properties, the depth of penetration, as well as the frequency of microwave [49]. The dielectric properties of materials can in principle be considered as one of the most important features to evaluate the effects of heating due to microwaves, and the ability of a dielectric material to absorb microwave energy is given by its permittivity.

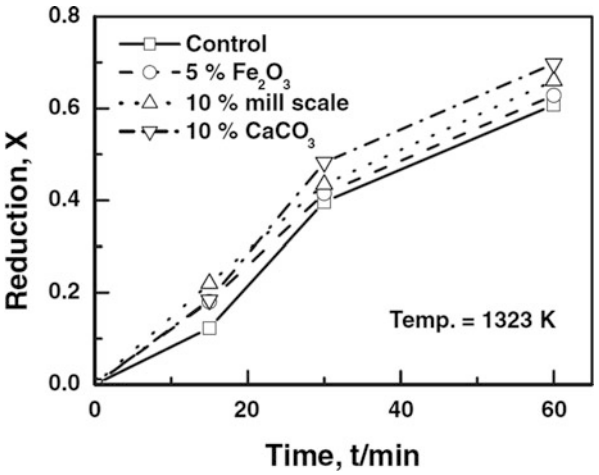

Fig. 2.11 Effect of additives on the ZnO carbon reaction system (Figure from Ref. [46] with permission from The Japan Institute of Metals)

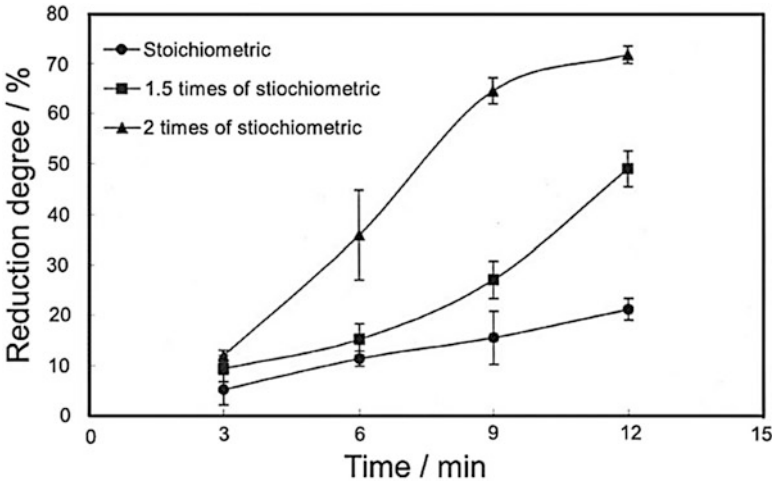

Fig. 2.12 Effect of carbon stoichiometry on microwave reduction of zinc oxide concentrate (Figure from Ref. [52] with permission from Elsevier)

Although the permittivity (and dielectric loss) of ZnO increases by increasing the temperature [50], its value is small at room temperature, resulting in a slower heating in the presence of microwaves [51]. However, carbon sources present high-microwave absorption and are the main responsible for the heating, which consequently promote the reduction of ZnO. A higher reduction rate can be achieved by increasing the carbon concentration in the mixture. Figure 2.12 shows the percentage of the ZnO reduction as function of time for different stoichiometries of ZnO and carbon source using microwave as a heating source.

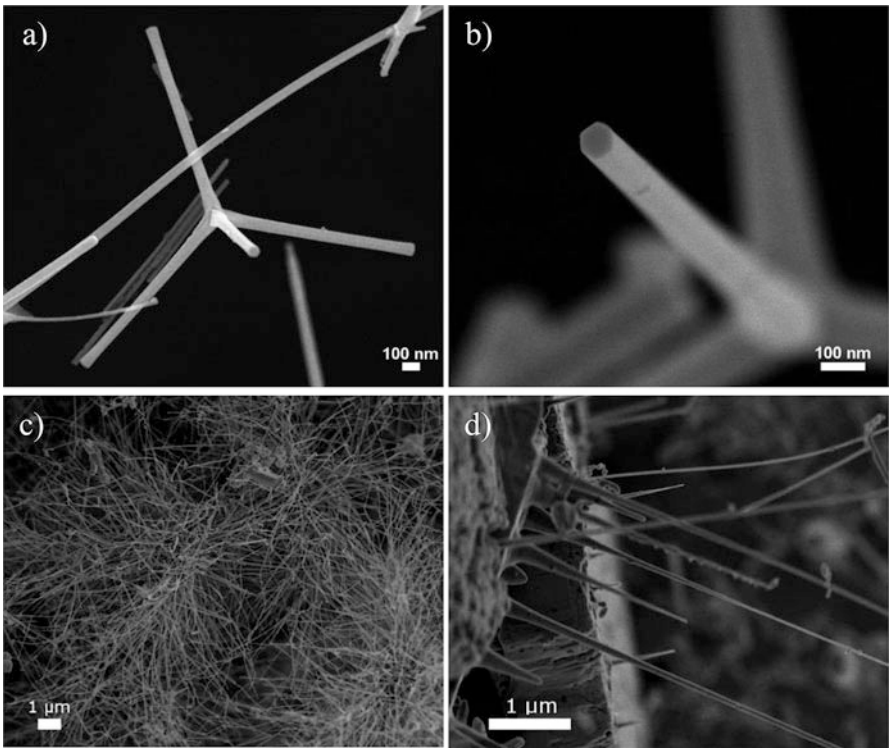

Fig. 2.13 FE-SEM images of ZnO tetrapods synthesized by the carbothermal reduction process, (**a**) an individual tetrapod, (**b**) detail of the hexagonal shape, (**c**) nanowires grown on a silicon substrate, and (**d**) growth of ZnO nanowires from plates

Using the carbothermal reduction process associated with other techniques, different ZnO nanostructured morphologies with peculiar properties can be obtained, and tetrapods and nanowires are the most common shapes.

From Fig. 2.13a–d, it is possible to observe the effectiveness of the method for obtaining tetrapods (Fig. 2.13a, b) [14] and nanowires (Fig. 2.13c, d). The carbon black was used as carbon source in the molar ratio of 1:1, and the synthesis was performed at 1,100 °C. Tetrapods have a hexagonal cross-section and a diameter lower than 100 nm. In this case, no support substrate or any types of metal catalyst were necessary to induce the growth, which is based on the VS model. For the ZnO nanowires, silicon substrates with Au catalyst layer were used to induce the growth. However, the wires grow from a layer containing ZnO plates over the silicon substrate. There is considerable homogeneity of wires with a circular cross-section, and their diameters are below 100 nm. ZnO usually crystallizes in the hexagonal wurtzite crystal structure, which is composed of Zn^{2+} and O^{2-} arranged in a tetrahedral shape and stacked alternately along the direction of the c-axis.

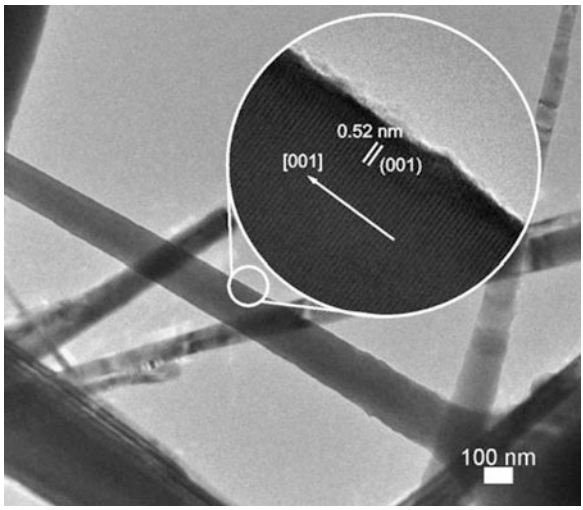

Fig. 2.14 Image of an individual ZnO tetrapod. In the inset, a HRTEM image is shown (Figure from Ref. [14] with permission from Hindawi Publishing Corporation)

Figure 2.14 shows the crystallinity degree of the tetrapods from the HRTEM image, where it is possible to confirm that material grows free of defects, featuring each "foot" of the tetrapod as a single crystal. The interplanar distance of the crystal planes in the growth direction has 0.52 nm, which refers to the (001) plane. This plane makes an angle of 90° to the growth direction of each tetrapod foot. Therefore, the [001] is the growth direction of ZnO tetrapods, which is preferred due to the self-catalytic property of the (001) plane for the ZnO structure [53].

6 Indium Tin Oxide Nanowires

Indium tin oxide (ITO) is one of the most studied transparent and conductor oxides (TCOs) used in optical electronics applications to combine high-optical transparency and high electrical conductivity [54–56]. It may be formed either by tin-doped indium oxide or vice versa, having the replacement of some indium atoms by the tin atoms. The growth of 1D ITO nanostructures has been reported by several groups since the first study on In_2O_3 nanobelts in 2001 [13, 57–59]. ITO nanowires, which have a large surface area, high electrical conductivity, and high crystallinity, can allow novel applications such as it interconnects in integrated nanoscale devices and electrodes for solar cells [58, 60, 61].

Due to the practical importance of ITO material, many methods have been used to prepare ITO nanostructures (e.g., nanowires, nanobelts, and nanorods), such as sputtering [60], coprecipitation annealing [62], electrospinning [63], pulsed laser ablation process [64], thermal evaporation [58, 59, 65], and carbothermal reduction [13, 66, 67, 68].

Among these methods, the carbothermal reduction syntheses result in the production of nanowires with features such as excellent homogeneity and crystallinity, besides allowing the obtaining of materials at lower temperatures compared to conventional thermal evaporation [13, 67].

ITO nanowires were synthesized by a carbothermal reduction method using the co-evaporation of oxides (In_2O_3 e SnO_2) mixed with carbon black as the reducing agent. As discussed above, in this process, the reaction between carbon and oxides is crucial, and thus the temperature and atmosphere during the synthesis must be tightly controlled, especially for avoiding the presence of oxygen, given that this can react with carbon before it reduces the oxides. Accordingly, several parameters may alter the composition, morphology, and yield of the grown material; the most significant parameters are the composition of the starting material (proportion of carbon/oxide) and the inert gas flux, followed by the time and temperature of synthesis.

Results obtained by changing the oxide to carbon black ratio in the starting material allowed good control of the nanowire stoichiometry enabling to obtain ITO nanowires in In_2O_3 or SnO_2 structures. Thus, properly controlling the ratio between carbon black and the oxides, the In:Sn ratio in the nanowires, and consequently the doping level, can be controlled, which is a determining factor for the conductivity of the material [68].

The influence of synthesis parameters was studied in detail for obtaining ITO nanowires, and it was found that the growth parameters which combine characteristics such as homogeneity, transparency, conductivity, and yield were the molar ratio for the starting material of $1SnO_2 + 1C$ and $1In_2O_3 + 1C$, nitrogen flow rate of 80 cm^3/min, synthesis time of 60 min, and temperature of 1150 °C. Synthesis details are given in ref. [67].

The XRD pattern (Fig. 2.15) of the collected materials can be indexed by the following phases: $In_{0.2}Sn_{0.8}$ (JCPDS card # 48-1547) and ITO (card # 89-4597). It is important to mention that it is not possible to distinguish the ITO and In_2O_3 phases without Rietveld refinement. The Al peaks are related to the aluminum sample holder used in the XRD measurements and have no correlation with the sample. The ITO phase is present in a higher amount than the metallic alloy, and have preferential orientation for the (400) planes (35.5°). No tin oxide phases were observed because following the phase diagram of In_2O_3 and SnO_2 [69], up to about 15 mol% of tin atoms can be in the solid solution in the In_2O_3 matrix without any secondary phase.

From the FE-SEM images in Fig. 2.16, it is possible to observe that ITO material is composed of 1D structures with well-defined edges, having homogeneous width along their lengths and no apparent superficial defects. Besides, we note that materials have a square cross-section due to the cubic phase of ITO, meaning ITO structures are nanowires. The metallic spheres at one extremity of wires suggest that growth mechanism of the wires follows a vapor-liquid-solid (VLS) process.

Using HRTEM characterization, it was possible to confirm that the wires grow in the (100) planes of the ITO phase (Fig. 2.17). This result agrees with the XRD analysis, which showed preferential orientation for this family of planes and also

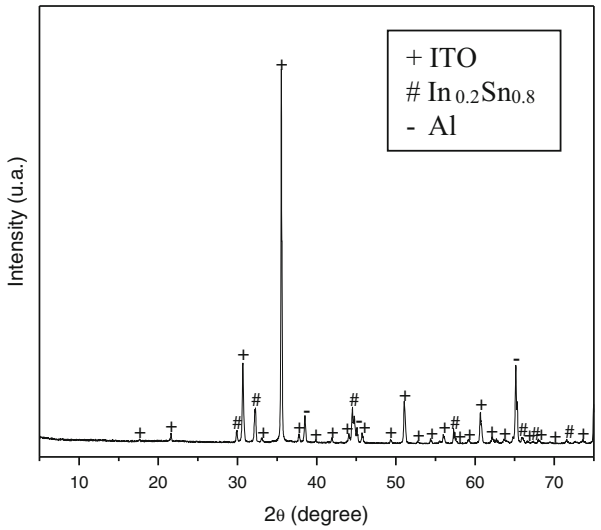

Fig. 2.15 XRD pattern of the collected material after the synthesis

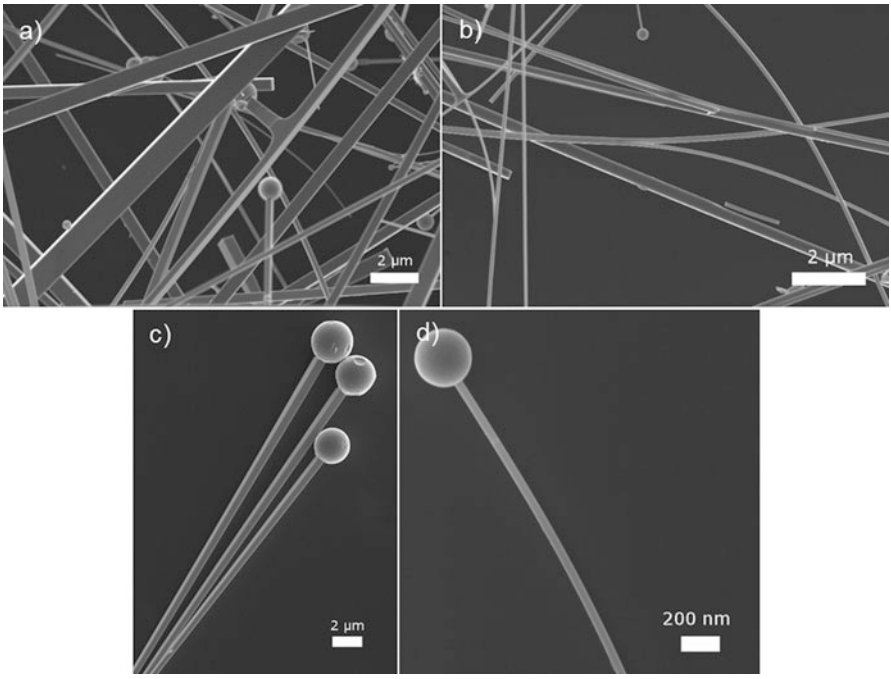

Fig. 2.16 (**a**,**b**) Low magnification FE-SEM images of typical ITO nanowires obtained at 1,150 °C. (**c**,**d**) High magnification images of ITO nanowires presenting metallic droplets at extremities

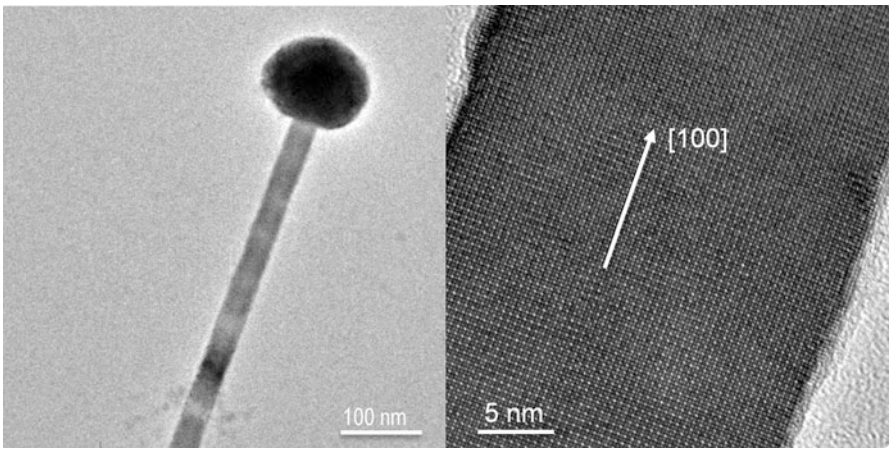

Fig. 2.17 TEM image of a typical ITO nanowire and the respective high-resolution (HRTEM) image showing the growth direction of wires

explains the origin of the square cross-section of ITO nanowires. The EDS study revealed that the wires are constituted of indium, tin, and oxygen atoms with a In:Sn proportion of 89:11 at%, confirming that carbothermal reduction is an efficient method to obtain 1D ITO nanostructures. Meanwhile, the chemical analysis showed that the spheres are composed of a Sn-rich Sn-In alloy with the same proportion obtained by XRD [67].

When obtaining ITO nanowires, the catalyst is generated in its own synthesis, meaning that the growth mechanism is related to a self-catalytic VLS process. The reactions that occur from the mixture of indium oxide with carbon during synthesis are:

$$In_2O_{3(s)} + C_{(s)} \rightarrow In_2O_{(g)} + CO_{2(g)} \tag{2.7}$$

$$In_2O_{(g)} + CO_{(g)} \rightarrow 2In^0{}_{(l)} + CO_{2(g)} \tag{2.8}$$

Then, the SnO_2 is reduced to metallic tin through the Eqs. (2.2) and (2.5). The In_2O_3 can also be reduced to metallic indium by means of the Eqs. (2.7) and (2.8) when the In_2O reacts with the carbon monoxide generated by the Eq. (2.2). These equations indicate how the catalyst metals are generated to adsorb vapor and allow growth of ITO nanowires.

It is known that these reactions occur more readily at higher temperatures, and ITO nanowires were synthesized from 1,000 to 1,200 °C. However, results indicated that at higher temperatures the carbothermal reduction process produces a significant increase of tin amount in the synthesis atmosphere. Another consequence of performing synthesis at higher temperatures is the increased width/thickness ratio of the nanowires (Fig. 2.18a). In some cases, it leaves the formation of microwires

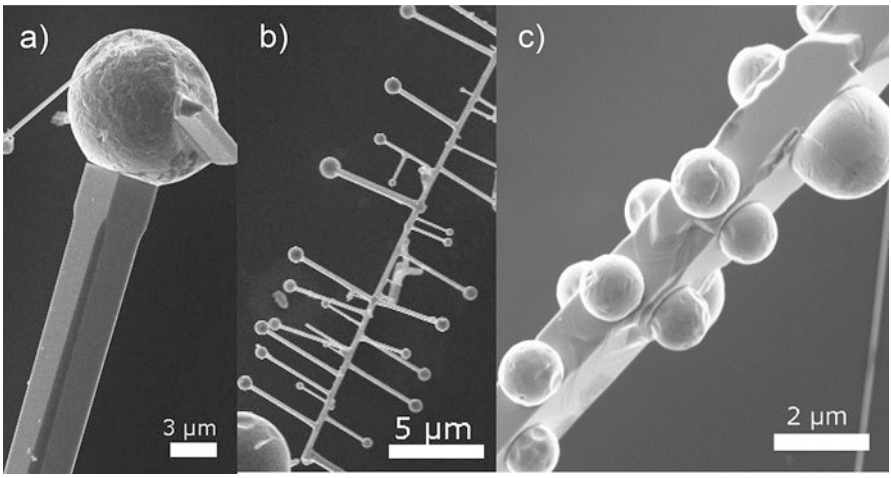

Fig. 2.18 (**a**) Detail of a ITO nanowire presenting square cross section. (**b**) A ITO nanowire with perpendicular dendrites and (**c**) initial stage of dendrite growth

(width greater than 1 μm) instead of nano-sized structures. The increase in the nanowire's width is related to the increased diameter of the catalyst metallic drop at higher temperatures. Some synthesized nanowires showed a great concentration of dendrites, which is related to the increased amount of metallic tin available in the atmosphere of synthesis (Fig. 2.18b). Figure 2.18c illustrates the deposited metallic spheres on a nanowire edge that would give rise to dendrites.

From the results shown above, it is possible to note the versatility to produce ITO nanowires by carbothermal evaporation method. Wires grow by a self-catalytic VLS process, which avoid contamination by an external catalytic agent. However, when there is a need for growing nanowires on specific sites on a substrate, it is possible to use the catalyst VLS growth (usually using gold as catalyst), which allows a more controlled growth position [65, 70].

In short, it can be concluded that the ITO nanowire's synthesis by carbothermal reduction enables, besides versatility and high performance, to control the doping level, the width/thickness ratio, and the presence of dendrites, depending on the desired application. Therefore, it is possible to choose the optimal synthesis conditions, which certainly will facilitate obtaining more complex materials with properties/characteristics desired for a wide range of technological applications.

References

1. Lu W, Lieber CM (2007) Nanoelectronics from the bottom up. Nat Mater 6(11):841–850
2. Zhang Q, Ha ST, Liu X, Sum TC, Xiong Q (2014) Room-temperature near-infrared high-Q perovskite whispering-gallery planar nanolasers. Nano Lett 14(10):5995–6001
3. Zhu H, Fu Y, Meng F, Wu X, Gong Z, Ding Q, Gustafsson MV, Trinh MT, Jin S, Zhu XY (2015) Lead halide perovskite nanowire lasers with low lasing thresholds and high quality factors. Nat Mater 14(6):636–642

4. Mao Y, Banerjee S, Wong SS (2003) Large-scale synthesis of single-crystalline perovskite nanostructures. J Am Chem Soc 125(51):15718–15719
5. Zhou W, Liu H, Boughton RI, Du G, Lin J, Wang J, Liu D (2010) One-dimensional single-crystalline Ti-O based nanostructures: properties, synthesis, modifications and applications. J Mater Chem 20(29):5993–6008
6. Yu S-H (2001) Hydrothermal/solvothermal processing of advanced ceramic materials. J Ceram Soc Jpn 109(1269):S65–S75
7. Xiao Z, Xia Y, Ren Z, Liu Z, Xu G, Chao C, Li X, Shen G, Han G (2012) Facile synthesis of single-crystalline mesoporous [small alpha]-Fe2O3 and Fe3O4 nanorods as anode materials for lithium-ion batteries. J Mater Chem 22(38):20566–20573
8. He C, Chang S, Huang X, Wang Q, Mei A, Shen PK (2015) Direct synthesis of pure single-crystalline Magneli phase Ti8O15 nanowires as conductive carbon-free materials for electrocatalysis. Nanoscale 7(7):2856–2861
9. Hu X, Tang Y, Xiao T, Jiang J, Jia Z, Li D, Li B, Luo L (2010) Rapid synthesis of single-crystalline SrSn(OH)6 nanowires and the performance of SrSnO3 nanorods used as anode materials for Li-ion battery. J Phys Chem C 114(2):947–952
10. Suman PH, Orlandi MO (2011) Influence of processing parameters on nanomaterials synthesis efficiency by a carbothermal reduction process. J Nanopart Res 13(5):2081–2088
11. Orlandi MO, Leite ER, Aguiar R, Bettini J, Longo E (2006) Growth of SnO nanobelts and dendrites by a self-catalytic VLS process. J Phys Chem B 110(13):6621–6625
12. Suman PH, Longo E, Varela JA, Orlandi MO (2014) Controlled synthesis of layered Sn3O4 nanobelts by carbothermal reduction method and their gas sensor properties. J Nanosci Nanotechnol 14(9):6662–6668
13. Orlandi MO, Aguiar R, Lanfredi AJC, Longo E, Varela JA, Leite ER (2005) Tin-doped indium oxide nanobelts grown by carbothermal reduction method. Appl Phys A 80(1):23–25
14. Silva RA, Orlandi MO (2016) Influence of synthesis route on the radiation sensing properties of ZnO nanostructures. J Nanomater 2016:9
15. Suman PH, Felix AA, Tuller HL, Varela JA, Orlandi MO (2013) Giant chemo-resistance of SnO disk-like structures. Sensors Actuators B Chem 186:103–108
16. Suman PH, Felix AA, Tuller HL, Varela JA, Orlandi MO (2015) Comparative gas sensor response of SnO2, SnO and Sn3O4 nanobelts to NO2 and potential interferents. Sensors Actuators B Chem 208:122–127
17. Zhong Y, Shaw LL, Manjarres M, Zawrah MF (2010) Synthesis of silicon carbide nanopowder using silica fume. J Am Ceram Soc 93(10):3159–3167
18. Huang B, Zheng X, Fan X, Song G, Lu M (2011) Enhanced rate performance of nano–micro structured LiFePO4/C by improved process for high-power Li-ion batteries. Electrochim Acta 56(13):4865–4868
19. Samsonov GV (1973) The oxide handbook. IFI/Plenum. Springer, New York
20. Dai ZR, Pan ZW, Wang ZL (2001) Ultra-long single crystalline nanoribbons of tin oxide. Solid State Commun 118(7):351–354
21. Dai ZR, Gole JL, Stout JD, Wang ZL (2002) Tin oxide nanowires, nanoribbons, and nanotubes. J Phys Chem B 106(6):1274–1279
22. Yang P, Lieber CM (1996) Nanorod-superconductor composites: a pathway to materials with high critical current densities. Science 273(5283):1836–1840
23. Yang P, Lieber CM (1997) Columnar defect formation in nanorod/Tl2Ba2Ca2Cu3Oz superconducting composites. Appl Phys Lett 70(23):3158–3160
24. Ya-Juan H, Jakob BW, Dang Sheng S, Guo-Qiang J, Xiang-Yun G (2006) Beaded silicon carbide nanochains via carbothermal reduction of carbonaceous silica xerogel. Nanotechnology 17(12):2870
25. Wagner RS, Ellis WC (1964) Vapor-liquid-solid mechanism of single crystal growth. Appl Phys Lett 4(5):89–90
26. Zhang Y, Wang N, Gao S, He R, Miao S, Liu J, Zhu J, Zhang X (2002) A simple method to synthesize nanowires. Chem Mater 14(8):3564–3568

27. Devan RS, Patil RA, Lin J-H, Ma Y-R (2012) One-dimensional metal-oxide nanostructures: recent evelopments in synthesis, characterization, and applications. Adv Funct Mater 22(16):3326–3370
28. Zhai T, Li L, Ma Y, Liao M, Wang X, Fang X, Yao J, Bando Y, Golberg D (2011) One-dimensional inorganic nanostructures: synthesis, field-emission and photodetection. Chem Soc Rev 40(5):2986–3004
29. Wang S, Yang J, Zhang H, Wang Y, Gao X, Wang L, Zhu Z (2015) One-pot synthesis of 3D hierarchical SnO2 nanostructures and their application for gas sensor. Sensors Actuators B Chem 207(Part A):83–89
30. Nagasawa K, Takao S, S-i N, Samjeské G, Sekizawa O, Kaneko T, Higashi K, Yamamoto T, Uruga T, Iwasawa Y (2015) Surface-regulated nano-SnO2/Pt3Co/C cathode catalysts for polymer electrolyte fuel cells fabricated by a selective electrochemical Sn deposition method. J Am Chem Soc 137(40):12856–12864
31. Yuan J, Li H, Wang Q, Zhang X, Cheng S, Yu H, Zhu X, Xie Y (2014) Facile fabrication of aligned SnO2 nanotube arrays and their field-emission property. Mater Lett 118:43–46
32. Yu S, Li L, Xu D, Dong H, Jin Y (2014) Characterization of SnO2/Cu/SnO2 multilayers for high performance transparent conducting electrodes. Thin Solid Films 562:501–505
33. Pan ZW, Dai ZR, Wang ZL (2001) Nanobelts of semiconducting oxides. Science 291(5510):1947–1949
34. Guan C, Wang X, Zhang Q, Fan Z, Zhang H, Fan HJ (2014) Highly stable and reversible lithium storage in SnO2 nanowires surface coated with a uniform hollow shell by atomic layer deposition. Nano Lett 14(8):4852–4858
35. Hu D, Han B, Deng S, Feng Z, Wang Y, Popovic J, Nuskol M, Wang Y, Djerdj I (2014) Novel mixed phase SnO2 nanorods assembled with SnO2 nanocrystals for enhancing gas-sensing performance toward isopropanol gas. J Phys Chem C 118(18):9832–9840
36. Zhang J, Guo J, Xu H, Cao B (2013) Reactive-template fabrication of porous SnO2 nanotubes and their remarkable gas-sensing performance. ACS Appl Mater Interfaces 5(16):7893–7898
37. Seko A, Togo A, Oba F, Tanaka I (2008) Structure and stability of a homologous series of tin oxides. Phys Rev Lett 100(4):045702
38. Wang X, Liu W, Yang H, Li X, Li N, Shi R, Zhao H, Yu J (2011) Low-temperature vapor–solid growth and excellent field emission performance of highly oriented SnO2 nanorod arrays. Acta Mater 59(3):1291–1299
39. Dai ZR, Pan ZW, Wang ZL (2002) Growth and structure evolution of novel tin oxide diskettes. J Am Chem Soc 124(29):8673–8680
40. Ma XL, Li Y, Zhu YL (2003) Growth mode of the SnO2 nanobelts synthesized by rapid oxidation. Chem Phys Lett 376(5–6):794–798
41. Hsu YF, Xi YY, Yip CT, Djurišić AB, Chan WK (2008) Dye-sensitized solar cells using ZnO tetrapods. J Appl Phys 103(8):083114
42. Chen W, Zhang H, Hsing IM, Yang S (2009) A new photoanode architecture of dye sensitized solar cell based on ZnO nanotetrapods with no need for calcination. Electrochem Commun 11(5):1057–1060
43. Duclère J-R, Doggett B, Henry MO, McGlynn E, Rajendra Kumar RT, Mosnier J-P, Perrin A, Guilloux-Viry M (2007) (20 − 23) ZnO thin films grown by pulsed laser deposition on CeO2-buffered r-sapphire substrate. J Appl Phys 101(1):013509
44. Gorla CR, Mayo WE, Liang S, Lu Y (2000) Structure and interface-controlled growth kinetics of ZnAl2O4 formed at the (1120)ZnO/(0112)Al2O3 interface. J Appl Phys 87(8):3736–3743
45. Lim YS, Park JW, Kim MS, Kim J (2006) Effect of carbon source on the carbothermal reduction for the fabrication of ZnO nanostructure. Appl Surf Sci 253(3):1601–1605
46. Kim B-S, Yoo J-M, Park J-T, Lee J-C (2006) A kinetic study of the carbothermic reduction of zinc oxide with various additives. Mater Trans 47(9):2421–2426
47. Fagury Neto E, Kiminami RHGA (2014) Synthesis of silicon nitride by conventional and microwave carbothermal reduction and nitridation of rice hulls. Adv Powder Technol 25(2):654–658

48. Renato de Castro E, Breda Mourão M, Jermolovicius LA, Takano C, Thomaz Senise J (2012) Carbothermal reduction of iron ore applying microwave energy. Steel Res Int 83(2):131–138
49. Chandrasekaran S, Ramanathan S, Basak T (2012) Microwave material processing—a review. AICHE J 58(2):330–363
50. L-b Z, Ma A-y, C-h L, W-w Q, J-h P, Luo Y-g, Y-g Z (2014) Dielectric properties and temperature increase characteristics of zinc oxide dust from fuming furnace. Trans Nonferrous Metals Soc China 24(12):4004–4011
51. Martin LP, Dadon D, Rosen M, Gershon D, Rybakov KI, Birman A, Calame JP, Levush B, Carmel Y, Hutcheon R (1998) Effects of anomalous permittivity on the microwave heating of zinc oxide. J Appl Phys 83(1):432–437
52. Ali Saidi KA (2005) Carbothermic reduction of zinc oxide concentrate by microwave. J Mater Sci Technol 21(05):724–728
53. Wang ZL, Kong XY, Zuo JM (2003) Induced growth of asymmetric nanocantilever arrays on polar surfaces. Phys Rev Lett 91(18):185502
54. Jiang L, Sun G, Zhou Z, Sun S, Wang Q, Yan S, Li H, Tian J, Guo J, Zhou B, Xin Q (2005) Size-controllable synthesis of monodispersed SnO2 nanoparticles and application in electrocatalysts. J Phys Chem B 109(18):8774–8778
55. Ginley DS, Bright C (2000) Transparent conducting oxides. MRS Bull 25(8):15–18
56. Wang ZL (2004) Functional oxide nanobelts: materials, properties and potential applications in nanosystems and biotechnology. Annu Rev Phys Chem 55(1):159–196
57. Chen YQ, Jiang J, Wang B, Hou JG (2004) Synthesis of tin-doped indium oxide nanowires by self-catalytic VLS growth. J Phys D Appl Phys 37(23):3319
58. Wan Q, Dattoli EN, Fung WY, Guo W, Chen Y, Pan X, Lu W (2006) High-performance transparent conducting oxide nanowires. Nano Lett 6(12):2909–2915
59. Li L, Chen S, Kim J, Xu C, Zhao Y, Ziegler KJ (2015) Controlled synthesis of tin-doped indium oxide (ITO) nanowires. J Cryst Growth 413:31–36
60. Kim H, Park H-H, Kim J (2016) Electrical and optical properties of Ni-assisted grown single crystalline and transparent indium-tin-oxide nanowires. Mater Sci Semicond Process 48:79–84
61. Meng G, Yanagida T, Nagashima K, Yoshida H, Kanai M, Klamchuen A, Zhuge F, He Y, Rahong S, Fang X, Takeda S, Kawai T (2013) Impact of preferential indium nucleation on electrical conductivity of vapor–liquid–solid grown indium–tin oxide nanowires. J Am Chem Soc 135(18):7033–7038
62. Yu D, Wang D, Yu W, Qian Y (2004) Synthesis of ITO nanowires and nanorods with corundum structure by a co-precipitation-anneal method. Mater Lett 58(1–2):84–87
63. Dandan L, Hui W, Rui Z, Wei P (2007) Preparation and electrical properties of electrospun tin-doped indium oxide nanowires. Nanotechnology 18(46):465301
64. Savu R, Joanni E (2006) Low-temperature, self-nucleated growth of indium–tin oxide nanostructures by pulsed laser deposition on amorphous substrates. Scr Mater 55(11):979–981
65. Wan Q, Wei M, Zhi D, MacManus-Driscoll JL, Blamire MG (2006) Epitaxial growth of vertically aligned and branched single-crystalline tin-doped indium oxide nanowire arrays. Adv Mater 18(2):234–238
66. Seu Yi L, Chia Ying L, Pang L, Tseung Yuen T (2005) Low temperature synthesized Sn doped indium oxide nanowires. Nanotechnology 16(4):451
67. Arlindo EPS, Lucindo JA, Bastos CMO, Emmel PD, Orlandi MO (2012) Electrical and optical properties of conductive and transparent ITO@PMMA nanocomposites. J Phys Chem C 116(23):12946–12952
68. Orlandi MO, Lanfredi AJC, Longo E (2010) Study of indium tin oxide nanomaterials obtained from vapor phase by electron microscopy. In: Mendez-Vilas A, Díaz J (eds) Microscopy: science, technology, applications and education, 4th edn, vol 3. Formatex, Badajoz, pp 1667–1673
69. Enoki H, Echigoya J, Suto H (1991) The intermediate compound in the In2O3-SnO2 system. J Mater Sci 26(15):4110–4115
70. Shen Y, Turner S, Yang P, Van Tendeloo G, Lebedev OI, Wu T (2014) Epitaxy-enabled vapor–liquid–solid growth of tin-doped indium oxide nanowires with controlled orientations. Nano Lett 14(8):4342–4351

Chapter 3
Modification of Complex Materials Using a Pressure-Assisted Heat Treatment

Thiago Sequinel, Samara Schmidt, Evaldo Toniolo Kubaski, José Arana Varela, and Sergio Mazurek Tebcherani

1 Pressure-Assisted Heat Treatment

Pressure-assisted heat treatment (denoted PAHT) is based on a hermetically closed chamber from especially designed for this method [1, 2]. Thermodynamic laws and gas properties drive this method, in which the initial air pressure inside the chamber and chamber's temperature are increased simultaneously. Air pressure is distributed inside the chamber homogeneously, which enables a better action of the pressure on each particle of materials that undergoes to PAHT, as shown in Fig. 3.1.

Recent advances in the PAHT chamber, in particular, offer the ability to reach pressures higher than 2 MPa at temperatures of about 485 °C or lower. Indeed, the use of relatively low temperatures is one of the greatest advantages of this versatile synthetic strategy. The temperature of 350 °C normally used in PAHT is well lower than the temperatures of thermal annealing used in other methods of thin film deposition. Furthermore, many substrates can be decomposed or can suffer alterations in their physical properties at temperatures higher than 350 °C.

T. Sequinel (✉)
Federal University of Grande Dourados (Universidade Federal da Grande Dourados), Dourados, MS, Brazil
e-mail: sequinel.t@gmail.com

S. Schmidt
Federal University of Technology – Paraná, Ponta Grossa, PR, Brazil
e-mail: samaraschmidt@live.com

E.T. Kubaski • S.M. Tebcherani
State University of Ponta Grossa, Ponta Grossa, PR, Brazil
e-mail: evaldotk@outlook.com; sergiomt@uepg.br

J.A. Varela
Institute of Chemistry – UNESP, Araraquara, SP, Brazil
e-mail: varela@iq.unesp.br

E. Longo, F.A. La Porta (eds.), *Recent Advances in Complex Functional Materials*,
DOI 10.1007/978-3-319-53898-3_3

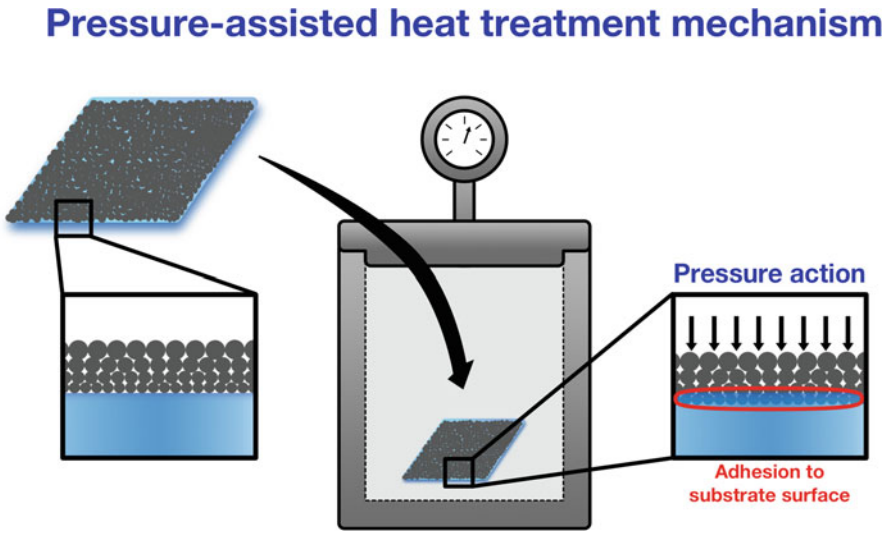

Fig. 3.1 Schematic representation of the air pressure action on oxide particles inside the chamber

Consequently, PAHT has opened a new possibility for treating a large variety of substrates at the low temperature, such as polymers, glass, and wood. The growing interest by using of low-temperature substrates are potential candidates for the production of less expensive devices, opening the possibility of creating a new series of products in the future.

From a fundamental point of view, the mechanism of PAHT process can in principle be described by the impregnation and mass transport from the oxide particles into the substrate surface caused by the air pressure in association with the thermal annealing and time of treatment. An increase in temperature during the PAHT process, in principle, facilitates the mass transport from the oxide particles to the substrate surface (e.g., similar to the coalescence mechanism observed in a densification of ceramics). Therefore, a denser and homogeneous surface will be obtained at longer treatment times. Furthermore, the use of higher air pressures facilitates the impregnation of the oxide particles onto the substrate surface, increases the impregnation rate, as well as depth of particle penetration.

The mechanism of PAHT is also related to the specific characteristics of the substrate surface. By means of the deposition of thin films on porous or soft low-hardness substrates resulted in an impregnation of the oxide particles onto the substrate surface by the air pressure applied. On the other hand, when thin films are deposited on rigid and dense substrates, the mechanism of thin film is driven by the mass transport from the oxide particles to the substrate surface, generating a film with the same morphology of the initial oxide particles.

Furthermore, the PAHT is applied to study the influence of air pressure in the structural parameters of films and oxide particles. In some cases, distortion in the angle between cluster units of the formed materials was observed. This chapter

will detail the use of PAHT to deposit thin films and its use to promote structural modifications in materials, especially oxide powders. Physicochemical properties of thin films and oxides after PAHT will also be considered.

2 Deposition/Impregnation of Ceramic Particles on Glass Substrate Using PAHT

PAHT was developed to create a new physical method of deposition of thin films. The objective was to reduce the deposition temperature to become possible the application of thin films on substrates that are unstable at higher temperatures. The idea to develop the PAHT method was first driven to found a new way to deposit oxide particles on cheaper substrates such as glass, polymers, and woods. Looking for a methodology involving low temperatures to preserve the characteristic of the substrate, the PAHT was studied to deposit crystalline oxide powders on glass substrates [3]. Different oxide particles (such as SnO_2, Al_2O_3, Co_3O_4, TiO_2, among others) were deposited on commercial float glass using PAHT. The deposition consisted of the oxide powder on the substrate surface. Afterward, the substrate/oxide system was placed inside the PAHT chamber, and pressurized cold air was injected into the chamber using a compressor increasing the chamber's pressure. Simultaneously, the substrate oxide system was thermally annealed at temperatures lower than the glass transition temperature. This range of temperature avoids any deterioration on the glass substrate. Toward that end, the parameters used in this process were 485 °C, 2 MPa of air pressure for 32 h. These parameters were sufficient to produce the impregnation of the oxide particles into the glass surface, resulting in a glass-ceramic composite with the same visual appearance of the original glass substrate. In other words, the development of the PAHT was able to generate new surface properties for the glass substrate.

The glass-ceramic composites were characterized by X-ray diffraction (XRD) and X-ray fluorescence (XRF) to evaluate the present phases and composition of the thin films. Scanning electron microscopy (SEM) micrographs of the surface and cross-section glass-ceramic composites revealed the presence of the oxide particles deposited on the glass surface. Two mechanisms were proposed for film formation on glass surface: an initial nucleation and a final grain growth resulted from the nucleation of the oxide powder/substrate interface. The glass surface is smoothed which favors the initial nucleation due to the minimum free-energy configuration, and the final growth is favored by the energetic instability of the nuclei in the plane parallel to the substrate surface.

The main advantage of using PAHT is the possibility of depositing crystalline oxide particles on the glass substrate (e.g., oxide powders). On the other hand, conventional chemical methods of film deposition crystalizes the film after deposition, which can alter the substrate characteristics due to the elevate temperatures necessary to obtain crystalline oxides.

2.1 The Influence of Time in PAHT

Several studies were to optimize PAHT parameters to obtain high-quality thin films on a wide variety of substrate surfaces. For example, Sequinel et al. [4] used temperature and air pressure fixed at 485 °C and 1.72 MPa, respectively, and varied PAHT time from 0 to 32 h. This study evaluates the most adequate time to obtain a homogeneous thin film on the substrate surface. Oxide films (SnO_2) were deposited on glass substrate by PAHT, and all films were characterized by XRD, XRF, SEM, and infrared (IR) reflectance spectroscopy. The influence of time on PAHT during the deposition process of oxide particles is described in five steps.

Initially, only the substrate surface, without any film deposition, was observed. After 8 h, some nucleation regions were already present, which is an indication of the initial growth of the film. After 16 h, nucleation regions increase indicating a large growth of the film. Small grain growth occurred after 24 h, and a complete densification of the film occurred after 32 h of PAHT, finalizing the growth cycle of the film deposited by PAHT, as shown in Fig. 3.2.

XRF showed the presence of SnO_2 on the glass substrate after PAHT. IR reflectance indicated characteristic bonding of SnO_2 in both sides of the glass substrate, indicating the presence of SnO_2 inside the glass matrix. The IR reflectance of the top surface with oxide film showed a significant band attributed to the stretching vibration of Si-O-Si bonds shifted to smaller energy after SnO_2 film deposition. The presence of SnO_2 causes the decrease in Si-O-Si bond angles. In the bottom side of the glass substrate (without film), a similar IR spectrum was observed, but in lower intensity, which indicates the impregnation of SnO_2 particles onto glass matrix after the high pressure used in PAHT. The impregnation of oxide particles inside the substrate matrix will be further discussed in Sect. 2.3. These results revealed that 32 h of treatment is necessary to deposit/impregnate a homogeneous and dense film on the substrate surface.

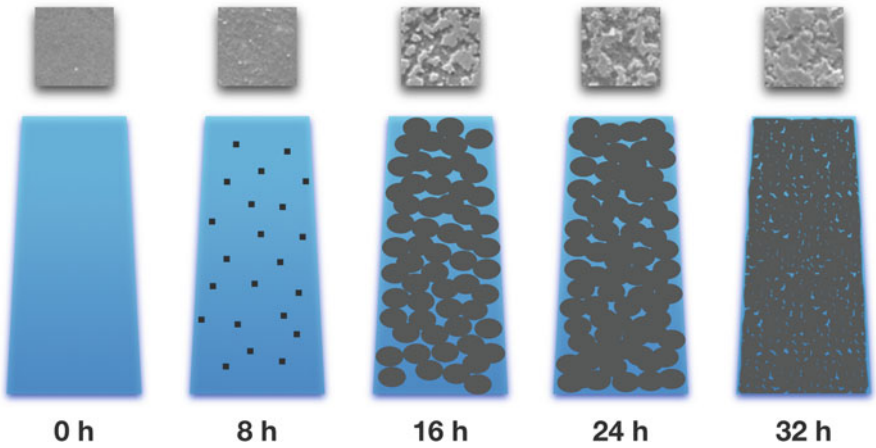

Fig. 3.2 Schematic representation of thin film deposition by PAHT at different times

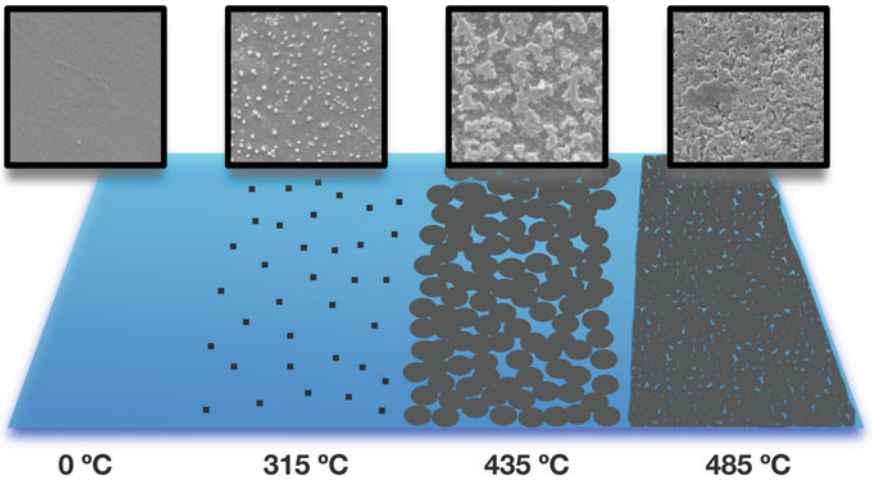

Fig. 3.3 Schematic representation and SEM micrographs (inset) showing the formation of thin film on glass substrate by PAHT at different annealing temperatures

2.2 *The Influence of Temperature in the PAHT*

The optimal temperature to produce homogeneous and dense SnO_2 films on glass substrates by PAHT was studied in a similar test as that describe in Sect. 2.1. The time and air pressure of PAHT were fixed at 32 h and 1.72 MPa, respectively. However, the temperature of thermal annealing varied from room temperature to 485 °C [5]. Influence of temperature is presented in Fig. 3.3 that shows SEM micrographs of four temperature steps. When thermal annealing was performed at 315 °C, SEM image shows an initial region of nucleation. At 435 °C a large film growth was verified, while at 485 °C a homogeneous and dense film was obtained.

In this study, results showed that the SnO_2 content in the film/substrate system increased with the temperature of the thermal annealing. A maximum of 5.6% (wt.%) of SnO_2 was found when thermal annealing temperature in PAHT was 485 °C. Another interesting fact observed in the influence of temperature was the reduction of the Na_2O content in glass composition. As the temperature increased, the amount of Na_2O decreased, indicating the impregnation of SnO_2 particles in glass substrate is facilitated by the particle exchange between sodium and tin oxide particles.

2.3 *The Influence of Crystallite Size in the Deposition of Film by PAHT*

Other important parameters like temperature and crystallite sizes of the oxide powder used can in principle favor the thin film deposition by the PAHT method [6]. Nanoparticles present elevated surface area that covers a higher substrate surface

area, and this characteristic could be related to the favoring in the mass transport of the oxide particles to the substrate surface. As result, the nucleation of the thin film deposition is originated at lower temperature and time of PAHT, reducing the kinetic energy barrier for this methodology.

In this study, two different SnO_2 powders were deposited on glass substrates. The first SnO_2 powder has a hollow microsphere morphology and was obtained by the chemical route using a calorimetric pump (CR powder) [7]. CR powder showed a crystallite size of 3.7 nm calculated by the Scherrer's equation. The second SnO_2 powder was obtained by of the polymeric precursor method (PPR powder) [8]. PPR showed an average crystallite size of 22.4 nm. The CR powder has a crystallite size six times smaller than PPR powder, favoring the discussion about the influence of the crystallite size in the deposition using PAHT.

The effect of pressure and the quality of the thin films produced by CR and PPR powders using the PAHT were evaluated by their physical-chemical properties. Micrographs (SEM and FEG-SEM) of the film surfaces showed the dependence on the crystallite size to reduce the temperature necessary to obtain a dense and homogeneous film. While the CR film (smaller crystallite size) reached the final film growth at 485 °C, the PPR film reached only an intermediated level of the growth showing a porous surface film at this same temperature, indicating the necessity of higher temperature to complete film growth. Furthermore, micrographs of the film surface showed that film morphology is similar to the starting oxide particles morphology, indicating the mechanism of mass transport from the oxide particles to the substrate surface. Figure 3.4 presents the comparison between oxide particles and film morphology, illustrating the similarity between both particle and film. FEG-SEM micrographs of the cross section of CR film produced by PAHT (485 °C, 32 h and 1.72 MPa) indicated a thickness of 700 nm. The cross section of the film also shows a smaller particle size near the substrate surface and a higher particle size at the top of the film (Fig. 3.4).

The same film thickness (700 nm) was estimated during the measurement of the elastic modulus by the nanoindentation [6]. Nanoindentation tests showed an increase about 55% in the elastic modulus in regions about 200 nm of depth when compared to the original glass substrate. As nanoindentation test increases the depth of the penetration, it was observed a decrease in the influence of the film in the elastic modulus of the substrate, presenting a modulus 33% higher in the depth between 200–400 nm and reaching a 20% higher than original substrate at depths of 700 nm.

In short, both micrographs and nanoindentation measurements contribute to defining the 700 nm of the thickness of the films deposited by PAHT methodology. Nanoindentation tests also indicated that the cover layer deposited on the substrate surface could be applied to increase the hardness and toughness of this substrate. On the other hand, the mechanical properties reveal that the film produced by PAHT can be applied to cover and protect a wide variety of fragile substrates, such as glass, polymers, and others. However, the protection promoted by films deposited by the PAHT does not affect the original visual aspect of the substrate since the films are transparent. Therefore, this is another advantage of PAHT method in comparison with other techniques for deposition of thin films.

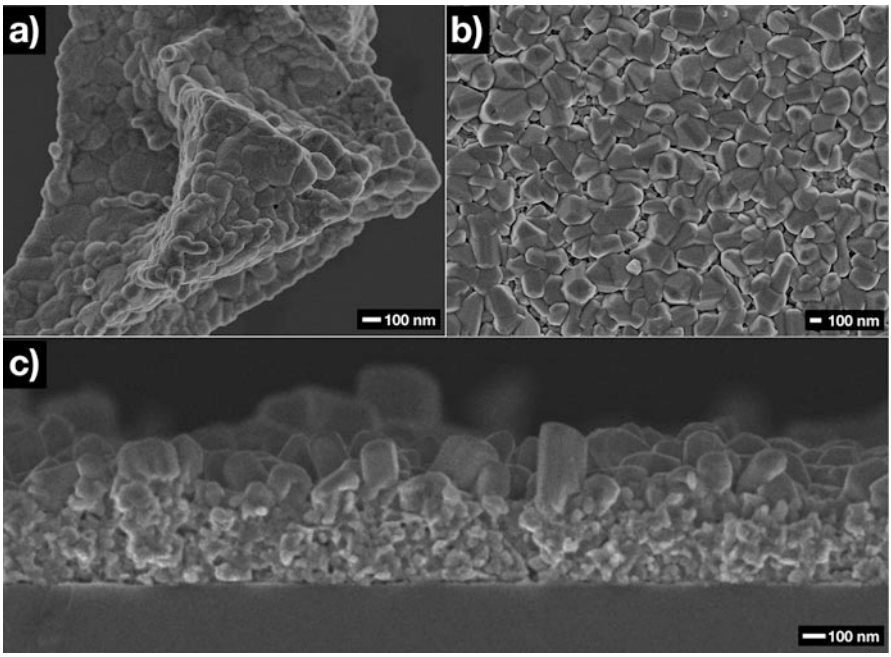

Fig. 3.4 Micrographs of (**a**) oxide particles, (**b**) film surface, and (**c**) film cross section

3 Study of the PAHT on Thin Films and Oxide Powders Structures

After all, development to find the optimal parameters to deposit films and impregnate oxide particles on less expensive substrates, in particular, the PAHT method was used to study some structural modifications in crystalline thin films and oxide powders. In this case, thin films and oxide powders were obtained by other methods of synthesis (e.g., chemical routes of oxide synthesis and depositions). These studies were conducted to find the effect of high air pressure on the crystalline structures, and these studies are described in the next sections.

3.1 Influence of PAHT on Thin Films Obtained by Chemical Route

Thin films produced by means of the chemical routes were subjected to a PAHT, in order to verify the pressure effect on properties of these films. Chemical films were based on a polymeric solution of the desired complex materials (Pechini method) and were deposited by the spin coating. The polymeric solution is converted to

the oxide thin film after a thermal annealing at temperatures higher than 500 °C, according to the crystallization temperature of each inorganic oxide. One chemical film tested was calcium and copper titanate (CCTO).

Thin films CCTO were chemically deposited on Pt(111)/Ti/SiO_2/Si substrates using a spin coater equipment [9]. CCTO chemical film depositions were performed after spinning the CCTO polymeric solution (Pechini method) on substrate surface. After the deposition of the polymeric solution, the CCTO crystalline thin film structure was obtained on substrate surface by a thermal annealing at temperatures higher than 500 °C. Due to the elevate temperature necessary to convert the polymeric solution to a crystalline thin film, there was the need of using a substrate that was able to support this range of temperature.

CCTO chemical films were characterized by XRD, FEG-SEM micrographs, and photoluminescence (PL) measurements. Results showed that after the chemical deposition, a thermal annealing of 700 °C was necessary to obtain crystalline thin films. This temperature does not allow the less expansive substrates (e.g., polymers and glass) that have their physical and chemical properties altered at temperatures higher than 500 °C. After all characterization of CCTO chemical films, they were subjected to PAHT to evaluate the effect of the air pressure in their optical properties.

Structural order-disorder effects were observed when CCTO thin films deposited by chemical methods were underwent the PAHT. Ordered clusters could be disordered due to the pressure action, increasing in the PL emission intensity of such materials [9]. Furthermore, the effect of pressure on the thin film structure revealed a medium-range disorder of the cluster structure after PAHT and caused a red-shift displacement in the PL emissionof the thin film, as shown in Fig. 3.5. Red shift in the PL emission after PAHT was also associated by a decrease in the band gap of the thin films, where the air pressure could lead to the formation of new intermediate levels, probably due to the presence of the interstitial oxygen. These facts favored the creation of intermediate levels associated with the defect structure

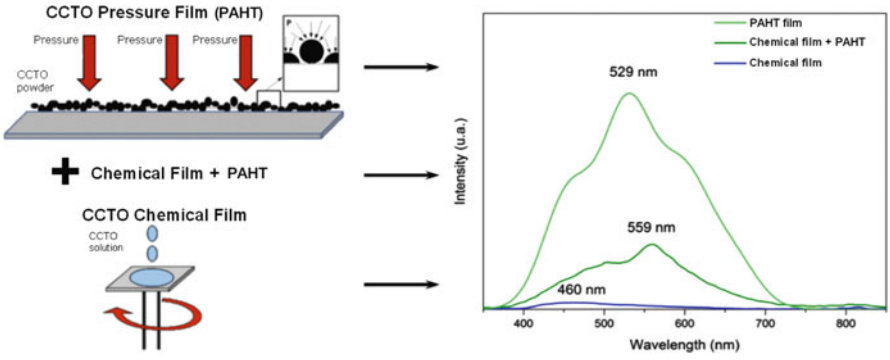

Fig. 3.5 Schematic representation of the chemical and physical deposition of CCTO films and their PL spectra (Adapted with permission from Sequinel et al. [9]. Copyright (2013) Elsevier)

caused by PAHT. Red shift in the PL emission means the presence of band emission at higher wavelengths (lower energies) indicating the transition of an electron from the valence (VB) to the conduction (CB) band is, in part, facilitated.

The pressure effect on the CCTO thin films prepared by physical and chemical methods was compared. Physical films were deposited on the same substrate by PAHT using CCTO oxide particles. The CCTO physical film was prepared under an air pressure of 2 MPa at 340 °C for 32 hours. They were characterized by the same techniques of the chemical films. CCTO physical films showed a higher PL intensity than CCTO chemical films (Fig. 3.5), with a similar red-shift displacement found in chemical films after PAHT. The comparison of the PL emission of CCTO films (i.e., prepared by chemical and physical methods), before and after PAHT, shows a great advantage of oxide particle depositions by PAHT. It can be highlighted the relatively low temperatures necessary to deposit films on substrates by PAHT using oxide particles. The temperature of 340 °C used in PAHT enables this method to deposit films with improved optical properties on less expansive substrates without changing substrates' original properties.

Similar results were observed in ZnO thin films [10], indicating that PAHT can enforce similar structures distortions at different crystalline thin films. ZnO chemical thin films were also obtained by spinning a ZnO polymeric solution (Pechini solution) using spin coater equipment on ITO/silicon substrate surface. The ZnO chemical thin film became crystalline after a thermal annealing at 760 °C for 2 h in ambient atmosphere. The crystalline ZnO thin film also underwent the PAHT to verify the pressure effect on PL emission. After PAHT, the ZnO thin films also showed a red-shift displacement on the PL emission (Fig. 3.6). This behavior indicates that air pressure can lead to medium-range disorder in different crystalline structures. This fact can change the state of defect states inside the band gap and can favor the formation of new interstitial oxygen in the crystalline structures.

3.2 Influence of PAHT on Oxide Powder

The effect of the air pressure on crystalline powders structures was studied by subjecting inorganic oxide powders to PAHT [11]. α-Bi_2O_3 was obtained by microwave-assisted hydrothermal (MAH). The α-Bi_2O_3 was obtained after 30 minutes at 80 °C with a heating rate of 10 °C/min in a MAH system and then calcined at 400 °C for 1 h. α-Bi_2O_3 powder was characterized by the following techniques: X-ray diffraction with refinements carried out by the Rietveld method using fundamentals parameters, FEG-SEM micrographs to analyze their morphology, PL measurements, Raman spectroscopy to analyze the short- and medium-range order, and X-ray photoelectron spectroscopy (XPS) to analyze the chemical states of the elements. In addition, first-principles total-energy calculations were carried out within periodic density functional theory. All these characterizations were performed in the α-Bi_2O_3 obtained by MAH before and after PAHT.

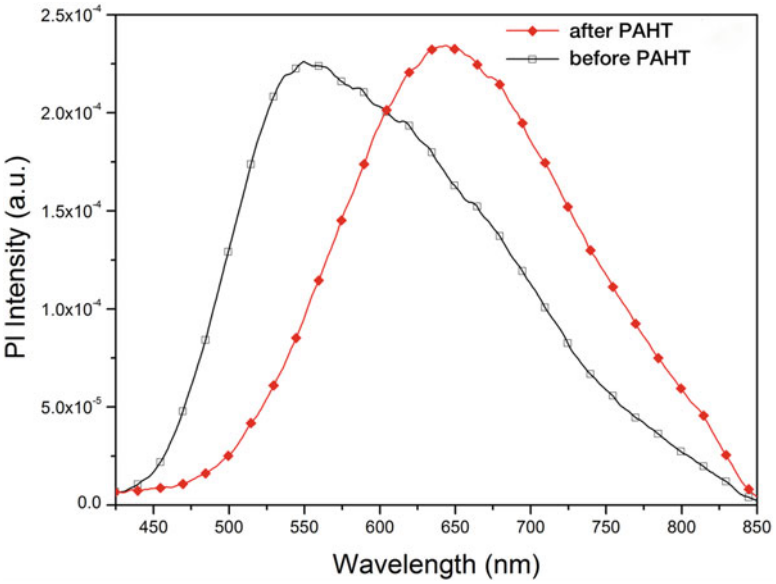

Fig. 3.6 PL spectra of ZnO thin films before and after PAHT (Reprinted with permission from Berger et al. [10]. Copyright (2012) John Wiley & Sons, Ltd.)

Rietveld refinements showed no alteration in the lattice parameters and in the crystallite size for α-Bi_2O_3 after PAHT when compare with the oxide obtained by MAH before PAHT. However, simulation of the material structure revealed that PAHT leads to an increase of approximately 2° in the angle between the clusters [BiO_6]-[BiO_6] (Fig. 3.7), even though with the coordination of the polyhedral, cell volume and crystallite size did not suffer any variation. Moreover, no change in powder morphology, before and after PAHT, was observed.

PAHT also affected of the PL emission, increasing the PL emission intensity and the contribution of direct transitions between the CB and VB. A direct transition between the CB and VB is associated to the band gap, which was not changed after PAHT. A deconvolution of the PL spectra showed an increase in the contribution of the violet region from 9 to 19% after PAHT. PAHT also leads to a significant decrease at PL low-energy region (red and orange emission region) from 26% to only 9% after pressure treatment (Fig. 3.8). PL emission in the low-energy spectral range is attributed to the oxygen vacancies that form defect donor states.

Raman spectroscopy revealed an increase in the spectrum intensity at frequencies higher than 284 cm^{-1}, which can be associated to changes in the electronic density of the crystal after PAHT. The increase in the average electronic density is caused by the distortion in the angles between [BiO_6]-[BiO_6] clusters, as reported in the simulation of the crystal structure. These results are supported by other's experimental and theoretical studies [12, 13, 14]. In addition, the XPS did not detect any signal of Bi^{+2} ions in α-Bi_2O_3, which confirms the PL emission in the low-energy of emission is associated to oxygen vacancies that form defect donor states. The PAHT

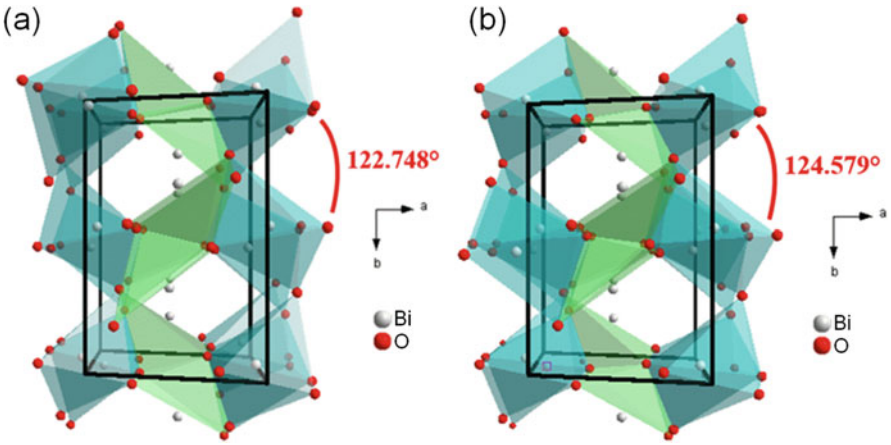

Fig. 3.7 Coordination polyhedral for α-Bi_2O_3 in the simulated structures for (**a**) before PAHT and (**b**) after PAHT (Reprinted with permission from Schmidt et al. [11]. Copyright (2015) American Chemical Society)

decreased the emission at the low-energy region, revealing a decrease in the oxygen vacancies in crystalline oxide after PAHT. The oxygen-rich atmosphere present in PAHT caused this, and this ambient was disadvantageous to the formation oxygen vacancies in the oxide powder. All these variations in electronic density, oxygen vacancies, and PL emission reported after PAHT are directly related to the disorder caused by an increase in the angles between $[BiO_6]$-$[BiO_6]$ clusters. These facts are in good agreement with the results obtained by Raman and XPS spectroscopies.

Theoretical calculation showed that O 2p states have an important role in photoelectron transfers in both samples (before and after PAHT). Changes in angles between $[BiO_6]$-$[BiO_6]$ clusters can change the polarization of O 2p states and, consequently, can lead to changes on electric density of crystals. Our theoretical results are in good agreement with the experimental data.

4 PAHT Influence on Thin Film Versus Oxide Powders

Both thin film and oxide powders had their photoluminescence properties changes after PAHT. The rich oxygen atmosphere favors the formation of intermediate levels inside the band gap, reducing the energy of the PL emission, which was observed in the red-shift displacement in the PL emission after PAHT. However, the thin film showed a significant increase in the PL intensity, while oxide powders had a small difference in the PL emission when compare the emission behavior before and after PAHT. PL intensity is directly affected by the disorder effects at medium range in the structure of these complex materials. This increase in the PL emission observed to thin film after PAHT could be explained due to capacity of the air pressure to penetrate in the sample. Particles and clusters of thin films are more exposed to

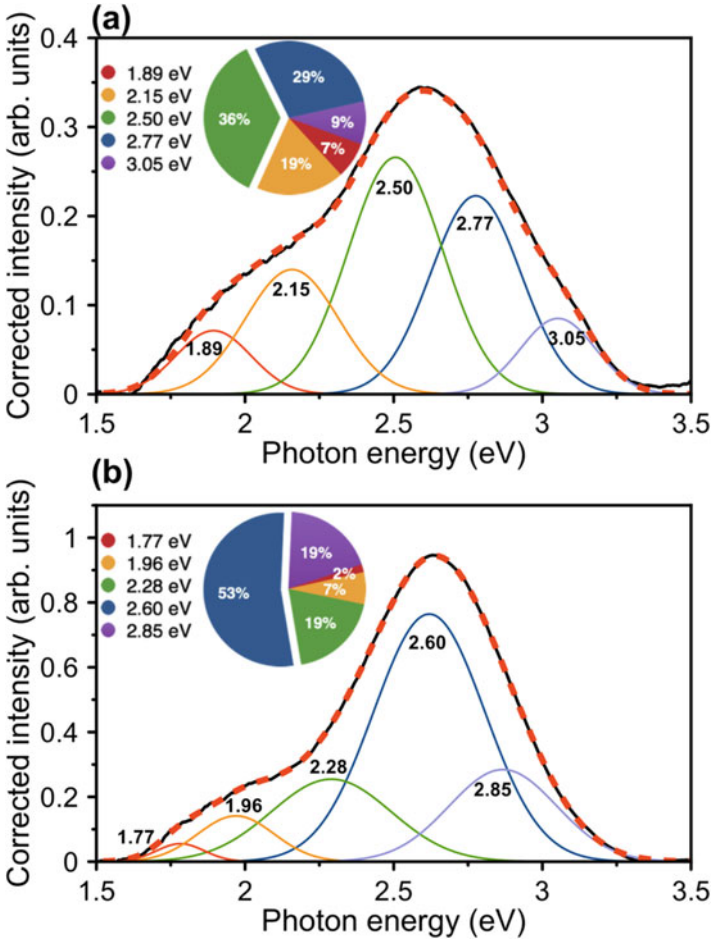

Fig. 3.8 Deconvolution of PL spectra of (**a**) before PAHT and (**b**) after PAHT (Reprinted with permission from Schmidt et al. [11]. Copyright (2015) American Chemical Society)

action of the air pressure, once all of their clusters are located close to surface in touch with the air atmosphere. The air pressure is more efficient on surface area, or in a small depth of materials samples, being able to force the medium-range disorder at the whole thin film sample.

5 Summary

This chapter described the pressure-assisted heat treatment (PAHT) as a method of deposition/impregnation of films on a variety of substrates, including substrates unstable at elevated temperatures, such as polymers and glass. The PAHT method is based on low temperatures (e.g., 350 °C), elevated air pressure (higher than

2 MPa), and a long period of treatment (about 32 h). The mechanism of deposition is based on mass transport from the oxide particles to the substrate surface and on the impregnation of oxide particles inside small depth at the soft or porous substrate surfaces. The physical film produced by PAHT is homogenous and dense, with a great adhesion that makes strong film/substrate interfaces. PAHT can also be applied to modify crystalline structures, increasing their photoluminescence emission intensity due to a medium-range disorder caused by PAHT. PAHT method is able to change the angle between clusters of crystal, which can lead to changes in the electron density of the material and to an increase in photoluminescence emission intensity.

References

1. Cava S, Tebcherani SM, Lazaro SR, Chinelatto ASA, Chinelatto AL, Oliveira CR (2008a) Equipamento para manufatura de filmes finos ou ultra-finos e nanocompósitos de óxidos metálicos e/ou metais impregnados e/ou depositados em substratos vítreos, poliméricos, madeiras, metais e outros. Brasil Patent PI 0806010–0 A2
2. Cava S, Tebcherani SM, Mandalozzo SSN, Berger D, Garcia JR, Wohnrath K (2008b) Processo de preparação de filmes finos ou ultra-finos e nanocompósitos de nanopartículas de óxidos metálicos e/ou metais impregnados e/ou depositados em substratos vítreos, poliméricos, madeiras, metais e outros. Brasil Patent PI 0806015–0 A2
3. Cava S, Sequinel T, Tebcherani SM, Michel MD, Lazaro SR, Pianaro SA (2009) Microstructure of ceramic particles infiltrated into float glass surfaces by high gas pressure impregnation. J Alloys Compd 484(1–2):877–881. doi:10.1016/j.jallcom.2009.05.061
4. Sequinel T, Cava S, Pimenta JO, Pianaro SA, Tebcherani SM, Varela JA (2011) IR reflectance characterization of glass–ceramic films obtained by high pressure impregnation of SnO_2 nanopowders on float glass. Ceram Int 37(5):1533–1536. doi:10.1016/j.ceramint.2011.01.013
5. Cava S, Sequinel T, Tebcherani SM, Lazaro SR, Pianaro SA, Varela JA (2010a) Effect of temperature on glass-ceramic films prepared by impregnation of commercial float glass surfaces with oxide powders under pressure. Thin Solid Films 518(21):5889–5891. doi:10.1016/j.tsf.2010.05.087
6. Cava S, Sequinel T, Tebcherani SM, Michel MD, Lepienski CM, Varela JA (2010b) Nanomechanical properties of glass–ceramic films obtained by pressure impregnation of oxide powders on commercial float glass surfaces. J Non-Cryst Solids 356(4–5):215–219. doi:10.1016/j.jnoncrysol.2009.11.006
7. Sequinel T, Cava S, Berger D, Tebcherani SM, Pianaro SA, Schmidt S (2009) Synthesis and characterization of microspheres composed of SnO_2 nanoparticles processed via a chemical route. Powder Technol 196(2):180–183. doi:10.1016/j.powtec.2009.07.019
8. Pechini MP (1966) Barium titanatium, citrate, barium titanate and processes for producing same. United Stade Patent U.S. 3231328
9. Sequinel T, Garcia IG, Tebcherani SM, Kubaski ET, Oliveira LH, Siu Li M, Longo E, Varela JA (2014) Red shift and higher photoluminescence emission of CCTO thin films undergoing pressure treatment. J Alloys Compd 583:488–491. doi:10.1016/j.jallcom.2013.08.210
10. Berger D, Kubaski ET, Sequinel T, da Silva RM, Tebcherani SM, Varela JA (2013) Effect of pressure-assisted thermal annealing on the optical properties of ZnO thin films. Lumin J Biol Chem Lumin 28(6):942–947. doi:10.1002/bio.2463
11. Schmidt S, Kubaski ET, Volanti DP, Sequinel T, Bezzon VDN, Beltrán A, Tebcherani SM, Varela JA (2015) Effect of pressure-assisted heat treatment on photoluminescence emission of α-Bi_2O_3 needles. Inorg Chem 54:10184–10191. doi:10.1021/acs.inorgchem.5b01237

12. Ghedia S, Locherer T, Dinnebier R, Prasad DLVK, Wedig U, Jansen M, Senyshyn A (2010) High-pressure and high-temperature multianvil synthesis of metastable polymorphs of α-Bi_2O_3: crystal structure and electronic properties. Phys Rev B 82(2):024106
13. Locherer T, Prasad DLVK, Dinnebier R, Wedig U, Jansen M, Garbarino G, Hansen T (2011) High-pressure structural evolution of α-Bi_2O_3. Phys Rev B 83(21):214102
14. Pereira ALJ, Errandonea D, Beltrán A, Gracia L, Gomis O, Sans JA, García-Domene B, Miquel-Veyrat A, Manjón FJ, Muñoz A, Popescu C (2013) Structural study of α-Bi_2O_3 under pressure. J Phys Condens Matter 25(47):475402

Chapter 4
Preparation of Polymeric Mats Through Electrospinning for Technological Uses

Elisangela Corradini, Priscila Schroeder Curti, Regiane da Silva Gonzalez, Antonio Guilherme B. Pereira, Douglas Cardoso Dragunski, Alessandro Francisco Martins, and Edvani Curti Muniz

1 Introduction

1.1 Basic Aspects of Electrospinning

The electrospinning is an emergent technique that presents a great technological potential to produce continuous fibers from the submicron diameter down to the nanometer diameter. Furthermore, this technique presents a simple, versatile, and cost-effective technology to produce fibers, which present high surface area/volume ratio. It is indispensable the correct adjustment and optimization of electrospinning parameters, for obtaining fibers with distinct/desired morphologies, with average

E. Corradini
Programa de Pós-gradução em Ciência e Engenharia de Materiais (PPGCEM), Universidade Tecnológica Federal do Paraná (UTFPR-LD), Avenida dos Pioneiros, 3131, 86036-370, Londrina, PR, Brazil

P.S. Curti
Departamento Acadêmico de Química, Universidade Tecnológica Federal do Paraná (UTFPR-LD), Avenida dos Pioneiros, 3131, 86036-370, Londrina, PR, Brazil

R. da Silva Gonzalez
Departamento Acadêmico de Química, Universidade Tecnológica Federal do Paraná (UTFPR-CM), Via Rosalina Maria dos Santos, 1233, CEP 87301-899, Campo Mourão, PR, Brazil

A.G.B. Pereira
Engenharia de Bioprocessos e Biotecnologia, Universidade Tecnológica Federal do Paraná (UTFPR-DV), Estrada para Boa Esperança, 85660-000, Dois Vizinhos, PR, Brazil

D.C. Dragunski
Centro de Engenharias e Ciências Exatas, Universidade do Oeste do Paraná (UNIOESTE), Rua da Faculdade, 645, 85903-000, Toledo, PR, Brazil

Programa de Pós-graduação em Biotecnologia Aplicada a Agricultura, Paranaense University (UNIPAR), 87502-210, Umuarama, PR, Brazil

E. Longo, F.A. La Porta (eds.), *Recent Advances in Complex Functional Materials*,
DOI 10.1007/978-3-319-53898-3_4

diameters in a given range, and having roughness and other important properties tuned for a specific application of interest. Both synthetic and natural polymers, in solution, have been electrospun in order to obtain varied kinds of fibers, which could be successfully applied in different fields, such as tissue engineering scaffolds [1–9], filtration [10–16], biomedical [17–26], pharmaceutical [27–32], wound dressing [33–40], optical electronics [41–48], protective textile [14, 49–54], among others.

Since the 1990s the interest on the electrospinning technique usage has increased significantly, due to the increase of the research employing the technique. Before that, the electrospraying phenomenon was first observed in 1897 by Rayleigh and was studied in detail by Zeleny in 1914. The electrospinning principle was firstly proposed by Formhals in 1934, who applied several patents of the process in the years 1934–1944 [55–57], despite some studies before 1934 (done by Cooley in 1902; by Morton in 1929; and by Hagiwara in 1929) can be found [58].

In 1969, Taylor focused on electrically driven jets, being an important basis for the electrospinning [56]. But, only from the mid 1990s, the electrospinning technique started to be used by Reneker et al. being widely studied until nowadays [59–69].

Electrospinning process consists in to apply an electric field between the tip of a capillary needle (electrode) and a grounded collector plate (counter electrode), inducing the formation of the polymeric fluid jet in a fiber form. Using a polymer solution, in a preestablished flow and under the influence of a strong electric field, the electric charges are generated on the polymer solution surface drop formed at the needle tip, and repulsion forces appear on the liquid surface. Such repulsive forces act oppositely to surface tension. When the electrostatic repulsion imposed on the polymer spherical droplet surface overcomes the surface tension of the liquid, the drop deforms into a cone shape, called Taylor's cone [70, 71]. Increasing the elongational Taylor's cone deformation, the charged polymer solution is ejected, and hence, the polymer stretching between the needle tip and the collector occurs, inducing fiber formation. At the same time, the charge density on the polymer jet interacts with the electrical field producing instabilities. These phenomena are known as whipping. It causes bending and spreading of main jet into numerous secondary fibers, with a diameter approximately equal (or smaller) to the main jet.

A.F. Martins
Universidade Tecnológica Federal do Paraná (UTFPR-AP), Rua Marcilio Dias, 635, CEP 86812-460, Apucarana, PR, Brazil

E.C. Muniz (✉)
Programa de Pós-gradução em Ciência e Engenharia de Materiais (PPGCEM), Universidade Tecnológica Federal do Paraná (UTFPR-LD), Avenida dos Pioneiros, 3131, 86036-370, Londrina, PR, Brazil

Programa de Pós-graduação em Biotecnologia Aplicada a Agricultura, Paranaense University (UNIPAR), 87502-210, Umuarama, PR, Brazil

Departamento de Quimica, Universidade Estadual de Maringa (UEM), Av. Colombo, 5790, CEP, 87020-900, Maringá, PR, Brazil
e-mail: ecmuniz@uem.br; curtimuniz@gmail.com; edvanimuniz@utfpr.edu.br

In the jet course, the solvent evaporates and the polymer solidifies, and fibers are obtained due to the entanglements in the loaded fluid, which are randomly deposited on the collector [72, 73]. These electrospun fibers can present diameters in the range of nanometers to few micrometers. Although the apparatus presents simple construction, the electrospinning technique presents several key physical phenomena that affect the jet during the process, such as (a) solution parameters (concentration, viscosity, molecular weight, surface tension, conductivity), (b) processing parameters (applied voltage, flow rate, needle tip-to-collector distance, needle shape, types of collector), and (c) ambient parameters (temperature, humidity) [19, 56, 71–74]. The control and optimization of these parameters can result in micro- or nanofibers with very interesting properties and various application areas.

In addition to the importance of the electrospinning experimental parameters in the final properties of electrospun fibers, another relevant factor that greatly influences the process is the geometry configuration (horizontal or vertical) of the electrospinning setup used, which is discussed next.

1.2 Experimental Devices Used in Electrospinning

Basically, the conventional electrospinning device consists on a high-voltage supplier, an injection pump connected to a syringe plugged in a flat tip of the capillary needle (nozzle) and a metallic collector. The device can be built in horizontal or vertical setup, as shown in Fig. 4.1a, 4.1b, respectively. In these cases, the jet suffers instabilities during the electrospinning process, known whipping, and random fibers are obtained on a static collector.

The high-voltage supplier is connected between the tip of capillary needle and the collector. It is important to use voltage values in scale of kV, due to compulsory condition of overcoming the surface tension of polymer solution to form the uniaxial stretching jet, which can be properly collected in a static or mobile collector.

The nozzle used may have a single or coaxial shape. The single nozzle shape has just only one polymer solution output [75]. Thus, just one kind of polymer solution (one polymer or a polymer-physical mixture) can be electrospun. In addition, it is possible to use more than one nozzle, in multiple spinnerets, in order to produce mats with different morphologies (Fig. 4.1c) [6, 76–79]. In a coaxial shape (Fig. 4.1d), the nozzle presents two concentric tubes, in which two distinct solutions could be electrospun. In this case, the two polymer solutions do not come in physical contact until they reach the end of the spinneret, where the process of fiber formation begins. Several studies have shown that is possible to get hollow fibers [80] or core-sheath fibers [24, 34, 81].

Some difficulties may arise due to the clogging of the needle preventing the flow of solution. Therefore, a needless (nozzle-less) apparatus can be used in an electrospinning device. In this setup, a thin layer of polymer solution covers a rotating drum surface that is exposed to a high voltage (up to100 kV), and several jets are created simultaneously and distributed on the collector (Fig. 4.1e). Dubsky et al. [5] pointed out that nozzle-less is an advance as compared to needle setup

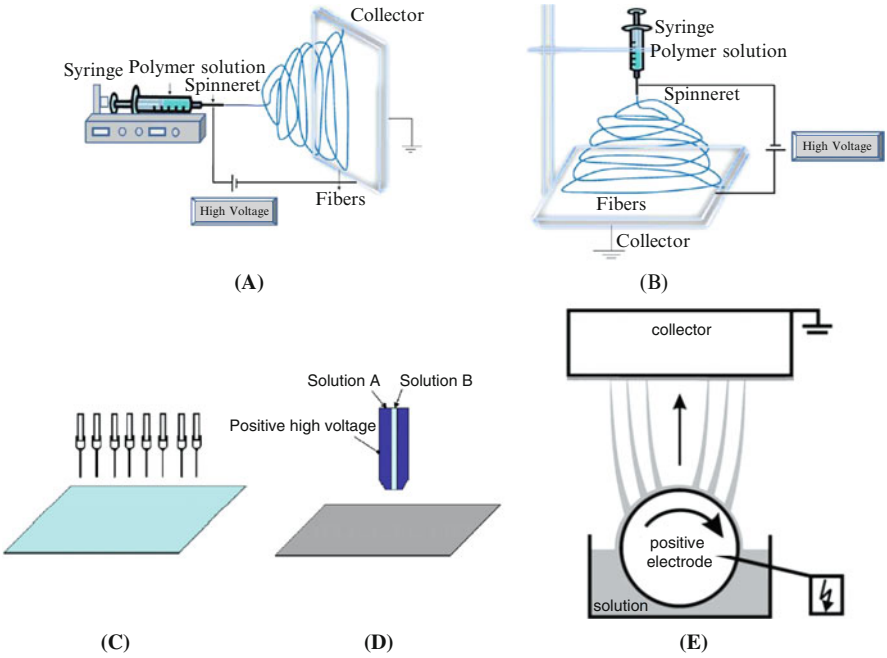

Fig. 4.1 Schematic setup of electrospinning apparatus and some typical typed nozzle: (**a**) typical horizontal setup and (**b**) vertical setup [56], (**c**) multiple spinnerets nozzles, (**d**) coaxial nozzle [58], and (**e**) nozzle-less electrospinning apparatus [5] (Reprinted with permissions from Refs. [5, 56, 58])

used in conventional electrospinning, because it allows continual manufacturing and larger amounts of fiber mats in a given time scale. On the other hand, the use of this kind of setup in an industrial scale is a disadvantage due to undesired residual solvent generated during the process.

Teo and Ramakrishna [58] published a review about electrospinning devices, in which comments about not conventional needle setups are found. For instance, the gas jacket electrospinning, using coaxial needle, can be used to obtain smooth fibers using gas flowing in a controlled speed, as core, during the electrospinning; bicomponent spinneret that uses a nozzle shape has two outputs to get single fibers from two different materials carefully chosen to reduce mixing of the materials. Other not conventional setups can be cited: (i) hole electrospinning (needleless setup) that produces simultaneously a large amount of fibers, but presenting different diameters; (ii) multiple spikes electrospinning that avoids needle clogging, producing fibers in high rate, but presenting a complicated setup and the large variation of fiber diameter; and (iii) pointed tip electrospinning source, no needle clogging occurs, solutions can be electrospun over short distances to collector, but it needs low solution flows.

Sambaer et al. [11] used a rotating electrode with 4 cotton cords spinning elements, using needleless electrospinning method allowing to produce nonwoven polyurethane nanofibers. The rotating electrode was immersed in a polymer solution, and the cotton cords work as spinning elements, avoiding the use of needle.

The collector is another very important part of the electrospinning device. It can be static or mobile. The chosen collector setup influences significantly the morphological and the physical characteristics of the electrospun mat. According to Baji et al. [73], the use of metal and conductive collectors helps to dissipate the electrical charges and also reduced the repulsion between the fibers. Teo and Ramakrishna [58] and Baji et al. [73] presented and discussed advantages and disadvantages of different setups for collector to be used in electrospinning. Figure 4.2 is a schematic representation of different kinds of collectors [73, 58].

When a plate is used as static collector, fibers can be obtained in a random orientation due to the instabilities of stretched jet. On the other hand, when two parallel plates are used as collector, with a predetermined distance between them (gap), aligned fibers can be produced [82, 83]. Compared to randomly distributed fibers, oriented fibers present better mechanical properties [24]. In another situation, using an array of four counter-electrodes, disposed in opposite directions in a predetermined gap, fibers oriented in two different directions were produced [58]. Teo and Ramakrishna [58] mentioned the gap-distance between the arrays of four counter-electrodes is typically less than 100 mm, because the electrospun jet may not deposit across the gap at larger distances. In addition, the ring collector placed in parallel is also used to obtain aligned fibers [84]. Thus, the characteristics of fibers can be completely changed as the kind of static collector used in the electrospinning process is altered.

Furthermore, many kinds of mobile collectors can be used in electrospinning setup. In these cases, the chances of getting aligned fibers are higher [73]. The collector used can be a drum, a rod, or a disc (Fig. 4.2). The drum or the rod shape can rotate on its own axis, and this axis still can undergo a translational movement in the parallel direction to the rotation. The rotating disc collector can just rotate in a fixed axis, without the translational movement. This kind of setup is very simple, and it is possible to get aligned fibers, and the fiber diameter can be controlled depending on the speed of the drum [58, 73]. But, the electrospun-aligned fibers remain concentrated in a small area.

The drum and rod collectors can be configured in different ways. In the rotating drum collector that presents a simple setup with a large area, aligned fibers can be fabricated, circumferentially oriented, and such alignment depends on the speed of the drum rotation [6, 8, 12, 14, 51, 75, 85]. At low speed, randomly fibers can be obtained because the amount of fibers deposited on the collector is higher for a given low speed low drum speed rotation. On the other hand, if the drum speed rotation is too high, discontinuous fibers are produced, due to the extensive fiber elongation. In the rotating wire drum, it is possible to obtain aligned fibers using a simple setup. Further, the kinds of collector in a rod shape, found in literature [58], can be (i) rotating rod collector with knife-edge electrodes, (ii) controlling electrospinning jet using knife-edge electrodes, and (iii) yarn collection using water bath.

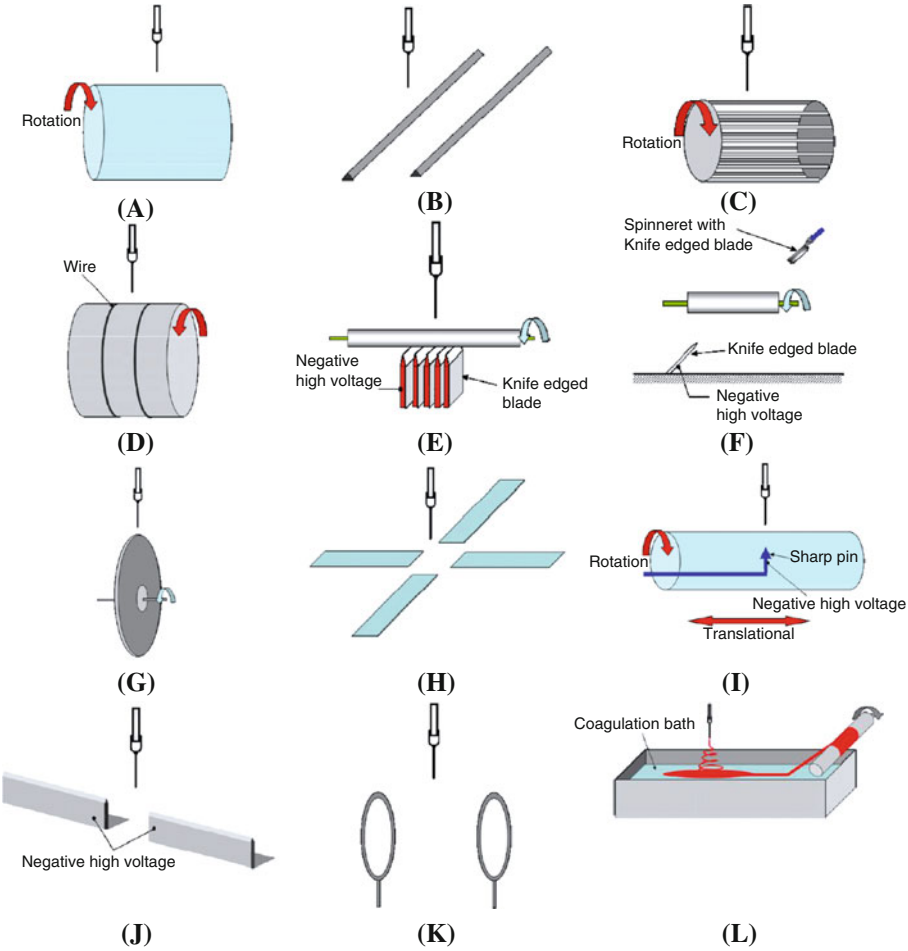

Fig. 4.2 Kinds of collectors used in electrospinning apparatus: (**a**) rotate drum, (**b**) parallel electrodes, (**c**) rotating wire drum collector, (**d**) drum collector with wire wound on it, (**e**) rotating tube collector with knife-edge electrodes below, (**f**) controlling electrospinning jet using knife-edge electrodes, (**g**) disc collector, (**h**) array of counter-electrodes, (**i**) rotating drum with sharp pin inside, (**j**) blade placed in line, (**k**) ring collector placed in parallel, (**l**) yarn collection using water [58] (Reprinted with permission of Ref. [58])

Mi et al. [9] used a rotating rod collector aiming to fabricate thermoplastic polyurethane (TPU)/silk triple-layered vascular scaffolds with various structures using a novel approach that combines electrospinning, braiding, and thermally induced phase separation (TIPS) methods. The inner layer was produced by electrospinning the TPU solution on a rotating aluminum rod. The silk yarn braiding was performed using a rod with the inner layer as the mandrel via a 36-carrier braiding machine (Kokubun, Japan). The outer layer of the vascular scaffold was

prepared by the TIPS method. The average diameter of the scaffolds was 3.18 mm, and the average thickness was 1.05 mm. The authors concluded the triple-layered scaffolds had desirable toe regions in the tensile tests, as well as sufficient modulus, suture retention, and burst pressure for vascular graft applications.

In addition, other kinds of collectors setup are found in literature [28, 32, 41, 50, 77]. Holzmeister et al. [77] evaluated the use of a rotating metal plate collector using two single syringes filled with PA-6 and PLLA, respectively, in the final properties of fiber mats. They had succeeded in electrospinning nonwovens that were heterogeneous in either diameter or chemical composition or both.

Rose et al. [50] used a rotating metal plate and a single syringe to get composite fiber mats of polystyrene (PS), poly(vinylpyrrolidone) (PVP), and polyaniline (PAN) with metal-organic framework (MOF) particles, for the production of functional textile-like layers. This kind of collector allows obtaining MOFs entrapped among the polymer fibers, during the electrospinning process. In such study, they verified that PAN was a suitable material, due to the immobilization of MOFs among the polymer fibers. They pointed out that morphology, mechanical properties, and water resistance of fibers were better than the other studied polymers, probably due to the nonpolar behavior of PAN. Lowering the fiber diameter and decreasing of the MOF particle size allowed entrapping higher MOF amounts (80%).

Aligned light-emitting fibers of mixtures of poly[2-methoxy-5-(2-ethylhexyloxy)-1,4-phenylenevinylene]/poly(ethyelene oxide) (MEH-PPV/PEO) (1:100 w/w) were deposited over a SiO_2/Si substrate, placed on a metallic plate [41]. Grounded collector with x–y and z stages was used allowing control the collector movement through dedicated software. So, the electrospun fibers were deposited in parallel and crossed shapes, obtaining nanostructures with a diameter of about 500 nm, emitting light at 560 nm.

Haromi et al. [32] purposed different collector setup to get nanofiber mats to be applied in pharmaceutical area. They used a metallic collector plate made from copper with an attached stainless steel conductor-rod, which was located in the center of the plate. This setup could enable to efficiently collect nanofibers by concentrating on a conductor-rod with guided electric force to electrospin methacrylic acid copolymer S (MAC S; commercial name EUDRAGIT® S-100). They observed that applying a prescribed voltage, nanofibers were collected, at the beginning, within a copper-mesh and then gradually got to pitch a tent round a fixed conductor-rod to become a layered structure. Consequently, a nanofiber sheet surrounding the metallic collector plate was obtained. At the end, the nanofiber sheet was easily peeled off from the collector plate, compared to the flat plate. After parameter optimization, the authors observed the best range of electrospun fiber average diameter (a.d.) was 271 to 526 nm. Haromi et al. [32] developed nanofiber-based tablets with acetaminophen (AAP), using the same electrospinning device cited earlier, for controlled release systems. They verified the electrospinning method is a useful technique to prepare nanofibers and showed promising results as an oral delivery system for sustained-release regulation.

1.3 Influences of Internal and External Parameters

1.3.1 Solution Parameters

Concentration

The polymer solution concentration is an important parameter that needs to be studied and controlled in the electrospinning. Recently, several studies have been published focusing on this parameter in the electrospun fiber morphology [86–92]. The solution viscosity increases sharply with the concentration due to the occurrence of polymer chain entanglements. The entanglements stabilize the droplets and produce free-beads nanofibers, which can show great uniformity. At very low polymer concentrations, the polymer chain entanglements do not exist, and the jet presents instabilities leading to sprayed droplets, fiber disruptions, or even the occurrence of defect formation in the polymer fibers, called beads [25]. On the other hand, at too high concentrations, the viscosity increases too much, and the interruption in the fiber formation can occur, due to the needle clogging [56]. It is well known that the higher solution viscosity, obtained when the polymer concentration increased, resulted in an increase in the fiber diameter [68]. Thus, the optimal concentration differs with the polymer and can be adjusted accordingly to the molecular weight and the type of solvent.

Al-Qadhi et al. [90] evaluated the effect of the polysulfone (PSf) solution in different concentrations in the electrospun fibers morphology. They observed beads structure when the PSf solution was 5 wt% or less. For solutions with 15 wt% of PSf, beads-on-string structures were obtained. The shape of beads changed from spherical to spindle-like when PSf concentration increased to 20 wt%, and when the solution concentration exceeded 20 wt%, free-beads fibers were formed. The authors attributed the beads absence to the relatively high concentration solution that increases the viscosity and polymer chain entanglements keeping the continuity of fibers and overcoming the surface tension during the electrospinning process. Further, they also observed that if there is an increase in the polymer solution concentration there is also an increase in fiber diameter.

Molecular Weight

The polymer molecular weight presents relevant effects in the rheological and electric properties, such as viscosity, tension surface, and dielectric strength [93], which affect the fiber uniformity, morphology, and size. Molecular weight is directly related to the polymer chains entanglement. Solutions from low molecular weight polymer can present very few entanglement fraction and lead to beads formation even in high concentrations. Accordingly, as the molecular weight of polymer increases, the viscosity of solution and the entanglement of polymer chains raise abruptly, obtaining uniform electrospun fibers with larger diameter [56]. It has been

reported that the relaxation of the polymeric chain becomes more difficult as the molecular weight increases, and the jet splitting and splaying processes are not too effective [94]. As the polymer molecular weight increases, the electrospun fiber's diameter increases as well.

Ramji and Shah [7] studied the morphological behavior of PEO/SPI (isolated soy protein) electrospun blends and verified increase in solution viscosity and decrease in surface tension as the PEO molecular weight was increased, leading to continuous fibers with lesser defects and larger fiber diameters.

Viscosity

The viscosity is a very important parameter to define the fiber diameter and morphology. According to Sukigara et al. [95], it is difficult to obtain continuous electrospun polymeric fibers from solutions with low viscosity. Nevertheless, if the viscosity is very high, it is very difficult to get the polymer jet during the electrospinning process. Thereby, the viscosity is directly related to the molecular weight of polymer and its concentration, used during the electrospinning [25, 56]. The optimal concentration depends on the polymer used to prepare the solution.

Erencia et al. [91] evaluated the viscosity effect in electrospinnability of gelatin solubilized in acetic acid at different concentrations. They observed the gelatin viscosity increased as the amount of acetic acid in solution increased. Moreover, they confirmed the improved electrospinnability of gelatin solution not only with high acetic acid concentration combined with low gelatin concentration but also that the gelatin electrospun fibers can also be obtained for low acetic acid concentrations (25%, v/v) combined with high gelatin concentrations (>300 mg/mL). According to these authors, in the first case, the acetic acid content was high enough to provide electrical conductivity and, the most important, to dissolve gelatin avoiding gelling. In the latter case, the concentration of gelatin was high enough to induce the necessary viscosity and polymer chain entanglement for adequate electrospinning.

Surface Tension

The surface tension is mainly associated with the nature of the solvent and the polymer concentration used in the preparation of the solution. Thus, depending on the solvent used and in moderate polymer concentration, a decrease in the solution surface tension can occur, and the mats obtained may have few or without beads. If the low concentration polymer solution is used, the surface tension increases, and it can cause the jet instabilities during the electrospinning process, occurring the electrospray instead of electrospinning, due to the formation of ejected dropletsand

not continuous fibers, as expected [89]. To overcome the surface tension increasing it is necessary to use higher voltages in the electrospinning process to reduce or eliminate the presence of beads and drops on nanofibers [56, 93].

Conductivity

The electrical conductivity of the solution is the easiness of solution to conduct electricity. This parameter depends directly on both solvent and polymer used to prepare the solution. In some cases, salts or nanoparticles may be used to improve conductivity [96]. According to Bhardwaj and Kundu [56], the use of polymer solutions with higher conductivity favors finer fibers formation. On the other hand, electrospun polymeric fibers obtained from solutions with low conductivity do not exhibited uniformity, due to the presence of beads. The electric conductivity is increased in the presence of dissolved salts allowing reduction in fibers diameter [15]. The electrolyte or surfactant addition and the suitable solvent with high dielectric constant can facilitate the achievement of smaller nanofibers, since the polymer solution conductivity increases and viscosity may decrease to an appropriate value, favoring a greater jet stretching [97, 98]. On the other hand, one excessively charged solvent (ionized) can greatly increase the solution conductivity, avoiding good electrospinnability. The formation of hyaluronic acid fibers (0.8–1.2 wt%) was suppressed by increasing the formic acid level (>25% wt.) and maintaining the water concentration to 25 wt% toward H_2O/N,N-dimethylformamide/formic acid system [98]. In this sense, there is a minimum voltage as a threshold for the electrospinning occurrence, and the presence of ions with greater mobility promotes larger jet stretching and smaller fiber formation [98].

Okutan et al. [89] evaluated some solution and processing parameters in the gelatin electrospinning studies. Using the gelatin solution at 20%, they observed higher electrical conductivity and lower surface tension as compared to the gelatin solution at 7%. They pointed out that the electrical conductivity increasing and/or the surface tension of the feed solution decreasing may help to obtain regular gelatin nanofibers. Similar observations were found by Ramji and Shah [7] during the electrospinning of blends constituted by PEO and SPI (isolated soy protein). They verified slight decrease in surface tension, and significant increase in viscosity occurred as the concentration of either SPI or PEO was increased. So, in these conditions, continuous fibers were formed with lesser defects.

1.3.2 Processing Parameters

Applied Voltage

Applied voltage is a very important parameter to be controlled as the target is to obtain nice fibers through electrospinning process. High positive charge density can be induced on the droplet situated on tip-capillary needle at threshold values

of applied voltage. This allows overcoming the surface tension and starting the jet formation, between the tip and the collector. In many instances, applied voltage higher than 12–15 kV imposes a rise in Coulomb forces in the jet, which lead a greater elongation degree of the polymer chains. This effect decreases the fiber diameter [21, 23, 99]. There is a trend to form beads at high applied voltages, as a consequence of increased instabilities in the electrical-charged jet and in the Taylor's cone [100]. According to Yang et al. [100], high voltages could be used to obtain more uniform and stable electric field that is more adequate for electrospinning. They observed the more uniform electric field provides a suitable electric field distribution for producing thinner fibers due to the larger bending speed, which sufficiently stretches the fiber. Furthermore, high-applied voltages can affect negatively the fiber crystallinity [101–103]. This is, much probably, due to the high stretching force which decreases the molecular orientation of nanofibers by rapid solvent evaporation during the electrospinning process that reduces the interactions between the polymer chains. Thereby, it is interesting to define an optimal applied voltage and work distance, to control the diameter, homogeneity, and degree of crystallinity, aiming desired applications.

Flow Rate

The flow rate of polymer solution is related to the amount of electric-charged solution that is ejected during the electrospinning process at a given time. The correct setting of this parameter, joined to the voltage applied, allows producing fibers without defects (beads or pores) [56, 71, 104]. Low flow rate is adequate for low volatile solvent, in order for the solvent to evaporate before the fiber reaches the collector. Instead, for volatile solvents, it is interesting to use higher flow rate to avoid solvent evaporation at the needle tip, before being ejected. But high flow rates, even using volatile solvents, can result in beaded fibers due to short drying time during the jet traveling from the needle to the collector [104, 105].

Tip-To-Collector Distance

In electrospinning process, it is important adjust the tip-to-collector distance to obtain enough time for drying process before fiber reaching the collector. When the tip-to-collector distance is too close, jet accelerating to the collector occurs leading to very little time for solvent evaporating, producing flat and/or thick fibers [106, 107]; beyond this, the jet presents instabilities and beads on fibers can be observed [108]. On the other hand, when the tip-to-collector distance increases, the nanofiber diameter decreases [82, 107]. The increasing tip-to-collector distance displayed similar results as observed in case of low voltage. Thus, in an optimal tip-to-collector distance, the fibers present round morphology and smaller diameter. But it also depends on the polymer-solvent pair studied.

1.3.3 Ambient Parameters

Temperature and Humidity

The ambient parameters affecting the electrospinning process are directly related to the experimental atmospheric conditions, which can be adjusted and controlled. The temperature influences the solvent evaporation rate and the viscosity of the polymer solution. The control of temperature is paramount to adjust these parameters. At moderate and controlled temperatures, for instance, 40 °C, the solubility of polymer in the used solvent can be improved in relation to room temperature but at the same time decreases the solution viscosity. In this case, the proper jet stretching and the polymer elongation lead to the formation of well-distributed fibers presenting low diameters [15, 109]. Decreasing in the fiber diameter of electrospun polymer with temperature increases were observed in some researches due to the inversely proportional relationship of solution viscosity and temperature [109], besides the solvent evaporation rate also increases.

The relative humidity has a great influence on both electrospinning process and morphology of electrospun fibers. Therefore, control of humidity is also important. At high relative humidity, fibers reach the collector before complete solvent evaporation leading to fiber fusion, beads, and other defects [109]. For electrospinning of a hydrophobic polymer, water acts as a nonsolvent, and during the solvent evaporation, a dry thick polymer film is formed around the liquid jet and allowing pore formation [112]. In this case, porous electrospun hydrophobic fibers can be formed [109–111]. On the other hand, depending on the solvent volatility, at low relative humidities (very dry ambient conditions), the solvent evaporation rate is higher than the solution flow rate allowing polymer solidification at the needle tip [113].

Pelipenko et al. [114] electrospun poly(vinyl alcohol) (PVA), hyaluronic acid (HA), poly(ethylene oxide) (PEO), and chitosan (CS) at controlled relative humidity. It showed the diameter of electrospun nanofibers can be regulated by controlling the relative humidity. At low relative humidity conditions (<20%), rapid solvent evaporation occurs and results in the thicker nanofibers (>400 nm). At higher relative humidity values (>70–80%), the slower solvent evaporation occurs, resulting in thinner nanofibers.

2 Electrospun Fibers and Characterization

2.1 Based on Natural and Synthetic Polymers

Natural polymers belong to the most important class of polymers used for nanofibers manufacturing via electrospinning technique. Regarding the natural biopolymers, proteins such as collagen, silk fibroin (SF), and gelatin are highlighted [115–117]. All these proteins are nontoxic, biodegradable, and biocompatible; they are able to

mimic the extracellular matrix in the body as well as easily degraded by enzymes [117, 118]. These properties are required for some biomedical applications. Collagen and SF received great attention because they have excellent mechanical properties, bioactivity for tissues developing (promote minimal inflammatory reaction toward cells), and occur naturally as fibers, having great electrospinnable potential [117]. However, collagen is relatively expensive, and, when appropriate, it can be replaced by gelatin (a biopolymer derived from natural collagen), which is easily obtained from skins and skeletons of bovine and porcine [116]. On the other hand, gelatin has less structural consistency regarding to collagen [116].

Few polysaccharides as cellulose and hyaluronic acid (HA) also received attention for electrospinning due to their properties of tissue regeneration, chemical resistance, stability, appropriate solubility into organic solvents [98], biodegradability, and biocompatibility [119, 120]. Cellulose is the most abundant linear polysaccharide of the earth, being its application economically viable in this point of view. However, the cellulose has restricted solubility. But the cellulose acetate, one of the most famous acetate ester derivatives processed from cellulose, can be used producing very nice electrospun nanofiber mats, which are applicable in several fields, such as medicine, pharmacy, food industry, and environment [120–123]. The electrospun cellulose acetate can be deacetylated to give back the cellulose nanofibers. Although HA presents great potential to be electrospinnable, it is more expensive than cellulose. The HA biopolymer is commonly found in specialized tissues (extracellular matrix of connective tissue), dermis, cartilages, and synovial fluids [98].

Polycaprolactone (an aliphatic polyester, PCL), poly(lactic acid) (an aliphatic polyester, PLLA), and poly(vinyl alcohol) (PVA) are the most important synthetic biopolymers used to obtain mats by electrospinning [124–127]. These biopolymers also have nontoxicity, biocompatibility, slow biodegradability, and renowned mechanical property. PCL, PLLA, and PVA are electrospinnable polymers to offer nanomaterials with applicability in biomedical field on delivery devices, scaffolds, and healing agents, toward tissue engineering [124–127]. Table 4.1 depicts those based biopolymers of greater importance regarding the electrospinning procedure, as well as some important parameters used such as solvent, flow, concentration solution, and the average diameter of the obtained fiber.

As mentioned in Sect. 1.3 of this chapter, several parameters affect the electrospinning process, being those associated with the characteristic of the polymeric solutions [126] the most important. In this case, the surface tension, viscosity, conductivity, polymer solubility, solvent type and its volatility, and dielectric constant, among others, are important parameters [117]. For example, the electrospinnable solution must contain electrical charges to be stretched. So, polymer solution with zero conductivity cannot give nice nanofibers through electrospinning [98]. So, the increase of conductivity should cause higher elongation on the jet [98]. In general, nanofiber obtainment is considered a challenge, whereas the electrospinning process is complex and it depends on many parameters [89]. Many parameters associated with the electrospinning were discussed in Sect. 1.2 and 1.3 and will be recalled when necessary.

Table 4.1 Electrospun biopolymer fibers

Biopolymer	Solvent	Flow (mL h^{-1})	Concentration (wt.%)	Size (nm)	Year
Collagen	EtOH/PBS [117] HFP [118]	0.5 [117, 118]	16 [117] 6 [118]	420 [117] 127 [118]	2012 [117] 2016 [118]
SF	EtOH/H_2O [128] HCOOH/$CaCl_2$ [97]	[128][a] 1.5 [97]	15–21 [128] 8–12 [97]	183 [128] [97][a]	2014 [97] 2016 [128]
Gelatin	H_2O [116] AcOOH [89, 129]	[116][a] 0.1or 1.0 [89] [129][a]	10 [116] 7 or 20 [89] 11–30 [129]	292 [116] 46–88 [89] 184 [129]	2014 [129] 2015 [89, 116]
Cellulose acetate	Ac/DMAc/EtOH [123] Ac/DMF [120] CF_3COOH [121] Ac/DCM or Ac/AcOOH [122]	1.0 [122, 123] 1.8 [120] 0.3 [121]	9.17 or 11 [123] 12–16 [120] 15 [121] 17 [122]	240–650 [123] 800 [120] 120–130 [121] 200–500 [122]	2012 [123] 2016 [120–122]
Hyaluronic acid	H_2O/HCOOH/DMF [98] NH_4OH/DMF [119] NaOH/DMF [119]	0.3 [98] ≈0.09 [119]	0.8–1.2 [98] 1.5 or 3.0 [119]	100 [98, 119] 39 [119]	2011 [98] 2012 [119]
Polycaprolactone	$HCCl_3$ [127] HCOOH/AcOOH [127]	1.0–5.0 [127]	10 [127]	222–266 [127]	2011 [127]
Poly(lactic acid)	$HCCl_3$/DMF [126]	[126][a]	8–12 [126]	730–1119 [126]	2014 [126]
Poly(vinyl alcohol)	H_2O/HCl/Ac [124] H_2O [130]	10 μL/min [124] 0.3 [130]	8 [124] 10 [130]	290 [124] [130][a]	2016 [124, 130]

Ac acetone, *DMAc* N,N-dimethylacetamide, *EtOH* ethanol, *DMF* N,N-dimethylformamide, *CF_3COOH* trifluoroacetic acid, *DCM* dichloromethane, *AcOOH* acetic acid, *PBS* buffer solution, *HFP* 1,1,1,3,3,3-hexafluoro-2-propanol

[a]The dates were not informed

Nanofibers with desired mechanical strength, stability in water, homogeneity, and low diameter size are required in many applications. PVA, gelatin, collagen, and SF fibers have low stability to humidity (due to high aqueous polymer solubility) and in contact with water can lead to rupture of material structure reducing the potential for application [116, 124]. In this sense, nanofibers based on gelatin (a.d. = 292 nm) and PVA (a.d. = 290 nm) were cross-linked with glutaraldehyde (cross-linking between -OH groups on polymer chains and aldehyde) to offer nanomaterials with excellent mechanical resistance and better water stability [116, 124]. However, the high glutaraldehyde toxicity is a disadvantage for these procedures, decreasing the applicability of this nanomaterial in biomedical field. Undoubtedly, the use of a cross-linking agent with lesser cytotoxicity like 1-ethyl-3-(3-dimethylaminopropyl)-1-carbodiimide hydrochloride (EDC) is essential to give suitable biocompatibility to the end material [128].

The system based on N-hydroxysuccinimide/EDC (NHS/EDC) is one of the best to promote cross-linking toward polymers due to its nontoxicity and selectivity [128]. SF (a.d. = 183 nm) and collagen (a.d. = 420 nm) fibers were obtained under NHS/EDC presence from "*in situ*" procedure, and the as-obtained nanofibers did not have good water stability, suppressing applications like scaffolds and as drug delivery agents. After cross-linking, such nanofibers were more resistant and more stable against humidity [117, 128]. Citric acid was also used as a cross-linking agent for PVA nanofibers (a.d. = 270 nm), leading to formation of more stable materials when exposed to water [125]. The higher humidity also promoted an increase on PCL fiber diameters [127].

Solutions with low viscosity do not favor the electrospinning process because the solution jet can be easily broken [89, 98, 123]. In this case, the surface tension has a dominant influence onto electrospinning jet, leading to formation of beaded fibers ("bead-on-string") [89, 98, 123]. Currently, it is a challenge to obtain bead-free fibers in the nanoscale range [127]. Indeed, the surface tension of the solution may be reduced by an appropriate solvent, namely, by a "good" solvent [98, 127]. Cellulose acetate (9.17 wt.%), SF (<15 wt.%), gelatin (7.0 wt.%), and hyaluronic acid (HA) (0.6 wt.%) solutions were prepared at acetone/N,N-dimethylacetamide/ethanol (4:1:1), ethanol/H_2O (95:5 v/v), acetic acid, and H_2O/N,N-dimethylformamide (DMF)/formic acid (1:2:1), respectively, leading to formation of fibers with "bead-on-string" morphologies [89, 98, 123, 128] (Fig. 4.3). In all these cases, the "bead-on-string" shape may be suppressed by increasing the polymer concentration [89, 98, 123, 128].

The use of an appropriate solvent with higher dielectric constant reduced the likelihood of beads occurrence. For example, the formic acid/acetic acid binary system was used to obtain polycaprolactone (PCL) nanofibers [127]. Formic acid insertion in suitable amount (1:2 formic acid/acetic acid) assigned the formation of smaller PCL nanofibers (a.d. = 266 nm) with smoother morphology [127]. Formic acid has dielectric constant (58) much higher than acetic acid (6.2), being the binary system (formic acid/acetic acid is a less harmful mixture) a better choice for preparing PCL fibers in the nanoscale range, concerning those systems containing chloroform (a toxic solvent commonly used for PCL fibers preparation), due to its

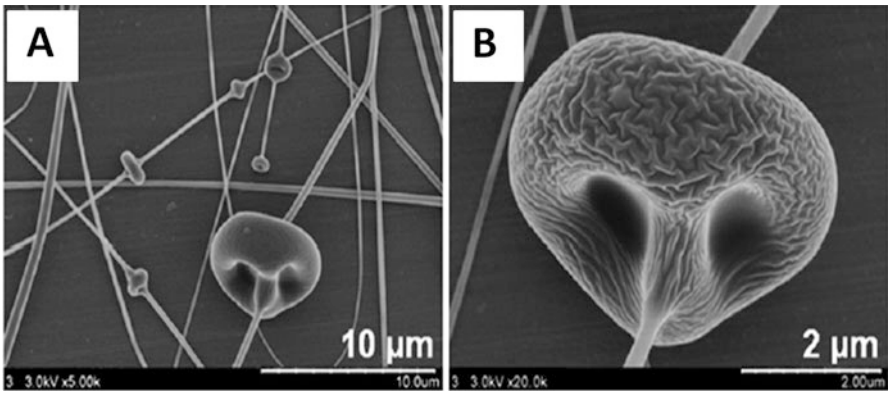

Fig. 4.3 Cellulose acetate fibers with "bead-on-string" morphology: at the low (**a**) and high magnifications (**b**) (Reprinted with permission of Ref. [123])

higher toxicity [127]. The acid medium did not degrade the PCL chains within 3 days, implying a suitable time frame for PCL electrospinning [127]. So a solvent with a higher dielectric constant causes an increase on electrospinning instability of the jet, and the interaction between the charges present on jet and solution must be critical to determine the material shape.

CS is a widely studied polymer due to its important properties such as non-toxicity, biocompatibility, biodegradability, and antimicrobial [131]. CS can easily bind to toxic metal ions, which can be beneficial for use in air cleaning and water purification applications [132]. The repulsive forces between ionic groups within polymer backbone that arise due to the application of a high electric field during electrospinning restrict the formation of continuous fibers and often produce beads. So, it is difficult to prepare nanofibers from CS. Okawa et al. used trifluoroacetic acid (TFA) for obtaining mats of CS. The TFA is a suitable solvent for electrospinning of CS because TFA can form salt with CS, so the interchains CS-interactions are destroyed facilitating the CS nanofibers [133]. The addition of dichloromethane (DCM) to TFA-CS solution improved the homogeneity of CS fibers without interconnected fibrous networks [134]. Using the ratio DCM/TFA as 30/70, nanofibers with a.d. $= 126 \pm 20$ nm were produced [135].

If the solvent used is not appropriated (does not interact with the polymeric matrix), the effect may be the contrary of that described previously. Poly(lactic acid) (PLLA) nanofibers were prepared from binary system, composed by chloroform/DMF (9:1, 8:2, and 7:3). Increasing the DMF concentration led to formation of PLLA nanofibers with "bead-on-string" morphology [126]. In this case, the DMF (with dielectric constant of 38) was not a suitable solvent for PLLA, decreasing its solubility into binary system (composed mainly by chloroform, which has dielectric constant of 4.8) and even more promoted an increase in surface tension to give beaded PLLA fibers [126].

The solution should have a suitable viscosity. Viscous solutions become unworkable to be electrospinnable into the syringe, leading the spinneret cloggings [98, 119, 123, 128]. Hyaluronic solutions (1.2 and 3.0 wt.%) promoted the clogging of the needle capillary, and the fiber formation was interrupted within 1 min for 1.2 wt.% solution [98]. The adjustment of concentrations for SF (17 wt.%), gelatin (20 wt.%), and HA (1.0 wt.%) allowed the formation of clear cylindrical fibers with lowest a.d. (183 nm for silk, 46–88 nm for gelatin, and 100 nm for HA) [98, 119, 123, 128]. HA solution (3.0 wt.%) in NH_4OH/DMF (2:1) failed to produce any fibers [119].

Increasing the SF concentration to 21 wt.% promoted higher a.d. of nanofibers up to 630 nm [128]. Another study showed solutions at low SF (8–12 wt.%) concentrations were suitable to obtain fibers without "bead-on-string." This is possible because many parameters, such as solvent type, polymer molar mass (which is related to the silk type), temperature, and governing variables (electrical field strength, fluid flow rate, and distance tip-to-collector plate), can be changed in the electrospinning process to control nanofiber production with desired morphologies. So, when SF was electrospinnable from solutions at 8–12 wt.% concentration range, using formic acid/$CaCl_2$ solution, the a.d. for fibers were 297 nm at 8 wt% and 689 nm for 12 wt.% solution [128].

An appropriate solvent or solvent mixture can facilitate the nanofiber obtainment [98] with porous morphology or favors the formation of flattened or ribbonlike fibbers. Flattened cellulose acetate fibers were obtained using DMF/acetone, mainly when the concentration of cellulose acetate was increased to 16 wt.% [120]. As already mentioned, the increased concentration enhances the viscosity, slowing the solvent evaporation, and when the wet fibers are collected, they are flattened by the impact. Figure 4.4 depicts the cellulose acetate fibers with flattened morphology.

HA nanofibers (a.d. = 100 nm) were obtained only when the ratio between H_2O/DMF/formic acid solvents was 1:2:1. Other proportions were investigated, but led to negative outcomes. Increasing DMF concentration became the HA solution

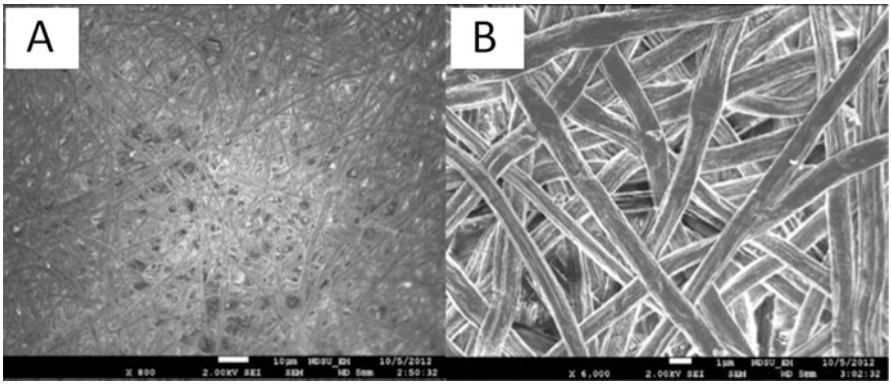

Fig. 4.4 Cellulose acetate fibers with ribbonlike morphology: at 50× (**a**) and 6000× magnifications (**b**) (Reprinted with permission of Ref. [120])

(0.8–1.2 wt.%) electrospinnable [98] due to the lowering of surface tension. In this case, the higher HA molar weight (10^6 $gmol^{-1}$) considerably decreased the appropriate concentration for electrospinning, regarding those used for the proteins (Table 4.1). Larger molar weight leads to a much higher viscosity for HA dilute solutions. This factor becomes a tough challenge to find the critical concentration, enough to promote the HA chain entanglement to be electrospinnable [119].

When HA molar weight was increased to 2,000,000 $gmol^{-1}$, 1.5 and 3.0 wt% solutions were electrospinnable, using NaOH/DMF (4:1) and NH_4OH/DMF mixtures (2:1 and 2:3) [119]. Strong alkaline condition (NaOH) causes polysaccharide degradation, leading to formation of fibers with 100 nm diameters. On the other hand, under NH_4OH/DMF (2:1) system (a weak alkaline condition), 1.5 wt% HA solution was better electrospun, and nanofibers with much lower size and narrow diameter distribution were obtained (39 ± 12 nm) [119]. In this case, the key to give thinner nanofibers was the lesser NH_4OH/DMF solution conductivity, concerning the NaOH/DMF solution. According to Brenner et al. [119], the solvent mixture disrupts the strong H-bonds on biopolymer structure improving chain entanglement to be electrospinnable.

Porous fibers were obtained using solvents with high volatility. Cellulose acetate fibers with a high pore density were taken in dichloromethane/acetone (2:1), because the mixture had boiling temperature at 40 °C. The large volatility for binary system favored pores formation [122]. The fast solvent evaporation leads to phase separation on electrospinning jet; one phase has polymer excess, while the other is richer in solvent. The poor polymer phase is responsible by the pores formation. Thus, the vapor pressure of the system has a critical influence on the nanofiber porous morphology [122].

2.2 Based on Polymeric Blends

The physical mixture of polymers generates a polymeric blend [136–140]. Sometimes combining two or more polymers can benefit the electrospinning process and also improve the application spectrum of such nanofibers due to new important properties of the system [136–140]. For example, some biopolymers have greater medicinal importance, such as CS, SA, and SF. Depending on the final destination/application, they may not have adequate mechanical properties to generate nanofiber with technological interest [136–140]. Besides the hydrodynamic responses, repulsive forces regard the polyanion or polycation solutions (composed by polysaccharides or proteins), and several chain conformations adopted by these charged macromolecules promote lesser electrospinning efficiency, being the process of lower reproducibility. This is a challenge, because protein or polysaccharide nanofibers were not obtained with desired uniformity, limiting their practical applications. Other parameters associated to polysaccharide/protein solutions are due to higher surface tension and conductivity [136–140].

On the other hand, biopolymers such as PCL, PLLA, and PVA have renowned mechanical property and do not have ionizable side groups in their structures, such as -NH_2 or -COOH, which occur on CS and on several anionic polysaccharides and proteins, respectively. Such groups are associated with the greatest potential for biocompatibility of these materials. However, depending on the desired application, nanofiber based on synthetic biopolymers must have their biocompatibility improved [136–140]. For example, the most challenging objective of 3D cell culture is the manufacture of scaffolding materials with outstanding favorable mechanical strength and excellent biocompatibility [139]. In this case, the combination of natural and synthetic biopolymers can give blended systems that overcome limitations of simple polymer systems [136–140]. All the parameters described in previous section significantly change the electrospinning process of polymeric blends. Regarding the blended solution, it must be depicted the effect of some parameters (specially the solvent type and polymer concentration) on morphology of fibers [138, 140].

PVA/CS (60:40 wt.%) and PVA/SA fibers cross-linked with glutaraldehyde were carried out and applied as filter for chromium removal and as scaffold matrices, respectively [136, 137]. The effect on chromium ion removal was maximized by the CS presence on PVA/CS matrix, since the amino group is an excellent chelating agent for metals. Cross-linking with glutaraldehyde improved the fiber stability against water [136, 137]. From PLLA and CS combination, it was possible to obtain more stable nanofibers against humidity, while neat PLLA fibers in contact with buffer solution (PBS) were completely disintegrated in just 2 weeks. Nanofibers (a.d. = 167 to 525 nm) could be generated from PLLA/CS solutions at desired concentration [138].

Porous nanofibers based on PCL/collagen were prepared with smooth morphology, and higher collagen concentrations led to formation of smaller fibers (a.d. = 480 or 689 nm) [139, 141]. Again, the polymeric system viscosity was the key factor to obtain fibers with suitable morphology [139, 141]. The addition of collagen decreased the solution viscosity of binary systems composed by chloroform/H_2O or chloroform/methanol and improved the materials mechanical properties [141]. Generally, blended systems composed by several biopolymers have been obtained and studied [140]. Blends of SF/PVA, SF/PCL, SF/PLLA, SF/CS, SF/gelatin, SF/HA, among others, were investigated as well [140]. SF nanofibers with suitable diameter are challenging because the electrospinning of SF aqueous solution often leads to the formation of ribbonlike fibers. Therefore, the SF and its association with other components are carried out to give better mechanical properties to the smooth nanofibers [140].

2.3 Nanofibers Containing Nanoparticles

The addition of organic or inorganic nanoparticles (NPs) into electrospun nanofiber mats has different purposes, which might be improving or inducing new properties in the final material such as optical, mechanical, electrical, thermal, and biological,

among several others, as well as improving the electrospinnability of the polymer solution by changing key solution properties, e.g., surface tension, conductivity, viscosity, etc., that are essential in controlling the process, the homogeneity, and sizes (average diameter, a.d.) of final electrospun fibrous mats.

A quick search at ISI™ database with the words "electrospinning" and "nanoparticles" showed ca. 3500 papers, while more than 8000 papers appeared using the same keywords at Scopus™ database. Independent of the database chosen, the oldest papers date from the year 2002. This impressive number of recent papers published in such a short period of time pictures on how this topic (electrospinning evolving NPs) is paramount in many fields of science with potential uses as purification systems, catalysts, sensors, tissue engineering, energy storage devices, and drug delivery, among others, that are still yet to be glimpsed by creative researchers.

The addition of NPs is always a challenging task since solution properties are generally changed, and therefore processing parameters (working distance, applied voltage, solution flow rate, etc.) have to be adjusted in order to obtain nanofibers with specific features. Besides, the added NPs should be easily dispersed in the solvent to avoid precipitation and heterogeneous distribution into the fibrous polymer matrix. The use of surfactants, vigorous mechanical stirring, ultrasonication, and *in situ* polymerization has been reported as convenient means to achieve satisfactory filler dispersion throughout the polymer matrix. Among the organic NPs, single or multiwalled carbon nanotubes [142–144], cellulose nanocrystals [145–150], and chitin nanocrystals [151–155] have been the most reported in the preparation of electrospun composite mats.

In general, carbon nanotubes (CNTs) have been incorporated into fibrous mats owing its electrical features and high Yong's moduli ($\approx$1000 GPa) [156], to induce electrical conductivity and improve mechanical properties. For instance, Seoul et al. [157] used CNTs to modify conductivity of poly(vinylidene fluoride) (PVDF) in DMF solutions and electrospun fibrous mats. CNTs addition (0.002 and 0.004-wt%) to PVDF solutions caused significant increase in the solution viscosity from 1200 to 1800 cP, while further increment on CNTs contents did not significantly alter such feature. Homogeneous electrospun nanofibers (a.d. = 70 nm) were obtained from 20-wt% PVDF solutions with 0.0004 wt-% CNTs, using voltage of 5 kV, 18-gauge needle (solution flow rate was not provided), and 5 cm of tip-to-collector distance. At 0.1-wt% CNTs the electrospun fibrous mats presented an outstanding 6 orders of magnitude increment in electrical conductivity properties from 1×10^{-12} S/cm to 1×10^{-6} S/cm. Another study reports the effect of multiwalled carbon nanotubes (MWNTs) in the electrical features of poly(methyl methacrylate) (PMMA) electrospun fibers [158]. Electrical conductivity of pure PMMA film was ca. 10^{-15} S/cm while 1.4×10^{-2} S/cm for cast films at 5 wt-% MWNTs. Surprisingly, the electrical conductivity for electrospun MMA/MWNT fibers decreased to 10^{-10} S/cm, regardless of the concentration of carbon nanotubes (1–5 wt-%). That behavior was explained by the high porosity of the fibrous mats and by the fact that the fillers were completely embedded by the PMMA chains.

Sen et al. [159] demonstrated the effects of single walled carbon nanotubes (SWNTs) and ester-functionalized SWNTs on the tensile strength of electrospun polyurethane and polystyrene nanofibers. The addition of either fillers at a ratio of 1:100 (filler/polymer) increased more than 200% the tensile strength of electrospun fibers.

Bio-based nanoparticles such as polysaccharide nanocrystals (cellulose or chitin), which are easily obtained from biomass residues, are biodegradable and biocompatible and present high Young's modulus (∼150 GPa), and have been employed as reinforcement in polymeric materials. Naseri et al. [154] tested the surface chemistry of polysaccharide nanocrystals (at 50 wt-%) in the electrospinnability of CS/PEO solutions. It was found that surface charges have significant impact on spinnability, dispersion of nanofillers and final aspects of fibrous mats. Fibrous mats containing chitin nanocrystals were easier to electrospin, and the fibers were more homogeneous than those mats prepared from cellulose. The basic difference resides on the surfaces of nanocrystals; cellulose was negatively charged due to the presence of sulfate groups, while chitin was positively charged due to the presence of amine groups (protonated at the solution acid pH). The main reason was that solution with chitin presented higher viscosity, higher conductivity, and lower surface tension as compared to those with cellulose. Moreover, samples containing chitin whiskers presented higher water wettability (drop water contact angle =18°).

The inorganic NPs usually employed in the preparation of electrospun nanofibers composites are gold [160, 161], silver [162–164], hydroxyapatite [165, 166], clay minerals [167–169], bioactive glass [170], metal oxides [171, 172], silicon [173], among others.

Wong et al. [174] showed that the presence of hydroxyapatite (HAP) nanopowder in PCL nanofiber also affects the tensile modulus of mats. It was observed that tensile modulus increased with increasing HAP concentration on electrospun polymer composites. This was due to HAP particles being carried by the nanofibers and to confine the segmental motion of the PCL chains, which results on enhancing the tensile strength of the composites. In this case, the electrospinning process leads to molecular chains reordering, like in a melt flow fashion. The tensile strength was improved by increase on anisotropy, molecular conformation, and the transition from flaw-sensitive domain.

2.4 Physical and Chemical Changes on Surfaces of Electrospun Fibers

Surface chemistry and physical aspects of electrospun nanofibers (e.g., surface to volume ratio, roughness, porosity, porous size distribution, etc.) are paramount to design functional materials for specific applications [175]. Therefore, chemical and physical changes on electrospun fibers surfaces targeting different goals have been reported and are subject of some review papers [176–179].

Many different physical approaches to modify surfaces including etching methods and laser ablation, plasma, differential solubility, and thermal stability of

fiber components have been reported [180–182]. Chemical methods are virtually unlimited and depend mostly on surfaces composition [178, 183, 184]. Surface modifications targeting technological applications, including tissue engineering, antibacterial agents, water/oil separation, biosensor, drug delivery, enzyme immobilization, among others, are explored in this section.

Tan et al. [185] prepared vascular grafts based on PCL, gelatin (GT), and PVA using electrospinning and tested the material ability to improve tissue regeneration using subcutaneous implants in rat models. Faster degradation rate and higher solubility of PVA under physiological conditions, related to PCL and GT, provided fibrous membranes with large porous allowing cell infiltration and migration within the scaffolds improving cell regeneration and healing process. Therefore, PVA was used as a sacrifice material with differentiated solubility parameters to generate high porosity. Furthermore, chemical modification was provided by functionalizing the fibrous mats surfaces with heparin, which is an antithrombogenic (i.e., inhibits blood clot formation) agent. In this case, both physical and chemical modifications were performed on the surfaces to achieve electrospun scaffolds with adequate biomechanical and biocompatible features to be used in tissue engineering.

Several water-soluble polymers can be successfully turned into nanofibers through electrospinning. However, the high surface area to volume ratio of electrospun materials induces fast solubilization in aqueous media hindering many possible applications. In order to prevent undesirable solubility, physical and chemical cross-linking approaches have been reported. For instance, Liu et al. [124] reported the preparation of cross-linked PVA nanoporous fibrous mats from electrospinning. Fe_3O_4 NPs were added to PVA aqueous solutions (8 wt-%) and then electrospun at 10 μL mL^{-1} by a syringe pump, voltage of 9.0 kV, and working distance of 10 cm. PVA fibers were chemically cross-linked through the formation of acetal bonds by reacting the hydroxyl groups from PVA with glutaraldehyde. Further, Fe_3O_4 NPs were removed by differential dissolution in HCl solutions producing highly porous cross-linked PVA membranes. The membranes presented a.d. = 290 nm with pores (14∼20 nm, as indicated by N_2 isotherms) throughout the polymer matrix. The authors suggest the possibility of such material to be used as biomaterial. Similar approaches for cross-linking PVA electrospun fibers with glutaraldehyde have been also reported [186, 187]. Physical stabilization of polymers by increasing crystallinity with either thermal or nonsolvent treatment has been reported [188].

Hydrophobic NPs such as Ag nanoclusters and hydrophobic nanosilica have also been incorporated on electrospun nanofiber surfaces to impart hydrophobicity in water/oil separation systems [189–191].

Layer-by-layer (LbL) assembly of oppositely charged materials has also been reported in electrospun mats surfaces modification. He et al. [192] developed poly-L-lactide (PLLA) electrospun scaffolds to be further modified with polysaccharide-protein (CS-gelatin) by LbL self-assembly. The modifier polymers were chosen due to similarity of extracellular matrix (ECM). The modified electrospun mats were used in nerve regeneration. It was showed that both number of layers and top layer influence neurons attachment and outgrowth enhancing cell matrix interactions in relations to pure PLLA membranes.

A myriad of physical and chemical modifications of electrospun fibers have been reported, and the most adequate one depends on fiber composition, toxicity of reactants, single or multiple reaction steps, and final material application. Therefore, it is up to us to decide which path is more adequate and beneficial when considering specific fibrous mats surface changes.

2.5 Techniques Often Used for Characterization of Electrospun Fibers

The electrospinning process is highly versatile to obtain materials structured in the form of nanofibers [193]. As stated before, due to the electrospun fiber being formed by extremely thin line with nano- and/or submicrometric scale, their meshes have a high surface to volume ratio [194]. Moreover, the nanofibers often exhibit high porosity and ductility and can be formed into a wide variety of sizes and shapes [195, 196]. Among the advantages of using electrospinning for fiber forming, the control of composition thinking in terms of polymer blend or polymer-containing nanoparticles to achieve desired properties and functionality can be mentioned. So, different techniques need to be applied for a complete characterization of electrospun nanofibers for anticipating a specific (or a set) of use. According to thermal, structural, morphological, and mechanical properties, several techniques can be used allowing a complete characterization of electrospun material.

It is very common to see papers highlighting the morphology of electrospun materials using the microscopies: optical (OM), atomic force (AFM), and electronic scanning/transmission (SEM/TEM), in which the most common is the SEM [197]. In addition, several studies have analyzed the fibers through thermal analysis (TGA, DSC, DTA, etc.), highlighting the use of DSC [198] to study the thermal behavior of electrospun polymer alone or mixed with other polymers or bioactive substances, for example [194]. Regarding the addition of bioactive substance or mixture of polymers, or synthesis, spectroscopic techniques (FTIR, NMR, XPS, etc.) are also often used to evaluate the chemical structure of electrospun material [198] and mechanical characterization through DTA, DMA, etc., to assess the effect of the polymer mixture or compound addition on the fiber strength [199]. The presence of metallic NPs in polymeric nanofibers can be done through atomic absorption technique [200].

2.5.1 Thermal Analysis

Thermal analyses, such as TGA, DSC, DTA, etc., are extensively used to characterize polymer materials, in general, due to the easy sample preparation, to sensibility to changes in physical and chemical structures, and to the facile data interpretation. Specifically, these techniques can provide information of structural organization of electrospun polymeric fibers. It is possible, for instance, to check whether the electrospinning process leads to a modification from thermal properties

of electrospun material such as crystallinity, glass transition, melting temperature, thermal stability, phase transition, or weight loss due to temperature-induced decomposition or evaporation, as compared to pristine polymers.

Bizarria et al. produced membranes of CS/PEO 80/20 w/w through electrospinning process [196]. They observed by thermal analysis (TG and DSC) that the electrospinning process did not considerably affect the thermal properties compared to raw (not electrospun) polymers. However, the presence of CS significantly interfered on the PEO crystallization and leads the PEO melting peak to shift to lower values. Besides disfavoring the crystallization, the presence of CS also delayed the crystallization of the PEO.

Awal et al. [201] developed nanoscale composite fibers from wood pulp, modified wood pulp, and PEO, through induced electrostatic interactions using two parallel collector discs. Fibers with a.d. ranging from 339 to 612 nm were observed through SEM. These authors showed by DSC analysis that such composite fibers presented lower melting temperature than PEO powder. Moreover, they also observed by TG that the composite fibers presented thermal stability relatively lower than PEO powder. Furthermore, spreading of crystalline structure in the composite fibers and acetylated wood pulp was reduced.

Waseem et al. [199] investigated electrospun nanocomposite fibers from poly(vinyl pyrrolidone) (PVP) solutions with incorporated MWCNTs. The electrical resistance decreased with increase of temperature due to the phase transition occurred on polymer chains. The phase transition ranges from 37 to 60 °C, as confirmed by DSC studies. Moreover, no significant effect was observed on the glass transition temperature (Tg) of PVP/MWCNTs nanocomposite. These results suggested that no significant covalent bonds occurred between the MWCNTs and the PVP chains.

Ibrahim et al. studied PAN-based electrospun nanofibers followed by oxidation at 270 °C and subsequently carbonization at 750, 850, and 950 °C for 1 h [198]. The carbonization process removed all non-carbonaceous material and preserved the carbon fibers. This process leads to highly purified carbon nanofiber mats with adequate property for possible use as a sensor material in a structural health monitoring (SHM). Such electrospun PAN fibers were lightweight and less costly and did not interfere with the adequate structural monitoring. The PAN fibers before and after the carbonization process were characterized through electrochemical impedance spectroscopy (EIS), X-ray diffraction (XRD), TGA, DSC, FTIR, and drop water contact angle measurements. The results indicated the carbonization process improved the physical properties, such as carbon amount, hydrophobicity, and ionic conductivity of PAN nanofibers. Chemical reactions, such as cyclization, degradation, and thermal cross-linking occurred during the heating of the PAN fibers. Moreover, factors such as heating rate, the environment, the mass of the polymer, and the type and nature of material filler can modify these processes. The authors observed that beyond the stabilization, time has been increased, the peak attributed to cyclization expanded, and the cyclization temperature considerably increased. During cyclization of nitrile groups, releasing of heat occurred, and this exothermic process was able to fragment the chains. The exothermic process can be

observed in the DSC thermograms through a peak attributed to the cyclization of the nitrile groups, in PAN-based on the free radicals.

Fouad et al. [202] prepared electrospun poly(DL-lactide-co-glycolide), (PLGA), nanofibers and analyzed by TG and DSC. As a relevant result, the authors observed that Tg of the electrospun sheet is lower than that of the raw PLGA. This event was associated to occurrence of molecular chains orientation in the electrospun polymer nanofibers and to a larger area-to-volume ratio of electrospun mats. Moreover, the electrospinning process reduced the chain entanglements and, consequently, decreased the crystallinity of the fiber as compared to PLGA bulk material. Also, TG analyses allowed observing the weight loss due to thermal decomposition or evaporation occurred at a higher temperature for bulk as compared to PLGA fibers. This result was attributed to the presence of residual solvents in the nanofiber sheet.

2.5.2 Structural Chemical-Physical Analysis

Spectroscopic techniques such as FTIR, NMR, XPS, and others are suitable for studying the chemical structure of polymeric materials, in general way, and, obviously, can be employed to study electrospun meshes. For instance, these techniques allow evaluating if during electrospinning process occurs or not modification on chain structure such as chemical or physical events. Beyond this, the occurrence of intermolecular interaction forces, covalent bond formation, or also structural deformation can be observed on electrospun material and on another eventually present substance.

Composite fibers from wood pulp and PEO were studied by Awal et al. [201] through FTIR. The characteristic peak of PEO was observed since less wood pulp was incorporated in the composite system.

FTIR analysis made by Wei et al. [194] on poly(L-lactic acid) (PPLA)/captopril composite nanofibers indicated the electrospinning process changed the physical form of captopril, but its chemical structure remained unchanged. This was possible once the characteristic peaks in the composite shifted to higher wavenumbers in the FTIR spectra of the composite. Probably, the process occurred by mechanism related to weakening the association of the hydrogen atoms with the addition of PLLA, highlighting that the oxygen of the carbonyl group in PLLA could form the hydrogen bond with the hydroxyl of captopril carbonyl.

CS and PVA blend solutions were investigated by Zhou et al. [203] , and they observed that blends were homogeneous and optically clear and, thus, present only one phase indicating complete miscibility. Moreover, analysis by FTIR on such blends demonstrated that the absorption band at 3420 cm^{-1} concerned the –OH and –NH stretching vibrations, broadened, and shifted to a lower wave number. This matches on addition of PVA in the blends, and it is due to the formation of H-bonds among CS and PVA chains. Moreover, such authors observed that intermolecular interactions between PVA and CS disturb the crystallization of CS.

Electrospun fibers of Nylon 11 were characterized by Dhanalakshmi et al. (2008) through XRD [204]. The Nylon 11 is a polymer with about five crystalline phases

(**α**, **β**, **γ**, **δ**, **δ'**, and **α'**). The authors pointed out the electrospinning process transformed the **a** phase of Nylon 11 to **g** phase, and such fact was attributed to fast evaporation of the solvent combined to the elongation of the fibers during electrospinning process that lead to a mechanical deformation. Moreover, the rapid solidification of the polymer solution limited the development of crystallinity. Using the same technique, Oliveira et al. [205] showed that different mechanisms and timescales are important key factors for fiber crystallinity of electrospun fibers from PLA, PEO, and PCL solutions. It is well known that the crystalline structure and chain orientations in electrospun nanofibers depend on molecular weight, polymer-solvent interactions, and process timescale.

Using a mixture of trifluoroacetic acid/dichloromethane (TFA/DCM) as solvent, Sencadas et al. [206] obtained electrospun CS (CS) nanofibers. They observed through FTIR that strong acids such as the mixture of trifluoroacetic/hidrochloridric (TFA/HCl) can charge the polymer. In this case, strong electrostatic interactions and rotational distortion are induced around the main polymer chain. Moreover, the electrospun CS nanofibers can be cross-linked using glutaraldehyde (GA) once an increase of methylene groups resulting from condensation reaction occurred. The resulting product presented more elongated chain due to intermolecular cross-links and inhomogeneities of the reaction. These authors calculated the degree of deacetylation (DD), being around 86% for CS, using a method developed by Brugnerotto et al. (2001) [207], through FTIR and ^{1}HNMR experiments. It was observed that the electrospinning, neutralization, cross-linking, and neutralization followed by cross-linking processes did not change the degree of deacetylation. Once CS can exhibit two crystalline structures (form I and form II), the crystallinity of electrospun CS was further studied by X-ray diffraction. It was observed decreasing on degree of crystallinity of CS due to electrospinning process. Due to exposure to strong electric field in the flight needle tip/collector, the diffusion of CS chains to incorporate to growing crystals was compromised, resulting in lower crystallinity and a formation of a less homogeneous crystalline structure. Finally, the authors pointed out the cross-linking process induced reorganization of polymer chains through rearrangement of intra- and intermolecular hydrogen bonds from CS network and introduced discontinuities along the polymer chains, which hindered crystal formation.

2.5.3 Morphological Analyses (OM, SEM, TEM, etc.)

The information that one gets on the morphology and the dimensions of the physical structure of the material depend on microscopy technique used: OM, SEM, TEM, or AFM. The SEM has been largely used to assess the structure and morphology of electrospun materials. In general, information about the average and diameters distribution of fibers and some structural characteristics are obtained from SEM micrographs. Several papers have been published highlighting the structure of electrospun materials describing on how electrospinning inputs change the morphological structure of electrospun nanofibers [208]. For instance, Dhanalakshmi

et al. (2008) showed by SEM images that electrospun fibers of Nylon 11 present two different morphologies [204]. Uniform nanofibers of Nylon 11 from electrospinning of 10 wt% concentration solution, with a.d. ∼300 nm, were obtained. At higher polymer concentration (20 wt%), however, ribbons and circular fibers, with diameter ranging from 400 nm to few micrometers, were obtained.

2.5.4 Mechanical Properties

The mechanical properties of electrospun materials depend on many factors such as polymer fiber composition, the solvent type, operating conditions, and the setup used as collector. Shing-Chung Wong et al. [174] showed the tensile strength, stiffness, and draw ratio of electrospun PCL nanofibers increased, in an abrupt fashion, by decreasing the fiber diameter. In same work a study evaluating the dependence of crystallinity and molecular orientation with tensile properties was performed through X-ray diffraction (RXD). Reduction of PCL nanofibers diameter improved the crystallinity and molecular orientation. The abrupt change in tensile properties was raised from enhanced orderliness of the amorphous phase and more crystalline regions.

The mechanical properties of PCL nanofibers were investigated by Baker et al. [209], using AFM. An optical adhesive substrate was used for anchoring the PCL nanofibers. The AFM results indicate the fiber no longer slipped over the ridges following the curing of optical glue anchoring points. Moreover, the anchoring process was able to create condition that allowed for the determination of fiber mechanical properties. However, slippage of the fiber off the AFM tips still occurred during extensibility measurement giving a lower limit for the maximum extension of a PCL fiber.

PVA/CS electrospun nanofibers were properly prepared with heat-mediated chemical cross-linking. The mechanical properties of mats were dependent on PVA amount [203]. Increasing the PVA content lead to improvement in mechanical properties (tensile strength, elongation at break) of such material and also the swelling ratio, beyond contributing for intensification of intermolecular interaction among CS and PVA chains (hydrogen bonds evolving hydroxyl oxygen atoms of PVA and -NH_2 or -OH groups of CS).

The effects of external loads and temperatures on the resistance of electrospun nanocomposite fibers based on PVP with MWCNTs (incorporated before electrospinning) were investigated by Waseem et al. [199]. The main factors that influenced the resistance of fibers were the porosity, charge carrier concentration, and polarizability of inclusions in the polymer matrix. Moreover, charge carrier concentration and polarizability could be increased by addition of MWCNTs. However, increase on MWCNTs content reduced the porosity of the electrospun fiber films under the load. Electrospun PLGA nanofibers were investigated by Fouad et al. [202] through dynamic mechanical analysis (DMA). Their results indicated a strong dependence of the viscoelastic behavior of PLGA nanofibers in terms of frequency. The storage modulus (G') increased as the time elapsed, but the loss modulus (G") decreased with rise of frequency.

Plenty of techniques may be used for characterizing the nanofibers made by electrospinning. Exception for the mechanical properties, the techniques used for characterizing a pristine material can be used, as a rule, to characterize the mats made through electrospinning.

3 Technological Application of Electrospun Fibers

3.1 As Scaffolds for Cell Growth

Polymeric mats made through electrospinning belong to a very important class of materials that may be used as scaffolds for cell growth in tissue engineering, among other uses [56, 210, 211]. For instance, using the keywords electrospinning, nanofibers, and tissue engineering in the ISI™ database, almost 1800 works were found being ca. 97% of them published in last 10 years. This data show this technological use of electrospun nanofibers is a hot topic in materials science and in biomedical/biotechnological fields [211–213].

The replication of the native cell in an environment that simulates the living environment is very important and should be taken into account when designing scaffolds for tissue engineering [214]. This is why scaffolds often simulate the native extracellular matrix (ECM). Three methods can be used for manufacturing polymeric nanofiber-based scaffolds, which are phase separation, self-assembly, and electrospinning [215]. The electrospinning is the unique that enables the production of polymeric fibers having a diameter ranging from tens of nanometers to micrometers [216]. The development of scaffold consisting of nano- and microfiber made by electrospinning technique has been extensively explored, as fibers can be prepared with similar diameters to natural fibers found in the ECM [217].

Electrospinning ultrafine fibers from biodegradable and biocompatible polymers fashioned interesting opportunities for biomedical applications due to their inherent properties such as high surface to area ratio, suitable porosity, stiffness, and also to topographic-structure aspects. Despite these advantageous properties, the nature of the surface chemistry of the fibers of most natural and synthetic materials has repressed the development of nanofibers for use in tissue engineering [218]. In addition, hydrophobic, the unwanted adsorption of nonspecific protein, attachment, and bacterial growth are factors that limit final use of nanofibers. The lack of surface functionality in many cases and an incomplete understanding of the myriad of interactions among cells and the ECM proteins are still a challenge to improve the implementation of these systems. In this way, physical and chemical treatments were applied in order to modify or control the surface properties of electrospun fibers. A lot of information is presented in review from Yoo et al. (2009) [177] for readers interested in this specific issue. Chemical functionalization for achieving sustained delivery through physical adsorption of diverse bioactive molecules is deeply discussed in that review.

Plasma treatment, wet chemical method, surface graft polymerization, and co-electrospinning of surface-active agents and polymers are the most used methodology for nanofiber surface modification. Bioactive compounds including anticancer drugs, enzymes, cytokines, and polysaccharides were entrapped inside (or outside) the nanofiber and/or physically immobilized on the surface, for controlled drug delivery or for improving the cytocompatibility. The surfaces of electrospun nanofibers can be also chemically modified with immobilizing cell-specific bioactive ligands to enhance cell adhesion, proliferation, and differentiation by mimicking morphology and biological functions of extracellular matrix. For instance, SF nanofibers, prepared by electrospinning and further immobilization of sodium heparin at the mat surface, were done by Cestari et al. [219], targeting improvements in the hemocompatibility for application as scaffolds in tissue engineering. The authors showed that the SF nanofibers having heparin immobilized (at maximum 5%) at surface improved the VERO cells growth as compared to pristine SF nanofibers.

3.2 As Matrix for Drug Carriers

The Drug Delivery technology (DDt) has been widely studied in recent years as an efficient way to combat health problems. A material can be considered as belonging to DDt category as it has the ability for prolonging the drug release time, maintaining constant the concentration of released drug turn forward through physical, chemical, or biological stimulus. In this technology, the matrix is known as excipient or drug carrier. Electrospun nanofibers can be engineered to act as vehicles for delivering agents that hasten wound healing. Their large surface to volume ratio and easy manipulation makes electrospun nanofibers ideal candidates as excipientes (or carriers) of immobilized antibiotics, enzymes, antimicrobial peptides, and growth factors. Many tests should be performed in these excipients in order to ensure the respect of its biocompatibility or no toxicity [220–222].

Natural polymers have advantages in biocompatibility since they have often both biodegradability and bioactivity. Chitosan is renowned due to its antifungal and antimicrobial activities. Recent studies show CS can also be used as DD for nasal therapeutic [221]. Spherical nanoparticles of N,N,N-trimethyl CS (TMC) with diameters of 66, 76, and 85 nm were synthesized by reaction with methyl iodide, showing efficiency in controlling release to act as hepatitis B antigen [223]. Applications like this are due to the mucoadhesive property of CS, which extends the residence time in a given body area such as the colon [224, 225]. Another study showed that curcumin can be incorporated into cellulose films (natural polymer) by electrospinning. The cellulose fibers produced by electrospinning showed good homogeneity in all studied curcumin concentrations of 5–20% w/w. Curcumin is well known for its antioxidant, anti-inflammatory, and antitumor properties, so the interest in this compound significantly increased targeting to develop devices based on DDt for cancer treatment [226]. DDt was used for treatment of oral candidiasis

infections using PVA and PVP electrospun with cellulose acetate for cetylpyridine chloride transporting [227] and for controlled releasing of gentamicin sulfate [228].

The principle behind polymer-based nanofibers for DDt is that the dissolution rate of drug particles increases as the surface area of both drug and the corresponding carrier are increased. For controlled drug delivery, apart from their large surface area to volume ratio, polymer nanofibers also have other additional advantages such as the ease of drug incorporation into nanofibers. Therapeutic compounds can be conveniently incorporated into the carrier polymers using electrospinning. The resultant nanofibrous membrane containing drugs can be applied topically for tissue engineering as wound healing specific use [195].

Hydrophobic polymers provided a backbone and degrade over a longer period, whereas the more hydrophilic polymers degraded or dissolved faster. The choice of polymer or polymer blends is important in wound dressings aimed at controlled release [229].

The release of a pharmaceutical dosage can be rapid, immediate, delayed, or modified dissolution depending on the polymer carrier used. It was found that drug dissolution was facilitated by the dispersion of amorphous drug on electrospun polymer nanofibers [230].

Kenawy and co-workers [231] fabricated electrospun mats from nondegradable polymer, polyethylene-co-vinyl acetate (EVA), and a biodegradable polymer polylactic acid (PLA) and a 50:50 EVA/PLA blend for tetracycline hydrochloride release. The electrospun EVA matrices showed faster release kinetics as compared to electrospun PLA and blend matrices. Burst release followed by a slower release was exhibited. Tetracycline's release rate from EVA/PLA blend mats was intermediate between that of PEVA and PLA, which showed the possibility of controlling release rate by varying the ratio of polymer blend. Antibiotic electrospun mats of PLAGA and their PEG-based copolymers retained the activity of encapsulated Mefoxin (cefoxitin) and successfully inhibited the in vitro growth of *Staphylococcus aureus* and promoted wound healing in vivo in a rat model [232].

The most popular polymer solutions used for DDt are the aliphatic polyester blends of the copolymer PLGA, due to its biocompatibility and degradability [233] capabilities. However, the quick aqueous dissolution of PLGA components limits the use due to burst release when encapsulating drugs. Numerous drugs and blends can be simultaneously electrospun or intermittently layered into a single material with a more complex distribution of drug component. For instance, Thakur and coworkers used a multi-spinneret system to produce a composite mat composed of lidocaine- and mupirocin-loaded poly(L-lactide) (PLLA) electrospun fibers [234].

3.3 As Adsorbent Material

Water pollution by potentially toxic metals and drugs caused by industrial, agricultural, and domestic sources sewer is one of the most serious environmental and public problems. For Manzetti and Ghisi [235], the domestic wastes are the

principal sources of antibiotics in the water contamination, in which the current decontamination process does not completely remove the compounds of antibiotics, resulting in a low, but steady, concentration of remaining contaminants. Also, it is stated that the second largest source of contamination comes from agricultural activities, where antibiotics are transferred to the environment from compounds present in feces and urine of animals and mud. The contaminants result in a local cycle of antibiotic transfer to soil and pasture returning to animals through food, reaching therefore man [235]. For Kemper [236] the majority of the antibiotic is water soluble, eliminating about 90% of the drug in the urine and 75% in feces.

Conventional treatments such as coagulation, filtration, and chlorination can remove about 50% of drugs in water. However, advanced treatments such as ozonation, advanced oxidation, active carbon, and membrane processes (nanofiltration and reverse osmosis, RO) can remove much higher concentrations. A promising alternative to these treatments is the use of membranes containing nanoscale fibers, which have a high degree of porosity. High porosity composite nanofibers can be obtained by the electrospinning process [237].

For the electrospun fibers from polymer solutions, the presence of residual solvent in the fiber facilitates interlocking connection of these, creating a cohesive and strong structure [238].

For common filtration application, the most intuitive and in fact the most effective and strong filters consist of a mesh kind of structure made of fibrous material. These fibrous structures provide narrow pore size distribution which ensures high selectivity and better mechanical strength. Since it is very difficult to produce fibrous membranes with nanopores for nanofiltration or RO applications, researchers started to play around with chemistry of molecules and chemistry of surfaces to make such nanostructures. Electrospun nanofibrous membranes (ENM) have already showed good results in microfiltration uses. So ENMs have very good potential in microfiltration as well as ultrafiltration industry. For instance, the pore size observed in SPEEK electrospun membrane (a.d. = 26–200 nm) is suitable for ultrafiltration. The narrow pore size distribution observed here is very promising because the selectivity of the filter improved so much [239]. For instance, poly(methacrylic acid) and cellulose acetate (PMAA-modified CA) membrane could be used for the adsorption of heavy metal ions from water. Adsorption experimental results indicated that higher initial pH value corresponds to higher adsorption capacity [240].

The thin-film composite nanofibrous filtration membranes containing a hydrophilic calcium alginate/carboxyl multiwalled carbon nanotubes hydrogel barrier layer and a polyhydroxybutyrate nanofibrous substrate (PHB-CaAlg/CMWCNT) were prepared by electrospinning technique. The hydrophilic top hydrogel nanofibers layer were further redissolved and combined with Ca^{2+} cross-linking to form a barrier layer with several micrometers thick on PHB nanofibrous substrate. The obtained PHB-CaAlg nanofibrous membrane by synchronization electrospinning could improve the hydrophilic property of PHB nanofibrous substrate as transitional layer and closely integrate with the top hydrogel layer. The results showed the tensile strength and the breaking elongation rate of PHB-CaAlg/CMWCNT membrane reached 2.59 MPa and 120%, respectively. The water contact angle of PHB-CaAlg/CMWCNT membrane was 19.4° indicating the

membrane had good mechanical strength and hydrophilic nature. The dye Brilliant blue adsorption capacity of PHB-CaAlg/CMWCNT membrane was twice higher than PHB-CaAlg membrane. The flux for oil emulsions and Brilliant blue was 84.01% and 89.73% for pure water flux, respectively, indicating that the membrane had excellent antifouling property [241].

Also, the electrospun CS/PEO nanofibers have been used to adsorb potentially toxic metals such as copper, lead, cadmium, and nickel ions from aqueous solution [240, 241]. Adsorption experiments were carried out using electrospun CS/PEO nanofibers to investigate adsorption of copper (II) ions from aqueous solutions. An optimal adsorption of 94.7% was obtained by using 75 mg of nanofibers in 200 min at pH 5.5 and a temperature of 55.7 °C with initial copper concentration of 100 ppm [242]. This membrane has promising applications as nano-filtration membrane to remove small organic and inorganic molecules in wastewater.

The electrospun nanofibrous membrane possesses three-dimensional network and completely interconnected pore structures. So, the qualitatively controlled pore size distribution from submicron level to a few micrometers and high porosity have been widely used for wastewater treatments. However, the irreversible fouling of traditional electrospun filtration membrane materials with poor hydrophilic property results in the membrane pores blocking and flux significantly decreasing. Many efforts have been exerted to modify the hydrophilic property of membranes, including polymer blending, surface coating, and surface grafting [241].

3.4 Other Technological Applications of Nanofibers

As already mentioned, the contamination of water bodies by drugs is a worldwide environmental problem. An example of these pollutants is the metronidazole, an antibiotic used to treat infections caused by protozoa and anaerobic bacteria [243, 244]. The presence of the drug in aquatic environments indicates the need to monitor such pollutant, as several studies have emphasized their high toxicity, low biodegradability, carcinogenic and mutagenic effects, bioaccumulation potential, as well as high solubility in water [243, 245, 246].

Electrochemical methods stand out for being simple and accessible, moreover having high sensitivity and selectivity, and the possibility of measurement is performed directly in the environmental matrix without the need of pretreatments, allowing considerable reduction of costs and time in analysis. So electrochemical methods constitute simple and affordable alternatives for the determination of emerging pollutants such as metronidazole [247, 248].

Electrospinning has been used to manufacture nanofibers with potential application as a sensor, since the nanofibers have a remarkable porous structure, proximity between the same and high surface area, providing good contact with the analyte [249]. This technique has been extensively studied for production of various types of nanofibers or nanowires of different polymers, such as PVP [250], PLA [251], PVA [252], among many others. New frontiers in the application of polymers

have been investigated, involving obtaining new precursor molecules, structures, arrangements, and molecular rearrangement synthesis and processing steps [253, 254].

Thus, the development of electroactive polymer nanofibers by electrospinning has presented unique properties and many potential uses, such as in fabrication of nanoelectronic and optical devices, in biomedical materials, protective garments, filtration media, charge accumulating devices, actuators, and sensors.

4 Future Trends

Despite electrospinning being a widely researched issue with technological application in several fields [175], there are still, undoubtedly, many opened windows for opportunities to overcome some existing challenges and also to meet new structures, morphologies, and properties.

As discussed in Sects. 1 and 2 of this chapter, the physical-chemistry structure and properties of nanofibers are dependent of operational, external, and ambient conditions as well as the setup. The versatility of electrospinning allows the researchers to design a myriad of setups. So, virtually there is no limit for different structures and properties of nanofibers obtained through electrospinning. One important problem is to scale up the structures obtained in lab scale, in terms of reproducibility, controlling the distribution of fiber diameters, orientations, etc. One very important challenge for electrospinning of polymer solutions is the cost associated to the solvent that is effectively lost because the solvent evaporates during the process considering the difficulties to recover it. Depending on the solvent used, the inflammability may turn the process dangerous [255]. Therefore, the developments of process using green and not flammable solvents or aqueous media are very important tasks for facilitating the scale-up and industrial production of electrospun fibrous mats.

A very important opened window in electrospinning is the melt electrospinning technology that does not use solvent. Melt electrospinning has emerged as an alternative to polymer processing technology to mitigate concerns related to conventional solvent electrospinning [256, 257]. The use of this technology resulted in the production of ultrafine fibers of a growing range of synthetic polymers and composite systems for materials, including ceramics; driving new applications in technical fields such as textiles, filtration, environment, and energy; as well as biomedicine. The review recently published by Brown et al. [258] shows several aspects of this new technology in terms of setup designs and the morphologies that can be obtained. One very important issue to highlight is the possibility of extending the use of technique for ceramic and metallic materials, as pointed out by Ding et al. [259].

5 Concluding Remarks

This chapter shows the electrospinning is a very exciting technique for obtaining nanofibers in submicro- or nanoscales. Plenty of possibilities for morphologies and structures can be obtained and are related to the final properties of the nanofibers. The versatility of the technique and the equipment's low cost allow to design plenty of setups and are the main responsible factors for the quick spread of technique. This chapter also showed that the as-obtained materials through electrospinning can be applied in several technological fields, such as scaffolds for cell growth, drug delivery, adsorbent, sensors, etc. This review highlights the electrospinning of polymer solutions. Yet, the electrospinning molten polymers appear as a new technology avoiding the use of solvent, to overcome some challenges in the field. Moreover, ceramic and metals can also be electrospun on the molten state. Although much progress has been made in the field, electrospinning has not reached yet its full potential and will remain, undoubtedly, as one of the most promising techniques for developing new materials for technological applications in the next years.

References

1. Luu YK, Kim K, Hsiao BS, Chu B, Hadjiargyrou M (2003) Development of a nanostructured DNA delivery scaffold via electrospinning of PLGA and PLA-PEG block copolymers. J Control Release 89:341–353
2. Ramakrishna S, Fujihara K, Teo WE, Yong T, Ma Z, Ramaseshan R (2006) Electrospun nanofibers: solving global issues. Mater Today 9:40–50
3. Welle A, Kröger M, Döring M, Niederer K, Pindel E, Chronakis IS (2007) Electrospun aliphatic polycarbonates as tailored tissue scaffold materials. Biomaterials 28:2211–2219
4. Del Valle LJ, Roa M, Díaz A, Casas MT, Puiggalí J, Rodríguez-Galán A (2012) Electrospun nanofibers of a degradable poly(ester amide). Scaffolds loaded with antimicrobial agents. J Polym Res 19:251
5. Dubský M, Kubinová Š, Širc J, Voska L, Zajíček R, Zajícová A, Lesný P, Jirkovská A, Michálek J, Munzarová M, Holáň V, Syková E (2012) Nanofibers prepared by needleless electrospinning technology as scaffolds for wound healing. J Mater Sci Mater Med 23: 931–941
6. He J, Qin T, Liu Y, Li X, Li D, Jin Z (2014) Electrospinning of nanofibrous scaffolds with continuous structure and material gradients. Mater Lett 137:393–397
7. Ramji K, Shah RN (2014) Electrospun soy protein nanofiber scaffolds for tissue regeneration. J Biomater Appl 29:411–422
8. Cho SJ, Jung SM, Kang M, Shin HS, Youk JH (2015) Preparation of hydrophilic PCL nanofiber scaffolds via electrospinning of PCL/PVP-b-PCL block copolymers for enhanced cell biocompatibility. Polymer (U K) 69:95–102
9. Mi HY, Jing X, Yu E, McNulty J, Peng XF, Turng LS (2015) Fabrication of triple-layered vascular scaffolds by combining electrospinning, braiding, and thermally induced phase separation. Mater Lett 161:305–308
10. Qin XH, Wang SY (2006) Filtration properties of electrospinning nanofibers. J Appl Polym Sci 102:1285–1290
11. Sambaer W, Zatloukal M, Kimmer D (2011) 3D modeling of filtration process via polyurethane nanofiber based nonwoven filters prepared by electrospinning process. Chem Eng Sci 66:613–623

12. Chegoonian P, Feiz M, Ravandi SAH, Mallakpour S (2012) Preparation of sulfonated poly(ethylene terephthalate) submicron fibrous membranes for removal of basic dyes. J Appl Polym Sci 124:E190
13. Yin G, Zhao Q, Zhao Y, Yuan Y, Yang Y (2013) The electrospun polyamide 6 nanofiber membranes used as high efficiency filter materials: filtration potential, thermal treatment, and their continuous production. J Appl Polym Sci 128:1061–1069
14. Li C, Chen R, Zhang X, Xiong J, Zheng Y, Dong W (2011) Fabrication and characterization of electrospun nanofibers of high DP natural cotton lines cellulose. Fibers Polym 12:345–351
15. Balgis R, Kartikowati CW, Ogi T, Gradon L, Bao L, Seki K, Okuyama K (2015) Synthesis and evaluation of straight and bead-free nanofibers for improved aerosol filtration. Chem Eng Sci 137:947–954
16. Langner M, Greiner A (2016) Wet-laid meets electrospinning: nonwovens for filtration applications from short electrospun polymer nanofiber dispersions. Macromol Rapid Commun 37:351–355
17. Boland ED, Coleman BD, Barnes CP, Simpson DG, Wnek GE, Bowlin GL (2005) Electrospinning polydioxanone for biomedical applications. Acta Biomater 1:115–123
18. Venugopal J, Ramakrishna S (2005) Applications of polymer nanofibers in biomedicine and biotechnology. Appl Biochem Biotechnol Part A Enzyme Eng Biotechnol 125:147–157
19. Agarwal S, Wendorff JH, Greiner A (2008) Use of electrospinning technique for biomedical applications. Polymer 49:5603–5621
20. Shin TJ, Park SY, Kim HJ, Lee HJ, Youk JH (2010) Development of 3-D poly(trimethylenecarbonate-co-ε-caprolactone)-block-poly(p-dioxanone) scaffold for bone regeneration with high porosity using a wet electrospinning method. Biotechnol Lett 32: 877–882
21. Nirmala R, Navamathavan R, Kang HS, El-Newehy MH, Kim HY (2011) Preparation of polyamide-6/chitosan composite nanofibers by a single solvent system via electrospinning for biomedical applications. Colloids Surf B Biointerfaces 83:173–178
22. Rodríguez K, Gatenholm P, Renneckar S (2012) Electrospinning cellulosic nanofibers for biomedical applications: structure and in vitro biocompatibility. Cellulose 19:1583–1598
23. Panthi G, Barakat NAM, Risal P, Yousef A, Pant B, Unnithan AR, Kim HY (2013) Preparation and characterization of nylon-6/gelatin composite nanofibers via electrospinning for biomedical applications. Fibers Polym 14:718–723
24. Kai D, Liow SS, Loh XJ (2015) Biodegradable polymers for electrospinning: towards biomedical applications. Mater Sci Eng C Mater Biol Appl 45:659–670
25. Maeda T, Hagiwara K, Yoshida S, Hasebe T, Hotta A (2014) Preparation and characterization of 2-methacryloyloxyethyl phosphorylcholine polymer nanofibers prepared via electrospinning for biomedical materials. J Appl Polym Sci 131:40606
26. Leong MF, Toh JKC, Du C, Narayanan K, Lu HF, Lim TC, Wan ACA, Ying JY (2013) Patterned prevascularised tissue constructs by assembly of polyelectrolyte hydrogel fibres. Nat Commun 4:2353
27. Liu H, Ding X, Zhou G, Li P, Wei X, Fan Y (2013) Electrospinning of nanofibers for tissue engineering applications. J Nanomater 2013:11
28. Hamori M, Yoshimatsu S, Hukuchi Y, Shimizu Y, Fukushima K, Sugioka N, Nishimura A, Shibata N (2014) Preparation and pharmaceutical evaluation of nano-fiber matrix supported drug delivery system using the solvent-based electrospinning method. Int J Pharm 464: 243–251
29. Hu X, Liu S, Zhou G, Huang Y, Xie Z, Jing X (2014) Electrospinning of polymeric nanofibers for drug delivery applications. J Control Release 185:12–21
30. Bruni G, Maggi L, Tammaro L, Canobbio A, Di Lorenzo R, D'Aniello S, Domenighini C, Berbenni V, Milanese C, Marini A (2015) Fabrication, physico-chemical, and pharmaceutical characterization of budesonide-loaded electrospun fibers for drug targeting to the colon. J Pharm Sci 104:3798–3803
31. Tonglairoum P, Ngawhirunpat T, Rojanarata T, Kaomongkolgit R, Opanasopit P (2015) Fabrication of a novel scaffold of clotrimazole-microemulsion-containing nanofibers using an electrospinning process for oral candidiasis applications. Colloids Surf B Biointerfaces 126:18–25

32. Hamori M, Nagano K, Kakimoto S, Naruhashi K, Kiriyama A, Nishimura A, Shibata N (2016) Preparation and pharmaceutical evaluation of acetaminophen nano-fiber tablets: application of a solvent-based electrospinning method for tableting. Biomed Pharmacother 78:14–22
33. Maleki H, Gharehaghaji AA, Dijkstra PJ (2013) A novel honey-based nanofibrous scaffold for wound dressing application. J Appl Polym Sci 127:4086–4092
34. Sofokleous P, Stride E, Edirisinghe M (2013) Preparation, characterization, and release of amoxicillin from electrospun fibrous wound dressing patches. Pharm Res 30:1926–1938
35. He T, Wang J, Huang P, Zeng B, Li H, Cao Q, Zhang S, Luo Z, Deng DYB, Zhang H, Zhou W (2015) Electrospinning polyvinylidene fluoride fibrous membranes containing anti-bacterial drugs used as wound dressing. Colloids Surf B Biointerfaces 130:278–286
36. Liao N, Unnithan AR, Joshi MK, Tiwari AP, Hong ST, Park CH, Kim CS (2015) Electrospun bioactive poly (e{open}-caprolactone)-cellulose acetate-dextran antibacterial composite mats for wound dressing applications. Colloids Surf A Physicochem Eng Asp 469:194–201
37. Tan L, Hu J, Zhao H (2015) Design of bilayered nanofibrous mats for wound dressing using an electrospinning technique. Mater Lett 156:46–49
38. Kim S, Park SG, Kang SW, Lee KJ (2016) Nanofiber-based hydrocolloid from colloid electrospinning toward next generation wound dressing. Macromol Mater Eng 301:818–826
39. Unnithan AR, Ghavami Nejad A, Sasikala ARK, Thomas RG, Jeong YY, Murugesan P, Nasseri S, Wu D, Park CH, Kim CS (2016) Electrospun zwitterionic nanofibers with in situ decelerated epithelialization property for non-adherent and easy removable wound dressing application. Chem Eng J 287:640–648
40. Kong Q, Wang J, Dong X, Yu W, Liu G (2013) Synthesis and luminescence properties of LaOCl:Eu3+ nanostructures via the combination of electrospinning with chlorination technique. J Mater Sci Mater Electron 24:4745–4756
41. Di Camillo D, Fasano V, Ruggieri F, Santucci S, Lozzi L, Camposeo A, Pisignano D (2013) Near-field electrospinning of light-emitting conjugated polymer nanofibers. Nanoscale 5:11637–11642
42. Wang L, Gai G, Xiao X, Gao S (2014) Fabrication of magnetic-luminescent bifunctional composite nanofibers via facile electrospinning. J Mater Sci Mater Electron 25:3147–3153
43. Yu H, Fan H, Wang X, Wang J (2014) Synthesis and optical properties of Co-doped ZnO nanofibers prepared by electrospinning. Optik 125:2361–2364
44. Choi J, Panthi G, Liu Y, Kim J, Chae SH, Lee C, Park M, Kim HY (2015) Keratin/poly (vinyl alcohol) blended nanofibers with high optical transmittance. Polymer (U K) 58:146–152
45. Fasano V, Moffa M, Camposeo A, Persano L, Pisignano D (2015) Controlled atmosphere electrospinning of organic nanofibers with improved light emission and waveguiding properties. Macromolecules 48:7803–7809
46. Ramasundaram S, Son A, Seid MG, Shim S, Lee SH, Chung YC, Lee C, Lee J, Hong SW (2015) Photocatalytic applications of paper-like poly(vinylidene fluoride)-titanium dioxide hybrids fabricated using a combination of electrospinning and electrospraying. J Hazard Mater 285:267–276
47. Wang T, Fu H, Duan X, Li Z (2015) An electrospun micro/nanofibrous mesh based nontoxic sensor for optical detection of high humidity. Anal Methods 7:3676–3679
48. Park M, Lee KS, Shim J, Liu Y, Lee C, Cho H, Kim MJ, Park SJ, Yun YJ, Kim HY, Son DI (2016) Environment friendly, transparent nanofiber textiles consolidated with high efficiency PLEDs for wearable electronics. Org Electron phys Mater Appl 36:89–96
49. Lee S, Obendorf SK (2007) Use of electrospun nanofiber web for protective textile materials as barriers to liquid penetration. Text Res J 77:696–702
50. Rose M, Böhringer B, Jolly M, Fischer R, Kaskel S (2011) MOF processing by electrospinning for functional textiles. Adv Eng Mater 13:356–360
51. Gorji M, Jeddi AAA, Gharehaghaji AA (2012) Fabrication and characterization of polyurethane electrospun nanofiber membranes for protective clothing applications. J Appl Polym Sci 125:4135–4141

52. Varesano A, Rombaldoni F, Tonetti C, Di Mauro S, Mazzuchetti G (2014) Chemical treatments for improving adhesion between electrospun nanofibers and fabrics. J Appl Polym Sci 131:39766
53. Serbezeanu D, Popa AM, Stelzig T, Sava I, Rossi RM, Fortunato G (2015) Preparation and characterization of thermally stable polyimide membranes by electrospinning for protective clothing applications. Text Res J 85:1763–1775
54. Zhu F, Xin Q, Feng Q, Zhou Y, Liu R (2015) Novel poly(vinylidene fluoride)/thermoplastic polyester elastomer composite membrane prepared by the electrospinning of nanofibers onto a dense membrane substrate for protective textiles. J Appl Polym Sci 132(26):42170. doi:10.1002/app.42170
55. Anton F (1934) Process and apparatus for preparing artificial threads. In: Google Patents
56. Bhardwaj N, Kundu SC (2010) Electrospinning: a fascinating fiber fabrication technique. Biotechnol Adv 28:325–347
57. F Anton (1938) Artificial fiber construction, in, Google Patents
58. Teo WE, Ramakrishna S (2006) A review on electrospinning design and nanofibre assemblies. Nanotechnology 17:R89–r106
59. Doshi J, Reneker DH (1995) Electrospinning process and applications of electrospun fibers. J Electrost 35:151–160
60. Reneker DH, Chun I (1996) Nanometre diameter fibres of polymer, produced by electrospinning. Nanotechnology 7:216–223
61. Fong H, Chun I, Reneker DH (1999) Beaded nanofibers formed during electrospinning. Polymer 40:4585–4592
62. Reneker DH, Yarin AL, Fong H, Koombhongse S (2000) Bending instability of electrically charged liquid jets of polymer solutions in electrospinning. J Appl Phys 87:4531–4547
63. Koombhongse S, Liu W, Reneker DH (2001) Flat polymer ribbons and other shapes by electrospinning. J Polym Sci B 39:2598–2606
64. Yarin AL, Koombhongse S, Reneker DH (2001) Bending instability in electrospinning of nanofibers. J Appl Phys 89:3018–3026
65. Kataphinan W, Teye-Mensah R, Evans EA, Ramsier RD, Reneker DH, Smith DJ (2003) High-temperature fiber matrices: electrospinning and rare-earth modification. J Vac Sci Technol A 21:1574–1578
66. Yarin AL, Kataphinan W, Reneker DH (2005) Branching in electrospinning of nanofibers. J Appl Phys 98:064501
67. Dosunmu OO, Chase GG, Kataphinan W, Reneker DH (2006) Electrospinning of polymer nanofibres from multiple jets on a porous tubular surface. Nanotechnology 17:1123–1127
68. Thompson CJ, Chase GG, Yarin AL, Reneker DH (2007) Effects of parameters on nanofiber diameter determined from electrospinning model. Polymer 48:6913–6922
69. Xin Y, Reneker DH (2012) Garland formation process in electrospinning. Polymer (U K) 53:3629–3635
70. Elsabee MZ, Naguib HF, Morsi RE (2012) Chitosan based nanofibers, review. Mater Sci Eng C 32:1711–1726
71. Rogina A (2014) Electrospinning process: versatile preparation method for biodegradable and natural polymers and biocomposite systems applied in tissue engineering and drug delivery. Appl Surf Sci 296:221–230
72. Pham QP, Sharma U, Mikos AG (2006) Electrospinning of polymeric nanofibers for tissue engineering applications: a review. Tissue Eng 12:1197–1211
73. Baji A, Mai YW, Wong SC, Abtahi M, Chen P (2010) Electrospinning of polymer nanofibers: effects on oriented morphology, structures and tensile properties. Compos Sci Technol 70:703–718
74. Subbiah T, Bhat GS, Tock RW, Parameswaran S, Ramkumar SS (2005) Electrospinning of nanofibers. J Appl Polym Sci 96:557–569
75. Valizadeh A, Farkhani SM (2014) Electrospinning and electrospun nanofibres. IET Nanobiotechnol 8:83–92

76. Kim G, Cho YS, Kim WD (2006) Stability analysis for multi-jets electrospinning process modified with a cylindrical electrode. Eur Polym J 42:2031–2038
77. Holzmeister A, Rudisile M, Greiner A, Wendorff JH (2007) Structurally and chemically heterogeneous nanofibrous nonwovens via electrospinning. Eur Polym J 43:4859–4867
78. Bjorge D, Daels N, De Vrieze S, Dejans P, Van Camp T, Audenaert W, Hogie J, Westbroek P, De Clerck K, Van Hulle SWH (2009) Performance assessment of electrospun nanofibers for filter applications. Desalination 249:942–948
79. Tian L, Zhao C, Li J, Pan Z (2015) Multi-needle, electrospun, nanofiber filaments: effects of the needle arrangement on the nanofiber alignment degree and electrostatic field distribution. Text Res J 85:621–631
80. Kaerkitcha N, Chuangchote S, Sagawa T (2016) Control of physical properties of carbon nanofibers obtained from coaxial electrospinning of PMMA and PAN with adjustable inner/outer nozzle-ends. Nanoscale Res Lett 11:186
81. Park JS (2010) Electrospinning and its applications. Adv Nat Sci Nanosci Nanotechnol 1:043002
82. Kirecci A, Özkoç Ü, Içoĝlu HI (2012) Determination of optimal production parameters for polyacrylonitrile nanofibers. J Appl Polym Sci 124:4961–4968
83. Cordie T, Harkness T, Jing X, Carlson-Stevermer J, Mi HY, Turng LS, Saha K (2014) Nanofibrous electrospun polymers for reprogramming human cells. Cell Mol Biol 7:379–393
84. Walser J, Ferguson SJ (2016) Oriented nanofibrous membranes for tissue engineering applications: electrospinning with secondary field control. J Mech Behav Biomed Mater 58:188–198
85. El-hadi AM, Al-Jabri FY (2016) Influence of electrospinning parameters on fiber diameter and mechanical properties of poly(3-Hydroxybutyrate) (PHB) and polyanilines (PANI) blends. Polymer 8:97
86. Jacobs V, Anandjiwala RD, Maaza M (2010) The influence of electrospinning parameters on the structural morphology and diameter of electrospun nanofibers. J Appl Polym Sci 115:3130–3136
87. Neo YP, Ray S, Easteal AJ, Nikolaidis MG, Quek SY (2012) Influence of solution and processing parameters towards the fabrication of electrospun zein fibers with sub-micron diameter. J Food Eng 109:645–651
88. Hekmati AH, Rashidi A, Ghazisaeidi R, Drean JY (2013) Effect of needle length, electrospinning distance, and solution concentration on morphological properties of polyamide-6 electrospun nanowebs. Text Res J 83:1452–1466
89. Okutan N, Terzi P, Altay F (2014) Affecting parameters on electrospinning process and characterization of electrospun gelatin nanofibers. Food Hydrocoll 39:19–26
90. Al-Qadhi M, Merah N, Matin A, Abu-Dheir N, Khaled M, Youcef-Toumi K (2015) Preparation of superhydrophobic and self-cleaning polysulfone non-wovens by electrospinning: influence of process parameters on morphology and hydrophobicity. J Polym Res 22:207
91. Erencia M, Cano F, Tornero JA, Fernandes MM, Tzanov T, Macanás J, Carrillo F (2015) Electrospinning of gelatin fibers using solutions with low acetic acid concentration: effect of solvent composition on both diameter of electrospun fibers and cytotoxicity. J Appl Polym Sci 132:42115
92. Senthil T, Anandhan S (2015) Fabrication of styrene-acrylonitrile random copolymer nanofiber membranes from N,N-dimethyl formamide by electrospinning. J Elastomers Plast 47:327–346
93. Haghi AK, Akbari M (2007) Trends in electrospinning of natural nanofibers. Phys Status Solidi (a) Appl Mater Sci 204:1830–1834
94. Koski A, Yim K, Shivkumar S (2004) Effect of molecular weight on fibrous PVA produced by electrospinning. Mater Lett 58:493–497
95. Sukigara S, Gandhi M, Ayutsede J, Micklus M, Ko F (2003) Regeneration of *Bombyx mori* silk by electrospinning – part 1: processing parameters and geometric properties. Polymer 44:5721–5727

96. Zhou Y, Yang H, Liu X, Mao J, Gu S, Xu W (2013) Electrospinning of carboxyethyl chitosan/poly(vinyl alcohol)/silk fibroin nanoparticles for wound dressings. Int J Biol Macromol 53:88–92
97. Sasithorn N, Martinová L (2014) Fabrication of silk nanofibres with needle and roller electrospinning methods. J Nanomater 2014:947315
98. Liu Y, Ma G, Fang D, Xu J, Zhang H, Nie J (2011) Effects of solution properties and electric field on the electrospinning of hyaluronic acid. Carbohydr Polym 83:1011–1015
99. Megelski S, Stephens JS, Bruce Chase D, Rabolt JF (2002) Micro- and nanostructured surface morphology on electrospun polymer fibers. Macromolecules 35:8456–8466
100. Yang Y, Jia Z, Liu J, Li Q, Hou L, Wang L, Guan Z (2008) Effect of electric field distribution uniformity on electrospinning. J Appl Phys 103:104307
101. Zhao S, Wu X, Wang L, Huang Y (2004) Electrospinning of ethyl–cyanoethyl cellulose/tetrahydrofuran solutions. J Appl Polym Sci 91:242–246
102. Liao C-C, Wang C-C, Chen C-Y (2011) Stretching-induced crystallinity and orientation of polylactic acid nanofibers with improved mechanical properties using an electrically charged rotating viscoelastic jet. Polymer 52:4303–4318
103. Hernández-Navarro N, González-González V, Moreno-Cortez IE, Garza-Navarro MA (2016) Electrospun polyvinylidene fluoride nanofibers by bubble electrospinning technique. Mater Lett 167:34–37
104. Salles THC, Lombello CB, d'Ávila MA (2015) Electrospinning of gelatin/poly (vinyl pyrrolidone) blends from water/acetic acid solutions. Mater Res 18:509–518
105. Wang M, Jin H-J, Kaplan DL, Rutledge GC (2004) Mechanical properties of electrospun silk fibers. Macromolecules 37:6856–6864
106. Hekmati AH, Rashidi A, Ghazisaeidi R, Drean J-Y (2013) Effect of needle length, electrospinning distance, and solution concentration on morphological properties of polyamide-6 electrospun nanowebs. Text Res J 83:1452
107. Vashisth P, Pruthi PA, Singh RP, Pruthi V (2014) Process optimization for fabrication of gellan based electrospun nanofibers. Carbohydr Polym 109:16–21
108. Neubert S, Pliszka D, Góra A, Jaworek A, Wintermantel E, Ramakrishna S (2012) Focused deposition of electrospun polymer fibers. J Appl Polym Sci 125:820–827
109. De Vrieze S, Van Camp T, Nelvig A, Hagström B, Westbroek P, De Clerck K (2008) The effect of temperature and humidity on electrospinning. J Mater Sci 44:1357
110. Fashandi H, Ghomi A (2015) Interplay of phase separation and physical gelation in morphology evolution within nanoporous fibers electrospun at high humidity atmosphere. Ind Eng Chem Res 54:240–253
111. Lu P, Xia Y (2013) Maneuvering the internal porosity and surface morphology of electrospun polystyrene yarns by controlling the solvent and relative humidity. Langmuir 29:7070–7078
112. Medeiros ES, Mattoso LHC, Offeman RD, Wood DF, Orts WJ (2008) Effect of relative humidity on the morphology of electrospun polymer fibers. Can J Chem 86:590–599
113. De Vrieze S, De Schoenmaker B, Ceylan Ö, Depuydt J, Van Landuyt L, Rahier H, Van Assche G, De Clerck K (2011) Morphologic study of steady state electrospun polyamide 6 nanofibres. J Appl Polym Sci 119:2984–2990
114. Pelipenko J, Kristl J, Janković B, Baumgartner S, Kocbek P (2013) The impact of relative humidity during electrospinning on the morphology and mechanical properties of nanofibers. Int J Pharm 456:125–134
115. Aznar-Cervantes SD, Lozano-Pérez AA, García Montalbán M, Víllora G, Vicente-Cervantes D, Cenis JL (2015) Importance of refrigeration time in the electrospinning of silk fibroin aqueous solutions. J Mater Sci 50:4879–4887
116. Lu W, Ma M, Xu H, Zhang B, Cao X, Guo Y (2015) Gelatin nanofibers prepared by spiral-electrospinning and cross-linked by vapor and liquid-phase glutaraldehyde. Mater Lett 140:1–4
117. Meng L, Arnoult O, Smith M, Wnek GE (2012) Electrospinning of in situ crosslinked collagen nanofibers. J Mater Chem 22:19412–19417

118. Haghjooy Javanmard S, Anari J, Zargar Kharazi A, Vatankhah E (2016) In vitro hemocompatibility and cytocompatibility of a three-layered vascular scaffold fabricated by sequential electrospinning of PCL, collagen, and PLLA nanofibers. J Biomater Appl 31:438–449
119. Brenner EK, Schiffman JD, Thompson EA, Toth LJ, Schauer CL (2012) Electrospinning of hyaluronic acid nanofibers from aqueous ammonium solutions. Carbohydr Polym 87:926–929
120. Zhou Z, Lin W, Wu XF (2016) Electrospinning ultrathin continuous cellulose acetate fibers for high-flux water filtration. Colloids Surf A Physicochem Eng Asp 494:21–29
121. Omollo E, Zhang C, Mwasiagi JI, Ncube S (2016) Electrospinning cellulose acetate nanofibers and a study of their possible use in high-efficiency filtration. J Ind Text 45:716–729
122. Wang K, Ma Q, Wang SD, Liu H, Zhang SZ, Bao W, Zhang KQ, Ling LZ (2016) Electrospinning of silver nanoparticles loaded highly porous cellulose acetate nanofibrous membrane for treatment of dye wastewater. Appl Phys Mater Sci Process 122:1–10
123. Yu DG, Yu JH, Chen L, Williams GR, Wang X (2012) Modified coaxial electrospinning for the preparation of high-quality ketoprofen-loaded cellulose acetate nanofibers. Carbohydr Polym 90:1016–1023
124. Liu J, Chang MJ, Du HL (2016) Facile preparation of cross-linked porous poly(vinyl alcohol) nanofibers by electrospinning. Mater Lett 183:318–321
125. López-Córdoba A, Castro GR, Goyanes S (2016) A simple green route to obtain poly(vinyl alcohol) electrospun mats with improved water stability for use as potential carriers of drugs. Mater Sci Eng C 69:726–732
126. Smyth M, Poursorkhabi V, Mohanty AK, Gregori S, Misra M (2014) Electrospinning highly oriented and crystalline poly(lactic acid) fiber mats. J Mater Sci 49:2430–2441
127. Van Der Schueren L, De Schoenmaker B, Kalaoglu OI, De Clerck K (2011) An alternative solvent system for the steady state electrospinning of polycaprolactone. Eur Polym J 47:1256–1263
128. Singh BN, Panda NN, Pramanik K (2016) A novel electrospinning approach to fabricate high strength aqueous silk fibroin nanofibers. Int J Biol Macromol 87:201–207
129. Naghibzadeh M, Adabi M (2014) Evaluation of effective electrospinning parameters controlling gelatin nanofibers diameter via modelling artificial neural networks. Fibers Polym 15:767–777
130. Vuddanda PR, Mathew AP, Velaga S (2016) Electrospun nanofiber mats for ultrafast release of ondansetron. React Funct Polym 99:65–72
131. Mi FL, Tan YC, Liang HF, Sung HW (2002) In vivo biocompatibility and degradability of a novel injectable-chitosan-based implant. Biomaterials 23:181–191
132. Selmer-Olsen E, Ratnaweera HC, Pehrson R (1996) A novel treatment process for dairy wastewater with chitosan produced from shrimp-shell waste. Water Sci Technol 34:33–40
133. Hasegawa M, Isogai A, Onabe F, Usuda M (1992) Dissolving states of cellulose and chitosan in trifluoroacetic acid. J Appl Polym Sci 45:1857–1863
134. Ohkawa K, Minato K-I, Kumagai G, Hayashi S, Yamamoto H (2006) Chitosan nanofiber. Biomacromolecules 7:3291–3294
135. Sangsanoh P, Suwantong O, Neamnark A, Cheepsunthorn P, Pavasant P, Supaphol P (2010) In vitro biocompatibility of electrospun and solvent-cast chitosan substrata towards Schwann, osteoblast, keratinocyte and fibroblast cells. Eur Polym J 46:428–440
136. Santos C, Silva CJ, Büttel Z, Guimarães R, Pereira SB, Tamagnini P, Zille A (2014) Preparation and characterization of polysaccharides/PVA blend nanofibrous membranes by electrospinning method. Carbohydr Polym 99:584–592
137. Yang JM, Yang JH, Tsou SC, Ding CH, Hsu CC, Yang KC, Yang CC, Chen KS, Chen SW, Wang JS (2016) Cell proliferation on PVA/sodium alginate and PVA/poly(γ-glutamic acid) electrospun fiber. Mater Sci Eng C 66:170–177
138. Tanir TE, Hasirci V, Hasirci N (2014) Electrospinning of chitosan/poly(lactic acid-co-glycolic acid)/hydroxyapatite composite nanofibrous mats for tissue engineering applications. Polym Bull 71:2999–3016

139. Choi DJ, Choi SM, Kang HY, Min HJ, Lee R, Ikram M, Subhan F, Jin SW, Jeong YH, Kwak JY, Yoon S (2015) Bioactive fish collagen/polycaprolactone composite nanofibrous scaffolds fabricated by electrospinning for 3D cell culture. J Biotechnol 205:47–58
140. Zhang JG, Mo XM (2013) Current research on electrospinning of silk fibroin and its blends with natural and synthetic biodegradable polymers. Front Mater Sci 7:129–142
141. Zhang Q, Lv S, Lu J, Jiang S, Lin L (2015) Characterization of polycaprolactone/collagen fibrous scaffolds by electrospinning and their bioactivity. Int J Biol Macromol 76:94–101
142. Kaur N, Kumar V, Dhakate SR (2016) Synthesis and characterization of multiwalled CNT–PAN based composite carbon nanofibers via electrospinning. Springerplus 5:483
143. Ko F, Gogotsi Y, Ali A, Naguib N, Ye H, Yang GL, Li C, Willis P (2003) Electrospinning of continuous carbon nanotube-filled nanofiber yarns. Adv Mater 15:1161–1165
144. Shilpa, Das SK, Afzal MAF, Srivastava S, Patil S, Sharma A (2016) Enhanced electrical conductivity of suspended carbon nanofibers: effect of hollow structure and improved graphitization. Carbon 108:135–145
145. Rahmat M, Karrabi M, Ghasemi I, Zandi M, Azizi H (2016) Silane crosslinking of electrospun poly (lactic acid)/nanocrystalline cellulose bionanocomposite. Mater Sci Eng C Mater Biol Appl 68:397–405
146. Wanasekara ND, Santos RPO, Douch C, Frollini E, Eichhorn SJ (2016) Orientation of cellulose nanocrystals in electrospun polymer fibres. J Mater Sci 51:218–227
147. Arrieta MP, López J, López D, Kenny JM, Peponi L (2016) Biodegradable electrospun bionanocomposite fibers based on plasticized PLA–PHB blends reinforced with cellulose nanocrystals. Ind Crop Prod 93:290–301
148. Sun C, Boluk Y, Ayranci C (2015) Investigation of nanofiber nonwoven meshes produced by electrospinning of cellulose nanocrystal suspensions in cellulose acetate solutions. Cellulose 22:2457–2470
149. Dong H (2015) Polymer nanofibers reinforced with cellulose nanocrystals. In: Pandey JK, Takagi H, Nakagaito AN, Kim H-J (eds) Handbook of polymer nanocomposites. Processing, performance and application: volume C: polymer nanocomposites of cellulose nanoparticles. Springer, Berlin/Heidelberg, pp 323–341
150. Naseri N, Mathew AP, Oksman K (2016) Electrospinnability of bionanocomposites with high nanocrystal loadings: the effect of nanocrystal surface characteristics. Carbohydr Polym 147:464–472
151. Liu H, Liu W, Luo B, Wen W, Liu M, Wang X, Zhou C (2016) Electrospun composite nanofiber membrane of poly(l-lactide) and surface grafted chitin whiskers: fabrication, mechanical properties and cytocompatibility. Carbohydr Polym 147:216–225
152. Goetz LA, Jalvo B, Rosal R, Mathew AP (2016) Superhydrophilic anti-fouling electrospun cellulose acetate membranes coated with chitin nanocrystals for water filtration. J Membr Sci 510:238–248
153. Ji Y, Liang K, Shen X, Bowlin GL (2014) Electrospinning and characterization of chitin nanofibril/polycaprolactone nanocomposite fiber mats. Carbohydr Polym 101:68–74
154. Naseri N, Algan C, Jacobs V, John M, Oksman K, Mathew AP (2014) Electrospun chitosan-based nanocomposite mats reinforced with chitin nanocrystals for wound dressing. Carbohydr Polym 109:7–15
155. Zhu L, Liang K, Ji Y (2015) Prominent reinforcing effect of chitin nanocrystals on electrospun polydioxanone nanocomposite fiber mats. J Mech Behav Biomed Mater 44:35–42
156. Yu M-F, Files BS, Arepalli S, Ruoff RS (2000) Tensile loading of ropes of single wall carbon nanotubes and their mechanical properties. Phys Rev Lett 84:5552–5555
157. Seoul C, Kim Y-T, Baek C-K (2003) Electrospinning of poly(vinylidene fluoride)/dimethylformamide solutions with carbon nanotubes. J Polym Sci B 41:1572–1577
158. Sung JH, Kim HS, Jin H-J, Choi HJ, Chin I-J (2004) Nanofibrous membranes prepared by multiwalled carbon nanotube/poly(methyl methacrylate) composites. Macromolecules 37:9899–9902
159. Sen R, Zhao B, Perea D, Itkis ME, Hu H, Love J, Bekyarova E, Haddon RC (2004) Preparation of single-walled carbon nanotube reinforced polystyrene and polyurethane nanofibers and membranes by electrospinning. Nano Lett 4:459–464

160. Jamil AKM, Izake EL, Sivanesan A, Agoston R, Ayoko GA (2015) A homogeneous surface-enhanced Raman scattering platform for ultra-trace detection of trinitrotoluene in the environment. Anal Methods 7:3863–3868
161. Nam SH, Shim H-S, Kim Y-S, Dar MA, Kim JG, Kim WB (2010) Ag or Au nanoparticle-embedded one-dimensional composite TiO2 nanofibers prepared via electrospinning for use in lithium-ion batteries. ACS Appl Mater Interfaces 2:2046–2052
162. Zhang S, Tang Y, Vlahovic B (2016) A review on preparation and applications of silver-containing nanofibers. Nanoscale Res Lett 11:80
163. Son WK, Youk JH, Park WH (2006) Antimicrobial cellulose acetate nanofibers containing silver nanoparticles. Carbohydr Polym 65:430–434
164. Doğan G, Özyıldız F, Başal G, Uzel A (2013) Fabrication of electrospun chitosan and chitosan/poly(ethylene oxide) nanofiber webs and assessment of their antimicrobial activity. Int Polym Process 28:143–150
165. Kim H-W, Lee H-H, Knowles JC (2006) Electrospinning biomedical nanocomposite fibers of hydroxyapatite/poly(lactic acid) for bone regeneration. J Biomed Mater Res A 79A:643–649
166. Kim HW, Song JH, Kim HE (2005) Nanofiber generation of gelatin–hydroxyapatite biomimetics for guided tissue regeneration. Adv Funct Mater 15:1988–1994
167. Ji Y, Li B, Ge S, Sokolov JC, Rafailovich MH (2006) Structure and nanomechanical characterization of electrospun PS/clay nanocomposite fibers. Langmuir 22:1321–1328
168. Raj KK, Anil KS, Rajesh Kumar K (2017) Novel approaches for drug delivery. IGI Global, Hershey, pp 1–515
169. Yu L, Cebe P (2009) Crystal polymorphism in electrospun composite nanofibers of poly(vinylidene fluoride) with nanoclay. Polymer 50:2133–2141
170. Goh Y-f, Akram M, Alshemary A, Hussain R (2016) Antibacterial polylactic acid/chitosan nanofibers decorated with bioactive glass. Appl Surf Sci 387:1–7
171. Rezaee O, Mahmoudi Chenari H, Ghodsi FE, Ziyadi H (2017) Preparation of PVA nanofibers containing tungsten oxide nanoparticle by electrospinning and consideration of their structural properties and photocatalytic activity. J Alloys Compd 690:864–872
172. Zhu J, Wei S, Chen X, Karki AB, Rutman D, Young DP, Guo Z (2010) Electrospun polyimide nanocomposite fibers reinforced with core − shell Fe-FeO nanoparticles. J Phys Chem C 114:8844–8850
173. Hwang TH, Lee YM, Kong B-S, Seo J-S, Choi JW (2012) Electrospun core–shell fibers for robust silicon nanoparticle-based lithium ion battery anodes. Nano Lett 12:802–807
174. Wong S-C, Baji A, Leng S (2008) Effect of fiber diameter on tensile properties of electrospun poly(ε-caprolactone). Polymer 49:4713–4722
175. Huang ZM, Zhang YZ, Kotaki M, Ramakrishna S (2003) A review on polymer nanofibers by electrospinning and their applications in nanocomposites. Compos Sci Technol 63: 2223–2253
176. Agarwal S, Wendorff JH, Greiner A (2010) Chemistry on electrospun polymeric nanofibers: merely routine chemistry or a real challenge? Macromol Rapid Commun 31:1317–1331
177. Yoo HS, Kim TG, Park TG (2009) Surface-functionalized electrospun nanofibers for tissue engineering and drug delivery. Adv Drug Deliv Rev 61:1033–1042
178. Duque Sánchez L, Brack N, Postma A, Pigram PJ, Meagher L (2016) Surface modification of electrospun fibres for biomedical applications: a focus on radical polymerization methods. Biomaterials 106:24–45
179. Ma W, Zhang Q, Hua D, Xiong R, Zhao J, Rao W, Huang S, Zhan X, Chen F, Huang C (2016) Electrospun fibers for oil-water separation. RSC Adv 6:12868–12884
180. Cui Q, Dong X, Wang J, Li M (2008) Direct fabrication of cerium oxide hollow nanofibers by electrospinning. J Rare Earths 26:664–669
181. Yalcinkaya F, Yalcinkaya B, Pazourek A, Mullerova J, Stuchlik M, Maryska J (2016) Surface modification of electrospun PVDF/PAN nanofibrous layers by low vacuum plasma treatment. Int J Polym Sci 2016:4671658
182. Ngadiman NHA, Yusof NM, Idris A, Misran E, Kurniawan D (2017) Development of highly porous biodegradable γ-Fe_2O_3/polyvinyl alcohol nanofiber mats using electrospinning process for biomedical application. Mater Sci Eng C 70:520–534

183. Schaub NJ, Le Beux C, Miao J, Linhardt RJ, Alauzun JG, Laurencin D, Gilbert RJ (2015) The effect of surface modification of aligned poly-l-lactic acid electrospun fibers on fiber degradation and neurite extension. PLoS One 10:e0136780
184. Chen W, He S, Pan W, Jin Y, Zhang W, Jiang X (2010) Strategy for the modification of electrospun fibers that allows diverse functional groups for biomolecular entrapment. Chem Mater 22:6212–6214
185. Tan Z, Wang H, Gao X, Liu T, Tan Y (2016) Composite vascular grafts with high cell infiltration by co-electrospinning. Mater Sci Eng C 67:369–377
186. Tang C, Saquing CD, Harding JR, Khan SA (2010) In situ cross-linking of electrospun poly(vinyl alcohol) nanofibers. Macromolecules 43:630–637
187. Shaikh RP, Kumar P, Choonara YE, Toit LCD, Pillay V (2012) Crosslinked electrospun PVA nanofibrous membranes: elucidation of their physicochemical, physicomechanical and molecular disposition. Biofabrication 4:025002
188. Miraftab M, Saifullah AN, Çay A (2016) Physical stabilisation of electrospun poly(vinyl alcohol) nanofibres: comparative study on methanol and heat-based crosslinking. J Mater Sci 50:1943–1957
189. Li X, Wang M, Wang C, Cheng C, Wang X (2014) Facile immobilization of Ag nanocluster on nanofibrous membrane for oil/water separation. ACS Appl Mater Interfaces 6:15272–15282
190. Wang L, Yang S, Wang J, Wang C, Chen L (2011) Fabrication of superhydrophobic TPU film for oil-water separation based on electrospinning route. Mater Lett 65:869–872
191. Su C, Li Y, Dai Y, Gao F, Tang K, Cao H (2016) Fabrication of three-dimensional superhydrophobic membranes with high porosity via simultaneous electrospraying and electrospinning. Mater Lett 170:67–71
192. He L, Shi Y, Han Q, Zuo Q, Ramakrishna S, Xue W, Zhou L (2012) Surface modification of electrospun nanofibrous scaffolds via polysaccharide-protein assembly multilayer for neurite outgrowth. J Mater Chem 22:13187–13196
193. Frenot A, Chronakis IS (2003) Polymer nanofibers assembled by electrospinning. Curr Opin Colloid Interface Sci 8:64–75
194. Wei A, Wang J, Wang X, Hou D, Wei Q (2012) Morphology and surface properties of poly (L-lactic acid)/captopril composite nanofiber membranes. J Eng Fibers Fabr 7:129–135
195. Liang D, Hsiao BS, Chu B (2007) Functional electrospun nanofibrous scaffolds for biomedical applications. Adv Drug Deliv Rev 59:1392–1412
196. Bizarria MTM, D'Ávila MA, Mei LHI (2014) Non-woven nanofiber chitosan/PEO membranes obtained by electrospinning. Braz J Chem Eng 31:57–68
197. Zander NE (2013) Hierarchically structured electrospun fibers. Polymer 5:19–44
198. Alarifi IM, Alharbi A, Khan WS, Swindle A, Asmatulu R (2015) Thermal, electrical and surface hydrophobic properties of electrospun polyacrylonitrile nanofibers for structural health monitoring. Materials 8:7017–7031
199. Khan WS, Asmatulu R, Eltabey MM (2013) Electrical and thermal characterization of electrospun PVP nanocomposite fibers. J Nanomater 2013:160931
200. Feng Q, Xia X, Wei A, Wang X, Wei Q, Huo D, Wei A (2011) Preparation of Cu(II)-chelated poly(vinyl alcohol) nanofibrous membranes for catalase immobilization. J Appl Polym Sci 120:3291–3296
201. Awal A, Sain M, Chowdhury M (2012) Thermal analysis and spectroscopic studies of electrospun nano-scale composite fibers. J Therm Anal Calorim 107:1237–1242
202. Fouad H, Elsarnagawy T, Almajhdi FN, Khalil KA (2013) Preparation and in vitro thermomechanical characterization of electrospun PLGA nanofibers for soft and hard tissue replacement. Int J Electrochem Sci 8:2293–2304
203. Zhou YS, Yang DZ, Nie J (2007) Effect of PVA content on morphology, swelling and mechanical property of crosslinked chitosan/PVA nanofibre. Plast Rubber Compos 36:254–258
204. Dhanalakshmi M, Jog JP (2008) Preparation and characterization of electrospun fibers of nylon 11. Express Polym Lett 2:540–545
205. Oliveira JE, Mattoso LHC, Orts WJ, Medeiros ES (2013) Structural and morphological characterization of micro and nanofibers produced by electrospinning and solution blow spinning: a comparative study. Adv Mater Sci Eng 2013:409572

206. Sencadas V, Correia DM, Ribeiro C, Moreira S, Botelho G, Gómez Ribelles JL, Lanceros-Mendez S (2012) Physical-chemical properties of cross-linked chitosan electrospun fiber mats. Polym Test 31:1062–1069
207. Brugnerotto J, Lizardi J, Goycoolea FM, Argüelles-Monal W, Desbrières J, Rinaudo M (2001) An infrared investigation in relation with chitin and chitosan characterization. Polymer 42:3569–3580
208. Costa RGF, De Oliveira JE, De Paula GF, De Picciani PHS, De Medeiros ES, Ribeiro C, Mattoso LHC (2012) Electrospinning of polymers in solution. Part I: theoretical foundation. Polimeros 22:170–177
209. Baker SR, Banerjee S, Bonin K, Guthold M (2016) Determining the mechanical properties of electrospun poly-ε-caprolactone (PCL) nanofibers using AFM and a novel fiber anchoring technique. Mater Sci Eng C 59:203–212
210. Greiner A, Wendorff JH (2007) Electrospinning: a fascinating method for the preparation of ultrathin fibers. Angew Chem Int Ed Engl 46:5670–5703
211. Kong B, Mi S (2016) Electrospun scaffolds for corneal tissue engineering: a review. Materials 9:614
212. Jiang Min WM, Shiyong W, Zhibao C, Shichun M (2016) Aligned nanofibers based on electrospinning technology. Prog Chem 28:711–726
213. Jiang T, Carbone EJ, Lo KWH, Laurencin CT (2015) Electrospinning of polymer nanofibers for tissue regeneration. Prog Polym Sci 46:1–24
214. Li W-J, Laurencin CT, Caterson EJ, Tuan RS, Ko FK (2002) Electrospun nanofibrous structure: a novel scaffold for tissue engineering. J Biomed Mater Res 60:613–621
215. Mo XM, Xu CY, Kotaki M, Ramakrishna S (2004) Electrospun P(LLA-CL) nanofiber: a biomimetic extracellular matrix for smooth muscle cell and endothelial cell proliferation. Biomaterials 25:1883–1890
216. Sill TJ, von Recum HA (2008) Electrospinning: applications in drug delivery and tissue engineering. Biomaterials 29:1989–2006
217. Matthews JA, Wnek GE, Simpson DG, Bowlin GL (2002) Electrospinning of collagen nanofibers. Biomacromolecules 3:232–238
218. Duque Sanchez L, Brack N, Postma A, Pigram PJ, Meagher L (2016) Surface modification of electrospun fibres for biomedical applications: a focus on radical polymerization methods. Biomaterials 106:24–45
219. Cestari M, Muller V, Rodrigues JH, Nakamura CV, Rubira AF, Muniz EC (2014) Preparing silk fibroin nanofibers through electrospinning: further heparin immobilization toward hemocompatibility improvement. Biomacromolecules 15:1762–1767
220. Villanova JCO, Oréfice RL, Cunha AS (2010) Pharmaceutical applications of polymers. Polimeros 20:51–64
221. Bennet D. and Kim S. (2014) Polymer nanoparticles for smart drug delivery, application of nanotechnology in drug delivery, PhD. Sezer AD (ed), InTech, doi: 10.5772/58422. Available from: http://www.intechopen.com/books/application-of-nanotechnology-in-drug-delivery/polymer-nanoparticles-for-smart-drug-delivery
222. Porto I. C. C. M. Porto (2012) Polymer biocompatibility, polymerization, Dr. Gomes A. de S. (ed.), InTech, doi: 10.5772/47786. Available from: http://www.intechopen.com/books/polymerization/polymer-biocompatibility
223. Subbiah R, Ramalingam P, Ramasundaram S, Kim DY, Park K, Ramasamy MK, Choi KJ (2012) N,N,N-trimethyl chitosan nanoparticles for controlled intranasal delivery of HBV surface antigen. Carbohydr Polym 89:1289–1297
224. Varum FO, Basit AW, Sousa J, Veiga F (2008) Mucoadhesion studies in the gastrointestinal tract to increase oral drug bioavailability. Revista Brasileira de Ciencias Farmaceuticas Braz J Pharm Sci 44:535–548
225. Säkkinen M, Linna A, Ojala S, Jürjenson H, Veski P, Marvola M (2003) In vivo evaluation of matrix granules containing microcrystalline chitosan as a gel-forming excipient. Int J Pharm 250:227–237

226. Suwantong O, Opanasopit P, Ruktanonchai U, Supaphol P (2007) Electrospun cellulose acetate fiber mats containing curcumin and release characteristic of the herbal substance. Polymer 48:7546–7557
227. Santos VA (2013) Preparo e caracterização físico-química de filmes nanofibrílicos contendo cloreto de cetilpiridíneo: futura alternativa aos antifúngicos para o tratamento de infecções orais por Candida, in: Faculdade de Odontologia, Universidade de São Paulo
228. Nista SVG (2012) Desenvolvimento e caracterização de nanofibras de acetato de celulose para liberação controlada de fármacos in, Universidade Estadual de Campinas
229. Dicks LMT, Heunis TDJ (2010) Nanofibers offer alternative ways to the treatment of skin infections. J Biomed Biotechnol 2010:510682. doi:10.1155/2010/510682
230. Verreck G, Chun I, Peeters J, Rosenblatt J, Brewster ME (2003) Preparation and characterization of nanofibers containing amorphous drug dispersions generated by electrostatic spinning. Pharm Res 20:810–817
231. Kenawy E-R, Bowlin GL, Mansfield K, Layman J, Simpson DG, Sanders EH, Wnek GE (2002) Release of tetracycline hydrochloride from electrospun poly(ethylene-co-vinylacetate), poly(lactic acid), and a blend. J Control Release 81:57–64
232. Kim CH, Khil MS, Kim HY, Lee HU, Jahng KY (2006) An improved hydrophilicity via electrospinning for enhanced cell attachment and proliferation. J Biomed Mater Res B Appl Biomater 78:283–290
233. Anderson JM, Shive MS (1997) Biodegradation and biocompatibility of PLA and PLGA microspheres. Adv Drug Deliv Rev 28:5–24
234. Thakur RA, Florek CA, Kohn J, Michniak BB (2008) Electrospun nanofibrous polymeric scaffold with targeted drug release profiles for potential application as wound dressing. Int J Pharm 364:87–93
235. Manzetti S, Ghisi R (2014) The environmental release and fate of antibiotics. Mar Pollut Bull 79:7–15
236. Kemper N (2008) Veterinary antibiotics in the aquatic and terrestrial environment. Ecol Indic 8:1–13
237. Harada NS (2014) Desenvolvimento de membranas compósitas de poliuretano pelo processo de eletrofiação. Escola Politécnica de São Paulo, São Paulo
238. Gibson P, Schreuder-Gibson H, Rivin D (2001) Transport properties of porous membranes based on electrospun nanofibers. Colloids and Surf A Physicochem Eng Asp 187–188: 469–481
239. Rajesh KP, Natarajan TS (2009) Electrospun polymer nanofibrous membrane for filtration. J Nanosci Nanotechnol 9:5402–5405
240. Tian Y, Wu M, Liu R, Li Y, Wang D, Tan J, Wu R, Huang Y (2011) Electrospun membrane of cellulose acetate for heavy metal ion adsorption in water treatment. Carbohydr Polym 83: 743–748
241. Guo J, Zhang Q, Cai Z, Zhao K (2016) Preparation and dye filtration property of electrospun polyhydroxybutyrate–calcium alginate/carbon nanotubes composite nanofibrous filtration membrane. Sep Purif Technol 161:69–79
242. Lakhdhar I, Mangin P, Chabot B (2015) Copper (II) ions adsorption from aqueous solutions using electrospun chitosan/peo nanofibres: effects of process variables and process optimization. J Water Process Eng 7:295–305
243. Chianeh FN, Parsa JB (2016) Electrochemical degradation of metronidazole from aqueous solutions using stainless steel anode coated with SnO_2 nanoparticles: experimental design. J Taiwan Inst Chem Eng 59:424–432
244. Ammar HB, Brahim MB, Abdelhédi R, Samet Y (2016) Green electrochemical process for metronidazole degradation at BDD anode in aqueous solutions via direct and indirect oxidation. Sep Purif Technol 157:9–16
245. Gurcu B, Koca YB, Ozkut M, Tuglu MI (2016) Matrix changes due to the toxic effects of metronidazole in intestinal tissue of fish (Onchorhynchus mykiss). Chemosphere 144:1605–1610

246. Carrales-Alvarado DH, Ocampo-Perez R, Leyva-Ramos R, Rivera-Utrilla J (2014) Removal of the antibiotic metronidazole by adsorption on various carbon materials from aqueous phase. J Colloid Interface Sci 436:276–285
247. Chen D, Deng J, Liang J, Xie J, Hu C, Huang K (2013) A core–shell molecularly imprinted polymer grafted onto a magnetic glassy carbon electrode as a selective sensor for the determination of metronidazole. Sensors Actuators B Chem 183:594–600
248. Xiao N, Deng J, Cheng J, Ju S, Zhao H, Xie J, Qian D, He J (2016) Carbon paste electrode modified with duplex molecularly imprinted polymer hybrid film for metronidazole detection. Biosens Bioelectron 81:54–60
249. Li M, Han G, Yang B (2008) Fabrication of the catalytic electrodes for methanol oxidation on electrospinning-derived carbon fibrous mats. Electrochem Commun 10:880–883
250. McCann JT, Li D, Xia Y (2005) Electrospinning of nanofibers with core-sheath, hollow, or porous structures. J Mater Chem 15:735–738
251. Picciani PHS, Soares BG, Medeiros ES, de Souza FG, Wood DF, Orts WJ, Mattoso LHC (2009) Electrospinning of polyaniline/poly(lactic acid) ultrathin fibers: process and statistical modeling using a non-Gaussian approach. Macromol Theory Simul 18:528–536
252. Costa RGF, Oliveira JEd, Paula GFd, Picciani PHds, Medeiros ESd, Ribeiro C, Mattoso LHC (2012) Eletrofiação de Polímeros em Solução: parte I: fundamentação TeÃ^{3}rica. Polímeros 22:170–177
253. Brannon-Peppas L (1995) Recent advances on the use of biodegradable microparticles and nanoparticles in controlled drug delivery. Int J Pharm 116:1–9
254. Reneker DH, Yarin AL (2008) Electrospinning jets and polymer nanofibers. Polymer 49:2387–2425
255. Agarwal S, Burgard M, Greiner A, Wendorff J (2016) Electrospinning, a practical guide to nanofibers. De Gruyter, Berlin/Boston
256. Ogata N, Yamaguchi S, Shimada N, Lu G, Iwata T, Nakane K, Ogihara T (2007) Poly(lactide) nanofibers produced by a melt-electrospinning system with a laser melting device. J Appl Polym Sci 104:1640–1645
257. Zhang L-H, Duan X-P, Yan X, Yu M, Ning X, Zhao Y, Long Y-Z (2016) Recent advances in melt electrospinning. RSC Adv 6:53400–53414
258. Brown TD, Dalton PD, Hutmacher DW (2016) Melt electrospinning today: an opportune time for an emerging polymer process. Prog Polym Sci 56:116–166
259. Ding B, Wang M, Wang X, Yu J, Sun G (2010) Electrospun nanomaterials for ultrasensitive sensors. Mater Today 13:16–27

Part II
Probing the Functionality and Applications of Novel Complex Functional Materials

Chapter 5
Morphology and Optical Properties of $SrWO_4$ Powders Synthesized by the Coprecipitation and Polymeric Precursor Methods

Júlio César Sczancoski, Máximo Siu Li, Valmor Roberto Mastelaro, Elson Longo, and Laécio Santos Cavalcante

1 Introduction

In recent years, the electrooptical industries have searched to minimize the size of electronic systems, increase the efficiency of optical devices, employ materials safe for the human life and the environment, and use synthesis or fabrication techniques with low costs and simple handling. These factors are fundamental for the improvement of electronic components and equipments, for example, as solid-state lasers (Blu-ray players, medical surgery), light-emitting diodes (traffic light signals, automotive lighting), lamps (illuminated advertising panels), displays (cell phones, computer monitors), and scintillators (radiation detectors) [1–3]. The materials belonging to the scheelite group are considered promising candidates for these technological purposes, especially the strontium tungstate ($SrWO_4$) because of its blue and green luminescence emissions [4–9]. In general, the origin of these emissions has been attributed to many effects, such as structural order-disorder, quantum size effect, crystalline imperfections, surface roughness, particle sizes and shapes, etc. [10–13]. In principle, all these factors are dependent on the synthesis methods and some experimental parameters like heat treatment temperature,

J.C. Sczancoski (✉)
CDMF – Department of Chemistry, Universidade Federal de São Carlos (UFSCar), São Carlos, SP, Brazil
e-mail: jcsfisica@gmail.com

M.S. Li • V.R. Mastelaro
IFSC – Instituo de Física de São Carlos, Universidade de São Paulo (USP), São Carlos, SP, Brazil

E. Longo
LIEC-IQ – Department of Chemistry, Universidade Estadual Paulista (UNESP), Araraquara, SP, Brazil

L.S. Cavalcante
PPGQ-GERATEC, Universidade Estadual do Piauí (UESPI), Teresina, PI, Brazil

E. Longo, F.A. La Porta (eds.), *Recent Advances in Complex Functional Materials*,
DOI 10.1007/978-3-319-53898-3_5

pressure in closed systems, processing time, form of the material (single crystal, thin film, or powder), reaction medium (solid or liquid), type of solvent, gaseous atmosphere, and so on [14–16].

In materials science, the bottom-up approach is a good strategy to prepare oxide materials, which is based on smaller units (ions, molecules, or nanocrystals) that are self-assembled up to build a more complex unit (nano-, meso-, or microparticles) [17, 18]. Typical examples of materials made by bottom-up approaches include the coprecipitation reaction (CP) and polymeric precursor method (PPM) [19]. CP involves the mixture of different chemical salts in a liquid medium in order to obtain the required final composition. The success of this reaction, in part, depends on the control of the concentration of reactants, pH, and temperature of the solution to produce a specific material with the desired chemical homogeneity [20]. Xing et al. [21] reported the molar ratio and concentration of reactants are two fundamental parameters able to control the particle shapes of strontium molybdate in a CP reaction. On the other hand, PPM is a versatile route in which the metal complexes are dissolved in a mixture of citric acid and ethylene glycol in aqueous medium [22]. The main features of this chemical route are the capability of reducing the phase segregation and ensuring the compositional homogeneity at the molecular scale [23]. Anicete-Santos et al. [24] described an experimental and theoretical correlation on the effect induced by the structural order-disorder phenomenon in the photoluminescence (PL) response of $SrWO_4$ powders prepared by PPM.

Since 1970, the microwave heating opened a new research line in the area of materials science, mainly focused on studying the sintering and calcining mechanisms of ceramic oxides (e.g., thin films, powders, composites). However, this type of heating is very complex and depends on several parameters, such as dielectric properties, penetration depth, operating frequency, operating mode (single or multimode), placement inside the oven, load geometry, and oven geometry [25, 26]. Hence, understanding the individual or joint influence of these factors in the formation and crystallization mechanisms as well as its effects on the physicochemical properties of solids is still a major challenge for materials engineers and scientists. In a study on the growth of $CaMoO_4$ thin films deposited on silicon substrates, Marques et al. [27] analyzed the surface morphological behavior of this scheelite after heat treatments performed at 600 °C for 2 h (resistive furnace (RF)) and 10 min (microwave oven (MO)), respectively. Their results revealed the formation of the homogeneous and crack-free surface for thin films heat-treated in MO. However, the authors did not report any information on the growth of these films using the same conditions of heat treatment times in both furnaces.

Therefore, the present chapter was focused on the direct influence of two chemical methods (CP and PPM) and heat treatment conditions performed in distinct furnaces (RF and MO) on the morphological features and optical properties of $SrWO_4$ powders.

2 Experimental Procedure

2.1 Synthesis

In order to perform this study, the following synthesis procedure was adopted to prepare $SrWO_4$ powders:

Coprecipitation (*CP*) strontium nitrate [Sr $(NO_3)_2$] (99%) and tungstic acid [H_2WO_4] (99%) were purchased from Aldrich and used as received. Initially, Sr $(NO_3)_2$ precursor (5 mmol) was added in 50 ml of deionized water contained in a plastic tube (Falcon™; 50 mL). This mixture was stirred for 10 min at room temperature using an MS3 basic vortex shaker (IKA Werke GmbH & Co. KG, Germany). In a beaker, a second solution was prepared with H_2WO_4 precursor (5 mmol) dissolved in 75 mL of deionized water, which was heated at 85 °C for 15 min. In order to favor the H_2WO_4 solubilization in the aqueous medium, 6 mL of ammonium hydroxide (NH_4OH) [28–30% in NH_3, Aldrich] was added to this solution and maintained under constant stirring for 5 min. Thereafter, both solutions were quickly mixed, stirred for a further 15 min with the temperature maintained at 85 °C. After these steps, the formation of solid $SrWO_4$ precipitates (white coloration) was verified at the bottom of the beaker. This solution containing the precipitates was naturally cooled to room temperature and then washed and centrifuged several times with deionized water. Finally, the collected powders were heat-treated at 500, 600, and 700 °C for 2 h using an RF (EDG 1800 model, EDG Equipamentos, Brazil) [28] and an MO (FTR-1100 model, Fornos INTI, Brazil) [29]. The heating rate in both furnaces was controlled and fixed at 1 °C/min. The powder denoted as CP was not subjected to any heat treatment and considered as a standard sample.

Polymeric precursor method (*PPM*) Sr $(NO_3)_2$ (99%), H_2WO_4 (99%), citric acid ($C_6H_8O_7$) (99.5%), and ethylene glycol ($C_2H_6O_2$) (99%) were used as raw materials. Sr $(NO_3)_2$ (99%) and H_2WO_4 (99%) precursors were purchased from Aldrich, while the $C_6H_8O_7$ and $C_2H_6O_2$ were purchased from Mallinckrodt and J.T. Baker, respectively. Initially, $C_6H_8O_7$ was dissolved in 150 mL of deionized water heated at 90 °C under constant stirring for 45 min. In a second beaker, 5 mmol of H_2WO_4 was dissolved in 100 mL of deionized water and heated at 90 °C during 1 h. 15 mL of NH_4OH [28–30% in NH_3, Aldrich] was added in this solution to assist in the H_2WO_4 dissolution. In a third beaker, 5 mmol of $Sr(NO_3)_2$ precursor was solubilized in 75 mL of deionized water at room temperature. In the sequence, all these solutions previously prepared were mixed and stirred at 90 °C for 1 h. The pH value of the solution was maintained at 6. After homogenization, $C_2H_6O_2$ was added to this solution to promote the polyesterification reaction. The molar ratio of $C_6H_8O_7$/metal cations was fixed at 6:1, while the mass ratio of $C_6H_8O_7/C_2H_6O_2$ was adjusted at 60:40. The volume of this solution was reduced to obtain a viscous polymeric resin, which was then placed inside an RF and heat-treated at 350 °C for 12 h. This procedure was employed to minimize the presence of residual organic compounds arising from the $C_6H_8O_7$ and $C_2H_6O_2$. The precursor powder was

deagglomerated using an agate mortar with pestle and then heat-treated at 500, 600, and 700 °C for 2 h in RF (EDG 1800 model, EDG Equipamentos, Brazil) [28] and MO (FTR-1100 model, Fornos INTI, Brazil) [29] with the heating rate maintained at 1 °C/min. This low heating rate was chosen to verify the influence of microwaves on the heat treatment process of $SrWO_4$ in MO. Besides the microwave radiation, MO was projected with interior walls composed of susceptor material (silicon carbide), favoring also in the thermal conduction (converting microwave energy into thermal energy).

2.2 Characterizations

The powders were structurally characterized by X-ray diffraction (XRD) using a D/Max-2500PC diffractometer (Rigaku, Japan) with Cu$K\alpha$ radiation (λ = 1.5406 Å) and scanning rate of 2 °/min. The thermogravimetric (TG) analysis was performed in a TG 209 F1 Iris equipment (Netzsch, Germany), using synthetic air as oxidative atmosphere and collected over ranging from 30 to 900 °C with a heating rate of 10 °C/min. Raman spectra of the powders prepared by CP were measured with a LabRAM HR 800 spectrophotometer (Horiba Jobin Yvon, Japan) equipped with He-Ne laser (λ = 632.8 nm). In samples synthesized by PPM, Raman spectra were recorded by means of an RFS100 spectrophotometer (Bruker, Germany) equipped with Nd:YAG laser (λ = 1064 nm), operating at 100 mW. The use of different Raman spectrophotometers for the samples was adopted to suppress the fluorescence phenomenon and obtain well-defined vibrational bands. Morphological aspects were observed in an Inspect F50 field emission-scanning electron microscope (FE-SEM) (FEI Company, Netherlands) operated at 5 kV. Ultraviolet-visible (UV-vis) absorption spectra were taken using a Cary 5G spectrophotometer (Varian, USA) in the diffuse reflection mode. The electronic and local atomic structures around tungsten (W) atoms were checked by X-ray absorption near-edge structure (XANES). W L_3-edge XANES spectra were collected at the National Synchrotron Light Laboratory (LNLS) in Brazil, using the D04BXAFS1 beam line. XANES data were collected in transmission mode at room temperature with the samples deposited on a polymeric membrane. These spectra were recorded for each sample using an energy step of 1.0 eV, before and after the edge, and 0.7 eV near the edge. The tungsten oxide (WO_3) ($\geq$99%) purchased from Aldrich was employed as reference compound in these measurements. PL spectra were obtained with a Monospec 27 monochromator (Thermal Jarrel Ash, USA) coupled to an R446 photomultiplier (Hamamatsu Photonics, Japan). A krypton ion laser (Coherent Innova 200 K, USA) (λ = 350 nm) was used as excitation source. The incident laser beam power on the sample was maintained at 14 mW. All experimental measurements were performed at room temperature.

3 Results and Discussion

3.1 Thermogravimetric Analysis

The thermal decomposition behavior of $SrWO_4$ powders synthesized by CP and PPM is illustrated in Fig. 5.1. TG profiles indicated the existence of two main weight loss regions. The first is caused by the dehydration or evaporation of the residual aqueous solvent (from 50 to 200 °C), while the second is due to the decomposition of organic compounds (from 200 °C to 770 °C → CP and from 230 °C to 670 °C → PPM). A notable feature was the predominance of a larger amount of organic matter in the samples prepared by PPM (≈57%) in relation to those obtained by CP (≈3.5%). It is a typical consequence of this synthesis method, i.e., a direct response due to the use of $C_6H_8O_7$ and $C_2H_6O_2$ in the chelation and polyesterification stages of metal ions, respectively. This result is in good agreement with other published papers [30, 31].

3.2 Structural Analyses

Figure 5.2 illustrates the diffractograms of $SrWO_4$ powders synthesized by CP and PPM and heat-treated at different temperatures in RF and MO, respectively. Firstly, all XRD patterns were perfectly indexed to the scheelite-type tetragonal structure with space group $I4_1/a$, as described in the Inorganic Crystal Structure Data (ICSD) No. 155425 [32]. Diffraction peaks associated to secondary phases were not detected in the samples. According to the literature [8], the existence of intense and well-defined peaks in the diffractograms is a common nature of crystalline solids with a high degree of periodicity at long range. This aspect was

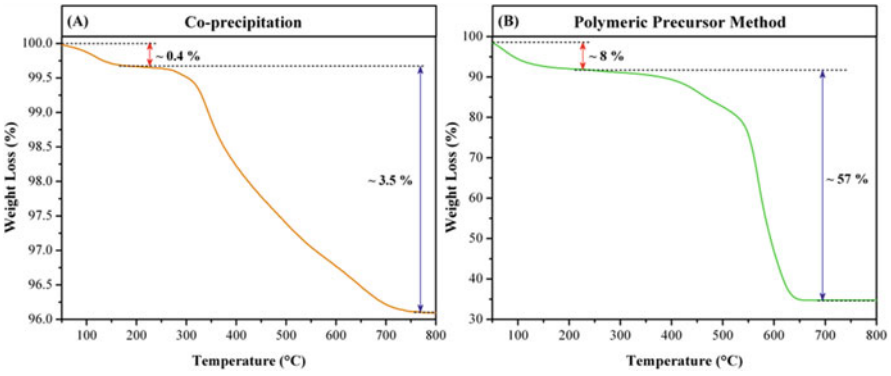

Fig. 5.1 Thermal decomposition analyses of $SrWO_4$ powders synthesized by (**a**) CP and (**b**) PPM, respectively

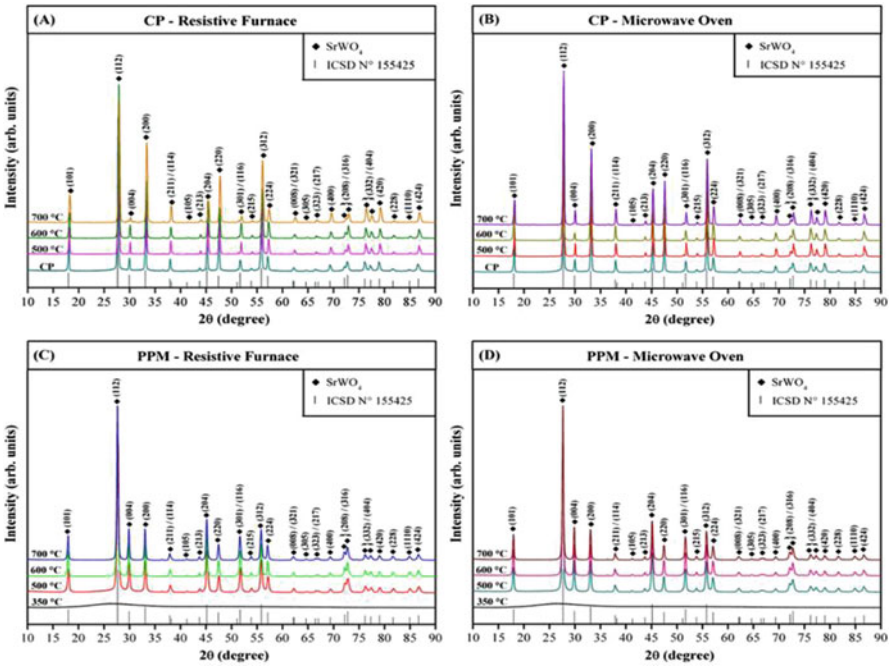

Fig. 5.2 XRD patterns of $SrWO_4$ powders synthesized by CP (**a**, **b**) and PPM (**c**, **d**), which were heat-treated at different temperatures in RF and MO, respectively. The vertical lines indicate the positions and relative intensities of diffraction peaks in ICSD No. 155425

observed in all $SrWO_4$ powders synthesized by CP and heat-treated in both furnaces (Fig. 5.2a, b). On the other hand, the precursor powders obtained by PPM and heat-treated at 350 °C for 12 h did not reveal the presence of diffraction peaks, which were only verified after heat treatments performed at 500, 600, and 700 °C for 2 h. Thus, the precursor powder is amorphous or highly disordered, containing an enormous concentration of organic substances, as detected in TG measurements (Fig. 5.1b). The excess of organics has an influence on the interactions between $[SrO_8]$ and $[WO_4]$ clusters as well as on the matter diffusion. When the temperature is increased, there is an elimination of organic matter, which favors a better interaction between the clusters and a gradual crystallization of $SrWO_4$ phase. Analyzing in terms of synthesis methods (CP and PPM), when compared to all samples, it was possible to identify a partial effect of crystallographic orientation by means of diffraction peaks associated to (004)/(200) and (204)/(220) planes. The analysis performed on the normalized intensity (I_N) in diffractograms revealed $I_N(004) < I_N(200)$ and $I_N(204) < I_N(220)$ for the $SrWO_4$ synthesized by CP, while $I_N(004) \approx I_N(200)$ and $I_N(204) > I_N(220)$ for those obtained by PPM. According to experimental conditions (temperature and heating rate) adopted in the heat treatments, there is no conclusive evidence in XRD patterns in order to confirm the real effects induced by the conventional or microwave heating.

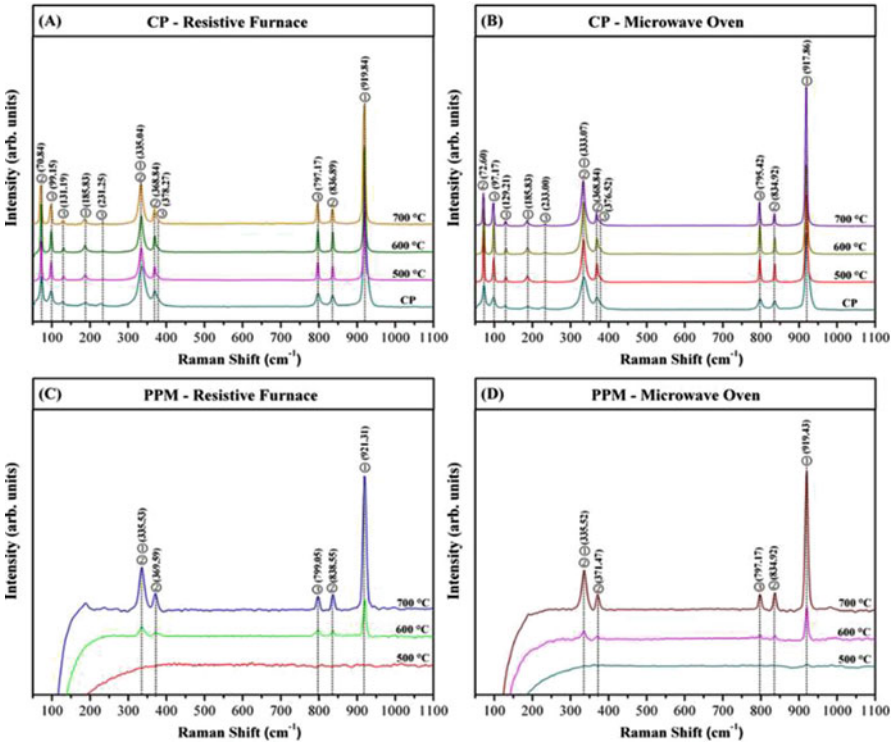

Fig. 5.3 Raman spectra of $SrWO_4$ powders synthesized by CP (**a**, **b**) and PPM (**c**, **d**), which were heat-treated at different temperatures in RF and MO, respectively (vibrational modes: A_g = ①; B_g = ②; E_g = ③)

3.3 Raman Spectra

Raman spectra of $SrWO_4$ powders obtained in our study are illustrated in Fig. 5.3. According to Basieve et al. [33], Raman-active modes of tungstates are composed of internal and external vibrational modes. In our case, the internal modes are arising from the vibrations associated with $[WO_4]$ clusters, while the external modes are caused by the motion of $[SrO_8]$ clusters in the lattice. Moreover, considering the Raman scattering theory in solids, some published papers describe that spectra containing intense and narrow bands are typical of materials with local or short-range structural ordering [8, 34]. Raman spectra of all samples prepared by CP have well-defined vibrational bands. On the other hand, the powders prepared by PPM exhibited a transition from amorphous (or disordered) to crystalline solid, according to the heat treatment evolution. This observation supports the affirmation that the excess of organics, inherent of the PPM, difficults the interactions between $[SrO_8]$ and $[WO_4]$ clusters in both long and short range. These results are in

good agreement with other papers found in the literature for other tungstates with scheelite-type structure [8, 12, 16, 24].

3.4 Morphological Aspects

The morphological features of $SrWO_4$ powders synthesized by CP and PPM obtained in the present study are illustrated in Figs. 5.4 and 5.5. FE-SEM micrographs in Figs. 5.4 and 5.5 revealed the presence of uncountable rice-shaped $SrWO_4$ microparticles. In a first approximation, we suppose the initial nucleation event during the CP reaction for the formation of these microstructures proceed according to the La Mer model [35, 36]. When the concentration of reactants was maintained above the critical level, the number of stable nuclei rapidly and instantaneously increased with the supersaturation via dissolution of unstable nuclei. These dissolved nuclei provide the solute, which is consumed by stable nuclei during its growth. As can be seen in FE-SEM micrographs, the rice-like particles present polydisperse particle size distribution and aggregated profiles. This experimental observation allows us to presume the nucleation and growth stages occur simultaneously, becoming a complication for the morphologic control. In this condition, the interactions between nanocrystals to produce larger structures are governed by particle-particle (collision events) and particle-solvent interactions [37]. When the system has reached an equilibrium condition between the solubilization and precipitation processes, the Ostwald ripening mechanism [38] occurred, resulting in the growth and final shape of rice-like microparticles.

A remarkable change in these morphologies was verified when the heat treatment temperature was increased. In powders synthesized by CP, it was verified that both sides of these rice-like microstructures are very similar (Fig. 5.4a–c). However, when subjected to the calcining in RF or MO, the temperature promoted a slight modification on just one side of these particles (appearing as if it were broken) (Fig. 5.4d–l). According to the literature [39, 40], particles having shapes similar to rice grains tend to grow along the [001] or [100] direction. Moreover, faces with low surface energy grow slowly and predominate in the final shape [38]. In our case, we do not know which crystallographic faces are exposed in $SrWO_4$ microparticles. Therefore, future theoretical calculations focused on the concept of surface energy on the main shapes of these microcrystals will be needed to provide fundamental responses on the morphological progress.

As was previously described, the heat treatment of $SrWO_4$ powders in MO (Fig. 5.5a–i) resulted in particles with morphological features similar to those found in RF (Fig. 5.4d–l). However, when the heat treatment was performed at 700 °C, imperfections or surface defects were noted in the microparticles. This behavior was not evidenced for the powders heat-treated at the same temperature in RF. Although there is the effect of thermal conduction induced from suscepter (SiC) to alumina crucible containing the $SrWO_4$ powders, an interaction phenomenon

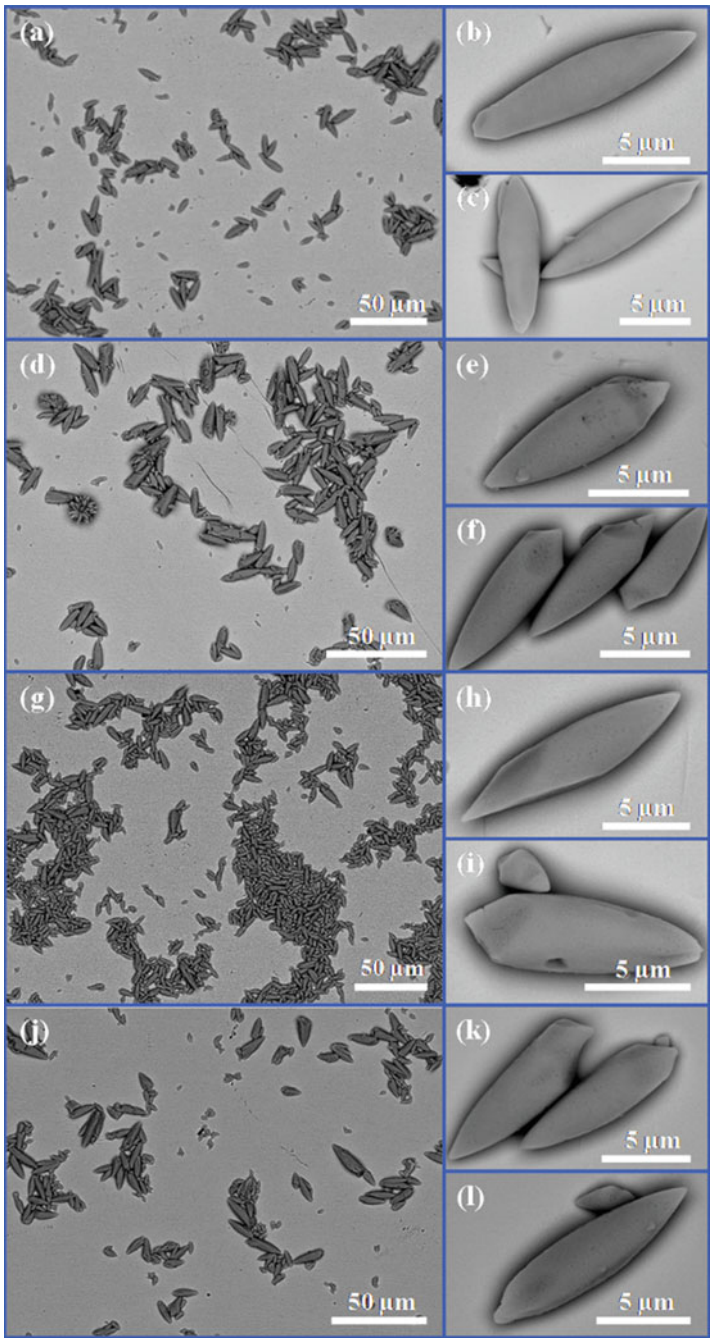

Fig. 5.4 Low- and high-magnification FE-SEM micrographs of rice-like $SrWO_4$ microparticles synthesized by CP (**a–c**) and heat-treated at 500 °C (**d–f**), 600 °C (**g–i**), and 700 °C (**j–l**) for 2 h in RF

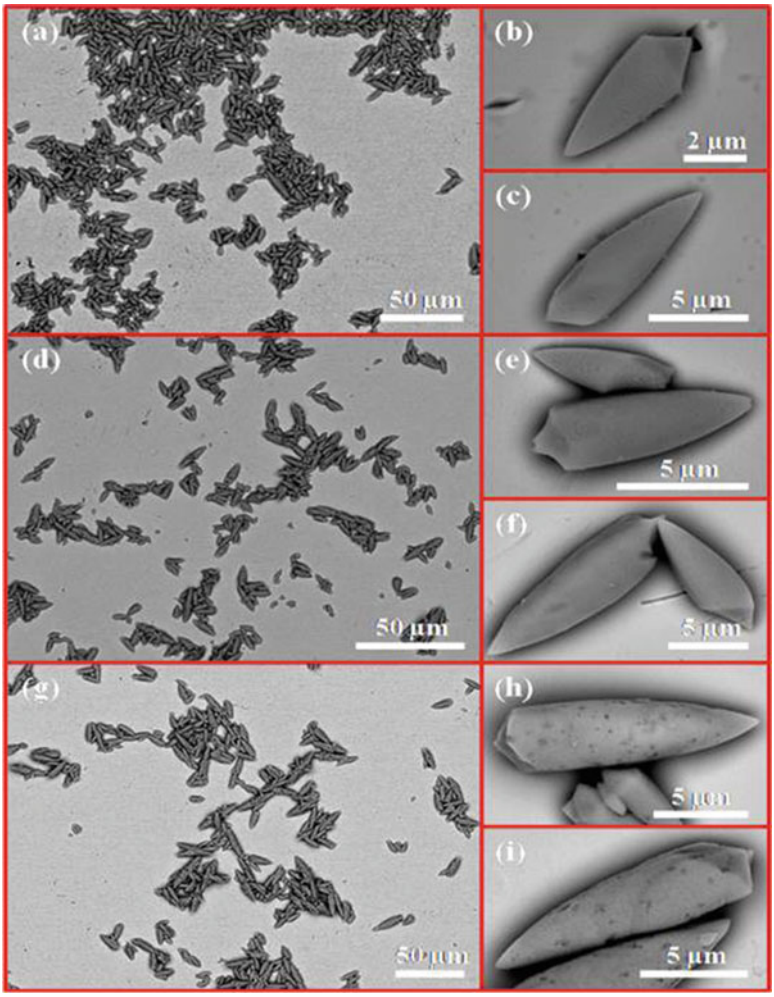

Fig. 5.5 Low- and high-magnification FE-SEM micrographs of rice-like $SrWO_4$ microparticles synthesized by CP and heat-treated at 500 °C (**a**–**c**), 600 °C (**d**–**f**), and 700 °C (**g**–**i**) for 2 h in MO

between solid particles and microwaves also occurs. In principle, in conventional heating using RF, the heating direction is from outside to inside of the powder, resulting in a higher temperature of the sample surface than in the core, while for microwaves, the direction is from inside to outside of the powder resulting in a higher temperature of the sample core than on the surface [41]. However, the use of electromagnetic waves as an energy source is able to induce the phenomenon known as temperature runaway, i.e., the specimen overheats catastrophically [42]. Based on these physical concepts, it is acceptable that the surface defects are originated by the

fast evaporation of residual solvent and decomposition of organic compounds by the microwave heating or due to local overheating points.

The difference of synthesis methods is evidenced in Figs. 5.6 and 5.7. While the particles formed by CP have well-defined shapes, those obtained by PPM exhibit aggregated assemblies of small particles with irregular shapes. The literature [19] reports the preparation of inorganic oxides by PPM which is dependent on the mixing level of different alkoxides in the precursor solution and reactivity of each alkoxide species in water. Also, the metal cations are trapped in the polymeric resin, reducing the growing controlled shapes. The high particle reactivity and the excess of organics in the polymeric resin favor the formation of partially sintered hard agglomerates. The slow heating rate and the increase of temperature on the polymeric resin promote a slow evaporation of the solvent and decomposition of the organic matter, causing the appearance of small pores. In this synthesis method, the growth process is governed by the matter transport in points of contact between the particles. This behavior can be seen for the powders heat-treated at different temperatures in RF (Fig. 5.6). After the heat treatment performed at 500 °C, a compact group made up of several small particles was noted (Fig. 5.6a–c). The occurrence of layer overlapping was identified at 600 °C, as a consequence of the interdiffusion of matter from one particle to another (Fig. 5.6d–f). The increase of temperature up to 700 °C promoted an increase in the diffusion rate, resulting in the appearance of thick and/or dense layers composed of several aggregated particles (Fig. 5.6g–i).

Figure 5.7 shows FE-SEM micrographs of $SrWO_4$ samples obtained by PPM and heat-treated at different temperatures in MO. All powders exhibited large assemblies of aggregated particles, resulting in irregular and dense blocks. These morphological features are not very different from the samples heat-treated in RF; however, the particles are slightly smaller. We believe the microwaves induced a rapid thermal heating inside the samples and strongly increased the particle densification and growth rate. The densification rate depends on the diffusion of ions between particles, and the growth rate is determined by the diffusion in the interface contact of the particles or by means of grain boundaries [41]. This behavior induced by the MO was also evidenced by Marques et al. [23] in the preparation of $BaMoO_4$ thin films heat-treated at 600 °C.

3.5 XANES Spectra

XANES is a quantum mechanical phenomenon based on the X-ray photoelectric effect, in which an X-ray photon incident on an atom within a sample is absorbed and liberates an electron from an inner atomic orbital [43]. The photoelectron wave scatters from atoms around the X-ray-absorbing atom, creating interferences between the outgoing and scattered parts of the photoelectron wave function. These quantum interference effects cause an energy-dependent variation in the X-ray absorption probability, which is proportional to the X-ray absorption coefficient

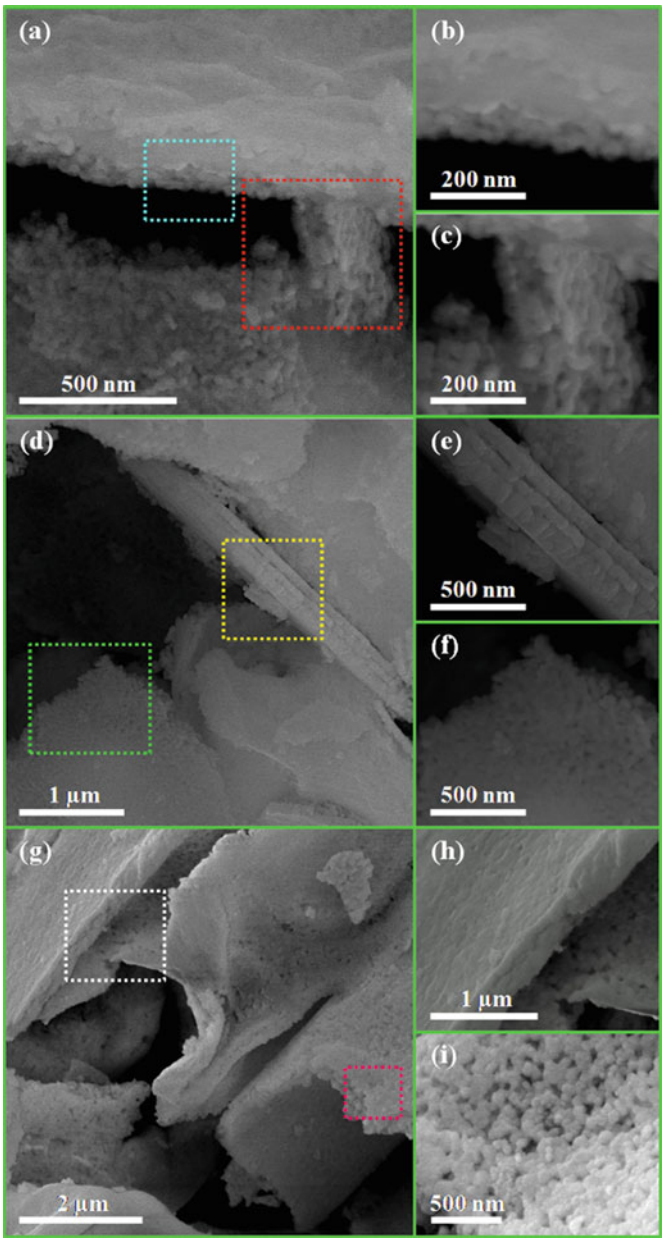

Fig. 5.6 FE-SEM micrographs of $SrWO_4$ particles synthesized by PPM and heat-treated at different temperatures in RF. (**a**) Aggregated assemblies of small particles with imperfect shapes (500 °C), (**b**, **c**) high-magnification images of regions chosen in (**a**) (*blue* and *red squares*), (**d**) low-magnification micrograph of compact blocks composed of several particles (600 °C), (**e**, **f**) high-magnification images of areas selected in (**d**) (*yellow* and *green squares*), (**g**) low-magnification micrograph showing the presence of a dense layer as well as some irregular particles (700 °C), and (**h**, **i**) high-magnification images of areas chosen in (**g**) (*white* and *pink squares*)

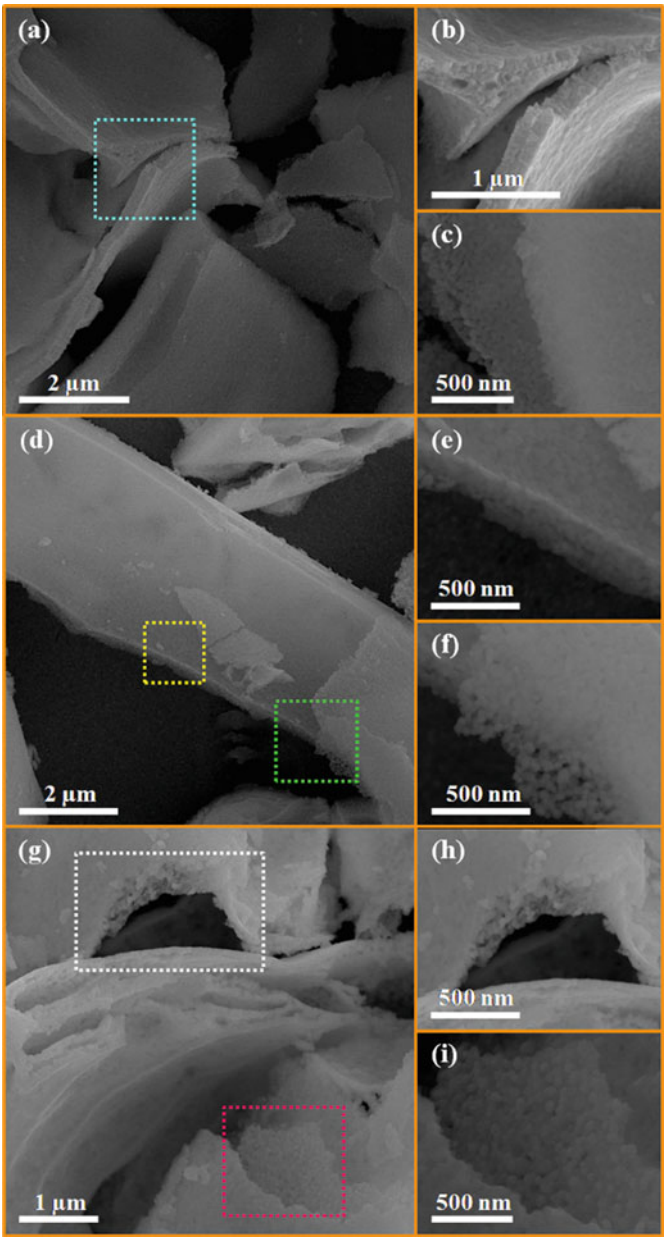

Fig. 5.7 FE-SEM micrographs of $SrWO_4$ particles synthesized by PPM and heat-treated at different temperatures in MO. (**a**) Uncountable aggregated particles forming compact layers (500 °C), (**b**) high-magnification images of the region chosen in (**a**) (*blue square*), (**c**) micrograph illustrating an assembly of these particles, (**d**) low-magnification micrograph of a compact block (600 °C), (**e**, **f**) high-magnification images of areas selected in (**d**) (*yellow* and *green squares*) showing the organization of the particles, (**g**) low-magnification micrograph demonstrating the overlapping of several layers with imperfect shapes (700 °C), and (**h**, **i**) high-magnification images of areas chosen in (**g**) (*white* and *pink squares*)

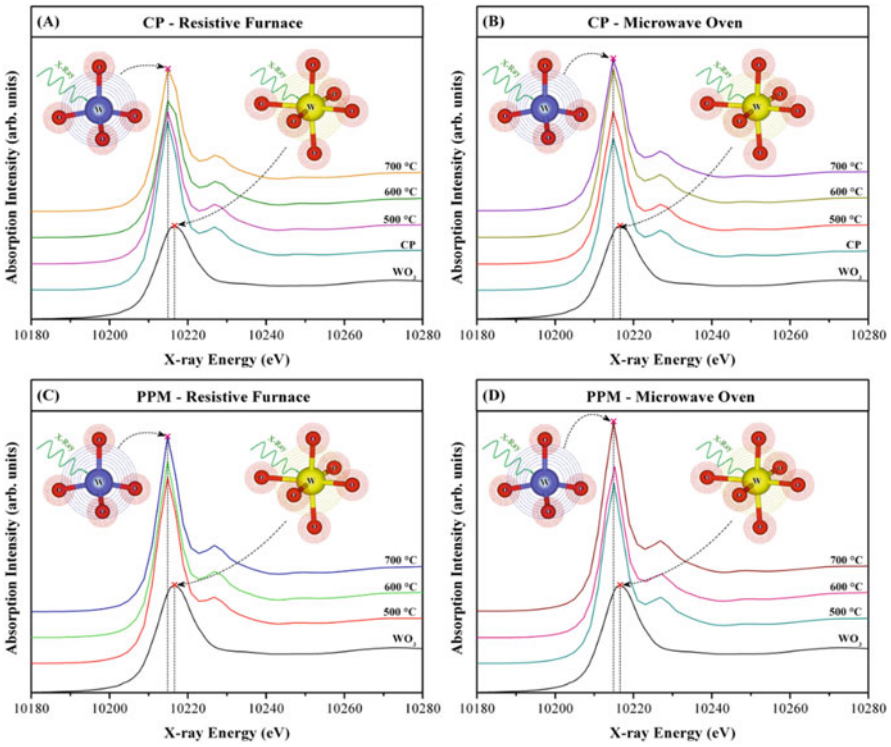

Fig. 5.8 XANES spectra of $SrWO_4$ powders synthesized by CP (**a**, **b**) and PPM (**c**, **d**) and heat-treated at different temperatures in RF and MO, respectively

(measurable quantity). When these modulations are decoded, XANES spectra become an essential and powerful tool to extract any information related to structure, atomic number, structural local order (no long range is needed), and thermal motions of neighboring atoms for a wide range of materials [43, 44]. Particularly, XANES technique has been especially employed to obtain responses on the structural order-disorder phenomenon of ceramic oxides with perovskite or scheelite-type structures [45, 46]. In the case of solids containing W atoms, W L_1- and L_3-edge XANES are the most used in this study. In our work, L_3-edge XANES spectra measured of $SrWO_4$ samples are illustrated in Fig. 5.8.

According to the literature [47, 48], the prominent peak in these spectra (highlighted with dotted lines) is associated to electron transitions from $2p_{3/2}$ state to a vacant *5d* state. Therefore, W L_3-edge XANES spectra are able to reveal the character of *5d* orbitals.

In XANES spectra presented in Fig. 5.8, there is a difference in the profile and intensity of the peaks (highlighted with dotted lines) when a comparison is made between the as-synthesized samples with the reference (WO_3). The low intensity of this peak for the WO_3 compound is directly related to the octahedral

environment exhibited by its W atoms ($[WO_6]$ clusters) (insets in Fig. 5.8). In $SrWO_4$ powders obtained in our study, W atoms are bonded to four oxygens, presenting a tetrahedral environment ($[WO_4]$ clusters). As a consequence of these differences in the coordination number, a shift in the respective position of these peaks was noted ($\approx$10,215 eV for $SrWO_4$ powders and $\approx$10,217 eV for WO_3). Another visible aspect in XANES spectra of as-synthesized samples was the occurrence of a small shoulder at around 10,227 eV, which is recognized for the small split in *5d* orbitals of tetrahedral W units [47]. The absence of this small peak in XANES spectra of solids composed by $[WO_6]$ clusters was also verified by Cavalcante et al. [49] in silver tungstate (α-Ag_2WO_4) microcrystals. All measured XANES spectra are very similar to those reported in the literature for materials belonging to the scheelite-type class [45, 50].

Based on this qualitative analysis, all XANES spectra have the same features, independent of synthesis routes (CP or PPM) or experimental conditions. This result confirms the first coordination shell is only composed of W atoms bonded to four oxygens ($[WO_4]$ clusters) for all studied samples.

3.6 Optical Properties

According to the classical theory of electronic conduction [51, 52], the conductivity in semiconductor materials can be modified by introducing impurities or dopants into their crystalline lattice. In a controlled way, the concentration and the type of doping in an intrinsic semiconductor are able to create energy levels (donors or acceptors) near the valence band (VB) or conduction band (CB), modifying the band gap energy (E_g). In this case, vacant states (holes) are created near the VB for *p*-type semiconductors, while electronic states are originated below the CB for *n*-type semiconductors [53]. However, in studies focused on the luminescence of solids, the existence of intermediary energy levels within the band gap can be arising from doping atoms or structural defects [54]. Particularly, the concentration and type of structural defect (cracks, pores, dislocations, grain boundaries, oxygen vacancies, distortion in atomic bonds, etc.) are impossible to control in the solid matrix. The nature of these defects has a key importance for the appearance of uncountable intermediary states between the VB and CB, which are known as deep donors and shallow holes [55]. Different from the band structure of *p-n* junction semiconductors, the wide band model predicts the existence of states occupied by electrons near the VB [56]. The existence of intermediary energy levels within the forbidden band can be estimated qualitatively by means of UV-vis spectra.

Typical UV-vis spectra of $SrWO_4$ powders obtained in this study are illustrated in Fig. 5.9. The E_g of all samples was estimated extrapolating the linear portion of the UV-vis curves, according to the Kubelka-Munk equation [57]. All results obtained by this methodology are listed in Table 5.1.

Perfect monocrystals do not exist; however, their good quality is ensured by the minimal percentage of imperfections or defects. Lacomba-Perales et al. [58] grew

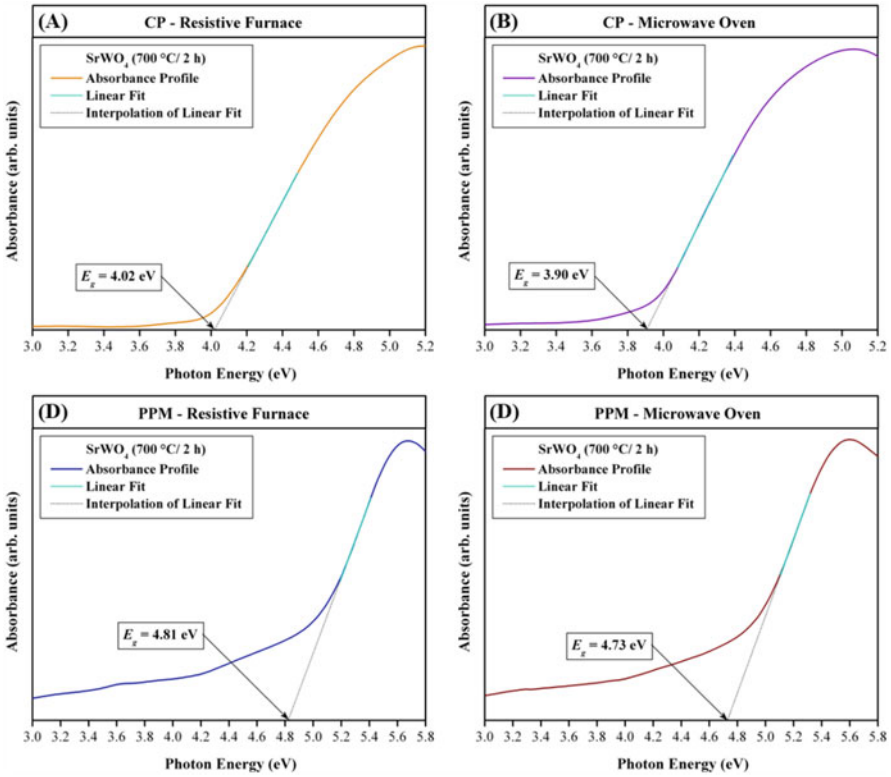

Fig. 5.9 Typical UV-vis spectra of $SrWO_4$ powders synthesized by CP (**a**, **b**) and PPM (**d**, **c**), which were heat-treated at 700 °C for 2 h in RF and MO, respectively

Table 5.1 Comparative results among the E_g values of $SrWO_4$ powders

Method	Temperature (°C)	Furnace	E_g (eV)
CP	85	–	4.73
CP	500	RF	3.95
CP	600	RF	4.08
CP	700	RF	4.02
CP	500	MO	4.00
CP	600	MO	3.99
CP	700	MO	3.90
PPM	600	RF	4.61
PPM	700	RF	4.81
PPM	600	MO	4.37
PPM	700	MO	4.73

$SrWO_4$ monocrystals by the Czochralski method and found an optical band gap of 5.08 eV for this scheelite. Assuming that these mentioned considerations are valid, we can point out that when there is a reduction in E_g values, the number of intermediary energy levels increases proportionally within the forbidden band, as a response to high density of surface and structural defects in the $SrWO_4$ matrix. Initially, analyzing the UV-vis spectra of $SrWO_4$ powders formed via CP without and with heat treatment, E_g results revealed distinct values from one sample to another. Actually, an increase in the E_g was expected with the temperature evolution (linear behavior) in both furnaces (RF and MO). In contrast, these results indicate the samples have different quantities and distributions of defects, independent of temperature or type of furnace. The nature of these defects can be correlated with the crystalline lattice initial formation first stages, such as creation of clusters, random interaction between these clusters, and beginning of the nucleation process. Firstly, primary $[WO_4]$ and $[SrO_8]$ clusters interact with the liquid phase having a partial passivation. The interaction between them promotes the instant origin of nuclei. After reaching a stability condition, the association of these nuclei causes the appearance of the first nanocrystals, which are able to collide among them. However, in this same stage, it is impossible to avoid the formation of a high defects density at short, medium, and/or long range. The arrangement and growth of these nanocrystals depend on the reaction medium as well as the type of chemical bond formed.

In the second case, for the samples prepared by PPM and heat-treated in both furnaces, UV-vis spectra demonstrated an increase in the E_g values with the temperature evolution (linear behavior) (Table 5.1). According to Anicete-Santos et al. [24], this phenomenon is due to the modification in the degree of structural order-disorder in the lattice (from disordered to ordered structure). Thus, the amorphous or disordered materials have a higher concentration of defects than those in the crystalline state, i.e., a high quantity of intermediary states within the forbidden band. Hence, it has been demonstrated that the temperature is a key variable in order to minimize these defects and increase the E_g. In addition, as a result of the gradual decomposition of organic matter along a temperature increase, we believe the slow interdiffusion of metal cations between the small particles also plays a crucial role in the distribution and organization of these intermediary energy levels.

Nonetheless, the high concentration of organic matter found in the samples heat-treated at 500 °C is not allowed in estimating their E_g values. Also, independent of the synthesis methods or furnaces employed in this study, for all E_g results of $SrWO_4$ are in good agreement with those previously described in the literature [8, 24].

PL property is an interesting physical phenomenon, not only because of its technological applications in electrooptical devices but as a complementary tool for UV-vis absorption measurements to assist in understanding on the band structure of solids. For example, in colloidal semiconductor nanocrystals (sizes from 2 to 10 nm), the quantum dots (dimensions close to the Bohr exciton radius) are very common. In this circumstance, the electronic energy levels are discrete, i.e., with finite, small distances between them. Thus, their luminescence spectra present a narrow emission band due to the quantum confinement effect, which is dependent on the size of the quantum dot [59, 60].

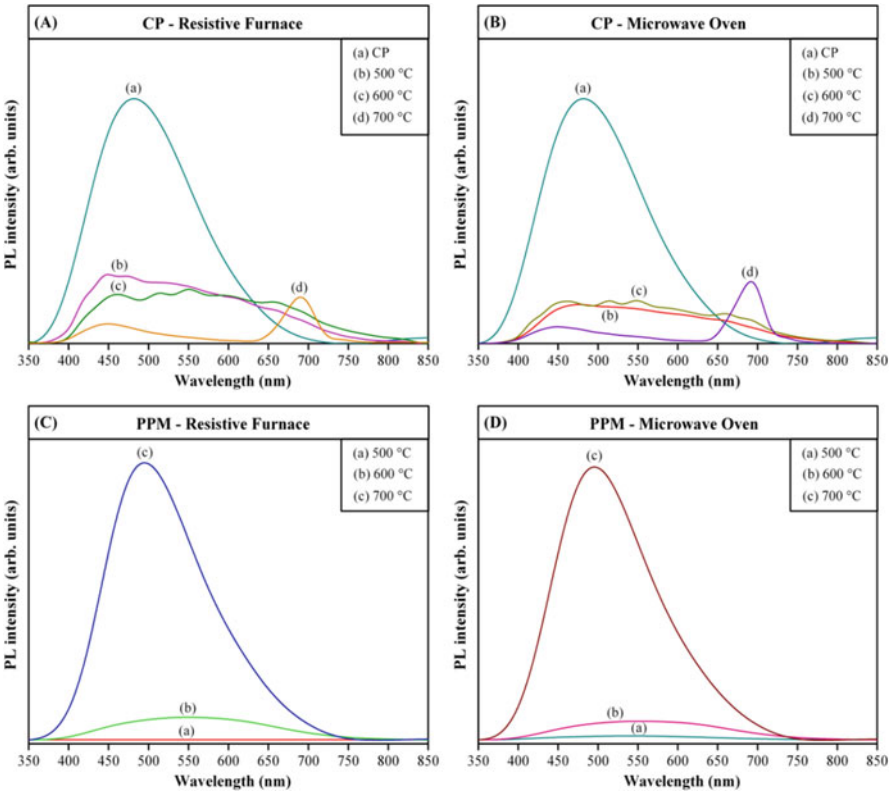

Fig. 5.10 PL spectra of $SrWO_4$ powders synthesized by CP (**a**, **b**) and PPM (**c**, **d**), which were heat-treated at different temperatures in RF and MO, respectively

Another situation found in materials science is related to PL emissions of bulk semiconductors. Generally, these types of materials exhibit wide band PL spectra, as a consequence of the participation of uncountable intermediary energy levels within the band gap. As previously described, these energy states arise from structural defects, which can be classified as deep donors and shallow holes. The deep donors are considered visible light emission centers responsible for the green, yellow, orange, and red PL at room temperature, while the shallow holes are directly associated with the violet and blue emissions [61]. Figure 5.10 shows the PL spectra at room temperature of all $SrWO_4$ powders obtained in this study under an excitation wavelength of 350 nm.

Initially, considering only the samples formed by CP without and with heat treatment (RF and MO), PL spectra showed a linear tendency, i.e., a reduction of intensity with the increase of the heat treatment temperature. Despite the wide band, the maximum emission of these powders was found in blue or green regions of the visible electromagnetic spectrum. The only exceptions were identified for the $SrWO_4$ samples heat-treated at 700 °C in both furnaces, where there is the presence

of two distinct bands located at around 448 nm (blue emission) and 690 nm (red emission), respectively. All these experimental observations suggest the temperature has a crucial role in the relaxation of defects as well as in the reorganization process of the intermediary states within the band gap.

In the case of $SrWO_4$ powders synthesized by PPM, PL spectra exhibited an increase in the PL intensity with the temperature evolution. In fact, this behavior is different from that described by Anicete-Santos et al. [24] and Campos et al. [34]. According to these authors, this optical behavior is directly related to the structural order-disorder phenomenon. In this concept, the lowest PL intensities are found in materials containing an elevated concentration of structural defects or exhibiting a high degree of crystallinity. The ideal circumstance in order to obtain an intense PL emission at room temperature is the equilibrium or simultaneous presence of order-disorder at long and short range in the lattice. Moreover, the charge transfer process in the $SrWO_4$ lattice is mainly attributed to oxygen vacancies $\left(\left[WO_3 \bullet V_0^z\right]\right.$ and $\left.\left[SrO_7 \bullet V_0^z\right]; V_0^z = V_0^x, V_0^{\bullet}$ or $V_0^{\bullet\bullet}\right)$ [34]. We believe these types of defects have a significant importance in PL spectra of $SrWO_4$, but the symmetry break responsible for the lattice polarization also can arise from distortions in dihedral bond angles (O-W-O and/or O-Sr-O) within the $[WO_4]$ and $[SrO_8]$ clusters, respectively. Hence, the increase of the PL intensity with the temperature in our samples is due to the influence of large quantities of organic compounds around the surface of the particles, as identified in TG curves (Fig. 5.1). Thus, as previously explained, the low heating rate (1 °C/min) and the increase of the temperature are able to allow the slow elimination of carbon, resulting in a gradual interdiffusion between the particles in contact. Considering this affirmation, the degree of structural order-disorder of $SrWO_4$ powders reported in our study is slightly different from that mentioned by Anicete-Santos et al. [24] under the same temperature conditions.

A comparative analysis among the PL emissions of all $SrWO_4$ powders under the viewpoint of heat treatment temperature is displayed in Fig. 5.11. In this situation, the results demonstrate the standard sample (CP) has the highest PL intensity than all samples heat-treated at 500 °C. For powders synthesized by CP and heat-treated at 500 °C in both MO and RF, the decrease in the PL emission can be explained by the reduction of defects and reorganization of intermediary states within the band gap, as previously explained. At this same temperature, the powders formed by PPM have a high degree of structural order-disorder and, therefore, a low emission. Another important point noted was the low PL intensity of the powder obtained by PPM and heat-treated in RF in relation to those subjected to the MO. This observation suggests the microwave heating contributed to a reduction of organic substances in the system. On the other hand, when the temperature was increased up to 600 °C, PL intensity of the powders prepared by PPM is superior to that synthesized by CP route. In this circumstance, these powders have a reduction of organic substances (TG curves in Fig. 5.1) and, therefore, favor a transition from highly disordered solid (containing many defects) to structurally ordered-disordered material (equilibrium condition between defects and local order). After heat treatment performed at 700 °C, the most notable feature is the equivalence of

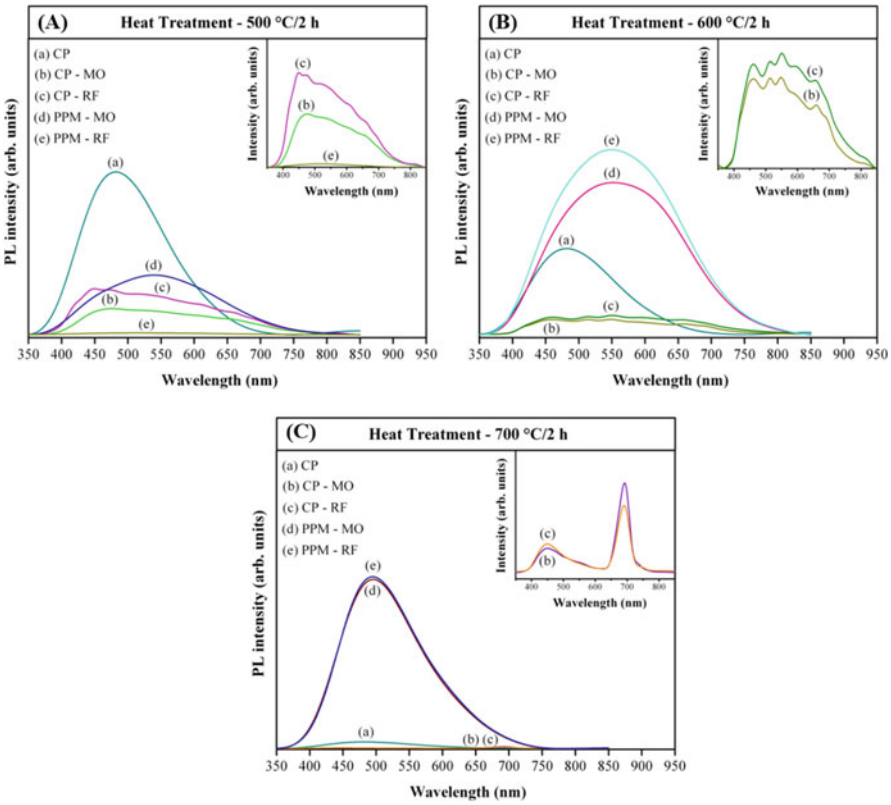

Fig. 5.11 PL spectra of $SrWO_4$ powders obtained in the present study in terms of heat treatment temperatures: (**a**) 500 °C/2 h, (**b**) 600 °C/2 h, and (**c**) 700 °C/2 h

PL profiles in both the powders synthesized by PPM. This result demonstrates that after the removal of the organic matter, there is an increase in the interaction of $[WO_4]$ and $[SrO_8]$ clusters, favoring the occurrence of the structural order-disorder phenomenon. Moreover, at this temperature, there is no direct influence of the type of furnace (RF or MO).

Despite the low organic matter concentration and more efficient morphological control on the powders formed by CP route, the highest PL emissions were identified in $SrWO_4$ powders synthesized by PPM with a subsequent heat treatment performed at 700 °C for 2 h.

4 Conclusion

In summary, $SrWO_4$ was synthesized by CP and PPM and heat-treated at different temperatures in two distinct furnaces (RF and MO). A high concentration of organic matter was detected in TG curves for the samples formed by PPM. This result

arises from the use of $C_6H_8O_7$ and $C_2H_6O_2$, which are commonly employed in this synthesis method. Independent of the conventional or microwave heating, XRD patterns showed all powders have a scheelite-type structure with a good degree of crystallinity (ordered at long range). Another important feature detected in these diffractograms was the existence of crystallographic orientation, indicating the synthesis method is a key factor in the formation process of $SrWO_4$ phase. Raman spectra revealed the powders obtained by CP, without and with heat treatment, have well-defined vibrational bands, suggesting a short-range structural ordering in the matrix. Moreover, Raman-active modes related to powders synthesized by PPM showed a structural transition from disordered to ordered material. This phenomenon was associated with the excess of organic substances, which retard the interaction between $[SrO_8]$ and $[WO_4]$ clusters. FE-SEM images revealed both synthesis routes (CP and PPM) induced the formation of distinct particle shapes. While the samples obtained by CP are composed of rice-like microparticles, the others synthesized by PPM formed dense layers composed of large assemblies of aggregated irregular particles. According to XANES spectra, all samples obtained in the present study have their W atoms bonded to four oxygens ($[WO_4]$ clusters). The different E_g values were associated with different quantities and/or distributions of structural defects in the lattice, independent of temperature or type of furnace. PL emissions exhibited an inverse behavior with the temperature evolution among the samples prepared by CP and PPM, respectively. The reduction of the PL intensity for the powders obtained by the CP was attributed to the relaxation of structural defects with the temperature, while the increase of PL intensity for the samples formed by PPM was explained by means of structural transition from disordered to ordered-disordered material.

Acknowledgments The authors are grateful to the FAPESP (#2012/14004-5), CNPq, and CAPES/PNPD (20131475) for the financial support. We also thank the National Laboratory of Synchrotron Light (LNLS), Campinas, SP, Brazil, for the X-ray absorption near-edge structure measurements (XD04B-XAFS1 - 11883). Special thanks to Mr. Rorivaldo Camargo and Mrs. Madalena Turssi for operating the FE-SEM and XRD equipments, respectively.

References

1. Minowa M, Itakura K, Moriyama S, Ootani W (1992) Measurement of the property of cooled lead molybdate as a scintillator. Nucl Instrum Methods Phys Res A 320(3):500–503. doi:http://dx.doi.org/10.1016/0168-9002(92)90945-Z
2. Ju Z, Wei R, Gao X, Liu W, Pang C (2011) Red phosphor $SrWO_4:Eu^{3+}$ for potential application in white LED. Opt Mater 33(6):909–913. doi:http://dx.doi.org/10.1016/j.optmat.2011.01.025
3. Jia G, Tu C, Li J, Zhu Z, You Z, Wang Y, Wu B (2007) Optical spectroscopy of Yb^{3+} doped $SrWO_4$ scheelite crystal. J Alloys Compd 436(1–2):341–344. http://dx.doi.org/10.1016/j.jallcom.2006.07.037
4. Parhi P, Karthik TN, Manivannan V (2008) Synthesis and characterization of metal tungstates by novel solid-state metathetic approach. J Alloys Compd 465(1–2):380–386. doi:10.1016/j.jallcom.2007.10.089

5. Wang A, Wang C, Jia G (2009) Recent advances in strontium tungstate scheelite material. Front Chem China 5(1):61–70. doi:10.1007/s11458-009-0099-3
6. Chen L, Gao Y (2007) Fabrication of luminescent $SrWO_4$ thin films by a novel electrochemical method. Mater Res Bull 42(10):1823–1830. doi:10.1016/j.materresbull.2006.12.002
7. Feng L-D, Chen X-B, Mao C-J (2010) A facile synthesis of $SrWO_4$ nanobelts by the sonochemical method. Mater Lett 64(22):2420–2423. doi:10.1016/j.matlet.2010.08.024
8. Sczancoski JC, Cavalcante LS, Joya MR, Espinosa JW, Pizani PS, Varela JA, Longo E (2009) Synthesis, growth process and photoluminescence properties of $SrWO_4$ powders. J Colloid Interface Sci 330(1):227–236. doi:10.1016/j.jcis.2008.10.034
9. Pan H, Hojamberdiev M, Zhu G (2012) Hydrothermal synthesis of quasi-monodisperse AWO_4 (A = Ca, Sr, and Ba) microspheres. J Mater Sci 47(2):746–753. doi:10.1007/s10853-011-5850-8
10. Orhan E, Anicete-Santos M, Maurera MAMA, Pontes FM, Paiva-Santos CO, Souza AG, Varela JA, Pizani PS, Longo E (2005) Conditions giving rise to intense visible room temperature photoluminescence in $SrWO_4$ thin films: the role of disorder. Chem Phys 312(1–3):1–9. doi:10.1016/j.chemphys.2004.11.013
11. Dong F-Q, Wu Q-S, Sun D-M, Ding Y-P (2008) Morphology-tunable synthesis of $SrWO_4$ crystals via biomimetic supported liquid membrane (SLM) system. J Mater Sci 43(2): 641–644. doi:10.1007/s10853-007-2165-x
12. Thongtem T, Phuruangrat A, Thongtem S (2008) Preparation and characterization of nanocrystalline $SrWO_4$ using cyclic microwave radiation. Curr Appl Phys 8(2):189–197. doi:10.1016/j.cap.2007.08.002
13. Sun L, Guo Q, Wu X, Luo S, Pan W, Huang K, Lu J, Ren L, Cao M, Hu C (2007) Synthesis and photoluminescent properties of strontium tungstate nanostructures. J Phys Chem C 111(2):532–537. doi:10.1021/jp064923d
14. Cui C, Bi J, Gao D (2008) Room temperature synthesis of crystallized luminescent $SrWO_4$ films by an adjustable galvanic cell method. J Cryst Growth 310(19):4385–4389. doi:10.1016/j.jcrysgro.2008.07.030
15. Marques VS, Cavalcante LS, Sczancoski JC, Alcântara AFP, Orlandi MO, Moraes E, Longo E, Varela JA, Siu Li M, Santos MRMC (2010) Effect of different solvent ratios (water/ethylene glycol) on the growth process of $CaMoO_4$ crystals and their optical properties. Cryst Growth Des 10(11):4752–4768. doi:10.1021/cg100584b
16. Cavalcante LS, Sczancoski JC, Lima LF, Espinosa JWM, Pizani PS, Varela JA, Longo E (2008) Synthesis, characterization, anisotropic growth and photoluminescence of $BaWO_4$. Cryst Growth Des 9(2):1002–1012. doi:10.1021/cg800817x
17. Rotello VM (2004) Nanoparticles: building blocks for nanotechnology. In: Skaff H, Emrick T (eds) Semiconductor nanoparticles. Springer Science & Business Media, New York, pp 32–33
18. Sattler KD (2010) Handbook of nanophysics: nanoparticles and quantum dots. In: Reiss G, Hütten A (eds) Magnetic nanoparticles. Taylor & Francis, New York, pp 1–2
19. Kakihana M (1996) Invited review "sol-gel" preparation of high temperature superconducting oxides. J Sol Gel Sci Technol 6(1):7–55. doi:10.1007/BF00402588
20. Rahaman MN (2003) Ceramic processing and sintering, 2nd edn. Taylor & Francis, New York
21. Xing G, Li Y, Li Y, Wu Z, Sun P, Wang Y, Zhao C, Wu G (2011) Morphology-controllable synthesis of $SrMoO_4$ hierarchical crystallites via a simple precipitation method. Mater Chem Phys 127(3):465–470. doi:10.1016/j.matchemphys.2011.02.034
22. Ho K-C, Greenberg CB, MacArthur DM (1997) Proceedings of the third symposium on electrochromic materials. In: Oliveira S, Faria RC, Terezo AJ, Pereira EC, Bulhões LOS (eds) The cerium addition effect on the electrochemical properties of niobium pentoxide electrochromic thin films. Electrochemical Society, New Jersey, pp 106–118
23. Marques APA, de Melo DMA, Longo E, Paskocimas CA, Pizani PS, Leite ER (2005) Photoluminescence properties of $BaMoO_4$ amorphous thin films. J Solid State Chem 178(7):2346–2353. doi:10.1016/j.jssc.2005.05.024

24. Anicete-Santos M, Picon FC, Escote MT, Leite ER, Pizani PS, Varela JA, Longo E (2006) Room-temperature photoluminescence in structurally disordered $SrWO_4$. Appl Phys Lett 88(21):211913. doi:10.1063/1.2207491
25. Rahaman NR (2007) Sintering of ceramics. CRC Press, New York
26. Barani K, Koleini SMJ, Rezai B, Khodadadi A (2012) The effect of sample geometry and placement of sample on microwave processing of iron ore. Int J Appl Phys Math 2:131–134. doi:10.7763/IJAPM
27. Marques APA, Longo VM, de Melo DMA, Pizani PS, Leite ER, Varela JA, Longo E (2008) Shape controlled synthesis of $CaMoO_4$ thin films and their photoluminescence property. J Solid State Chem 181(5):1249–1257. doi:10.1016/j.jssc.2008.01.051
28. http://www.edg.com.br. Accessed 16 Oct 2015
29. http://www.maitec.com.br/. Accessed 16 Oct 2015
30. Barros BS, de Lima AC, da Silva ZR, Melo DMA, Alves-Jr S (2012) Synthesis and photoluminescent behavior of Eu^{3+}-doped alkaline-earth tungstates. J Phys Chem Solids 73(5):635–640. doi:10.1016/j.jpcs.2011.12.026
31. Yoon J-W, Ryu JH, Shim KB (2006) Photoluminescence in nanocrystalline $MMoO_4$ (M = Ca, Ba) synthesized by a polymerized complex method. Mater Sci Eng B 127(2–3):154–158. doi:10.1016/j.mseb.2005.10.015
32. Errandonea D, Pellicer-Porres J, Manjón F, Segura A, Ferrer-Roca C, Kumar R, Tschauner O, Rodríguez-Hernández P, López-Solano J, Radescu S, Mujica A, Muñoz A, Aquilanti G (2005) High-pressure structural study of the scheelite tungstates $CaWO_4$ and $SrWO_4$. Phys Rev B 72(17). doi:10.1103/PhysRevB.72.174106
33. Basiev TT, Sobol AA, Voronko YK, Zverev PG (2000) Spontaneous Raman spectroscopy of tungstate and molybdate crystals for Raman lasers. Opt Mater 15(3):205–216. doi:http://dx.doi.org/10.1016/S0925-3467(00)00037-9
34. Campos AB, Simões AZ, Longo E, Varela JA, Longo VM, de Figueiredo AT, De Vicente FS, Hernandes AC (2007) Mechanisms behind blue, green, and red photoluminescence emissions in $CaWO_4$ and $CaMoO_4$ powders. Appl Phys Lett 91(5):051923. doi:10.1063/1.2766856
35. Rao CNR, Müller A, Cheetham AK (2007) Nanomaterials chemistry: recent developments and new directions. In: Viswanatha R, Sarma DD (eds) Growth of nanocrystals in solution. Wiley, Weinheim, pp 140–143
36. Tao AR, Habas S, Yang P (2008) Shape control of colloidal metal nanocrystals. Small 4(3):310–325. doi:10.1002/smll.200701295
37. Dalmaschio CJ, Ribeiro C, Leite ER (2010) Impact of the colloidal state on the oriented attachment growth mechanism. Nanoscale 2(11):2336–2345. doi:10.1039/c0nr00338g
38. Cöelfen H, Antonietti M (2008) Mesocrystals and nonclassical crystallization. Wiley, Chichester, pp 230–233
39. Yin Y, Yang F, Yang Y, Gan Z, Qin Z, Gao S, Zhou B, Li X (2011) Controlled synthesis of $BaWO_4$ hierarchical nanostructures by exploiting oriented attachment in the solution of H_2O and C_2H_5OH. Superlattice Microst 49(6):599–607. doi:10.1016/j.spmi.2011.03.010
40. Cavalcante LS, Sczancoski JC, Batista NC, Longo E, Varela JA, Orlandi MO (2013) Growth mechanism and photocatalytic properties of $SrWO_4$ microcrystals synthesized by injection of ions into a hot aqueous solution. Adv Powder Technol 24(1):344–353. doi:10.1016/j.apt.2012.08.007
41. Oghbaei M, Mirzaee O (2010) Microwave versus conventional sintering: a review of fundamentals, advantages and applications. J Alloys Compd 494(1–2):175–189. doi:10.1016/j.jallcom.2010.01.068
42. Spotz MS, Skamser DJ, Johnson DL (1995) Thermal stability of ceramic materials in microwave heating. J Am Ceram Soc 78(4):1041–1048. doi:10.1111/j.1151-2916.1995.tb08434.x
43. Bunker G (2010) Introduction to XAFS: a practical guide to X-ray absorption fine structure spectroscopy. Cambridge University Press, Cambridge

44. Gautier-Soyer M (1998) X-ray absorption spectroscopy: a tool to study the local atomic and electronic structure of ceramics. J Eur Ceram Soc 18(15):2253–2261. doi:http://dx.doi.org/10.1016/S0955-2219(98)00103-4
45. Gracia L, Longo VM, Cavalcante LS, Beltrán A, Avansi W, Li MS, Mastelaro VR, Varela JA, Longo E, Andrés J (2011) Presence of excited electronic state in $CaWO_4$ crystals provoked by a tetrahedral distortion: an experimental and theoretical investigation. J Appl Phys 110(4):043501. doi:10.1063/1.3615948
46. Cavalcante LS, Sczancoski JC, Espinosa JWM, Mastelaro VR, Michalowicz A, Pizani PS, De Vicente FS, Li MS, Varela JA, Longo E (2009) Intense blue and green photoluminescence emissions at room temperature in barium zirconate powders. J Alloys Compd 471(1–2): 253–258. doi:10.1016/j.jallcom.2008.03.080
47. Yamazoe S, Hitomi Y, Shishido T, Tanaka T (2008) XAFS study of tungsten L_1- and L_3-edges: structural analysis of WO_3 species loaded on TiO_2 as a catalyst for photo-oxidation of NH_3. J Phys Chem C 112(17):6869–6879. doi:10.1021/jp711250f
48. Yamamoto T (2008) Assignment of pre-edge peaks in K-edge x-ray absorption spectra of 3d transition metal compounds: electric dipole or quadrupole? X-Ray Spectrom 37(6):572–584. doi:10.1002/xrs.1103
49. Cavalcante LS, Almeida MA, Avansi W Jr, Tranquilin RL, Longo E, Batista NC, Mastelaro VR, Li MS (2012) Cluster coordination and photoluminescence properties of α-Ag_2WO_4 microcrystals. Inorg Chem 51(20):10675–10687. doi:10.1021/ic300948n
50. Rodríguez-Hernández P, López-Solano J, Radescu S, Mujica A, Muñoz A, Errandonea D, Pellicer-Porres J, Segura A, Ferrer-Roca C, Manjón FJ, Kumar RS, Tschauner O, Aquilanti G (2006) Theoretical and experimental study of $CaWO_4$ and $SrWO_4$ under pressure. J Phys Chem Solids 67(9–10):2164–2171. doi:10.1016/j.jpcs.2006.05.011
51. Gao W, Li Z, Sammes NM (2011) An introduction to electronic materials for engineers, 2nd edn. World Scientific, Singapore, pp 96–100
52. Lindroos V, Franssila S, Tilli M, Paulasto-Krockel M, Lehto A, Motooka T, Airaksinen VM (2009) Handbook of silicon based MEMS materials and technologies, 1st edn. Elsevier Science, Oxford, pp 37–38
53. Martin PM (2011) Introduction to surface engineering and functionally engineered materials. Wiley, Hoboken, pp 409–410
54. Kitai A (2008) Luminescent materials and applications. Wiley, Chichester
55. Lyons JL, Janotti A, Van de Walle CG (2012) Shallow versus deep nature of Mg acceptors in nitride semiconductors. Phys Rev Lett 108(15). doi:10.1103/PhysRevLett.108.156403
56. Longo VM, de Figueiredo AT, de Lázaro S, Gurgel MF, Costa MGS, Paiva-Santos CO, Varela JA, Longo E, Mastelaro VR, De Vicente FS, Hernandes AC, Franco RWA (2008) Structural conditions that leads to photoluminescence emission in $SrTiO_3$: an experimental and theoretical approach. J Appl Phys 104(2):023515. doi:10.1063/1.2956741
57. Tolvaj L, Mitsui K, Varga D (2010) Validity limits of Kubelka-Munk theory for DRIFT spectra of photodegraded solid wood. Wood Sci Technol 45(1):135–146. doi:10.1007/s00226-010-0314-x
58. Lacomba-Perales R, Ruiz-Fuertes J, Errandonea D, Martínez-García D, Segura A (2008) Optical absorption of divalent metal tungstates: correlation between the band-gap energy and the cation ionic radius. Europhys Lett 83(3):37002. doi:10.1209/0295-5075/83/37002
59. Marinescu DC (2011) Classical and quantum information. Elsevier Science, Oxford, pp 612–614
60. Cao G (2010) Annual review of nano research, vol 3. World Scientific, Singapore, pp 49–50
61. Rout SK, Cavalcante LS, Sczancoski JC, Badapanda T, Panigrahi S, Siu Li M, Longo E (2009) Photoluminescence property of $Ba(Zr_{0.25}Ti_{0.75})O_3$ powders prepared by solid state reaction and polymeric precursor method. Physica B 404(20):3341–3347. doi:10.1016/j.physb.2009.05.014

Chapter 6
Optical Properties of Semiconductor Nanocrystals into the Glass and Colloidal Environments for New Technological Applications

Sidney Alves Lourenço, Ricardo Souza da Silva, Marco Aurélio Toledo da Silva, Adriano César Rabelo, Gabriel Dornela Alves da Rocha, Anielle Christine Almeida Silva, and Noelio Oliveira Danta

1 Introduction

Semiconductor quantum dots (QDs) became in the last decade an important class of materials by present continuous tunability of electronic and optical properties by changing size and shape [1–4]. These new physical properties presented by QDs have demonstrated potential applications in different technologic areas as light-emitting devices [5–8], low-threshold lasers [9], optical amplifiers [10], photovoltaic devices [11–14], biological labels [15, 16], antibacterial control [17], and cancer therapy [18]. In the visible and violet spectral range, CdS- and CdSe-based QDs become a prototypical among QDs, for above applications, due to highly reproducible and controllable emission from violet to red. The ability to synthesize stable QDs via colloidal aqueous solutions is extremely important for same application areas. For medical and biotechnological applications, for example, water-soluble QDs are needed [19, 20], and appropriate functionalizations will define its specific applications [21–23]. Thus, surface passivation and functionalization of QD

S.A. Lourenço (✉) • M.A.T. da Silva • G.D.A. da Rocha
Engenharia de Materiais, Universidade Tecnológica Federal do Paraná - UTFPR, CEP 86.812-460, Londrina, PR, Brazil
e-mail: lourenco-sidney@hotmail.com

R.S. da Silva
Departamento de Física, Universidade Federal do Triângulo Mineiro, 38.025-440, Uberaba, MG, Brazil

A.C. Rabelo
Universidade Federal de Sao Carlos - LIEC, Rodovia Washington Luís km 235 Campus Sao Carlos, 13565-905, Sao Carlos, SP, Brazil

A.C.A. Silva • N.O. Danta
Laboratório de Novos Materiais Isolantes e Semicondutores (LNMIS), Instituto de Física, Universidade Federal de Uberlandia, CP 593, 38.400-902, Uberlândia, MG, Brazil

E. Longo, F.A. La Porta (eds.), *Recent Advances in Complex Functional Materials*,
DOI 10.1007/978-3-319-53898-3_6

systems are important methods that can improve their well-defined physical and chemical properties [24, 25]. Although QDs or QDs doped with impurities (metal or magnetic) are currently being synthesized by colloidal chemistry techniques [26, 27] or molecular beam epitaxy (MBE) [28], some possible applications of interest, technological, in particular, require nanoparticles to be embedded in robust and transparent host materials. In this context, the melting-nucleation approach appears as an appropriate synthesis technique since it allows the growth of diluted magnetic semiconductor NCs embedded in different glass matrices, which can avoid undesirable effects on the nanostructures, such as corrosion and humidity [29–31].

In this chapter, we will be discussing synthesis and same optical property results of CdSe nanocrystals in colloidal, semimagnetic $Pb_{1-x}Co_xSe$ nanocrystals into glass environment and thin-film CdS NCs.

2 Colloidal CdSe Quantum Dots and Its Surface Functionalization

The nanocrystalline semiconductors can in principle be divided into different groups of the periodic table, such as II-VI, III-V, and IV-VI. The synthesis of these materials can be performed either by the top-down method using physical techniques such as lithography or by the bottom-up method which employs colloidal chemistry techniques.

Through top-down method, it is possible to obtain a large amount of material. However, the size of these nanocrystals does not have uniformity, making this technique impractical in obtaining a narrow distribution of nanocrystals. In contrast, by colloidal chemistry, it is possible to obtain nanocrystals with size relatively uniform. Furthermore, it presents other advantages: (a) avoids the use of substrates for growth of nanostructures, (b) generation of a minimum amount of residues, (c) enables a surface modification for different applications, and (d) the possibility for large-scale production with lower cost compared to other techniques.

The synthesis of colloidal nanoparticles occurs by the reaction that can be controlled by the nucleation and growth. The precursor is a molecule or complex containing one or more atoms necessary for the growth of the nanocrystal. Once the precursors are introduced into the reaction, they decompose, forming a new reactive species (monomers). These will cause the nucleation and growth of the nanocrystals. For illustration, we consider the case of a simple addition reaction for forming a solid A_xB_y.

$$xA^{y+}_{(aq.)} + yB^{x-}_{(aq.)} \rightleftarrows A_xB_{y\ (sol.)} \tag{6.1}$$

The equilibrium relationship between the product of the reagent is expressed by the solubility product constant K_{sp}:

$$K_{sp} = (a_A)^x(a_B)^y \tag{6.2}$$

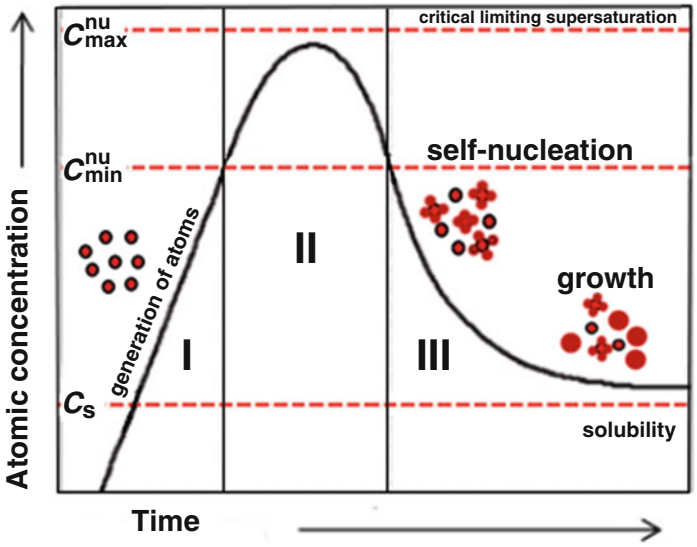

Fig. 6.1 Model of LaMer. Phase I, monomer concentration increases. Phase II critical concentration. Phase III nucleation process, growth of NCs (Adapted with permission from Ref. [32])

In this equation, a_A and a_b are activities of cation A and B of the anion in aqueous solution. The K_{sp} values tend to be too low for various hydroxides, carbonates, oxalates, and chalcogenides in aqueous solution. Precondition for all solid precipitation from a homogeneous solution is the occurrence of supersaturation. Supersaturation (S) is defined as:

$$S = \frac{a_A a_B}{K_{sp}} = \frac{C}{C_{eq}} \tag{6.3}$$

In which C and C_{eq} are the solute concentration in saturation and equilibrium, respectively. The solute will be referred to as monomer that is generated by the reaction of the precursors corresponding to the smallest unit of grown crystal.

The first theory treating the influence of such processes in obtaining colloidal dispersions is the model LaMer and Dinegar (Fig. 6.1), originally developed to describe the kinetics of nucleation and crystal growth in solution. At the present time, it is known that such a model is very private, and this system does not apply directly to most colloids. However, for its central idea of temporal separation of nucleation and growth, the model serves as the basis for the development of other models as well as for the development of several methods for obtaining monodisperse colloids. LaMer diagram is divided into three phases:

In phase I, the monomer concentration was constantly increased, but there was no formation of NCs. When a critical concentration $C_{crit.}$ is reached, in phase II, a nuclear explosion occurs by decreasing the oversaturation. The supersaturation has

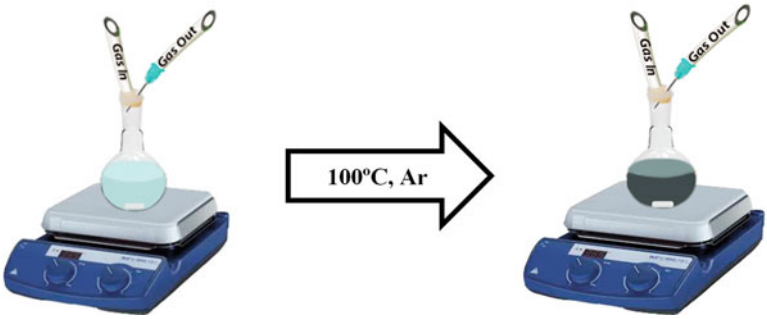

Fig. 6.2 The procedure of selenium dissolution with TOP

a natural limit on the concentration of monomer has reached its maximum value and then adding monomers only leads to an increase in nucleation rate. When the concentration of monomers, continually consumed by nucleation, goes below $C_{\min}^{\mathrm{nu}}$, it does not form more nuclei, and NCs begin to form in phase III. The growth rate reaches zero when the precursors are depleted and monomer concentration approaches the solubility product ($C_{\mathrm{eq}} = C_{\mathrm{s}}$), corresponding to $S = 1$. Moderate growth of NCs during supersaturation is controlled principally by the reaction of precursors, since a high concentration of monomers limits the growth rate by diffusion of monomers to the surface of the NCs. However, the concentration of monomers may not exceed S_{n} in order to avoid secondary nucleation because the rapid and efficient separation of nucleation and growth processes is a key step in the synthesis dispersed by NCs. Therefore, the initial conditions, such as temperature and concentration, strongly influence the equilibrium between nucleation and growth, which are important parameters for controlling the distribution and size of the nanocrystals.

Figure 6.2 presents a traditional example of the CdSe nanocrystal synthesis process. It begins with the preparation of two solutions: a solution of TOP-Se and the other of Cd. In preparing the first solution, trioctylphosphine (TOP)-Se, 30 mg of Se, and 5 ml of octadecene are added in a 10 ml flask; this first procedure basically consists of dissolving the selenium powder. The TOP is used to help in the dissolution of selenium and then will be used to cover the surface of the quantum dot to promote stability and protection of the surface. It is essential that this part of the experiment is performed in an inert atmosphere so there is no oxidation of the TOP. So it is done by heating the solution through a hot plate. Then add 0.4 mL of TOP via syringe. A stir bar is added to stir the solution; the change of color of a turbid gray solution to colorless color is noted, as illustrated in Fig. 6.2.

For second solution is used a three-necked flask to which is added 13 mg of CdO, 0.6 mL OLEA (oleic acid), and 10 ml of octadecene, in which there will be the dissolution of CdO in octadecene to isolate Cd^{+2} ions. The OLEA is also added to act as a surfactant as TOP. This process must be in an inert atmosphere to avoid that the oxygen released in the reaction does not oxidize the TOP when the injection is performed in the solution. Thus the flask containing all reagents is put on a hot plate in continuous agitation (Fig. 6.3).

Fig. 6.3 Scheme of the synthesis process

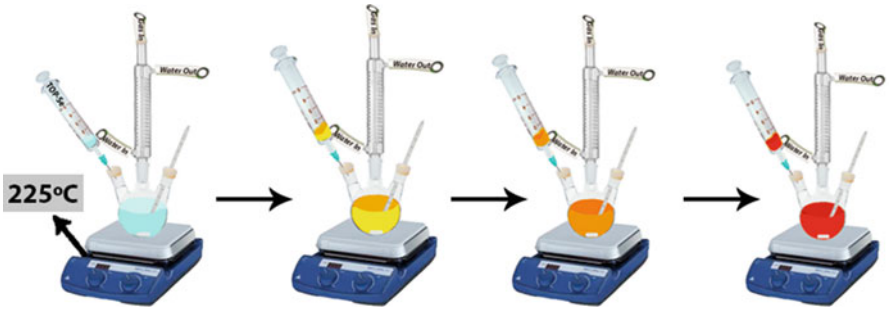

Fig. 6.4 Injection of TOP-Se and growth of nanocrystals with time, as evidenced by the color change

When the temperature reaches 225 °C, the solution is injected with TOP-Se within the Cd precursor solution to induce nucleation and growth of nanoparticles (Fig. 6.4). After the injection, the TOP-Se bonds are break and selenium ions are dissolved into the solution. This ion concentration of the addition of Se and Cd is observed in stage I of the nucleation and growth of nanocrystals chart at this stage no reaction occurs. Until stage II, concentrations reach a peak and overcome the energy barrier of nucleation.

The size of the NC grows with time; thus, samples of approximately 1 mL can be removed at frequent time intervals. The samples are washed and then dispersed in toluene.

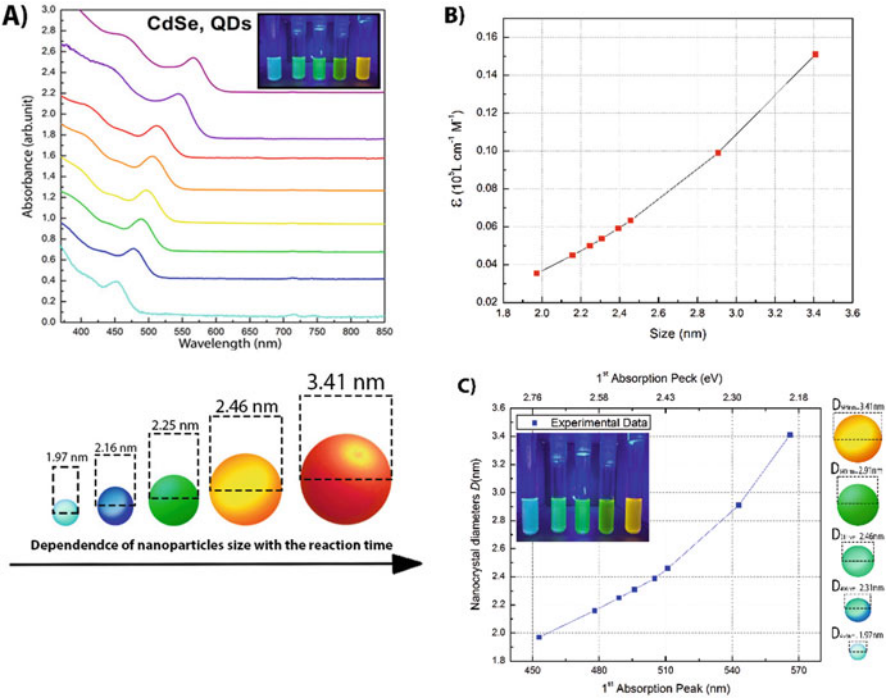

Fig. 6.5 (**a**) Absorption measurements of nanocrystals and the dependency of size with the reaction time; (**b**) relation between coefficient of excitation (ε) and nanoparticles size; (**c**) nanocrystals diameter related with the first excitonic peak, wavelength (nm), and energy (eV)

Figure 6.5 shows optical absorption spectra of CdSe NCs dissolved in toluene removed at frequent time intervals, with different sizes. As NCs size increases, there is a shift of the main peak of the optical absorption to longer wavelengths.

For many applications of NCs, it is important to determine the actual concentration or average concentration of nanocrystals in solution. It is also essential to determine the concentration to study the mechanisms of nucleation and growth of colloidal nanocrystals. If the material is known, extinction coefficient is relatively easy to obtain the concentration of the nanocrystals through the optical absorption spectrum; this method is often more practical and convenient to determine the concentration. Thus the first step to be performed in obtaining the extinction coefficient is to acquire the diameter of the nanocrystal CdSe, which can be obtained by the expression developed by William et al. [33]:

CdSe: $D = (1.6122 \times 10^{-9})\lambda^4 - (2.6575 \times 10^{-6})\lambda^3 + (1.6242 \times 10^{-3})\lambda^2 + (0.4277)\lambda + (41.57)$

In this expression, D (nm) is the size of the nanocrystal obtained, and λ (nm) is the wavelength of the first absorption peak. To illustrate the size calculation, consider the following figure of the characteristic absorption spectrum of a sample

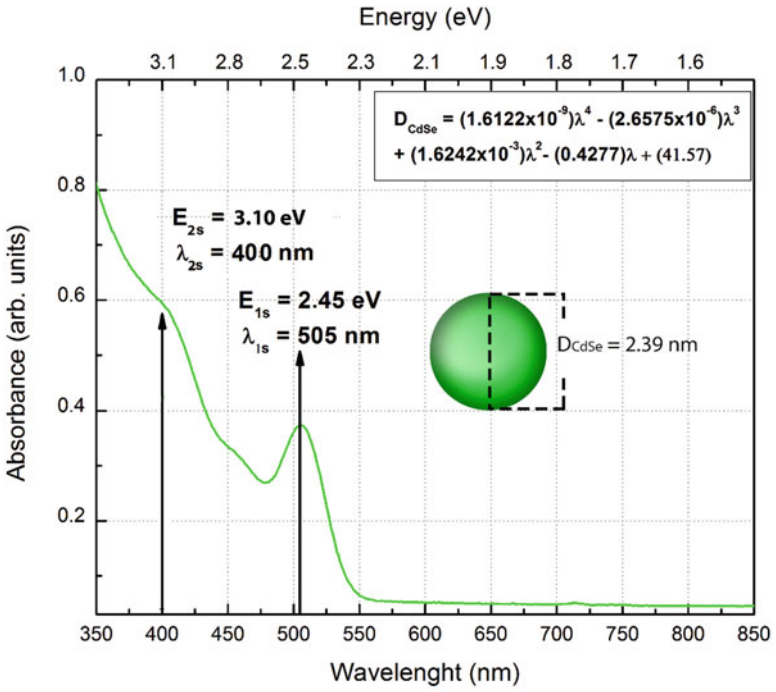

Fig. 6.6 Calculation of size, using absorption spectrum. The *up arrow* at 505 nm represents the first excitonic absorption band of QD, and 400 nm represents the second excitonic absorption band

of CdSe nanocrystals which can be seen in the first excitonic absorption peak $\lambda_{1s} = 505$ nm (Fig. 6.6).

In this particular case, the value of $D \cong 2.4$ *nm*.

The coefficient of excitation mol (ϵ) particles is calculated by Lambert-Beer Law:

$$A = \epsilon CL \tag{6.5}$$

In this equation, A is the absorbance of first excitonic peak, C is the molar concentration (mol/L) of the nanocrystals, and L is the optical path length of the cuvette fixed as 1 cm.

2.1 Surface Functionalization

Quantum dots have attracted considerable attention by exhibiting a high surface-to-volume ratio, which means that most of the atoms are located at the QD surface, thus becoming structures with high surface reactivity [34]. Generally, surface atoms, at QD surface, can generate surface defect sites (e.g., dangling bounds) which act as trap states for charged carriers. The trapping of charge carriers on surface defect sites results in an exciton delocalization that leads to non-radiative recombination

pathways, and therefore low photoluminescence quantum yields generally result in a decreased performance of emission-based devices. Intense efforts have been applied to understanding the role of carrier surface trapping on physical processes such as carrier relaxation and recombination dynamics.

A frequently used method to reduce defects and dangling bonds situated on the nanocrystal surface, and then the exciton delocalization, is the passivation of the QD surface with *organic ligands*, such as hexadecylamine (HDA) or trioctylphosphine oxide (TOPO), among others. It has been shown that the passivation of QDs with capping agents strongly influences the electron and hole transport from QDs, making them a critical factor for delivery of photoexcited carriers in photovoltaic devices [35, 36] or for biomedical and clinical imaging applications [37, 38].

The ligand exchange reaction method is a common procedure used to functionalize NC structures. The reaction can be obtained by put 0.09 g NaOH, 4 mL of Methanol and 38 μL of 1-Thioglycerol in a beaker of 10 mL. Then 2 mL of CdSe nanocrystals with a density of 16 mg/mL is added to the solution. The solution must be stirred for the ligand exchange process to occur. During the reaction time, note the transfer of nanocrystals from a nonpolar solvent such as toluene to a polar one such as water.

Then by measuring absorption, it was possible to visualize the shift of the first absorption peak, from 528 to 547 nm after 16 h (Fig. 6.7). Such exchange is slower for QDs because exchange reaction is controlled by mass transport processes. The intermediate broadness of the peak in 4 h can be rationalized as a large variation in

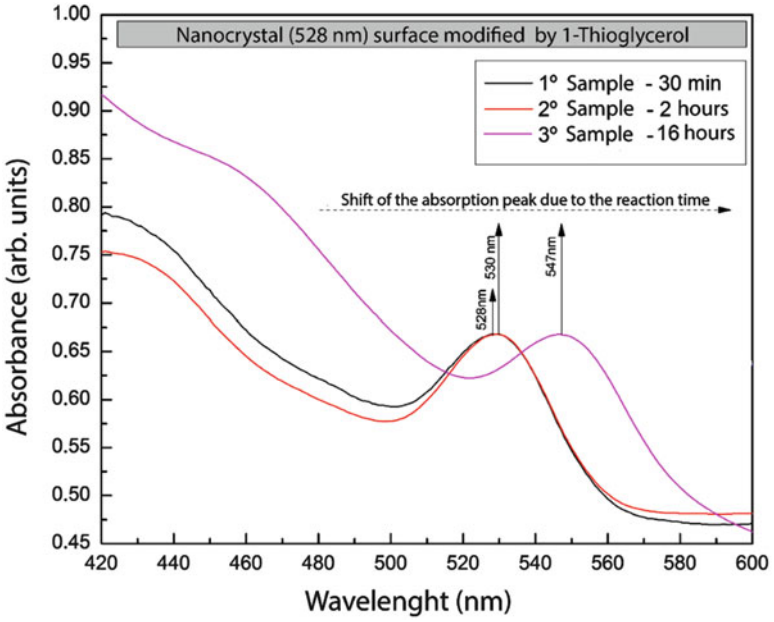

Fig. 6.7 Absorption spectra of CdSe nanocrystals functionalized with time reaction

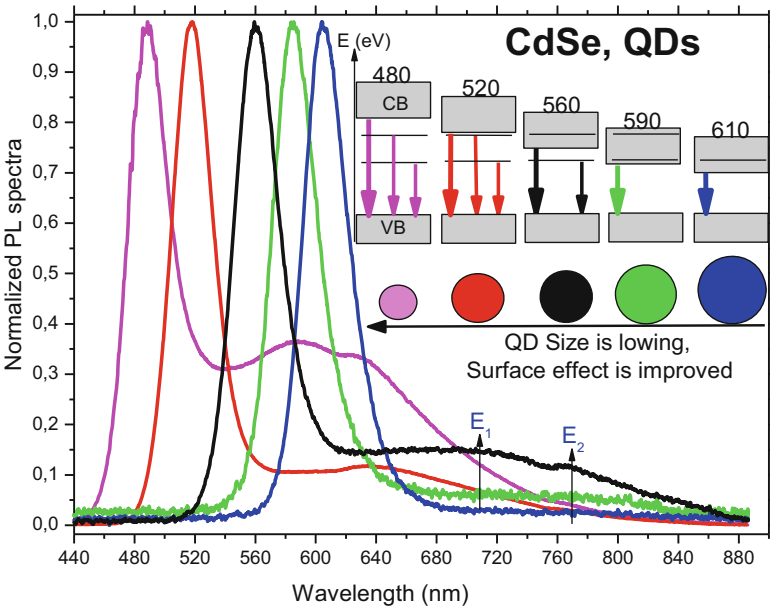

Fig. 6.8 Photoluminescence spectra of CdSe QDs functionalized with hexadecylamine. Inset shows the effect of QD size and the surface electronic levels. Here, CB and VB are conduction band and valence band, respectively. The values 480, 520, 560, 590, and 610 are emission peaks of the QDs

the ratio of the number of 1-thioglycerol ligands on the CdSe nanocrystals surface between different nanocrystals in solution. However, the final absorption peak of the ligand exchange reaction after 16 h is only slightly broader than the original CdSe NCs [39].

Figure 6.8 above shows normalized PL spectra of the core-type CdSe QDs' surface stabilized with hexadecylamine coating diluted in toluene. By reducing the QD size, one clearly observes an increase in the emission intensity of the shoulder band located for greater wavelength of the main excitonic transition of the QD. In the case of the sample with emission at 480 nm, from QD of smaller size, it is clearly observed that the shoulder can be resolved into two emission peaks. This issue is associated with the QD surface states, and PL spectra show that the emission from the surface becomes increasingly prevalent with reducing the QD size. The inset of the figure shows that with the reduction of the QD size, surface localized states can emit radiation because these states are into NCs band gap.

The synthesis using TOPO/TOP makes these NPs soluble in the apolar solvent. If the application requires, for example, which NPs are water soluble, a polar solvent with significant use in medical and pharmaceutical applications, then one must replace the linker of the NP surface. Just below, there is a list of linker molecules commonly used to change the NP solubilization properties. A good job of reviewing the medical and pharmaceutical application of NPs can be obtained from Ref. [40].

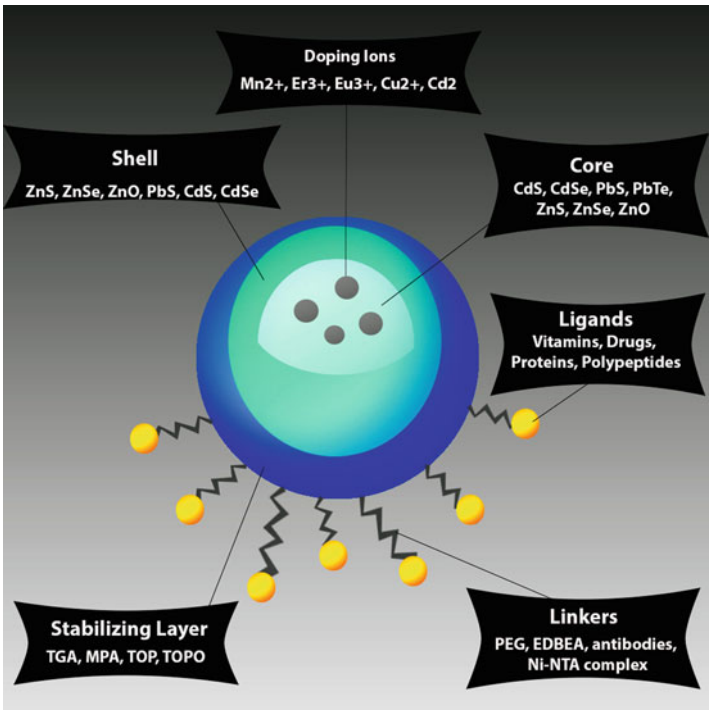

Fig. 6.9 Schematic possibilities presented by QDs depending on doping, stabilization, and functionalization of its surface

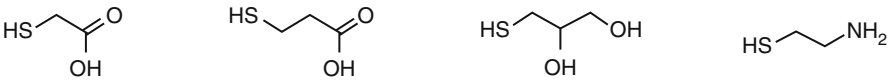

TGA MPA TG Cisteamine

The surface functionalization of these NPs provides improvements of their physicochemical properties according to the nature of the linker on the NP surface. The quantum confinement effect observed in QDs results in the tunability of the optical properties depending on their composition, particle size, and the presence of dopants [41]. Due to their excellent photophysical, magnetic, electric, and biological properties, QDs are widely applied in medicine as drug delivery [42], bioimaging [43], biosensors [44], detection for disease [45], photodynamic therapy [46], molecular biology [47], and cancer therapy [48].

Figure 6.9, below, summarizes different arrangements achieved with nanomaterials depending on doping, stabilization, and functionalization of its surface.

These possibilities in functionalization of QDs with linkers or functional molecules lead to different applications. For applications in photovoltaic systems, Robel et al. [49] used the (HS-R-COOH) which is a bifunctional surface modifier to

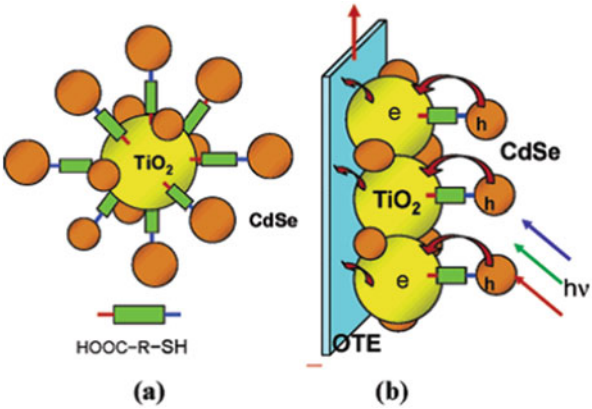

Fig. 6.10 This figure shows schematically the (**a**) ligand of CdSe QD particles of TiO_2 with bifunctional surface modifier and (**b**) light collection with transfer charges for TiO_2 (Reprinted with permission from Ref. [49]. Copyright 2017 American Chemical Society)

alter the collection of electrons from the quantum dot CdSe for TiO_2, as showed in Fig. 6.10. Here the SH-R-COOH molecule serves as a bridge to facilitate electron transport. It has been shown that the thiol functional group (HS) has a strong bond with the surface of the CdSe NP, while the other COOH functional group adheres to the surface of TiO_2.

Another procedure used to reduce surface trap states is from the synthesis of core/shell structures. In this case, two semiconductor materials with different energy band gaps are used. The core-type semiconductor has a smaller energy band gap than the shell semiconductor. This leaves a potential barrier at the semiconductor interface increasing the confinement potential of the charge carriers in the core region. That is, the core QD is encapsulated in a semiconductor shell of wider band gap to confine either both type-I or a single quasi-type-II charge carrier to the core and minimize their surface overlap [50].

This occurs by the formation of a potential barrier at the junction of the semiconductor which inhibits the carrier transfer by non-radiative processes to QD surface defects. As an example, the CdSe/CdS where the values of bulk material energy gaps at room temperature are 1.74 eV (CdSe) and 2.58 eV (CdS). The core/shell is a more stable material and has higher quantum efficiency than the case of quantum dot CdSe without surface protection (Fig. 6.11) [51].

However, the abrupt boundary between core and shell materials can induce strain due to lattice mismatch and introduce new trap states at the interface. Thus, more recently, it was proposed that a thick-graded shell can be a strategy to cover the semiconductor QD core and provide better enhancement of the fluorescence properties [52]. This structure has been shown to reduce Auger recombination process in semiconductor QDs, a non-radiative process, and particularly for the graded alloyed CdSe/$CdSe_xCdS_{1-x}$/CdS system; the delocalization of the electron wave function into the *thick* CdS shell reduces its overlap with the core-localized hole [53] and improves the multiexciton performance of QDs [54].

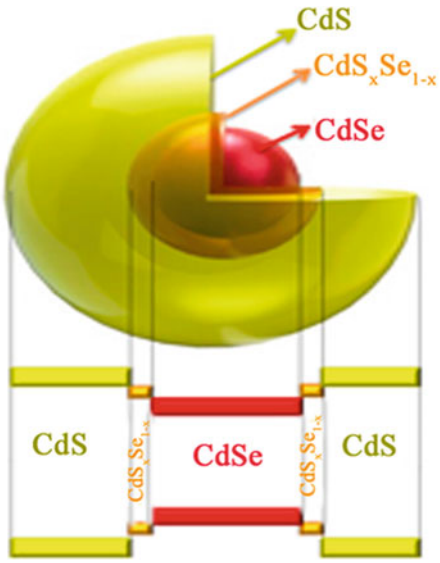

Fig. 6.11 Shell thickness modulation in $CdSe/CdS_xSe_{1-x}/CdS$ core/shell quantum dots via 1-thioglycerol. Energy gaps of the bulk materials at room temperature are 1.74 eV (CdSe) and 2.58 eV (CdS) (Reprinted with permission from Ref. [51]. Copyright (2017) American Chemical Society)

3 PbCoSe NCs in Glass Environment for Visible and Infrared Emission

The kinetic growth of the nanocrystals in glass matrices is the result of the thermodynamic process of the diffusion controlled by the precursors of chemical elements that are precipitated in an oversaturated solid solution in the glass matrix [55, 56]. In this way, the appearance of nanocrystals (solid phase) occurs, originated by diffusion controlled by the precursor elements (solute) in the glass matrix (solvent) [57]. The synthesis of nanocrystals grown in glassy matrices follows the following steps: (1) weighing of chemical elements, (2) mixture of chemical elements, (3) melting the chemical composition at a melting temperature established by thermal analysis measurements, (4) cooling the melt to room temperature, and (5) heat treatment around the glass transition temperature (T_g) for the formation and growth of the nanocrystals. The average size of the nanocrystal depends on the temperature and time at which the samples are subjected to the heat treatment. The schematic representation of the synthesis process is shown in Fig. 6.12.

Semiconductor nanocrystals (NCs) doped with transition metal (TM) are part of a class of materials in which a restricted portion of its cations are replaced by TM ions, named as diluted magnetic semiconductors nanocrystals (DMS NCs). In context, an exchange interaction is promoted between the *d*-electrons of the transition metal ion, usually located in the band gap region of the hosting semiconductor, and the *sp*-band electrons of the NC semiconductor [57–61]. These new materials show a change of optical, magnetic, electronic, and structural properties dependent of TM concentration, size, and shape of DMS NCs. Some kinds of DMS NCs have been grown in glass matrix such as TM (Mn^{2+} or Co^{2+})-doped Bi_2Te_3 [62], CdS [63], Bi_2S_3 [64], CdSe [65–67], ZnO [68, 69], ZnTe [70], and PbSe NCs [31].

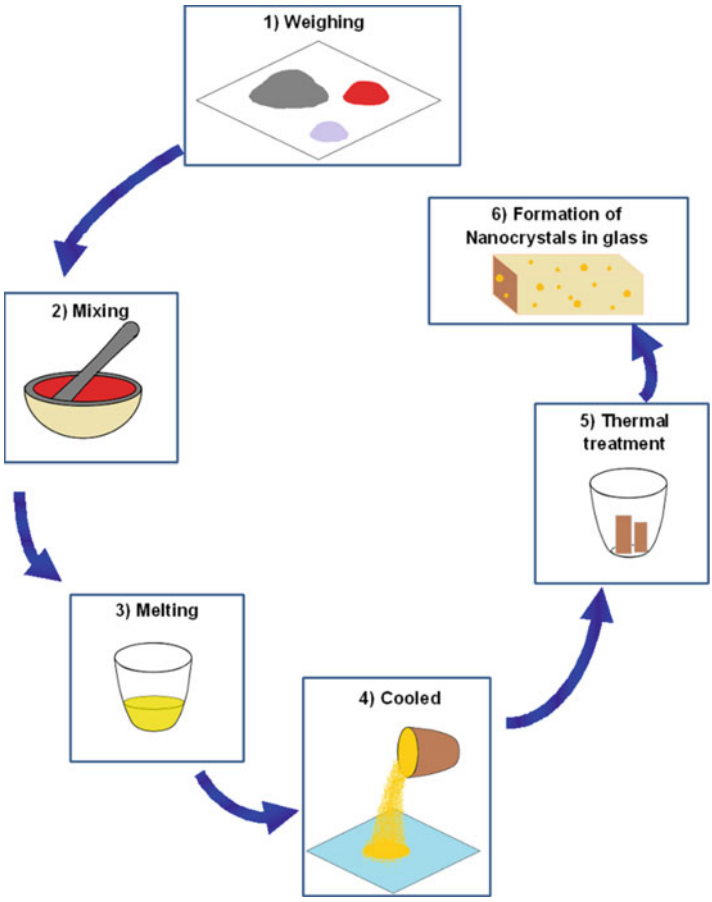

Fig. 6.12 Schematic representation of the synthesis process of nanocrystals embedded in a host glass matrix

In context, we investigated an interesting modification that occurs in PbCoSe nanocrystals which refers to the optical properties caused by the change in the band gap of NCs semiconductor with the incorporation of Co^{2+} ions, due to the exchange interactions *sp-d*, that is related in reference [71].

The samples investigated with semimagnetic PbCoSe NCs were produced by the fusion method in the glass matrix with the following nominal composition: $40SiO_2 \bullet 30Na_2CO_3 \bullet 1Al_2O_3 \bullet 25B_2O_3 \bullet 4PbO$ (%mol), herein quoted as SNABP glass matrix. The nominal composition of the nanocomposite was achieved by adding 2Se (%wt) plus xCo with respect to the $(1 - x)$Pb, with $x = 0.05$. For this sample, a thermal annealing of the previously melted glass matrix was carried out at 500 °C for two different times, 200 and 500 min, here denoted as PbCoSe200 and PbCoSe500 samples, respectively.

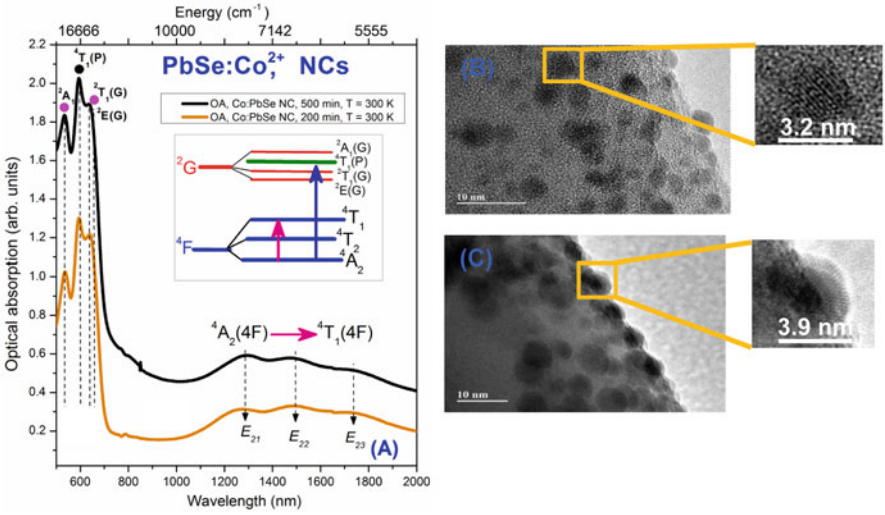

Fig. 6.13 (**a**) Room-temperature absorption spectra of PbSe:Co^{2+} NCs embedded in SNABP glass matrix annealed for 200 and 500 min at 500 °C. *Inset* shows the energy level diagram of Co^{2+} ($3d^7$) in a tetrahedral site next to $\Delta/B = 4.93$, in the Tanabe-Sugano diagram of $d^7(Td)$ for $C/B = 4.5$. Figures (**b**) and (**c**) show the TEM images of $Pb_{1-x}Co_xSe$ NCs, $x = 0.05$, annealed for 200 min and for 500 min, respectively (Ref. [71], Reproduced by permission of the PCCP Owner Societies: http://pubs.rsc.org/en/Content/ArticleLanding/2016/CP/C6CP04419K#!divAbstract)

The divalent ion $Co^{2+}(d^7)$ in the tetrahedral site exhibits electronic energy levels denoted by $^4T_1(^4P)$, $^4T_1(^4F)$, $^4T_2(^4F)$, and $^2E(^2G)$, which are strongly dependent of the crystal field intensity. Here, we analyze the visible and near-IR optical absorption and emission of Co^{2+}-doped PbSe nanocrystals embedded in glass by controlling the temperature (19–317 K) and NC size. Depending on crystal field intensity and sample temperature, the visible emission can be tuned from $^4T_1(^4P)$ to spin-flip-like $^2E(^2G)$ states. The near-IR absorption and emission spectra present component of delocalized, excitonic NC and localized Co^{2+} ion state, which can be tuned by changing the PbCoSe NC size. To the best of our knowledge, there is no report about the studies of Co^{2+}-doped PbSe nanocrystals embedded in glass matrices presenting optical properties in visible and near-IR electromagnetic spectral region as shown in Fig. 6.13.

Figure 6.14 shows the PL spectra as a function of temperature for PbCoSe200 and PbCoSe500 samples in the visible region. Comparing the PL spectra of the two samples, it was observed that the ZPL(^2E(G)) is more pronounced at lower temperatures, as expected, than the sample treated with a higher annealing time. The distribution of intensity between the ZPL and the PSB is strongly dependent on temperature. For low temperatures, there are low phonon excitations, and the ZPL is higher than PSB. At higher temperature, there is enough thermal energy to excite many phonons, and the probability of ZPL transition is close to zero. After a characteristic temperature, with thermal energy higher than Δ_{ZPL}, thermal

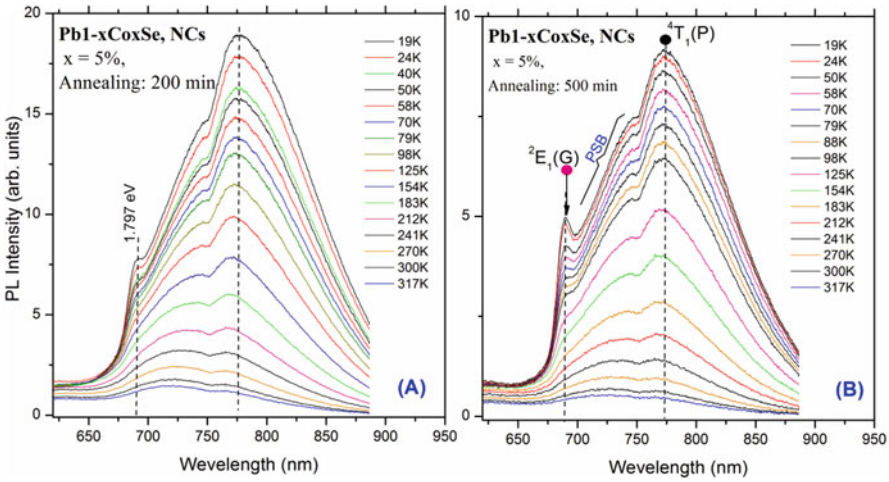

Fig. 6.14 Temperature dependence of PL spectra of the PbCoSe200 (**a**) and PbCoSe500 (**b**) samples (Ref. [71], reproduced by permission of the PCCP Owner Societies: http://pubs.rsc.org/en/Content/ArticleLanding/2016/CP/C6CP04419K#!divAbstract)

population from ^2E to $^4T_1$ states occurs, and after this temperature, an excited-state crossover occurs [$^4T_1$(P) ↔ ^2E(G)], which is responsible for the evolution of the emission spectrum from a broadband emission to a narrow peak emission.

In Fig. 6.15 the OA and PL spectra are shown with PbCoSe200, PbCoSe500, PbSe NCs, and SNABP matrix. The PL spectrum of the sample annealed for 500 min has an asymmetric behavior with an apparent exponential tail at the lower energy side, a characteristic of localized excitonic recombinations due to states below the conduction band. We believe that this shoulder in the lower energy side of the PL peak, observed for the sample treated at 500 °C, can be related with $^4T_1(^4F)$ states after interaction with the extended states of the NC conduction band. By reducing the energy position of the NC conduction band, after the thermal annealing process, there is an interaction between the $^4T_1(^4F)$ localized states and the delocalized states of the NC conduction band, so that electrons in the nanocrystal conduction band can relax by non-radiative recombination to accessible states $^4T_1(^4F)$ and recombine radiatively with the lower $^4A_2$ (^4F) state.

4 Tin Films of CdS NCs Growth By Chemical Bath Deposition

Chemical bath deposition technique has been used for deposition of CdS films since the 1960s [72–75] and since the late 1980s for use in photovoltaic devices [76]. The CdS was widely used as window material in the second generation of photovoltaic cells due to your absorption below 500 nm [77]. Moreover, that material can

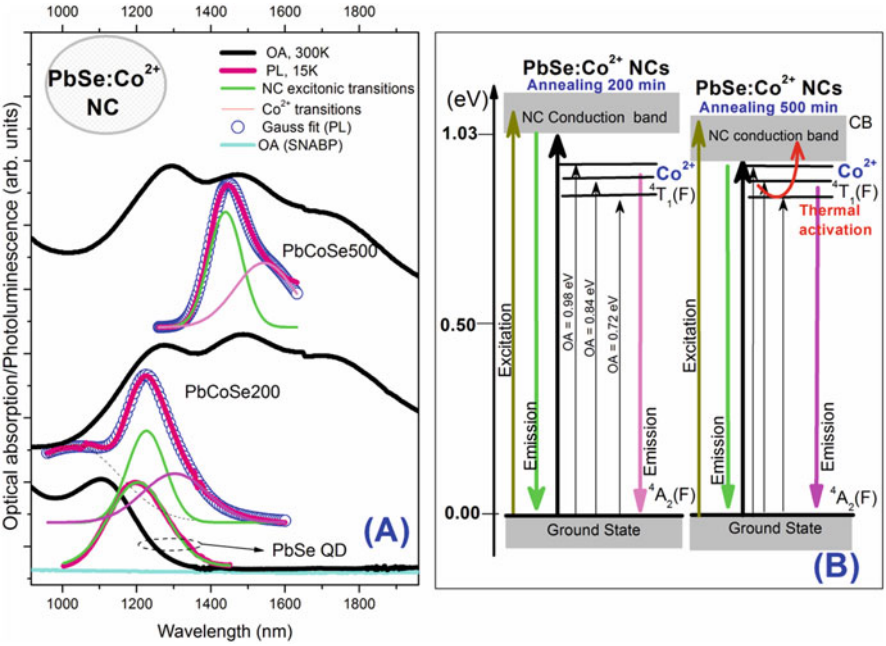

Fig. 6.15 Optical absorption and photoluminescence of PbSe:Co^{2+} and PbSe NCs. (**a**). *Green lines* represent excitonic NC transitions, and *magenta lines* represent emission from Co^{2+} ion states, $^4T_1(^4F)$ to $^4A_2(^4F)$. (**b**) It shows possible diagram energy for PbSe:Co^{2+}, with optical activity in near-IR region (Ref. [71], reproduced by permission of the PCCP Owner Societies: http://pubs.rsc.org/en/Content/ArticleLanding/2016/CP/C6CP04419K#!divAbstract)

be deposited on flexible substrates attending the new proposal to photovoltaic technology. In chemical bath deposition technique of CdS, the substrate is dipped in an alkaline solution containing a source of chalcogenide and one metal ion, wherein the film is deposited by precipitation due to the concentration of ions reaching the maximum value predicted by the solubility constant. The reactions involved at process are presented in Eqs. (a) and (b) below.

$$SC(NH_2)_{2\,(aq)} + 2OH^-_{(aq)} \rightarrow S^{2-}{}_{(aq)} + CH_2N_2\,(aq) + H_2O_{(l)} \qquad (a)$$

$$Cd^{2+}{}_{(aq)} + S^{2-}{}_{(aq)} \leftrightarrows CdS_{(s)} \qquad (b)$$

The process begins with the decomposition of thiourea in alkaline medium. This process provides for several complex medium containing cadmium which is shown in Table 6.1 with their respective equilibrium constants. In addition to the cadmium complex, there are also free cadmium ions in solution. The formation of the CdS occurs when the concentration of free sulfide and cadmium ions is high enough to initiate precipitation of CdS.

Table 6.1 Chemical species present in an aqueous solution containing cadmium ions and acetate

Chemical equations	Log K
$Cd^{2+}_{(aq)} + CH_3COO^-_{(aq)} \rightleftharpoons [CdCH_3COO]^+_{(aq)}$	1.90
$Cd^{2+}_{(aq)} + CH_3COO^-_{(aq)} \rightleftharpoons [Cd(CH_3COO)_2]_{(aq)}$	3.20
$Cd^{2+}_{(aq)} + H_2O_{(l)} \rightleftharpoons [CdOH]^+_{(aq)} + H^+_{(aq)}$	−10.1
$Cd^{2+}_{(aq)} + 2H_2O_{(l)} \rightleftharpoons Cd(OH)_{2\,(aq)}\, 2H^+_{(aq)}$	−20.3
$Cd^{2+}_{(aq)} + 3H_2O_{(l)} \rightleftharpoons [Cd(OH)_3]^-_{(aq)} + 3H^+_{(aq)}$	−31.7
$Cd^{2+}_{(aq)} + 4H_2O_{(l)} \rightleftharpoons [Cd(OH)_4]^{2-}_{(aq)} + 4H^+_{(aq)}$	−47.3
$2Cd^{2+}_{(aq)} + H_2O_{(l)} \rightleftharpoons [Cd_2OH]^{3+}_{(aq)} + H^+_{(aq)}$	−9.40
$4Cd^{2+}_{(aq)} + 4H_2O_{(l)} \rightleftharpoons [Cd_4(OH)_4]^{4+}_{(aq)}\, 4H^+_{(aq)}$	−32.8
$CH_3COO^-_{(aq)} + H^+_{(aq)} \rightleftharpoons CH_3COOH_{(aq)}$	4.73

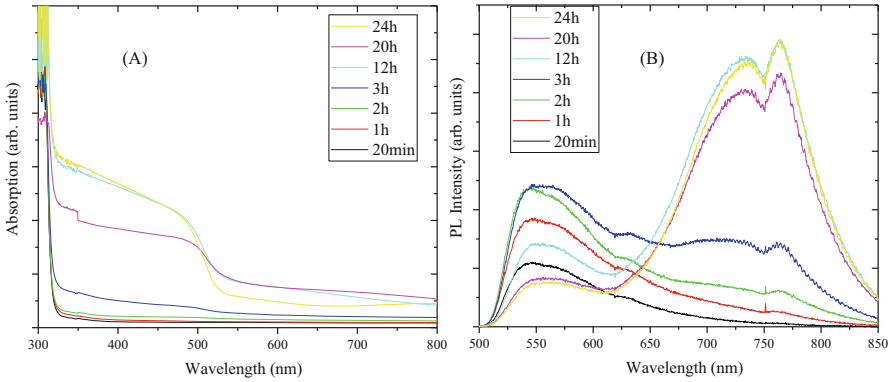

Fig. 6.16 (**a**) Absorption spectra and (**b**) photoluminescence emission spectra of CdS films obtained in different t_{CBD}

We have analyzed CdS films deposited on polyester by chemical bath deposition technique varying the bath time, $t_{CBD,}$ and the film was characterized by scan electronic microscopy, SEM. Moreover, optical properties of films have been investigated by absorption and photoluminescence, PL, spectroscopies. The average size of the nanoparticles can vary from 50 to 400 nm depending on the deposition time.

Figure 6.16 shows absorption and photoluminescence spectra obtained at room temperature through a Varian spectrophotometer, model Cary 5G, and a laser setup exciting the sample at 488 nm line (1 mW) of Ar^+ laser. PL signal has been analyzed by USB 4000 Ocean Optics spectrometer.

Absorption and PL spectra show that after 12 h in reaction bath occurs saturation in the absorption and emission intensities. The PL emission due to the band to band emission (540 nm) increases until 3h. After this, the emission decreases until t_{CBD} is 20 and 24 h. The transition at 730 nm is due to electrons and holes trapped in surface defects [78]. The exciton trapped in CdS composite vacancies can recombine with emission at 760 nm [79].

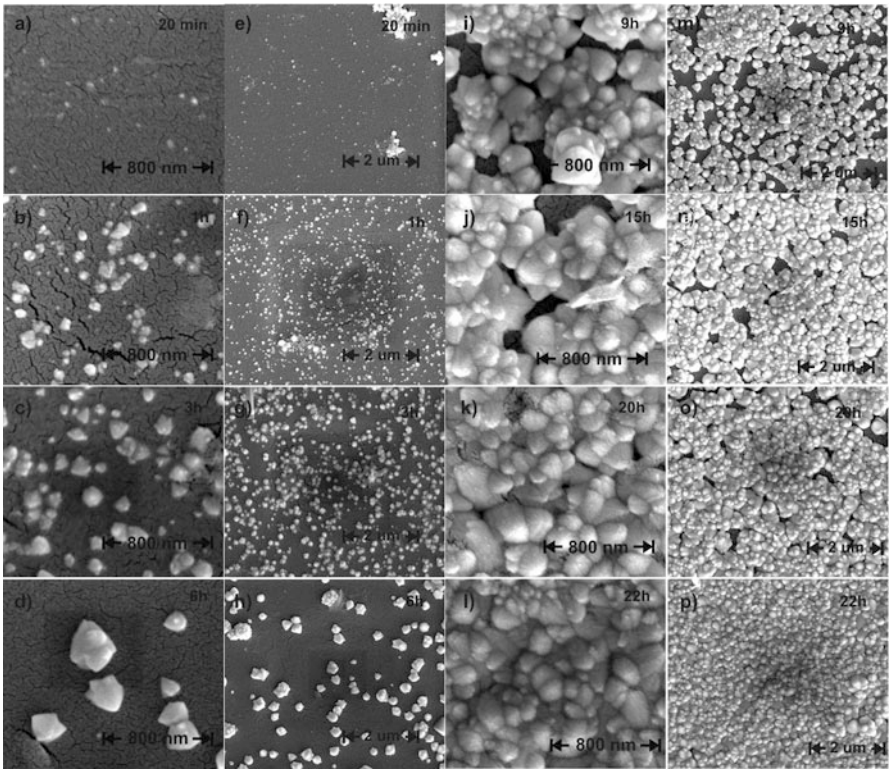

Fig. 6.17 Scanning electron microscopy images at magnifications of 50,000 to 200,000× for films with different deposition times

Figure 6.17 shows different magnification images obtained through the scanning electron microscopy of different CdS films. It can be seen through Fig. 6.17a–h that for a deposition time of up to 6 h, the particles are not in contact with each other. For deposition times over 9 h (see Fig. 6.17i–p), particles begin to establish contact with each other, and the film feature becomes more pronounced. The covering of the entire substrate as shown in Fig. 6.17o–p occurs only once between 20 and 22 h.

References

1. Talapin DV, Haubold S, Rogach AL, Kornowski A, Haase M, Weller H (2001) J Phys Chem B 105:2260–2263
2. Talapin DV, Rogach AL, Kornowski A, Haase M, Weller H (2001) Nano Lett 1:207–211
3. Murray CB, Norris DJ, Bawendi MG (1993) J Am Chem Soc 115:8706–8715
4. Alivisatos AP (1996) Science 271:933–937
5. Colvin VL, Schlamp MC, Alivisatos AP (1994) Nature 370:354–357

6. Park SS, Kim DH, Jeon YP, Kim TW (2013) J Nanosci Nanotechnol 13:7194–7197
7. Kim Y, Greco T, Ippen C, Wedel A, Oh MS, Han CJ, Kim J (2013) Nanosci Nanotechnol Lett 5:1065–1069
8. Shen HB, Lin QL, Wang HZ, Qian L, Yang YX, Titov A, Hyvonen J, Zheng Y, Li LS (2013) ACS Appl Mater Interfaces 5:12011–12016
9. Klimov VI, Mikhailovsky AA, Xu S, Malko A, Hollingsworth JA, Leatherdale CA, Eisler HJ, Bawendi MG (2000) Science 290:314–317
10. Harrison MT, Kershaw SV, Burt MG, Rogach AL, Kornowski A, Eychmuller A, Weller H (2000) Pure Appl Chem 72:295–307
11. Amgar D, Aharon S, Etgar L (2016) Adv Funct Mater 26:8576–8593
12. Tang JA, Sargent EH (2011) Adv Mater 23:12–29
13. Li XM, Li YF, Zeng HB (2013) Sci Adv Mater 5:1585–1595
14. Chen Z, Zhang H, Yu W, Li Z, Hou J, Wei H, Yang B (2013) Adv Energy Mater 3:433–437
15. Bruchez M, Moronne M, Gin P, Weiss S, Alivisatos AP (1998) Science 281:2013–2016
16. Dong MT, Fu SS, Liu SX, Xu JY, Huang CB (2013) J Chin Chem Soc 60:1328–1332
17. Ouay BL, Stellacci F (2015) Nano Today 10:339–354
18. Purushotham S, Ramanujan RV (2010) J Appl Phys 107:114701
19. Wu Z, Zhao Y, Qiu F, Li Y, Wang S, Zhang B, Yang B, Zhang Y, Gao R, Wang J (2009) J Lumin 129:1125–1131
20. Yu WW, Chang E, Drezek R, Colvin VL (2006) Biochem Biophys Res Commun 348:781–786
21. Salata OV (2004) NanoBiotechnology 2:3
22. Drbohlavova J, Adam V, Kizek R, Hubalek J (2009) Int J Mol Sci 10:656–673
23. Pilla V, Alves LP, de Santana JF, da Silva LG, Ruggiero R, Munin E (2012) J Appl Phys 112:104704
24. Datta A, Panda SK, Chaudhuri S (2007) J Phys Chem C 111:17260–17264
25. Vempati S, Ertas Y, Uyar T (2013) J Phys Chem C 117:21609–21618
26. Vlaskin VA, Janssen N, van Rijssel J, Beaulac R, Gamelin DR (2010) Nano Lett 10:3670–3674
27. Beaulac R, Archer PI, Ochsenbein ST, Gamelin DR (2008) Adv Funct Mater 18:3873–3891
28. Papaj M, Kobak J, Rousset JG, Janik E, Nawrocki M, Kossacki P, Golnik A, Pacuski W (2014) J Cryst Growth 401:644–647
29. Freitas Neto ES, Dantas NO, Lourenco SA, Teodoro MD, Marques GE (2012) Phys Chem Chem Phys 14:3248–3255
30. Dantas NO, Silva AS, Freitas Neto ES, Lourenco SA (2012) Phys Chem Chem Phys 14:3520–3529
31. Lourenco SA, Dantas NO, Silva RS (2012) Phys Chem Chem Phys 14:11040–11047
32. LaMer VK, Dinegar RH (1950) J Am Chem Soc 72:4847–4854
33. William Yu W et al (2003) Experimental Determination of the Extinction Coefficient of CdTe, CdSe, and CdS. Nanocrystals 125:2854–2860
34. Kim BH, Hackett MJ, Park J, Hyeon T (2014) Chem Mater 26:59–71
35. Baker DR, Kamat PV (2010) Langmuir 26:11272–11276
36. Park Y-S, Bae WK, Padilha LA, Pietryga JM, Klimov VI (2014) Nano Lett 14:396–402
37. Larson DR, Zipfel WR, Williams RM, Clark SW, Bruchez MP, Wise FW, Webb WW (2003) Science 300:1434–1436
38. Pelley JL, Daar AS, Saner MA (2009) Toxicol Sci 112:276–296
39. Teunis MB, Dolai S, Sardar R (2014) Effects of surface-passivating ligands and ultrasmall CdSe nanocrystal size on the delocalization of exciton confinement. Langmuir 30(26):7851–7858
40. Geszke M, Moritz M (2013) Quantum dots as versatile probes in medical sciences: Synthesis, modification and properties. Mater Sci Eng C Mater Biol Appl 33(3):1008–1021
41. Lommens P, Smet PF (2006) Photoluminescence properties of Co2 + −doped ZnO nanocrystals. J Lumin 118(2):245–250
42. Adeli M, Hakimpoor FE (2011) Quantum dot-pseudopolyrotaxane supramolecules as anticancer drug delivery systems. Polymer 52(11):2401–2413

43. Ishikawa M, Biju V (2011) Luminescent quantum dots, making invisibles visible in bioimaging. Nanoparticles Transl Sci Med A Villaverd 104:53–99
44. Saran AD, Sadawana MM et al (2011) An optimized quantum dot-ligand system for biosensing applications: evaluation as a glucose biosensor. Colloids Surf Physicochem Eng Aspects 384(1–3):393–400
45. Sharma AC, Pandey CM et al (2012) Chitosan encapsulated quantum dots platform for leukemia detection. Biosens Bioelectron 38(1):107–113
46. Wang Y, Chen L (2011) Quantum dots, lighting up the research and development of nanomedicine. Nanomed Nanotechnol Biol Med 7(4):385–402
47. Biju V, Anas A et al (2012) FRET from quantum dots to photodecompose undesired acceptors and report the condensation and decondensation of plasmid DNA. ACS Nano 6(5):3776–3788
48. Peer D, Karp JM (2007) Nanocarriers as an emerging platform for cancer therapy. Nat Nanotechnol 2(12):751–760
49. Robel IV, Subramanian V et al (2006) Quantum dot solar cells. Harvesting light energy with CdSe nanocrystals molecularly linked to mesoscopic TiO2 films. J Am Chem Soc 128(7):2385–2393
50. Kim S, Fisher B, Eisler HJ, Bawendi M (2003) Type-II quantum dots: CdTe/CdSe(core/shell) and CdSe/ZnTe(core/shell) heterostructures. J Am Chem Soc 125:11466–11467
51. Silva ACA, Silva SW, Moraes PC Dantas NO (1014) ACS Nano 8 (2): 1913–1922
52. McBride J, Treadway J, Feldman LC, Pennycook SJ, Rosenthal SJ (2006) Structural basis for near unity quantum yield core/shell nanostructures. Nano Lett 6:1496–1501
53. Park YS, Bae WK, Padilha LA, Pietryga JM, Klimov VI (2014) Effect of the core/shell interface on auger recombination evaluated by single-quantum-dot spectroscopy. Nano Lett 14:396–402; Keene et al. (2014) ACS Nano 8:10665–10673
54. Garcia-Santamaria F, Chen Y, Vela J, Schaller RD, Hollingsworth JA, Klimov VI (2009) Suppressed auger recombination in "giant" nanocrystals boosts optical gain performance. Nano Lett 9:3482–3488
55. Woggon U. Optical properties of semiconductor quantum dots. Berlin: Springer; 1997. ISBN: 3540609067
56. Gaponenko SV (1998) Optical properties of semiconductor nanocrystals. Cambridge University Press, Cambridge. ISBN: 0521582415
57. Zarzycki J (1991) Glasses and the vitreous state. Cambridge University Press, Cambridge. ISBN: 0521355826
58. Erwin SC, Zu LJ, Haftel MI, Efros AL, Kennedy TA, Norris DJ (2005) Nature 436:91–94
59. Norris DJ, Efros AL, Erwin SC (2008) Science 319:1776–1779
60. Archer PI, Santangelo SA, Gamelin DR (2007) Nano Lett 7:1037–1043
61. Furdyna JK (1988) J Appl Phys 64:R29–R64
62. Silva RS, Mikhail HD, Pavani R, Cano NF, Silva ACA, Dantas NO (2015) Synthesis of diluted magnetic semiconductor $Bi_{2-x}Mn_xTe_3$nanocrystals in a host glass matrix. J Alloys Compd 648:778–782
63. Freitas Neto ES, Silva ACA, da Silva SW, Morais PC, Gómez JA, Baffa O, Dantas NO (2013) Raman spectroscopy of very small $Cd_{1-x}Co_xS$ quantum dots grown by a novel protocol: direct observation of acoustic-optical phonon coupling. J Raman Spectrosc 44:1022–1032
64. Silva RS, Silva JTT, Rocha VR, Cano NF, Silva ACA, Dantas NO (2014) J Phys Chem C 118:18730–18735
65. Freitas Neto ES, Dantas NO, Lourenco SA (2012) Phys Chem Chem Phys 14:1493–1501
66. Vlaskin VA, Barrows CJ, Erickson CS, Gamelin DR (2013) J Am Chem Soc 135:14380–14389
67. Hanif KM, Meulenberg RW, Strouse GF (2002) J Am Chem Soc 124:11495–11502
68. Hodges JM, Fenton JL, Gray JL, Schaak RE (2015) Nanoscale 7:16671–16676
69. Phan T-L, Yu SC (2013) J Phys Chem C 117:6443–6453
70. Silva AS, Lourenco SA, Pereira-da-Silva MA, Duarte JL, Renzi W, Alcalde AM, Dantas NO (2014) Chem Phys Lett 599:146–153

71. Lourenco SA, Silva RS, Dantas NO (2016) Tunable dual emission in visible and near-infrared spectra using Co-doped PbSe nanocrystals embedded in a chalcogenide glass matrix. PCCP Phys Chem Chem Phys (Print) 18:23036–23043
72. Mokrushin SG, Tkachev YD (1961) Kolloidn Zh 23:438
73. Kitaev GA (1965) Kolloidn Zh 27:51
74. Kitaev GA (1965) Zh Fig Khim 39:2065
75. Kitaev GA, Vritakaya AA (1966) Izv Nauk SSSR Neorg Mater 2:1554
76. Chandra S, Pandey RK, Agrawal RC (1980) J Phys D Appl Phys 13:1757–1760
77. Merdes S, Mainz R, Klaer J, Meeder A, Rodriguez-Alvarez H, Schock HW, Ch Lux-Steiner M, Klenk R (2011) Solar Energy Mater Solar Cells 95:864–869
78. Boev VI, Silva CJR, Hungerford G, Gomes MJM (2004) J Sol-Gel Sci Technol 31:131–135
79. Xu GQ, Liu B, Xu SJ, Chew CH, Chua SJ, Gana LM (2000) J Phys Chem Solids 61:829–836

Chapter 7
X-Ray-Excited Optical Luminescence

M. A. Cebim, H. H. S. Oliveira, M. O. Krauser, and M. R. Davolos

X-ray-excited optical luminescence (XEOL) is a spectroscopic technic historically related to scintillator materials and X-ray phosphors.

Scintillators and X-ray phosphors are materials which can efficiently convert ionizing radiation (photons or particles) into UV-Vis radiation.

Due to this property, such materials can in principle be applied to high-energy physics, industrial inspection, dosimetry, and nuclear medicine and in the detection systems of radiation [1] for image diagnosis [2]. In fact, all applications related to medical imaging require the detection of high-energy photons [3], which includes planar X-ray imaging, computed tomography, and positron emission tomography.

The applied and basic research in the scintillation field is a fundamental step in the development of new technologies and has increased significantly in recent years, because all the materials used in this myriad of applications can present improvements in its physical and chemical properties [4]. With the development of new luminescent materials along with the enhancement of characterization

M.A. Cebim (✉) • M.R. Davolos
Universidade Estadual Paulista (Unesp), Instituto de Química, Araraquara Departamento de Química Geral e Inorgânica, Laboratório de Materiais Luminescentes, Araraquara, SP, Brazil
e-mail: mcebim@iq.unesp.br

H.H.S. Oliveira
Universidade Estadual Paulista (Unesp), Instituto de Química, Araraquara Departamento de Química Geral e Inorgânica, Laboratório de Materiais Luminescentes, Araraquara, SP, Brazil

Instituto Federal de Educação, Ciência e Tecnologia de São Paulo - IFSP, Campus de Matão, SP, Brazil

M.O. Krauser
Universidade Estadual Paulista (Unesp), Instituto de Química, Araraquara Departamento de Química Geral e Inorgânica, Laboratório de Materiais Luminescentes, Araraquara, SP, Brazil

Universidade Federal do Tocantins - UFT, Química Ambiental, Campus Universitário de Gurupi, Gurupi, TO, Brazil

E. Longo, F.A. La Porta (eds.), *Recent Advances in Complex Functional Materials*,
DOI 10.1007/978-3-319-53898-3_7

techniques that contributes to the elucidation of the processes involved with the scintillation mechanism, it is possible to design high-performance scintillators, which can be characterized by a high density, reasonable mechanical and chemical stabilities, low radiation damage, and high luminescent quantum yield, and, beyond that, present feasible chemical synthesis and reasonable preparation coasts [5].

The improvement of scintillator characteristics and the knowledge of theoretical limits of relevant properties implies in the study of structural and luminescent features, as well as the mechanisms related to the scintillation process. Therefore, one must describe in general terms all the processes which manifest during scintillation.

The scintillation process can be divided into three stages [6]. In the first, incident radiation ionizes the material with the formation of holes in the most energetic shells of the material constituents. The ionization triggers a series of phenomena which includes radiative decay of electrons followed by the emission of secondary X-rays, non-radiative decays (Auger electrons), and electron-electron inelastic scattering. Typically, this stage requires two to seven times the energy for the creation of an electron-hole pair, with a time interval of 10^{-15}–10^{-13} s. The second stage is characterized by the gradual release of the absorbed energy until it reaches the ionization threshold. At this point, despite the evolved energy is inferior to promote further ionizations, it can be used to promote interband transitions leading to the creation of electron-hole pairs. Electron-phonon relaxation and intraband transitions promote pairs thermalization. Charge carriers can return to the diffuse band (in the case of semiconductors), being trapped in defects or impurities, self-trapped to its own structure or the formation of excitons, all of these in a time scale of 10^{-12}–10^{-11} s. At this stage, the luminescent centers can be excited by the impact of "hot electrons," by the subsequent capture of electron-hole pairs or by the energy transfer between a sensitizer and the activator, in a time scale of 10^{-12}–10^{-8} s. Finally, at the third stage, the excited luminescent center returns to the ground state by photon emission or non-radiative suppression. The radiative process can be short (10^{-9}–10^{-3} s) for pair recombination and for exciton emission or electronic recombination or take several minutes for the case of high prohibitive processes.

Due to the capacity of conversion of high-energy radiation into lower-energy radiation, these materials can be widely applied in fields of detection [7], dosimetry [8], and diagnosis applications [9] and as medical imaging technologies.

Nowadays, the science of scintillator materials is focused on the development of high-performance materials [10] and the understanding of the scintillation mechanism in nanostructured materials [11]. In general, scintillator materials and X-ray phosphors are prepared in the form of crystals, polycrystalline powders, and densified ceramics. The introduction of nanostructured materials in scintillation expands the possibility of new conformations such as composite films, vitroceramics, thin films, coordination compounds, metal-organic frameworks (MOFs), and organic-inorganic hybrid materials in the detection of ionizing radiation.

X-ray-excited optical luminescence (XEOL) is directly related to X-ray-induced photoelectron spectroscopy and X-ray fluorescence [12]. The majority of papers in physics and chemistry of materials relate XEOL as a complement of the structural

and spectroscopic analysis [13]. Thus, XEOL apparatus and measurements depend on the instrumentation of photoelectron spectroscopy, which is coupled with the necessary instrumentation for UV-Vis spectroscopy. However, the diffusion and popularization of XEOL as an analytic-structural characterization of materials depend on the development of a simple and low-cost instrumentation to realize quick and precise XEOL measurements.

XEOL is being tested and used in our lab in the characterization of materials with different conformations, such as nanostructured materials, composite films, coordination compounds, and MOFs, in addition to thin films and hybrid organic-inorganic materials.

Particularly, regarding lanthanide-based materials (with trivalent lanthanide cations, i.e. Ln^{3+}) which is the focus of a number of research papers due to its importance in luminescence and illumination [14], in the production of batteries and fuel cells [15], sunscreens [14], and mainly in strategic fields, such as nanostructured catalysts [16] and critical materials. In all these applications, the coordination number and the covalence degree for the lanthanide crystallographic site define the luminescent properties of the lanthanide-based material and are of fundamental value for the engineering of high-performance materials. The XEOL technique was already presented as a tool for the characterization of multisite lanthanide-based materials [17]; however, XEOL was poorly explored in this way. XEOL can be most valuable when performed along with UV-Vis-excited luminescence, since different excitation radiations can stimulate the luminescence of different Ln^{3+} sites.

Here we discuss the use of XEOL as an analytic tool for the characterization of materials, that is, the correlation of XEOL characterization with traditional structural and spectroscopic characterization and the influence of defects in luminescence properties of Eu^{3+}-doped Y_2O_3 and the XEOL analysis of materials with different conformations – phosphors/PMMA (polymethylmethacrylate) composite films – as scintillators and X-ray phosphors.

1 Influence of Structural Defects on Scintillation Properties

1.1 Method Influence

In this section, the structural defects produced by different methods and its influence on the scintillation properties will be discussed, evaluating the luminescent properties of the Y_2O_3:Eu^{3+} prepared by Pechini [18] and homogeneous precipitation (HP) [19] methods. Materials obtained by both synthetic methods, even using the same conditions – thermal treatment at 1100 °C for 4 h – present different structural and morphological properties. While HP method produces spherical and monodispersed particles, in particular, the same material prepared by Pechini method present agglomerates of nanoparticles, as observed in Fig. 7.1.

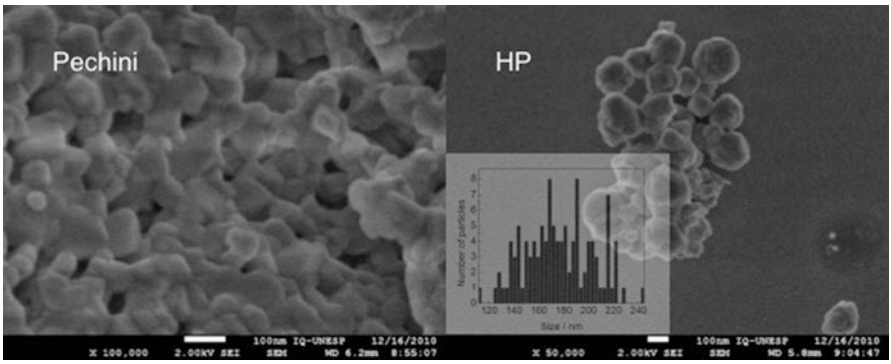

Fig. 7.1 Scanning electron microscopy of Y_2O_3:Eu^{3+} 1% a.t., obtained from Pechini and homogeneous precipitation (*HP*) methods

It is important to remember that both synthetic methods are based on different precursors, which leads to materials with different structural characteristics. In the Pechini method, the noncrystalline polymeric resin used as a precursor presents a morphology not well defined, favoring the formation of the aggregates. In HP methods, yttrium hydroxycarbonate nanoparticle precursors present size and shape defined, which are maintained after thermal treatment, resulting in dispersed nanoparticles. Despite these differences, the samples prepared from both synthetic methods reveal a mean size around 150 nm.

Another difference observed in the Y_2O_3:Eu^{3+} materials is related to the presence of precursor subproducts after thermal treatment, as observed in the infrared spectra (Fig. 7.2).

When Y_2O_3:Eu^{3+} is obtained by HP method, bands assigned to carbonate anions are observed [20]. These anions probably are trapped at oxide structure due to incomplete decomposition of the precursor, leading to the formation of the structural defects in the material.

X-ray diffraction data allows to evaluate the crystalline structure of the materials prepared from both synthetic methods (i.e., Pechini and HP methods), as observed in Fig. 7.3.

Analyzing X-ray diffraction data, the samples present structural phase related to Y_2O_3 (JCPDS-PDF 41-1105), independent of the synthesis method used. Crystallographic parameters can be obtained from X-ray diffraction data by Scherrer [21] and Williamson-Hall [22] (WH) methods, and these parameters are shown in Table 7.1.

As observed in Table 7.1, the material prepared via the HP method presents better values of the crystallographic parameters (e.g., higher crystallite size and minor crystalline structure strain) when compared with the material obtained by Pechini method. These structural parameters can be related to the luminescent properties of the Y_2O_3:Eu^{3+} under ultraviolet (UV) and X-ray-excited.

Photoluminescent (PL) measurements – excitation and emission spectra – of both samples recorded at room temperature are shown in Fig. 7.4.

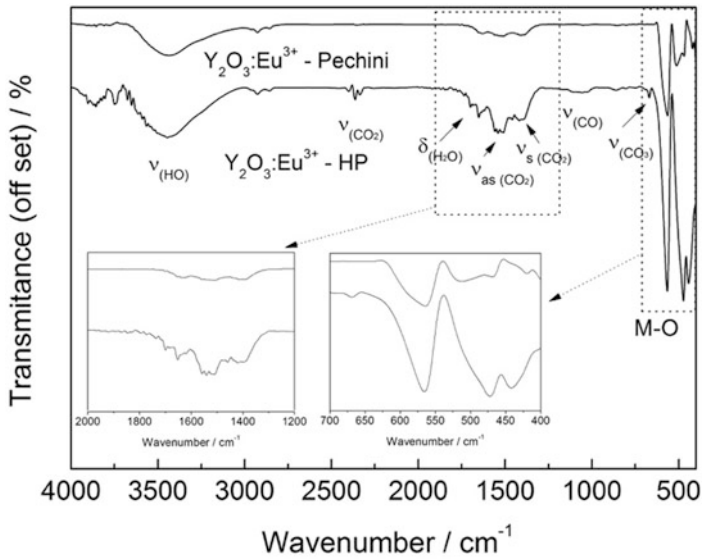

Fig. 7.2 Fourier transform infrared spectra of Y_2O_3:Eu^{3+} 1% a.t., obtained from Pechini and (*HP*) homogeneous precipitation methods

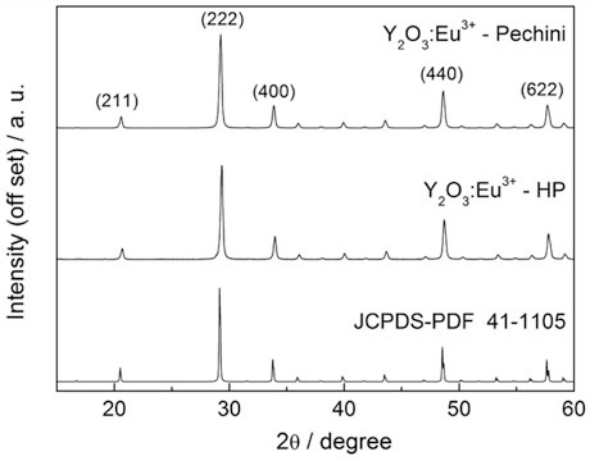

Fig. 7.3 X-ray diffraction data of the Y_2O_3:Eu^{3+} 1% a.t., obtained from Pechini and homogeneous precipitation (HP) methods

Emission spectra (λ_{ex} = 270 nm) of the samples present the characteristic bands assigned to $^5D_0 \rightarrow {}^7F_J$ (J = 0, 1, 2, 3, and 4) electronic transitions of the Eu^{3+} ion, and the emission profiles are similar for both samples, independent of the preparation method used [23]. However, the excitation spectra present some differences. It is possible to observe a redshift of the band assigned to charge transfer (CT) $O^{2-} \rightarrow Eu^{3+}$ of the sample obtained by Pechini method when compared with the same band of the sample prepared by HP method [24]. The redshift probably

Table 7.1 Crystallite sizes and strain lattice of Y_2O_3:Eu^{3+} obtained from Pechini and homogeneous precipitation (HP) methods

Sample	hkl	Position (2θ)	FWHM (2θ)	Crystallite size Scherrer method (nm)	Crystallite size WH method (nm)	Strain
Pechini method						
Y_2O_3:Eu^{3+}	*h22*				45.1	0.0032
	222	29.24	0.25036	44.3		
	622	57.68	0.32486	32.6		
Y_2O_3:Eu^{3+}	h11				42.8	0.0024
	211	20.60	0.24084	46.8		
	411	36.00	0.25053	45.0		
	611	53.26	0.30663	34.7		
Y_2O_3:Eu^{3+}	*4* k0				47.8	0.0036
	400	33.88	0.25509	43.3		
	440	48.62	0.29474	36.0		
Homogeneous precipitation (HP) method						
Y_2O_3:Eu^{3+}	*h22*				46.3	0.0030
	222	29.34	0.24287	46.9		
	622	57.76	0.31425	34.2		
Y_2O_3:Eu^{3+}	h11				43.7	0.0026
	211	20.70	0.23567	48.9		
	411	36.06	0.25346	44.0		
	611	53.38	0.30344	35.2		
Y_2O_3:Eu^{3+}	*4* k0				46.5	0.0028
	400	33.96	0.24822	45.5		
	440	48.70	0.28192	38.5		

is associated to additional electronic levels created from the higher structural defect concentration in the sample obtained by Pechini method, as indicated by the higher values of crystalline structure strain presented in Table 7.1.

Defect concentration in the material can be associated, indirectly, to X-ray-excited optical luminescence (XEOL) results. The third stage of the scintillation mechanism involves the energy transfer from e^-/h^+ pairs to luminescent center. This process can be affected by the presence of the defects that capture the energy from e^-/h^+ pairs and promote non-radiative decay rates. Therefore, the emission intensity measured by XEOL technique can be associated to the defects concentration in the materials analyzed.

Figure 7.5 shows emission spectra of the Y_2O_3:Eu^{3+} samples obtained by Pechini and/or HP method recorded by XEOL spectroscopy. As observed at PL measurements, the emission profiles under X-ray-excited present the characteristic bands assigned to $^5D_0 \rightarrow {}^7F_J$ ($J = 0, 1, 2, 3$, and 4) electronic transitions of the Eu^{3+} ion and are similar for both samples, i.e., independent of the preparation method used.

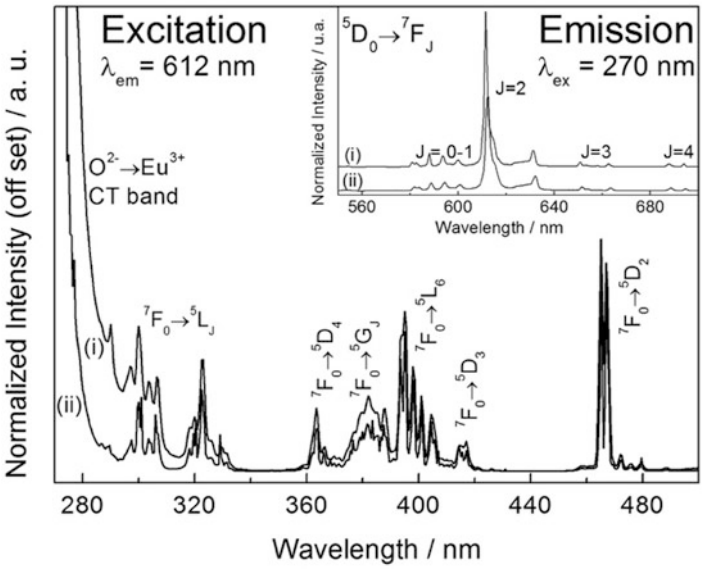

Fig. 7.4 Photoluminescence spectra recorded at room temperature of Y_2O_3:Eu^{3+} obtained from (*i*) Pechini and (*ii*) homogeneous precipitation (HP) methods

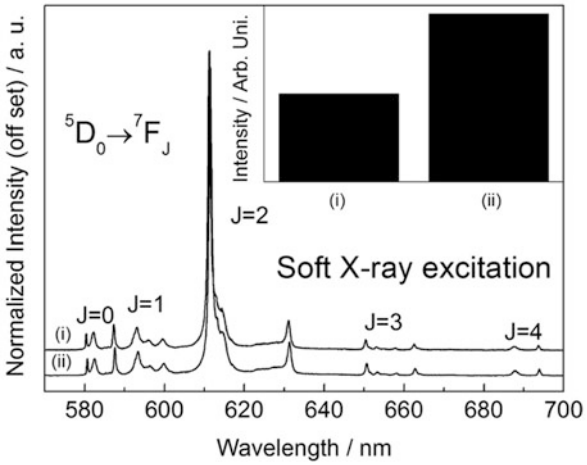

Fig. 7.5 X-ray-excited optical luminescence spectra recorded at room temperature and integrated emission intensity on the $^5D_0 \rightarrow {}^7F_2$ transition of Y_2O_3:Eu^{3+} obtained from (*i*) Pechini and (*ii*) homogeneous precipitation (HP) methods

However, it is possible to observe a significant emission intensity difference between the samples. As discussed in this section, the sample prepared by Pechini method presents a higher concentration of defects, and hence these defects can act as suppressors of the luminescence. Because of that, the emission intensity of the Y_2O_3:Eu^{3+} prepared by Pechini method is almost half from that observed in the sample prepared by HP method.

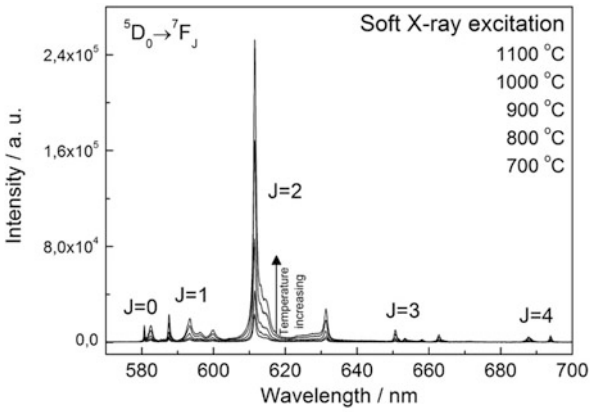

Fig. 7.6 X-ray-excited optical luminescence spectra recorded at room temperature of Y_2O_3:Eu^{3+} obtained from homogeneous precipitation (HP) method at 700, 800, 900, 1000, and 1100 °C

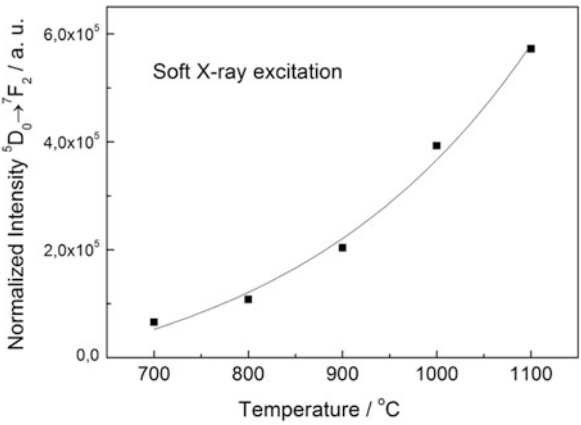

Fig. 7.7 Integrated emission intensity on the $^5D_0 \rightarrow {}^7F_2$ transition (from XEOL spectra) of Y_2O_3:Eu^{3+} obtained from homogeneous precipitation (HP) methods at 700, 800, 900, 1000, and 1100 °C

1.2 Temperature Influence

Besides the method influence, the temperature also may contribute to defining a higher or lower concentration of the defects in a material. This effect is observed for Y_2O_3:Eu^{3+} samples prepared by HP method using different thermal treatment (e.g., 700, 800, 900, 1000, and 1100 °C) for 4 h. Figure 7.6 shows the emission spectra of the samples prepared at different temperatures recorded under X-ray-excited, while that in Fig. 7.7 are shown the integrated emission intensity as a function of the thermal treatment temperature.

It is evident that emission intensity increases exponentially (first order) with the thermal treatment temperature. Increasing the temperature of the thermal treatment, the crystallinity of the resulting material is higher, and consequently, structural defect concentration decreases, minimizing non-radiative processes and increasing of the emission intensity [25].

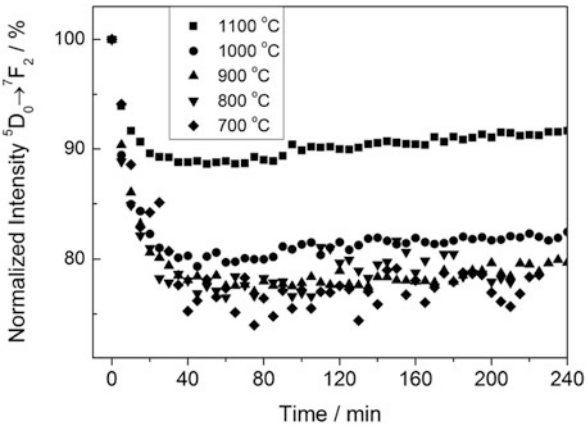

Fig. 7.8 Radiation damage of Y_2O_3:Eu^{3+} obtained from homogeneous precipitation (HP) method in 700, 800, 900, 1000, and 1100 °C

This influence also can be observed when the samples are exposed to the X-ray radiation for long periods – radiation damage. Figure 7.8 shows the emission intensity (on the $^5D_0 \rightarrow {}^7F_2$ transition) as a function of the time exposure of the samples to the X-rays [26].

The X-ray incidence on the sample creates defects that contribute to non-radiative processes, leading to decreasing of the emission intensity. However, when the sample is prepared at higher temperatures, the higher structural organization minimizes the creation of these defects. As a result, the emission intensity of the sample prepared at 1100 °C reduces, under X-ray exposure, to 90% from initial intensity, while the reduction observed for the samples treated below 1000 °C is higher, and it achieves to 80%.

2 New Conformations of Scintillators Materials

The science of ionizing radiation detection has received great attention in recent years due to the search for materials with high performance and for better understanding of the scintillation mechanisms in nanoparticles, thin films, and composite materials [27].

The structural conformation of scintillator materials is an important factor to be considered in the quest for efficient scintillation systems and devices because it has a direct impact on the application of these materials in ionizing radiation detectors and in the final cost of the devices [28]. The preparation of the sintered materials, compact ceramic, or single crystals involves high temperatures and pressures, elevated power consumption, expensive procedures, and relatively large amounts of raw and final product materials [29].

In this way, the preparation of nanocrystalline powders scintillators is the aim of several research since it enables the possibility of new application for powdered scintillator materials and may be considered an alternative to sintered compact ceramic and single-crystal scintillators [30, 31].

In nanocrystalline powders, it is possible to optimize the luminescent properties by controlling the nanoparticle characteristics, such as grain and particle sizes, allowing the preparation of structures with higher light yield than single crystals [32]. The application of nanocrystalline scintillators in radiation detectors may improve the efficiency of the X-ray volume imaging devices, increasing the light yield, sensitivity, and radiation hardness, accelerating the registration rate of the ionizing radiation decreasing irradiated doses, scanning durations and the cost of the device [33].

The use of inorganic nanocrystalline powders as scintillator materials supported into a polymeric film is also an interesting alternative for improvement of scintillation devices [34–39]. The preparation of inorganic phosphor/polymer films has a facile control of its shape, area, and thickness. Moreover, the use of composite films allows the maintenance of optical properties of supported materials with a significant decrease of the phosphor amount used in relation to compact ceramic or single-crystal samples and enables the construction of devices that require flexible systems, which cannot be achieved by single crystals [30, 32], sintered ceramic [31], and vitroceramic materials [40].

This section presents some aspects of the preparation and the optical properties of composite polymethylmethacrylate (PMMA) films containing $GdAlO_3:Eu^{3+}$ and $Gd_2O_2S:Pr^{3+}$ nanoparticles as scintillator materials [41–43].

Eu^{3+}-doped $GdAlO_3$ powder samples can be prepared by the Pechini method with thermal treatment at 1100 °C/4 h [41] and Pr^{3+}-doped Gd_2O_2S powder samples can be prepared by the thermal treatment (750, 780, and 900 °C for 2 h) of the corresponding hydroxycarbonate precursor in a dynamic H_2/N_2 atmosphere with sulfur vapor (S_8) [42, 43]. Previously characterizations of the luminescent properties of these solids were described in the literature [41–43].

Inorganic phosphor/polymer films can be prepared by dispersion of the $GdAlO_3:Eu^{3+}$ or $Gd_2O_2S:Pr^{3+}$ powders in a 10% (wt./v) polymethylmethacrylate (PMMA) solution in dichloromethane using the ultrasonic processor. The powder to PMMA mass ratio (χ) can be varied according to the desired characteristics of the films. The composition of the scintillator powder/PMMA films discussed in this section is shown in Table 7.2.

PMMA polymer has low X-ray absorption coefficient, presenting high transparency with respect to such radiation. However, if any radiation damage occur to the polymer that compromises the properties of the films, it is possible to recycle the film by dissolution in dichloromethane, followed by filtration of the powder and subsequent dispersion of the powder in a PMMA-dichloromethane solution. Figure 7.9 shows the flow scheme for the process of composite films preparation.

The dependence of the composite film mean thickness obtained from 2D profiles against the powder to polymer mass ratio, are shown in Fig. 7.10, varies linearly for all composite films. Depending on the powder composition used in the film's preparation, several powder to polymer mass ratios can be defined in order to verify the simplicity and feasibility of the composite film preparation.

The relative regularity of rugosity in the film's profile (Fig. 7.10 – inset) can be assigned to the uniform distribution of the powder in the PMMA polymeric

Table 7.2 Composition of the scintillator powder/PMMA films

Powder	Powder mass/mg	PMMA polymer mass/mg (PMMA solution volume)[a]	Powder to polymer mass ratio. χ ($\times 10^{-3}$)
$GdAlO_3:Eu^3$	1.0	1000 (10 mL)	1.0
	2.5	1000 (10 mL)	2.5
	5.0	1000 (10 mL)	5.0
	7.5	1000 (10 mL)	7.5
	10.0	1000 (10 mL)	10.0
$Gd_2O_2S:Pr^{3+}$	5.0	1000 (10 mL)	5.0
	5.0	700 (7 mL)	7.14
	5.0	333 (3.3 mL)	15.0

[a]PMMA solution in dichloromethane $=100$ mg mL^{-1}

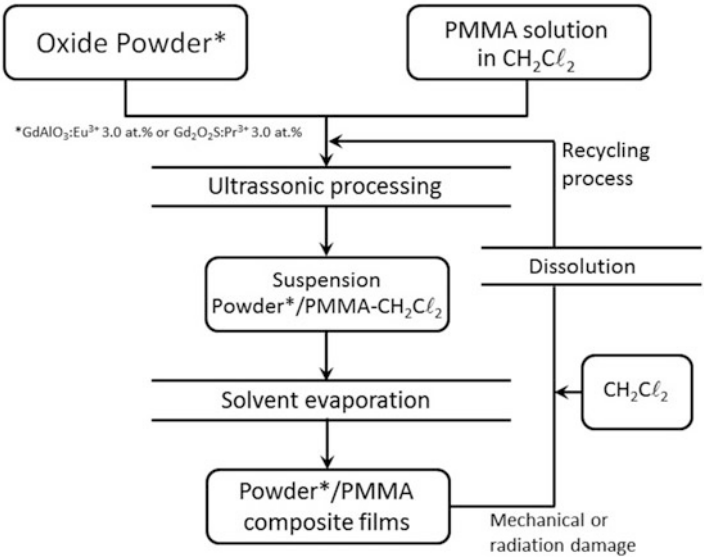

Fig. 7.9 Preparation flow scheme of scintillator powder/PMMA films

matrix. The thickness of the films directly depends on the powder to polymer ratio. Therefore, it is possible to control the film thickness using different compositions with different χ values. Despite of the film thickness dependence with powder to polymer mass ratio, the powder mass exerts minor influence in the film thickness when compared to the polymer mass. Therefore, $GdAlO_3:Eu^{3+}$ films, prepared using a constant polymer mass (Table 7.2), presented a minor variation of film thickness when compared with $Gd_2O_2S:Pr^{3+}$. In $Gd_2O_2S:Pr^{3+}$ films, the standard deviation of mean thickness is higher when compared to $GdAlO_3:Eu^{3+}$ films but is probably due to the presence of powder agglomeration. However, these deviation values are acceptable for the film thickness, which is around 235 μm.

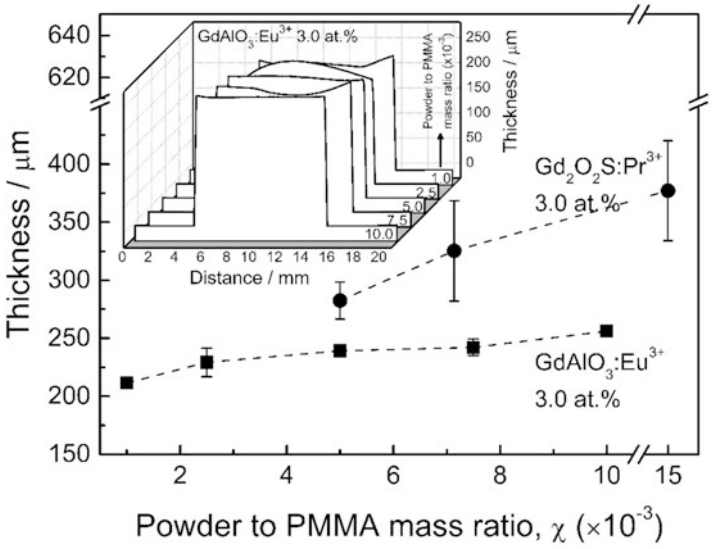

Fig. 7.10 Dependence of composite films mean thickness with the powder to PMMA mass ratio. The inset shows the 2D profiles of the $GdAlO_3:Eu^{3+}$/PMMA composite films

The dependence of the film mean transmittance (400–800 nm) derived from UV-VIS transmittance spectrum against the powder to polymer mass ratio is shown in Fig. 7.11.

The transmittance spectra of the composite films (Fig. 7.11 – inset) present the same profile, with different transmittance intensities. The bands observed at 299 and 341 nm are assigned to $\pi \rightarrow \pi^*$ *e* $n \rightarrow \pi^*$ transitions of the carbonyl group (C═O) of PMMA. A higher transmittance in the 400–800 nm spectral range was observed, except for the $Gd_2O_2S:Pr^{3+}$/PMMA composite films, which present mean transmittance around 20%, due to the high homogeneity of particle distribution. The mean transmittance in the 400–800 nm range decreases with χ values. Increasing the amount of powder dispersed with relation to the amount of PMMA polymer, i.e., increasing χ values, the visible light scattering increases and consequently, the transmitted light decreases. Hence, depending on the transmittance in the 400–800 nm range desired, it is also possible to control it by the use of films with different compositions and different χ values.

Scanning electron micrograph of $Gd_2O_2S:Pr^{3+}$ 5.0 at.%/PMMA composite film ($\chi = 5.0 \times 10^{-3}$) is shown in Fig. 7.12.

$Gd_2O_2S:Pr^{3+}$ 5.0 at.% spherical particles (mean diameter ~200 nm) are easily dispersed in PMMA/CH_2Cl_2 solution and form a stable suspension. After solvent evaporation, the composite films show a homogeneous distribution of powder particles (Fig. 7.12a, b). Figure 7.12c shows the energy-dispersive X-ray spectra of the polymeric matrix (EDS 1) and $Gd_2O_2S:Pr^{3+}$ 5.0 at.% particles (EDS 2). In contrast to vitroceramics [40], polymeric composite films can be prepared using particle

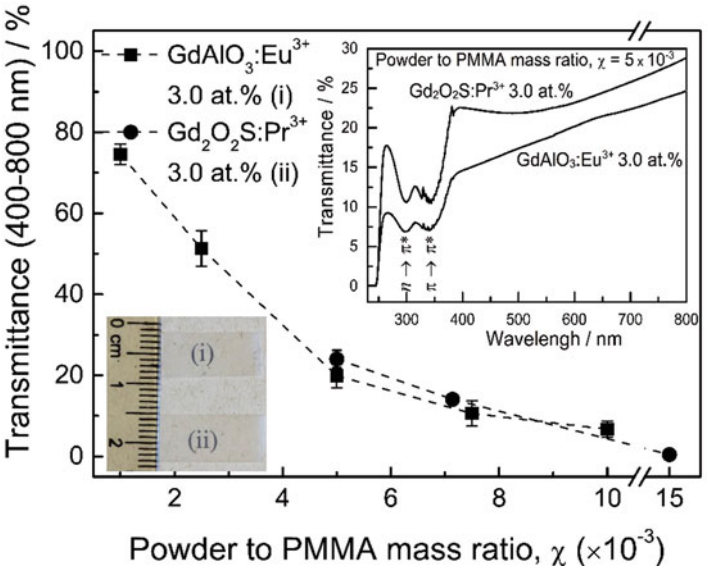

Fig. 7.11 Dependence of composite films mean transmittance (400–800 nm) with the powder to PMMA mass ratio. The inset shows the UV-VIS transmittance spectra of the composite films in the 200–1100 nm range. The image at the left shows (*i*) $GdAlO_3:Eu^{3+}$/PMMA and (*ii*) $Gd_2O_2S:Pr^{3+}$/PMMA composite films ($\chi = 5 \times 10^{-3}$)

powders of high crystallinity and can exhibit optimized functional electrooptical properties. Particles prepared by the polymeric precursor method ($GdAlO_3:Eu^{3+}$ 3.0 at.%, 50–120 nm) tend to form aggregates. Despite the presence of aggregates, the material distribution in the composite films remains homogeneous, since the aggregates can be homogeneously distributed in PMMA.

Figure 7.13 shows a comparison between UV (*straight line*) and X-ray (*dashed line*) excited luminescence [44] for (a) $GdAlO_3:Eu^{3+}$ 3.0 at.%/PMMA and (b) $Gd_2O_2S:Pr^{3+}$ 3.0 at.%/PMMA composite films ($\chi = 5.0 \times 10^{-3}$).

The $GdAlO_3:Eu^{3+}$ 3.0 at.%/PMMA and $Gd_2O_2S:Pr^{3+}$ 3.0 at.%/PMMA films exhibit the same spectral profiles for both UV and X-Ray-Excited. The UV-excited luminescence for the $GdAlO_3:Eu^{3+}$ 3.0 at.%/PMMA film (Fig. 7.13a) was recorded with excitation wavelength fixed at 274.5 nm ($^8S_{7/2} \rightarrow {}^6I_J$ transition of the Gd^{3+} ion). The typical transitions of the Eu^{3+} ions, $^5D_0 \rightarrow {}^7F_J$ ($J = 0$–4), are observed. In the case of the $Gd_2O_2S:Pr^{3+}$ 3.0 at.%/PMMA composite film, the emission spectrum obtained when the sample is excited at 262 nm (VB → CB, Gd_2O_2S) presents transitions from $^3P_0$ and $^1D_2$ in the wavelength range of 480–780 nm. All transitions are assigned in Fig. 7.13b.

Finally, for all composite films, the luminescence intensity is directly proportional to χ, and the films prepared with different powder to polymer mass ratio present the same spectral profiles. The employment of powder materials in the PMMA polymeric matrix in relation to sintered compact ceramics, single crystals,

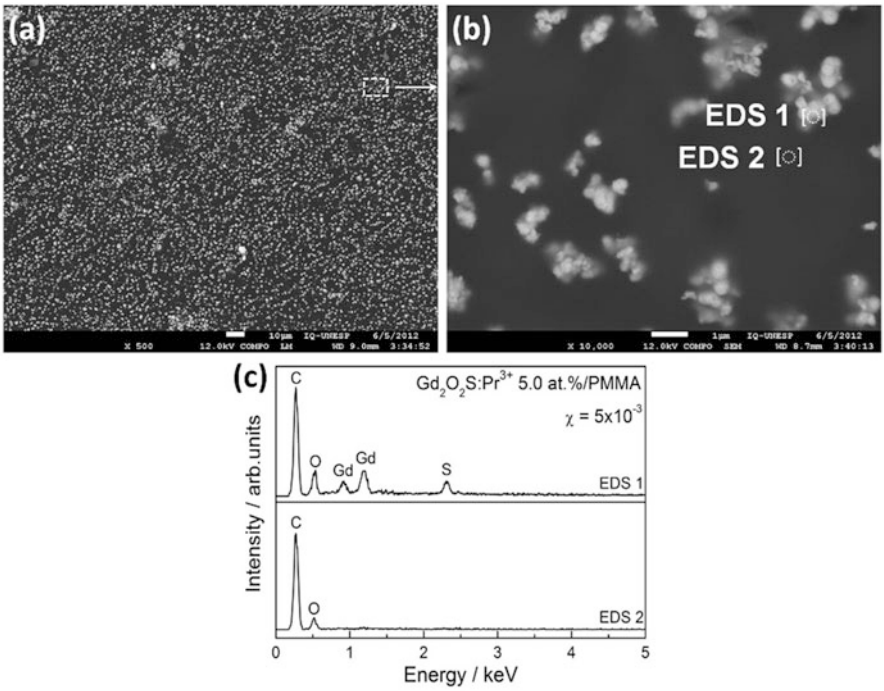

Fig. 7.12 Scanning electronic microscopy images of $Gd_2O_2S:Pr^{3+}$ 5.0 at.%/PMMA composite film ($\chi = 5 \times 10^{-3}$). (**a**) $Gd_2O_2S:Pr^{3+}$ 5.0 at.% particle distribution in the PMMA polymeric matrix. (**b**) Magnification of $Gd_2O_2S:Pr^{3+}$ 5.0 at.% particle distribution in the PMMA polymeric matrix. (**c**) Energy-dispersive X-ray spectra of the composite film: EDS 1 – $Gd_2O_2S:Pr^{3+}$ 5.0 at.% particle and EDS 2 – PMMA polymeric matrix

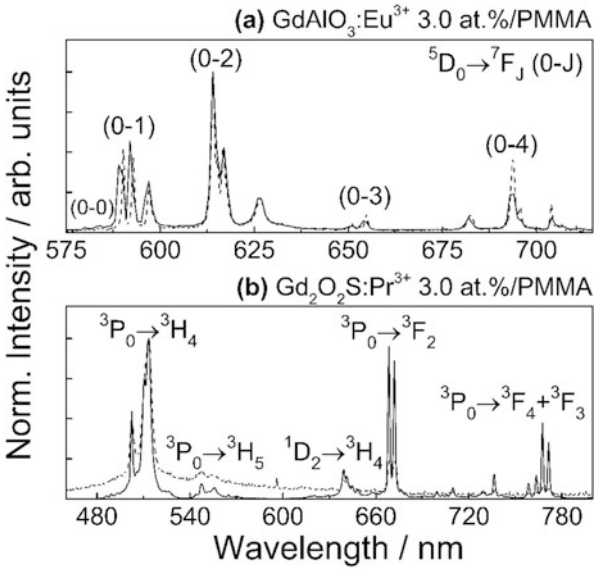

Fig. 7.13 Emission spectra of composite films. Photoluminescence spectra profile (continuous line) was recorded with excitation wavelength $\lambda_{GdAlO3} = 274.5$ nm and $\lambda_{Gd2O2S} = 262.5$ nm. XEOL profile (*dashed line*) was recorded with ~8.0 keV X-Ray-Excited (copper Kα, with the X-ray tube operating at 35 kV and 20 mA)

and vitroceramics [30, 31, 40] is interesting because the materials maintain its luminescent properties and the composite films conformation allows to reduce the amount of powder required, enabling the preparation of improved flexible devices, with controlled shape, thickness, visible light transmittance, and luminescent properties.

References

1. Lecoq P et al (2006) Scintillation and inorganic scintillators. In: Inorganic scintillators for detectors systems: physical principles and crystal engineering, vol 1, cap. 1. Springer, New York, pp 1–34
2. Greskovich C, Duclos S (1997) Ceramic scintillators. Ann Rev Mater Sci Palo Alto 27(1):69–88
3. Kandarakis I et al (2005) Evaluation of ZnS:cu phosphor as X-ray to light converter under mammographic conditions. Radiat Meas 39(3):263–275
4. Weber M, Inorganic J (2002) Scintillators: today and tomorrow. J Lumin 100:35–45
5. Derenzo SE et al. (2003) The quest for the ideal inorganic scintillator. Nucl Instrum Methods Phys Res A. 505:111–117. Grabmaier BC (1994) Luminescent materials for medical application. J Lumin. 60&61:967–970. Lecoq P (1994) The high energy physics demand for a new generation of scintillators. J Lumin. 60&61:948–955
6. Nikl M, Laguta VV, Vedda A (2008) Complex oxide scintillators: materials defects and scintillation performance. Physica Status Solidi B, Weiheim 245(9):1701–1722
7. Lucchini M et al (2014) Response of inorganic scintillators to neutrons of 3 and 15 MeV energy. IEEE Trans Nucl Sci, Piscataway 61(1):472–478
8. Yusoff AL et al (2005) Review of development of themoluminescence dosimeters. Radiat Chem Phys 74(6):459–481
9. Maghraby AM et al (2013) New approaches for improvement of TOF-PET. Nucl Inst Methods Phys Res A 732:560–563
10. Dujardin C et al (2010) Luminescence and scintillation properties at the nanoscale. IEEE Trans Nucl Sci, Piscataway 57(3):1348–1354
11. Soderholm L et al (1998) X-ray excited optical luminescence (XEOL) detection of x-ray absorption fine structure (XAFS). J Chem Phys 109(16):6745–6752
12. JYP K et al (2009) XANES and XEOL studies of Eu-doped calcium tungstate in silica synthesized by sol-gel method. J Phys 190:0120781–0120785
13. Blasse G (1995) Luminescent materials: is there still news? J Alloys Compounds, Lausanne 225(1-2):529–533
14. Yabe S, Sato T (2003) Cerium oxide for sunscreens cosmetics. J Solid State Chem 171(1-2):7–11
15. Vert VB, Serra JM (2010) Improvement of the electrochemical performance of $Ln_{0.58}Sr_{0.40}Fe_{0.8}Co_{0.2}O_3$ – IT-SOFC cathodes by ternary lanthanide combinations (La-Pr-Sm). Fuel Cells 10(4):693–702
16. Chen Y, Ma SQ (2012) Microporous lanthanide metal-organic frameworks. Rev Inorg Chem 32(2-4):81–100
17. Tola P et al (1982) On the use of X-ray-excited optical luminescence (XEOL) for the analysis of multisite rare-earth systems. Chem Phys 78(3):339–345
18. Pechini MP (1967) Method of preparing lead and alkaline earth titanates and niobates and coating method using the same to form capacitor. US3330697
19. Gaspar RDL, Mazali IO, Sigoli FA (2010) Particle size tailoring and luminescence of europium(III)-doped gadolinium oxide obtained by the modified homogeneous precipitation method: dielectric constant and counter anion effects. Colloids Surf A Physicochem Eng Asp 367(1-3):155–160

20. Nakamoto K (1997) Infrared and Raman spectra of inorganic and coordination compounds, 5th edn. John Wiley, New York, pp 338–338
21. Fu Z et al (2007) Preparation and luminescent properties of cubic Eu3+:Y2O3 nanocrystals and comparison to bulk Eu3+:Y2O3. J Lumin 124(2):213–216
22. Srinivasan R, Yogamalar R, Bose AC (2010) Structural and optical studies of yttrium oxide nanoparticles synthesized by co-precipitation method. Mater Res Bull 45(9):1165–1170
23. Blasse G, Grabmaier BC (1994) Luminescent materials, 1st edn. Springer-Verlag Telos, New York, p 232
24. Shang CY et al (2011) Investigation on the red shift of charge transfer excitation spectra for nano-sized Y_2O_3:Eu^{3+}. Chem Phys Lett 501(4-6):480–484
25. Lempicki A, Wojtowicz AJ, Berman E (1993) Fundamental limits of scintillator performance. Nucl Instrum Methods Phys Res Section A Accelerators Spectrometers Detectors Assoc Equip 333:304–311
26. Blasse G (1994) Scintillator materials. Chem Mater 6(9):1465–1475
27. Peurrung A (2008) Materials science for nuclear detection. Mater Today 11:50–54
28. Derenzo SE, Weber MJ, Bourret-Courchesne WE, Klintenberg MK (2003) The quest for the ideal inorganic scintillator. Nucl Instrum Methods Phys Res Sect A 505:111–117
29. Wisniewski DJ, Boatner LA, Neal JS, Jellison GE, Ramey JO, North A, Wisniewska M, Payzant AE, Howe JY, Lempicki A, Brecher C, Glodo J (2008) Development of novel polycrystalline ceramic scintillators. IEEE Trans Nucl Sci 55:1501–1508
30. Jalabadze NV, Chedia R, Kukava T, Nadaraia L (2008) Development of new technologies for the manufacturing of nanocrystalline scintillation materials. IEEE Trans Nucl Sci 55: 1514–1522
31. Tissue BM (1998) Synthesis and luminescence of lanthanide ions in nanoscale insulating hosts. Chem Mater 10:2836–2845
32. Shmurak SZ, Strukova GK, Smyt'ko IM, Klassen NV, Kobelev NP, Derenzo SE, Weber MJ (2005) Studies of nanocrystalline rare earth gallate and aluminate scintillators prepared by a new method. Nucl Instrum Methods Phys Res Sect A 537:149–153
33. Klassen NV, Kedrov VV, Kurlov VN, Ossipyan YA, Shmurak SZ, Shmyt'ko IM, Strukova GK, Kobelev NP, Kudrenko EA, Krivko OA, Kiselev AP, Bazhenov AV, Fursova TN (2008) Advantages and problems of nanocrystalline scintillators. IEEE Trans Nucl Sci 55:1536–1541
34. Nowotny R, Taubeck A (2009) A method for the production of composite scintillators for dosimetry in diagnostic radiology. Phys Med Biol 54:1457–1468
35. Vasil'chenko VG, Solov'ev AS (2004) New composite scintillators (in static and dynamic states). Instrum Exp Tech 47:602–610
36. Astakhov MV, Belanov GS, Vasil'chenko VG, Rodin AO, Samoilenko VD, Solov'ev AS (2006) Properties of composite scintillators based on severely deformed powder fillers. Instrum Exp Tech 49:645–650
37. Goubard F, Vidal F, Bazzi R, Tillement O, Chevrot C, Teussié D (2007) Synthesis and luminescent properties of PEO/lanthanide oxide nanoparticle hybrid films. J Lumin 126: 289–296
38. Tkaczyk S, Galceran M, Kret S, Pujol MC, Aguilo M, Díaz F, Reshak AH, Kityk IV (2008) UV-excited piezo-optical effects in oxide nanocrystals incorporated into PMMA matrices. Acta Mater 56:5677–5684
39. Musbah SS, Radojević V, Rradović I, Uskoković PS, Stojanović DC, Dramićanin M, Aleksić R, (2012) Preparation, characterization and mechanical properties of rare-earth-based nanocomposites. Metall Sect B 48:309–318
40. Vedda A, Chiodini N, Fasoli M, Lauria A, Moretti F, Martino DD, Baraldi A, Buffagni E, Capelletti R, Mazzera M, Bohacek P, Mihokova E (2010) Evidences of rare-earth nanophases embedded in silica using vibrational spectroscopy. IEEE Trans Nucl Sci 57:1361–1369
41. Oliveira HHS, Cebim MA, Da Silva AA, Davolos MR, Alloys J (2009) Structural and optical properties of GdAlO3:RE3+ (RE = Eu or Tb) prepared by the Pechini method for application as X-ray phosphors. Compd 488:619–623

42. Cebim MA, Da Silva AA, Davolos MR (2009) Spectroscopy properties and energy level location of $Gd_2O_2S:Pr^{3+},Ce^{3+}$. Phys Status Solidi C 6:S171–S174
43. Da Silva AA, Cebim MA, Davolos MR (2008) Excitation mechanisms and effects of dopant concentration in $Gd_2O:Tb^{3+}$ phosphor. J Lumin 128:1165–1168
44. Cebim MA, Oliveira HHS, Barelli N, Davolos MR (2011) Sistema para realiza ção de medidas de luminescência com excitação por raios X. Química Nova 34:1057–1062

Chapter 8
Piezoelectric Composites: Fabrication, Characterization, and Its Application as Sensor

Alex Otávio Sanches, José Antônio Malmonge, and Walter Katsumi Sakamoto

1 Introduction

Smart materials are those that under some stimulus are able to change, significantly, one or more of its properties (e.g., mechanical, optical, or electrical) [1]. Often called "sensitive materials" because they possess susceptibility to external stimuli, smart materials show a wide area of interest opening up new possibilities in various sectors such as engineering, medicine, biology, and so on. Among smart materials, piezoelectric materials have an important role, since they can function as actuator and sensor materials, mainly in harvesting field driven by size reduction and proliferation of so-called gadgets, and other portable electronics that require less and less power, opening doors to use batteries to continually store energy from other interconverted sources like human movement [2]. Several good papers have been published in the last decade focusing the sensing and the energy harvesting characteristics of them [3–6].

The existence of piezoelectricity in certain synthetic and biological polymers has been known for a long time, as described by Wada [7]. The piezoelectric activity of these polymers is low, limiting their studies to scientific interest. However, in 1969 the interest in this research field has changed with the work of Kawai [8], which showed the existence of significant piezo and pyroelectric activity in synthetic polymers, i.e., when subjected to a high electric field.

Due to its flexibility and ease of obtaining in various forms, polymers have opened a wide possibility of applications previously limited to the conventional piezoelectric ceramics. Thus, numerous studies have been developed mainly in order to use these complex materials as a sensor [9–15].

A.O. Sanches • J.A. Malmonge • W.K. Sakamoto (✉)
Faculdade de Engenharia – Universidade Estadual Paulista – UNESP – Câmpus de Ilha Solteira, Avenida Brasil, 56, 15385-000, Ilha Solteira, SP, Brazil
e-mail: sakamoto@dfq.feis.unesp.br

E. Longo, F.A. La Porta (eds.), *Recent Advances in Complex Functional Materials*,
DOI 10.1007/978-3-319-53898-3_8

If flexibility and resistance to mechanical shocks made piezoelectric polymer material more suitable than conventional ceramics for certain applications, despite the lower piezo and pyroelectric activity, a high dielectric loss and low figure of merit compromise its performance in various applications such as sensors. Hence, for some specific applications, both of them may not work adequately due to some properties of each one, such as low dielectric constant for polymers or mechanical fragility for ceramics.

To overcome this problem, the ceramic/polymer composite becomes an alternative material since it can combine the properties of each single phase, providing a new complex material with tailored performance as active or sensing material. In general, the properties of a composite are determined by the number single phase involved, volumetric fraction of each phase, the properties of the phases, and particularly the manner in which they are interconnected. The connectivity describes the configuration in which the phases of the composite material are interconnected. Each phase can itself connect up to three directions. The numbers used to identify the type of connectivity are given as a combination; the first number refers to the connectivity of the dispersed phase and the second connectivity of the matrix. According to Newnham and co-workers [16] for a two-phased system, there are ten possible connectivities. The most widely studied ferroelectric composite is the connectivity 0-3, mainly because it is the easiest to fabricate, but the composite with connectivity 1-3 has been also characterized mainly for its use as sensor due to higher piezoelectric activity in comparison with the 0-3 one. Several pyro- and piezoelectric composites were prepared and characterized using epoxy resin or polyvinylidene fluoride (PVDF) as matrix [17–19]. A review of the piezo- and pyroelectric properties of polymers and composites can be found in the works of Furukawa [20] and Das-Gupta [21].

Although the composite piezo- and pyroelectric has been studied for a long time, the large range of applications and the growing technological interest for the development of sensors and actuators left this field of research open to the search for new materials with better qualities. By changing the polymer matrix or ferroelectric ceramics, many papers have been published [22–27], showing that the polymer/ceramic composite stands as a good alternative for applications in sensors and actuators.

Another important parameter for obtaining samples with significant piezo- and pyroelectric activities is its effective polarization. Because of the difference of the dielectric constant of the ceramic and polymer, the effective electric field to the polarization of the ferroelectric is much smaller than the applied field, and hence the poling process requires an expressive electric field. SA-Gong and co-workers [28] proposed the addition of semiconducting ceramics to create a continuous path to the electrical flow between the particles of lead zirconate titanate PZT. Interesting results were obtained by these researchers.

As predicted a few decades ago, by several researchers, the development of the electronic industry greatly extended the scope of piezo- and pyroelectric composites in a wide variety of new applications. Amplifier circuits have allowed the use of composites with relatively low activities as piezo- and pyroelectric sensors.

The automotive industry has used piezoelectric sensors to determine the acceleration [29] and to measure the damping force in semi-active suspensions [30]. In the medical field, some studies have reported the extensive use of piezoelectric composites in ultrasonic transducers [31, 32]. The range of applications of piezoelectric materials goes from microphones and hydrophones to telephone communication systems [33, 34].

On these grounds, our aim in this chapter is to describe the development process and characterization of polymer-based piezo composite and cement-based piezo composite with 0-3 and 1-3 connectivity focusing its application as soil humidity sensor and the sensor for structural health monitoring. The result obtained indicates that it can be proposed as an alternative material to those used so far.

2 Soil Water Retention Curve Detection

The major development in the area of remote sensing and increasing miniaturization of sensors made possible the emergence of so-called precision agriculture, which seeks means to observe, access, and control over agricultural practices. An important parameter to be controlled is undoubtedly the amount of water retained in the soil. Thus, knowledge of the soil water characteristic curve is paramount since being a hydraulic property depends on the structure of soil and its constituents.

Water into the soil as any other body in nature can be characterized by an energy state. The movement of the water in the system soil-plant-atmosphere is very low, and the kinetic energy in most of the cases can be neglected. On the other hand, the potential energy is very important to characterize the energy state of the water as a function of its position and internal conditions.

Thermodynamics describe the energy state using the so-called Gibbs free energy [35], which is known as a total potential of water in the soil-plant-atmosphere system. The motion of the water into the system is due to the difference of the total potential between different position and the water follows the "universal law" that is: Every system tries to reach the low energy state. The internal energy variation dU can be written as [35]

$$\mathrm{d}U = T\mathrm{d}S - p\mathrm{d}V + \sum_{i=1}^{n} x_i \mathrm{d}y_i + \sum_{i=1}^{n} \mu_i \mathrm{d}n_i \tag{8.1}$$

where TdS is the heat (T = temperature and dS = entropy variation), pdV is the expansion work (p = external pressure and dV = volume variation), $\sum_{i=1}^{n} x_i \mathrm{d}y_i$ is any other kind of conservative energy, and $\sum_{i=1}^{n} \mu_i dn_i$ is the chemical work due to the variation of number of moles of each compound i. The Gibbs free energy in the differential form is

$$\mathrm{d}G = S\mathrm{d}T - V\mathrm{d}p + \sum_{i=1}^{n} x_i \mathrm{d}y_i + \sum_{i=1}^{n} \mu_i \mathrm{d}n_i \tag{8.2}$$

and finally,

$$dG = d\Psi = SdT - Vdp + gdz + \omega d\theta + \mu dn \tag{8.3}$$

with g = gravity, n = number of water moles, μ = chemical potential of water, and ω is related with the interactions water/air/soil; Ψ = total potential and $d\theta$ = variation of water content in the system. Ψ represents the Gibbs free energy difference between the state of water into the soil and one standard state. The standard state is chosen as the potential energy of pure water with zero force acting on it, atmospheric pressure, reference temperature, and elevation, and the energy of this state is taken as zero potential [36]. So, the total potential of water is the sum of the pressure, gravitational, osmotic, and matric components:

$$\Psi = \Psi_p + \Psi_g + \Psi_{os} + \Psi_m \tag{8.4}$$

Ψ_{os} is due to mineral salt content in the soil water, and Ψ_m (matric potential) relates the interaction between the soil and the water such as capillary and absorption and is related to the soil humidity θ.

For each homogeneous sample soil, the matric potential Ψ_m has a characteristic value for each water content. The graph Ψ_m versus θ is a characteristic of the soil sample and is commonly called the characteristic curve or soil moisture retention curve. Knowing the characteristic curve of the soil, it can estimate the matric potential or vice versa. Actually, the soil humidity is easier to measure and the matric potential is estimated by the retention curve.

The relation between Ψ_m and θ can be obtained by two different ways [37]:

1. Drying: by taking a soil sample initially saturated with water and applying gradually sucks
2. Wetting: taking a soil sample initially dried in air and allowing its gradual wetting

Each method provides a continuum curve but they are distinct. This phenomenon is called hysteresis. Since Ψ_m versus θ is obtained experimentally, there is a need to define the best fit to the experimental data. The model used is the Genuchten model, which is [38]

$$\theta = \theta_r + \frac{(\theta_s - \theta_r)}{[1 + (\alpha\Psi_m)^n]^b} \tag{8.5}$$

where θ_r is the residual volumetric humidity, θ_s the saturation value of the volumetric humidity, and α, n, and b are soil parameters.

In general, under isothermal and isobaric conditions, the total water potential in soil can be regarded as the sum of the gravitational and matric potential since the variation of osmotic potential varies slightly from point to point within the soil. One of the simplest tools to measure the water potential is the tensiometer. The measure is based on the vacuum produced by sucking water out of a tube by a porous tip and passes into the soil. The negative pressure is measured by the mercury

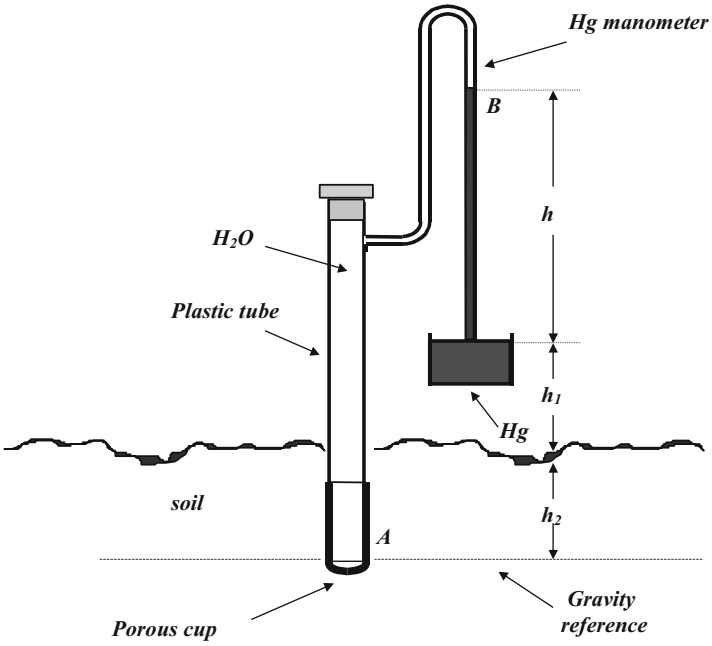

Fig. 8.1 Tensiometer

manometer attached to the tube. When placed into the soil, the water inside the tensiometer comes in contact with the water into the soil, and the equilibrium tends to be established. As the water in the ground is at a lower pressure, water from the tensiometer is sucked into the soil. The flow stops when the pressures are equalized, and the pressure in the tensiometer can be measured.

In Fig. 8.1, the gauge reading is given in -h cm of Hg, which corresponds to the water potential at point B. To determine the potential of the point A (point within the ground), it has [39]

$$\Psi_{\mathrm{m}}(\mathrm{A}) = -13.6h + h + h_1 + h_2 \tag{8.6}$$

or

$$\Psi_{m}(\mathrm{A}) = -12.6h + h1 + h2 \tag{8.7}$$

where h = reading Hg cm, h_1 = manometer height in relation to the soil surface, and h_2 = depth of the porous capsule in relation to the ground surface.

This paper proposes to replace the mercury manometer for a piezoelectric sensor for measuring the water potential according to Fig. 8.2 [39].

Figure 8.3 shows the apparatus with the composite sample as a pressure sensor. A frequency generator continuously drives a steel-carbon film which excites

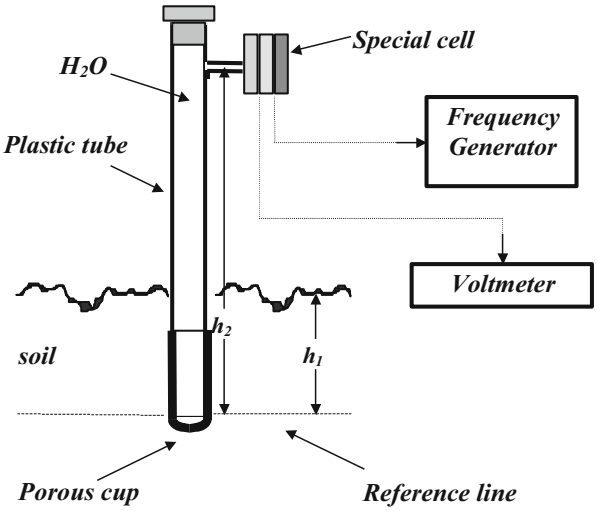

Fig. 8.2 Tensiometer with a special cell containing the piezoelectric sensor

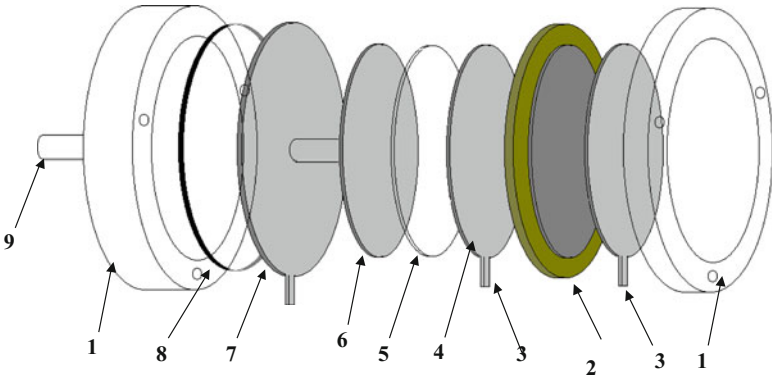

(1)- nylon cell;
(2)- PU/PZT sample;
(3)- electric connection;
(4)- metal plate for contact with the sample;
(5)- insulate film;
(6)- metal plate for contact with the oscillating electric field;
(7)- steel-carbon diaphragm;
(8)- rubber ring;
(9)- connection with the tensiometer.

Fig. 8.3 Special cell with piezoelectric composite sensor (*2*)

the composite sample. When the tensiometer water flows into the ground, the pressure will change in the composite film which responds with an electrical signal corresponding to the potential of water.

3 Acoustic Emission

Acoustic emission waves are elastic transient waves that arise from the sudden release of energy from a source located in a material [40–49]. Common sources of acoustic emission materials include mechanisms of initiation and growth of cracks, impact sources, delamination, etc. [40–42]. Waves resulting from acoustic emissions, in principle, are basically consisted of waves [40, 42]:

- Primary/longitudinal, known as type P waves.
- Shear/transverse known as type S waves.
- Rayleigh/surface basically consists of type P waves which are primary longitudinal waves and waves of S type.
- In addition it has reflected and refracted waves.

The speed at which an elastic wave propagates in a material will depend on the characteristics of the medium and the propagation mode. In planar structures, the propagation velocity of a longitudinal wave (C_L) and transverse (C_T) are given by the relationship [40, 42]:

$$C_L = \sqrt{\frac{E}{\rho}} \tag{8.8}$$

and

$$C_T = \sqrt{\frac{E}{2\rho\,(1+\nu)}} \tag{8.9}$$

where E = Young's modulus, ρ = density, and ν = Poisson modulus.

As the acoustic wave (signal) propagates, Lamb waves become the dominant mode of propagation and play an important role in AE tests. These originate from the vibration of the planar structure (plate) [42]. Lamb waves are formed by extensional or symmetric and antisymmetric or flexural waves so that flexural waves have lower frequencies than extensional one [40, 41]. The speed of Lamb waves directly depends on the thickness, frequency, and propagation mode. The speeds for extensional and flexural modes of a wave in a planar isotropic medium are given by the relations [42]:

$$C_e = \left[\frac{E}{\rho\,(1-\nu^2)}\right]^{1/2} \tag{8.10}$$

$$C_f = \left[\frac{EL^2}{12\rho\,(1-\nu^2)}\right]^{1/4} \omega^{1/2} \tag{8.11}$$

in which L is the thickness of the flat and ω the angular frequency. According to the classical theory of elastic wave propagating, waves with various propagation modes can simultaneously move in the material without directly interfering each other. Thus, the motion of a material point is the sum of the various modes of propagation of an elastic wave. As the elastic waves are propagating in a medium, they suffer attenuation processes characterized by a decrease in its amplitude. The elastic wave attenuation is given by the ratio between the energy of the wave, and its variation ΔE suffered along the propagation of a wavelength:

$$Q = \frac{2\pi E}{\Delta E} \tag{8.12}$$

For complex materials with pure elastic behavior, Q goes to infinite because ΔE is zero.

Thus, acoustic emission (AE) technique is to measure and store information of elastic waves by means of sensors arranged on the surface or in situ in a given material so as to extract information about the nature of the emission source. Lamb waves in flexural mode play an important role in acoustic emission technique mainly due to its high amplitude. Piezoelectric materials are commonly used as acoustic emission sensors. Among them, the most used are the ferroelectric ceramics by having mostly high piezoelectric coefficient, high Curie temperature, and low manufacturing cost, and PZT is the most used commercially. Acoustic emission sensors must have a good response over a wide frequency range, and this response is flat; acoustic and electrical impedance of the material must be very close to the studied material, and the sensor should have a low mechanical quality factor. These requirements generate limitations or reduction in the performance of such sensors fabricated from ferroelectric ceramics depending on the material to be monitored. In civil engineering, acoustic emission technique has been extensively studied over the years for the nondestructive monitoring structures. In this case, the most common material used in building processes is concrete. Problems associated with high differences in the values of dielectric constant and acoustic impedance between the concrete and piezoelectric sensors generate scattering and attenuation of elastic waves, and distortions appear on the electric signal generated by them.

In civil engineering, concrete is the most widely used material, and monitoring the structural integrity continuously is of great interest [50]. Determining quickly and accurately some problems in buildings can be the difference between life and death of many and can reduce maintenance costs by preventing or detecting damage sooner [51]. Among the nondestructive techniques, the use of piezoelectric transducers deserves special attention by the property of transforming a mechanical deformation into an electrical signal [52]. However, transducers made from conventional materials (PZT ferroelectric and polymer) are not suitable for

concrete structures. Due to the difference in electromechanical properties between the ceramic and concrete or between the pure polymer and concrete, the electric signals that come from the structure and represent its internal behavior can be distorted not allowing an accurate evaluation [53].

One of the devices widely used to evaluate structures in civil engineering is the "strain gauge" which measures the deformation of the object. However, the sensor elements (wires) are disposed on a dielectric (usually a polymer) which is stuck on the structure being evaluated. Thus, the strain measurement is actually the deformation of the polymer and not of the structure. Then, the cement-based composite becomes the nearest sensor of the concrete structure, and the signals from the structure to be analyzed will be more real. The motivation for the development of piezoelectric composite materials results from the need to achieve particular properties of a material, which cannot be found in materials with a single phase [54]. One of the advantages of the composite compared to the pure ferroelectric ceramic or pure ferroelectric polymer is the combination of properties of the constituents of the composite material, resulting in increased resistance against shocks and increased figure of merit which influences the sensitivity of the material, and also there is possibility to change the dielectric constant of the material, which is related with the poling process.

4 0-3 Connectivity Pattern Composite Fabrication

The composite polymer/ceramic was obtained by mixing piezoelectric ceramic (PZT) in the powder form with castor oil-based polyurethane (PU). Through the technique of "spin coating," the composite was obtained in the form of films with thicknesses between 70 and 300 μm. In this case, the desired film thickness can be partially controlled by the rotational speed of the spin coating system. The composite PZT/PU was obtained with 0-3 connectivity, where ceramic particles are dispersed in the polymer matrix without any contact between them. The diagram below gives an idea of the process to obtain the composite film.

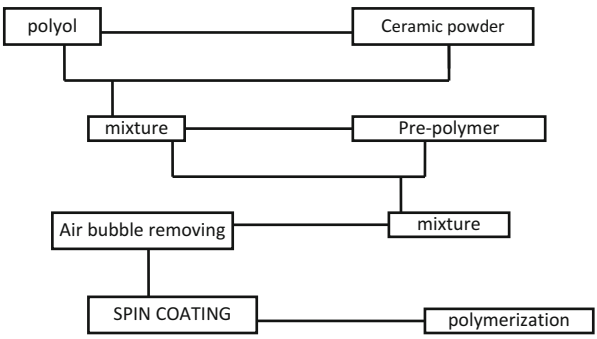

Schematic diagram to obtain PZT/PU composite

The vegetable-based PU results from the reaction of isocyanate and ester of ricinoleic acid. The composition of PZT:/PU used was 33:67 vol% of ceramic. The composition is obtained using the Eq. (8.13). Aluminum electrodes of a circular area of 1.0 cm diameter were deposited on both sides of the sample for electrical contact. The samples were poled at 373 K for 1 h by applying a DC electric field of 10 MV/m. The composites samples were placed in silicone oil bath during poling to avoid premature breakdown.

$$M_c = M_p \frac{\rho_c}{\rho_p} \left(\frac{\varnothing_c}{1 - \varnothing_c} \right) \tag{8.13}$$

here M is the mass, ρ is the density, and ϕ the ratio: c is related with the ceramic phase and p to the polymer.

5 1-3 Connectivity Pattern Composite Fabrication

To make 1-3 composite, first PZT was obtained in the wire form making up a mixture of PZT powders with water-based polyurethane in a proportion of 95 vol% ceramic calculated by Eq. (8.13). Using a syringe, the mixture PZT/PU was extruded onto a glass plate (Fig. 8.4a), and dried in an oven at 70 °C for 20 min. After that, the PZT wire was sintered at 1260 °C for 2 h when the polymer phase is removed (Fig. 8.4b).

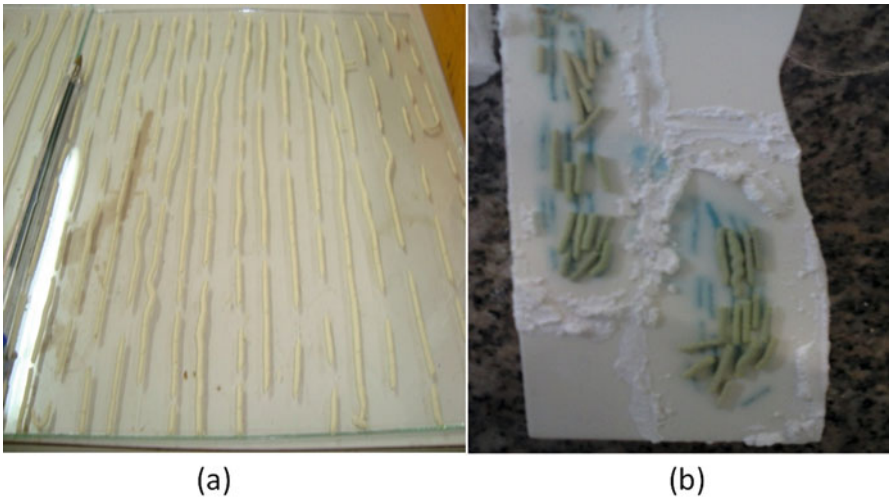

Fig. 8.4 (**a**) PZT wire extruded onto glass plate; (**b**) After sintering

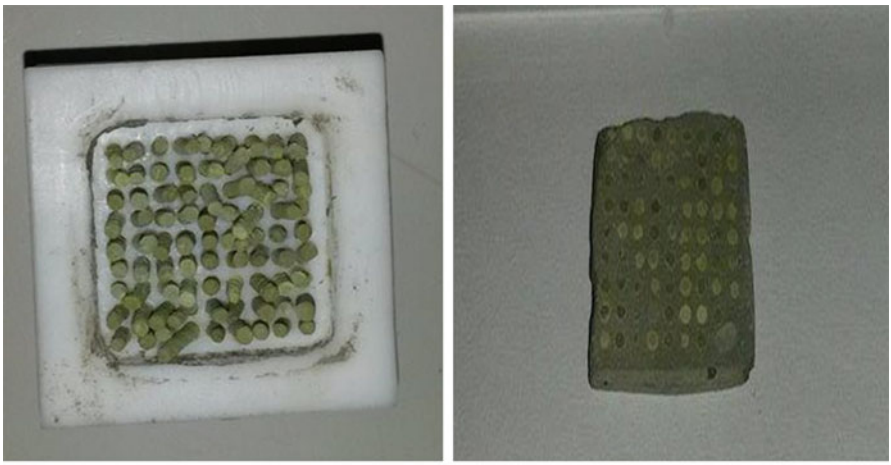

Fig. 8.5 (**a**) PZT wires in Teflon mold. (**b**) Final sample: lighter color is PZT

Table 8.1 d_{33} x poling electric field for a 0-3 PZT/PU 33 vol% composite

E (MV/m)	t (min.)	T (°C)	d_{33}(pC/N)
6	60	110	12.5
10	60	110	15.6
12	60	110	24.0

The composite PZT/cement was obtained using a Teflon mold where the PZT wires were placed as shown in Fig. 8.5a; for further filling with cementitious mass and drying, the sample was sanded to reduce the thickness and uniformity of the surface (Fig. 8.5b). Silver paint electrodes were placed on both sides of the sample to the polarization process and subsequent electromechanical measurement. The samples are of square shape with 18 mm side and an average thickness of 1 mm.

6 Composite Characterization

The poling process of a two-phased sample requires a higher bias field and also a greater polarization time since part of the electric field is lost in the polymer phase and does not reach the ferroelectric ceramic particles. The studies of the poling process of a 0-3 PZT/PU composite with 33 vol% of ceramic dispersed in the castor oil-based polymer were published in early work [55], and it can be summarized as shown in Tables 8.1, 8.2, and 8.3. which means, the better condition to poling the composite sample is $T = 110$ °C, $t = 60$ min, and $E = 12$ MV/m. For higher poling electric field, the piezoelectric coefficient should be higher, but the breakdown of the polymer is a limitation.

Table 8.2 d_{33} x poling time for a 0-3 PZT/PU 33 vol% composite

E (MV/m)	*t* (min.)	*T* (°C)	d_{33}(pC/N)
12	30	110	11.0
12	60	110	23.8
12	90	110	24.0

Table 8.3 d_{33} x poling temperature for a 0-3 PZT/PU 33 vol% composite

E (MV/m)	*t* (min.)	*T* (°C)	d_{33}(pC/N)
10	60	60	7.3
10	60	900	10.0
10	60	110	11.50

Table 8.4 d_{33} as a function of poling field

E (MV/m)	*T* (°C)	*t* (min)	d_{33} (pC/N)
0.60	60	60	158
0.76	60	60	163
0.91	60	60	189
1.01	60	60	213
1.21	60	60	226

Sample with 3.3 mm thickness

The poling process of the 1-3 composite samples is easier than of the 0-3 one because the applied electric field goes straight to the ceramic phase without any loss in the polymer phase. The first consequence is the lower electric field used in the process. Table 8.4 shows the piezoelectric coefficient behavior of a 1-3 PZT/cement composite.

Figure 8.6 shows the behavior of the relative dielectric constant in the frequency range of 1 kHz to 1 MHz. In that range of frequency, there is no significant variation in the constant value. It can be seen in Fig. 8.6 the decreasing of the constant for increasing PU content in relation to the cement. The target is to bring the dielectric constant of the composite closer to the concrete. The presence of the polymer in the matrix makes the composite material mechanically more resistant (Table 8.5).

7 The 0-3 PZT/PU Composite as Soil Humidity Sensor

Figure 8.7 shows the vegetable-based piezoelectric composite (different color) placed in a special cell (Fig. 8.3) and excited by an oscillating electric field that provides the AC signal required for piezoelectricity. The vacuum pump changes the pressure in the system and is monitored by the pressure gauge. The voltmeter measures the electrical signal from the piezoelectric sensor. The applied exiting square wave had 2.4 kHz frequency and 5.0 V peak-to-peak amplitude, and the pressure range was 0–608 mmHg. The calibration curve is shown in Fig. 8.8 [39].

To test the composite PZT/PU as a sensor, a soil sample, which had already been analyzed using an Hg manometer by the Department of Soil Science and

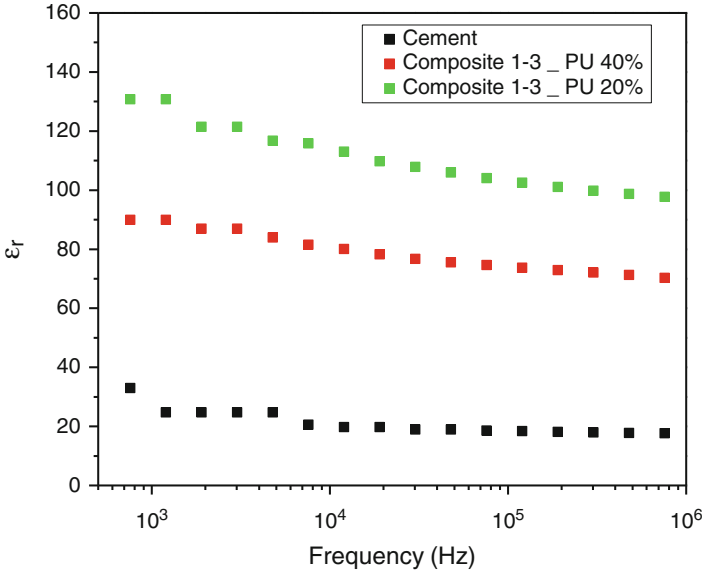

Fig. 8.6 Relative dielectric constant of cement and 1-3 composite with different PU rate as a function of frequency

Table 8.5 Comparison of relative dielectric constant $\mathbf{d}_{33}$ of some 1-3 cement-based composites

Matrix	Ceramic	Connectivity	d_{33} (pC/N)	ε_r	Ref.
Cement	PMN	1-3	213	278	[56]
Cement	PMN	1-3	264	450	[57]
Cement + PU 20%	PZT	1-3	226	131	This work
Cement + PU 40%	PZT	1-3	226	90	This work

Rural Engineering, UNESP/Ilha Solteira, was used. Experimental data were fitted by a computer program together with the Van Genuchten model. Table 8.6 shows the experimental data for three depths commonly used in soil analysis and the Genuchten parameters in Eq. 8.5 and that are listed in Table 8.7.

With the data from Tables 8.6 and 8.7, the soil retention curve can be obtained as shown in Figs. 8.9 and 8.10 using sensors, Hg manometer, and PZT/PU composite, respectively [39].

As it can be seen, there is good agreement between the two results, and the piezo composite can be proposed as a soil humidity sensor with the advantage that the monitoring of soil conditions can be made remotely.

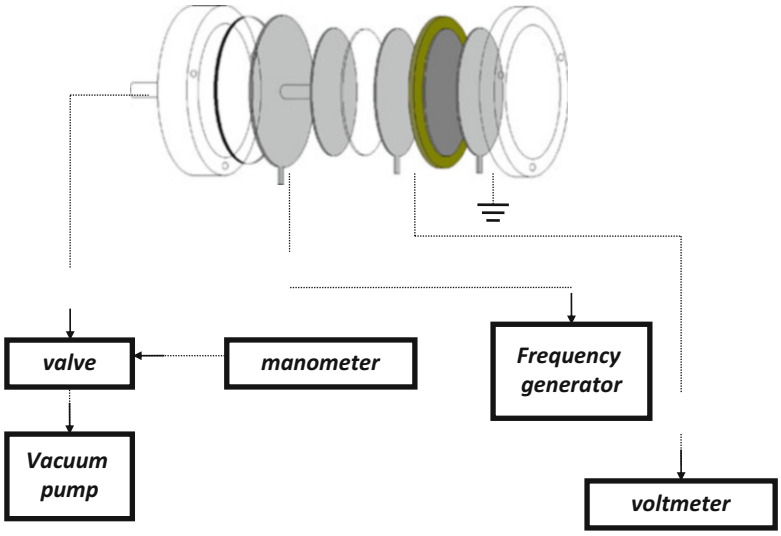

Fig. 8.7 Simulation of a tensiometer, for measures piezoelectric transduction of the sensor in relation to pressure variation in the system

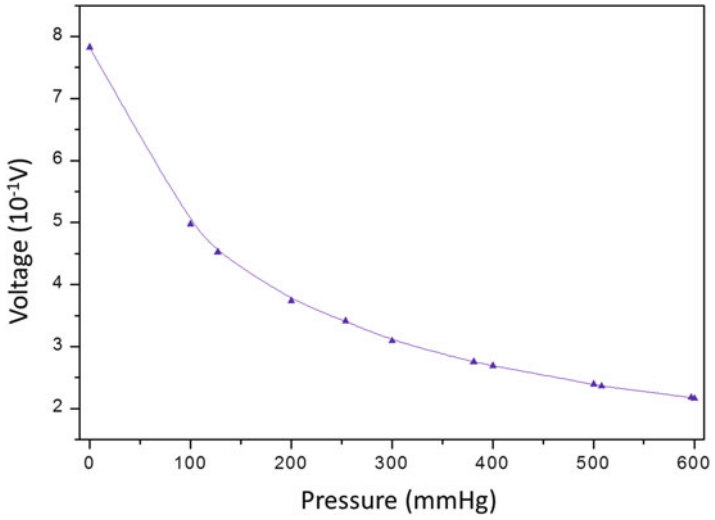

Fig. 8.8 Electrical signal from the sensor in response to the pressure variation

8 1-3 PZT/Cement/PU Composite as Acoustic Emission (AE) Sensor

As mentioned in many works [46, 53, 58–60], acoustic emission is a transient phenomenon in which elastic waves are generated by the rapid release of energy from a source of the material or structure. Thus, this technique is well suited

Table 8.6 Matric potential and volumetric humidity at three different depths [39]

Ψ_m(mmHg)	θ (cm^3/cm^3) 15 cm	θ (cm^3/cm^3) 30 cm	θ (cm^3/cm^3) 45 cm
0	0.281	0.330	0.370
0.735	0.281	0.320	0.350
2.941	0.280	0.290	0.280
7.353	0.200	0.240	0.230
22.059	0.170	0.210	0.200
36.765	0.150	0.180	0.181
73.529	0.140	0.150	0.170
367.647	0.102	0.140	0.150
1102.941	0.100	0.130	0.130

Table 8.7 Genuchten model parameters in Eq. 8.5 [39]

Parameters	15 cm	30 cm	45 cm
α	0.0286	0.018	0.0643
m	0.0183	0.4602	0.2128
n	27.443	10,182	2.085
θ_r	0.100	0.130	0.130
θ_s	0.281	0.330	0.370

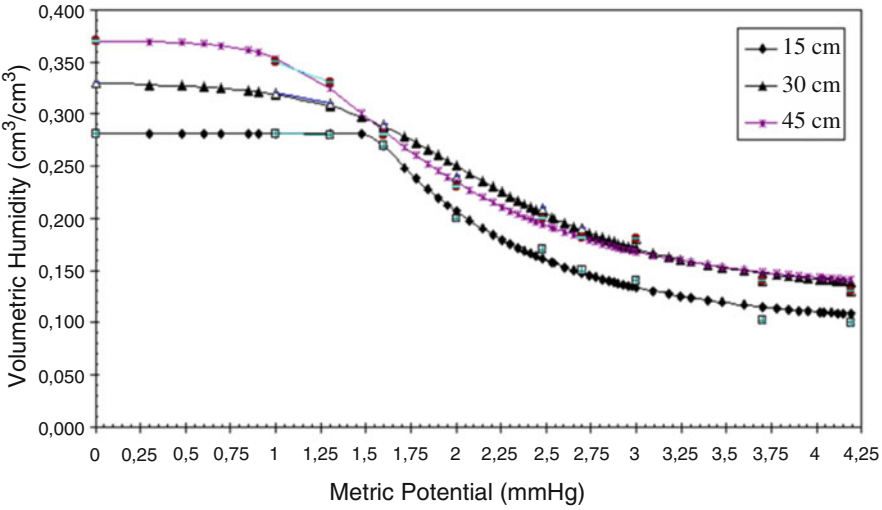

Fig. 8.9 Retention curve using conventional Hg manometer

for monitoring the structure in an accurate, fast, and nondestructive way. Early determination of the beginning of a structural failure can be the difference between life and death for many. Also, the maintenance of the structure may be less costly if done at the proper time.

Embedded into or surface mounted on the structure the acoustic emission sensor can provide a quick response to crack growth inside the structure transforming the

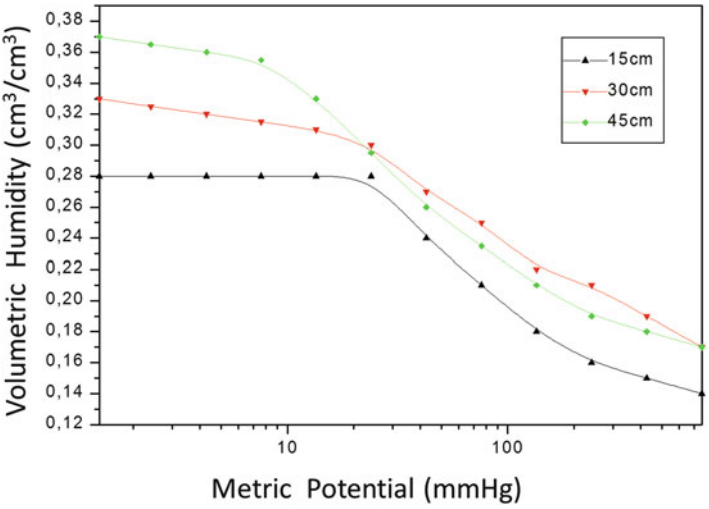

Fig. 8.10 Retention curve using PZT/PU sensor

received mechanical stress of the elastic waves into an electrical signal. In this work the composite PZT/cement/polymer was surface mounted onto a concrete block, and to characterize it as AE sensor, the block was excited with two different simulated AE sources: ball bearing drop, which provides relatively large amplitude and low-frequency stress waves and pencil lead break (Hsu-Nielsen) [61] producing stress waves with low amplitude and high frequency. The sensor response can be observed and stored in an oscilloscope.

To monitor structure in civil engineering, the AE sensor should match acoustic impedance with the concrete, which is the most used material. Also, the sensor should respond in a broadband frequency. Figure 8.11 shows the electrical response of the sensor to a pencil lead break test, which was carried out according to Hsu-Nielsen. Silver paint was used on the two faces of the composite as electrodes and the sensor response was stored in an oscilloscope Agilent model DSO6012A – 100 MHz.

The sensor was mounted on the surface of the concrete block and the graphite was broken close to it. This test simulates the release of energy when, for example, a crack in concrete block occurs. Applying the Fourier transform of the measured signal in the time domain, it has the behavior of the sensor response in the frequency domain, as shown in Fig. 8.12. It can be seen a flat sensor response in a wide range of frequency as expected for an AE sensor.

It can be seen in Fig. 8.12 and 8.14 the difference in the amplitude and frequency of the AE events as predicted by theory. The higher signal from the ball bearing simulated AE source is very clear (Fig. 8.13) in comparison with the pencil lead break response (Fig. 8.11).

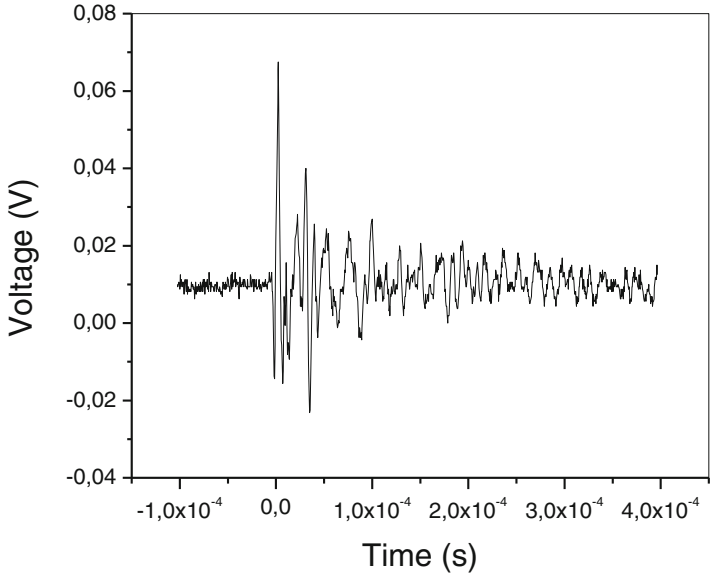

Fig. 8.11 Waveform from the surface mounted 1-3 sensor in time domain

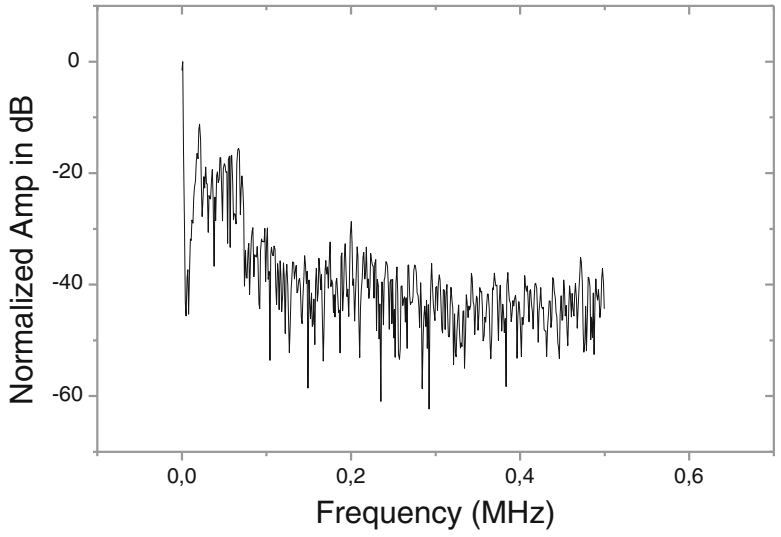

Fig. 8.12 dB spectrum in frequency domain

9 Concluding Remarks

Polymer matrix and cement-polymer matrix composites were obtained with 0-3 and 1-3 connectivity, respectively. After appropriate polarization process, the composites have been used as sensors because they can transform mechanical energy into

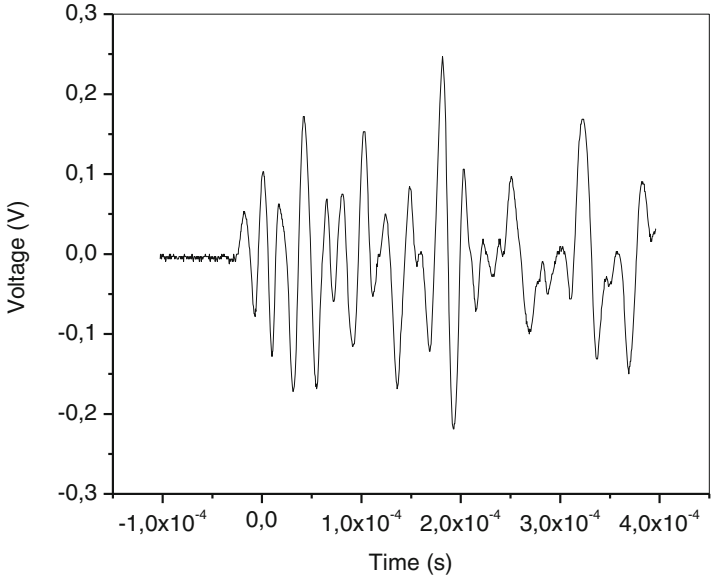

Fig. 8.13 Time domain sensor response for a ball bearing drop

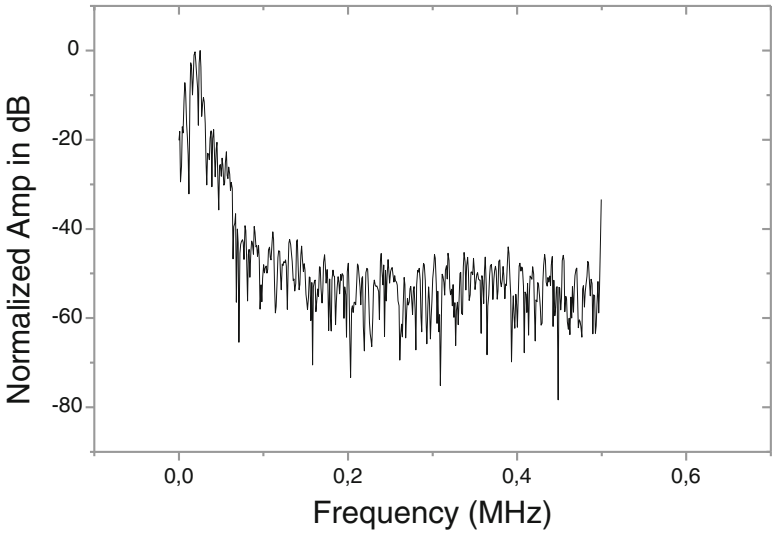

Fig. 8.14 dB spectrum in frequency domain of the ball bearing test response.

electric energy. The 0-3 composite was obtained in the film form, and using a special nylon cell, it was proposed as a substitute for mercury manometer in a tensiometer to measure the matric potential of soil water.

The negative pressure caused by the flow of water from the tensiometer to the soil is determined by PZT/PU sensor, and through a calibration curve of pressure x electrical voltage, the water retention curve can be obtained using the Genuchten equation. For measurements in standard depths of soil analysis, the obtained result is in agreement with the measurements of a mercury manometer. The advantage of using this sensor instead of the conventional Hg manometer is the possibility of automating all control systems of soil water content measurement and helping in the wireless sensor networks in precision agriculture.

Composites with 1-3 connectivity were obtained using cement and water-based polyurethane as a matrix. A Teflon mold was used to arrange the PZT wires, spaced homogeneously to avoid contact between them. The use of the polyurethane in the matrix is to obtain a sensor material with dielectric constant closer to the concrete due to problems encountered with the large difference in properties between the structure to be observed and the sensor material.

Increasing the percentage of PU in relation to the cement, it is observed that a decrease in the dielectric constant and the value begins to approach to the value of the dielectric constant of the concrete. The piezoelectric composite was surface mounted on a concrete block and subjected to the acoustic emission test, namely, ball bearing drop and pencil lead break. As expected from an AE sensor, the response is flat in a quite large range of frequency. The sensitivity is enough to detect AE events, and there is no need for signal amplification to be observed. Given the above, it can be stated that the composite PZT/PU and PZT/cement/PU can be used as a soil humidity sensor and acoustic emission sensor, respectively.

Acknowledgments Thanks are due to Fundação de Amparo à Pesquisa do Estado de São Paulo – FAPESP – a Brazilian funding agency (CEPID 2013/0796-2) for the partial financial support.

References

1. Reece PL (2006) Smart materials and structures: new research, 2nd edn. Science Publishers, New York, 292 p
2. Qi Y et al (2010) Piezoelectric ribbons printed onto rubber for flexible energy conversion. Nano Lett Washington 10(2):524–528
3. Ramadan KS, Sameoto D, Evoy S (2014) A review of piezoelectric polymers and functional materials for electromechanical transducers. Smart Mater Struct 23(3):033001
4. Park KI et al (2012) Flexible nanocomposite generator made of $BaTiO_3$ nanoparticles and graphitic carbons. Adv Mater 24:2999–3004
5. Lai X, Halpert JE, Wang D (2012) Recent advances in micro/nano-structured hollow spheres for energy applications: from simple to complex systems. Energy Environ Sci 5:5604–5618
6. Hua WX, Jic Y, Lin JY, Chao N-Y (2015) Simulation experiment on acoustic emission of pipeline leakage. Int J Smart Home 9(2):243–252
7. Wada Y (1982) Electronic properties of polymers. In: Mort J, Pfister G (eds) Piezoelectricity and pyroelectricity. Wiley, New York, pp 109–159
8. Kawai H (1969) The piezoelectricity of poly (vinylidene fluoride). Jpn J Appl Phys 8:975
9. Das-Gupta DK (1991) Pyroelectricity in polymers. Ferroelectrics 118:165
10. Wada Y (1984) Theoretical analysis of temperature dependence of complex piezoelectric constant and pyroelectric constant of poly (vinylidene fluoride). Ferroelectrics 57:343

11. Dias CJ, Das-Gupta DK (1994) Piezo-and pyroelectricity in ferroelectric ceramic-polymer composites. Key Eng Mater 92-93:217
12. Wong CK, Wong YW, Shin FG (2002) Effect of interfacial charge on polarization switching of lead zirconate titanate particles in lead zirconate titanate/polyurethane composites. J Appl Phys 92(7):3974–3978
13. Safari A (1994) Development of piezoelectric composites for transducers. J Physique III 4:1129
14. Sripada S, Unsworth SJ, Krishnamurty M (1996) PZT/polymer composites for medical ultrasound. Mat Res Bul 31(6):731–739
15. Cui C, Baughman RH, Iqbal Z, Dazmar T, Dahlstrom D (1998) Improved piezoelectric s for hydrophone applications based on calcium-modified lead titanate/poly(vinylidene fluoride) composites. Sensors Actuators A 65:76–85
16. Newnham RE, Skinner DP, Cross LE (1978) Connectivity and piezoelectric-pyroelectric composites. Mater Res Bull 13:525–536
17. Furukawa T, Fujino K, Fukada E (1976) Electromechanical properties in the composites of epoxy resin and PZT ceramics. Jpn J Appl Phys 15(11):2119–2129
18. Das-Gupta DK, Abdullah J (1988) Electroactive properties of polymer-ceramic composites. Ferroelectrics 87:213
19. Takeuchi H, Jyomura S, Nakaya C (1985) New piezoelectric materials for ultrasonic transducers. Jpn J Appl Phys 24(Suppl. 2):36–40
20. Furukawa T (1989) Piezoelectricity and pyroelectricity in polymers. IEEE Trans Electr Insul 24:375
21. Abdullah MJ, Das-Gupta DK (1990) Electrical properties of ceramic/polymer composites. IEEE Trans Electr Insul 25(3):605–610
22. Clegg WW, Jenkins DF, Cunningham MJ (1997) The preparation of piezoceramic–polymer thick films and their application as micromechanical actuators. Sensors Actuators A 58: 173–177
23. Ramazanov MA, Panakhova ZG (1997) Composite piezoelectric transducer for the registration of arterial pulse waves. Instrum Exp Tech 40(5):708–710
24. James NK et al (2014) Piezoelectric and mechanical properties of fatigue resistant, self-healing PZT-ionomer composites. Smart Mater Struct 23:055001–055008
25. Dias CJ, Das-Gupta DK (1996) Inorganic ceramic/polymer ferroelectric composite electrets. Ferroelectrics 3(5):706–734
26. James NK et al (2013) Piezoelectric and mechanical properties of structured PZT-epoxy composites. J Mater Res 28:635–641
27. Chen Y, Chan HLW, Choy CL (1998) Pyroelectric properties of PbTiO3/P(VDF–TrFE) 0–3 nanocomposite films. Thin Solid Films 323(1–2):270–274
28. Sa-Gong G, Safari A, Jang SJ, Newnham RE (1986) Poling flexible piezoelectric composites. Ferroelectr Lett 5:131
29. Macdonald GA (1990) A review of low cost accelerometers for vehicle dynamics. Sensors Actuators A A21-A23:303–307
30. Shiozaki M, Kamiya S, Kuroyanagi M, Matsui K, Kizu R (1991) High speed control of damping force using piezoelectric elements. SAE Trans 100:884
31. Bhalla S, Suresh R (2013) Condition monitoring of bones using piezo-transducers. Meccanica 48:2233–2244
32. Gururaja TR, Schulze WA, Cross LE, Newnham RE (1985) Piezoelectric composite materials for ultrasonic transducer applications. I. Resonant modes of PZT rods-polymer composites. IEEE Trans Sonics Ultrasonics SU-32:499
33. Mort J, Pfister G (1982) Electronic properties of polymers. Wiley, New York
34. Richerson DW (1982) Modern ceramic engineering properties, processing and use in design. Marcel Dekker Inc, New York
35. Callen HB (1985) Thermodynamics and an introduction to thermostatistics, 2nd edn. Wiley, Canadá
36. Whalley WR, Ober ES, Jenkins M (2013) Measurement of the matric potential of soil water in the rhizosphere. J Exp Bot. doi:10.1093/jxb/ert044

37. Yang X, You X (2013) Estimating parameters of van Genuchten model for soil water retention curve by intelligent algorithms. Appl Math Inf Sci 7(5):1977–1983
38. Van Genuchten M (1980) A closed-form equation for predicting the hydraulic conductivity of unsaturated soils. Soil Sci Soc Am J 44:892–898
39. Sakamoto WK, Malmonge JA, Fernandes SH (2004) Ferroelectric ceramic/polymer composite for soil-humidity detection. Sens Transducers Mag 39(1):112–120
40. Grosse CU, Ohtsu M (eds) (2008) Acoustic emission testing. Springer, Leipzig/Berlin Heidelberg
41. The Japanese Society for Non-Destructive Inspection (2006) Practical acoustic emission testing. Springer, Tokio
42. Kaphle M, Tan A, Andy C, Thambiratnam D (2009) Structural health monitoring of bridges using acoustic emission technology and signal processing techniques. 13th Asia Pacific Vibration Conference. University of. Canterbury, Christchurch, pp 1–11
43. Zhao P, Kim S, Hinderliter B (2015) Investigation of cement–sand-based piezoelectric composites. J Intell Mater Syst Struct 27:1–7
44. Qin L et al (2009) The application of 1–3 cement-based piezoelectric transducers in active and passive health monitoring for concrete structures. Smart Mater Struct 18:1–8
45. Li Z et al (2007) An investigation on 1–3 cement based piezoelectric composites. Smart Mater Struct 16:1–8
46. Qin L, Ren H-W, Dong B-Q, Xing F (2014) Acoustic emission behavior of early age concrete monitored by embedded sensors. Materials 7:6908–6918
47. Or SW, Chan HLW, Choy CL (2000) P(VDF-TrFE) copolymer acoustic emission sensors. Sensors Actuators 80:237–241
48. Iliopoulos SN, El Khattabi Y, Aggelis DG (2016) Towards the establishment of a continuous nondestructive monitoring technique for fresh concrete. J Nondestruct Eval 35:35–37
49. Sakamoto WK et al (2006) PTCa/PEEK composite acoustic emission sensors. IEEE Trans Dielectr Electr Insul 13:1177–1182
50. Yang Y, Hu Y, Lu Y (2008) Sensitivity of PZT impedance sensors for damage detection of concrete structures. Sensors 8:327–346
51. Dong B, Xing F, Li Z (2011) Cement-based piezoelectric ceramic composite and its sensor applications in civil engineering. ACI Mater J 108(5):543–549
52. Grosse CU, Kruger M, Glaser SD (2006) Wireless acoustic emission sensor networks for structural health monitoring in civil engineering. 9th European Conference on Non-destructive Testing. Berlin. ECNDT, Tu1.7.3:1–8
53. Nair A, Cai CS (2010) Acoustic emission monitoring of bridges: review and case studies. Eng Struct 32:1704–1714
54. Giurgiutiu V, Zagrai A, Bao JJ (2002) Piezoelectric wafer embedded active sensors for aging aircraft structural health monitoring. Struct Health Monit 1:41–61
55. Sakamoto WK, Shibatta-Kagesawa S, Kanda DHF, Fernandes SH, Longo E, Chierice GO (1999) Piezoelectric effect in composite polyurethane-ferroelectric ceramics. Phys Stat Sol A 172:265–271
56. Jinrui H et al (2015) A new smart traffic monitoring method using embedded cement-based piezoelectric sensors. Smart Mater Struct 24:1–8
57. Youyuan L, Zongjin L (2008) Cement-based piezoelectric sensor for acoustic emission detection in concrete structures. Earth Space Int Conf Eng Sci Constr Oper Challenging Environ ASCE Am Soc Civil Eng 1–12. doi:http://dx.doi.org/10.1061/40988(323)155
58. Gorman MR (1991) Plate wave acoustic emission. J Acoust Soc Am 90:358–364
59. Chan HLW, Or SW, Choy CLP (2000) P(VDF – TrFE), copolymer emission sensors. Sensors Actuators A 80:237–241
60. Wenger MP, Blanas P, Shuford RJ, Das-Gupta DK (1999) Characterization and evaluation of piezoelectric composite bimorph for in situ acoustic emission sensors. Polym Eng Sci 39(3):508–518
61. Sause MGR (2011) Investigation of pencil-lead breaks as acoustic emission sources. J Acoustic Emission 29:184–196

Chapter 9
Functional Nanomaterials for Applications in Energy Storage and Conversion

Mario Godinho Junior, Rosana de Fátima Gonçalves, Kellen Cristina Mesquita Borges, Murillo Henrique de Matos Rodrigues, Maurício Roberto Bomio Delmonte, Fabiana Villela da Motta, and Rubens Maribondo do Nascimento

1 Electrochemical Power Source

Up to the mid-1970s, energy demands could be successfully supplied by fossil fuels. The conventional technology was adapted to the requirements of the consumer electronics and of the automobile market. Since that time, the situation abruptly changed as consequence of a series of major events, namely, the oil crisis, the worldwide extent of the consumer electronic market, miniaturization and portability of electronic devices, and concerns about air pollution.

The consumption of energy provided by fossil fuels, such as natural gas, coal, and crude oil, has abruptly increased during the twentieth century. In fact, it involves as far as an 85% of worldwide energy consumption [1]. These energy resources of widespread use are not obviously renewable, which may risk to bring to an end these limited natural resources.

In the transport domain, some debate is set between the predominance of classical gasoline propulsion [2] and alternatives fuels. Proposal exists to substitute propelled by electric vehicles (EVs) or, at least, hybrid electric vehicles (HEVs), which are much more environmentally friendly and more economic [3].

The term "battery" is, in fact, a general word that can be referred to many subjects. It is usually used to describe an assembly of units connected to achieve

M.G. Junior (✉) • K.C.M. Borges • M.H. de Matos Rodrigues
Federal University of Goiás (UFG), Goiania, Brazil
e-mail: godinho.mj.ufg@gmail.com; kellen_cmb@hotmail.com; murillo.matos@live.com

R. de Fátima Gonçalves
Federal University of São Paulo (UNIFESP), São Paulo, Brazil
e-mail: rosanaf.gon@gmail.com

M.R.B. Delmonte • F.V. da Motta • R.M. do Nascimento
Federal University of Rio Grande do Norte (UFRN), Natal, Brazil
e-mail: mauricio.bomio@ct.ufrn.br; fabiana@ct.ufrn.br; rmaribondo@ufrnet.br

E. Longo, F.A. La Porta (eds.), *Recent Advances in Complex Functional Materials*,
DOI 10.1007/978-3-319-53898-3_9

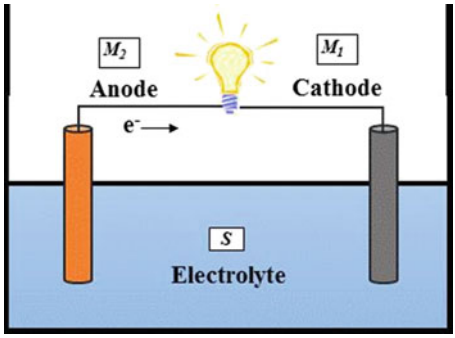

Fig. 9.1 Schematic design of a galvanic cell

a common goal. Thus, the assembly of galvanic cells, both on parallel or series, to reach the adequate capacity or potential, respectively, is also designed as a battery.

A typical galvanic cell is a simple device that enables the energy released in a spontaneous redox reaction to be directly converted into electricity [4]. In its basic scheme, an electrochemical cell is constituted by two electrodes (e.g., M_1 and M_2) which act as electrons carriers, in general, separated by an electrolyte (e.g., S) which provides ionic transport between the electrodes and also electric isolation. A schematic design of a galvanic cell is shown in Fig. 9.1.

At the contact between the metal M phase and the electrolyte phase S, a potential $E_{M/S}$ arises from the balance of the Fermi energy levels F_M and F_S. This balance is set by charge transfer from the electrode to the electrolyte or vice versa, according to the redox properties of the electrode materials. This, in turn, is associated with the establishment of a redox equilibrium leading to an oxidation process at one electrode/electrolyte interphase,

$$M_2 \rightleftarrows {M_2}^{n+} + n\,\mathrm{e}^- \tag{9.1}$$

The electrons produced may be driven by an external circuit to the second electrode where are involved in reduction process at the interphase:

$$M_1 + n\,\mathrm{e}^- \rightleftarrows {M_1}^{n-} \tag{9.2}$$

Hence, the electric current circulating through the external circuit yields an *electromotive force* E between the electrodes, which may be expressed as the difference of their potentials:

$$E = E_{M1/S} - E_{M2/S} \tag{9.3}$$

and is notably associated with the overall process:

$$M_1 + M_2 \rightleftarrows {M_1}^{n-} + {M_2}^{n+} \tag{9.4}$$

$E_{M1/S}$ is the potential of the positive electrode, e.g., the electrode which provides electrons to the electrolyte species (reduction process), and$E_{M2/S}$ is the potential of the negative electrode, e.g., the electrode which accepts electrons from the electrolyte species (oxidation process). In the most common convention, the positive electrode is called *cathode* and the negative electrode *anode*. The overall potential of the galvanic cell is measured as the difference of both electrode potentials:

$$\Delta E^{\circ} = E^{\circ}{}_{\text{Cathode}} - E^{\circ}{}_{\text{Anode}} \tag{9.5}$$

By operating as a power source, the electrochemical cell converts chemical energy to electrical energy:

$$\Delta G^{\circ} = -n\,F\Delta E^{\circ} \tag{9.6}$$

Where ΔG° is the Gibbs free energy, n is the number of transferred electrons into the overall reaction Eq. (9.6), and $\Delta E^{\circ}$is the cell electromotive force.

When an external load is connected to cell, the anode starts to suffer the oxidation process giving electrons to the external circuit. At the other extreme, the cathode receives the incoming electrons to suffer the reduction process. The balance of charge is ensured by the ionic transport in the electrolyte. For this reason, the electrolyte must be an ionic conductor but an electronic isolator.

2 Lithium Batteries

Research on lithium batteries began in the late 1950s, and the first publication about the subject was written by Harris in 1958 [5]. Many different materials were considered for the active cathode material: sulfur dioxide, manganese dioxide, iron disulfide, and carbon monofluoride. The term "lithium battery," therefore, applies to many different types of chemistries, each using lithium as the anode but differing in cathode material, electrolyte, and chemistry as well as in design and other physical and mechanical features.

Among all the possible anode materials, lithium is perhaps the most attractive since it combines a favorable thermodynamic electrode potential with a very high specific capacity (3.86 Ah/g; 7.23 Ah/cm^3) and typical energy densities of up to 250 Wh/kg, which are twice as high as the best conventional aqueous systems [6].

The main goal of the initial developments of secondary lithium batteries was to research for materials which react reversibly with lithium as follows in Eq. (9.7):

$$x\text{Li}^{+} + A_zB_y\,(\text{s}) + x\text{e}^{-} \rightleftarrows \text{Li}_x A_z B_y\,(\text{s}) \tag{9.7}$$

Layered intercalation compounds, such as TiS_2, MoS_2, and V_6O_{13}, were profoundly investigated as a positive electrode due to their ability to host lithium ions in vacant sites, while charge transfer reaction takes place. This insertion reaction

is topotactic, which means that the structural changes induced in the host matrix are not too large and can be reverted when lithium is removed during the reverse reaction. Hence, in principle, these materials behave as a mixed ionic-electronic conductor. Meanwhile, the main drawbacks of these materials were the low cell voltage, near 2 V, and the safety problems arising from the use of metallic lithium as anode [7].

A great number of compounds have been researched including layered transition metal chalcogenides and metal oxides with either layered structure, as Li_xMO_2 (where M = Ni, Co, or Mn) [8, 9] or spinel structure as $LiMn_2O_4$ [10]. Nevertheless, these rechargeable lithium batteries, based on the use of lithium metal, were abandoned for the same reasons as in the case of primary lithium cells.

The most relevant characteristics of lithium cells are as follows:

- *High cell voltage.* They have working cell voltages of 3 V or even higher.
- *Flat discharge.* Cells in which the activities of the oxidized and reduced forms are invariant and offer highly stable working potentials during cell discharging.
- *Long shelf life.* Due to the formation of the passivating layer on the lithium anode surface, the self-discharge is minimized.

Wide operating temperature range Because of the low freezing point of nonaqueous solvents, in general, the lithium cells can work at temperatures ranging from −40 to 60 °C.

In contrast, several drawbacks need to be overcome. Namely, lithium metal rapidly oxidizes in aqueous media due to its high electropositive nature. Commonly, lithium salts are dissolved in aprotic organic solvents; however, these solvents are inherently less conductive than water. Moreover, some improvement in safety was requested because almost all organic solvents are flammable. It was soon demonstrated that lithium metal was stable in a number of organic electrolyte systems due to the formation of a passivating layer (*solid state interface or solid electrolyte interface*) which prevented chemical corrosion, ensures long shelf life, and permits cell discharge due to its ionic conductivity. A scheme of SEI is shown in Fig. 9.2.

A crucial impediment for an extended commercialization of lithium metal-based batteries was the nonhomogenous back-deposition of Li ions upon charging. This phenomenon leads to a kind of dendrite growth from the anode, crossing through the separator and arriving at the cathode which eventually induces a cell short circuit. Consequently, the internal temperature increases and further venting and flame of the cell may provoke accidents. In order to undertake a responsibility between high efficiency and safety, in 1980s, legions of scientists moved their research line to develop a new concept for rechargeable lithium batteries changing the lithium metallic by other anode materials.

In the early 1980s, a new concept of secondary lithium batteries was described [11]. Lithium-ion (Li-ion) batteries are comprised of cells that employ lithium intercalation compounds as the positive and negative materials. As a battery is cycled, lithium ions exchange between the positive and negative electrodes. They are

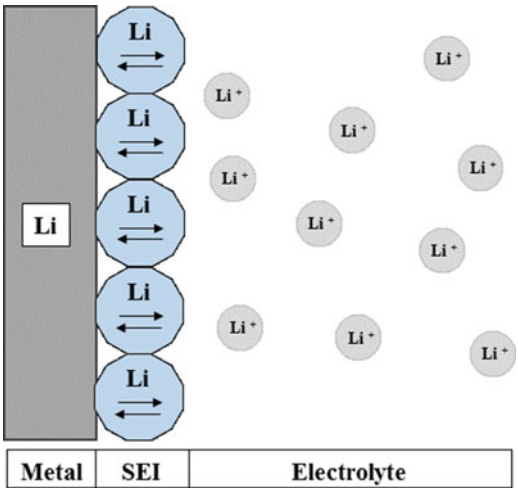

Fig. 9.2 Scheme of a solid electrolyte interface (SEI)

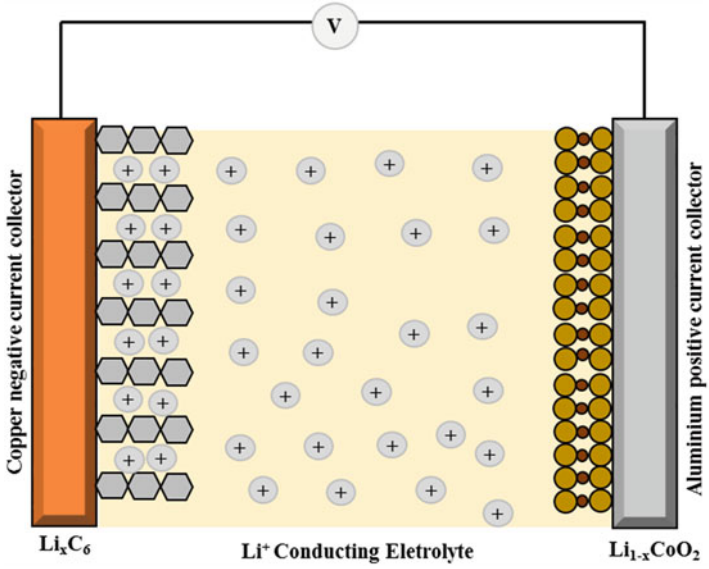

Fig. 9.3 Commercial lithium ion battery introduced in the marked by Sony Company

also referred to as rocking-chair batteries as the lithium ions "rock" back and forth between the positive and negative electrodes as the cell is charged and discharged. A scheme of the cell is shown in Fig. 9.3.

These systems are assembled in a discharged state – which is favorable to manufacturers – because lithium is initially present in the stoichiometry of the cathode material. Hence, a previous charge is needed before becoming entirely operational. Therefore, they must not be considered as one primary source of energy rather than energy storage devices (secondary batteries).

Eventually, in 1991, the Sony Company introduced the first commercial lithium-ion battery based on $LiCoO_2$ as a positive active material and as negative one's constituted by one or several forms of carbons, which the most usual is graphite, with an open circuit of 4.2 V and an operational voltage of 3.6 V [12]. Taking, for example, the Sony model previously commented, during the first charge the cell obeys an electrochemical process in which the negative Li_xC_6 electrode acts as a lithium ion sink, while a positive $LiCoO_2$ electrode acts as a lithium ion source. The overall process involves the cyclic transfer of x moles of lithium ions between the two insertion electrodes as follows in Eq. (9.8):

$$LiCoO_2\,(s) + 6\,C \underset{\text{Discharge}}{\overset{\text{Charge}}{\rightleftarrows}} Li_{1-x}CoO_2\,(s) + Li_xC_6\,(s) \tag{9.8}$$

The substitution of metallic lithium by graphite, which reversibly intercalates lithium into its structure, considerably improved the battery safety and long-term cycling.

3 Anode Materials

3.1 Carbonaceous Materials

Carbonaceous materials constitute a wide family of allotropes with structural and morphological diversity. Their classification is not an easy task, but we may distinguish between graphitized and nongraphitized carbons. In the latter group, it is usual to distinguish between glass-like carbons (hard carbons) which do not graphitize even if they are submitted to elevated temperatures, and soft carbon, readily graphitizable upon suitable thermal treatment. Hexagonal graphite is the allotrope most commonly used in lithium ion batteries, which has a layered structure, consisting of hexagonal graphene sheets of sp^2-carbon weakly bonded together by van der Walls forces into an ABAB ... stacking sequence along the c-axis. The lattice belongs to space group $P6_3/mmc$, with cell parameters $a = 0.246$ nm and $c = 0.6708$ nm, respectively, at room temperature.

Several types of carbonaceous materials, as well as graphite, can be intercalated or doped with different atoms and atomic groups between the layers to form the so-called graphite intercalation compounds (GICs). Lithium is not an exception to this phenomenon, and lithium-GIC is formed by doping graphite with lithium. At room temperature, graphite accepts sufficient lithium to form LiC_6 which in delithiation can deliver 372 mAh/g, as follows:

$$Li^+ + 6C + e^- \underset{\text{Charge}}{\overset{\text{Discharge}}{\rightleftarrows}} LiC_6 \tag{9.9}$$

It has been confirmed that the electrochemical intercalation of lithium in an aprotic organic electrolyte containing complex lithium salts, such as $LiPF_6$, $LiBF_4$, $LiAsF_6$, and $LiClO_4$, reduces graphite to form Li-GIC. Then, it can be electrochemically oxidized by lithium deintercalation to restore the raw material.

3.2 Tin Compounds

Lithium alloy-based electrodes have been developed since 1971 by Dey [13], who demonstrated by electrochemical experiments the Li-alloys formation in liquid organic electrolytes, a reaction that takes place reversibly in a Li-anode cell as follows.

$$\mathrm{Li_xM} \underset{\text{Charge}}{\overset{\text{Discharge}}{\rightleftarrows}} x\mathrm{Li}^+ + x\mathrm{e}^- + \mathrm{M} \tag{9.10}$$

During charge, the formation of the alloy is followed by several characteristic steps and/or slopes that are due to a reversible formation of the alloys. These steps can also be observed in the discharge process.

Metals, such as Al, Si, Sn, Pb, In, Bi, Sb, and Ag, which combine electrochemically with lithium, have been intensely studied due to the structural changes while alloying with lithium. An example of the changes, pure aluminum when reacting with approximately 7% of Li, the formation of α phase can be observed and when this amount increases around 47–56% a nonstoichiometric β phase can be achieved [14].

The brittle mechanical properties of the lithium alloys Li_xM are associated to highly ionic character. Therefore, the mechanical stresses during charge/discharge cycles causes marked specific volume changes in the alloys that can lead crack formation inducing loss of electrical contact and rapid decay in the capacity due to "pulverization" of the electrode.

The metallurgical structure and morphology of Li alloys (grain's size, shape, and texture) strongly affect their dimensional stability [15]. One possibility for counteracting the mechanical degradations is by the use of thin layers of alloys with small particle size (nanomaterials); thus, the changes in specific volume can be minimized avoiding the pulverization of the electrode.

Recently Fujifilm Celltech Co, Ltd. developed a material based in an "amorphous tin-based composite oxide" [16] for the negative electrode. The improvements in this material are a promising cycle life and high specific charge (>600 Ah/Kg) as well as charge density (>2200 Ah/L) [17].

A mechanism was suggested for high specific charge [18] in which the tin oxide reacts to form Li_2O and metallic Sn as follows:

$$2\mathrm{Li} + \mathrm{SnO} \underset{\text{Charge}}{\overset{\text{Discharge}}{\rightleftarrows}} \mathrm{Li_2O} + \mathrm{Sn} \tag{9.11}$$

The difference in the values of Gibbs free energies formation (−562.1 kJ/mol for Li_2O and −256.8 kJ/mol for Sn), tin oxide that is less stable than lithium oxide will provide the thermodynamic driving force for displacement reaction in which Li_2O will be formed at the expense of SnO.

As the formation of Li_2O is not reversible, the electrode will maintain a composite microstructure and behave as a binary lithium-tin alloy after the first cycle. The initial Li_2O formation represents a significant initial capacity loss.

Now it is well established that elemental Sn and additional Li brought into the electrode will tend to react further to form the various Li-Sn alloys.

3.3 Transition Metal Oxides

Decades ago, a survey of the reactivity of numerous binary compounds M_xO_y towards Li at low voltage was carried out. The research efforts were focused on those systems prompted to yield insertion reactions. The well-established reversibility of this mechanism assured the rechargebility of the battery built with the electrode material. These electrochemical reactions were commonly tested at voltages higher than 1.0 V. Above this cut off voltage, the electron consumption usually justifies both the partial reduction of the metallic atoms and the occupancy of empty sites into the structure. For lower cell potentials, some electrochemical and structural data obtained by Thackeray's group on iron oxides were regarded as the consequence of an insertion of lithium into, and iron extrusion from, the cubic close-packed lattice to yield the final discharge products Li_2O and α-Fe [19].

Binary transition metal oxides ($M_xO_y$with M = Fe, Cu, Co, and Ni) have been recently reviewed as anode materials for lithium ion batteries [20]. The mechanism of the lithium reaction differs from either classical lithium insertion/extraction in graphite or lithium-tin alloys. The authors proposed a new mechanism which involves the reversible reduction of the transition metal to the metallic state along the formation of Li_2O, according with Eq. (9.12).

$$M_xO_y + 2ye^- + 2yLi^+ \underset{\text{Charge}}{\overset{\text{Discharge}}{\rightleftarrows}} xM^0 + yLi_2O \tag{9.12}$$

The extended reduction of the metal atoms allows the cell to reach capacity values as higher as 700 mAh/g for CoO [21]. If the ΔG_f° (Li_2O) = −561.2 kJmol^{-1} is compared with that of CoO = −214.2 kJmol^{-1}, it is clear that reaction (9.12) is nearly exoergic and can be reversed in a cell voltage value useful for a lithium-ion battery.

The profile of the first electrochemical discharge is characterized by two relevant features. First, a voltage plateau around 1 V whose extent agrees well with the expected metal reduction and a sloping voltage to 0 V which is ascribed to the formation of an organic polymer layer. The final product of the reduction is

the decomposition of the transition metal oxide into a composite matrix made of metallic nanograins (M^0) dispersed into Li_2O.

Nevertheless, the reduction potential of M_xO_y/Li cells (especially during the first discharge) is quite low compared with the theoretical predictions. For instance, the cobalt monoxide reduction takes place at about 0.8 V, as compared to the predicted $E = 1.798$ V vs. Li^+/Li^0. Such deviation is of kinetic nature and represents the important overpotential needed to initiate and continue with the decomposition reaction.

Bearing in mind that the only condition for the feasibility of this redox reaction is the occurrence of transition metal compounds which accomplishes the exoergicity, other transition metal compounds have been researched to evaluate the electrochemical performance in lithium cells. Such family includes chalcogenides [22, 23], halides [24], phosphides [25], oxysalts [26], etc. However, some drawbacks as the Li_2S solubility or low electronic conductivity of fluorides hinder an electrochemical behavior as performing as that of the oxides.

A different way of research consists of the evaluation of mixed transition metal oxides. Tirado and coworkers have demonstrated the feasibility of the conversion reaction in compounds such as $NiCo_2O_4$ [27], $CoFe_2O_4$, and $NiFe_2O_4$ [28] with a spinel structure and $Ni_xMg_{6-x}MnO$ series [29] with a distorted rock salt structure.

4 Fuel Cell

Progressing limits on pollutant emissions oblige ship owners to reduce the environmental impact of their operations. In this direction, increases the demand for eco-friendly buildings, sustainable transport, efficient energy and water use and improving air quality, among others. To achieve the ambitious goals of the blueprint, we believe that the use of hydrogen technologies along with solar, energy storage, and other sustainable technologies is necessary.

In this context, fuel cells may provide a suitable solution, since they are fuel efficient, while they emit few hazardous compounds and are a competitive alternative to supply energy by converting chemical energy into electricity via electrochemical reaction with high efficiency and low emissions.

Fuel cells are electrical generators, that is, the energy conversion process will theoretically remain unaltered as long as the fuel and oxidant feed the system. The fuel or oxidant flows through the anode or cathode, opposite the electrolyte, and generates electrical energy by the electrochemical oxidation of the fuel and the electrochemical reduction of the oxidant [30–32]. Thus, fuel cells can be used as nonintermittent electricity and heat sources that are powered by solar and wind-renewable hydrogen or the by-product hydrogen available from local chemical and petrochemical industries. In such scenario, hydrogen is a clean energy carrier allowing to potentially increase the energy conversion efficiency, resolve intermittency issue of renewable energy, and provide more environmentally friendly energy system.

Various choices can be made with regard to the type of fuel cell system and logistic fuel. It is shown that low-temperature fuel cells using liquefied hydrogen provide a compact solution for ships with a refueling interval up to a tens of hours, but may result in total system sizes up to five times larger than high-temperature fuel cells and more energy dense fuels for vessels with longer mission requirements. Among the possible alternatives, fuel cells are considered to be one of the most promising future technologies. Fuel cell systems for residential applications have proven their ability to produce electricity with lower heating value (LHV) efficiencies up to 60% using natural gas (NG). Efficiencies over 70% are projected when they are combined with gas turbines or reciprocating internal combustion engines.

So, a variety of fuel cell types with distinct characteristics has been developed. Today, there are five different types of fuel cells, all named after their electrolyte materials:

- Alkaline fuel cells (AFCs)
- Polymer exchange membrane fuel cells (PEMFCs)
- Phosphoric acid fuel cells (PAFCs)
- Molten carbonate fuel cells (MCFCs)
- Solid oxide fuel cells (SOFCs)

Depending on the electrolyte, each fuel cell has certain characteristics such as operation temperature, electric efficiency, and demands for fuel composition. Some relevant characteristics are summarized in Table 9.1 [33, 34].

Low-temperature fuel cells (AFC, PEMFC, and PAFC) have potential for the propulsion of cars, where a short heating time is needed and the efficiency has to be compared with about 20% for a combustion engine, whereas high-temperature fuel cells (MCFC and SOFC) are suitable for continuous power and heat production, where the cell temperature can be maintained. The high-temperature fuel cells have higher efficiency and are more tolerant to the choice of fuel compared to the low-temperature fuel cells [35].

The AFC is one of the first practical fuel cells to be developed for powering electrical systems on spacecraft. It exploits the high conductivity and boiling point of a concentrated alkaline solution (potassium hydroxide) and runs at 65–220 °C. Nickel and silver electrodes are used. The alkaline electrolyte means that carbon

Table 9.1 Overview of commonly applied fuel cell systems, their temperature range, fuel requirements, and the opportunity to reform fuel directly in the fuel cell

Fuel cell type	Temperature (°C)	Fuel	Internal reforming	Charge carrier
AFC	65–220	H_2	No	OH^-
PEMFC	65–130	H_2	No	H^+
PAFC	140–200	H_2	No	H^+
MCFC	650–700	H_2, CO	Yes	CO_3^{2-}
SOFC	400–1000	H_2, CO	Yes	O^{2-}

dioxide, which degrade (carbonate) the electrolyte must be completely eliminated and only highly purified hydrogen and oxygen can be used, the cost of which imposes a severe limitation to applications other than space.

The PEMFC has shown rapid development in the last decades and achieved high power densities and good transient performance. Its membrane consists of a proton-conducting wetted solid polymer [36]. The necessity of a wet membrane, while the gas-diffusion pores have to remain dry, dictates an operational temperature of 65–85 °C and complicates water management [37]. At low temperatures, the use of platina is required to catalyze the electrochemical reaction [38]. Another important disadvantage of the low operational temperature is the limited tolerance to fuel impurities. In particular, carbon monoxide (CO) deactivates the catalyst, because of its strong surface adsorption at low temperatures [39, 40].

The selection of fuel cell for an application depends on the purpose of use and limitation on operating temperature [41]. PEMFC is generally used as a portable electricity source. Typically, PEMFC utilize hydrogen as fuel particularly in high purity that is the main limitations, including storage and handling [42]. Methanol is an attractive fuel because of its high energy density and easy in storage and transportation. Hence, MCFC got attention to overcome difficulties on hydrogen use. Conventional MCFC operates with polymer electrolyte membranes (PEMs) for portable application. However, PEMFC system requires a humid condition, which limits the operating temperature to below 100 °C, limiting the scope of this type of fuel cell. Furthermore, the poor permeability of PEM in PEMFC to methanol and hydrogen lowers fuel efficiency. This problem originates from the humid conditions needed for the electrolyte. In contrast, solid acids can transport protons under humid conditions and remain stable at high temperature (up to 250 °C). The efficiency of MCFC may therefore be increased using anhydrous solid acid as electrolyte to increase fuel permeability [43].

The membrane of the PAFC consists of a silicon carbide matrix saturated with liquid phosphoric acid. The higher operating temperature, 140–200 °C, reduces the required platinum loading and increases CO tolerance. The low power density and durability issues have so far limited the commercial success of the PAFC. A new membrane operating in the same temperature region has been developed in the past decade in an attempt to overcome these issues. This membrane essentially combines a polymer electrolyte and phosphoric acid membrane, and is therefore known as the high-temperature (HT)-PEMFC [44, 45].

Platinum can be replaced with cheaper catalysts, such as nickel, in the high-temperature fuel cell classes. Furthermore, CO becomes a fuel rather than a contaminant to the fuel cell. Another advantage is the opportunity to use high-temperature waste heat and steam, for example, in a bottoming cycle or for fuel processing. The MCFC is a relatively mature high-temperature fuel cell and operates in a range of 650–700 °C. MCFCs are commercially available, but still struggle with high cost, limited lifetime, and low power density [46, 47].

However, SOFCs are considered by many researchers to be the most suitable for generating electricity from hydrocarbons because of their simplicity, efficiency, and ability to tolerate some degree of impurities.

4.1 Solid Oxide Fuel Cells (SOFCs)

Among all types of fuel cells, solid oxide fuel cells (SOFCs) are regarded as the most efficient ones with excellent fuel flexibility. The development of high-performance SOFCs to be operated at low temperature is vital to effectively reduce the cost of the SOFCs system, thus realizing industrialization [48]. There are many advantages of SOFC with respect to other fuel cells such as the highest efficiencies of all fuel cells (50–60%), few problems with electrolyte management, high-grade waste heat is produced, for combined heat and power (CHP) applications increasing overall efficiencies to over 80%, and internal reforming of hydrocarbon fuels is possible.

The SOFC has been heavily investigated during recent decades, and various classes of SOFCs have been developed over the years, with operating temperatures ranging from 400 to 1000 °C. The low-temperature classes are mainly applied in stand-alone fuel cell products, with electrical efficiencies up to 60% [49], while the high-temperature SOFCs are targeted for combined operation with gas turbines, where efficiencies over 70% are projected. Besides the general advantages of fuel cells, including clean and quiet operation, solid oxide fuel cells (SOFCs) as being one of the high-temperature fuel cells also provide a relatively high efficiency due to enhanced reaction kinetics at high operating temperatures. The high operation temperature of SOFC also enables internal reforming of most hydrocarbons and can tolerate small quantities of impurities in the fuel. SOFC can be considered to be one of the most efficient fuel cells. In addition to pure hydrogen, gaseous hydrocarbon fuels can be used as a fuel in SOFC directly or after a reforming process. Although a promising type, their limited development state, mechanical vulnerability and high cost have so far limited widespread adoption of SOFC technology [50].

4.1.1 Ionic-Conducting SOFC

Conventional SOFC with an oxide ion-conducting electrolyte can be called SOFC-O^{2-}. This type of electrolyte allows oxide ions to move through it to transport electrons from the anode section to the cathode section via load as electricity (Fig. 9.4a).

H_2 and O_2 as feed fuels are introduced at the anode and cathode sections, respectively, and then react as shown in reactions Eqs. (9.13), (9.14), and (9.15):

$$\text{Cathode}: O_2 + 4e^- \rightarrow 2O^{2-} \tag{9.13}$$

$$\text{Anode}: 2H_2 + 2O^{2-} \rightarrow 2H_2O + 4\,e^- \tag{9.14}$$

$$\text{Overall}: O_2 + 2H_2 \rightarrow 2H_2O \tag{9.15}$$

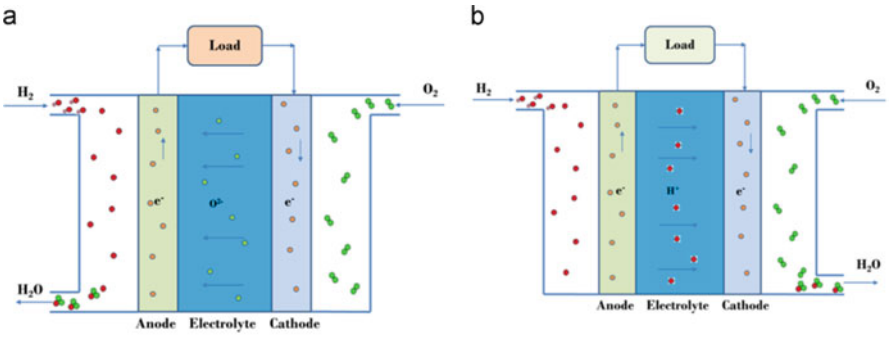

Fig. 9.4 Schematic diagram of an oxide ion-conducting solid oxide fuel cell (**a**) and a proton-conducting solid oxide fuel cell (**b**) [51]

The conventional SOFCs consist of cathode $LaSrMgO_{3-\delta}$ (LSM/YSZ), electrolyte (YSZ), and anode (NiO/YSZ), which are usually operated at above 900 °C due to the low conductivity of yttria-stabilized zirconia (YSZ) [52, 53]. However, it has been reported that high operating temperature leads to cell degradation, which reduces the life of the SOFC. To decrease the operating temperature, two approaches are studied; one is the reduction of the thickness of the electrolyte as thin as few tens of micrometers, another is the application of alternative electrolyte materials such as $La(Sr)Ga(Mg)O_{3-\delta}$ (LSGM) and samarium or gadolinium-doped CeO_2 (SDC or GDC). Therefore, new electrolyte materials with high conductivity at lower operating temperature have been investigated. $LaGaO_3$-based materials with perovskite structure have been kept attention on electrolyte systems with high ionic conductivity at below 800 °C. Strontium and magnesium-doped lanthanum gallate composition (LSGM, $La_{0.8}Sr_{0.2}Ga_{0.8}Mg_{0.2}O_{3-\delta}$) is one of the candidate materials for intermediate temperature solid oxide fuel cells (IT-SOFCs). However, it has also been reported that there are some difficulties on synthesizing LSGM material of single phase with high ionic conductivity and when LSGM material was applied as electrolyte layer of SOFC single cell, side reaction products were created such as $LaNiO_3$ or La_2NiO_4. They were formed at the interface of LSGM electrolyte and anode layer at high sintering temperature, resulting in the degradation of SOFC cell. Therefore, it is reported that design of electrolyte-support type is usually applied for the fabrication of LSGM-based SOFC cell, in which first of all, electrolyte support with thick electrolyte thickness of above 300 mm is prepared by sintering process. And then, the anode layer and the cathode layer are printed and sintered on both sides of LSGM electrolyte support, respectively.

Therefore, decreasing the operating temperature from the current regime of 800–1000 °C to 400–600 °C has been a longstanding goal in the SOFC's study. Such low-temperature (400–600 °C) operation can allow for the use of inexpensive alloy interconnects, simplify the gas sealing challenge, reduce the materials, system cost, and enhance the fuel cell durability [54, 55].

In order to operate efficiently at these reduced temperatures and to develop the next generation of hydrogen-related energy devices, new materials are required and the utilized processing routes must be optimized [56].

Carbonate/doped ceria composite electrolyte has shown enhanced properties compared to pure ceria [57], such as high ionic conductivity, improved stability, and low electron conductivity at low temperatures (400–600 °C), which has been considered promising electrolyte for using in low-temperature solid oxide fuel cells (LT-SOFCs), with ionic conductivities as high as 0.01–0.1 S cm^{-1} achieved at 400–600 °C [58, 59]. However, to reduce the cost of cell fabrication by co-sintering, it is desirable to develop new SOFC single cell with anode-supported electrolyte [60]. Moreover, although oxide ion conductors are typically used in SOFC, they possess disadvantages like material mismatch, small range of operating conditions, and poor fuel efficiency. To solve these problems, use of proton conductors to facilitate electricity generation in SOFC at intermediate temperature (400–650 °C) has been widely investigated [61].

4.1.2 Proton-Conducting SOFC

Compared with traditional SOFCs using oxygen-ion conductor as electrolyte, the use of proton-conducting oxides as electrolyte provides an alternative choice for SOFC development [62]. The ability to transport protons enables a greater range of oxygen-free fuel reforming and chemical synthesis. However, lowering the operating temperature of solid oxide fuel cells (SOFCs) possessing high energy conversion efficiency and low impact to environment to intermediate or lower temperatures (below 700 °C) is a actual research trend for the commercial development, because conventional SOFCs using yttria-stabilized zirconia (YSZ) electrolyte require high operating temperature of 800–1000 °C [63].

Proton conductors are promising electrolytes of low-temperature SOFCs due to their high proton conductivity and low activation energy of proton transport [64]. Thus, these advantages of proton-conducting SOFCs make it a hot topic in the community [65, 66].

In this context, among the new generation of materials, those with ABO_3-type perovskite structures stand out due to their great versatility. Several perovskite-type electrolytes with the structure ABO_3 have shown proton conductivity in the temperature range of 400–650 °C [67]. To overcome the limitations of oxide ion conductors, proton conductors have been studied to lower the operating temperature and enhance the efficiency of SOFC (Fig. 9.4b). Barium cerate ($BaCeO_3$) and barium zirconate ($BaZrO_3$) have been broadly studied as proton-conducting electrolytes for SOFC because of their favorable properties [68]. Therefore, up to now, the most studied proton-conducting oxide is $BaCeO_3$-based material that shows high conductivity [69, 70].

$BaCeO_3$-based oxides are the most widely and intensively studied materials as representative of the solid proton conductors' class [71, 72]. The proton conductivity in such unique systems appears due to the interaction between water steam and

oxygen vacancies. Barium cerate–based materials are considered as perspective electrolytes for solid oxide fuel elements due to their high ionic (including proton) conductivity. However, low thermodynamic stability prevents their application in solid oxide electrochemical devices. Nowadays, different strategies of stability improving of $BaCeO_3$-based oxide systems are developed [73].

The reaction in cathode, anode, and overall is given in the following Eqs. (9.16), (9.17), and (9.18):

$$\text{Cathode}: O_2 + 4e^- + 4H^+ \rightarrow 2H_2O \tag{9.16}$$

$$\text{Anode}: 2H_2 \rightarrow 4e^- + 4H^+ \tag{9.17}$$

$$\text{Overall}: O_2 + 2H_2 \rightarrow 2H_2O \tag{9.18}$$

4.1.3 Internal Reforming

Internal reforming is an attractive option offering a significant cost reduction, higher efficiencies, and faster load response of a solid oxide fuel cell (SOFC) power plant [74]. Hydrogen and carbon monoxide are used as the fuel for SOFC. In order to supply these components to the fuel cell, the steam-reforming reaction is used to reform hydrocarbon fuels such as natural gas. Due to the high operating temperature of SOFC, the steam reforming occurs very efficiently. In the case of high-temperature fuel cells such as SOFC's, there is high-grade waste heat which can be used to facilitate internal reforming. In lower temperature fuel cells such as PAFC types, the waste heat is low grade and external reforming is required.

Most natural gas combustion-based power plants currently operate at efficiencies in the low 30%. Conversion of natural gas in solid oxide fuel cells (SOFCs) promises to increase system level conversion efficiencies to above 60%, doubling the current efficiencies and significantly reducing the CO_2 emissions by a factor of 2. Such dramatic improvements in conversion efficiency and ease of CO_2 capture are currently out of reach for the combustion-based power generation technologies. Natural gas makes up a significant segment of the global energy portfolio and is rapidly becoming the preferred fuel for thermoelectric power generation partly because of its relatively lower carbon intensity compared to other fossil fuels such as coal and oil. As the least carbon-intensive fossil fuel with abundant reserves, especially after the recent finds of shale gas reservoirs in the USA and around the world, natural gas may serve as the "bridge fuel" during the next several decades to transition into a low-carbon energy economy. The high H/C ratio of nearly 4 for natural gas, as opposed to that for oil (H/C $\sim$ 2) or coal (H/C $\sim$ 1), translates into much larger amounts of energy generated per unit quantity of CO_2 released into the environment upon combustion. Natural gas is a critically important primary energy source, fuel and chemical feedstock for a wide range of industrial and societal needs, and especially for electricity generation [75].

The most interesting fuel for SOFC systems is natural gas consisting mainly of methane, that is, 80–95% CH4. Understanding the mechanistic details and technical challenges of methane conversion in SOFCs is the logical first step toward realizing natural gas utilization in SOFCs for electricity generation. Methane chemistry is rich as it can undergo many reactions. Several of the industrially important net reactions pertinent to this chapter and the associated enthalpy changes are listed in Eqs. (9.19), (9.20), (9.21), (9.22), (9.23), and (9.24).

Full oxidation (or, complete combustion)

$$CH_4 + 2O_2 \rightarrow CO_2 + 2H_2O \qquad \Delta H^\circ_{298K} = -802\ \text{kJ/mol} \tag{9.19}$$

Partial oxidation

$$CH_4 + 1/2\ O_2 \rightarrow CO + 2H_2 \qquad \Delta H^\circ_{298K} = -36\ \text{kJ/mol} \tag{9.20}$$

Steam reforming

$$CH_4 + H_2O \rightarrow CO + 3H_2 \qquad \Delta H^\circ_{298K} = +206\ \text{kJ/mol} \tag{9.21}$$

Dry reforming

$$CH_4 + CO_2 \rightarrow 2CO + 2H_2 \qquad \Delta H^\circ_{298K} = +247\ \text{kJ/mol} \tag{9.22}$$

Water–gas shift

$$CO + H_2O \rightarrow CO + H_2 \qquad \Delta H^\circ_{298K} = -41\ \text{kJ/mol} \tag{9.23}$$

Boudouard reaction

$$CO_2 + C \rightarrow 2CO \qquad \Delta H^\circ_{298K} = +171\ \text{kJ mol} \tag{9.24}$$

In the reaction environment at the SOFC anode, it is possible that several of these reactions may compete or proceed concurrently. This provides an exceptionally high ceiling of 100% for the theoretical conversion efficiency of electrochemical oxidation of methane, which also is significantly higher than for the typical and preferred SOFC fuel H_2, as shown in Fig. 9.5.

Besides hydrocarbons, alcohols like methanol and ethanol are also attractive for distributed generation of electrical energy and transportation applications [76]. Use of a liquid as fuel can realize high energy density, which can decrease the size, complexity, and cost of fuel cell systems. Methanol is a competitive fuel that remains liquid over a wide temperature range, so it is able to tolerate a range of operating conditions.

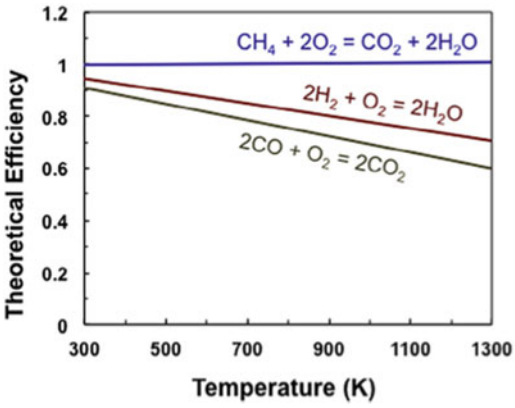

Fig. 9.5 Calculated theoretical efficiencies for electrochemical oxidation of methane, hydrogen, and carbon monoxide [71]

4.2 Photoelectrochemical Production of Hydrogen

Solar hydrogen production from direct photoelectrochemical (PEC) water splitting is the ultimate goal for a sustainable, renewable, and clean hydrogen economy. The interest in extracting hydrogen from water is fueled by the need to find a renewable, sustainable, and environmentally safe alternative energy source. Hydrogen is considered as a viable option to today's fossil fuel–based energy source especially when it is produced from water and only sunlight as the energy input. This completes the consumption and regeneration cycle of hydrogen, Eqs. (9.25) and (9.26).

$$\text{Generation}: H_2O + \text{energy (solar)} \rightarrow H_2 + 1/2\ O_2\ (\text{PEC reactor}) \tag{9.25}$$

$$\text{Consumption}: H_2 + 1/2O_2{}^{-} \rightarrow H_2O + \text{energy (Fuel cell)} \tag{9.26}$$

Photoelectrochemical (PEC) water splitting has the potential to be an efficient and cost effective way to produce hydrogen where the PE in PEC system absorb sunlight and split water directly into hydrogen and oxygen [77]. The basic PEC consists of two electrodes immersed in an aqueous electrolyte contained within a vessel, where one or both of the electrodes are photoactive. The vessel containing the aqueous electrolyte is transparent to light or fitted with an optical window that allow light to reach the photoactive electrode or also known as photoelectrode (PE). Water splitting will occur when the energetic requirements are met where the practical potential will be much higher than the minimum required to overcome overpotential and other system losses, Fig. 9.6 and Eqs. (9.27), (9.28), and (9.29).

Photoanode:

$$2\ h\nu \rightarrow\ 2\ e^{-} + 2h^{\cdot} \tag{9.27}$$

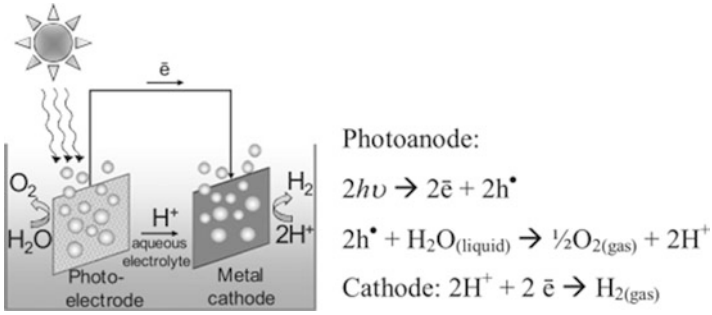

Fig. 9.6 Schematic of PEC water splitting [73]

$$2h^{\cdot} + H_2O_{(liquid)} \rightarrow \frac{1}{2}\, O_{2(gas)} + 2H^{+} \tag{9.28}$$

$$\text{Cathode}: 2H^{+} + 2\, e^{-} \rightarrow\ H_2\ (\text{gas}) \tag{9.29}$$

Hematite (α-Fe_2O_3) as a potential material for photoelectrochemical devices due to its ability to absorb visible light as well as its chemical stability in an alkaline medium and the abundance of this element 1 [78]. Many excellent research projects have demonstrated good photoelectrochemical performance for hematite thin which can be associated with morphological control at the nanoscale through a suitable thin film deposition process [79, 80].

5 Summary

Thus, the use of rechargeable batteries has been proposed as a means to accumulate the energy excess to be further supplied on demand. The advantages that these electrochemical devices offer are low cost, size, power, and easy transport. One additional reason why batteries are to be found in all aspects of modern life is that electronic devices have become much more portable and convenient to use. For the modern society, whether the source is renewable energy or nuclear energy, the energy supplied will be in the form of electricity in most cases, and people would need energy storage systems capable high energy and power density. Moreover, reliability, free maintenance, durability, safety, and low cost are desirable characteristics to compete with combustion engines in the car market.

On the other hand, contrary to batteries, fuel cells are not energy storage devices but electrical generators, that is, the energy conversion process will theoretically remain unaltered as long as the fuel and the oxidant feed the system.

Fuel cells are a competitive alternative to supply energy by converting chemical energy into electricity via electrochemical reaction with high efficiency and low emissions.

The development of high-performance SOFCs to be operated at low temperature is vital to effectively reduce the cost of the SOFCs system, thus realizing industrialization a new class of functional materials with possible applications in energy storage and production many areas.

References

1. Dresselhaus MS, Thomas JL (2001) Nature 414:332
2. Heather LM, Lester BL (2003) Prog Energy Combust Sci 29:1
3. Menahem A (2004) J Power Sources 127:2
4. Harris WS (1958) Ph.D. Thesis UCRL-8381. University of California, Berkeley
5. Vincent CA, Scrosati B (1997) Modern batteries an introducton to electrochemical power sources, 2nd edn. Arnold, London
6. Van Schalkwijk WA, Scrosati B (2002) Kluwer advances in lithium-ion batteries. Academic/Plenum Publishers, New York
7. Winter M, Besenhard JO, Spahr ME, Novak P (1998) Adv Mater 10:725
8. Mizushima K, Jones PC, Wiseman PJ, Goodenough JB (1980) Mater Res Bull 158:783
9. Thackeray MM, David WIF, Bruce PG, Goodenough JB (1983) Mater Res Bull 18:461
10. Tarascon JM, Guyomard D, Baker JL (1993) J Power Sources 43–44:689
11. Pietro B, Patriarca M, Scrosati B (1982) J Power Sources 8:289
12. Masataka W (2001) Mat Sci Eng R 33:109
13. Dey AN (1971) J Electrochem Soc 118:1547
14. Wen CJ, Boukamp BA, Huggins RA, Weppner W (1979) J Electrochem Soc 126:2258
15. Besenhard JO, Yang J, Winter M (1997) J Power Sources 68–69:87
16. Nippo enki Shinbum, March 11, 1996
17. Idota Y, Kubota T, Matsufuji A, Maekawa Y, Miyasaka T (1997) Science 276:1395
18. Huggins RA (1998) Solid State Ionics 113–115:57
19. Thackeray MM, David WIF, Goodenough JB (1982) Mater Res Bull 17(6):785
20. Poizot P, Laruelle S, Grugeon S, Dupont L, Tarascon JM (2000) Nature 407:496
21. Poizot P, Laruelle S, Grugeon S, Tarascon JM (2002) J Electrochem Soc 149(9):1212
22. Debart A, Dupont L, Patrice R, Tarascon J-M (2006) Solid State Sci 8(6):640
23. Shao-Horn Y, Osmialowski S, Quinn CH (2002) J Electrochem Soc 149(12):A1547
24. Badway F, Pereira N, Cosandey F, Amatuccia GG (2003) Electrochem Soc 150(9):A1209
25. Pralong V, Souza DCS, Leung KT, Nazar LF (2002) Electrochem Commun 4:516–520
26. Laruelle S, Poizot P, Baudrin E, Briois T, Tarascon JM (2001) J Power Sources 97–98:251
27. Alcantara R, Jaraba M, Lavela P, Tirado JL (2002) Chem Mater 14(7):2847–2848
28. Lavela P, Tirado JL, Alcantara R, Jaraba M, Jumas J, Olivier F (2003) Arcachon, Burdeos, (France)
29. Alcantara R, Jaraba M, Lavela P, Tirado JL (2002) Solid State Chem 166(2):330–335
30. Steele BC, Heinzel A (2001) Materials for fuel-cell technologies. Nature 414(6861):345–352
31. Williams MC (2001) Status and promise of fuel cell technology. Fuel Cells 1(2):87–91
32. Mekhilef S, Saidur R, Safari A (2012) Renew Sustain Energy Rev 16(1):981–989
33. Biert L van, Godjevac M, Visser K, Aravind PV (2016) J Power Sources 327:345–364
34. de Larramendi IR, Ortiz-Vitoriano N, Dzul-Bautista IB, Rojo T. Designing perovskite oxides for solid oxide fuel cells. http://dx.doi.org/10.5772/61304

35. Primdahl S (1999) Nickel/Yttria-stabilized zirconia cermet anodes for solid oxide fuel cells [thesis]. University of Twente, Faculty of Chemical Technology, The Netherlands and Risø National Laboratory, Materials Research Department, Denmark
36. Wang Y, Chen KS, Mishler J, Cho SC, Adroher XC (2011) Appl Energy 88(4):981–1007
37. Dai W, Wang H, Yuan X-Z, Martin JJ, Yang D, Qiao J, Ma J (2009) Int J Hydrog Energy 34(23):9461–9478
38. Ço€genli M, Mukerjee S, Yurtcan AB (2015) Fuel Cells 15(2):288–297
39. Baschuk J, Li X (2001) Int J Energy Res 25(8):695e713
40. Cheng X, Shi Z, Glass N, Zhang L, Zhang J, Song D, Liu Z-S, Wang H, Shen J (2007) J Power Sources 165(2):739–756
41. McGrath KM, Surya Prakash GK, Olah GA (2004) J Ind Eng Chem 10(7):1063–1080
42. Iulianelli A, Ribeirinha P, Mendes A, Basile A (2014) Renew Sustain Energy Rev 29:355–368
43. Boysen DA, Uda T, Chisholm CRI, Haile SM (2004) Science 303:68–70
44. Jensen JO, Li Q, Pan C, Bjerrum NJ, Rudbeck HC, Steenberg T, Stolten D, Grube T (2010) Report Nr, Schriften des Forschungszentrums Jülich/Energy & Environment
45. Zhang J, Xie Z, Zhang J, Tang Y, Song C, Navessin T, Shi Z, Song D, Wang H, Wilkinson DP (2006) J Power Sources 160(2):872–891
46. Huijsmans J, Kraaij G, Makkus R, Rietveld G, Sitters E, Reijers HTJ (2000) J Power Sources 86(1):117–121
47. Kulkarni A, Giddey S (2012) J Solid State Electrochem 16(10):3123–3146
48. Boudghene Stambouli A, Traversa E (2002) Renew Sustain Energy Rev 6:433–455
49. Leah RT, Bone A, Selcuk A, Corcoran D, Lankin M, Dehaney-Steven Z, Selby M, Whalen P (2011) ECS Trans 35(1):351–367
50. Pellegrino S, Lanzini A, Leone P (2015) Appl Energy 143:370e382
51. Radenahmad N, Afif A, Petra PI, Rahman SMH, Eriksson S-G, Azad AK (2016) Renew Sust Energ Rev 57:1347–1358
52. Bozza F et al (2009) Electrochem Comm 11(8):1680
53. Hosomi T, Matsuda M, Miyake M (2007) J Eur Ceram Soc 27(1):173
54. Liu XJ, Meng X, Han D, Wu H, Zeng FR, Zhan ZL (2013) J Power Source 222:92–96
55. Muhammed ASA, Muchtar A, Sulong AB, Muhamad N, Majlan EH (2013) J Ceram Int 39(5):5813–5820
56. Fergus JW, Hui R, Li X, Wilkinson DP, Zhang J (2009) CRCPress, BocaRaton
57. Jing Y, Janne P, Lund Peter D, Bin Z (2013) Int J Hydrogen Energy 38(36):16532–16538
58. Bin Z (2003) J Power Source 114:1–9
59. Benamira M, Ringuede A, Hildebrandt L, Lagergren C, Vannier R-N, Cassir M (2012) Int J Hydrogen Energy 37(24):19371–19379
60. Kim K-J, Choi S-W, Kim M-Y, Lee M-S, Kim Y-S, Kim H-S (2016) J Ind Eng Chem 42:69–74
61. Kreuer KD (2003) Annu Rev Mater Res 33(1):333–359
62. Kreuer KD (2003) Annu Rev Mater Res 33:333–359
63. Sengodan S, Choi S, Jun A, Shin TH, Ju YW, Jeong HY, Shin J, Irvine JTS, Kim G (2015) Nature Mater 14:205–209
64. He B, Zhang L, Zhang Y, Ding D, Xu J, Ling Y, Zhao L (2015) J Power Sources 287:170–176
65. Bi L, Boulfrad S, Traversa E (2014) Chem Soc Rev 43:8255
66. Fu XZ, Luo JL, Sanger AR, Luo N, Chuang KT (2010) J Power Sources 195:2659
67. Sawant P, Varma S, Wani BN, Bharadwaj SR (2012) Int J Hydrog Energy 37(4):3848–3856
68. Radenahmad N, Afif A, Petra PI, Rahman SMH, Eriksson S-G, Azad AK (2016) Renew Sust Energ Rev 57:1347–1358
69. Fu XZ, Luo JL, Sanger AR, Luo N, Chuang KT (2010) J Power Sources 195:2659
70. Tao Z, Zhang Q, Xi X, Hou G, Bi L (2016) Electrochem Commun 72:19–22
71. Medvedev D, Murashkina A, Pikalova E, Podias A, Demin A, Tsiakaras P (2014) Prog Mater Sci 60:72–129
72. Bi L, Traversa E (2014) J Mater Res 29(1):1–15
73. Medvedev DA, Lyagaeva JG, Gorbova EV, Demin AK, Tsiakaras P (2016) Prog Mater Sci 75:38–79

74. Peters R, Dahl R, Kluttgen U, Palm C, Stolten D (2002) J Power Sources 106:238–244
75. Gür TM (2016) Prog Energy Combust Sci 54:1–64
76. Lo Faro M, Stassi A, Antonucci V, Modafferi V, Frontera P, Antonucci P, Aric AS (2011) Int J Hydrog Energy 36(16):9977–9986
77. Minggu LJ, Daud WRW, Kassim MB (2010) Int J Hydrog Energy 35:5233–5244
78. Hardee KL, Bard AJJ (1976) Electrochem Soc 123:1024–1026
79. Tilley DS, Cornuz M, Sivula K, Gratzel M (2010) Angew Chem Int Ed 49:1–5
80. Gonçalves RH, Leite ER (2014) Energy Environ Sci 7:2250–2254

Chapter 10
Electrochemistry: A Powerful Tool for Preparation of Semiconductor Materials for Decontamination of Organic and Inorganic Pollutants, Disinfection, and CO_2 Reduction

Juliano Carvalho Cardoso, Guilherme Garcia Bessegato, Juliana Ferreira de Brito, Bárbara Camila A. Souza, and Maria Valnice Boldrin Zanoni

1 Overview

One-dimensional nanostructures exhibit excellent physical and chemical properties that have attracted great interest in many scientific and technological applications. In particular, 1D nanotube (NT) arrays have received increasing attention in recent years, since they exhibit an exceptional combination of well-defined electrical, optical, and chemical properties with an organized geometry, instigating tremendous advances in the fields of nanotechnology and microelectronics. Additionally, when compared to bulk materials, the 1D nanotubes feature superior characteristics, such as high-electron mobility, quantum size-related effects, very high specific surface area, and mechanical strength. These properties are of vital importance for numerous applications in physics, chemistry, materials science, and medicine [1–3].

Since the discovery of carbon nanotubes [4] and their proven impact on nanotechnology [4, 5], research efforts have been extended to a large number of inorganic materials, mainly oxides and sulfides of metals and transition metals [6–8]. The oxide/sulfide nanotubes can be synthesized by various methods, such as hydrothermal [9, 10], sol-gel, or template-assisted methods [11, 12]. In recent years, the most frequently adopted and straightforward approach for the growth of highly ordered 1D nanostructures is the self-organized electrochemical anodization process [13, 14].

J.C. Cardoso • G.G. Bessegato • J.F. de Brito • B.C.A. Souza • M.V.B. Zanoni (✉)
UNESP, Universidade Estadual Paulista Júlio de Mesquita Filho, Instituto de Química de Araraquara, Departamento de Química Analítica, Rua Francisco Degni, 55, Bairro Quitandinha, 14800-900, Araraquara, SP, Brazil
e-mail: boldrinv@iq.unesp.br

E. Longo, F.A. La Porta (eds.), *Recent Advances in Complex Functional Materials*,
DOI 10.1007/978-3-319-53898-3_10

The growth and the use of electrochemical nanostructures were first reported by Rummel [15] with the fabrication of porous-type aluminum oxide layers. The work of Thompson and Wood [16] first highlighted the great potential of porous alumina for dispersion of organic dyes and loading of inorganic pigments for corrosion protection.

Owing to the extended control over nanoscale geometry, direct back-contacting, and the versatility involving the controlled growth of nanotubular structures of various metal oxides and mixed oxide compounds, the electrochemical anodization process is the most widely explored method for the fabrication of NTs. The self-organized nanotubular structures find applications in a broad range of fields. For example, TiO_2 NTs are widely used in dye-sensitized solar cells (DSSCs), photocatalysis, and biomedical applications, α-Fe_2O_3 and Ta_3N_5 NTs are used as anodes for (photo)electrochemical water-splitting reactions [17–19], ordered nanoporous V_2O_5 and Co_3O_4 structures are utilized for batteries and ion intercalation devices or as oxygen evolution catalysts [20], and WO_3 nanochannels are used for gas sensing and electrochromic applications [21].

Interestingly, TiO_2 has become the most investigated metal oxide [17, 20, 22–26], and many functional applications rely on the specific ionic and electronic properties of the main shapes of TiO_2. Nonetheless, this metal oxide has also been widely used because of its nontoxic, environment-friendly, corrosion-resistant, and biocompatible characteristics. The most common applications of TiO_2 are in the areas of photo-electrochemistry (e.g., photocatalytic splitting of water into oxygen and hydrogen, self-cleaning surfaces, and degradation of organic pollutants) and solar cells (mostly in Grätzel-type DSSCs) [27].

2 Introduction

The electrochemical production of highly ordered nanomaterials of TiO_2 (TiO_2 NTs) is a simple process and includes the anodization of a pure titanium metal electrode in a one-compartment cell with any other metal (typically platinum) acting as the cathode.

Anodization refers to the electrochemical process of converting a metallic surface into a durable, corrosion-resistant, anodic oxide finish [28]. It is generally considered as the process of treating metals, in which the “sample” to be treated acts as the positive electrode in an electrical circuit. This process usually involves the deposition of oxide coatings aimed at improving the properties of the metal surface.

From the early 1900s, considerable efforts were devoted toward protecting and improving the properties of precious metals, such as aluminum and titanium. The first and the most important consequence of these efforts was the development of the anodizing process [28]. The process of anodization completely integrates the film with the underlying sample substrate, i.e., it cannot chip or peel like paint or plating [29]. In this process, the sample to be anodized (Al/Ti) is immersed

into an acid electrolyte bath, and electric current is passed through the medium. The sample to be anodized acts as the anode, whereas any other suitable material can function as the cathode. Oxygen ions are then released from the electrolyte, and they react with the sample atoms at the surface of the part being anodized [28]. At the sample/oxide interface, the anodic film grows as a result of the continuous formation and dissolution of the oxide layer, known as the barrier layer (or base layer). Ultimately, a very hard, relatively inert and an electrically insulating oxide (Al_2O_3/TiO_2) film is formed at the surface. The sample substrate is entirely composed of the anodic oxide (Al/Ti) structure. A highly ordered, porous structure is formed, which can be used for secondary processes.

The thickness of the oxide layer is a function of the voltage and is determined from the current per unit area and time. The influence of the time on the growth of the anodic film on the substrate increases with resistance, and the process voltage also increases correspondingly. However, increasing the thickness does not necessarily improve the performance. Thicker coatings are beneficial when thermal or electrical insulation is required, but the resistance declines while the cost increases more than proportionally to the film thickness [30].

2.1 Growth of TiO_2 NTs

TiO_2 NT arrays can be easily grown via the electrochemical anodization of titanium in fluoride-based baths by applying an electrical current between a Ti electrode and a counter electrode. Typically, the diameter of nanotube is controlled by the applied anodization voltage [31], while its length can be varied by the anodization time and by using different electrolytes containing fluoride ions. The anodization under constant voltage conditions leads to an ordered layer consisting of a distinct morphology of smooth tubes with well-defined cylindrical or hexagonal cross sections [31], as shown in Fig. 10.1.

Hence, TiO_2 NT arrays are formed in a fluoride-containing electrolyte as the result of three processes that occur simultaneously at the surface:

1. Field-assisted oxidation of the Ti metal to form TiO_2
2. Field-assisted dissolution of the Ti metal ions in the electrolyte
3. Chemical dissolution of Ti and TiO_2 due to etching by the fluoride ions

From this perspective, it appears that the key to achieving very long TiO_2 NT arrays is the use of polar organic electrolytes with water content less than 5%. The organic electrolytes pose difficulties with respect to the donation of oxygen in comparison to water and reduce the tendency toward oxide formation [31–33]. Concomitantly, the reduction in the water content that results in the formation of thinner or lower quality barrier layers through ionic transport may be enhanced.

The first synthesis of the TiO_2 NTs via anodization of Ti using hydrofluoric acid (HF) as the electrolyte was reported in 1999 by Sounart et al. [34]. Zwilling et al. [35] in the same year reported the formation of a porous titanium oxide layer using

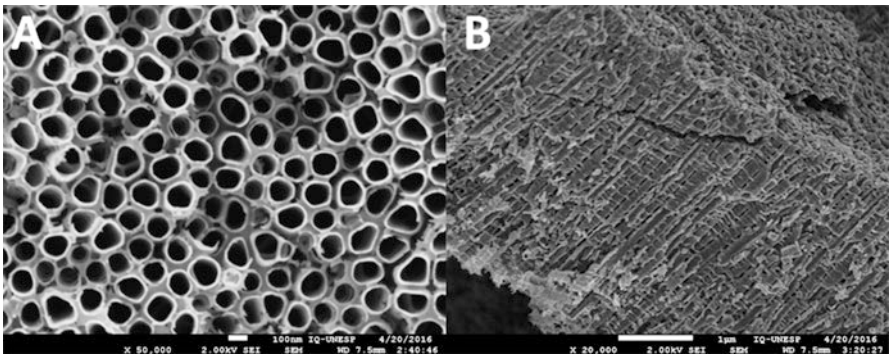

Fig. 10.1 FEG-SEM images of TiO_2 nanotube arrays prepared by electrochemical anodization, where (**a**) shows a top view and (**b**) a cross-sectional view

chromic acid solution with a small amount of HF. Gong et al. [33] demonstrated the necessity to control the experimental conditions to obtain high-quality and well-ordered TiO_2 NTs in HF electrolytes. Great breakthroughs in the fabrication of TiO_2 nanotubular structures were achieved by Macak et al. [36] and Paulose et al. [32]. They reported the preparation of aligned, regular, and very long nanotubes using fluoride in the presence of organic viscous electrolytes. Since then, different electrolytes based on HF, aqueous glycerol, aqueous carboxymethyl cellulose, and ethylene glycol containing ammonium fluoride (NH_4F) have been successfully used for the preparation of TiO_2 NTs.

The use of phosphoric acid and sodium fluoride or HF as electrolytes has also been reported for the anodization of titanium [26]. However, the TiO_2 NTs prepared using these electrolytes are not well ordered, and it takes several hours to prepare micron-length nanotubes in a high-pH electrolyte.

According to Macak et al. [37], anodization is an interesting technique owing to the fact that the diameter, the length, and the smoothness of the NTs can be easily controlled by adjusting the electrochemical parameters, such as the type of electrolyte, concentration, potential, time, and so on. Mohapatra et al. used ethylene glycol as an electrolyte and a sonoelectrochemical method [17] with an applied potential of 5–20 V to synthesize self-ordered arrays of TiO_2 NTs with diameters in the range of 30–100 nm and lengths of 300–1000 nm. They also demonstrated that the rate of formation of the TiO_2NTs via the sonoelectrochemical method was almost twice as that of the magnetic stirring technique.

Zhao et al. [38] have also synthesized TiO_2 NT arrays on titanium substrates at constant voltages in HF electrolytes. Yang et al. [39] reported the use of H_2SO_4 solution for the anodic oxidation of the titanium surface. They analyzed the modified structure focusing on the bioactivity of titanium for biomedical applications. Macak et al. [40] reported the synthesis of self-organized layers of TiO_2 NTs by the electrochemical anodization of Ti in various electrolytes containing fluoride anions. Sul et al. [41] studied the growth behavior of anodic oxide on

a commercially pure titanium sample after modifying its surface by changing the anodizing parameters. They also reported the effects of different electrolytes, such as acetic acid, phosphoric acid, calcium hydroxide, and sodium hydroxide on the anodization process performed under galvanostatic mode.

Gong et al. [33] reported the formation of TiO_2 nanoporous structures with limited thickness in an HF-containing aqueous electrolyte. More recently, Beranek et al. [23] have shown that a highly ordered porous titania can be produced in H_2SO_4 electrolytes containing HF. However, the thicknesses of the pores are still limited up to 500 nm. Grimes et al. [33] found that the use of an electrolyte solution consisting of fluorinated dimethyl sulfoxide (DMSO) and ethanol mixture for the anodization of titanium resulted in a highly ordered surface architecture of NT arrays with inner diameter of 60 nm and thickness of 40 nm. They also reported the formation of 2.3 μm thick nanotubular structures using DMSO/ethanol/HF electrolyte.

Ali et al. [26] reported the fabrication of highly oriented anodic TiO_2 nanoporous structures with uniform and parallel nanochannels at room temperature, using a two-step anodization method in two different viscous organic electrolytes. Beranek et al. [23] and Macak et al. [40] fabricated TiO_2 NTs by the anodization of Ti in H_2SO_4-HF and Na_2SO_4-HF electrolytes. However, scanning electron microscopy analyses revealed the formation of tubular structures instead of porous ones.

Choi et al. [42] prepared TiO_2 NTs using nanoimprint lithography and successive anodization of Ti in ethanolic HF. They obtained a network of pores with interpore distance of 500 nm. Zhang et al. [43] reported the obtained highly ordered TiO_2NTs structure by applying a three-step anodization approach. The structure was only formed at the top surface after the third anodization. Schmuki's [24] group used nonaqueous mixtures of ethanol and ammonium fluoride and reported the formation of nanotubular structures without using an imprinting treatment. However, the depth of the TiO_2NTs was limited to a few 100 nm.

Cai and coworkers [44] reported the formation of 4.4 μm long TiO_2 NT arrays by the anodization of Ti using NaF or KF as electrolytes. According to Kumar et al. [45], the nucleation-growth type of phase transformation leads to reductions in the porosity and/or the surface area of TiO_2 NTs with sintering. Hence, it is important to use low temperatures to fabricate TiO_2 NT arrays with high crystallinity and isomorphic structures.

Mohamed et al. [46] synthesized TiO_2 NTs in glycerol, ethylene glycol, and carboxymethyl cellulose with inner diameter ranging from 16 to 91 nm and wall thickness in the range of 7–29 nm. Ge et al. [47] synthesized TiO_2 NT arrays via anodization in ethylene glycol and glycerol electrolytes, and they demonstrated the tuning effects of DMSO on the length, the wall thickness, the dimension, and the morphology of the nanotubes.

Smith et al. [48] summarized the recent advances in solar-based applications achieved using metal oxide NT arrays formed via anodization. Gurrapa [49] used a Ti alloy instead of the metal and recently reported the synthesis of highly ordered TiO_2 NT by the electrochemical anodization of IMI-834 alloy in 0.5 wt.% HF and 1 M phosphoric acid electrolytes.

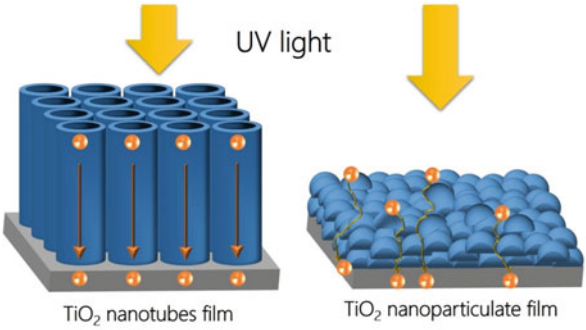

Fig. 10.2 Representation of electronic transfer on TiO_2 nanotubes and TiO_2 nanoparticulate films. In the nanotubes, the transfer of photogenerated electron to the metal substrate is vectorial, while it takes place randomly in the nanoparticulate film

The various applications of semiconductors based on their electronic properties include photovoltaics (e.g., DSSCs) [50, 51], sensing [52], electrochromics and photochromics [53, 54], self-cleaning surfaces [55], photocatalysis [56–59], and photoelectrocatalysis (PEC) [60–67]. In the following sections, we present a few examples of the applications of the semiconductors prepared by electrochemical anodization.

2.2 TiO_2 NTs for Photoelectrocatalysis

Among the nanostructured TiO_2 films, considerable attention has been focused on TiO_2 NTs, especially those prepared by the anodization of titanium in fluoride-based baths. The important advantages of these NTs include the precise control of the dimensions of the tubes, resulting in a large internal surface area where reactions may take place, and the outstanding charge transport and carrier lifetime properties owing to the excellent electron percolation pathways through the oriented structures [30, 68–70], as shown in Fig. 10.2.

The unique properties of the TiO_2 NTs enable their diverse applications in a wide range of areas including supercapacitors, solar cells, drug-eluting surfaces, hydrogen sensors, biofiltration membranes, photoelectrochemical cells for hydrogen generation, and photocatalytic degradation of contaminants, among others [68].

The photocatalytic reactions merit a relatively broader attention due to the possibility of generating electrons, holes, hydroxyl radicals, and/or superoxide radicals for different applications such as oxidation of organic compounds [67, 71, 72], reduction of inorganic ions [65, 73], inactivation of microorganisms [66, 74], reduction of CO_2 [75, 76], and production of electricity and hydrogen [77–80].

Upon the absorption of photons with energy greater than the bandgap of TiO_2, electrons are excited from the valence band (VB) to the conduction band (CB), creating electron-hole pairs (e^-/h^+) (Eq. 10.1). The holes and the electrons subsequently diffuse or migrate to the semiconductor surface and react with a suitable redox species in the environment. The oxidizing character of the hole

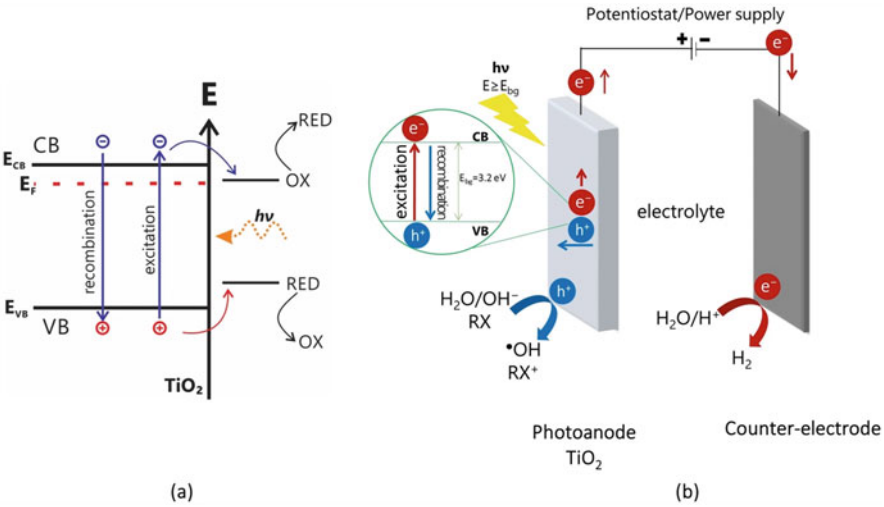

Fig. 10.3 (**a**) Mechanism of charges generation and reactions that may occur at a TiO_2 semiconductor/electrolyte interface under irradiation. (**b**) Scheme of a photoelectrochemical arrangement and reactions that take place when TiO_2 is under irradiation with bias potential

(h^+) leads to the generation of hydroxyl radicals ($^{\bullet}OH$) by the oxidation of H_2O molecules or OH^- ions adsorbed on the semiconductor surface besides enabling the direct oxidation of the organic molecules (Eqs. 10.2 and 10.3). The electrons in the CB, on the other hand, may be transferred to H_2O or H^+ contributing finally toward the production of H_2 in an aqueous environment (Fig. 10.3). However, if O_2 is present in the aqueous solution, the predominant reaction of the electrons shall be with O_2, resulting in the formation of superoxide (Eq. 10.4), hydrogen peroxide, or water. Apart from the reactions of electrons and holes with the redox species on the surface, they may recombine by an electronic transition from the CB to VB, which is referred to as electron-hole recombination [59–61, 81, 82] (Eq. 10.5).

$$TiO_2 - h^+_{VB} + H_2O_{ads} \rightarrow TiO_2 - HO^{\bullet}_{ads} + H^+ \tag{10.1}$$

$$TiO_2 - h^+_{VB} + HO^-_{ads} \rightarrow TiO_2 - HO^{\bullet}_{ads} \tag{10.2}$$

$$TiO_2 - h^+_{VB} + RX_{ads} \rightarrow TiO_2 + RX^{\bullet +}_{ads} \tag{10.3}$$

$$TiO_2 - e^-_{CB} + O_2 \rightarrow TiO_2 + O_2^{\bullet -} \tag{10.4}$$

$$TiO_2 - e^-_{CB} + TiO_2 - h^+_{VB} \rightarrow TiO_2 + \text{heat} \tag{10.5}$$

The main factors that affect the photocatalytic activity are the light absorption properties (light absorption spectrum and coefficient), the reduction and the oxidation rates of the charges at the surface, as well as the electron-hole recombination rate [59, 83]. Thus, a large surface area with a constant surface density of adsorbents leads to faster rates of the surface photocatalytic reactions, and this can be achieved using the morphology of the TiO_2 NTs. The combination of electrochemical and photocatalysis processes, known as photoelectrocatalysis, offers the possibility to efficiently separate the charge carriers and reduce the electron-hole recombinations [60, 61, 81, 82, 84].

In a PEC system, the electrochemical processes create a potential gradient in the photocatalyst, which is attached to a conductive substrate, and hence modify the properties of the substrate/electrolyte interface. The photogenerated holes on the surface of semiconductor afford oxidation reactions, and the electrons migrate to the counter electrode due to the potential gradient, where the reduction reactions take place. Thus, the charge recombination process is minimized, while the quantum yield of the photocatalytic activity is improved. Excellent reviews on the properties of TiO_2 and its photocatalytic and photoelectrocatalytic behaviors are available in the literature [59, 60, 81, 82, 85–87].

The main drawback of powder forms employed in heterogeneous photocatalysis is the use of catalyst suspensions that necessitates the separation of the material following the reaction. In PEC, however, the photocatalyst is immobilized at the surface of a solid conductive substrate, thus rendering the subsequent filtration step dispensable [88].

An important development in the area of PEC was the work of Fujishima and Honda in 1972 [89]. They demonstrated that photoelectrocatalytic water splitting is possible when n-type TiO_2 and Pt electrodes are used as the anode and the cathode, respectively. This breakthrough opened an essentially important window in the area of PEC [56, 89].

A notable contribution of the PEC process lies in the treatment of organic pollutants. The occurrence of contaminants of emerging concern (CEC) in surface water, such as pesticides, hormones, pharmaceuticals, phenols, surfactants, and dyes, has been an appalling problem to the environment and human health [90–92]. These contaminants are causes of concern because they can bioaccumulate, and some of the CECs have been recognized as endocrine-disrupting chemicals, i.e., they can interfere with the functioning of the endocrine system. The presence of CECs in the environment is mainly attributed to the direct discharge of industrial and domestic wastewater or even treated wastewater from wastewater treatment plants [91]. This is because conventional wastewater treatments involve either the modification of the organic pollutants into different phases or their concentration into a single phase, without actually destroying them.

The advanced oxidative process has been established as an efficient method for the degradation of contaminants. The *in situ* generation of $^{\bullet}OH$, which is a highly oxidizing agent and a nonselective reagent, has been found to be effective for the oxidation of any organic substance. The reaction of organic molecules with $^{\bullet}OH$ leads to complete mineralization which involves the conversion of organic molecules into CO_2, H_2O, and inorganic ions [60, 81, 82, 84].

The first studies on the photoelectrocatalytic degradation of organic contaminants were reported by Vinodgopal et al. [88], Haque and Husling [93], and Kim and Anderson [94]. Films of TiO_2 were deposited on conductive glass substrates, such as fluorine-doped tin oxide (FTO) and/or indium tin oxide (ITO). These studies showed that the photocatalysis efficiency can be significantly enhanced by using a suitable bias potential.

Recent progress in the area of PEC is closely related to the development of nanomaterials. Highly ordered nanomaterials such as NTs have been proven to be endowed with the most suitable morphology as evident from their superior properties, such as high surface area and excellent electronic transport compared to other types of semiconducting electrodes [59, 60, 87]. This was illustrated by the study on the influence of structure and surface morphology of TiO_2 (i.e., nanotubes, nanowires, and nanoporous morphology) on the photoelectrocatalytic oxidation of 4,4-oxydianiline. While 100% removal of total organic carbon (TOC) was obtained after 120 min of treatment using the TiO_2 NT electrodes, only 68% and 47% were obtained with the nanowires and the nanoporous morphology, respectively [67]. Xin et al. showed that the degradation rate of alachlor herbicide increased from 59% by using the wormhole TiO_2 electrodes to 94% by using TiO_2 NTs photoelectrodes [95].

The photoelectrochemical studies demonstrate the excellent stability of TiO_2 NT arrays for long-term applications [96]. The efficiency of the PEC process can be improved by the precise control of the dimensions of the tubes in the TiO_2 NT arrays prepared by electrochemical anodization [61, 68]. This is because the length of the TiO_2 nanotube arrays directly affects the photoelectrocatalytic activity [97]. The increase in the length of the tubes increases the resistance of the TiO_2 NTs, which reduces the intensity of the electric field within TiO_2 and decreases the charge separation. There is also an increased probability of recombination as a result of the enlarged path through the nanotubes to the substrate.

2.3 *Doping of TiO_2 NTs for Improved Photoelectrocatalytic Performance*

The electrochemical process has also contributed to the modification of the properties of the TiO_2 NTs fabricated for different applications. A typical example is the improvement in the photoactivation properties of TiO_2 which are limited to the ultraviolet (UV) region ($\lambda \leq 387$ nm). Since the UV radiation corresponds to only 5% of the sun's radiation, the extension of the optical response of TiO_2 to the visible region would be more beneficial for photocatalysis [59, 69, 87]. This has been achieved by doping (anion and/or cation) or surface decoration with noble metals (such as Pt, Pd, Au, and Ag) or coupling with other semiconductors with small bandgap energy (such as CdS and Sb_2S_3) using the electrochemical process.

The anion and/or cation doping of TiO_2 systems by the electrochemical technique can be carried out in three different ways: (i) electrodeposition, (ii) addition of a precursor of the element in the electrolyte during electrochemical anodization for oxide formation, and (iii) use of a Ti alloy during anodization.

The substitutional doping of TiO_2 with N is the most widely explored and effective technique because the nitrogen *p* states contribute significantly to the bandgap narrowing by mixing with O *2p* states. Nitrogen can be easily introduced in the TiO_2 structure due to its comparable atomic size with oxygen, apart from its small ionization energy and high stability. The following examples describe the use of electrochemical techniques for N-doping. Shankar et al. [98] performed the N-doping of TiO_2 fabricated by the anodic oxidation of a pure titanium sheet in an electrolyte composed of 0.07 M HF, NH_4NO_3 (from 0.2 to 2.5 M), and NH_4OH to adjust the pH to 3.5. The material exhibited optical absorption in the visible wavelength range of 400–530 nm. Kim et al. [99] prepared N-doped TiO_2 NTs by the anodization of a highly pure Ti alloy with approximately 5 at.% N in glycerol + water (50:50 vol.%) + 0.27 M NH_4F electrolyte. The UV response of the N-doped TiO_2 NTs was found to be lower compared to the pure TiO_2 NTs, though the former showed a strongly increased photoresponse in the visible region. Li et al. [100] prepared N-doped TiO_2 NTs by electrochemical anodization in glycerol electrolyte, followed by electrochemical deposition in NH_4Cl solution. Both the photoelectrochemical properties and the photocatalytic activity under visible light irradiation were enhanced after the N-doping of the TiO_2 NT arrays.

Similar methods were used for anion doping with B [71, 101, 102] and C [103, 104] and cation doping with W [105] and Zr [106]. Another method of doping is based on the incorporation of more than one anion (or an anion and a cation) in the structure of TiO_2 and is known as codoping. Examples include N-F-codoped [107], B-N-codoped [108], Si–W-codoped [109], and N/Zr-codoped [110] TiO_2 NTs prepared using electrochemical methods.

The visible light absorption mechanism associated with the anion/cation doping has not been fully understood by the scientific community [61, 86, 111]. Some researchers are inclined to the proposition that anion doping tends to shift the absorption edge of TiO_2 to lower energies through the narrowing of the TiO_2 bandgap. However, some others believe that TiO_2 doped with anion/cation exhibits electronic transitions from localized states in the bandgap to the CB of the semiconductor. In addition to the aforementioned distinct views, a hypothesis defended by other researchers is based on the redshift of the absorption edge which is considered to be related to the formation of color centers including Ti^{3+} centers and oxygen vacancies [111]. Although several proposals have been made to explain the redshift, the role of dopants has not been clearly described, and no consensus has been reached on this topic till date within the scientific community.

The absorption of visible light can also be achieved by coupling two semiconductors with appropriate energies of the CB and the VB. Depending on the bandgap energy of the semiconductor used with TiO_2, the composite can be activated in the visible region [86], and this junction reduces the recombination of the e^-/h^+ pairs due to the transfer of the carriers from one semiconductor to the other [60]. The use

of electrochemical techniques is hardly reported in this case. Cadmium sulfide (CdS) is the most common semiconductor coupled with TiO_2 due to its small bandgap energy ($E_g = 2.4$ eV) that is capable of absorbing visible light. Li et al. [112] produced CdS nanoparticle-modified TiO_2 NT arrays by electrodeposition via direct current, in which the electrolyte was a mixed solution of 0.01 M $CdCl_2$ in DMSO with saturated elemental sulfur. The photocurrent of the CdS/TiO_2 NTs was found to be much larger compared to that of the pure TiO_2 NTs.

The photoactivity of TiO_2 can be enhanced by decorating the surface of TiO_2 with nanoparticles of noble metals (such as Ag, Au, Pt, and Pd). Because of the difference in the Fermi levels of TiO_2 and the metal nanoparticles, a Schottky barrier is formed in the new material. Thus, a rectification of the charge carrier transfer takes place wherein the difference in the energies at the semiconductor/metal interface drives the e^- from the CB of the TiO_2 to the metal nanoparticles. In other words, the metal acts as an electron trap, promoting interfacial charge transfer and thereby minimizing the recombination of the e^-/h^+ pairs [86]. The metal nanoparticles are usually deposited via an electrochemical technique. Xie et al. [113] prepared Ag-loaded TiO_2 NTs by pulsed-current deposition technique in 0.01 M $AgNO_3$ and 0.1 M $NaNO_3$ electrolytes. Another important work on the surface decoration of TiO_2 with noble metals is that of Xing et al. [114]. They prepared Pt nanoparticles-decorated TiO_2 NTs using cyclic voltammetry electrodeposition in 19.3 mM H_2PtCl_6 solution in the voltage range of −0.4 to 0.5 V at a scan rate of 10 $mV{\cdot}s^{-1}$ (controlling the number of cycles). Furthermore, Qin et al. [115] also reported the decoration of the TiO_2 surface using Pd particles deposited by pulse electrodeposition technique in $PdCl_2$ (2 $g{\cdot}L^{-1}$) electrolyte solution (pH of 1.5). All these materials demonstrated massive improvements in the photoelectrocatalytic performance.

The use of TiO_2 nanostructured materials for the removal of contaminants has been successful for the treatment of contaminated water. A number of works published in the literature have reported the photoelectrocatalytic degradation of organochlorinated compounds [116, 117], pesticides [118, 119], aromatic amines [67], biological microorganisms [66, 74, 120], hormones and pharmaceuticals (endocrine disrupters) [72, 121–123], flame retardants [124], and dyes [63, 71, 125–127]. The process of PEC using TiO_2 nanotubes as the photoanode has proven to be a suitable alternative with high efficiency.

Some microorganisms can spread potential pathogens causing contamination of water. The photoelectrocatalytic oxidation has been demonstrated to be a powerful method for water disinfection [60, 74, 120]. This method promotes the inactivation of several microorganisms within a short treatment time. It is noteworthy that the PEC process is an alternative to conventional chlorination methods that result in toxic by-products such as the carcinogenic trihalomethanes. In addition, this method is effective for the demobilization of microorganisms that are resistant to chlorine disinfection [128]. The TiO_2 NT arrays and TiO_2 decorated with silver nanoparticles have been utilized for the disinfection of water containing *Mycobacterium smegmatis*. Under UV irradiation, the photoelectrochemical treatment achieved 100% inactivation after 3 min of treatment [74].

As electrons are directed to the cathode in a PEC system, reduction reactions are likely to take place at the cathode. Thus, it may be possible, for instance, to reduce heavy metals at the cathode. In this regard, the simultaneous degradation of organic compounds and reduction of Cr(VI) to Cr(III) has been demonstrated in a simulated tannery effluent [129]. Another very important application based on the reaction at the cathode is the generation of hydrogen [77]. In a PEC cell used for water splitting, the TiO_2 electrode (anode) and the counter electrode (cathode) are separated in a two-compartment cell by a Nafion membrane. Usually, ethanol, glycerol, methanol, and compounds derived from biomass are useful for providing electrons to the photoanode [130–132], although recently reported works have employed a large number of organic substances that are contaminants. These electrons flow to the cathode where water is reduced to molecular hydrogen.

2.4 WO_3 Electrodes for Photoelectrocatalytic Treatments

The use of TiO_2 as a semiconductor for photoelectrocatalytic applications has been well established in the literature [66, 74, 133–135]. Nevertheless, this material exhibits a bandgap energy of approximately 3.2 eV and is photoexcited only in the ultraviolet region, requiring wavelengths below 400 nm [136, 137]. The photocatalytic and photoelectrocatalytic applications of TiO_2 are attributed to its high stability, nontoxicity, and low cost. The development of new materials with a better performance than TiO_2 is a huge challenge due to two reasons: (i) rapid recombination of the photogenerated electron-hole pairs and (ii) low utilization of the solar energy [138]. In this context, active systems for the photodegradation of organic contaminants and use in photoelectrochemical reactions can be obtained by investigating semiconductors that exhibit highly efficient absorption in the visible region.

Tungsten trioxide (WO_3) is a widely studied material like TiO_2 and presents a wide range of bandgap values depending on the crystalline phases [139] besides the fact that it can also be obtained by electrochemical processes. An increase in the absorption of visible radiation as well as a reduction in the recombination of charges (e^-/h^+) has been obtained by the coupling of WO_3 and TiO_2. This has been attributed to the difference in the bandgap values of these materials as reported by several authors [140].

Tungsten trioxide is a promising alternative to TiO_2 for photoelectrocatalytic treatments as it exhibits a smaller bandgap (2.4–2.8 eV for monoclinic phase) and can be photoexcited at wavelengths in the visible region. However, most of the studies have explored the use of WO_3 for electrochromic applications and solar energy conversion [141]. The applicability of WO_3 in electrochemical processes is due to the position of its conduction band, which is more positive compared to the water reduction potential. This means that this material has the ability to directly reduce H^+ to H_2 [142]. As a result, numerous reports have been published regarding

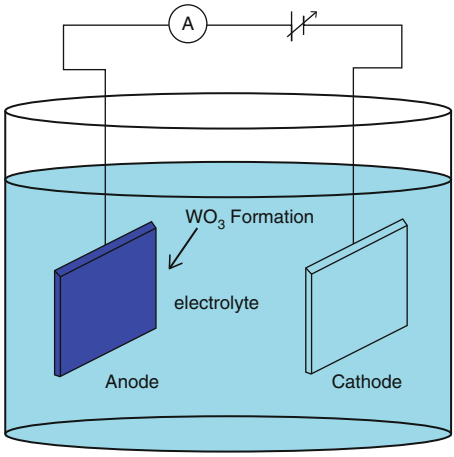

Fig. 10.4 Schematic representation of the anodizing process

the synthesis of nanostructured WO_3 thin films using different methods, especially via the electrochemical routes, such as electrochemical anodization and cathodic electrodeposition for applications in PEC and water splitting [143].

A wide range of structures can be obtained by the distortion of the hydrated octahedral crystal structure of WO_3, by the replacement of an oxygen octahedron by a water molecule or by the intercalation of H_2O molecules between layers of the octahedral structure of WO_3. The synthesis of WO_3 polymorphs crystallized in monoclinic, orthorhombic, hexagonal, tetragonal, and cubic systems has been reported [144]. Among the studies involving the use of WO_3 structures, the synthesis method employed is regarded as the key to the development of nanostructures with desirable properties for specific applications and reproducible catalysts for industrial applications. However, a controlled synthesis process without the contamination of the final material is required to obtain heterostructures with high photoelectrocatalytic activity. Thus, simple and clean methods for the controlled synthesis of the semiconductor without the use of additives are being extensively explored [143, 145, 146].

The most widely used electrochemical method for the preparation of WO_3 films is based on electrochemical anodization and cathodic electrodeposition. Electrochemical anodization is an electrochemical treatment process used for the growth of an oxide film of interest from a metal surface in an electrolytic solution under the application of a potential difference [147], as shown in Fig. 10.4.

The formation of WO_3 films on a tungsten plate via the electrochemical method has been well reported in the literature by Zhu et al. [143]. The electrochemical growth of WO_3 in an aqueous medium is due to the initial anodic oxidation of tungsten that results in a mixture of oxides such as WO_2, WO_3, and W_2O_5, among which the tungsten-containing species with $+6$ oxidation state prevails in the system, as shown in Eqs. 10.6, 10.7, 10.8, and 10.9. The presence of fluoride in the reaction medium contributes to the formation of the desired morphology [26, 148].

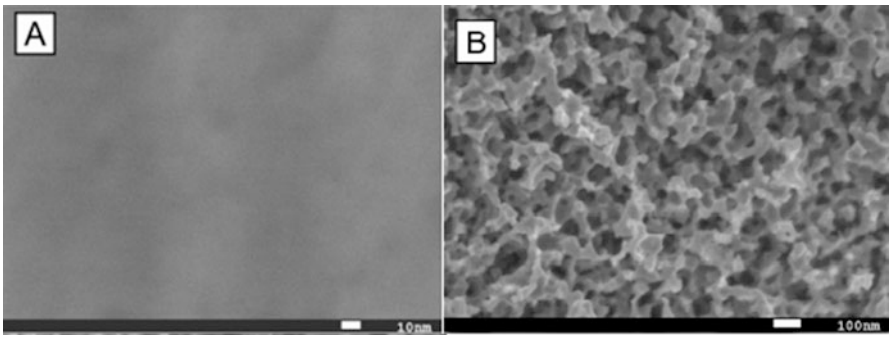

Fig. 10.5 FE-SEM images of (**a**) W foil, (**b**) nanoporous W/WO_3 thin film electrode obtained by electrochemical anodization of tungsten foil in 0.15 mol L^{-1} NaF at 60 V for 2 h, annealed at 450 °C (30 min)

Cathode

$$2H_2O + 2e^- \rightarrow H_2 + 2OH^- \tag{10.6}$$

Anode

$$W + H_2O \longrightarrow WO_2 + 4H^+ + 4e^- \tag{10.7}$$

$$2WO_2 + H_2O \longrightarrow W_2O_5 + 2H^+ + 2e^- \tag{10.8}$$

$$W_2O_5 + H_2O \longrightarrow 2WO_3 + 2H^+ + 2e^- \tag{10.9}$$

The work done by Fraga et al. in 2011 [147] reports the satisfactory synthesis of nanoporous electrodes of W/WO_3 by the electrochemical anodization method, where they detected the formation of the monoclinic phase of WO_3 which is the photoactive crystalline phase of this oxide (Fig. 10.5). The application of the electrodes in the photoelectrocatalytic degradation of the hair dye Basic Red 51 showed very promising results. The electrode was found to promote complete decolorization of the investigated Basic Red 51 dye after 60 min of photoelectrocatalytic oxidation. Furthermore, 61% mineralization of all the organic materials was observed after 1 h of the treatment, revealing the potential of this material for the decontamination of water.

Films of WO_3 with nanotubular morphologies were obtained by the anodization process as reported by Lai Wei [149]. The nanotubes were produced by anodizing a tungsten foil in the middle of NH_4F and Na_2SO_4. The optimization of various synthesis parameters such as electrolyte concentration, reaction time, and applied potential resulted in an interesting material for photoelectrocatalytic applications. The WO_3 nanostructures exhibited substantial enhancement in the degradation of methyl orange (MO) dye and generation of H_2 via the water-splitting process.

According to Zhu et al. [150], the electrodeposition method of synthesis has received increasing attention due to the advantages that include low capital cost, ambient temperature, and pressure conditions for synthesis, direct control of film thickness, and the possibility of scaling-up and commercialization. In their study, they reported the importance of systematically optimizing the electrodeposition parameters in order to achieve a higher photocurrent density on the nanostructured WO_3 thin films. The nanostructured WO_3 films were obtained by galvanostatic electrodeposition under tungsten trioxide Fe-SnO_2 wire at room temperature using a conventional three-electrode electrochemical cell system submerged in a W precursor solution with a high ion concentration of $W_2O_{11}{}^-$. The optimum process conditions of the study were reported as deposition time, 60 min; precursor concentration of W, 0.15 mol·L^{-1}; annealing temperature, 600 °C; and pH 1.0. The photocurrent density at these conditions was found to be 120 μA·cm^{-2}.

Guaraldo et al. explored nanostructured films composed of TiO_2/WO_3 bicomponent electrodes prepared by the template method. In this work, the electrodes consisting of WO_3 were obtained by electrodeposition, using polystyrene beads as the template for the growth of the film. After electrodeposition, the template was removed by dissolution in tetrahydrofuran resulting in a macroporous film, the structure of which was determined by the original template. The prepared electrode was subjected to the photoelectrocatalytic treatment of indigo carmine dye. Following 2 h of treatment, 97% decolorization and 62% mineralization of the organic materials were obtained, which demonstrate the great potential of the prepared bicomponent electrode [151].

Another work published by Guaraldo et al. [152] showed the application of this electrode for the degradation of dyes and the simultaneous generation of hydrogen gas, indicating the versatility of PEC. A good photoactivity response (11 mA·cm^{-2}) was obtained under UV and visible light irradiation, while the optimization of the photoelectrochemical conditions revealed that the pH had a major impact on H_2 production. The optimized pH resulted in a satisfactory hydrogen generation efficiency (46%), 100% decolorization of the system, and 85% removal of TOC.

It is worth noting that several works have reported the preparation of WO_3 by electrodeposition using W foil as the precursor [151]. When the appropriate potential (−0.45 V) is applied, occurs the formation of the WO_3, yielding the desired coating. The material is subjected to a calcination process at a temperature greater than or equal to 450 °C for the formation of the appropriate crystalline phase [151].

The study published in 2011 by Hepel and Luo [153] pioneered the use of WO_3 for photoelectrocatalytic treatments. This study investigated the photoelectrochemical degradation process of the dye Naphthol Blue Black (NBB) in an aqueous solution, and we intended at creating an effective method for the degradation of diazo dyes. The nanocrystalline WO_3 film was electrodeposited on a platinum surface and applied satisfactorily for the degradation of the NBB dye. This study is of great importance since it reports some mechanistic details of the WO_3 film functioning as the photoanode, such as the sensitivity degradation of the dye with respect to the potential applied on the electrode and the strong dependence of the degradation of the dye on the pH of the chloride medium. Another significant work

involves photobleaching of the dye Remazol Black B. In this study, the treatment of the dye using the W/WO_3 electrode was found to be more efficient when compared to the Ti/TiO_2 electrode with the same roughness, demonstrating the potential of this material for photoelectrocatalytic applications. Moreover, the system was examined with a model similar to Langmuir-Hinshelwood in order to explain the adsorption of the dye on the electrode surface [154].

Fraga et al. have also investigated the applications of W/WO_3 electrodes for active chlorine formation and degradation of microcystin produced by *M. aeruginosa* [141] and obtained similar results as those reported by Hepel and Luo in their aforementioned work.

The work carried out by Emuakpor et al. [155] shows the degradation of a persistent chlorophenol (2,4-dichlorophenol; 2,4-DCP) using visible-light-active W/WO_3 electrodes. The degradation of 2,4-DCP was monitored using a combination of chemical and bacterial biosensor toxicity assessments. The results showed that the concentration of 2,4-DCP dsecreased by 74% after a period of 24 h out of which 54% was attributed to the degradation processes and 20% was associated with losses of pollutants by adsorption or volatilization. The formation of more toxic intermediates was a subject of investigation in this study. Therefore, analyses by liquid chromatography-mass spectrometry were performed to study the intermediate degradation products. The results showed the occurrence of stable dimers within the first few hours of the process of degradation and the formation of intermediate products with higher toxicity compared to the parent compound.

Tungsten trioxide electrodes with nanoporous morphology and monoclinic phase were prepared by electrochemical anodization in 0.25 wt.% HF under a potential of 50 V and subsequent calcination at 500 °C. The photoelectrocatalytic capability of this material was verified by the degradation of MO dye under visible light. High decolorization and mineralization of the MO dye were observed, and the photoanode proved to be extremely stable. These results were attributed to the bandgap of 2.77 eV and the greater separation of the photogenerated charges [156].

Previously reported studies show the great potential of WO_3 electrodes for the photoelectrochemical degradation of pollutants in wastewater. Tungsten trioxide electrodes are also very effective in the treatment of microorganisms that are potentially harmful to humans. This has been highlighted in the work conducted by Souza in 2015. The aim of the work was to investigate the capability of W/WO_3 photoanode for the disinfection of water contaminated by *Candida parapsilosis* (which is found in hemodialysis water) using PEC. To this end, WO_3 was synthesized using electrodes via electrochemical anodization through the growth of WO_3 films on a tungsten foil as the substrate. This work resulted in the establishment of a new method for the disinfection of dialysates. Under photoexcitation with visible light, total destruction of the microorganisms was achieved after 1 h of treatment, while the mineralization of the organic material was found to be 60%. Thus, this study unfolded new perspectives in the research of this material for the destruction and the mineralization of microorganisms [157].

Recently, the disinfection of *Escherichia coli* was investigated using an immobilized WO_3 thin film photocatalyst in a visible light-driven photoelectrocatalytic

batch cell. The best disinfection efficiency (> 99% within 15 min) was obtained when the WO_3 catalyst was illuminated under closed-circuit conditions along with the occurrence of cell death. Thus, the WO_3 photocatalyst is a potential disinfectant; the utilization of its visible parts of the solar spectrum optimizes energy for treatment of contaminated water [158].

The applications of PEC processes are not limited to degradation of organic compounds, removal of microorganisms, and remediation of pollutants. An equally important application is the reduction of CO_2 to obtain chemicals with high commercial and energetic values using not only TiO_2NTs as catalysts but also other important materials like CuO and Cu_2O.

2.5 *Generation of Products with Commercial Values Using Copper Electrodes*

Among the nanostructured semiconductors, the copper oxide catalysts, copper (I) oxide (Cu_2O), and copper (II) oxide (CuO) are among the few known p-type semiconductors [159] that can be produced by electrochemical processes. Owing to the poor electronic conductivity of stoichiometric Cu_2O, the two oxides coexist with copper [160]. These semiconductors are attractive by virtue of their photoactive properties, natural abundance of copper, good environmental compatibility, low thermal emittance, nontoxicity, and simple and low-cost production process [159, 161–163].

Copper (II) oxide is a p-type semiconductor that absorbs light in the visible region, exhibiting a bandgap energy between 1.2 and 1.7 eV [164] which is close to the ideal bandgap for a single-junction photovoltaic cell [165]. As a result, CuO has been investigated for its potential use in photoelectrochemical cells [164, 166], as the active layer in solid-state solar cells [165], for the reduction of CO_2 by photo- and photoelectrocatalysis [167, 168], and as a cathode in DSSCs [169].

Copper (I) oxide is also a p-type material with a bandgap of around 2.2 eV [170]. This means that Cu_2O absorbs light radiation in the range of 300–620 nm, covering about 50% of the photons of the solar spectrum [162]. Copper (I) oxide is a semiconductor with a reported resistivity varying from a few ohm-centimeters to 10^{14} Ω cm, depending on the preparation technique [171]. As compared to CuO, Cu_2O is more widely explored as a photocathode [159]. It is suitable for hydrogen generation as a result of the position of its conduction band which is 0.7 V more negative compared to the reduction potential of hydrogen [172]. The Cu_2O semiconductor is also applied for photo- and photoelectrocatalytic reduction of CO_2 [173–176].

Despite the photoactive properties of Cu_2O, it was generally not preferred for photoelectrochemical applications owing to its slow stability when illuminated in an aqueous solution [159, 172, 173]. However, reports on the improved stability of electrodeposited polycrystalline Cu_2O as photocathodes in aqueous solutions

[73, 171, 172, 177] gradually increased the interest in the photoelectrochemical applications of p-Cu_2O. Besides the essential stability, the electrochemical synthesis of copper oxide provides flexibility, relatively low cost, and control of morphology, structure, and orientation of the final products [159].

A variety of methods have been reported for the preparation of CuO which include solution phase [170], dip coating [167, 178], alcohothermal [165], hydrothermal [179], combustion synthesis [180], microemulsion [181], and electrodeposition [163, 164, 182]. Among these methods, electrodeposition is particularly attractive as it provides inexpensive and mild conditions for the preparation of high-quality films with easily tunable film thickness and offers a facile route toward controlling the morphology or structure of interfacial films [163, 164].

Since the electrodeposition method improved the photostability of both the types of copper oxides, there has been a remarkable increase in their application as catalysts for CO_2 reduction, and the results obtained demonstrate their relatively good efficiency in most of the cases. Brito et al. [173, 174] studied the photoelectrocatalytic reduction of CO_2 using Cu_2O which was electrodeposited under a copper plate. The copper plates were treated with hydrogen peroxide/ammonium hydroxide (1:1) solution to improve the adhesion of the Cu_2O film on the surface. The electrodeposition was performed with 0.4 $mol{\cdot}L^{-1}$ cupric sulfate solution containing 3.0 $mol{\cdot}L^{-1}$ lactic acid. The pH of the solution was adjusted to 12.0 using 12.0 $mol{\cdot}L^{-1}$ NaOH, and the substrate was subjected to a potential of −0.40 V for 30 min at a temperature of 60 °C. The authors presented the evaluation of different parameters that resulted in the formation of methanol, ethanol, formaldehyde, acetaldehyde, and acetone.

Le et al. [183] presented the direct reduction of CO_2 to methanol (CH_3OH) using electrodeposited Cu_2O thin films. Cuprous oxide thin films were electrodeposited on stainless steel substrates at −0.555 V (saturated calomel electrode; SCE) and 333 K for 30 min. The electrolyte employed was a lactate solution consisting of 0.4 M copper sulfate ($CuSO_4$) and 3 M lactic acid at a pH of 9.0 using Cu foil as the anode. The yield of CH_3OH was found to be 43 $\mu mol{\cdot}cm^{-2}{\cdot}h^{-1}$ and the faradaic efficiency reached up to 38%. According to the authors, these values were higher than those of air-oxidized or anodized Cu electrodes prepared in the same study, and they suggested that the electrodeposited Cu (I) species play a critical role in electrode activity and selectivity to CH_3OH.

Ren et al. [183] performed electrochemical reduction of CO_2 to ethylene and ethanol using copper (I) oxide catalysts. Flat Cu disks were used as substrates for the catalysts after polishing. The Cu_2O layers were then galvanostatically deposited onto these Cu disks from a copper lactate solution for different durations in the range of 1–60 min, generating Cu_2O films of different thicknesses. The results revealed that the faradaic yields of C2 products can be systematically tuned by varying the thicknesses of the Cu_2O overlayers. The most efficient C−C bond formation was obtained with 1.7−3.6 μm-thick films, resulting in faradaic efficiencies of 34−39 and 9−16% for ethylene and ethanol, respectively.

Ghadimkhani et al. [184, 185] reported the preparation of hybrid CuO-Cu_2O semiconductor nanorod arrays for the photoelectrocatalytic reduction of CO_2 with methanol formation. First, the CuO nanorod arrays were prepared by thermal oxidation in the presence of air using a box furnace at 400 °C for 4 h. In the second step, Cu_2O crystallites were electrodeposited on the thermally grown CuO nanorods from the same basic solution of lactate-stabilized copper sulfate. The electrodeposition was performed at −0.2 V vs. standard hydrogen electrode in 0.4 M $CuSO_4$ + 3 M lactic acid and pH of 9 at 60 °C for preselected times (1–30 min) on the surfaces of the CuO nanorods. The methanol formation as a result of the photoelectrocatalytic reduction of CO_2 was found to be 85 $\mu mol \cdot L^{-1}$ after 90 min with the faradaic efficiency ranging from 94% to 96%.

Li et al. [186] prepared a wedged N-doped CuO with a more negative CB and a low overpotential for the photoelectric conversion of CO_2 to methanol. The catalyst was prepared under a Cu foil polished with sand papers. The electrolytes (water-ethanol = 3:1) consisted of 3.200 g NaOH and 0.002 g polyvinyl alcohol. The anodization was performed at 3 $mA \cdot cm^{-2}$ and 15 °C for 1 h. After the anodization, the sample was placed in a muffle furnace under a nitrogen atmosphere with a flow rate of 60 sccm and heated to 300 °C at a rate of 2 $°C \cdot min^{-1}$ for 3 h. The authors affirm that the material not only exhibited excellent PEC reduction of CO_2 but also promoted the efficient separation of the photoelectrons and the holes. The reduction of CO_2 by PEC resulted in the predominant formation of methanol (3.6 $mmol \cdot L^{-1} \cdot cm^{-2}$) with efficiency of 84.4%. However, the copper oxides were not the only products of electrodeposition. The electrodeposition resulted in the combination of the different metallic supports as well as the merging of the copper oxides with other p- or n-type oxides. Copper oxides are a good material for heterojunctions due to their ability to act as an electron trapper, which is necessary to avoid the accumulation of charge on the surface [187]. For instance, Cu^{2+} has an unfilled 3d shell, making its reduction thermodynamically feasible. Thus, CuO can trap the electrons generated on the other surface of the semiconductor, and as a result, the rate of the electron-hole recombination is slowed down, and more holes and electrons are available for the redox reactions [167, 187].

Siripala et al. [188] prepared the Cu_2O/TiO_2 heterojunction thin film cathode for photoelectrocatalytic applications. The electrodeposition of the Cu_2O film was performed under a clean titanium substrate using a three-electrode electrochemical cell containing aqueous solutions of 0.05 $mol \cdot L^{-1}$ sodium acetate and 0.05 $mol \cdot L^{-1}$ cupric acetate. The temperature of the electrolyte was maintained at 60 °C under continuous magnetic stirring. The counter electrode was a platinum wire, and Ag/AgCl electrode was used as the reference electrode. The electrodeposition was carried out under potentiostatic control at −200 mV for 45 min, and the resulting films were calcined in air at 150 °C for 30 min. Finally, the heterojunction was formed by electron beam evaporation of TiO_2 over the electrodeposited Cu_2O under high vacuum. The Cu_2O/TiO_2 electrode presented efficient light-induced charge carrier generation at the p–n junction. In addition, the authors affirm that the TiO_2 film protects the Cu_2O film against photocorrosion without diminishing its performance.

In the paper published by Kecsenovity et al. [176], the decoration of ultra-long carbon nanotubes with Cu_2O nanocrystals was studied as a hybrid platform for enhancing the photoelectrocatalytic reduction of CO_2. Cuprous oxide was electrodeposited under the carbon nanotubes from an alkaline solution (pH of 9) of lactate-stabilized copper sulfate, containing 0.4 mol·L^{-1} cupric sulfate and 3 mol·L^{-1} lactic acid in deionized water at 60 °C. To ensure complete coverage of the carbon nanotubes, nuclei formation was initialized by introducing a seed nucleation step at a more negative potential (−0.35 V) until the first 50 mC·cm^{-2} of charge was passed (15 s). After that, the deposition was performed at a less negative potential (−0.25 V, steps of 20 s) to achieve uniform and homogenous crystal growth. After each 50 mC of charge was passed, the deposition was interrupted for 60 s to avoid the depletion of the solution. The photoelectrocatalytic reduction of CO_2 using this new material resulted in the formation of methanol, ethanol, and formic acid. On the other hand, Li et al. [189] electrodeposited Cu_2O under hematite nanotubes (Fe_2O_3 NTs) for the conversion of CO_2 to methanol. The Cu_2O/Fe_2O_3 NTs were prepared by the potentiostatic electrodeposition method by depositing Cu_2O films on the surface of Fe_2O_3 NTs. The electrodeposition experiments were performed at 0.5 V for 30 min (20 °C) using 0.4 mol·L^{-1} $CuSO_4$ and 3 mol·L^{-1} lactic acid as electrolytes. The growth mechanism of the Cu_2O/Fe_2O_3 NTs was investigated in detail by the authors; the Cu_2O film showed various structures during the course of the electrodeposition. Furthermore, the photoelectric properties of the materials varied with the morphologies. The faradaic efficiency for CO_2 reduction and the yield of methanol reached 93% and 4.94 mmol·L^{-1}·cm^{-2}, respectively, after 6 h of the reaction.

Kang et al. [190] also studied the combination of copper oxide and iron oxide for the photoelectrocatalytic reduction of CO_2. The researchers reported the preparation of $CuFeO_2$ and CuO mixed p-type catalysts for solar conversion of carbon dioxide into formate. The electrode fabrication was performed under FTO substrates which were maintained at −0.36 V vs. SCE for 2 h due to the highest efficiency in aqueous 50 mmol·L^{-1} $KClO_4$ solution with 4 mmol·L^{-1} $Cu(NO_3)_{2\cdot3}H_2O$ and 12 mmol·L^{-1} $Fe(ClO_4)_3$·H2O. Following the electrodeposition, the samples were annealed at 650 °C in air for 3 h, resulting in the formation of $CuFeO_2$/CuO. This electrode was used for the reduction of CO_2 to formate, simultaneously leading to the oxidation of water to molecular oxygen at circumneutral pH without any external bias. This stand-alone system operated for a period of 1 week with continued production of formate.

Despite the difficulties related to the stability of copper oxide, electrodeposition has been proven to be a good option for the preparation of pure copper oxide catalysts or junctions of semiconductors based on copper oxides. These p-type catalysts have become the most popular materials for the conversion of carbon dioxide to products with high energetic values. The PEC using Cu_2O and CuO semiconductors is a potential technique for the reduction of CO_2 and the formation of different types of products with high yields.

3 Final Consideration

Overall, different methods for the preparation of semiconductors as catalyst materials involving the formation of different types of nanostructures, such as nanowires, nanotubes, and nanoporous, have been proposed in the literature among others. Conventional techniques such as thermal, hydrothermal, sol-gel, sputtering, and dip coating have been reported to be useful for the preparation of these materials, which are potential candidates for environmental applications, sensors, and other commercial applications. Electrochemical methods deserve considerable attention when it comes to the production of these nanomaterials. It has several advantages over the previously mentioned processes, namely, ease of manufacture, simple instrumentation, speedy preparation process, low generation of chemical residues, reproducibility of the samples produced, and low cost.

Titania is one of the most studied compounds in materials science and easy to produce by electrochemical methods. Owing to its outstanding properties, it is used in photocatalysis with focus on environmental protection, DSSCs, and biomedical devices. The feasibility of growing highly ordered arrays of TiO_2 nanotubes by a simple but optimized electrochemical anodization of a titanium metal sheet has gained considerable attention in the last decade. This finding stimulated intense research activities focused on growth, modification, properties, and applications of these one-dimensional nanostructures. The combination of extreme molecular geometry and exciting properties has not only inspired the field of nanotechnology but also instigated enormous efforts in physics, chemistry, and materials science. These 1D nanostructures exhibit unique electronic properties, such as high-electron mobility or quantum confinement effects, high specific surface area, and high mechanical strength that have revolutionized the industry considerably. Although carbon is still the most explored nanotube material, a considerable range of other materials, which are mainly transition metal oxides and sulfides, have been synthesized in the 1D geometry (e.g., nanowires, nanorods, nanofibers, or nanotubes) and have also shown fascinating properties.

Electrochemistry has contributed significantly to the production of 1D nanostructures, such as WO_3 and CuO, besides its remarkably important applications including catalytic conversion of CO_2, reduction of inorganic pollutants, and disinfection processes.

References

1. Lieber CM (1998) One-dimensional nanostructures: chemistry, physics & applications. Solid State Commun 107:607–616. doi:10.1016/S0038-1098(98)00209-9
2. Khudhair D, Bhatti A, Li Y et al (2016) Anodization parameters influencing the morphology and electrical properties of TiO2 nanotubes for living cell interfacing and investigations. Mater Sci Eng C Mater Biol Appl 59:1125–1142. doi:10.1016/j.msec.2015.10.042

3. Riboni F, Nguyen NT, So S, Schmuki P (2016) Aligned metal oxide nanotube arrays: key-aspects of anodic TiO_2 nanotube formation and properties. Nanoscale Horiz. doi:10.1039/C6NH00054A
4. Iijima S (1991) Helical microtubules of graphitic carbon. Nature 354:56–58. doi:10.1038/354056a0
5. Ebbesen TW, Ajayan PM (1992) Large-scale synthesis of carbon nanotubes. Nature 358:220–222. doi:10.1038/358220a0
6. Spahr ME, Stoschitzki Bitterli P, Nesper R et al (1999) Vanadium oxide nanotubes. A new nanostructured redox-active material for the electrochemical insertion of lithium. J Electrochem Soc 146:2780. doi:10.1149/1.1392008
7. Krumeich F, Muhr H-J, Niederberger M et al (1999) Morphology and topochemical reactions of novel vanadium oxide nanotubes. J Am Chem Soc 121:8324–8331. doi:10.1021/ja991085a
8. Remškar M, Škraba Z, Stadelmann P, Lévy F (2000) Structural stabilization of new compounds: MoS2 and WS2 micro- and nanotubes alloyed with gold and silver. Adv Mater 12:814–818. doi: 10.1002/(SICI)1521-4095(200006)12:11<814::AID-ADMA814>3.0.CO;2-0
9. Kasuga T, Hiramatsu M, Hoson A et al (1998) Formation of titanium oxide nanotube. Langmuir 14:3160–3163. doi:10.1021/la9713816
10. Wang W, Varghese OK, Paulose M et al (2004) A study on the growth and structure of titania nanotubes. J Mater Res 19:417–422. doi:10.1557/jmr.2004.19.2.417
11. Hoyer P (1996) Formation of a titanium dioxide nanotube array. Langmuir 12:1411–1413. doi:10.1021/la9507803
12. Sander MS, Côté MJ, Gu W et al (2004) Template-assisted fabrication of dense, aligned arrays of titania nanotubes with well-controlled dimensions on substrates. Adv Mater 16:2052–2057. doi:10.1002/adma.200400446
13. Xie S, Zhang Q, Liu G et al (2016) Photocatalytic and photoelectrocatalytic reduction of CO2 using heterogeneous catalysts with controlled nanostructures. Chem Commun 52:35–59. doi:10.1039/C5CC07613G
14. Loget G, Yoo JE, Mazare A et al (2015) Highly controlled coating of biomimetic polydopamine in TiO2 nanotubes. Electrochem Commun 52:41–44. doi:10.1016/j.elecom.2015.01.011
15. Rummel T (1936) Uber Wachstum und Aufbau elektrolytisch erzeugter Aluminiumoxydschichten. Z Phys 99:518–551
16. Thompson GE, Wood GC (1983) Treatise on materials science and technology, 1st edn. Academic Press, New York
17. Mohapatra SK, Misra M, Mahajan VK, Raja KS (2007) A novel method for the synthesis of titania nanotubes using sonoelectrochemical method and its application for photoelectrochemical splitting of water. J Catal 246:362–369. doi:10.1016/j.jcat.2006.12.020
18. Lee C-Y, Wang L, Kado Y et al (2014) Anodic nanotubular/porous hematite photoanode for solar water splitting: substantial effect of iron substrate purity. ChemSusChem 7:934–940. doi:10.1002/cssc.201300603
19. Lee C-Y, Wang L, Kado Y et al (2013) Si-doped Fe2O3 nanotubular/nanoporous layers for enhanced photoelectrochemical water splitting. Electrochem Commun. doi:10.1016/j.elecom.2013.07.024
20. Yang Y, Albu SP, Kim D, Schmuki P (2011) Enabling the anodic growth of highly ordered V2O5 nanoporous/nanotubular structures. Angew Chem Int Ed 50:9071–9075. doi:10.1002/anie.201104029
21. Li W, Li J, Wang X et al (2010) Visible light photoelectrochemical responsiveness of self-organized nanoporous WO3 films. Electrochim Acta 56:620–625. doi:10.1016/j.electacta.2010.06.025
22. Lee K, Mazare A, Schmuki P (2014) One-dimensional titanium dioxide nanomaterials: nanotubes. Chem Rev 114:9385–9454. doi:10.1021/cr500061m

23. Beranek R, Hildebrand H, Schmuki P (2003) Self-organized porous titanium oxide prepared in H_2SO_4/HF electrolytes. Electrochem Solid-State Lett 6:B12. doi:10.1149/1.1545192
24. Wei W, Berger S, Hauser C et al (2010) Transition of TiO2 nanotubes to nanopores for electrolytes with very low water contents. Electrochem Commun. doi:10.1016/j.elecom.2010.06.014
25. Yasuda K, Ghicov A, Nohira T et al (2008) Preparation of organized Ti nanorods by successive electrochemical processes in aqueous solution and molten salt. Electrochem Solid-State Lett 11:C51. doi:10.1149/1.2943666
26. Ali G, Chen C, Yoo S et al (2011) Fabrication of complete titania nanoporous structures via electrochemical anodization of Ti. Nanoscale Res Lett 6:332. doi:10.1186/1556-276X-6-332
27. O'Regan B, Grätzel M (1991) A low-cost, high-efficiency solar cell based on dye-sensitized colloidal TiO2 films. Nature 353:737–740. doi:10.1038/353737a0
28. What is Anodizing? – Aluminum Anodizers Council. Aluminun Anodizers Council 1 (2016). Available at:http://www.anodizing.org/?page=what_is_anodizing.
29. Anodizing Services, Anodizing Vancouver | Altech Anodizing. Altech Anodizing 1 (2011). Available at:http://www.altechanodizing.com/home/anodizing/.
30. Roy P, Berger S, Schmuki P (2011) TiO2 nanotubes: synthesis and applications. Angew Chem Int Ed Eng 50:2904–2939. doi:10.1002/anie.201001374
31. Cardoso JC, Zanoni MVB (2010) Structural effects of nanotubes, nanowires, and nanoporous Ti/TiO2 electrodes on photoelectrocatalytic oxidation of 4,4-oxydianiline. Sep Sci Technol 45:1628–1636. doi:10.1080/01496395.2010.487721
32. Paulose M, Prakasam HE, Varghese OK et al (2007) TiO_2 nanotube arrays of 1000 μm length by anodization of titanium foil: phenol red diffusion. J Phys Chem C 111:14992–14997. doi:10.1021/jp075258r
33. Gong D, Grimes CA, Varghese OK et al (2001) Titanium oxide nanotube arrays prepared by anodic oxidation. J Mater Res 16:3331–3334. doi:10.1557/JMR.2001.0457
34. Sounart TL, Liu J, Voigt JA et al (2006) Sequential nucleation and growth of complex nanostructured films. Adv Funct Mater 16:335–344. doi:10.1002/adfm.200500468
35. Zwilling V, Darque-Ceretti E, Boutry-Forveille A et al (1999) Structure and physicochemistry of anodic oxide films on titanium and TA6V alloy. Surf Interface Anal 27:629–637. doi:10.1002/(SICI)1096-9918(199907)27:7<629::AID-SIA551>3.0.CO;2-0
36. Macak JM, Sirotna K, Schmuki P (2005) Self-organized porous titanium oxide prepared in Na2SO4/NaF electrolytes. Electrochim Acta 50:3679–3684. doi:10.1016/j.electacta.2005.01.014
37. Macak JM, Hildebrand H, Marten-Jahns U, Schmuki P (2008) Mechanistic aspects and growth of large diameter self-organized TiO2 nanotubes. J Electroanal Chem 621:254–266. doi:10.1016/j.jelechem.2008.01.005
38. Wang X, Zhao J, Kang Y et al (2014) Photoelectrochemical properties of Fe-doped TiO2 nanotube arrays fabricated by anodization. J Appl Electrochem 44:1–4. doi:10.1007/s10800-013-0617-3
39. Yang B, Uchida M, Kim H-M et al (2004) Preparation of bioactive titanium metal via anodic oxidation treatment. Biomaterials 25:1003–1010. doi:10.1016/S0142-9612(03)00626-4
40. Macak JM, Tsuchiya H, Taveira L et al (2005) Smooth anodic TiO2 nanotubes. Angew Chem Int Ed Eng 44:7463–7465. doi:10.1002/anie.200502781
41. Sul YT, Johansson CB, Jeong Y, Albrektsson T (2001) The electrochemical oxide growth behaviour on titanium in acid and alkaline electrolytes. Med Eng Phys 23:329–346
42. Choi J, Wehrspohn RB, Lee J, Gösele U (2004) Anodization of nanoimprinted titanium: a comparison with formation of porous alumina. Electrochim Acta 49:2645–2652. doi:10.1016/j.electacta.2004.02.015
43. Zhang G, Huang H, Zhang Y et al (2007) Highly ordered nanoporous TiO2 and its photocatalytic properties. Electrochem Commun. doi:10.1016/j.elecom.2007.10.014
44. Cai Q, Paulose M, Varghese OK, Grimes CA (2005) The effect of electrolyte composition on the fabrication of self-organized titanium oxide nanotube arrays by anodic oxidation. J Mater Res 20:230–236. doi:10.1557/JMR.2005.0020

45. Kumar K-NP, Fray DJ, Nair J et al (2007) Enhanced anatase-to-rutile phase transformation without exaggerated particle growth in nanostructured titania–tin oxide composites. Scr Mater 57:771–774. doi:10.1016/j.scriptamat.2007.06.039
46. Mohamed AER, Kasemphaibulsuk N, Rohani S, Barghi S (2010) Fabrication of titania nanotube arrays in viscous electrolytes. J Nanosci Nanotechnol 10:1998–2008
47. Ge Y, Zhu W, Liu X, Liu S (2012) Electrochemical fabrication of titania nanotube arrays with tunning nature of dimethyl sulfoxide and its application for hydrogen sensing. J Nanosci Nanotechnol 12:3026–3034
48. Smith Y, Ray R, Carlson K et al (2013) Self-ordered titanium dioxide nanotube arrays: anodic synthesis and their photo/electro-catalytic applications. Mater 6:2892–2957. doi:10.3390/ma6072892
49. Yashwanth, IVS, Gurrappa I (2014) Synthesis and characterization of titania nanotubes on titanium alloy IMI 834 by electrochemical anodization process. J Nanomater Mol Nanotechnol. doi:10.4172/2324-8777.1000141
50. Grätzel M (2001) Photoelectrochemical cells. Nature 414:338–344. doi:10.1038/35104607
51. Grätzel M (2004) Conversion of sunlight to electric power by nanocrystalline dye-sensitized solar cells. J Photochem Photobiol A Chem 164:3–14. doi:10.1016/j.jphotochem.2004.02.023
52. Mor GK, Carvalho MA, Varghese OK et al (2004) A room-temperature TiO2-nanotube hydrogen sensor able to self-clean photoactively from environmental contamination. J Mater Res 19:628–634. doi:10.1557/jmr.2004.19.2.628
53. Biancardo M, Argazzi R, Bignozzi CA (2005) Solid-state photochromic device based on nanocrystalline TiO2 functionalized with electron donor − acceptor species. Inorg Chem 44:9619–9621. doi:10.1021/ic0514593
54. Ohko Y, Tatsuma T, Fujii T et al (2003) Multicolour photochromism of TiO2 films loaded with silver nanoparticles. Nat Mater 2:29–31. doi:10.1038/nmat796
55. Bozzi A, Yuranova T, Kiwi J (2005) Self-cleaning of wool-polyamide and polyester textiles by TiO2-rutile modification under daylight irradiation at ambient temperature. J Photochem Photobiol A Chem 172:27–34. doi:10.1016/j.jphotochem.2004.11.010
56. Hashimoto K, Irie H, Fujishima A (2005) TiO2 photocatalysis: a historical overview and future prospects. Jpn J Appl Phys Part 1-Regul Pap Brief Commun Rev Pap 44:8269–8285. doi:10.1143/jjap.44.8269
57. Nakata K, Fujishima A (2012) TiO2 photocatalysis: design and applications. J Photochem Photobiol C: Photochem Rev 13:169–189. doi:10.1016/j.jphotochemrev.2012.06.001
58. Rajeshwar K, Osugi ME, Chanmanee W et al (2008) Heterogeneous photocatalytic treatment of organic dyes in air and aqueous media. J Photochem Photobiol C: Photochem Rev 9:171–192. doi:10.1016/j.jphotochemrev.2008.09.001
59. Paramasivam I, Jha H, Liu N, Schmuki P (2012) A review of photocatalysis using self-organized TiO2 nanotubes and other ordered oxide nanostructures. Small (Weinheim an der Bergstrasse, Germany) 8:3073–3103. doi:10.1002/smll.201200564
60. Bessegato GG, Guaraldo TT, de Brito JF et al (2015) Achievements and trends in photoelectrocatalysis: from environmental to energy applications. Electrocatalysis 6:415–441. doi:10.1007/s12678-015-0259-9
61. Bessegato GG, Guaraldo TT, Zanoni MVB (2014) Enhancement of photoelectrocatalysis efficiency by using nanostructured electrodes. In: Aliofkhazraei M (ed) Modern electrochemical methods in nano, surface and corrosion science. InTech, Rijeka, pp 271–319
62. Egerton TA (2011) Does photoelectrocatalysis by TiO2 work? J Chem Technol Biotechnol 86:1024–1031. doi:10.1002/jctb.2616
63. Ferraz ERA, Oliveira GAR, Grando MD et al (2013) Photoelectrocatalysis based on Ti/TiO2 nanotubes removes toxic properties of the azo dyes disperse red 1, disperse red 13 and disperse Orange 1 from aqueous chloride samples. J Environ Manag 124:108–114. doi:10.1016/j.jenvman.2013.03.033

64. Bessegato GG, Cardoso JC, da Silva BF, Zanoni MVB (2016) Combination of photoelectrocatalysis and ozonation: a novel and powerful approach applied in acid yellow 1 mineralization. Appl Catal B Environ 180:161–168. doi:10.1016/j.apcatb.2015.06.013
65. Paschoal FMM, Pepping G, Zanoni MVB, Anderson MA (2009) Photoelectrocatalytic removal of bromate using Ti/TiO 2 coated as a photocathode. Environ Sci Technol 43:7496–7502. doi:10.1021/es803366d
66. Brugnera MF, Miyata M, Zocolo GJ et al (2013) A photoelectrocatalytic process that disinfects water contaminated with mycobacterium kansasii and Mycobacterium Avium. Water Res 47:6596–6605. doi:10.1016/j.watres.2013.08.027
67. Cardoso JC, Lizier TM, Zanoni MVB (2010) Highly ordered TiO2 nanotube arrays and photoelectrocatalytic oxidation of aromatic amine. Appl Catal B Environ 99:96–102. doi:10.1016/j.apcatb.2010.06.005
68. Grimes CA, Mor GK (2009) TiO2 nanotube arrays: synthesis, properties, and applications doi: 10.1007/978-1-4419-0068-5
69. Nah Y-C, Paramasivam I, Schmuki P (2010) Doped TiO2 and TiO2 nanotubes: synthesis and applications. ChemPhysChem 11:2698–2713. doi:10.1002/cphc.201000276
70. Grimes CA (2007) Synthesis and application of highly ordered arrays of TiO2 nanotubes. J Mater Chem 17:1451–1457. doi:10.1039/b701168g
71. Bessegato GG, Cardoso JC, Zanoni MVB (2014) Enhanced photoelectrocatalytic degradation of an acid dye with boron-doped TiO2 nanotube anodes. Catal Today 240:100–106. doi:10.1016/j.cattod.2014.03.073
72. Brugnera MF, Rajeshwar K, Cardoso JC, Zanoni MVB (2010) Bisphenol a removal from wastewater using self-organized TiO2 nanotubular array electrodes. Chemosphere 78:569–575. doi:10.1016/j.chemosphere.2009.10.058
73. Paschoal FMM, Nuñez L, Lanza MRDV, Zanoni MVB (2013) Nitrate removal on a Cu/Cu 2 O photocathode under UV irradiation and bias potential. J Adv Oxid Technol 16:63–70
74. Brugnera MF, Miyata M, Zocolo GJ et al (2012) Inactivation and disposal of by-products from mycobacterium smegmatis by photoelectrocatalytic oxidation using Ti/TiO2-Ag nanotube electrodes. Electrochim Acta 85:33–41. doi:10.1016/j.electacta.2012.08.116
75. Tahir M, Amin NS (2013) Advances in visible light responsive titanium oxide-based photocatalysts for CO2 conversion to hydrocarbon fuels. Energy Convers Manag 76:194–214. doi:10.1016/j.enconman.2013.07.046
76. LaTempa TJ, Rani S, Bao N, Grimes CA (2012) Generation of fuel from CO2 saturated liquids using a p-Si nanowire parallel to n-TiO2 nanotube array photoelectrochemical cell. Nanoscale 4:2245–2250. doi:10.1039/c2nr00052k
77. Lianos P (2011) Production of electricity and hydrogen by photocatalytic degradation of organic wastes in a photoelectrochemical cell the concept of the photofuel cell: a review of a re-emerging research field. J Hazard Mater 185:575–590. doi:10.1016/j.jhazmat.2010.10.083
78. Zanoni MVB, Guaraldo TT (2013) Photoelectrochemical hydrogen generation and concomitant organic dye oxidation under TiO2 nanotube. ECS Trans 50:63–70. doi:10.1149/05036.0063ecst
79. Kakuta S, Abe T (2009) A novel example of molecular hydrogen generation from formic acid at visible-light-responsive photocatalyst. ACS Appl Mater Interfaces 1:2707–2710. doi:10.1021/am900707e
80. Abe R (2010) Recent progress on photocatalytic and photoelectrochemical water splitting under visible light irradiation. J Photochem Photobiol C: Photochem Rev 11:179–209. doi:10.1016/j.jphotochemrev.2011.02.003
81. Daghrir R, Drogui P, Robert D (2012) Photoelectrocatalytic technologies for environmental applications. J Photochem Photobiol A Chem 238:41–52. doi:10.1016/j.jphotochem.2012.04.009
82. Zhang Y, Xiong X, Han Y et al (2012) Photoelectrocatalytic degradation of recalcitrant organic pollutants using TiO2 film electrodes: an overview. Chemosphere 88:145–154. doi:10.1016/j.chemosphere.2012.03.020

83. Chen X, Mao SS (2007) Titanium dioxide nanomaterials: synthesis, properties, modifications, and applications. Chem Rev 107:2891–2959. doi:10.1021/cr0500535
84. Georgieva J, Valova E, Armyanov S et al (2012) Bi-component semiconductor oxide photoanodes for the photoelectrocatalytic oxidation of organic solutes and vapours: a short review with emphasis to TiO2-WO3 photoanodes. J Hazard Mater 211:30–46. doi:10.1016/j.jhazmat.2011.11.069
85. Sakthivel S, Shankar MV, Palanichamy M et al (2004) Enhancement of photocatalytic activity by metal deposition: characterisation and photonic efficiency of Pt, Au and Pd deposited on TiO2 catalyst. Water Res 38:3001–3008. doi:10.1016/j.watres.2004.04.046
86. Zhang H, Chen G, Bahnemann DW (2009) Photoelectrocatalytic materials for environmental applications. J Mater Chem 19:5089. doi:10.1039/b821991e
87. Shankar K, Basham JI, Allam NK et al (2009) Recent advances in the use of TiO2 nanotube and nanowire arrays for oxidative photoelectrochemistry. J Phys Chem C 113:6327–6359. doi:10.1021/jp809385x
88. Vinodgopal K, Hotchandani S, Kamat PV (1993) Electrochemically assisted photocatalysis: titania particulate film electrodes for photocatalytic degradation of 4-chlorophenol. J Phys Chem 97:9040–9044. doi:10.1021/j100137a033
89. Fujishima A, Honda K (1972) Electrochemical photolysis of water at a semiconductor electrode. Nature 238:37–38. doi:10.1038/238037a0
90. Stuart M, Lapworth D, Crane E, Hart A (2012) Review of risk from potential emerging contaminants in UK groundwater. Sci Total Environ 416:1–21. doi:10.1016/j.scitotenv.2011.11.072
91. Petrie B, Barden R, Kasprzyk-Hordern B (2014) A review on emerging contaminants in wastewaters and the environment: current knowledge, understudied areas and recommendations for future monitoring. Water Res 72:3–27. doi:10.1016/j.watres.2014.08.053
92. Richardson SD, Ternes TA (2014) Water analysis: emerging contaminants and current issues. Anal Chem 86:2813–2848. doi:10.1021/ac500508t
93. Haque IU, Rusling JF (1993) Photodegradation of 4-chlorophenol to carbon dioxide and HCl using high surface area titanium dioxide anodes. Chemosphere 26:1301–1309. doi:10.1016/0045-6535(93)90183-6
94. Kim DH, Anderson MA (1994) Photoelectrocatalytic degradation of formic acid using a porous titanium dioxide thin-film electrode. Environ Sci Technol 28:479–483. doi:10.1021/es00052a021
95. Xin Y, Liu H, Han L, Zhou Y (2011) Comparative study of photocatalytic and photoelectrocatalytic properties of alachlor using different morphology TiO2/Ti photoelectrodes. J Hazard Mater 192:1812–1818. doi:10.1016/j.jhazmat.2011.07.005
96. Mahajan V, Mohapatra S, Misra M (2008) Stability of TiO2 nanotube arrays in photoelectrochemical studies. Int J Hydrog Energy 33:5369–5374. doi:10.1016/j.ijhydene.2008.06.074
97. Liu Z, Zhang X, Nishimoto S et al (2008) Highly ordered TiO2 nanotube arrays with controllable length for photoelectrocatalytic degradation of phenol. J Phys Chem C 112:253–259. doi:10.1021/jp0772732
98. Shankar K, Tep KC, Mor GK, Grimes CA (2006) An electrochemical strategy to incorporate nitrogen in nanostructured TiO2 thin films: modification of bandgap and photoelectrochemical properties. J Phys D-Appl Phys 39:2361–2366. doi:10.1088/0022-3727/39/11/008
99. Kim D, Fujimoto S, Schmuki P, Tsuchiya H (2008) Nitrogen doped anodic TiO2 nanotubes grown from nitrogen-containing Ti alloys. Electrochem Commun 10:910–913. doi:10.1016/j.elecom.2008.04.001
100. Li S, Lin S, Liao J et al (2012) Nitrogen-doped TiO2 nanotube arrays with enhanced photoelectrochemical property. Int J Photogr 2012:1–7. doi:10.1155/2012/794207
101. Li J, Lu N, Quan X et al (2008) Facile method for fabricating boron-doped TiO2 nanotube array with enhanced photoelectrocatalytic properties. Ind Eng Chem Res 47:3804–3808. doi:10.1021/ie0712028

102. Lu N, Zhao H, Li J et al (2008) Characterization of boron-doped TiO2 nanotube arrays prepared by electrochemical method and its visible light activity. Sep Purif Technol 62:668–673. doi:10.1016/j.seppur.2008.03.021
103. Milad AMH, Minggu LJ, Kassim MB, Daud WRW (2013) Carbon doped TiO2 nanotubes photoanodes prepared by in-situ anodic oxidation of Ti-foil in acidic and organic medium with photocurrent enhancement. Ceram Int 39:3731–3739. doi:10.1016/j.ceramint.2012.10.209
104. Krengvirat W, Sreekantan S, Mohd Noor A-F et al (2012) Carbon-incorporated TiO2 photoelectrodes prepared via rapid-anodic oxidation for efficient visible-light hydrogen generation. Int J Hydrog Energy 37:10046–10056. doi:10.1016/j.ijhydene.2012.04.004
105. Das C, Paramasivam I, Liu N, Schmuki P (2011) Photoelectrochemical and photocatalytic activity of tungsten doped TiO2 nanotube layers in the near visible region. Electrochim Acta 56:10557–10561. doi:10.1016/j.electacta.2011.05.061
106. Liu H, Liu G, Zhou Q (2009) Preparation and characterization of Zr doped TiO2 nanotube arrays on the titanium sheet and their enhanced photocatalytic activity. J Solid State Chem 182:3238–3242. doi:10.1016/j.jssc.2009.09.016
107. Su Y, Zhang X, Zhou M et al (2008) Preparation of high efficient photoelectrode of N–F-codoped TiO2 nanotubes. J Photochem Photobiol A Chem 194:152–160. doi:10.1016/j.jphotochem.2007.08.002
108. Zhou X, Peng F, Wang H et al (2011) Preparation of B, N-codoped nanotube arrays and their enhanced visible light photoelectrochemical performances. Electrochem Commun 13:121–124. doi:10.1016/j.elecom.2010.11.030
109. Sun M, Cui X (2012) Anodically grown Si–W codoped TiO2 nanotubes and its enhanced visible light photoelectrochemical response. Electrochem Commun 20:133–136. doi:10.1016/j.elecom.2012.04.016
110. Liu H, Liu G, Shi X (2010) N/Zr-codoped TiO2 nanotube arrays: fabrication, characterization, and enhanced photocatalytic activity. Colloids Surf A Physicochem Eng Asp 363:35–40. doi:10.1016/j.colsurfa.2010.04.010
111. Serpone N (2006) Is the band gap of pristine TiO2 narrowed by anion- and cation-doping of titanium dioxide in second-generation photocatalysts? J Phys Chem B 110:24287–24293. doi:10.1021/jp065659r
112. Li J-TJ, Lin C-J, Li J-TJ, Lin Z-Q (2011) A photoelectrochemical study of CdS modified TiO2 nanotube arrays as photoanodes for cathodic protection of stainless steel. Thin Solid Films 519:5494–5502. doi:10.1016/j.tsf.2011.03.116
113. Xie K, Sun L, Wang C et al (2010) Photoelectrocatalytic properties of Ag nanoparticles loaded TiO2 nanotube arrays prepared by pulse current deposition. Electrochim Acta 55:7211–7218. doi:10.1016/j.electacta.2010.07.030
114. Xing L, Jia J, Wang Y et al (2010) Pt modified TiO2 nanotubes electrode: preparation and electrocatalytic application for methanol oxidation. Int J Hydrog Energy 35:12169–12173. doi:10.1016/j.ijhydene.2010.07.162
115. Qin Y-H, Yang H-H, Lv R-L et al (2013) TiO2 nanotube arrays supported Pd nanoparticles for ethanol electrooxidation in alkaline media. Electrochim Acta 106:372–377. doi:10.1016/j.electacta.2013.05.067
116. Quan X, Ruan X, Zhao H et al (2007) Photoelectrocatalytic degradation of pentachlorophenol in aqueous solution using a TiO2 nanotube film electrode. Environ pollut (Barking, Essex: 1987) 147:409–414. doi:10.1016/j.envpol.2006.05.023
117. Quan X, Yang S, Ruan X, Zhao H (2005) Preparation of titania nanotubes and their environmental applications as electrode. Environ Sci Technol 39:3770–3775. doi:10.1021/es048684o
118. Philippidis N, Sotiropoulos S, Efstathiou A, Poulios I (2009) Photoelectrocatalytic degradation of the insecticide imidacloprid using TiO2/Ti electrodes. J Photochem Photobiol A Chem 204:129–136. doi:10.1016/j.jphotochem.2009.03.007
119. Fang T, Yang C, Liao L (2012) Photoelectrocatalytic degradation of high COD dipterex pesticide by using TiO2/Ni photo electrode. J Environ Sci 24:1149–1156. doi:10.1016/S1001-0742(11)60882-6

120. Brugnera MF, Miyata M, Zocolo GJ et al (2014) Ti/TiO2 nanotubes enhance mycobacterium fortuitum, mycobacterium chelonae and mycobacterium abscessus inactivation in water. J Chem Technol Biotechnol 89:1686–1696. doi:10.1002/jctb.4243
121. Chang H-S, Choo K-H, Lee B, Choi S-J (2009) The methods of identification, analysis, and removal of endocrine disrupting compounds (EDCs) in water. J Hazard Mater 172:1–12. doi:10.1016/j.jhazmat.2009.06.135
122. Daghrir R, Drogui P, Dimboukou-Mpira A, El Khakani MA (2013) Photoelectrocatalytic degradation of carbamazepine using Ti/TiO2 nanostructured electrodes deposited by means of a pulsed laser deposition process. Chemosphere 93:2756–2766. doi:10.1016/j.chemosphere.2013.09.031
123. Nie X, Chen J, Li G et al (2013) Synthesis and characterization of TiO2 nanotube photoanode and its application in photoelectrocatalytic degradation of model environmental pharmaceuticals. J Chem Technol Biotechnol 88:1488–1497. doi:10.1002/jctb.3992
124. Liu H, Liu G, Fan J et al (2011) Photoelectrocatalytic degradation of 4,4′-dibromobiphenyl in aqueous solution on TiO_2 and doped TiO_2 nanotube arrays. Chemosphere 82:43–47. doi:10.1016/j.chemosphere.2010.10.013
125. Brillas E, Martínez-Huitle CA (2015) Decontamination of wastewaters containing synthetic organic dyes by electrochemical methods: an updated review. Appl Catal B Environ 166–167:603–643. doi:10.1016/j.apcatb.2014.11.016
126. Martínez-Huitle CA, Brillas E (2009) Decontamination of wastewaters containing synthetic organic dyes by electrochemical methods: a general review. Appl Catal B Environ 87:105–145. doi:10.1016/j.apcatb.2008.09.017
127. Bessegato GG, Cardoso JC, Silva BF da, Zanoni MVB (2014) Enhanced photoabsorption properties of composites of Ti/TiO2 nanotubes decorated by Sb2S3 and improvement of degradation of hair dye. J Photochem Photobiol A Chem 276:96–103. doi: 10.1016/j.jphotochem.2013.12.001
128. Malato S, Fernández-Ibáñez P, Maldonado MI et al (2009) Decontamination and disinfection of water by solar photocatalysis: recent overview and trends. Catal Today 147:1–59. doi:10.1016/j.cattod.2009.06.018
129. Paschoal FMM, Anderson MA, Zanoni MVB (2009) Simultaneous removal of chromium and leather dye from simulated tannery effluent by photoelectrochemistry. J Hazard Mater 166:531–537. doi:10.1016/j.jhazmat.2008.11.058
130. Kaneko M, Nemoto J, Ueno H et al (2006) Photoelectrochemical reaction of biomass and bio-related compounds with nanoporous TiO2 film photoanode and O2-reducing cathode. Electrochem Commun 8:336–340. doi:10.1016/j.elecom.2005.12.004
131. Ueno H, Nemoto J, Ohnuki K et al (2009) Photoelectrochemical reaction of biomass-related compounds in a biophotochemical cell comprising a nanoporous TiO2 film photoanode and an O2-reducing cathode. J Appl Electrochem 39:1897–1905. doi:10.1007/s10800-009-9897-z
132. Kaneko M, Ueno H, Saito R, Nemoto J (2009) Highly efficient photoelectrocatalytic decomposition of biomass compounds using a nanoporous semiconductor photoanode and an O2-reducing cathode with quantum efficiency over 100. Catal Lett 131:184–188. doi:10.1007/s10562-009-0011-2
133. Brugnera MF, Miyata M, Fujimura Leite CQ, Zanoni MVB (2014) Silver ion release from electrodes of nanotubes of TiO2 impregnated with Ag nanoparticles applied in photoelectrocatalytic disinfection. J Photochem Photobiol A Chem 278:1–8. doi:10.1016/j.jphotochem.2013.12.020
134. Bessegato GG, Cardoso JC, Silva BF Da, Zanoni MVB (2013) Enhanced photoabsorption properties of composites of Ti/TiO2 nanotubes decorated by Sb2S3 and improvement of degradation of hair dye. J Photochem Photobiol A Chem 276:96–103. doi: 10.1016/j.jphotochem.2013.12.001
135. Cho M, Chung H, Choi W, Yoon J (2004) Linear correlation between inactivation of *E. coli* and OH radical concentration in TiO2 photocatalytic disinfection. Water Res 38:1069–1077. doi:10.1016/j.watres.2003.10.029

136. García-Pérez UM, Sepúlveda-Guzmán S, Martínez-De La Cruz A (2012) Nanostructured BiVO 4 photocatalysts synthesized via a polymer-assisted coprecipitation method and their photocatalytic properties under visible-light irradiation. Solid State Sci 14:293–298. doi:10.1016/j.solidstatesciences.2011.12.008
137. Hong X, Wang Z, Cai W et al (2005) Visible-light-activated nanoparticle photocatalyst of iodine-doped titanium dioxide. Chem Mater 17:1548–1552. doi:10.1021/cm047891k
138. Charles Dismukes G, Brimblecombe R, Felton GAN et al (2009) Development of bioinspired Mn4O4-cubane water oxidation catalysts: lessons from photosynthesis. Acc Chem Res 42:1935–1943. doi:10.1021/ar900249x
139. Migas DB, Shaposhnikov VL, Rodin VN, Borisenko VE (2010) Tungsten oxides. I. Effects of oxygen vacancies and doping on electronic and optical properties of different phases of WO3. J Appl Phys. doi:10.1063/1.3505688
140. Lv K, Li J, Qing X et al (2011) Synthesis and photo-degradation application of WO3/TiO2 hollow spheres. J Hazard Mater 189:329–335. doi:10.1016/j.jhazmat.2011.02.038
141. Fraga LE, Anderson MA, Beatriz MLPMA et al (2009) Evaluation of the photoelectrocatalytic method for oxidizing chloride and simultaneous removal of microcystin toxins in surface waters. Electrochim Acta 54:2069–2076. doi:10.1016/j.electacta.2008.08.060
142. Hisatomi T, Kubota J, Domen K (2014) Recent advances in semiconductors for photocatalytic and photoelectrochemical water splitting. Chem Soc Rev. doi:10.1039/c3cs60378d
143. Zhu T, Chong MN, Chan ES (2014) Nanostructured tungsten trioxide thin films synthesized for photoelectrocatalytic water oxidation: a review. ChemSusChem 7:2974–2997. doi:10.1002/cssc.201402089
144. Saha D, Jensen KMØ, Tyrsted C et al (2014) In situ total X-ray scattering study of WO3 nanoparticle formation under hydrothermal conditions. Angew Chem Int Ed 53:3667–3670. doi:10.1002/anie.201311254
145. Katsumata H, Inoue K, Suzuki T, Kaneco S (2014) Facile synthesis of WO3 nanorod thin films on W substrate with enhanced photocatalytic performance. Catal Lett 144:837–842. doi:10.1007/s10562-014-1194-8
146. Ahsan M, Ahmad MZ, Tesfamichael T et al (2012) Low temperature response of nanostructured tungsten oxide thin films toward hydrogen and ethanol. Sensors Actuators B Chem 173:789–796. doi:10.1016/j.snb.2012.07.108
147. Fraga LE, Zanoni MVB (2011) Nanoporous of W/WO 3 thin film electrode grown by electrochemical anodization applied in the photoelectrocatalytic oxidation of the basic red 51 used in hair dye. J Braz Chem Soc 22:718–725. doi:10.1590/S0103-50532011000400015
148. Lee WH, Lai CW, Abd Hamid SB (2015) In situ anodization of WO3-decorated TiO2 nanotube arrays for efficient mercury removal. Mater 8:5702–5714. doi:10.3390/ma8095270
149. Lai CW (2014) Photocatalysis and photoelectrochemical properties of tungsten trioxide nanostructured films. TheScientificWorldJOURNAL 2014:843587. doi:10.1155/2014/843587
150. Zhu T, Chong MN, Phuan YW et al (2016) Effects of electrodeposition synthesis parameters on the photoactivity of nanostructured tungsten trioxide thin films: optimisation study using response surface methodology. J Taiwan Inst Chem Eng 61:196–204. doi:10.1016/j.jtice.2015.12.010
151. Guaraldo TT, Zanoni TB, de Torresi SIC et al (2013) On the application of nanostructured electrodes prepared by Ti/TiO2/WO3 "template": a case study of removing toxicity of indigo using visible irradiation. Chemosphere 91:586–593. doi:10.1016/j.chemosphere.2012.12.027
152. Guaraldo TT, Gonçales VR, Silva BF et al (2016) Hydrogen production and simultaneous photoelectrocatalytic pollutant oxidation using a TiO2/WO3 nanostructured photoanode under visible light irradiation. J Electroanal Chem 765:188–196. doi:10.1016/j.jelechem.2015.07.034
153. Hepel M, Luo J (2001) Photoelectrochemical mineralization of textile diazo dye pollutants using nanocrystalline WO3 electrodes. Electrochim Acta 47:729–740. doi:10.1016/S0013-4686(01)00753-8

154. Hepel MHS (2005) Photoelectrocatalytic degradation of diazo dyes on nanostructured WO3 electrodes. Electrochim Acta 50:5278–5291. doi:10.1016/j.electacta.2005.03.067
155. Scott-Emuakpor EO, Kruth A, Todd MJ et al (2012) Remediation of 2,4-dichlorophenol contaminated water by visible light-enhanced WO 3 photoelectrocatalysis. Appl Catal B Environ 123–124:433–439. doi:10.1016/j.apcatb.2012.05.010
156. Zheng Q, Lee C (2014) Visible light photoelectrocatalytic degradation of methyl orange using anodized nanoporous WO3. Electrochim Acta 115:140–145. doi:10.1016/j.electacta.2013.10.148
157. Souza B (2015) Desinfecção de águas contaminadas com *Candida parapsilosis* utilizando eletrodos de W/WO3 em tratamento fotoeletrocatalítico. UNESP, Araraquara
158. Scott-emuakpor E, Paton GI, Todd MJ, Macphee DE (2016) Disinfection of *E. coli* contaminated water using tungsten trioxide-based photoelectrocatalysis. Environ Eng Manag J 15:273105
159. Zhang Z, Wang P (2012) Highly stable copper oxide composite as an effective photocathode for water splitting via a facile electrochemical synthesis strategy. J Mater Chem 22:2456. doi:10.1039/c1jm14478b
160. Richardson TJ, Slack JL, Rubin MD (2001) Electrochromism in copper oxide thin films. Electrochim Acta 46:2281–2284. doi:10.1016/S0013-4686(01)00397-8
161. Paracchino A, Laporte V, Sivula K et al (2011) Highly active oxide photocathode for photoelectrochemical water reduction. Nat Mater 10:456–461. doi:10.1038/nmat3017
162. Ma Q-B, Hofmann JP, Litke A, Hensen EJM (2015) Cu2O photoelectrodes for solar water splitting: tuning photoelectrochemical performance by controlled faceting. Sol Energy Mater Sol Cells 141:178–186. doi:10.1016/j.solmat.2015.05.025
163. Nakaoka K, Ueyama J, Ogura K (2004) Photoelectrochemical behavior of electrodeposited CuO and Cu 2 O thin films on conducting substrates. J Electrochem Soc 151:C661–C665. doi:10.1149/1.1789155
164. Siegfried MJ, Choi K-S (2007) Conditions and mechanism for the anodic deposition of cupric oxide films in slightly acidic aqueous media. J Electrochem Soc 154:D674. doi:10.1149/1.2789394
165. Lim YF, Choi JJ, Hanrath T (2012) Facile synthesis of colloidal CuO nanocrystals for light-harvesting applications. J Nanomater. doi:10.1155/2012/393160
166. Li D, Chien CJ, Deora S et al (2011) Prototype of a scalable core-shell Cu2O/TiO2 solar cell. Chem Phys Lett 501:446–450. doi:10.1016/j.cplett.2010.11.064
167. Brito JF, Valnice M, Zanoni B (2016) On the application of Ti/TiO_2/CuO n-p junction semiconductor: a case study of electrolyte , temperature and potential influence on CO_2 reduction. Chem Eng J:15–18. doi:10.1016/j.cej.2016.08.033
168. Slamet NHW, Purnama E et al (2005) Photocatalytic reduction of CO2 on copper-doped titania catalysts prepared by improved-impregnation method. Catal Commun 6:313–319. doi:10.1016/j.catcom.2005.01.011
169. Anandan S, Wen X, Yang S (2005) Room temperature growth of CuO nanorod arrays on copper and their application as a cathode in dye-sensitized solar cells. Mater Chem Phys 93:35–40. doi:10.1016/j.matchemphys.2005.02.002
170. Bouzit S, Boualy B, Firdoussi L et al (2015) Fast room temperature solution-phase approach for selective synthesis of nanostructured Cu(OH)2, Cu2O and CuO. Int Res J Pure Appl Chem 8:157–164. doi:10.9734/IRJPAC/2015/17920
171. Golden TD, Shumsky MG, Zhou Y et al (1996) Electrochemical deposition of copper(I) oxide films. Chem Mater 8:2499–2504. doi:10.1021/cm9602095
172. Sowers KL, Fillinger A (2009) Crystal face dependence of p-Cu_2O stability as photocathode. J Electrochem Soc 156:F80. doi:10.1149/1.3089290
173. Brito JF, Silva AA, Cavalheiro AJ, Zanoni MVB (2014) Evaluation of the parameters affecting the photoelectrocatalytic reduction of CO_2 to CH_3OH at Cu / Cu_2O electrode. Int J Electrochem Sci 9:5961–5973

174. Brito JF, Araujo AR, Rajeshwar K, Zanoni MVB (2015) Photoelectrochemical reduction of CO_2 on Cu/Cu_2O films: product distribution and pH effects. Chem Eng J 264:302–309. doi:10.1016/j.cej.2014.11.081
175. Yuan Y-J, Yu Z-T, Zhang J-Y, Zou Z-G (2012) A copper(i) dye-sensitised TiO2-based system for efficient light harvesting and photoconversion of CO2 into hydrocarbon fuel. Dalton Trans 41:9594. doi:10.1039/c2dt30865g
176. Kecsenovity E, Endrodi B, Pápa Z et al (2016) Decoration of ultra-long carbon nanotubes with Cu 2 O nanocrystals: a hybrid platform for enhanced. J Mater Chem A:3139–3147. doi:10.1039/C5TA10457B
177. de Jongh PE, Vanmaekelbergh D, Kelly JJ (2000) Photoelectrochemistry of electrodeposited Cu2O. J Electrochem Soc 147:486. doi:10.1149/1.1393221
178. Perazolli L, Nuñez L, da Silva MRA et al (2011) TiO2/CuO films obtained by citrate precursor method for photocatalytic application. Mater Sci Appl 2:564–571. doi:10.4236/msa.2011.26075
179. Fan M, Bai Z, Zhang Q et al (2014) RSC advances aqueous CO_2 reduction on morphology controlled CuxO nanocatalysts at low overpotential. RSC Adv 4:44583–44591. doi:10.1039/C4RA09442E
180. Epifani M, Melissano E, Pace G, Schioppa M (2007) Precursors for the combustion synthesis of metal oxides from the sol – gel processing of metal complexes. J Eur Ceram Soc 27:115–123. doi:10.1016/j.jeurceramsoc.2006.04.084
181. Nandanwar SU, Chakraborty M (2012) Synthesis of colloidal $CuO/\gamma\text{-}Al_2O_3$ by microemulsion and its catalytic reduction of aromatic nitro compounds. Chin J Catal. doi:10.1016/S1872-2067(11)60433-6
182. Izaki M, Nagai M, Maeda K et al (2011) Electrodeposition of 1.4-eV-bandgap p-copper (II) oxide film with excellent photoactivity. J Electrochem Soc 158:D578. doi:10.1149/1.3614408
183. Le M, Ren M, Zhang Z et al (2011) Electrochemical reduction of CO2 to CH3OH at copper oxide surfaces. J Electrochem Soc 158:E45. doi:10.1149/1.3561636
184. Ghadimkhani G, de Tacconi NR, Chanmanee W et al (2013) Efficient solar photoelectrosynthesis of methanol from carbon dioxide using hybrid CuO-Cu2O semiconductor nanorod arrays. Chem Commun (Cambridge, England) 49:1297–1299. doi:10.1039/c2cc38068d
185. Rajeshwar K, De Tacconi NR, Ghadimkhani G et al (2013) Tailoring copper oxide semiconductor nanorod arrays for photoelectrochemical reduction of carbon dioxide to methanol. ChemPhysChem 14:2251–2259. doi:10.1002/cphc.201300080
186. Li P, Xu J, Jing H et al (2014) Wedged N-doped CuO with more negative conductive band and lower overpotential for high efficiency photoelectric converting CO2 to methanol. Appl Catal B Environ 156–157:134–140. doi:10.1016/j.apcatb.2014.03.011
187. Chiang K, Amal R, Tran T (2002) Photocatalytic degradation of cyanide using titanium dioxide modified with copper oxide. Adv Environ Res 6:471–485. doi:10.1016/S1093-0191(01)00074-0
188. Siripala W, Ivanovskaya A, Jaramillo TF et al (2003) A Cu2O/TiO2 heterojunction thin film cathode for photoelectrocatalysis. Sol Energy Mater Sol Cells 77:229–237. doi:10.1016/S0927-0248(02)00343-4
189. Li P, Jing H, Xu J et al (2014) High-efficiency synergistic conversion of CO2 to methanol using Fe2O3 nanotubes modified with double-layer Cu2O spheres. Nanoscale 6:11380–11386. doi:10.1039/C4NR02902J
190. Kang U, Choi SK, Ham DJ et al (2015) Photosynthesis of formate from CO2 and water at 1% energy efficiency via copper iron oxide catalysis. Energy Environ Sci:2638–2543. doi:10.1039/C5EE01410G

Chapter 11
Nanostructured Functional Materials: Silver Nanoparticles in Polymer for the Generation of Antimicrobial Characteristics

Luiz Fernando Gorup, Francisco N. Souza Neto, Andressa M. Kubo, José Antonio Santos Souza, Renan Aparecido Fernandes, Gabriela Lopes Fernandes, Douglas Roberto Monteiro, Debora Barros Barbosa, and Emerson Rodrigues Camargo

1 Synthesis of Silver Nanoparticles and Antimicrobial Proprieties

1.1 The Science of Nanotechnology

Nanoscience has been established recently as a new interdisciplinary science, which means that the potential of nanocomposites to improve the welfare of our society will be achieved only through an intensive and collaborative work of researchers and experts from different fields, such as biology, chemistry, materials science, and industry. The results of nanoscience are realized in nanotechnology as new materials to meet new demands of the society. Currently, the synthesis of nanocomposites prepared with polymer and silver nanoparticles is one of the main growing directions of nanoscience [18, 64, 109].

L.F. Gorup (✉) • F.N.S. Neto • A.M. Kubo • E.R. Camargo
LIEC – Laboratório Interdisciplinar de Eletroquímica e Cerâmica, Department of Chemistry, UFSCar-Federal, University of São Carlos, Rod. Washington Luis km 235 CP 676, São Carlos, SP, 13565-9905, Brazil
e-mail: lfgorup@gmail.com

J.A.S. Souza • R.A. Fernandes • G.L. Fernandes • D.B. Barbosa
Department of Dental Materials and Prosthodontics, Araçatuba Dental School, UNESP – Univ Estadual Paulista, 16015-050 Araçatuba, São Paulo, Brazil

D.R. Monteiro
Department of Pediatric Dentistry and Public Health, Araçatuba Dental School, UNESP – Univ Estadual Paulista, Araçatuba, São Paulo, Brazil

Department of Prosthodontics, University of Western São Paulo (UNOESTE), Presidente Prudente, São Paulo, Brazil

E. Longo, F.A. La Porta (eds.), *Recent Advances in Complex Functional Materials*,
DOI 10.1007/978-3-319-53898-3_11

Recently, considerable attention has been given to the use of inorganic nanoparticles in nanocomposites for creating materials with antimicrobial activity. These materials are used in various technological fields, particularly in bionanotechnology [65]. Among these, metallic particles at the nanoscale are the most promising, which include copper, zinc, titanium, magnesium, gold, and silver [1, 9, 17, 75, 134, 140].

Nanometric metallic particles show unique and considerably changed chemical, physical, and biological properties compared to their macroscaled counterparts, mainly due to their high surface-to-volume ratio [123]. At the same time, these materials provide innovative solutions in technological and environmental fields related to medicine, water treatment, and food preservation, as they offer an alternative way for the control of the proliferation of pathogenic bacteria and fungi [63, 97].

1.2 Silver Nanoparticles

Metallic nanoparticles, in particular silver nanoparticles (AgNPs), have long been known to exhibit strong toxic effects on a wide range of microorganisms. Thanks to these broad-spectrum antimicrobial properties, silver has been extensively used for biomedical applications and other environmental disinfection processes for centuries.

Although there are several studies where AgNPs are used as antimicrobial agents, their mechanism of action is still not completely understood. McShan et al. [25] and Fu et al. [92] related their antimicrobial action to the toxicity resulting from free metal ion dissolution from the surface of the AgNPs [46]. For decades, people have been using colloidal silver for their own health benefits, but detailed studies on its effect in the environment have only recently started. Initial studies have demonstrated that cells and microbes are primarily affected by a low level of silver ion (Ag^+) released from the nanoparticle [100].

Due to the increasing use of silver nanoparticles in products for daily use, such as shampoos, soaps, detergents, cosmetics, toothpastes, and medical and pharmaceutical products, there has been a remarkable effort worldwide in order to verify the safety related to the use of silver nanoparticles and to understand how these effectively kill several microorganisms [112]. Moreover, this has encouraged the textile industry to use AgNPs in different textile fabrics [53, 91], given that cotton fibers containing AgNPs have antibacterial activity.

Silver nanoparticles coated in a polymer matrix increase the efficiency of antimicrobial action with a controlled release of Ag^+ ions. Also, the combination of silver with polymeric material significantly reduces the transmission of infectious agents [50, 141]. Scientists are also studying how these characteristics affect the mechanism of cell killing [10, 126]. For instance, the antibacterial activity of different metal nanoparticles depends directly to the particle size [42, 111]. Generally, the morphological control is achieved by varying the methods of synthesis and its parameters (e.g., like reducing agents, stabilizers, and so on).

With the currently available technology, there are several synthetic routes of silver nanoparticles, which include chemical [8], electrochemical [78], radiation [135], photochemical [108], and biological methods [71]. There are several wet chemical routes to obtain silver nanoparticles, which typically involve the reduction of silver ions by a reducing agent in the presence of a colloidal stabilizer. When the particles are very small, the colloidal suspension has a yellowish color with an intense band in the 380–400 nm range and other less intense or smaller bands at longer wavelengths [107].

The band results from the collective excitation of the free electrons of the metallic particles at the surface of the nanoparticle, which is known as surface plasmon absorption [90]. Commonly used reductants are hydrazine [122], sodium borohydride [93], ascorbate, hydrogen gas, citrate (Gorup et al. 2010), and sugar, among others. The stabilization of nanoparticles can be achieved by two main methods of stabilization, i.e., steric and electrostatic. The steric stabilization is achieved by the presence of bulky, typically organic materials that cause the steric impediment in the surface of the particle, preventing coalescence of the particles. Electrostatic stabilization, on the other hand, is achieved by the coordination of anionic species on the surface of particles, such as carboxylates, halides, or polyoxoanions. This results in the formation of an electrical double layer (in fact, a diffuse electrical multilayer), which causes coulombic repulsion among the nanoparticles, preventing the contact among them. Polymers and large cations such as alkylammonium are examples of steric stabilizers. The choice of stabilizer also allows one to tune the solubility of the nanoparticles in the matrix polymeric. The more common stabilizer agents are undoubtedly the polyvinyl alcohol [117], poly(vinylpyrrolidone) [79], citrate, and cellulose [72, 88].

1.3 Antimicrobial Activity of Silver Ion and Silver Nanoparticles

Despite the bactericidal effect of silver compounds in microorganisms is well known, their mechanism of action is not fully understood [86]. Silver particles have high affinity for nucleophilic atoms such as sulfur and phosphorus, which are found both in the bacterial cell membranes and cytoplasm, so that silver nanoparticles interact with the cell membrane deregulating the process of cellular respiration [74] and, within these, interact with DNA by preventing cell division. Silver nanoparticles have been shown to interact with other microorganisms such as fungi, by preventing their adhesion to cells, thus expanding its range of antimicrobial activity [62]. Studies showed that silver nanoparticles have antifungal activity against *Trichophyton mentagrophytes* and some species of Candida [106]. The main hypotheses of the bactericidal mechanisms of action by which silver nanoparticles and ions lead to death of the bacteria are shown in Fig. 11.1 and described below [45, 76, 77, 80]:

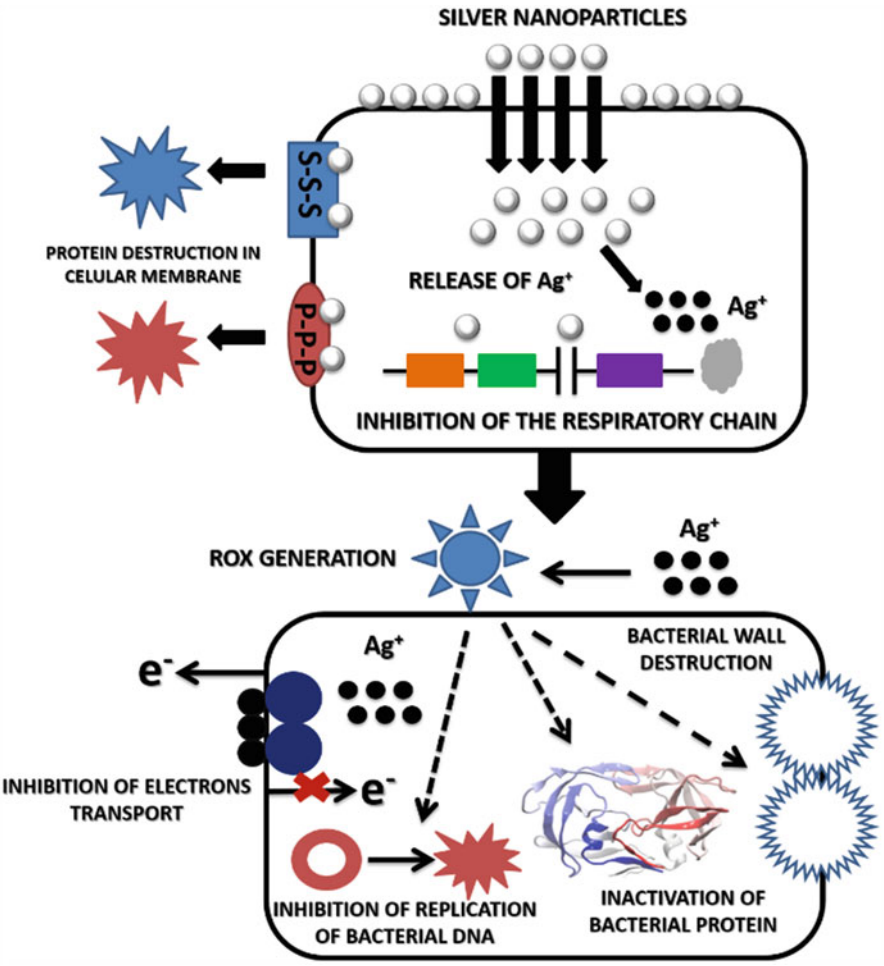

Fig. 11.1 Schematic representation of the bactericidal activity exerted by silver nanoparticles

- Silver nanoparticles have a strong interaction with the microorganisms due to their high surface area. Thus, these nanoparticles attack the bacterial surface, by penetrating into these organisms and leading to a disruption of the vital functions of the organism due to alteration of the membrane fluidity and hence increasing cell permeability.
- Bacterial membrane proteins contain sulfur and phosphorus in its structure. Both silver nanoparticles as silver ions can interact with these proteins and inhibit the DNA functions by interacting with these chemicals.
- Silver nanoparticles and/or silver ions can attack the respiratory chain in the bacterial mitochondria and lead to cell death.

- Silver nanoparticles may have a controlled release of Ag^+ once in the bacterial cells, which can form free radicals and induce oxidative stress, enhancing its bactericidal activity.

1.4 Composites with Silver Nanoparticles and Polymer

Polymer-metal nanocomposites can be prepared by two different approaches, namely, in situ and ex situ techniques [99]. By the in situ approach, AgNPs can be directly generated inside a polymer matrix by decomposition (e.g., thermolysis, photolysis, radiolysis, etc.) or by chemical reduction of a metallic precursor, conversely, by the ex situ approach; NPs are first produced by soft chemistry routes and then dispersed into polymeric matrices.

The term nanocomposite is described as a combination of two or more layers comprising a polymer matrix and a particle in which one of its dimensions is at the nanometer scale. The layers may be amorphous, semicrystalline, or crystalline. When combined, the phases can generate a synergistic behavior between the constituents of the nanocomposite.

There are several scientific types of research on the synthesis of uniform nanocomposites seeking a homogeneous load distribution in the polymer matrix and a good adhesion on the two-component interface. The main nanocomposite preparation routes from polymer latex and silver nanoparticles matrix are outlined in Fig. 11.2, but the principle is the same for other polymers.

I. Polymerization of the matrix in situ: The properties of a nanocomposite are generally determined by the matrix, which in this particular case is a polymeric material. Polymers provide an excellent support for the nanoparticles, protecting them from physical/chemical degradation and facilitating their

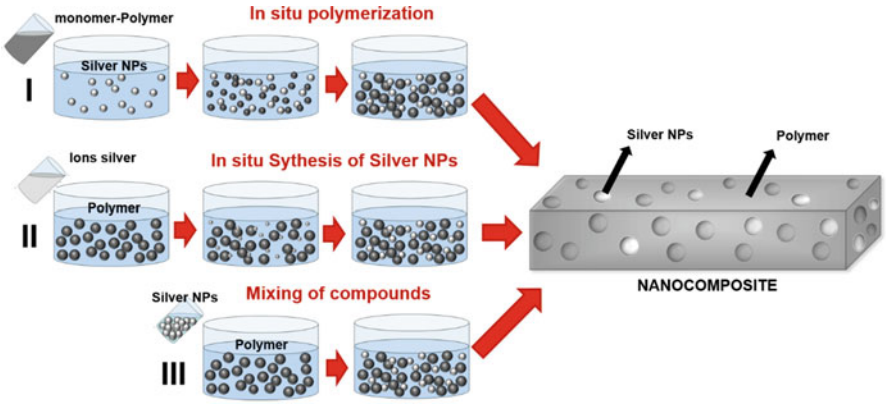

Fig. 11.2 Nanocomposite synthesis strategies: (*I*) synthesis of particles in situ; (*II*) polymerizing the matrix in situ; (*III*) mixing of components

handling/processing. The controlled synthesis of the polymer in the presence of inorganic nanoparticles enables strict control over the physicochemical properties of the matrix. It also allows a good dispersion of fillers, yielding homogeneous nanocomposites of easy processing and low production cost.

II. In situ synthesis of nanoparticles: The synthesis of the charges involves chemical methods of controlled preparation of inorganic solids. The materials prepared by this strategy are generally of chemical bonds between components, which results in more homogeneous hybrid materials and with greater consistency. The main methods for preparing nanocomposites by in situ synthesis of the loads are: solgel method and synthesis in the presence of structural materials.

III. The mixture of components: This method has been widely used in the preparation of composites, especially in nanocomposites in which the loads are lamellar or layered structures. Small lamellar inorganic compounds (montmorillonite) with nanometric dimensions are usually hydrophilic and before being dispersed in the polymer matrix must be chemically modified to make them compatible with the polymers.

The main reason for using a compound containing silver nanoparticles is one of the most powerful natural disinfectants known; therefore, its deposition onto prosthetic device surfaces (catheters, heart valves, etc.) would be an attractive approach for preventing bacterial attachment and biofilm formation, which can lead to serious infections. Another potential application is related to food processing equipment and packaging materials, where the presence of undesirable bacteria can cause food spoilage and foodborne diseases.

For this reason, an increasingly common application is the use of AgNPs for antimicrobial coatings, many textiles, polymer, and biomedical devices that contain AgNPs to provide protection against bacteria and fungi. AgNPs coated in the polymer matrix increases the efficiency of antimicrobial action with a controlled release of Ag^{+}. The combination of silver with polymeric material reduces the transmission of infectious agents.

2 Silver Nanoparticles for Consumer Products

2.1 Demands for Products with Silver Nanoparticles

Considering the current demands for better living conditions are pushing companies for a new era of sustainability and the search for new products [32]. Several countries introduced rigorous legislation regarding safety and environment requirements, including ethical obligations [67]. The relationship between companies and consumers is now much more complex, often surpassing business standards based exclusively in selling products. To survive in this competitive world, it is necessary

to stay focused in improved production processes in order to increase efficiency and efficacy, without compromising quality, convenience, or price. In this context, nanoparticles and nanotechnology emerged as a potential solution [57, 85].

2.2 A Brief History of the Use of Silver Nanoparticles

Nanoparticles can exhibit unique physicochemical properties, due to the presence of discrete energy level characteristics of confined nanometric systems [26, 70, 131]. In the case of noble metals, metallic silvers are largely used because of their known antimicrobial properties. Since antiquity, silver is used in filters or kitchenware for water disinfection [97, 110]. Historically, silver nitrate ($AgNO_3$) was reported as medical substance by Gabor [3], and in 980, Avicenna used $AgNO_3$ as a medicine for blood purifier, offensive breath, and to cure heart palpitations [87]. In the seventeenth and eighteenth centuries, $AgNO_3$ was used as a folk medicine to treat epilepsy, ulcers, and cholera [34], probably being effective only against diseases caused by microorganisms, without any antiepileptic action that is modernly treated with controlled anticonvulsants. In the nineteenth century, the Austrian surgeon Johann N. Rust used it to prevent infection in the treatment of burn [129] and Carl Crede used solutions of 0.5% $AgNO_3$ to treat *Ophthalmia neonatorum*, a neonatal conjunctivitis caused by virus or bacteria usually during the first month of life. Since 1954, colloidal AgNPs have been used in the United States as biocidal agent [104].

2.3 Toxicity and Legislation

A postantibiotic era far from a fantasy is a real possibility for our near future. Antimicrobial resistance within a wide range of infectious agents is considered a serious public health problem that urges for immediate action [86]. Increasingly new species of bacteria, both gram-negative and gram-positive, are becoming resistant to commercial drugs, requiring the production of new substances to combat them [115]. Thus, nanotechnological silver compounds may be used in combatting bacterial infections due to their low toxicity to human cells [66]. However, there is a lack of information about the risk of nanomaterials in consumer products, especially on their main side effects to human health [30]. Although international regulatory agencies successfully implemented safety procedures for a population about the problems related to exposures or ingestion of products based in nanotechnology [24], their impacts on human health and environment during long-term are still unknown [49].

Several government agencies or nongovernmental organizations approved products based in polymeric nanocomposites made with silver nanoparticles, such as the Society of Industrial Technology for Antimicrobial Articles in Japan, the National Sanitary Inspection Agency (ANVISA) in Brazil, and the Food and Drug

Administration (FDA) and the Environmental Protection Administration (EPA) in United States [2, 22]. Actually, EPA studied AgNPs especially evaluating their toxicity when in contact with the environment and biological systems, and the FDA elaborated a guidance for the use of nanotechnology in industries [19, 73, 116].

2.4 Applications

Considerable attention has been given to the widely use of inorganic nanoparticles in various fields of nanotechnology, particularly in bionanotechnology [65], in large part, because of their versatility in different areas [33]. Among the inorganic nanoparticles, metallic nanoparticles of copper, zinc, titanium, magnesium, gold, and silver are the most promising materials [102]. Indeed, copper and AgNPs effectively kill bacteria at low concentrations [35, 46, 82, 94], and their application in consumer products would be the logical next step.

Figure 11.3 shows the exponential interest in the last decade in applications of AgNPs in different fields, such as agriculture (germination and growth of plants) [56], health (dental treatment with sealers) [114], textile, and packaging industries (Fig. 11.4) [14, 37, 127].

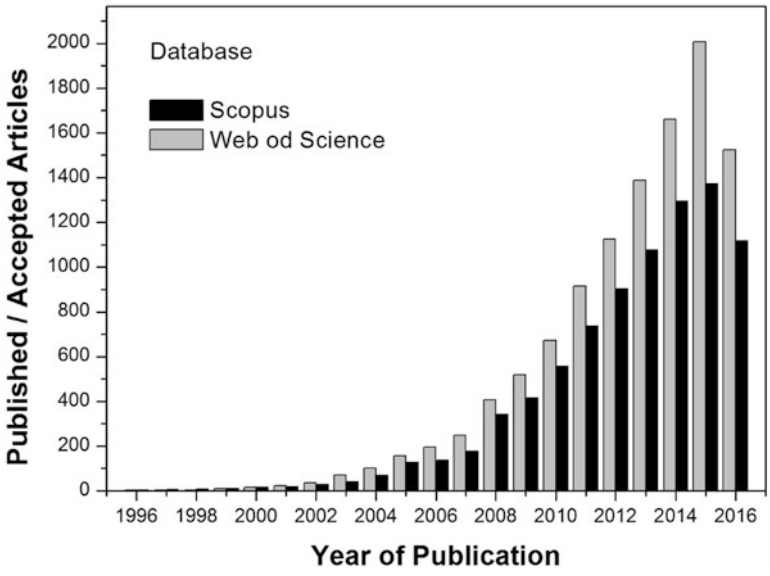

Fig. 11.3 Comparison of Scopus and Web of Science databases of published/accepted articles from 1996 to 2016 using the terms *silver nanoparticles* and *application*. In 2016, only the articles published/accepted up to September were considered

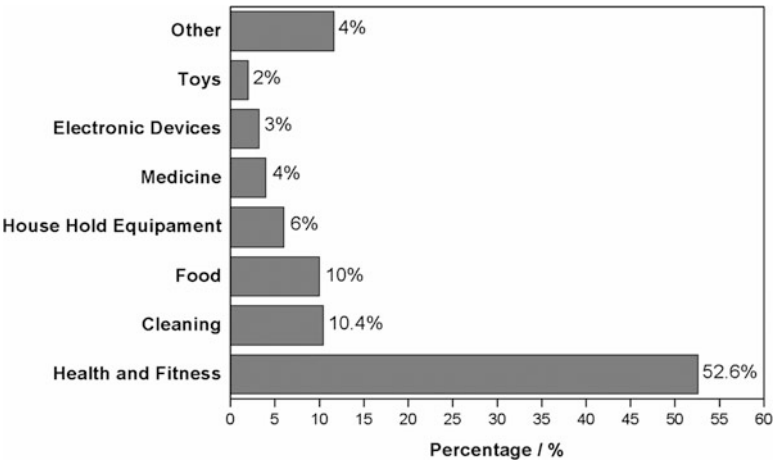

Fig. 11.4 Categories of products containing silver nanoparticles

2.5 Food Packaging

The production and use of plastics have been exponentially increasing worldwide [12, 128], with a great attention devoted to the use of coatings for fruits and vegetables [31]. The use of plastics as food packaging is relatively recent and still under development [96], their inherent advantages related to flexibility, strength, and ease of recycling [29].

Conventional petroleum-based packaging takes thousands of years to degrade, which led to the development of films and biofilms from renewable materials. Films made of polysaccharides, including cellulose derivatives, are widely used in the food industry due to their neutral sensory properties [40, 113]. One of the most promising concepts for packing is the incorporation of functional nanoparticles in biopolymers such as cellulose, agarose, chitosan, and starch [20, 38, 52]. Food industry has an increasing interest in antimicrobial packaging aiming to reduce the use of preservatives, to minimize potentially toxic and allergic responses [81]. At the same time, the food spoiling occurs due to the growth of microorganisms on the surface of food [83]. In this sense, instead of using chemical preservatives to protect food, AgNPs can be used due to their antimicrobial action to prevent the growth of microorganisms [6, 61].

Tankhiwale and Bajpai [119] investigated microbial properties of acrylamide onto cellulose and AgNPs nanocomposites against *Escherichia coli*, and Youssef et al. [136] prepared nanocomposite films of chitosan AgNPs which inhibited the growth of *Staphylococcus aureus*, *Pseudomonas aeruginosa*, *Aspergillus niger*, and *Candida albicans* and consequently increased the food shelf time.

2.6 Cosmetic Materials

Cosmetics are defined by the FDA as materials to be applied to the human body or any part thereof for cleansing, beautifying, promoting attractiveness, or altering the appearance [68]. Cosmetic products are exposed to bacteria and fungi, in particular during their manufacture or storage. Since cosmetics have a direct contact with human body, it is important to prevent their contamination against pathogenic microorganisms [44]. AgNPs have been also used for this purpose [58, 98].

The main applications of nanomaterials containing AgNPs in cosmetics include housecleaning, antiseptics, sunscreens, soap, and shampoos [11, 121]. Benn et al. [13] evaluated the likelihood of several different consumer products (shirt, medical mask and cloth, toothpaste, shampoo, detergent, towel) to release AgNPs into the environment (air, water, soil) when washed in water and concluded that they did not release significant amount of silver in the water, thus avoiding environmental and health problems to users of this products.

2.7 Clothing with Antimicrobial Activity

Nanoparticles have reached the textile industry as a way to add value to the consumer products, assigning properties to the initial material, which means a functional product in the end of the process [69]. In the case of silver nanoparticles, the properties are associated to the antibacterial and antifungal aspects [21].

Cotton fabrics are the most common materials to associate with the nanoparticles [133]. At first, because of the consumer market, and the ability of this functional material in eliminating the odor caused by microorganisms, such as bacteria, El-Rafie et al. [36] embedded AgNPs in cotton fabrics and tested their efficiency as antibacterial agent. The amount of *Staphylococcus aureus* and *Escherichia coli* is reduced by 97 and 91%, respectively. On the other hand, Hebeish et al. [47] have evaluated the antimicrobial activity of cotton fabrics with different quantities of AgNPs in two types of bacteria (*Staphylococcus aureus* and *Escherichia coli)* and one type of fungi (*Candida albicans),* showing that the greater the amount of AgNPs the higher the inhibition of bacteria and fungi growth.

Besides the use in clothing, cotton fabrics can be applied in medical area as a wound dressing. Ravindra et al. [103] have observed an excellent antibacterial behavior of cotton fibers with AgNPs against *Escherichia coli*. Also, their functional material presented an improvement of thermal stability and elongation properties which enhances its use as wound and burn dressing. Velazquez-Velazquez et al. [124] have shown that commercial cotton dressings embedded with AgNPs were able to avoid the growth of the bacteria *Pseudomonas aeruginosa*, present in chronic wounds of patients.

3 Polymer with Silver Nanoparticles for Medical and Health Applications

With the advances in nanotechnology, the incorporation of metal nanoparticles (such as silver nanoparticles) in a polymer matrix promotes the formation of polymer nanocomposites, and therefore a combination of the properties of these components (polymer and nanoparticles) yields a more effective material in many aspects [15, 27, 118]. In this case, the polymer not only functions as a support for the nanoparticles but can enhance the antibacterial performance of this material [118].

The control or prevention of microbial colonization is a necessity due to the several infectious diseases that affect human health. Medical devices such as vascular and urinary catheters, hip and knee prostheses, and endotracheal tube contamination are responsible for many cases of infections [27, 105].

The structural and morphological nature of polymers and chemical properties such as long polymeric chains are characteristics that allow the incorporation of silver nanoparticles, besides to prevent the agglomeration of these nanoparticles (which could decrease the antimicrobial effect of silver). In addition, the size of nanoparticles is of great importance, as it influences the surface reactivity and, consequently, its antimicrobial effect [23, 27, 51, 138].

The synthesis of polymer nanocomposites can be performed in two ways: (1) in situ, where the nanoparticles are synthesized in the middle of the polymer matrix, and (2) ex situ, meaning that AgNPs are synthesized prior to their incorporation in the matrix, so that this matrix is only used as a dispersion medium [46, 94].

The first method is mainly used for hydrogel polymers, where the presence of water improves the stability of the nanoparticles. The second method is most widely used for the thermoplastic nanocomposites, where high viscoelastic matrix in a melting state is used to improve the dispersion of nanoparticles [46, 94].

The development of hydrogel nanocomposites has been widely researched. For example, poly(acrylamide-co-acrylic acid) can be used as a template for the formation of AgNPs with a size of about 25–30 nm and with excellent antimicrobial activity [46, 94, 120]. Silver-hydrogel nanocomposite based on poly(vinyl alcohol) and sodium alginate has also been prepared and exhibited excellent antimicrobial activity against gram-positive and gram-negative [43, 46, 94].

A hydrophilic environment is excellent for antimicrobial applications, since water is necessary to facilitate the release of silver ions from the polymer matrix; in addition a moist environment or hydrate favors the healing of infected wounds [27, 84].

With all the benefits of the polymeric matrix associated with AgNPs and with the increase in the resistance of microorganisms to conventional antimicrobial agents, several studies have been carried out using different types of polymers. Some examples of these polymers and their microbial applicability are presented below.

While the use of carboxymethyl cellulose loaded with silver nanoparticles could be an alternative to prevent infections, the antimicrobial activity of this system was carried out against *E. coli*, *P. aeruginosa, S. aureus*, and *B. subtilis* and showed a good antimicrobial effect [48].

Biocompatibility tests have been carried out in vitro using fibroblasts and keratinocytes, in a study showing no inhibition of cell proliferation, thus safe for use as a topic material. The antimicrobial test against *S. aureus* (ATCC 6538) showed a great reduction in the number of colonies forming units at a concentration of 50 ppm of AgNPs [28].

The association between polymers is a common approach. A study used a gel of carboxymethyl cellulose with AgNPs bonded to cotton an antimicrobial test against *Staphylococcus aureus* (ATCC 6538) and *Klebsiella pneumonia* (ATCC 4352), showing a 99.9% reduction for both, thus being an alternative for wound dresses [16]. In addition, cotton with 250 ppm of AgNPs were tested against *E. coli* (AATCC 2784), *S. aureus* (AATCC 147), and *C. albicans* (AATCC 100–2004) showing an anti-inflammatory activity in an in vivo model [47].

Tampons and baby diapers are based on cellulose pulp. Although, these products are used worldwide, this substrate offers a good surface for the growth of microorganisms. The addition of AgNPs could help to prevent the initial microbial colonization phase. In this sense, AgNPs with size less than 100 nm at a concentration of 0.2 g/napkin showed no cytotoxic effects in rabbits, as well as in MTT assay, and had an excellent effect to control *Staphylococcus aureus* and *Klebsiella pneumonia* [54].

ICU pathogens have been considered a worldwide problem. A study was carried out to develop a nanobiomaterial containing carboxymethyl cellulose and AgNPs, whose antimicrobial activity was verified by Kirby-Bauer method. The silver nanoparticle – hydrogel composites – exhibited higher antibacterial activity against *Escherichia coli*, *Klebsiella pneumoniae*, *Pseudomonas aeruginosa*, *Proteus vulgaris*, *Staphylococcus aureus*, and *Proteus mirabilis* compared to a corresponding neat hydrogel [5].

Inflammation and infection are responsible for the maintenance of open wounds. AgNPs were used in an in vitro and in vivo model against a wound healing process. Bacterial cellulose gel membranes were impregnated with AgNPs and used to evaluate the antimicrobial and cytotoxic effect. *S aureus* (ATCC26085) was chosen to be tested, and the gel membranes exhibited significant antibacterial activity against these bacteria, as well as to present no side effect verified in MTT assay. The area of the wound was smaller in the treated groups when compared with the controls, thus being a good alternative to being used in treatments of wounds [130].

Nanobiomaterials with chitosan are also studied aiming to wound treatment. Membranes of chitosan and AgNPs were evaluated against *Staphylococcus aureus* (ATCC 25913), *Staphylococcus sciuri* (ATCC 29061), *Escherichia coli* (ATCC 35218), and *Pseudomonas aeruginosa* (ATCC 9028), as well as biocompatibility test in vitro and in vivo model. The membranes showed excellent biocompatible properties through in vitro and in vivo tests [89]. AgNPs with chitosan were also tested in an in vivo model showing a wound healing process greater than the groups with no treatment. Moreover, the antimicrobial efficacy of this hydrogel was observed against *E. coli* and *S. aureus*.

Other in vivo model using AgNPs and chitosan showed an antimicrobial effect against *E. coli* and *S. aureus* and nontoxicity effect at the concentration of 0.001% of silver oxide nanoparticles. The results of wound closure rate showed the treatment with this nanobiomaterial accelerated this process [7].

The process of storage of food is critical, given that contamination of food with microorganisms can be a problem for producers and consumers. It is known that AgNPs can prevent infections when incorporated into the packages. Films based on chitosan and AgNPs were developed and their antimicrobial activity was tested against *S. aureus*, *Pseudomonas aeruginosa*, *Candida albicans*, and *Aspergillus niger*, showing a good effect against these microorganisms. Moreover, because of the hydrophilic, biodegradable, biocompatible, and nontoxic character of chitosan/silver nanocomposites protected with chitosan layers, it can be used for biomedical, pharmaceutical, biosensor, and edible packaging applications [136].

Odor present in some leather or cotton clothes is a promising field for the companies to find strategies to control this inconvenience. Given that this odor is caused by some microorganisms, AgNPs were incorporated in lather and cotton, and their antimicrobial activity was evaluated against the major microorganisms which causes this problem. The results showed a good antimicrobial effect against *Brevibacterium linens*, in a study showing the great potential of AgNPs and their application in the process of manufacturing clothes [125].

Besides the use for medical approaches and in industry, 80% of gastrointestinal infectious and parasitic diseases are due to the use of non-potable water in the world. Contaminated water is regarded as the main vehicle involved in the transmission of bacteria, viruses, or parasites. Most pathogenic microorganisms contained in the water are removed in the early stages of treatment for water purification. So, AgNPs showed as a great alternative to treat water. The filter of nitrocellulose was prepared and tested against *E. coli* (ATCC 8739), *P. aeruginosa* (ATCC 9027), and *E. faecalis* (ATCC 29212). At a concentration of 1 mg L^{-1} , it was able to reduce the bacteria colony count by over five orders of magnitude [39].

Bacterial contaminations triggered by medical implants are still a major issue in hospital-acquired infections. These infections are often caused by the production of biofilms on the surface of medical implants mostly affecting the urinary tract, respiratory tract, and bloodstream [55].

Fuchs et al. [41] have evaluated the antibacterial properties of stable, uniform, high surface coverage films of poly(hydroxyethyl methacrylate-co-2-methacryloyloxyethyl phosphorylcholine) (p(HEMA-co-MPC)) with embedded, non-leaching AgNPs. Cultures of *Escherichia coli* were used in this study as a suitable bacterial model. They observed that the incorporated AgNPs showed antibacterial properties (99.9%) up to 1×10^5 CFU mL^{-1} after 1 h in nongrowing medium and 4 h under growing conditions. They hypothesize that the antibacterial effect occurs mainly by a contact active mechanism with contributions from a slow, nonmeasurable release of silver ions. Thus, it is envisioned that these films may prove effective for coating devices such as catheters, stents, and dialysis equipment.

High-density polyethylene is commonly used for long-term catheters, facial restoration, nasal dorsal augmentation, mandibular contours, ear reconstruction, and augmentation of facial contours. However, such devices may lead to a postoperative complication like bacterial infections and biofilm formation, which may not always be eradicated by antibiotics.

Zapata et al. [137] studied the incorporation of silver nanospheres (∼10 nm) into high-density polyethylene (HDPE) by in situ ethylene polymerization. The antibacterial effect of the silver-nanofiber composites was evaluated after incubation of *Escherichia coli* ATCC 25923 for 8 h on their surface. Bacterial viability tests showed that the silver-nanofiber composites inhibited the growth of *E. coli* ATCC 25923 by 88 and 56%. This behavior is attributed to increased silver ion release from the nanocomposite. Moreover, transmission electron microscopy (TEM) analysis showed that the antibacterial effect is associated with membrane disruption but not with changes in shape.

In another study, Ziabka et al. [139] synthesized a HDPE containing AgNPs. This new material was tested against gram-positive *Staphylococcus aureus* and gram-negative *Escherichia coli*. Antibacterial tests prove that nanosilver-modified materials have bactericidal activity against tested bacteria.

The development of hybrid nanofibers is of tremendous interest for the biomedical research community. They have been also used in wound dressing and healing where these scaffolds possess more homogeneity and oxygen penetration and prevent infections and dehydration. It has been reported that Ag nanoparticle-embedded nanofibers showed enhanced antimicrobial efficacy against gram-positive and gram-negative bacteria [59].

Xu et al. [132] synthesized Ag-loaded nylon nanofibers. Antibacterial performance tests were conducted. A strong antibacterial activity of Ag-loaded nylon was clearly demonstrated with bacterial killing rates reaching ∼100% for gram-negative *E. coli* and *Pseudomonas aeruginosa* microorganisms. Moreover, the authors concluded that both Ag nanoparticles and the Ag ions were found to be the reason for enhanced cell death in the bacterial solutions.

Perelshtein et al. [95] performed a study which AgNPs were deposited into the surface of different fabrics (nylon, polyester, and cotton) by ultrasound irradiation. The antimicrobial activity of these materials was tested against gram-negative (*E. coli*) and gram-positive (*Staphylococcus aureus*) bacteria. Cultures of the bacteria were eradicated completely after 1 h of treatment with the 6% (wt%) coated fabric and after approximately 1.5 h for the 1 wt% sample. Thus, these coated fabrics can have potential applications in wound dressing, in bed lining, and as medical bandages. Moreover, it can also be recommended for the purification of medical and food equipment, domestic cleaning, etc.

Controlled drug delivery systems have gained much attention in the last few decades. Polymers contain metal nanoparticles which are used as antimicrobial or drug delivery systems and have been captured attention, because of their novelty in being long-lasting biocidal materials with high-temperature stability and low volatility [60].

Poly(D,L-lactic-*co*-glycolic acid) polymers (PLGA) are ones of the most commonly used for preparing eroding drug-release devices. Almajhdi et al. [4] synthesized a new class of poly lactic-co-glycolic acid (PLGA) nanofibers containing AgNPs. They evaluated the anticancer activity of PLGA nanofibers containing different AgNP percentages against liver carcinoma cell line as well as antimicrobial efficacy against different types of bacteria. They observed that the anticancer activity of PLGA nanofibrous increased by increasing the concentration of the coated AgNPs. Moreover, PLGA/AgNPs (7%) inhibited all the strains used in this study (*E. coli* ATCC 51659, *Staphylococcus aureus* ATCC 13565, *Bacillus cereus* EMCC 1080, *Listeria monocytogenes* EMCC 1875, and *Salmonella typhimurium* ATCC 25566) with inhibition zone diameter of 10 ± 1.27 mm.

4 Trends and Future Perspectives for the Use of Polymer with Silver Nanoparticles

In summary, the combination of silver with polymeric material makes these materials promising commercial products, as they could be used in treating infectious pathogens, preventing microbial infections, and reducing the transmission of infectious agents. The application of polymeric material containing AgNPs is still far from achieving the maximal potential in the environmental, medical, or chemical fields. Considering that there are still many combinations and applications to be explored, these can be open a new generation of products for controlling and preventing further outbreak of diseases caused by fungi and bacteria. However, the emerging questions on the investigations assessing the efficacy of nanocomposites as disinfectants for real environmental contaminations are needed and especially the possible impacts on the contamination of the ecosystem.

References

1. Jesline A, John NP, Narayanan PM, Vani C, Murugan S (2015) Antimicrobial activity of zinc and titanium dioxide nanoparticles against biofilm-producing methicillin-resistant Staphylococcus aureus. Appl Nanosci 5(2):157–162. doi:10.1007/s13204-014-0301-x
2. Abou El-Nour KMM, Aa E, Al-Warthan A, Ammar RAA (2010) Synthesis and applications of silver nanoparticles. Arab J Chem 3:135–140
3. Alexander JW (2009) History of the medical use of silver. Surg Infect 10(3):289–292
4. Almajhdi FN, Fouad H, Khalil KA et al (2014) In-vitro anticancer and antimicrobial activities of PLGA/silver nanofiber composites prepared by electrospinning. J Mater Sci Mater Med 25:1045–1053
5. Alshehri SM, Aldalbahi A, Al-Hajji AB, Chaudhary AA, Panhuis MI, Alhokbany N, Ahamad T (2016) Development of carboxymethyl cellulose-based hydrogel and nanosilver composite as antimicrobial agents for UTI pathogens. Carbohydr Polym 138:229–236
6. Appendini P, Hotchkiss JH (2002) Review of antimicrobial food packaging. Innovative Food Sci Emerg Technol 3:113–126

7. Archana D, Singh BK, Dutta J, Dutta PK (2015) Chitosan-PVP-nano silver oxide wound dressing: in vitro and in vivo evaluation. Int J Biol Macromol 73:49–57
8. Khodashenas B, Ghorbani HR (2014) Synthesis of silver nanoparticles with different shapes. Arab J Chem, http://dx.doi.org/10.1016/j.arabjc.2014.12.014
9. Le Ouay B, Stellacci F (2015) Antibacterial activity of silver nanoparticles: a surface science insight. Nano Today 10(3):339–354, http://dx.doi.org/10.1016/j.nantod.2015.04.002
10. Ramalingam B, Parandhaman T, Das SK (2016) Antibacterial effects of biosynthesized silver nanoparticles on surface ultrastructure and nanomechanical properties of gram-negative bacteria viz. Escherichia coli and pseudomonas aeruginosa. ACS Appl Mater Interfaces 8(7):4963–4976. doi:10.1021/acsami.6b00161
11. Bansod SD, Bawaskar MS, Gade AK, Rai MK (2015) Development of shampoo, soap and ointment formulated by green synthesised silver nanoparticles functionalised with antimicrobial plants oils in veterinary dermatology: treatment and prevention strategies. Inst Eng Technol 9(4):165–171
12. Beltrán FR, Lorenzo V, de la Orden MU, Martínez-Urreaga J (2016) Effect of different mechanical recycling processes on the hydrolytic degradation of poly(l-lactic acid). Polym Degrad Stab 133:339–348
13. Benn T, Cavanagh B, Hristovski K, Posner JD, Westerhoff P (2010) The release of nanosilver from consumer products used in the home. J Environ Qual 39(6):1875
14. Blaser SA, Scheringer M, Macleod M, Hungerbuhler K (2008) Estimation of cumulative aquatic exposure and risk due to silver: contribution of nano-functionalized plastics and textiles. Sci Total Environ 390:396–409
15. Bourlinos AB, Stassinopoulos A, Anglos D, Herrera R, Anastasiadis SH, Petridis D et al (2006) Functionalized ZnO nanoparticles with liquidlike behavior and their photoluminescence properties. Small 2:513
16. Bozaci E, Akar E, Ozdogan E, Demir A, Altinisik A, Seki Y (2015) Application of carboxymethylcellulose hydrogel based silver nanocomposites on cotton fabrics for antibacterial property. Carbohydr Polym 134:128–135
17. Arijit Kumar C, Ruchira C, Tarakdas B (2014) Mechanism of antibacterial activity of copper nanoparticles. Nanotechnology 25(13):135101
18. Racles C, Stoica I, Doroftei F, Cozan V (2011) A simple method for the preparation of colloidal polymer-supported silver nanoparticles. J Nanopart Res 13(12):6971–6980. doi:10.1007/s11051-011-0608-4
19. Carbone M, Donia DT, Sabbatella G, Antiochia R (2016) Silver nanoparticles in polymeric matrices for fresh food packaging. J King Saud Univ Sci 28:273–279
20. Cha DS, Chinnan MS (2004) Biopolymer-based antimicrobial packaging: a review. Crit Rev Food Sci Nutr 44:223–237
21. Chaloupka K, Malam Y, Seifalian AM (2010) Nanosilver as a new generation of nanoproduct in biomedical applications. Trends Biotechnol 28(11):580–588
22. Chau C-F, Wu S-H, Yen G-C (2007) The development of regulations for food nanotechnology. Trends Food Sci Technol 18:269–280
23. Chen A, Wang H, Li X (2005) One-step process to fabricate Ag-polypyrrole coaxial nanocables. Chemical Communications. Chem Commun:1863–1864. doi:10.1039/B417744D
24. Choi JY, Ramachandran G, Kandlikar M (2008) The impact of toxicity testing costs on nanomaterial regulation. Environ Sci Technol 43(9):3030–3034
25. McShan D, Ray PC, Yu H (2014) Molecular toxicity mechanism of nanosilver. J Food Drug Anal 22(1):116–127, http://dx.doi.org/10.1016/j.jfda.2014.01.010
26. Dai J, Bruening ML (2002) Catalytic nanoparticles formed by reduction of metal ions in multilayered polyelectrolyte films. Nano Lett 2(5):497–501
27. Dallas P, Virender KS, Radek Z (2011) Silver polymeric nanocomposites as advanced antimicrobial agents: classification, synthetic paths, applications, and perspectives. Adv Colloid Interf Sci 166:119–135
28. Das A, Kumar A, Patil NB, Viswanathan C, Ghosh D (2015) Preparation and characterization of silver nanoparticle loaded amorphous hydrogel of carboxymethylcellulose for infected wounds. Carbohydr Polym 130:254–261

29. Davis G, Song JH (2006) Biodegradable packaging based on raw materials from crops and their impact on waste management. Ind Crop Prod 23:147–161
30. De Jong WH, Borm PJ (2008) Drug delivery and nanoparticles: applications and hazards. Int J Med 3(2):133–149
31. de Moura MR, Mattoso LHC, Zucolotto V (2012) Development of cellulose-based bactericidal nanocomposites containing silver nanoparticles and their use as active food packaging. J Food Eng 109:520–524
32. Deng Y, Li J, Pu Y, Chen Y, Zhao J, Tang J (2016) Ultra-fine silver nanoparticles dispersed in mono-dispersed amino functionalized poly glycidyl methacrylate based microspheres as an effective anti-bacterial agent. React Funct Polym 103:92–98
33. dos Santos CA, Seckler MM, Ingle AP, Gupta I, Galdiero S, Galdiero M, Gade A, Rai M (2014) Silver nanoparticles: therapeutical uses, toxicity, and safety issues. J Pharm Sci 103(7):1931–1944
34. Edwards-Jones V (2009) The benefits of silver in hygiene, personal care and healthcare. Lett Appl Microbiol 49:147–152
35. Egger S, Lehmann RP, Height MJ, Loessner MJ, Schuppler M (2009) Antimicrobial properties of a novel silver-silica nanocomposite material. Appl Environ Microbiol 75(9):2973–2976
36. El-Rafie MH, Mohamed AA, Shaheen TI, Hebeish A (2010) Antimicrobial effect of silver nanoparticles produced by fungal process on cotton fabrics. Carbohydr Polym 80:779–782
37. Fabrega J, Luoma SN, Tyler CR, Galloway TS, Lead JR (2011) Silver nanoparticles: behaviour and effects in the aquatic environment. Environ Int 37:517–531
38. Fernández JA, Fernández-Baldo MA, Berni E, Camí G, Durán N, Raba J, Sanza MI (2016) Production of silver nanoparticles using yeasts and evaluation of theirantifungal activity against phytopathogenic fungi. Process Biochem 51:1306–1313
39. Fernandez JG, Almeida CA, Fernandez-Baldo MA, Felici E, Raba J, Sanz MI (2016) Development of nitrocellulose membrane filters impregnated with different biosynthesized silver nanoparticles applied to water purification. Talanta 146:237–243
40. Ferreira AR, Alves VD, Coelhoso IM (2016) Polysaccharide-based membranes in food packaging applications. Membranes 6(2):22
41. Fuchs AV, Ritz S, Pütz S, Mailänder V, Landfester K, Ziener U (2013) Bioinspired phosphorylcholine containing polymer films with silver nanoparticles combuning antifouling and antibacterial properties. Biomater Sci 1:470–477
42. Martínez-Castañón GA, Niño-Martínez N, Martínez-Gutierrez F, Martínez-Mendoza JR, Ruiz F (2008) Synthesis and antibacterial activity of silver nanoparticles with different sizes. J Nanopart Res 10(8):1343–1348. doi:10.1007/s11051-008-9428-6
43. Ghasemzadeh H, Ghanaat F (2014) Antimicrobial alginate/PVA silver nanocomposite hydrogel, synthesis and characterization. J Polym Res 21:355–269
44. Grice EA, Segre JA (2011) The skin microbiome. Nat Rev Microbiol 9(4):244–253
45. Bao H, Yu X, Xu C, Li X, Li Z, Wei D, Liu Y (2015) New toxicity mechanism of silver nanoparticles: promoting apoptosis and inhibiting proliferation. PLoS One 10(3):e0122535. doi:10.1371/journal.pone.0122535
46. Palza H (2015) Antimicrobial polymers with metal nanoparticles. Int J Mol Sci 16(1):2099–2116. doi:10.3390/ijms16012099
47. Hebeish A, El-Rafie MH, El-Sheikh MA, Seleem AA, El-Naggar ME (2014) Antimicrobial wound dressing and anti-inflammatory efficacy of silver nanoparticles. Int J Biol Macromol 65:509–515
48. Hebeish A, Hashem M, El-Hady MM, Sharaf S (2013) Development of CMC hydrogels loaded with silver nano-particles for medical applications. Carbohydr Polym 92(1):407–413
49. Hoet PH, Bruske-Hohlfeld I, Salata OV (2004) Nanoparticles – known and unknown health risks. J Nanobiotechnol 2:12
50. Armentano I, Arciola CR, Fortunati E, Ferrari D, Mattioli S, Amoroso CF, Rizzo J, Kenny JM, Imbriani M, Visai L (2014) The interaction of bacteria with engineered nanostructured polymeric materials: a review. Sci World J 2014:410423. doi:10.1155/2014/410423

51. Ijeri VS, Nair JR, Gerbaldi C, Bongiovanni RM, Penazzi N (2010) Metallopolymer capacitor in “one pot” by self-directed UV-assisted process. ACS Appl Mater Interfaces 2:3192
52. Ji N, Liu C, Zhang S, Xiong L, Sun Q (2016) Elaboration and characterization of corn starch films incorporating silver nanoparticles obtained using short glucan chains. LWT- Food Sci Technol 74:311–318
53. Kulthong K, Srisung S, Boonpavanitchakul K, Kangwansupamonkon W, Maniratanachote R (2010) Determination of silver nanoparticle release from antibacterial fabrics into artificial sweat. Part Fibre Toxicol 7:8–8. doi:10.1186/1743-8977-7-8
54. Kavitha Sankar PC, Ramakrishnan R, Rosemary MJ (2016) Biological evaluation of nanosilver incorporated cellulose pulp for hygiene products. Mater Sci Eng C Mater Biol Appl 61:631–637
55. Khoo X, Grinstaff MW (2011) Novel infection-resistant surface coatings: a bioengineering approach. MRS Bull 36(5):357–366. doi:10.1557/mrs.2011.66
56. Khot LR, Sankaran S, Maja JM, Ehsani R, Schuster EW (2012) Applications of nanomaterials in agricultural production and crop protection: a review. Crop Prot 35:64–70
57. Kittler S, Greulich C, Diendorf J, Köller M, Epple M (2010) Toxicity of silver nanoparticles increases during storage because of slow dissolution under release of silver ions. Chem Mater 22:4548–4554
58. Kokura S, Handa O, Takagi T, Ishikawa T, Naito Y, Yoshikawa T (2010) Silver nanoparticles as a safe preservative for use in cosmetics. Nanomed Nanotechnol Biol Med 6:570–574
59. Kong H, Jang J (2008) Synthesis and antimicrobial properties of novel silver/polyrhodanine nanofibers. Biomacromolecules 9:2677–2681
60. Kumar R, Münstedt H (2005) Silver ion release from antimicrobial polyamide/silver composites. Biomaterials 26:2081–2088
61. Kuorwel KK, Cran MJ, Sonneveld K, Miltz J, Bigger SW (2011) Antimicrobial activity of biodegradable polysaccharide and protein-based films containing active agents. J Food Sci 76(3):R90–R102
62. Ge L, Li Q, Wang M, Ouyang J, Li X, Xing MMQ (2014) Nanosilver particles in medical applications: synthesis, performance, and toxicity. Int J Nanomedicine 9:2399–2407. doi:10.2147/IJN.S55015
63. Mpenyana-Monyatsi L, Mthombeni NH, Onyango MS, Momba MNB (2012) Cost-effective filter materials coated with silver nanoparticles for the removal of pathogenic bacteria in groundwater. Int J Environ Res Public Health 9(1):244–271. doi:10.3390/ijerph9010244
64. Zang L, Qiu J, Yang C, Sakai E (2016) Preparation and application of conducting polymer/Ag/clay composite nanoparticles formed by in situ UV-induced dispersion polymerization. Sci Rep 6:20470. doi:10.1038/srep20470
65. Ladj R, Bitar A, Eissa M, Mugnier Y, Le Dantec R, Fessi H, Elaissari A (2013) Individual inorganic nanoparticles: preparation, functionalization and in vitro biomedical diagnostic applications. J Mater Chem B 1:1381
66. Lara HH, Ayala-Núñez NV, Ixtepan Turrent LC, Rodríguez Padilla C (2009) Bactericidal effect of silver nanoparticles against multidrug-resistant bacteria. World J Microbiol Biotechnol 26:615–621
67. Llorens A, Lloret E, Picouet PA, Trbojevich R, Fernandez A (2012) Metallic-based micro and nanocomposites in food contact materials and active food packaging. Trends Food Sci Technol 24:19–29
68. Lohani A, Verma A, Joshi H, Yadav N, Karki N (2014) Nanotechnology-based cosmeceuticals. ISRN Dermatol 2014:843687
69. Lombi E, Donner E, Scheckel KG, Sekine R, Lorenz C, Goetz NV, Nowack B (2014) Silver speciation and release in commercial antimicrobial textiles as influenced by washing. Chemosphere 111:352–358
70. Luong ND, Lee Y, Nam J-D (2008) Highly-loaded silver nanoparticles in ultrafine cellulose acetate nanofibrillar aerogel. Eur Polym J 44:3116–3121
71. Sabri MA, Umer A, Awan GH, Hassan MF, Hasnain A (2016) Selection of suitable biological method for the synthesis of silver nanoparticles. Nanomater Nanotechnol 6:29. doi:10.5772/62644

72. Basuny M, Ali IO, El-Gawad AA, Bakr MF, Salama TM (2015) A fast green synthesis of Ag nanoparticles in carboxymethyl cellulose (CMC) through UV irradiation technique for antibacterial applications. J Sol-Gel Sci Technol 75(3):530–540. doi:10.1007/s10971-015-3723-3
73. Carbone M, Donia DT, Sabbatella G, Antiochia R (2016) Silver nanoparticles in polymeric matrices for fresh food packaging. J King Saud UnivSci 28(4):273–279, http://dx.doi.org/10.1016/j.jksus.2016.05.004
74. Chen M, Yang Z, Wu H, Pan X, Xie X, Wu C (2011) Antimicrobial activity and the mechanism of silver nanoparticle thermosensitive gel. Int J Nanomedicine 6:2873–2877. doi:10.2147/IJN.S23945
75. Guzman M, Dille J, Godet S (2012) Synthesis and antibacterial activity of silver nanoparticles against gram-positive and gram-negative bacteria. Nanomed Nanotechnol Biol Med 8(1):37–45, http://dx.doi.org/10.1016/j.nano.2011.05.007
76. Lopez-Heras M, Theodorou IG, Leo BF, Ryan MP, Porter AE (2015) Towards understanding the antibacterial activity of Ag nanoparticles: electron microscopy in the analysis of the materials-biology interface in the lung. Environ Sci Nano 2(4):312–326. doi:10.1039/C5EN00051C
77. Mollick MMR, Rana S, Dash SK, Chattopadhyay S, Bhowmick B, Maity D, Mondal D, Pattanayak S, Roy S, Chakraborty M, Chattopadhyay D (2015) Studies on green synthesized silver nanoparticles using Abelmoschus esculentus (L.) pulp extract having anticancer (in vitro) and antimicrobial applications. Arab J Chem, http://dx.doi.org/10.1016/j.arabjc.2015.04.033
78. Starowicz M, Stypuła B, Banaś J (2006) Electrochemical synthesis of silver nanoparticles. Electrochem Commun 8(2):227–230, http://dx.doi.org/10.1016/j.elecom.2005.11.018
79. Tejamaya M, Römer I, Merrifield RC, Lead JR (2012) Stability of citrate, PVP, and PEG coated silver nanoparticles in ecotoxicology media. Environ Sci Technol 46(13):7011–7017. doi:10.1021/es2038596
80. Yamanaka M, Hara K, Kudo J (2005) Bactericidal actions of a silver ion solution on Escherichia coli, studied by energy-filtering transmission electron microscopy and proteomic analysis. Appl Environ Microbiol 71(11):7589–7593
81. Malhotra B, Keshwani A, Kharkwal H (2015) Antimicrobial food packaging: potential and pitfalls. Front Microbiol 6:611
82. Marambio-Jones C, Hoek EMV (2010) A review of the antibacterial effects of silver nanomaterials and potential implications for human health and the environment. J Nanopart Res 12:1531–1551
83. Mastromatteo M, Conte A, Del Nobile MA (2010) Combined use of modified atmosphere packaging and natural compounds for food preservation. Food Eng Rev 2:28–38
84. Melaiye A, Sun Z, Hindi K, Milsted A, Ely D, Reneker DH et al (2005) Silver(I)-imidazole cyclophane gem-diol complexes encapsulated by electrospun tecophilic nanofibers: formation of nanosilver particles and antimicrobial activity. J Am Chem Soc 127:2285
85. Miller KP, Wang L, Benicewicz BC, Decho AW (2015) Inorganic nanoparticles engineered to attack bacteria. Chem Soc Rev 44:7787–7807
86. Morones JR, Elechiguerra JL, Camacho A, Holt K, Kouri JB, Ramirez JT, Yacaman MJ (2005) The bactericidal effect of silver nanoparticles. Nanotechnology 16:2346–2353
87. Muffly TM, Tizzano AP, Walters MD (2011) The history and evolution of sutures in pelvic surgery. J R Soc Med 104(3):107–112
88. Bastús NG, Merkoçi F, Piella J, Puntes V (2014) Synthesis of highly monodisperse citrate-stabilized silver nanoparticles of up to 200 nm: kinetic control and catalytic properties. Chem Mater 26(9):2836–2846. doi:10.1021/cm500316k
89. Nhi TT, Khon HC, Hoai NT, Bao BC, Quyen TN, Van Toi V, Hiep NT (2016) Fabrication of electrospun polycaprolactone coated withchitosan-silver nanoparticles membranes for wound dressing applications. J Mater Sci Mater Med 27(10):156
90. Yeshchenko OA, Dmitruk IM, Alexeenko AA, Kotko AV, Verdal J, Pinchuk AO (2012) Size and temperature effects on the surface plasmon resonance in silver nanoparticles. Plasmonics 7(4):685–694. doi:10.1007/s11468-012-9359-z

91. Rivero PJ, Urrutia A, Goicoechea J, Arregui FJ (2015) Nanomaterials for functional textiles and fibers. Nanoscale Res Lett 10:501. doi:10.1186/s11671-015-1195-6
92. Fu PP, Xia Q, Hwang H-M, Ray PC, Yu H (2014) Mechanisms of nanotoxicity: generation of reactive oxygen species. J Food Drug Anal 22(1):64–75, http://dx.doi.org/10.1016/j.jfda.2014.01.005
93. Van Dong P, Ha CH, Binh LT, Kasbohm J (2012) Chemical synthesis and antibacterial activity of novel-shaped silver nanoparticles. Int Nano Lett 2(1):9. doi:10.1186/2228-5326-2-9
94. Palza H (2015) Antimicrobial polymers with metal nanoparticles. Int J Mol Sci 16:2099–2116
95. Perelshtein I, Applerot G, Perkas N, Guibert G, Mikhailov S, Gedanken A (2008) Sonochemical coating of silver nanoparticles on textile fabrics (nylon, polyester and cotton) and their antibacterial activity. Nanotechnology 19(24):245705. doi:10.1088/0957-4484/19/24/245705
96. Piperigkou Z, Karamanou K, Engin AB, Gialeli C, Docea AO, Vynios DH, Pavao MS, Golokhvast KS, Shtilman MI, Argiris A, Shishatskaya E, Tsatsakis AM (2016) Emerging aspects of nanotoxicology in health and disease: from agriculture and food sector to cancer therapeutics. Food Chem Toxicol Int J Publ Br Ind Biol Res Assoc 91:42–57
97. Praveena SM, Aris AZ (2015) Application of low-cost materials coated with silver nanoparticle as water filter in Escherichia coli removal. Water Qual Expo Health 7(4):617–625
98. Pulit-Prociak J, Banach M (2016) Silver nanoparticles – a material of the future . . . ? Open Chem 14:76
99. Guo Q, Ghadiri R, Weigel T, Aumann A, Gurevich LE, Esen C, Medenbach O, Cheng W, Chichkov B, Ostendorf A (2014) Comparison of in situ and ex situ methods for synthesis of two-photon polymerization polymer nanocomposites. Polymers 6(7):2037–2050. doi:10.3390/polym6072037
100. Behra R, Sigg L, Clift MJD, Herzog F, Minghetti M, Johnston B, Petri-Fink A, Rothen-Rutishauser B (2013) Bioavailability of silver nanoparticles and ions: from a chemical and biochemical perspective. J R Soc Interface 10(87):20130396. doi:10.1098/rsif.2013.0396
101. Ladj R, Bitar A, Eissa M, Mugnier Y, Le Dantec R, Fessi H, Elaissari A (2013) Individual inorganic nanoparticles: preparation, functionalization and in vitro biomedical diagnostic applications. J Mater Chem B 1(10):1381–1396. doi:10.1039/C2TB00301E
102. Rai M, Yadav A, Gade A (2009) Silver nanoparticles as a new generation of antimicrobials. Biotechnol Adv 27:76–83
103. Ravindra S, Murali Mohan Y, Narayana Reddy N, Mohana Raju K (2010) Fabrication of antibacterial cotton fibres loaded with silver nanoparticles via "green approach". Colloids Surf A Physicochem Eng Asp 367:31–40
104. Reidy B, Haase A, Luch A, Dawson K, Lynch I (2013) Mechanisms of silver nanoparticle release, transformation and toxicity: a critical review of current knowledge and recommendations for future studies and applications. Materials 6:2295–2350
105. Richards MJ, Edwards JR, Culver RP (1999) Nasocomial infections in medical intensive care units in the United States. National nosocomial infections surveillance system. Crit Care Med 27:887–892
106. Ayatollahi Mousavi SA, Salari S, Hadizadeh S (2016) Evaluation of antifungal effect of silver nanoparticles against Microsporum canis, Trichophyton mentagrophytes and Microsporum gypseum. Iran J Biotechnol 13(4):38–42. doi:10.15171/ijb.1302
107. Agnihotri S, Mukherji S, Mukherji S (2014) Size-controlled silver nanoparticles synthesized over the range 5–100 nm using the same protocol and their antibacterial efficacy. RSC Adv 4(8):3974–3983. doi:10.1039/C3RA44507K
108. Yang SK, Li MY, Zhu X, Xu GQ, Wu JH (2015) Photochemical synthesis of hierarchical multiple-growth-hillock superstructures of silver nanoparticles on ZnO. J Phys Chem C 119(25):14312–14318. doi:10.1021/acs.jpcc.5b03521
109. Lin S, Cheng Y, Liu J, Wiesner MR (2012) Polymeric coatings on silver nanoparticles hinder autoaggregation but enhance attachment to uncoated surfaces. Langmuir 28(9):4178–4186. doi:10.1021/la202884f

110. Praveena SM, Aris AZ (2015) Application of low-cost materials coated with silver nanoparticle as water filter in Escherichia coli removal. Water Qual Expo Health 7(4):617–625. doi:10.1007/s12403-015-0167-5
111. Pal S, Tak YK, Song JM (2007) Does the antibacterial activity of silver nanoparticles depend on the shape of the nanoparticle? A study of the gram-negative bacterium Escherichia coli. Appl Environ Microbiol 73(6):1712–1720
112. Prabhu S, Poulose EK (2012) Silver nanoparticles: mechanism of antimicrobial action, synthesis, medical applications, and toxicity effects. Int Nano Lett 2(1):32. doi:10.1186/2228-5326-2-32
113. Shi Z, Zhang Y, Phillips GO, Yang G (2014) Utilization of bacterial cellulose in food. Food Hydrocoll 35:539–545
114. Silver S (2003) Bacterial silver resistance: molecular biology and uses and misuses of silver compounds. FEMS Microbiol Rev 27:341–353
115. Sondi I, Salopek-Sondi B (2004) Silver nanoparticles as antimicrobial agent: a case study on E. coli as a model for gram-negative bacteria. J Colloid Interface Sci 275:177–182
116. Suran M (2014) A little hard to swallow? The use of nanotechnology in the food industry might be both boon and bane to human health. EMBO Rep 15(6):638–641
117. Abdul Kareem T, Anu Kaliani A (2011) Synthesis and thermal study of octahedral silver nano-plates in polyvinyl alcohol (PVA). Arab J Chem 4(3):325–331, http://dx.doi.org/10.1016/j.arabjc.2010.06.054
118. Tamoyo L, Azócar M, Kogan M, Riveros A, Páez M (2016) Copper-polymer nanocomposites: An excellent and cost-effective biocide for use on antibacterial surfaces. Mater Sci Eng C 69:1391–1409
119. Tankhiwale R, Bajpai SK (2009) Graft copolymerization onto cellulose-based filter paper and its further development as silver nanoparticles loaded antibacterial food-packaging material. Colloids Surf B Biointerfaces 69:164–168
120. Thomas V, Yallapu MM, Sreedhar B, Bajpai SK (2007) A versatile strategy to fabricate hydrogel-silver nanocomposites and investigation of their antimicrobial activity. J Colloid Int Sci 315:389–395
121. Tulve NS, Stefaniak AB, Vance ME, Rogers K, Mwilu S, LeBouf RF, Schwegler-Berry D, Willis R, Thomas TA, Marr LC (2015) Characterization of silver nanoparticles in selected consumer products and its relevance for predicting children's potential exposures. Int J Hyg Environ Health 218(3):345–357
122. Chumachenko V, Kutsevol N, Rawiso M, Schmutz M, Blanck C (2014) In situ formation of silver nanoparticles in linear and branched polyelectrolyte matrices using various reducing agents. Nanoscale Res Lett 9(1):164–164. doi:10.1186/1556-276X-9-164
123. Mody VV, Siwale R, Singh A, Mody HR (2010) Introduction to metallic nanoparticles. Int J Pharm Bio Sci 2(4):282–289. doi:10.4103/0975-7406.72127
124. Velazquez-Velazquez JL, Santos-Flores A, Araujo-Melendez J, Sanchez-Sanchez R, Velasquillo C, Gonzalez C, Martinez-Castanon G, Martinez-Gutierrez F (2015) Anti-biofilm and cytotoxicity activity of impregnated dressings with silver nanoparticles. Mater Sci Eng C 49:604–611
125. Velmurugan P, Lee SM, Cho M, Park JH, Seo SK, Myung H, Bang KS, Oh BT (2014) Antibacterial activity of silver nanoparticle-coated fabric and leather against odor and skin infection causing bacteria. Appl Microbiol Biotechnol 98(19):8179–8189
126. Jung WK, Koo HC, Kim KW, Shin S, Kim SH, Park YH (2008) Antibacterial activity and mechanism of action of the silver ion in Staphylococcus aureus and Escherichia coli. Appl Environ Microbiol 74(7):2171–2178. doi:10.1128/AEM.02001-07
127. Walser T, Demou E, Lang DJ, Hellweg S (2011) Prospective environmental life cycle assessment of nanosilver T-shirts. Environ Sci Technol 45:4570–4578
128. Wang YP, Li XG, Fu T, Wang L, Turner NC, Siddique KHM, Li F-M (2016) Multi-site assessment of the effects of plastic-film mulch on the soil organic carbon balance in semiarid areas of China. Agric For Meteorol 228-229:42–51
129. White RJ (2001) An historical overview of the use of silver in wound management. Br J Community Nurs 6(1):4–8

130. Wu J, Zheng Y, Wen X, Lin Q, Chen X, Wu Z (2014) Silver nanoparticle/bacterial cellulose gel membranes for antibacterial wound dressing: investigation in vitro and in vivo. Biomed Mater 9(3):035005
131. Wuithschick M, Paul B, Bienert R, Sarfraz A, Vainio U, Sztucki M, Kraehnert R, Strasser P, Rademann K, Emmerling F, Polte J (2013) Size-controlled synthesis of colloidal silver nanoparticles based on mechanistic understanding. Chem Mater 25:4679–4689
132. Xu Z, Mahalingam S, Rohn JL et al (2015) Physio-chemical and antibacterial characteristics of pressure spun nylon nanofibres embedded with functional silver nanoparticles. Mater Sci Eng C 56:195–204
133. Xue C-H, Chen J, Yin W, Jia S-T, Ma J-Z (2012) Superhydrophobic conductive textiles with antibacterial property by coating fibers with silver nanoparticles. Appl Surf Sci 258:2468–2472
134. He Y, Ingudam S, Reed S, Gehring A, Strobaugh TP, Irwin P (2016) Study on the mechanism of antibacterial action of magnesium oxide nanoparticles against foodborne pathogens. J Nanobiotechnol 14(1):54. doi:10.1186/s12951-016-0202-0
135. Soliman YS (2014) Gamma-radiation induced synthesis of silver nanoparticles in gelatin and its application for radiotherapy dose measurements. Radiat Phys Chem 102:60–67. http://dx.doi.org/10.1016/j.radphyschem.2014.04.023
136. Youssef AM, Abdel-Aziz MS, El-Sayed SM (2014) Chitosan nanocomposite films based on Ag-NP and Au-NP biosynthesis by Bacillus Subtilis as packaging materials. Int J Biol Macromol 69:185–191
137. Zapata PA, Larrea M, Tamayo L, Rabagliati FM, Az´ocar M, P´aez M (2016) Polyethylene/silver-nanofiber composites: a material for antibacterial films. Mater Sci Eng C. doi:10.1016/j.msec.2016.08.039.
138. Zhang L, Shen Y, Xie A, Li S, Jin B, Zhang B (2006) One-step synthesis of monodisperse silver nanoparticles beneath vitamin E Langmuir monolayers. J Phys Chem B 110:6615
139. Ziabka M, Mertas A, Krol W, Bobrowski A, Chlopek J (2013) High density polyethylene containing antibacterial silver nanoparticles for medical applications. Macromol Sym 315:218–225
140. Chatterjee AK, Sarkar RK, Chattopadhyay AP, Aich P, Chakraborty R, Basu T (2012) A simple robust method for synthesis of metallic copper nanoparticles of high antibacterial potency against E. coli. Nanotechnology 23:1–11
141. Tran QH, Nguyenm VQ, Le AT (2013) Silver nanoparticles: synthesis, properties, toxicology, applications and perspectives. Adv Nat Sci Nanosci Nanotechnol 4:033001. doi:10.1088/2043-6262/4/3/033001

Chapter 12
Iron-Oxide-Filled Carbon Nanotubes

Carlos Eduardo Cava

1 Carbon Nanotube Development

Like diamond, graphite, fullerene, and other structures, carbon nanotubes (CNTs) also can be considered an allotropic form of carbon, as their composition contains only carbon–carbon bonds. Since its discovery in 1991 [1], several carbon nanotube applications have been suggested during the last 25 years [2–5], especially due to its combined hardness, strength, and electrical conduction properties [6, 7]. Carbon nanotubes can be divided into two classes: those that are formed by a single layer of graphene, called single-walled nanotubes (SWNTs) (see Fig. 12.1a), and those that are formed by several layers of graphene, called multiple wall nanotubes (MWNTs) (see Fig. 12.1b). Single-walled carbon nanotubes are divided into three categories, depending on the angle that the graphene sheet was rolled: armchair, zigzag, or chiral. The winding angle determines whether nanotubes are metallic conductors or semiconductors [8].

These three categories of SWNTs have different properties: all armchairs have metallic properties, and the other two structures can be metallic or semiconducting, depending on the diameter of the nanotube. The difference between the properties of SWNTs resides on how their atoms are arranged. In a carbon–carbon structure, the atoms have a covalent bond with different sp^3, sp^2, sp hybridizations. For instance, the sp^3, which has a full filled orbital p, is responsible for the hardness of the diamond. Other carbon structures as graphene, fullerenes, and carbon nanotubes have in most cases the sp^2 hybridization with a delocalized electron, creating the possibility of electrical conduction. The SWNTs are stable until to 750 °C in air. However, it is possible to observe an oxidation process at lower temperatures, which leads to the possibility of filling up the CNT inner with molecules [9].

C.E. Cava (✉)
Federal Technological University of Paraná (UTFPR), Londrina, Brasil
e-mail: carloscava@utfpr.edu.br

E. Longo, F.A. La Porta (eds.), *Recent Advances in Complex Functional Materials*,
DOI 10.1007/978-3-319-53898-3_12

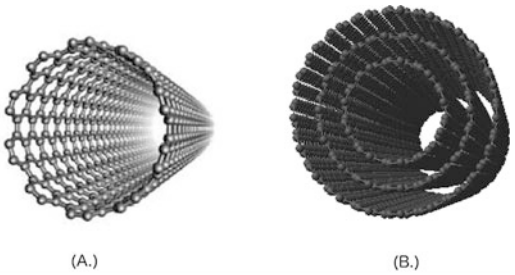

Fig. 12.1 Simulated structure of a (**a**) Single wall carbon nanotube, (**b**) Multiwall carbon nanotube

Typically, the total surface area of as-grown SWNTs ranges between 400 and $900\,m^2/g$ [10], and it can support high-current densities (max. $10^9\,A/cm^2$) [11]. However, structural defects can increase the material's electrical resistance. The tensile strength of a SWNT was calculated as 45 GPa [12], which is 20x larger than the steel. MWNTs with a structure free of defects have electronic properties similar to the metallic SWNT. The electronic conductance occurs preferentially at the surface of the nanotube; in most of the cases the interaction between the walls can be neglected. This property allows the nanotube to support a high level of electric current. MWNTs thermal conductivity measurements have shown an excellent heat transport rate (3000 W/mK), higher even than the natural diamond and the graphite (both 2000 W/mK) [13]. The surface area of a MWNT is directly related to its diameter, and most of the measured values are in the range of 200 and $400\,m^2/g$ [14].

1.1 Filled Carbon Nanotubes

An interesting aspect of CNTs is the possibility of filling their hollow core with foreign material. The resulting nanocomposite could provide new electrical, optical, and mechanical properties due to the synergistic effect between the CNTs themselves and the filling, which could lead to novel multifunctional materials. In some cases, the CNT can act as a shield, which increases the environment protection and lifetime of the material inside the CNT. Another improvement occurs in the crystalline and in the nanowire form of the inner material. An example is the possibility to manipulate the filled CNT whenever the inner material presents magnetic properties. Among the materials that may be part of this filling are those present at the growth process, enabling the formation of the nanocomposite in situ. Transition metals are considered good candidates for the formation of filled CNT because they have a binding energy favorable to the interaction with carbon. Another possibility is to fill up the CNT inside after its production using the capillarity effect proportioned by the nanometric size of the tube [15, 16]. The discovery of the carbon nanotube [1] motivated an expressive number of researchers to develop new methods to produce carbon nanotubes. Many of these methods ended to produce

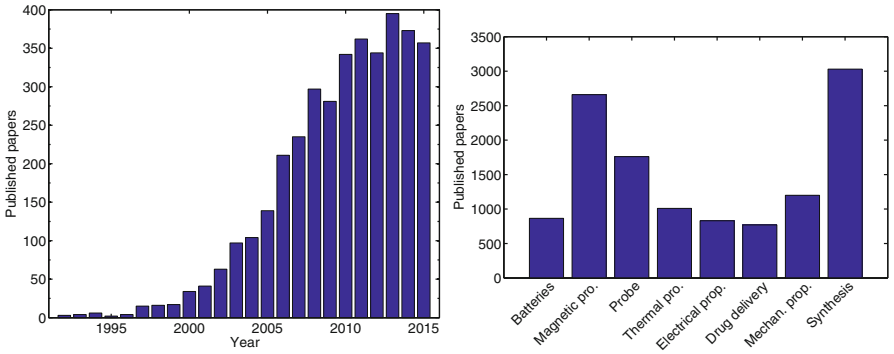

Fig. 12.2 Number of published papers per year related to filled carbon nanotubes and the applications mentioned on these publications. The search terms are ("filled carbon nanotubes" OR "filled carbon nanotube" OR "filled-CNTs" OR "filled-CNT" OR "filled-MWCNT" OR "filled-MWCNTs") between the years of 1992 and 2015

multiple derivatives forms of carbon nanotube, such as the filled CNTs. Since its first publication in 1993 [16, 17] the number of publications related to filled CNTs has grown expressively (see Fig. 12.2). After 2010 the average number of filled CNT related publications reached 350 papers per year. This is a significant number, which indicates the consolidation of this field of study.

Synthesis and magnetic properties showed to be the most common subjects in the researched papers. Actually, these are expected results because it is a novel class of materials. Therefore, a great effort had been done in order to understand the filled CNT synthesis. The addition of magnetic properties is a desired feature for many technological applications, so the possibility to add magnetism on carbon nanostructures rapidly pointed the researchers' efforts toward this direction. There are many possibilities of filling a carbon nanotube. The capillarity-induced process allows the insertion of many new materials such as the Buckminster fullerene (C60). The first molecule introduced into a CNT was a C60 [18]. This hybrid material was called nanopeapods. Figure 12.3a shows a high-resolution transmission electron microscopy (TEM) image of C60 filled CNT [19]. This is not only an exotic material, but the insertion of molecule inside a CNT can change their physical properties, their response to the presence of the absorbed molecules and electronic properties [20, 21]. Many other fullerenes species such as endohedral fullerenes can be added to a CNT in order to achieve new results from the regular carbon nanotube [22, 23]. This possibility is directly related to the ratio between the CNT diameter and the fullerene diameter [24]. Regarding other molecules inside the carbon nanotubes, water is a subject of interest in many studies, as shown in Fig. 12.3b. The possibility of having water inside a carbon nanotube has attracted the attention of many researchers in applications such as nanofluidic chips, cellular probes, and drug delivery. The water behavior in confined systems with tubular aspect promotes changes on its basic properties (i.e., crystallization [25])

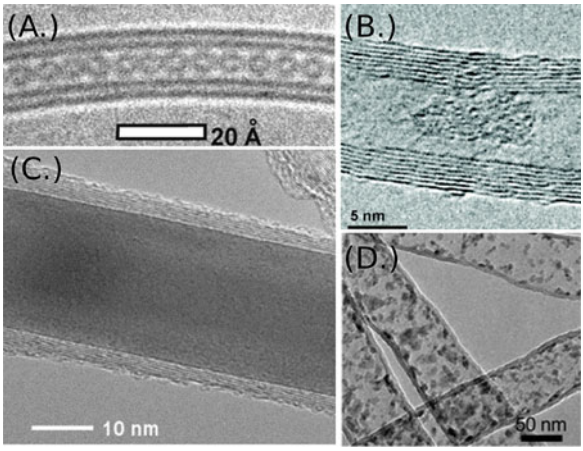

Fig. 12.3 (**a**) High-resolution image of C60-filled double-walled nanotubes. Adapted from [19]. Copyright 2005 American Chemical Society. (**b**) Observation of water confined in nanometer channels of closed MWNT. Adapted from [37]. Copyright 2004 American Chemical Society. (**c**) High-resolution images of an Ni-filled CNT. Adapted from [27] with permission from Elsevier. (**d**) Images of the Fe_2O_3-filled nanotubes. Adapted from [38] with permission from The Royal Society of Chemistry

and allows transportation through the carbon nanotube, which can be applied for osmotic processes such as desalinization [26]. Many other materials can be used to fill up CNTs, Fig. 12.3c [27] shows an example of nickel-filled CNT with high crystallinity. Actually, the most often used materials inside a CNT are those with magnetic properties, such as Fe, Ni, or Co [28–31], which can lead to a new material with new properties. Looking from another perspective, these materials can be used as a carbon-covered nanowires with significant potential for electronics due to their size and improved magnetic coercivity [32]. In addition, carbon shells provide an effective barrier against oxidation and, consequently, ensure the nanowire stability. Another possibility is to fill up the inner of a CNT with nanoparticles. In fact, almost any nanoparticle with the proper size can be added to the interior of the tube, which makes a great number of possible applications. Metals such as gold and silver [33, 34] inside the CNT can be used for medical and electronic applications. Particles like Si and Sn inside the CNT are interesting materials for energy storage. Well-oriented semiconductor nanoparticles inside the CNT can act as a nanobattery. In this case, the CNTs act as a buffer to accommodate the nanoparticle expansion during the lithiation process [35, 36]. Figure 12.3d shows an example of iron-oxide nanoparticles at the inner some CNTs.

1.2 Iron and Iron-Oxide-Filled CNTs

Iron is versatile and abundant in nature. It is considered the best-known transition metal and is present in many applications of our society. The iron atom can perform different types of connections due to its electron configuration ($3d^6$). This characteristic enables high chemical activity with other elements such as carbon. This fact reinforces the iron participation in the formation of CNTs [39].

Iron oxides are common compounds of iron (Fe) together with oxygen (O) and/or hydroxyl (OH). Usually iron oxides have a crystalline structure such as a hexagonal close packing (hcp) or a cubic close packing (ccp). There are many applications involving iron oxides in various technological fields such as electrochemistry, biology, chemical sensors, magnetic, and electronic devices [40–42]. At the iron-oxide structures, iron 3 d-orbitals have a large influence on the electronic and magnetic features of the material. There are five different available d-orbitals, each one with a different orientation on space. The ions of iron such as Fe^{3+} have five unpaired d-electrons and Fe^{2+} has two paired and four unpaired electrons. There are 16 iron oxides; the basic structure units are $Fe(OOH)_6$ or $Fe(O)_4$, and the various oxides differ in their arrangement in the space. The range of iron oxides is large, and the material properties are different for each structure. Here, the properties of hematite (α-Fe_2O_3) and magnetite Fe_3O_4 inside the CNTs will have special attention due to their applications in electromagnetic devices. The iron-oxide hematite complex structure has motivated many studies over the years in order to understand their properties [43–45]. The hematite unit cell structure is hexagonal with the following parameters: $a = 0.5034\,\text{nm}$, $c = 13.4\,\text{nm}$, and $\gamma = 120°$. It is also possible to describe as a rhombohedral $R\bar{3}c$ structure (see Fig. 12.4). Hematite presents an antiferromagnetic (AFM) behavior below $Tc = 955\,\text{K}$ [46] but is weakly ferromagnetic (FM) at room temperature [47]. The material normally exhibits *n*-type semiconductor characteristics with a band gap of 1.6–2.2 eV [48, 49]. The confinement inside a nanotube and the presence of interstitial atoms or vacancies can modify the electronic properties and its semiconductor characteristics [44, 50]. These studies indicated that this material is affected by its stoichiometry, which is strongly dependent on its growth conditions.

Magnetite is also a natural iron compound, which presents the Fe_3O_4 unit formula. This material is ferrimagnetic at room temperature; however, its properties are strongly dependent on temperature and stoichiometry. As showed in Fig. 12.5 magnetite unit cells are organized in a cubic inverse spinel structure *Fd3m* in a face-centered cubic crystalline structure with a crystal lattice parameter of $a = 0.8396\,\text{nm}$ [51]. However, the non-stoichiometric structure in which there is cation missing is often found. In its stoichiometric form magnetite the ratio Fe^{2+}/Fe^{3+} is 0.5. The Verwey transition occurs around 118 K, which is related with changes in the iron-oxygen stoichiometry at this temperature [51]. Magnetite presents a semi-metallic behavior with a low bandgap around 0.1 eV. These iron oxides have a complex structure, and its properties can be modified only by doing minor changes

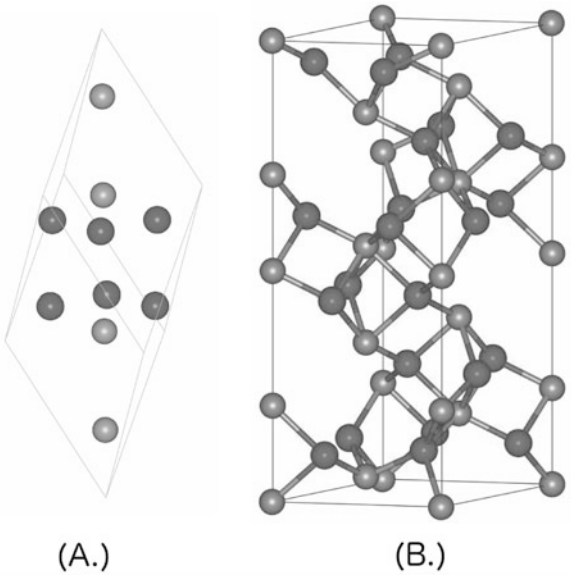

Fig. 12.4 Unit cell representation ball-and-stick model, the *light and dark grey* colors represent the iron and the oxygen atom, respectively: (**a**) rhombohedral; (**b**) hexagonal close pack (hcp) to Fe_2O_3

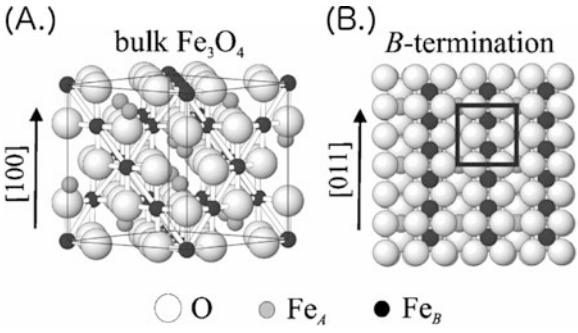

Fig. 12.5 (**a**) *Side* view of the inverse spinel Fe_3O_4 structure. (**b**) *Top* view of the $Fe_3O_4(100)$ bulk *B*-termination. The *black open square* in (**b**) marks the *p*(11) bulk unit cell. Reprinted with permission from [52]

on their crystal structures. Therefore, it is expected that both magnetite and hematite will have their properties strongly affected by the nanometric confinement inside the nanotube.

Inserting a new material into a CNT presents synergistic effects in order to form a nanocomposite with multiple properties. Such composites present better performance in many applications at the nanometric size. Transition metals are good materials to participate in the formation of CNTs. This fact is observed because the binding energy of transition metals presents a favorable interaction with carbon [53]. In fact, since the beginning of the CNT history, transition metals are used as catalysts at the CNT synthesis [54, 55]. Among the materials used to fill up a CNT, iron is one of the most popular. Pure iron or iron oxide confined in a SWCNT or a MWCNT can add magnetic properties to the CNT or, from another perspective, the CNT can provide stability and environmental protection to the iron nanowire.

Many examples of iron-filled CNTs applied for magnetic and medical studies have already been cited above. However, it is easy to find this material used in other applications as photovoltaic devices [56], electronic memory devices [57], polymer matrix composites [58], and electrochemical sensors [59]. The electrical properties of iron-oxide-filled CNTs are diverse from the regular CNTs, which allow the materials to be used in other applications [60, 61].

Several studies have suggested filled carbon nanotubes as vehicles for the delivery and targets for medical applications because of their biocompatibility. A promising biomedical application is the use of a CNT as a container for contrast agents (i.e., gadolinium) in magnetic resonance images [62]. This application can prevent the contrast from interacting with the human body thus mitigating the collateral effects. Concerning the improvement of images used for biomedical diagnosis, the approach is to fill up the CNT with some nanoparticles or molecules, which have a strong response to the excitation signal. An example is the improvement of fluorescence microscopy images, as shown in Fig 12.6a–d, by the addition of Fe_3O_4 nanoparticles inside CNTs, which are used to emphasize the studied cell [63]. In order to destroy a cancer cell, one approach is the use of iron-filled CNT, which, in the presence of an induced magnetic field [64], can heat and destroy the undesirable cells. Many other researches of filled CNTs applied for biomedicine are still ongoing, and some promissory results can be expected from this field of application. Regarding the magnetic properties of thin films, the use of iron-filled CNT presented improvements on the image resolution. Magnetic force microscopy (MFM) is a powerful tool to visualize the magnetic configuration at the materials surface. These images are acquired by scanning the magnetic forces between the probe and surface. Thus a probe with reduced size should improve the resolution of this equipment. When the iron-filled CNT is applied as the MFM probe, the equipment resolution and stability are improved [65]. An example of iron-filled CNTs applied as MFM probe is shown in Fig 12.6e, f.

The next sections are dedicated to the production, characteristics, and application of iron and iron-oxide-filled CNTs. The electrical and morphological properties of devices based on iron-oxide-filled CNT are also presented.

1.3 Routes to Obtain Iron-Oxide-Filled CNTs

The process and synthesis of CNTs have received great attention in the science industries in order to create large-scale production of SWNTs or MWNTs. The most common methods of manufacturing CNTs are voltaic arc-discharge, high power laser ablation, and chemical vapor deposition (CVD). The diameter of these nanotubes ranges from 0.4 to 3 nm for SWNTs and from 1.4 to 100 nm for MWNTs. All these growth techniques generate nanotubes with a high concentration of impurities as well as amorphous carbon material. These impurities, or amorphous carbon structures, can be removed with an acid treatment. However, this treatment involves additional damage to the nanotubes, which introduce other impurities

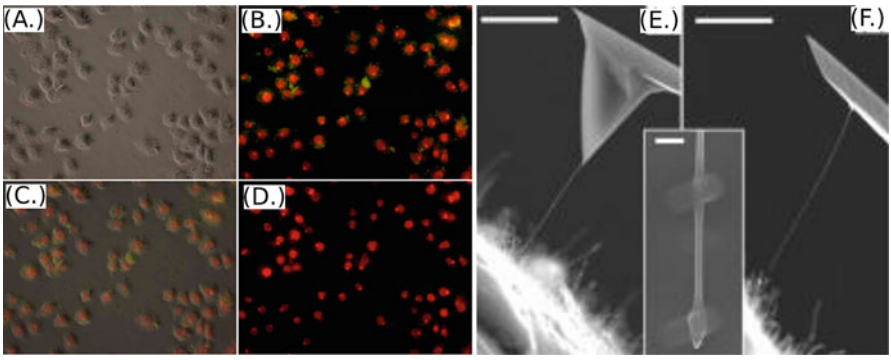

Fig. 12.6 Images of Fe_2O_3 nanoparticle-filled CNT used to enhance the fluorescent microscopic images of Hela cells (**a**) brightfield images; (**b**) fluorescent images by *blue light* excitation; (**c**) the merged images of (**a**) and (**b**); and (**d**) fluorescent images by *green light* excitation. Adapted from [63]. Copyright 2012 American Chemical Society. (**e**) Image of a Fe-CNTs attached to an AFM cantilever. (**f**) A cantilever without a tip. The inset shows the end of the nanotube attached to the AFM cantilever with two areas of deposited contamination. Scale bar: 10 μm, inset: 300 nm. Adapted from [28] with permission from AIP Publishing

or defects in the material. A challenge for CNT manufacturers is to achieve a synthesis in which all nanotubes have the same electrical and mechanical properties. The iron-oxide-filled CNT can be produced by in situ or ex situ techniques. The chosen approach will depend on the desired material. Commonly, CNTs filled with iron-oxide nanoparticles as Fe_3O_4, α-Fe_2O_3, and γ-Fe_2O_3 are obtained by ex situ techniques. The CNTs filled with iron-oxide nanowires as Fe_3O_4, α-Fe_2O_3 can be achieved by in situ techniques.

1.3.1 Ex situ Synthesis of Iron-Oxide-Filled CNTs

The ex situ method, also called post-synthesis method, of filling up a CNTs is a versatile method. Almost any material can be used to fill the CNT inner. This technique consists in opening the CNT by a chemical or thermal oxidation process and then inserting the desired material into the CNT. The capillarity presented in this CNT plays an important role on this technique. Interestingly, the pioneering studies on filled CNT [15, 16, 66] used this approach. This method can be done in one, two, or three steps, as detailed explained by Sloan et al. [67]. The opening tube process can be achieved by thermal oxidation in O_2 or Air. At temperatures around 400 °C the tube starts a process of oxidation. The tube tip has lower energy than the tube's body due to its curvature. Therefore, when the tube is heated in an oxygen-rich atmosphere, the carbon–carbon bonds at the tip are removed by oxidation first, then the carbon–carbon bonds at the tube's body. There are also chemical methods to open the CNT which are based on acid attach or other oxidization chemical process [66, 68]. The chemical and thermal oxidation are successful methods;

however, the chemical method has disadvantages due to issues in the removal of residues. Many iron species can be inserted in the CNTs by ex situ techniques. Nanoparticles of α-Fe_2O_3, γ-Fe_2O_3, and Fe_3O_4 are the most regular used due to their applications on biomedical and magnetic devices [38, 69–71].

1.3.2 In situ Synthesis of Iron-Oxide-Filled CNTs

The most regular in situ methods to fill up CNTs are arc-discharge (also called electric arc plasma) and CVD. The arc-discharge technique is a well-known method and was extensively used at the beginning of the research for filled CNTs [72–74]. This process consists in an electric arc plasma between two graphite electrodes in a chamber with a controlled atmosphere. The material, which will fill up the CNT, is placed in a coaxial hole within the graphite electrode. Many results can be achieved by the electric arc modulation changing its current, voltage, pressure, and atmosphere. Nowadays, this technique is not being considered for large-scale applications due to reproduction problems and relative high cost. The CVD method is capable of producing CNT in large quantities; due to its low cost, this technique is perfectly suited for the production of CNTs in industrial applications [75]. A regular CVD assembled to produce CNTs is a tubular furnace where the decomposition of a mixture of hydrocarbon gases (i.e., methane, ethylene) or carbon/metal compounds produces the CNTs. This decomposition process commonly occurs at temperatures of 500−1200 °C at atmospheric pressure. The presence of a metallic nanoparticles on the synthesis is important once it acts as catalyst and nucleation sites in the CNTs growth process. These nanoparticles can be located at the substrate or mixed with the vapor. The catalyst nanoparticle and preparation of substrate will determine the material inside the nanotube. Usually, Fe, Co, Ni nanoparticles are used as catalyst [28–31]. The excess of these materials will lead to a filled CNT. Porous silicon, alumina, and other ceramics are considered as good substrates for controlled growth of filled CNTs. The use of organometallic compounds in place of hydrocarbon gas is attractive in order to produce filled CNTs [76, 77]. Organometallic compounds work as a catalyst and carbon source at the same time. Using this approach, is it possible to achieve CNTs with a high fill rate. The iron-filled CNT produced by the use of organometallic compounds is obtained by the use of ferrocene [78]. This technique produces iron-filled CNTs as well as filled carbon nanostructures such as onions and rods. The route presented by Schitzler et al. [77] achieved good results using the sublimation of ferrocene at 300 °C. In this process, the ferrocene vapor was carried by the argon flow into a second furnace at 900 °C where the material's pyrolysis occurs. The argon gas used in this synthesis has a mixture of 4-5% of oxygen; this oxygen ends to produce iron oxide inside CNTs with multiple walls. The following sections will present the use of this filled CNT at magnetic and electronic applications. Figure 12.7 shows a high-resolution image of one iron-oxide-filled CNT produced by the method presented above.

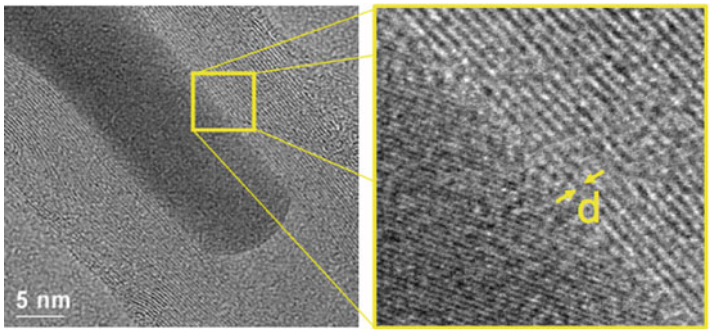

Fig. 12.7 High-resolution images of an iron-oxide-filled CNT. The inset highlights the iron-oxide crystal orientation, and "d" refers to the typical distance between the CNTs walls 0.34 nm. Adapted from [77] with permission from Elsevier

2 Iron-Oxide-Filled CNT Applications

2.1 Magnetic Properties

Iron-oxide nanoparticles and nanowires can transfer their magnetic properties to the iron-oxide-filled CNT. This has attracted attention to the use of this material in many applications that request magnetic features. As mentioned before, applications such as resonance images [62] and MFM [28] probes using filled CNTs can be achieved by using magnetic materials inside the CNT. In applications of magnetic material, many parameters should be considered. The material's response to a magnetic field applied determines if the material present diamagnetic, ferromagnetic, ferromagnetic, or paramagnetic behavior. However, the confinement in a nanometric tube can lead these materials to present unexpected behaviors in terms of coercivity and transition temperatures (i.e., Curie, Verwey, Néel temperature). Actually, the insertion of a material inside the CNT can motivate significant anisotropic behavior, due to the high aspect ratio induced by the CNT [41]. Another expected change is in the crystal lattice distances at the edge between the material and the CNT internal walls. The curvature in the inner tube should motivate some structure distortions at the crystal surface. These changes can have an effect in a positive or negative way depending on the desired feature. It is expected that, in small diameter tubes, disordering and the aspect ratio are increased. Araújo et al. found that iron and iron-oxide-filled CNTs presented a Verwey transition temperature of 125 K and a coercive field of 0.4 kOe [32]. The results can be seen in Fig. 12.8. Some works have applied the ferromagnetic or paramagnetic behavior of iron-oxide-filled CNTs to magnetically remove undesired residues in liquids [79, 80]. These studies used the CNTs to adsorb contaminants; further, as these CNTs had magnetic properties due to the filling, a magnetic field was used to attract and remove the filled CNT+contaminant.

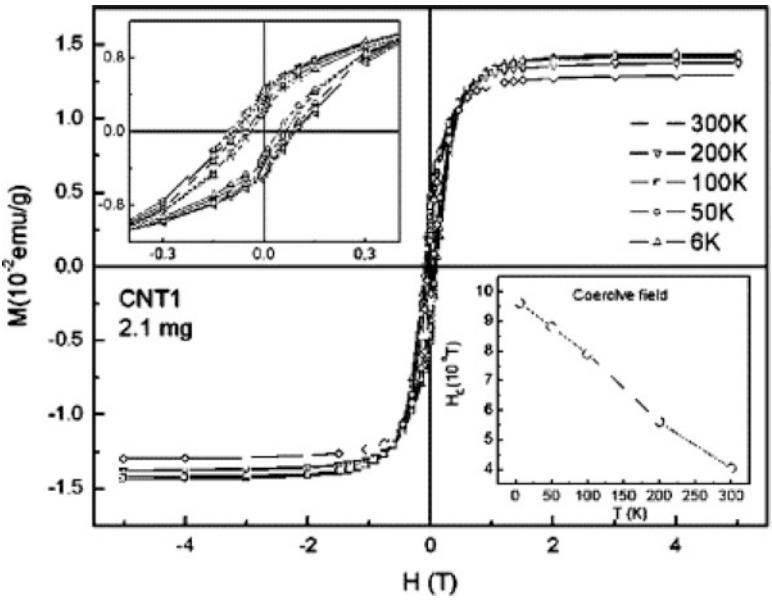

Fig. 12.8 Hysteresis loops taken at several values of temperature of iron-oxide-filled CNTs. The *right*-hand-side inset shows an amplification of the area of low field, whereas the *left*-hand-side inset displays the temperature dependence of the coercive field. Adapted from [32] with permission from Elsevier

2.2 Electronic Properties

The insertion of a new material inside a CNT can profoundly change its electronic properties. It is expected that the filling material transfers its electronic properties to the new hybrid material. This phenomena is well known in SWCNTs filled with many materials [24, 81]. However, there are few studies related to filled MWCNTs concerning their electrical properties. This may happen because of experimental conditions or even because of the impurities that are likely found on MWCNT samples. The inner diameter of a MWCNT is commonly higher than that of a SWCNT. Thus, it is possible to have more material inside a MWCNT than a SWCNT, which indicates a major possibility to observe the inner material effects on the electronic properties. However, as the MWCNT has many CNT walls, this effect can be mitigated by the shield formed by these walls. In addition, this is rarely explored by theoretical calculations due to the size of these systems with multiple walls. Another fact is that defects and impurities are crucial in the inter-layer electronic transport of a MWCNT [82]. In electronic devices, not only a single filled CNT can be used between two electrodes, but an entanglement of CNT also can be used to electronic applications. The use of a CNT net has potential applications due to the easiest manipulation. This method can save time and facilitate the use

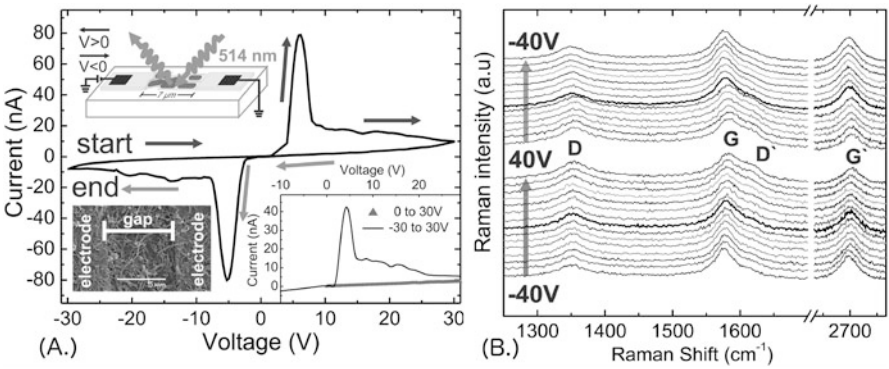

Fig. 12.9 (**a**) Characteristic current intensity versus voltage curve (I-V) for the iron-oxide-filled CNT planar device; the inset presents curves for different initial applied voltage, 0 to 30 V and −30 to 30 V; a schematic representation of the measurement setup, with the Raman laser incident; and a device SEM image. (**b**) Iron-oxide-filled CNT Raman spectra for an applied voltage range of −40 to 40 V in both directions (indicated by the *arrows*). The *darker line* indicates zero voltage applied. Adapted from [84] with permission from The Royal Society of Chemistry

of a filled CNT for certain applications. Here some features of entangled iron-oxide-filled CNTs applied in devices such as memories and gas sensors will be discussed. The current versus voltage analyses of an entanglement of iron-oxide-filled CNTs between two planar electrodes revealed an unexpected bipolar behavior. This behavior can be addressed to modifications of the material's electronic state. The inset in Fig. 12.9a shows an iron-filled CNT net covering both electrodes, allowing electronic transport between them. The electrical current versus applied voltage (I-V) on these devices can be made by a semiconductor parameter analyzer with applied voltage and is capable of reading a current in a nanoampere scale.

The I-V analyses shown in Fig. 12.9a exhibit the characteristic curve shape of an iron-filled CNT net between two identical electrodes. This measurement analyzes the electrical current intensity from an external voltage applied from 30 to 30 V (forward direction, increasing) and from 30 to 30 V (backward direction, decreasing), indicated by arrows on the figure, at a voltage step of 0.05 V with a scan rate of 2 V/s. Two intense electric current peaks are identified in the I-V curve: one in the positive region for the forward applied voltage, and the other in the negative region for the backward applied voltage. The highest positive electrical current peak, near 6 V, only occurs after the negative voltage has been applied; likewise, the negative electrical current peak near 6 V only occurs after the positive voltage has been applied. Thus, the application of the opposite voltage on the sample is necessary to yield a peak in the next voltage region. The inset in Fig. 12.9a demonstrates this feature; when the voltage is at 0 V, there is no electrical current peak. Therefore, if a new measurement is performed starting with a negative applied voltage, the peak appears in the same region as before. It is important to note that the I-V curve presents small perturbations after the peak, which can be attributed to

the different CNTs (sizes and diameters) present in this sample. For similar devices, this current peak is not detected when regular, unfilled CNTs are used, as tested by our group and in other studies [82, 83].

The I-V analyses revealed bipolar behavior, which should correspond to modifications of the material electronic state. One way to analyze this behavior is by the use of Raman spectroscopy with applied voltage in order to identify modifications due to the electron–phonon interactions on the material surface. Raman spectroscopy has been extensively applied to characterize carbon materials, such as carbon nanotubes and graphene. These carbon materials present a well-defined signature on Raman spectroscopy. So, a minor change on this signature can be addressed to a modification on its electronic configuration. A schematic illustration of the setup used simultaneously to apply an external voltage and acquire the Raman intensity is shown in Fig. 12.9a. A more detailed explanation about this measurement can be found in [84]. The main result of this measurement is shown in Fig. 12.9b. The Raman laser spot, with a diameter of approximately 1 mm, was focused exactly on the center of the gap to avoid any interference from the metal electrodes. The arrows in Fig. 12.9b indicate the applied voltage direction and reference values. All modes also exhibit a blueshift when the forward direction voltage is applied, regressing to the initial position as the voltage is applied backward. All the common intense active modes for MWCNTs are found between 1200 and 3000 cm^{-1}. For the Raman spectrum at zero applied voltage ($V = 0$), the Lorentzian line shape analyses revealed the G band, located at 1580 cm^{-1}, as well as the D band at 1354 cm^{-1}, the D· band at 1618 cm^{-1}, and the G· band at 2700 cm^{-1}; all of these wavenumber are in agreement with previously published values [85].

Analyzing the values presented with the forward voltage ramp between −40 and 40 V, the G band shifts are identified between 1576 and 1583 cm^{-1}, the first of which is typical for small CNT metallic tubes, and the second of which is characteristic of graphite-like materials [85, 86]. When the opposite voltage ramp is applied (backward voltage), the materials still present graphite-like frequencies, with an abrupt change for lower frequencies down to 40 V. However, our samples have a large diameter (40 to 100 nm) and a diameter reduction motivated by an applied voltage that cannot be used in order to explain the energy phonon reduction. To explain these results, it is important to remember that iron-oxide-filled CNTs are a strongly electron-doped material due to the iron oxides, which are strongly correlated materials. Thus, the CNTs tested here present a different electron charge distribution than do regular MWCNTs, and a metallic behavior is expected due to the electrical characteristics of the MWCNTs and the additional charge from the filling.

This results conclude that there are two different electronic states promoting phonons with different energies for the same applied voltage (6 V), which are related to the direction of the electric field. This difference occurs due to the reminiscent charge polarization. Once the voltage is applied in different directions, the device is still under the same electronic conditions until the space charge at the filling changes its polarization; for this sample, this phenomenon begins at 10 V. This feature leads to the possibility of using this material as a resistive memory device capable of

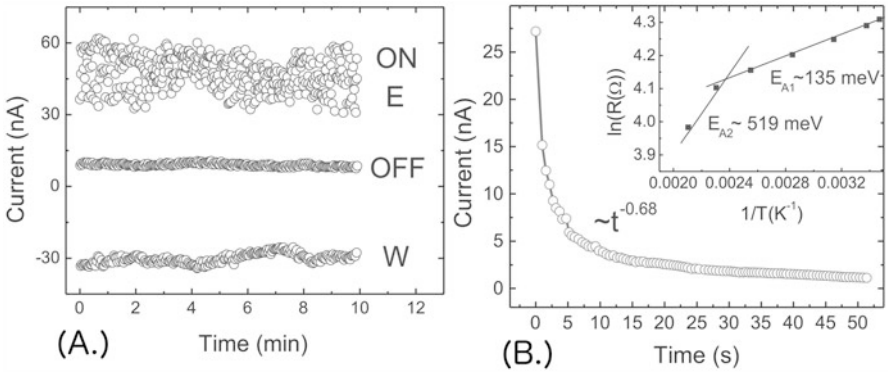

Fig. 12.10 (**a**) Iron-oxide-filled CNT resistive memory operating for 10 min with the voltage current dependence; the operation process is comprised of write (−10 V), read ON (+7 V), erase (+10 V), and read OFF (−7 V). (**b**) Current versus time (I-t) with 7 V applied after a pulse of −10 V; the inset is the resistance versus temperature curve (R-T) for Arrhenius analyses showing activation energies. Adapted from [84] with permission from The Royal Society of Chemistry

writing, reading, and erasing information many times. Figure 12.10a shows the same iron-oxide-filled CNT device working as a resistive memory device for 10 min. Here, it is possible to identify the processes of write (W), read (ON), erase (E), and read again (OFF). In this test, the information was written using an applied voltage of 10 V; the recorded information was read at 7 V, at which it is possible to identify the high-conductivity state (ON); the information was erased by applying 10 V; and the information was accessed again at 7 V, at which the low-conductivity state (OFF) can be verified. All of these processes (write, read, erase, and read again) were conducted within 28 ms with an ON/OFF difference of approximately 40 nA. This ON/OFF difference is related to the device construction parameters, and high values can be obtained by changing the device dimensions. The Raman analyses revealed the strong modification of the material's electronic state due to the applied external field and its reversibility. These measurements corroborate the electrical behavior of the iron oxide filling the CNT.

The time-dependent current under a constant applied voltage (7 V) after one pulse of the opposite voltage (10 V) is presented in Fig. 12.10b. This discharge curve can be described using the empirical Curie-von Schweidler equation [87], simplified as $I(t) \approx t^{\alpha}$, where it was found that $\alpha = 0.68$ at 300 K, which can be assigned to space-charge polarization and electron charge hopping [88, 89]. The energy needed to activate the electronic transport in this material was determined by measuring the electrical resistance versus temperature. The inset of Fig. 12.10b shows the Arrhenius analysis, which confirms the thermal-activated transport with two different activation energies: E_{A1}, with a value of 135 meV, and E_{A2}, with a value of 519 meV. These results were obtained by monitoring the temperature as a function of the device electrical resistivity in an inert atmosphere (N_2). Iron-oxide-filled CNTs are a complex material combining two different classes of materials.

Thus, it is important to consider that any electronic transport should occur in at least two different regions. Analyzing the activation energies, is it possible to attribute one portion of the charge transport to the MWCNT inter-shell transport and the other portion for electronic hopping between a metal or metal oxide to a carbon layer. Charge polarization is not often observed in CNTs; in fact, this feature is commonly found in metal-oxide materials [90]. Thus, it remains unclear as to how the filling contributes to the electronic transport on the carbon nanotube network. Considering these facts, it becomes evident that the filling strongly contributes to the electronic transport of the iron-oxide-filled CNTs.

Changes in the electrical conductivity also can motivate changes in the gas sensing materials properties. The interaction between a CNT and the filling could modify the electronic structure of the material and, consequently, change the kind of interaction between the CNT and different gases. Therefore, this kind of nanocomposite material could be useful in the preparation of versatile and durable solid-state sensors, with simple manufacturing and an appropriate size.

Achieving the right morphology is essential for a resistive gas sensor, and the right material distribution between the electrodes is essential for good operation of the sensor. The images of the iron-oxide-filled CNT and empty CNT films can be seen in Fig. 12.11a, b, respectively. This analysis shows that the CNT net covers the substrate in a way that allows good film formation. Although there is a difference in the diameter between the filled and nonfilled CNTs, the film formation is on a similar scale.

The resistivity at room temperature in a vacuum of 0.8 bar was initially measured for both devices; the iron-oxide-filled CNT and the empty CNT devices had values of 38.4 Ohm and 16.6 Ohm, respectively. The difference in the electrical resistivity of both devices was tested in vacuum and an oxygen atmosphere. Figure 12.11c presents the rate of resistance change (sensitivity) of the iron-oxide-filled CNT and the empty CNT devices under two atmospheric configurations changing every 2 min between vacuum and an oxygen atmosphere of 1 bar. The sensitivity magnitude shown in Fig. 12.11c is higher for the iron-oxide-filled CNT than for the empty CNT device. This result suggests that the oxygen atmosphere decreases the resistivity of the iron-oxide-filled CNT film more than the empty CNT film. In order to understand this interaction (oxygen/iron-oxide-filled CNT), the conductivity of the iron-oxide-filled CNT was monitored in a nitrogen (N_2) flow for 12 min, which was periodical interrupted by the addition of 1% of oxygen over 4 min. This measurement was made at the operating temperature of 160 °C, this temperature is characteristic for CNT films applied for oxygen sensors [91]. The results of this analysis are shown in Fig. 12.11d. The increase in conductivity in the presence of oxygen, although in the small amount presented in Fig. 12.11c, indicates a relatively strong interaction between the iron-oxide-filled CNT surface and the oxygen molecules. It is also important to note that the morphology of the empty CNT device is more favorable for achieving higher sensitivity. Figure 12.11a highlights some imperfections on the iron-oxide-filled CNT film due to a nonconformity in the CNT dispersion during the film production. Another important fact is that the iron-oxide-filled CNTs have a larger diameter compared with the empty CNTs.

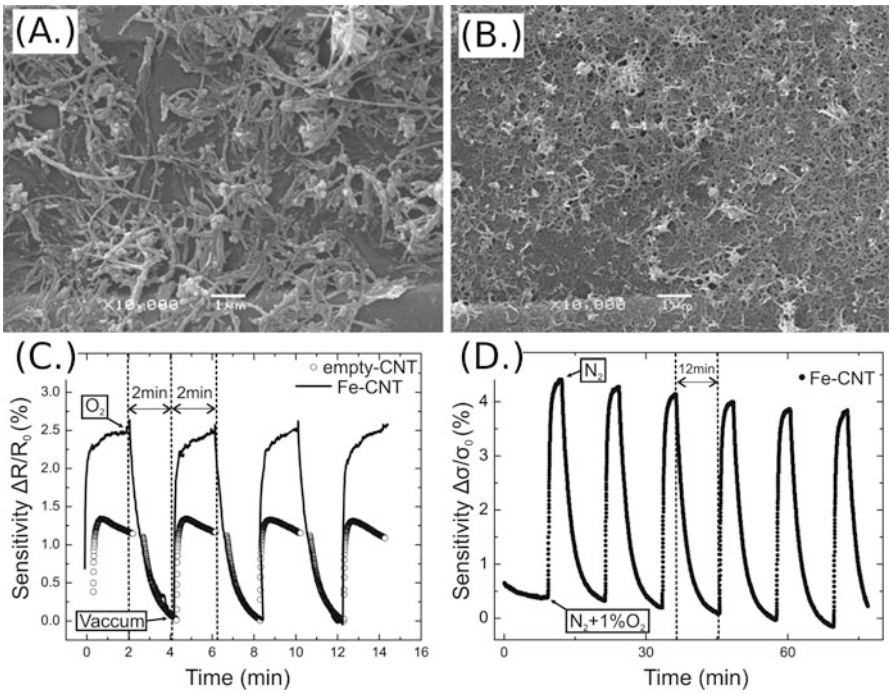

Fig. 12.11 Scanning electron microscopy (SEM) images: (**a**) iron-oxide-filled CNT film under the electrical contacts. (**b**) Empty CNT film under the electrical contacts. (**c**) Sensitivity in terms of resistance between a low pressure atmosphere of 0.8 bar (vacuum) and a dry oxygen gas atmosphere (O_2) at 1 bar, the atmosphere was changed every 2 min. The empty circles show the sensitivity measurement for the empty CNT device, and the solid line is for the iron-oxide-filled CNT device. (**d**) Sensitivity in terms of conductivity between a flow of nitrogen (N_2) and a flow of nitrogen mixed with oxygen (1% O_2) for the iron-oxide-filled CNT device. Adapted from [92] with permission from the PCCP owner societies

These characteristics should increase the activation energy for sensing oxygen and, consequently, decrease the sensitivity. Nevertheless, the iron-oxide-filled CNT device presented higher sensitivity for oxygen molecules than the empty CNT device, even under the above-mentioned conditions. The theoretical calculations also corroborate with these facts [92]. The same work also demonstrated that an iron-filled CNT is more sensitive and exchanges more electrons with the O_2 molecule than a regular CNT.

3 Summary

Although the CNT is a well-known material, many of its forms remain an interesting topic of study. The possibility of filling up CNTs opened a new class of multifunctional materials with possible applications in many areas. The iron oxide inside a

CNT is a new hybrid material where the electromagnetic properties of the inner are transferred to the carbon outside wall. The carbon nanotube acts as a shield protecting and inducing the shape of the iron-oxide nanowire. This material can present intriguing electric and magnetic properties. Its electrical behavior allows the construction of an electronic resistive memory with the possibility to write and read using an electronic pulse. Many studies should be made on this material before a satisfactory understand of these hybrids materials and its application. The combination of theoretical and experimental studies will be needed in order to accelerate better comprehension about these materials for its application in the near future.

Acknowledgements The author acknowledges the financial support from the Brazilian agencies CAPES, CNPq, F. Araucária.

References

1. Iijima S et al (1991) Helical microtubules of graphitic carbon. Nature 354(6348):56–58
2. Baughman RH, Zakhidov AA, de Heer WA (2002) Carbon nanotubes–the route toward applications. Science 297(5582):787–792
3. Abbas A, Al-Amer AM, Laoui T, Al-Marri MJ, Nasser MS, Khraisheh M, Atieh MA et al (2016) Heavy metal removal from aqueous solution by advanced carbon nanotubes: critical review of adsorption applications. Sep Purif Technol 157:141–161
4. Yan Y, Miao J, Yang Z, Xiao F-X, Yang HB, Liu B, Yang Y (2015) Carbon nanotube catalysts: recent advances in synthesis, characterization and applications. Chem Soc Rev 44:3295–3346
5. Mittal G, Dhand V, Rhee KY, Park S-J, Lee WR, A review on carbon nanotubes and graphene as fillers in reinforced polymer nanocomposites. J Ind Eng Chem 21:11–25
6. George N, Chandra J, Mathiazhagan A, Joseph R (2015) High performance natural rubber composites with conductive segregated network of multiwalled carbon nanotubes. Combust Sci Technol 116:33–40
7. Gong S, Zhu Z, Meguid S (2015) Anisotropic electrical conductivity of polymer composites with aligned carbon nanotubes. Polymer 56:498–506
8. Endo M, Iijima S, Dresselhaus M (2013) Carbon nanotubes. Elsevier Science, New York
9. Takenobu T, Takano T, Shiraishi M, Murakami Y, Ata M, Kataura H, Achiba Y, Iwasa Y (2003) Stable and controlled amphoteric doping by encapsulation of organic molecules inside carbon nanotubes. Nat Mater 2(10):683–688
10. Peigney A, Laurent C, Flahaut E, Bacsa R, Rousset A (2001) Specific surface area of carbon nanotubes and bundles of carbon nanotubes. Carbon 39(4):507–514
11. Dekker C et al (1999) Carbon nanotubes as molecular quantum wires. Phys Today 52:22–30
12. Wei C, Cho K, Srivastava D (2003) Tensile strength of carbon nanotubes under realistic temperature and strain rate. Phys Rev B 67(11):115407
13. Kim P, Shi L, Majumdar A, McEuen P (2001) Thermal transport measurements of individual multiwalled nanotubes. Phys Rev Lett 87(21):215502
14. Campos-Delgado J, Romo-Herrera JM, Jia X, Cullen DA, Muramatsu H, Kim YA, Hayashi T, Ren Z, Smith DJ, Okuno Y et al (2008) Bulk production of a new form of sp2 carbon: crystalline graphene nanoribbons. Nano Lett 8(9):2773–2778
15. Ugarte D, Støckli T, Bonard J, Châtelain A, De Heer W (1998) Filling carbon nanotubes. Appl Phys A Mater Sci Process 67(1):101–105

16. Ajayan PM et al (1993) Capillarity-induced filling of carbon nanotubes. Nature 361(6410):333–334
17. Seraphin S, Zhou D, Jiao J, Withers JC, Loutfy R (1993) Yttrium carbide in nanotubes. Nature 362(6420):503
18. Smith BW, Monthioux M, Luzzi DE (1998) Encapsulated c60 in carbon nanotubes. Nature 396:323–324
19. Khlobystov AN, Britz DA, Briggs GAD (2005) Molecules in carbon nanotubes. Acc Chem Res 38(12):901–909
20. Chiu P, Yang S, Yang S, Gu G, Roth S (2003) Temperature dependence of conductance character in nanotube peapods. Appl Phys A 76(4):463–467
21. Lee J, Kim H, Kahng S-J, Kim G, Son Y-W, Ihm J, Kato H, Wang Z, Okazaki T, Shinohara H et al (2002) Bandgap modulation of carbon nanotubes by encapsulated metallofullerenes. Nature 415(6875):1005–1008
22. Suenaga K, Tence M, Mory C, Colliex C, Kato H, Okazaki T, Shinohara H, Hirahara K, Bandow S, Iijima S (2000) Element-selective single atom imaging. Science 290(5500):2280–2282
23. Okazaki T, Suenaga K, Hirahara K, Bandow S, Iijima S, Shinohara H (2002) Electronic and geometric structures of metallofullerene peapods. Phys B Condens Matter 323(1):97–99
24. Shimada T, Ohno Y, Okazaki T, Sugai T, Suenaga K, Kishimoto S, Mizutani T, Inoue T, Taniguchi R, Fukui N et al (2004) Transport properties of c 78, c 90 and dy@ c 82 fullerenes-nanopeapods by field effect transistors. Phys E Low-dimens Syst Nanostruct 21(2):1089–1092
25. Koga K, Gao G, Tanaka H, Zeng XC (2001) Formation of ordered ice nanotubes inside carbon nanotubes. Nature 412(6849):802–805
26. Kalra A, Garde S, Hummer G (2003) Osmotic water transport through carbon nanotube membranes. Proc Natl Acad Sci 100(18):10175–10180
27. Leonhardt A, Ritschel M, Kozhuharova M, Graff A, Muhl T, Huhle R, Monch I, Elefant D, Schneider C (2003) Synthesis and properties of filled carbon nanotubes. Diam Relat Mater 12(3):790–793
28. Wolny F, Weissker U, Muhl T, Leonhardt A, Menzel S, Winkler A, Buchner B (2008) Iron-filled carbon nanotubes as probes for magnetic force microscopy. J Appl Phys 104(6):064908
29. Pradhan BK, Kyotani T, Tomita A (1999) Nickel nanowires of 4 nm diameter in the cavity of carbon nanotubes. Chem Commun (14):1317–1318
30. Hayashi T, Hirono S, Tomita M, Umemura S, Delaunay J-J (1997) Magnetic thin films of cobalt nanocrystals encapsulated in graphite-like carbon. In: MRS Proceedings, vol 475. Cambridge University Press, Cambridge, p 33
31. El Mel A-A, Gautron E, Angleraud B, Granier A, Tessier P (2011) Synthesis of nickel-filled carbon nanotubes at 350 ° c. Carbon 49(13):4595–4598
32. de Araújo A, Duque J, Knobel M, Schnitzler M, Zarbin A (2007) Evidence of Verwey transition in iron-and iron oxide-encapsulated carbon nanotubes. J Magn Magn Mater 312(1):32–34
33. Jiang L, Gao L (2003) Modified carbon nanotubes: an effective way to selective attachment of gold nanoparticles. Carbon 41(15):2923–2929
34. Chu A, Cook J, Heesom RJ, Hutchison JL, Green ML, Sloan J (1996) Filling of carbon nanotubes with silver, gold, and gold chloride. Chem Mater 8(12):2751–2754
35. Yu W-J, Liu C, Hou P-X, Zhang L, Shan X-Y, Li F, Cheng H-M (2015) Lithiation of silicon nanoparticles confined in carbon nanotubes. ACS Nano 9(5):5063–5071
36. Wang Y, Wu M, Jiao Z, Lee JY (2009) Sn@ cnt and sn@ c@ cnt nanostructures for superior reversible lithium ion storage. Chem Mater 21(14):3210–3215
37. Naguib N, Ye H, Gogotsi Y, Yazicioglu AG, Megaridis CM, Yoshimura M (2004) Observation of water confined in nanometer channels of closed carbon nanotubes. Nano Lett 4(11):2237–2243
38. Yu W-J, Hou P-X, Zhang L-L, Li F, Liu C, Cheng H-M (2010) Preparation and electrochemical property of fe2o3 nanoparticles-filled carbon nanotubes. Chem Commun 46:8576–8578
39. Hernadi K, Fonseca A, Nagy J, Bernaerts D, Lucas A (1996) Fe-catalyzed carbon nanotube formation. Carbon 34(10):1249–1257

40. Sivula K, Le Formal F, Grätzel M (2011) Solar water splitting: progress using hematite (α-fe2o3) photoelectrodes. ChemSusChem 4(4):432–449
41. Korneva G, Ye H, Gogotsi Y, Halverson D, Friedman G, Bradley J-C, Kornev KG (2005) Carbon nanotubes loaded with magnetic particles. Nano Lett 5(5):879–884
42. Weiss W, Ranke W (2002) Surface chemistry and catalysis on well-defined epitaxial iron-oxide layers. Prog Surf Sci 70(1):1–151
43. Morin F (1954) Electrical properties of α-fe 2 o 3. Phys Rev 93(6):1195
44. Cava CE, Roman LS, Persson C (2013) Effects of native defects on the structural and magnetic properties of hematite α-fe 2 o 3. Phys Rev B 88(4):045136
45. Pauling L, Hendricks SB (1925) The crystal structures of hematite and corundum. J Am Chem Soc 47(3):781–790
46. Searle C, Dean G (1970) Temperature and field dependence of the weak ferromagnetic moment of hematite. Phys Rev B 1(11):4337
47. Amin N, Arajs S (1987) Morin temperature of annealed submicronic α-f 2 o 3 particles. Phys Rev B 35(10):4810
48. Mochizuki S (1977) Electrical conductivity of α-fe2o3. Phys Status Solidi (a) 41(2):591–594
49. Leland JK, Bard AJ (1987) Photochemistry of colloidal semiconducting iron oxide polymorphs. J Phys Chem 91(19):5076–5083
50. Santilli CV, Bonnet JP, Dordor P, Onillon M, Hagenmuller P (1990) Influence of structural defects on the electrical properties of α-fe2o3 ceramics. Ceram Int 16(1):25–32
51. Cornell RM, Schwertmann U (1996) The iron oxide. VCH, New York
52. Fonin M, Pentcheva R, Dedkov YS, Sperlich M, Vyalikh DV, Scheffler M, Rüdiger U, Güntherodt G (2005) Surface electronic structure of the fe_3O_4(100): Evidence of a half-metal to metal transition. Phys. Rev. B 72:104436
53. Andriotis AN, Menon M, Froudakis GE (2000) Various bonding configurations of transition-metal atoms on carbon nanotubes: their effect on contact resistance. Appl Phys Lett 76(26):3890–3892
54. Saito Y, Yoshikawa T, Okuda M, Fujimoto N, Sumiyama K, Suzuki K, Kasuya A, Nishina Y (1993) Carbon nanocapsules encaging metals and carbides. J Phys Chem Solids 54(12):1849–1860
55. Guerret-Piecourt C, Le Bouar Y, Lolseau A, Pascard H (1994) Relation between metal electronic structure and morphology of metal compounds inside carbon nanotubes. Nature 372(6508):761–765
56. Canestraro CD, Schnitzler MC, Zarbin AJ, Da Luz M, Roman LS (2006) Carbon nanotubes based nanocomposites for photocurrent improvement. Appl Surf Sci 252(15):5575–5578
57. Cava CE, Possagno R, Schnitzler MC, Roman PC, Oliveira MM, Lepiensky CM, Zarbin AJ, Roman LS (2007) Iron-and iron oxide-filled multi-walled carbon nanotubes: electrical properties and memory devices. Chem Phys Lett 444(4):304–308
58. Salvatierra RV, Oliveira MM, Zarbin AJ (2010) One-pot synthesis and processing of transparent, conducting, and freestanding carbon nanotubes/polyaniline composite films. Chem Mater 22(18):5222–5234
59. Nossol E, Zarbin AJ (2009) A simple and innovative route to prepare a novel carbon nanotube/Prussian blue electrode and its utilization as a highly sensitive h2o2 amperometric sensor. Adv Funct Mater 19(24):3980–3986
60. Fagan SB, Mota R, da Silva AJ, Fazzio A (2003) Electronic and magnetic properties of iron chains on carbon nanotubes. Microelectron. J. 34(5):481–484
61. Chimowa G, Linganiso EC, Churochkin D, Coville NJ, Bhattacharyya S (2011) Origin of conductivity crossover in entangled multiwalled carbon nanotube networks filled by iron. Phys Rev B 84(20):205429
62. Marega R, Bonifazi D (2014) Filling carbon nanotubes for nanobiotechnological applications. New J Chem 38:22–27
63. Chen M-L, He Y-J, Chen X-W, Wang J-H (2012) Quantum dots conjugated with fe3o4-filled carbon nanotubes for cancer-targeted imaging and magnetically guided drug delivery. Langmuir 28(47):16469–16476

64. Yang F, Hu J, Yang D, Long J, Luo G, Jin C, Yu X, Xu J, Wang C, Ni Q et al (2009) Pilot study of targeting magnetic carbon nanotubes to lymph nodes. Nanomedicine 4(3):317–330
65. Wolny F, Muhl T, Weissker U, Lipert K, Schumann J, Leonhardt A, Büchner B (2010) Iron filled carbon nanotubes as novel monopole-like sensors for quantitative magnetic force microscopy. Nanotechnology 21(43):435501
66. Tsang S, Chen Y, Harris P, Green M et al (1994) A simple chemical method of opening and filling carbon nanotubes. Nature 372(6502):159–162
67. Sloan J, Monthioux M (2011) Filled carbon nanotubes:(X@CNTs). Carbon Meta-Nanotubes: Synth Properties Appl. John Wiley & Sons, p 225
68. Satishkumar B, Govindaraj A, Mofokeng J, Subbanna G, Rao C (1996) Novel experiments with carbon nanotubes: opening, filling, closing and functionalizing nanotubes. J Phys B At Mol Opt Phys 29(21):4925
69. Xu P, Han X, Liu X, Zhang B, Wang C, Wang X (2009) A study of the magnetic and electromagnetic properties of γ-fe 2 o 3–multiwalled carbon nanotubes (mwcnt) and fe/fe 3 c–mwcnt composites. Mater Chem Phys 114(2):556–560
70. Chen Y, Liu X, Mao X, Zhuang Q, Xie Z, Han Z (2014) γ-fe2o3 mwnt/poly (p-phenylenebenzobisoxazole) composites with excellent microwave absorption performance and thermal stability. Nanoscale 6(12):6440–6447
71. Rhee KY, Jung D-H, Kim H, Marroquin J (2012) Effect of fe 3 o 4 loading on the conductivities of carbon nanotube/chitosan composite films. Carbon Lett 13(2):126–129
72. Subramoney S, Ruoff RS, Lorents DC, Chan B, Malhotra R, Dyer MJ, Parvin K (1994) Magnetic separation of gdc2 encapsulated in carbon nanoparticles. Carbon 32(3):507–513
73. Liu M, Cowley JM (1995) Encapsulation of manganese carbides within carbon nanotubes and nanoparticles. Carbon 33(6):749–756
74. Ajayan PM, Redlich P, Rühle M (1997) Structure of carbon nanotube-based nanocomposites. J Microscopy 185(2):275–282
75. Zhang Q, Huang J-Q, Qian W-Z, Zhang Y-Y, Wei F (2013) The road for nanomaterials industry: a review of carbon nanotube production, post-treatment, and bulk applications for composites and energy storage. Small 9(8):1237–1265
76. Govindaraj A, Rao C (2002) Organometallic precursor route to carbon nanotubes. Pure Appl Chem 74(9):1571–1580
77. Schnitzler MC, Oliveira MM, Ugarte D, Zarbin AJ (2003) One-step route to iron oxide-filled carbon nanotubes and Bucky-onions based on the pyrolysis of organometallic precursors. Chem Phys Lett 381(5):541–548
78. Andrews R, Jacques D, Qian D, Rantell T (2002) Multiwall carbon nanotubes: synthesis and application. Acc Chem Res 35(12):1008–1017
79. Gupta V, Agarwal S, Saleh TA (2011) Chromium removal by combining the magnetic properties of iron oxide with adsorption properties of carbon nanotubes. Water Res 45(6):2207–2212
80. Gong J-L, Wang B, Zeng G-M, Yang C-P, Niu C-G, Niu Q-Y, Zhou W-J, Liang Y (2009) Removal of cationic dyes from aqueous solution using magnetic multi-wall carbon nanotube nanocomposite as adsorbent. J Hazard Mater 164(2):1517–1522
81. Carter R, Sloan J, Kirkland AI, Meyer RR, Lindan PJ, Lin G, Green ML, Vlandas A, Hutchison JL, Harding J (2006) Correlation of structural and electronic properties in a new low-dimensional form of mercury telluride. Phys Rev Lett 96(21):215501
82. Agrawal S, Raghuveer MS, Ramprasad R, Ramanath G (2007) Multishell carrier transport in multiwalled carbon nanotubes. IEEE Trans Nanotechnol 6(6):722–726
83. Fan S, Chapline MG, Franklin NR, Tombler TW, Cassell AM, Dai H (1999) Self-oriented regular arrays of carbon nanotubes and their field emission properties. Science 283(5401):512–514
84. Cava CE, Persson C, Zarbin AJ, Roman LS (2014) Resistive switching in iron-oxide-filled carbon nanotubes. Nanoscale 6(1):378–384
85. Jorio A, Saito R, Dresselhaus G, Dresselhaus M (2004) Determination of nanotubes properties by Raman spectroscopy. Philos Trans R Soc Lond A Math Phys Eng Sci 362(1824):2311–2336
86. Pimenta M, Dresselhaus G, Dresselhaus MS, Cancado L, Jorio A, Saito R (2007) Studying disorder in graphite-based systems by Raman spectroscopy. Phys Chem Chem Phys 9(11):1276–1290

87. Jonscher AK, Dielectric relaxation in solids. J Phys D Appl Phys 32(14):R57
88. Kliem H (2005) Kohlrausch relaxations: New aspects about the everlasting story. IEEE Trans. Dielectr Electr Insul 12(4):718
89. Tang X, Wang J, Zhang Y, Chan HL (2003) Leakage current and relaxation characteristics of highly (111)-oriented lead calcium titanate thin films. J Appl Phys 94(8):5163–5166
90. Yu S, Wu Y, Wong H-SP (2011) Investigating the switching dynamics and multilevel capability of bipolar metal oxide resistive switching memory. Appl Phys Lett 98(10):103514
91. Cava C, Salvatierra R, Alves D, Ferlauto A, Zarbin A, Roman L (2012) Self-assembled films of multi-wall carbon nanotubes used in gas sensors to increase the sensitivity limit for oxygen detection. Carbon 50(5):1953–1958
92. Bevilaqua RC, Cava CE, Zanella I, Salvatierra RV, Zarbin AJ, Roman LS, Fagan SB (2013) Interactions of iron-oxide filled carbon nanotubes with gas molecules. Phys Chem Chem Phys 15(34):14340–14346

Chapter 13
Characterization of Nanocarbons: From Graphene to Graphene Nanoribbons (GNRs) and Quantum Dots (GQDs)

Gabriela Borin Barin, Paulo T. Araujo, Iara de Fatima Gimenez, and Antonio G. Souza Filho

1 From Graphene to Graphene Nanoribbons (GNRs): The Effect of Quantum Confinement on Graphene-Based Material Electronic Properties

Carbon-based materials can be found in several different structural configurations (see Fig. 13.1) due to their bond flexibility [7], which allows for different hybridizations: sp, sp^2, and sp^3. Classical examples for each of the different hybridizations would be the diamond (displaying a sp^3 configuration), the graphite (displaying a sp^2 configuration), and the carbyne (displaying a sp configuration). Moreover, all these different hybridizations generate a wide variety of mechanical, electronic, thermal, and vibrational properties. Beyond the influence of the different hybridizations, these properties are intimately connected to these structures' dimensionality. Among systems with only carbon atoms, graphene – a two-dimensional (2D) allotrope of carbon – plays an important role since it is the basis for the understanding of the electronic properties in other allotropes, such as graphite, nanotubes, and fullerenes [1, 7], as shown in Fig. 13.2a.

G.B. Barin (✉) • I. de Fatima Gimenez
Materials Science and Engineering Department, Universidade Federal de Sergipe, Av. Marechal Rondom, s/n 49100-000, São Cristóvão, Sergipe, Brazil
e-mail: gabriela.borin@gmail.com; iara.gimenez@gmail.com

P.T. Araujo
Department of Physics and Astronomy and Center for Materials, The University of Alabama, for Info Tech – MINT, Tom Bevill Research Bldg, room 2050, Tuscaloosa, AL 35487, USA
e-mail: paulo.t.araujo@ua.edu

A.G. Souza Filho
Departamento de Física, Universidade Federal do Ceará, P.O. Box 6030, Fortaleza, Ceará, Brazil, CEP 60455-900
e-mail: agsf@fisica.ufc.br

E. Longo, F.A. La Porta (eds.), *Recent Advances in Complex Functional Materials*,
DOI 10.1007/978-3-319-53898-3_13

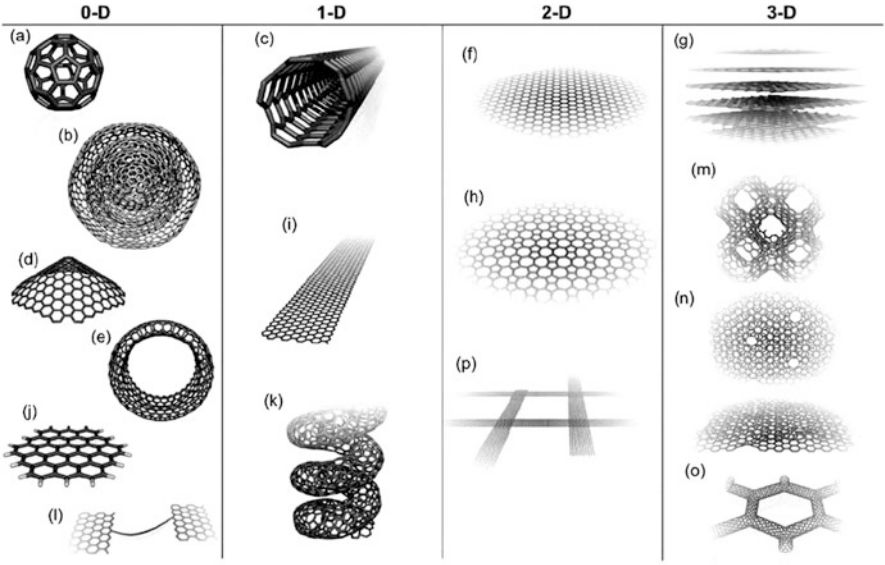

Fig. 13.1 Molecular models of different types of sp^2-like hybridized carbon nanostructures exhibiting different dimensionalities, 0D, 1D, 2D, and 3D: (**a**) C_{60}, buckminsterfullerene; (**b**) nested giant fullerenes or graphitic onions; (**c**) carbon nanotube; (**d**) nanocones or nanohorns; (**e**) nanotoroids; (**f**) graphene surface; (**g**) 3D graphite crystal; (**h**) haeckelite surface; (**i**) graphene nanoribbons; (**j**) graphene clusters; (**k**) helicoidal carbon nanotube; (**l**) short carbon chains; (**m**) 3D schwarzite crystals; (**n**) carbon nanofoams (interconnected graphene surfaces with channels); (**o**) 3D nanotube networks; and (**p**) nanoribbon 2D networks (Figure and caption adapted from Ref. [6]. Reproduced with permission from Elsevier Copyright © 2010)

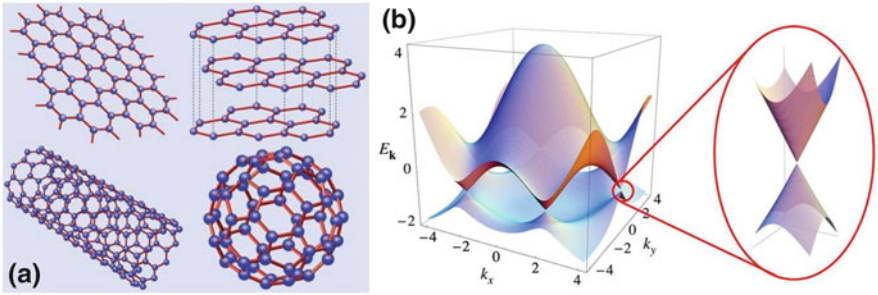

Fig. 13.2 (**a**) shows a graphene sheet (*top left corner*) and some of its allotropes: carbon nanotube (*bottom left corner*), fullerene (*bottom right corner*), and an AB-stacked trilayer graphene (*top right corner*). (**b**) shows the electronic structure of graphene. At the corners of the hexagons, in which the carbon atoms sit, the valence and the conduction bands touch each other giving rise to a conical linear dispersion called Dirac cones (Figures adapted from Ref. [7]. Reproduced with permission from American Physical Society. Copyright © 2009)

The band structure of graphene and graphite was first investigated by P.R. Wallace in 1946, in which study showed the unusual semimetallic behavior in these materials [8]. At that time, the idea of a purely 2D structure was still elusive, and Wallace's studies of graphene served him as a starting point to study graphite, an important material for nuclear reactors in the post-World War II era [7, 8]. Graphene is a flat monolayer of carbon atoms tightly packed into a two-dimensional (2D) honeycomb lattice [1], as illustrated in the top left corner of Fig. 13.2a. Graphene carbon atoms present sp^2 hybridization between one s orbital and two p orbitals which leads to a trigonal planar structure with a formation of a σ bond between carbon atoms that are separated by 1.42 Å [7]. The other $2p_z$ orbital, perpendicular to the graphene plane, is responsible for the π bond formation. The electrons from this orbital are less bounded to the atom and therefore can move freely in the crystal lattice. Also, they can be excited to the conduction band more easily than the σ electrons. In graphene, the electrons of the σ bond have no role in the electrical conduction. On the other hand, the electrons of the π bond originate the valence and conduction bands, π and π^*, and these electrons are the most important for the determination of optical and electrical transport properties in graphene [9].

The hexagonal graphene network has two carbon atoms per unit cell which results in a very unique band structure, as shown in Fig. 13.2b. As shown in Fig. 13.3a, there are two electrons per unit cell which fulfill the valence band (π band), the density of states at the Fermi level is null, and the π^* band is empty. This configuration gives 2D graphite a zero-bandgap semiconductor character. These two bands touch at six points, the so-called Dirac or neutrality points. Symmetry allows these six points to be reduced to a pair, K and K' (see Fig. 13.3b), which

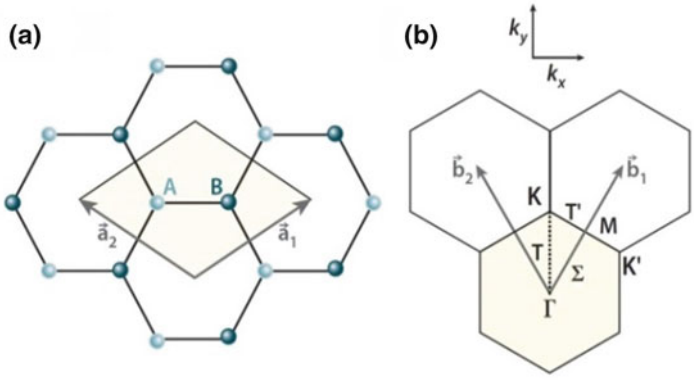

Fig. 13.3 (**a**) shows the graphene unit cell (*shaded diamond*) in the real space with its respective basis vectors $\overrightarrow{a_1}$ and $\overrightarrow{a_2}$. A and B are carbon atoms sitting on two inequivalent K and K' points, which are two inequivalent high-symmetry points in the graphene's Brillouin zone, as shown in (**b**). (**b**) shows the first Brillouin zone (*shaded hexagon*) of a graphene with its respective basis vectors $\overrightarrow{b_1}$ and $\overrightarrow{b_2}$. The main high-symmetry points Γ, M, and K are also shown (Figure adapted from Ref. [10]. Reproduced with permission from American Chemistry Society. Copyright© 2010)

are independent of one another. If we limit ourselves to low energies, which are the most relevant in electron transport and optical properties, the bands have a linear dispersion, and the band structure can be viewed as two cones touching at the Dirac points E_{Dirac}. This is because the orthogonal π and π^* states do not interact, so their crossing is allowed. Since the band structure is symmetric about the Dirac point, electrons and holes in pure, freestanding graphene should have the same properties [11].

Graphene layers were first isolated experimentally in 2004 by Novoselov and Geim et al. [12, 13] via mechanical exfoliation of graphite. The observation of the atomic-thick graphene layers was just possible due to the possibility of graphite to have isolated layers cleaved from its bulk, and the identification of such isolated layer was only possible after depositing the cleaved layer on top of an oxidized Si wafer followed by its surface scan in an optical microscope. So far, this detection technique has been demonstrated and widely used only for a SiO_2 thickness of 300 nm (purple to violet in color). It was observed that 5% change in the thickness (to 315 nm) can significantly lower the contrast [1]. Thin flakes were sufficiently transparent to add to an optical path, which changed their interference color with respect to an empty wafer [12, 13]. After this pioneer isolation of a graphene layer, other procedures to obtain this material were explored, being the epitaxial growth on SiC and the catalytical chemical vapor deposition (CVD) method, the two main approaches used to grow wafer-scale graphene [14]. Via the CVD method, growth is possible to obtain large-area graphene in a wide range of metal catalysts, such as Cu, Ni, Pt, Ru, and Ir. In most of the transition metals, graphene growth follows a two-step mechanism, the incorporation of carbon into the metal (dissolution) followed by segregation upon fast cooling. For transition metals with low-carbon solubility such as Cu, the graphene growth can be better understood via surface growth mechanism. Such mechanism is based on chemisorption/deposition in which the growth starts with the hydrocarbon dissociation step and stops as soon as the hydrocarbon supply is no longer provided [14, 15].

In order to exploit all the promising application of graphene in, for example, nanoelectronic and photoelectronic devices, it is necessary to transfer the graphene layers from the metal catalyst substrate to technologically relevant substrates [2]. Several techniques were exploited to transfer graphene such as polymer-based transfer [16], electrochemical delamination [17], and cold/hot lamination [18], among others. Graphene films are transparent, conductive, mechanically strong, and flexible which open up different possibilities of application such as conductive electrodes [19], radiofrequency devices [20], and flexible displays. Despite its potential, the absence of a bandgap indicates that graphene is not likely to be suitable for semiconductor application, such as digital switches. Different methodologies have been studied in order to progress in this direction and induce a gap opening in graphene, such as substrate-induced bandgap via epitaxial growth of graphene on SiC substrate [21], adsorption of atomic hydrogen onto the moiré superlattice positions of graphene [22], or bandgap induced between two layers of graphene [23].

The synthesis of ultra-narrow graphene nanoribbons [3, 4] (with widths down to 1 nm) also allows the opening of a bandgap due to the quantum confinement of the electronic bands in such narrow widths. Theoretical studies predict that

ribbons with a width smaller than 2 nm have bandgap comparable to that in silicon (1.1 eV) which makes this material really interesting for application in logic devices [24]. Graphene nanoribbons (GNRs) are narrow strips of graphene which have a sizeable bandgap due to lateral confinement. GNR semiconductor behavior raises interesting properties for electronic device application, which overcomes many of limitations of graphene [25, 26]. Besides the bandgap which decreases as the ribbon width increases, GNRs also present exceptional properties such as high thermal and electrical conductivity. However, in order to achieve such properties, it is of primary importance to develop techniques to synthesize graphene nanoribbons with atomically smooth and well-defined edges and width [27, 28]. Traditionally available methods to pattern GNRs from graphene, known as top-down methods, i.e., unzipping carbon nanotubes [29, 30] or e-beam lithography of graphene [31], result in GNRs with poorly defined edges and widths which degrade GNR electronic properties [32]. Therefore, these top-down techniques urge for further improvements if they are to be used in the nanofabrication of such ribbons.

A more recent alternative has shown the bottom-up approach to fabricate graphene nanoribbons with atomically smooth edges and well-defined width [3, 33]. The two main synthesis routes reported in the literature to fabricate graphene nanoribbons via bottom-up approach are the synthesis via chemical synthetic routes in solution [24, 34] and via on-surface synthesis, either using CVD [35] or more recently ultrahigh-vacuum (UHV) systems [3, 5, 36]. Solution-mediated synthesis achieved so far a variety of different defined GNRs; however, the solubility of the graphene nanoribbons remains a challenge and is limited by strong π–π interactions. Improving the solubility of GNRs is strongly linked to the addition of chemical groups, like alkyl chains in the GNR edges, which could compromise its electronic properties for further device application. On the other hand, GNR synthesis via on-surface methods allows the synthesis of single GNR, with hydrogen-terminated edges that can be characterized in situ via tunneling microscopy techniques as well as transfer to possible device integration [34].

Graphene nanoribbon growth via on-surface synthesis in ultrahigh-vacuum systems was first realized by Fasel et al. [3], and it is based on the surface-assisted covalent coupling of functionalized molecular precursors. The topology, edge structure, and width of the GNRs are controlled by monomer structure upon the polymerization step of the synthesis [37]. Further annealing allows for the closure of C–C bonds, upon the so-called cyclodehydrogenation step, forming the desired graphene nanoribbon. Defined electronic structure of the GNRs allows studies of charge transport and increases the potentiality of application in nanoscale electronic devices [25, 38]. GNRs have their electronic properties and bandgap tuned by their edge topology (armchair or zigzag) and their width (N = 5,7,9,11, etc.). Depending on the width, armchair GNRs can present both semiconductor (widths lower than 10 nm) and metallic behaviors [34, 39, 40]. For zigzag GNRs, the theory predicts that regardless of their width, they always show metallic behavior with strong localized edge states at the zigzag sites [34, 40]. Recently Ruffieux et al. [41] and Wang et al. [42] showed experimental results on GNRs with zigzag edges synthesized via on-surface synthesis on Au(111) in ultrahigh-vacuum conditions.

By combining finite-sized zigzag and armchair GNRs, it is possible to build up the graphene nanowiggles (GNWs) [3, 43, 44]. It is possible to construct four different arrangements regarding the edges (zigzag or armchair) and the parallel and oblique directions of the ribbons as indicated in Fig. 13.4a, b. Theory predicts that these GNWs exhibit emergent and versatile properties different from basic GNR counterparts. Similar to GNRs, the ground state for the GNWs with at least one zigzag sector is the antiferromagnetic configuration. In fact, the presence of at least one sector with zigzag edges allows the systems to exhibit many magnetic states as summarized in Fig. 13.5. The quantum mechanics explains the origin of these multiple magnetic states, and it is attributed mainly to the bipartition of the graphene lattice [43, 44].

Besides a lot of progress made so far, it should be pointed out that the full experimental realization of magnetism in graphene nanoribbon systems is still far from reaching the level of the body of theoretical predictions. The preservation of edge magnetism in zigzag ribbons depends strongly on keeping the C atoms at the edge in their sp^2 hybridization, and the right choice of chemical groups able to passivate and stabilize the edges preserving the magnetism is challenging [45].

2 Optical Absorption and Emission of Graphene-Based Materials

2.1 Pristine Graphene

The optical response of graphene depends upon the spectral region under investigation and may be dominated either by intraband or interband transitions, as reviewed by Heinz and coworkers [48] (see Fig. 13.6). In the far-infrared region, intraband transitions from free carriers dominate the optical response, while in the mid- and near-infrared regions, interband transitions from the valence to conduction band predominate.

In the case of interband transitions, the response is almost independent of the frequency, being equal to a universal value. This is regarded as the "universal" conductance of graphene and is determined only by fundamental constants, assuming the value of $\pi e^2/2\,h$, where e is the elementary charge of an electron and h is the Planck constant, and corresponding to an absorbance of $\approx$ 2.29% [49] (see Fig. 13.6). Thus, monolayer graphene represents an interesting example of a macroscopic manifestation of quantum mechanics [50]. In this context, the absorption spectrum of graphene has been predicted to exhibit particularly simple spectral features with a dependence on the number of stacked layers, which means that a bilayer absorbs 4.6% and a five-layer-thick flake near 11.5% [51].

This behavior remained to be experimentally observed until 2008 [52], and it has also been found that this type of optical absorption in graphene can be controlled through electrostatic gating, which induces Pauli blocking of the optical

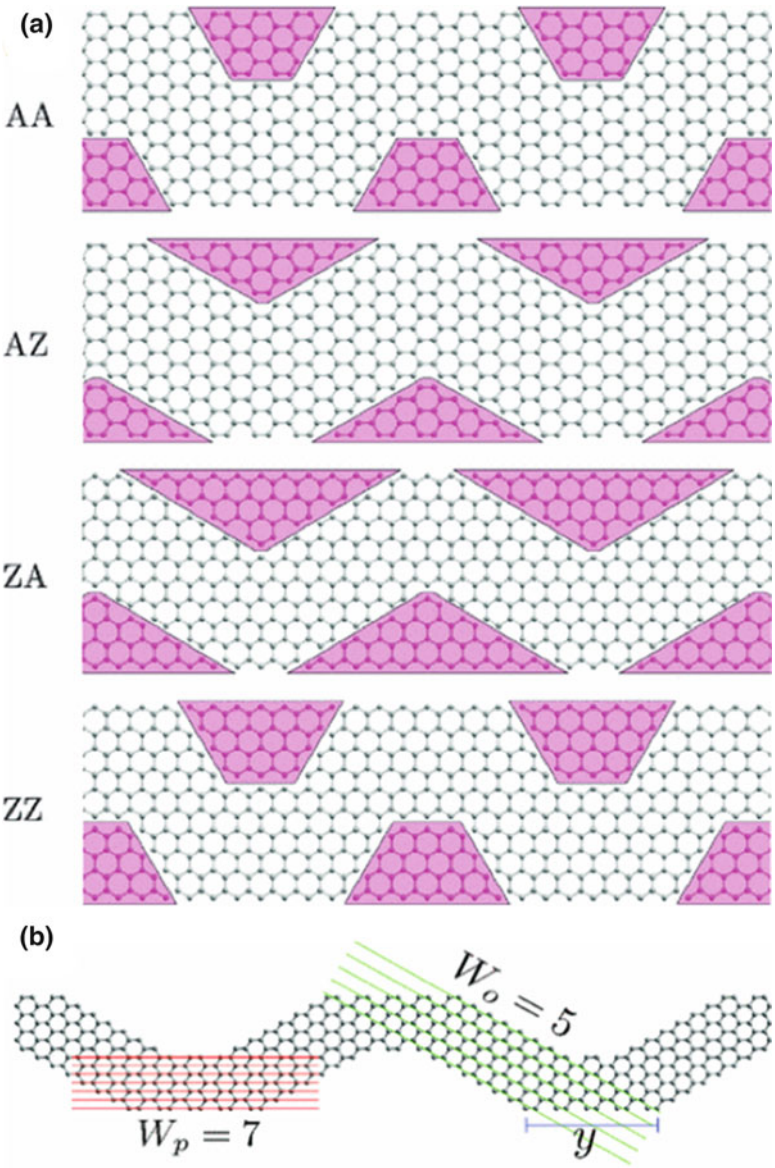

Fig. 13.4 (**a**) The four possible structures of graphene nanowiggles (GNWs). (**b**) Definition of the parallel width (W_p) and oblique width (W_o) parameters as the number of C–C lines or zigzag strips along the width of each sector and the length y of the outer edge of the parallel sector. The GNWs shown are (5_Z,7_A) [44] (Reproduced with permission from American Physical Society. Copyright © 2012)

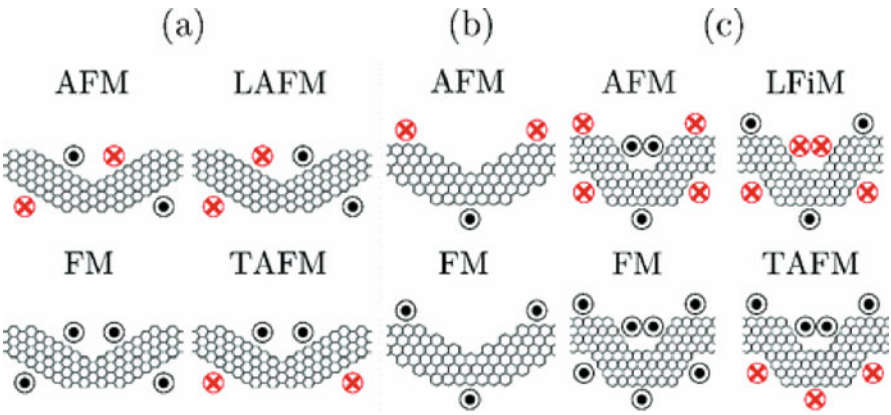

Fig. 13.5 Possible spin distributions in (**a**) AZ-GNWs, (**b**) ZA-GNWs, and (**c**) ZZ-GNWs. *Black dots* and a *red cross* stand for majority spin-up and spin-down, respectively. *AFM* antiferromagnetic, *LAFM* longitudinal antiferromagnetic, *LFiM* longitudinal ferrimagnet, *FM* ferromagnetic, and *TAFM* transversal antiferromagnetic [44] (Reproduced with permission from American Physical Society. Copyright © 2012)

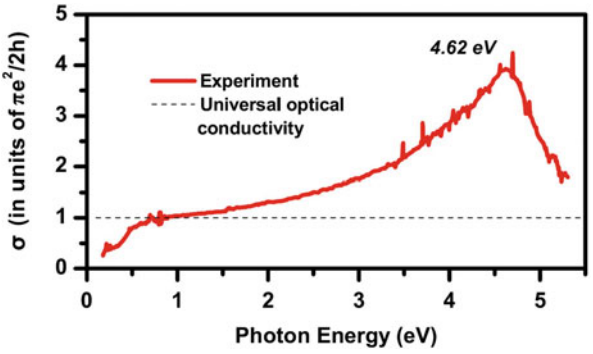

Fig. 13.6 Optical conductivity of graphene (*solid line*). The *dashed line* is the universal optical conductivity, which depends only on fundamental constants (Figure adapted from Ref. [54]. Reproduced with permission from American Physical Society. Copyright © 2011)

transitions [53]. In the ultraviolet region, the interband absorption was found to increase above the universal value and shows characteristics of excitonic signals.

The absorption for monolayer graphene is well behaved and smooth from 300 to 2500 nm (0.49 to 4.13 eV); the peak at $\lambda = 250$ nm in the UV region is attributed to the interband electronic transition from the unoccupied π^* states [2]. In photoluminescent materials, light emission by interband transitions is caused by the relaxation process that follows optical absorption. Since graphene, as an extended aromatic system, has sufficient light absorption, one could question about the possibility of observation of photoluminescence from this material. Single-layer graphene is considered a zero-bandgap semiconductor because its electronic structure exhibits two bands intersecting at inequivalent points K and K' – referred to as Dirac points – in the reciprocal space, where valence and conduction bands are degenerated [2], as shown in Fig. 13.2b. Thus, owing to the absence of

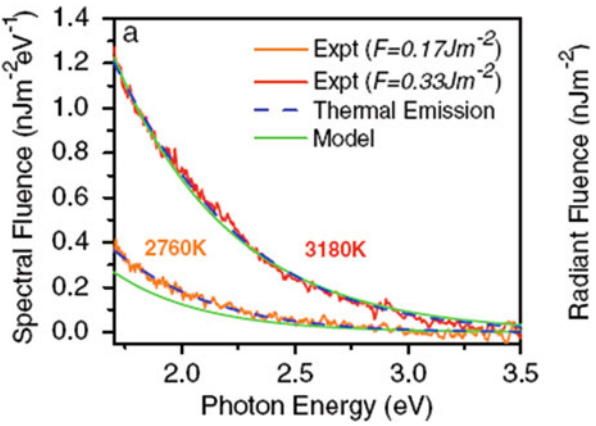

Fig. 13.7 Spectral fluence of light emission from graphene for excitation with 30-fs pulses. The spectra are compatible with the predictions for thermal emission (*dashed lines*) for T = 2760 K and 3180 K (Reproduced from Ref. [55] with permission from American Physical Society. Copyright© 2010)

a bandgap, the observation of photoluminescence from graphene is considered almost impossible, since carrier relaxation causes the energy of highly excited e–h pairs to return to low energies at very high rate. Nevertheless, Heinz and coworkers reported the observation of significant light emission from graphene under excitation by ultrashort (30-fs) laser pulses, discussing that ultrafast excitation can produce carriers with transient temperatures above 3000 K that give rise to emission in the visible spectral range [55] (Fig. 13.7). As further evaluated by Stöhr and coworkers, this broadband nonlinear PL was thought to result from radiative recombination of a high-density electron–hole plasma in graphene, generated by pulse laser irradiation [56].

A potentially successful way to make graphene photoluminescent is to open up its bandgap, which is zero because the two carbon atoms in the unit cell have identical properties. Thus, a bandgap can be formed through both chemical (or physical functionalization to reduce the connective long range π conjugations) [57] and structural modifications (reduction of size to give rise to quantum confinement) [58]. In the first strategy, oxidation is one of the most effective ways to open the bandgap of graphene by introducing the defects and confined islands of sp^2 conjugations [59].

2.2 Nanographenes

Since graphene exhibits an infinite exciton Bohr radius, it has been recognized that quantum confinement could take place in graphene of any finite size, being expected to result in many interesting phenomena that cannot be obtained in other materials such as the semiconductors. In principle, the bandgap of graphene can be tuned from 0 eV to that of benzene. For benzene, the HOMO–LUMO gap value is reported around 5–7 eV depending on the calculation method used [60] by varying the graphene dimensions. When the size of a material becomes equivalent to or falls

below the characteristic length scale for the motion of its electrons, its properties become dependent on the size and shape of the material. Specifically, as the size of a semiconductor crystal is reduced such that it becomes comparable to the exciton Bohr radius of the bulk material, the boundary significantly modifies the electron distribution, thus leading to size-dependent properties such as a bandgap and energy relaxation dynamics. This phenomenon, known as quantum confinement, has been demonstrated in many semiconductor materials including graphene itself [61]. Consequently, graphene quantum dots (GQDs), as a new class of quantum dots, have emerged and attracted tremendous research interest [58]. Colloidal graphene QDs with well-defined structures provide unique opportunities to study the evolution of properties with size in a two-dimensional crystal and may lead to useful applications [62]. Also, interesting semiconducting bandgaps were predicted in GNRs, laterally constrained graphene sheets, with widths under 100 nm [39]. As discussed before, GNRs are thin, elongated strips of graphene with straight edges. As their width decreases, GNRs can gradually transform from semimetals to semiconductors (i.e., the bandgap of GNRs is inversely proportional to the ribbon width) due to the quantum confinement and edge effects.

Theoretical and experimental studies [63] have shown that narrow GNRs (width less than 10 nm) exhibit substantial quantum confinement and edge effects that render GNR semiconducting character. By comparison, GQDs possess strong quantum confinement and edge effects when their sizes are down to 100 nm. If their sizes are reduced to 10 nm, comparable with the widths of semiconducting GNRs, the two effects will become more pronounced and, hence, induce new physical properties. Several works were dedicated to calculations of optical properties of pure graphene and its various forms such as GQDs and GNRs with different sizes and forms [64–66].

Optical absorption spectroscopy is frequently used for the characterization of GQDs [67–73] which typically show strong optical absorption in the UV region, with a tail extending into the visible range. For the UV–vis absorption spectrum of a graphene oxide (GO) sample, in particular, two kinds of peaks can be clearly seen: a peak at ~230 nm due to π–π^* transition of aromatic C = C bonds and a shoulder at ~300 nm assigned to n–π^* transition of C = O bonds [58]. In the case of extended graphene, the π–π^* transition peak shifts to ~270 nm with the disappearance of the n–π^* transition peak. These peaks can also be observed in the UV–vis absorption spectra of GQDs, with the π–π^* transition peak centered at a wavelength between 200 and 270 nm and the n–π^* transition peak at wavelength longer than 260 nm. For instance, Wu and coworkers observed a band at 230 nm (π–π^*) for oxidized graphene sheets, with the appearance of a second absorption at 320 nm (n–π^*) after cutting oxidized graphene sheets into GQDs [63]. Peak positions are sensitive to both GQD sizes and the presence of chemical groups. It has been shown that increasing the temperature in the preparation of GQDs from carbon fibers yields smaller particles, shifting the absorption peak to lower wavelengths [74]. This behavior is indicative of quantum confinement, although there are exceptions with size-independent spectroscopic properties [75, 76] (Fig. 13.8).

One of the most exciting properties of graphene nanostructures is the photoluminescence emission, as predicted from the fact that graphene should exhibit quantum confinement for any finite size, a result that was also studied by theoretical

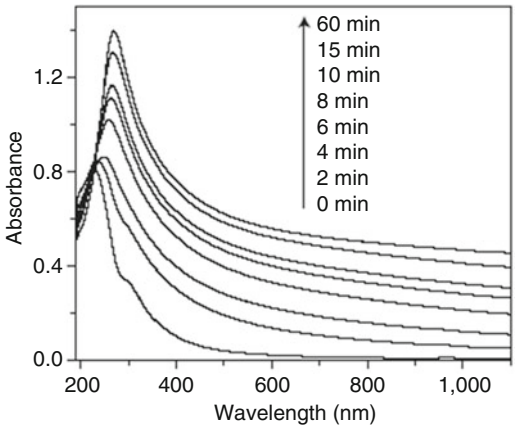

Fig. 13.8 UV–vis absorption spectra showing changes in spectral profile of graphene oxide under different reduction times with hydrazine (Reproduced from Ref. [76] with permission from Macmillan Publishers Limited, part of Springer Nature. Copyright © 2008)

calculations [77]. Several works have reported the synthesis of photoluminescent GQDs with different colors ranging from deep ultraviolet to near-infrared region [78–80]. However, most GQDs were in fact partially oxidized graphene quantum dots, for which the oxygen-containing functional groups on the surfaces introduce a series of emissive traps into the π–π^* gap influencing the emission mechanism [81]. In carbon materials containing a mixture of sp^2 and sp^3 bonding, the optoelectronic properties are determined by the π states of the sp^2 sites [71]. The π and π^* electronic levels of the sp^2 clusters lie within the bandgap of σ and σ^* states of the sp^3 matrix and are strongly confined, as they depend on the size of sp^2 domains.

Although the exact mechanism driving PL emissions in GQDs is still under debate, theoretical works proposed for this phenomenon include electron–hole (*e–h*) pair recombination with quantum size effect (band edge recombination), edge structure (when graphene sheets are cut along different crystallographic directions, diverse types of edges – armchair and zigzag edges), doping with impurities that introduce additional energy levels, free zigzag sites with a carbene-like triplet ground state, and surface defects in the functional groups of the GQDs [58]. As regards the existence of a bandgap, one could predict simple size dependences based on quantum confinement. However, the possibility that more than one mechanism occurs simultaneously increases the complexity of the GQD panorama. In fact, to the best of the authors' knowledge, no clear dependence of the emission colors on particle size was evidenced by detailed examination of literature data [58]. Several studies evaluated possible effects that may influence the photoluminescence emission of GQDs [82]. The formation of special molecule-like states containing carboxyl groups and carbonyl groups – parts of the so-called edge states – in carbon nanodots and graphene quantum dots has been shown to be responsible for their green fluorescence [81]. On the other hand, in chemically derived GO thin films, the presence of isolated sp^2 clusters within the carbon–oxygen sp^3 matrix leads to the localization of *e–h* pairs, facilitating radiative recombination and giving rise to blue emission [71]. The intrinsic state was found to depend on size for a series of GQDs (C42H18, C96H30, C132H34, C222H42) synthesized by organic methods, while the energy level offset between intrinsic state and edge state determined their optical

properties. As a result, the green fluorescence of these GQDs not only depends on the size but also results from bright edge state [83]. For well-crystallized GQDs prepared from glucose, sulfuric acid, and deionized water with ultraviolet and blue emission, the ultraviolet emission is originated from the recombination of *e–h* pairs localized in the C–C bonds, while the blue one originates from the electron transition from sp^2 domains [77].

In general, most luminescent GQDs exhibit excitation-dependent PL characteristics with an emission peak shift toward longer wavelength accompanied with an intensity decrease when the excitation wavelength is increased [84]. This behavior affords multi-PL colors under different excitation wavelengths, and this property is important for certain applications such as in bioimaging, biosensor, and biomolecule/drug delivery and may result from optical selection of differently sized GQDs and/or different emissive sites on GQDs. This effect has been called red edge effect and is unusual for other types of quantum dots as well as molecular fluorophores, but the position of the peak fluorescence of GO in a polar solvent is heavily dependent on the excitation wavelength [85]. Authors observed that, when GO sheets are present in a polar solvent, the solvation dynamics slows down to the same time scale as the fluorescence due to the local environment of the GO sheet. Consequently, the fluorescence peak of GO broadens and red-shifts up to 200 nm with an increase in the excitation wavelength, while the effect disappears in nonpolar solvents. Thus, there is no unified explanation to this effect, similarly to the photoluminescence mechanism itself [86].

3 ^{12}C and ^{13}C Isotopic Labeling: A Novel Route to Tune Properties and Characterize the Growth of Carbon Layers and Stacking Orders

As discussed throughout this chapter, the growth of carbon structures and the development/improvement of experimental techniques to characterize these carbon structures have been a major focus of research in the past decades [15, 19, 87]. Among these carbon structures, monolayer (SLG) and few-layer graphenes (FLG) have been extensively explored, since these structures are unique as regards their electronic, thermal, and mechanical properties [15, 19, 87]. Naturally derived from bulk graphite, SLG and FLG systems may be obtained by scotch-taping a piece of graphite and then transferring the flakes, which were extracted from the piece of graphite, to target substrates [1]. Although the quality of these scotch-taped flakes is outstanding, their dimensions are limited to a few microns. Notwithstanding, this limitation is a major drawback to a potential large-scale application by the industry [1, 15, 19, 87]. Fortunately, advances in the synthetic growth of SLG and FLG, which happened mainly in the past 10 years, allow us to envision these systems to be industrially scalable [1, 15, 19, 87]. Among the techniques available to synthesize graphene systems, the CVD technique is very convenient as it allows the use of a

large variety of catalyst substrates, and the size of the carbon layers is, in principle, limited by the dimensions of the catalyst substrate itself [1, 15, 19, 87].

As regards the CVD method, discussed in detail elsewhere in the chapter, copper (Cu) and nickel (Ni) have been the two main catalyst substrates used to grow SLG and FLG. Usually, the growth process can be established through four basic steps: (1) insertion of the catalyst substrate in the CVD chamber; (2) establishment of a gas flow constituted of 1/10 mixture of methane (CH_4) and hydrogen (H_2), respectively; (3) elevation of the temperature to the desired growth temperature, which changes with changing the catalyst substrate as well as its crystallographic orientation; and (4) fast cooling down of the specimens [15, 19, 87]. The growth mechanisms are different for each substrate. In Cu, the solubility of C is not very high so that the carbon atoms left at the Cu surface by the dissociation of CH_4 molecules will diffuse across the Cu bulk surface and form nucleation centers from which the carbon layers start growing [14, 88–95]. Since each nucleation center may be oriented in different directions, the carbon layers grow on the Cu surface several grains with different crystallographic orientations connected to each other. There is the formation of grain boundaries at the intersection of several differently oriented grains, which impoverishes the resulting carbon layers. On the other hand, in Ni, the solubility of carbon atoms if fairly high and diffusion of carbon atoms into the bulk Ni and segregation of carbon atoms from the bulk Ni rule the growth process [1, 15, 19, 87, 93, 96]. In Ni, SLG may be grown in the Ni(111) and Ni(110) crystallographic directions, while FLG may be grown in all the three Ni(111), Ni(110), and Ni(100) directions. In the Ni(111) direction, the growth of carbon layers will be epitaxial, and, therefore, the SLG layers are expected to be continuous producing high-quality layers. However, in the Ni(110) direction, the growth is no longer epitaxial, and similarly to the growth in Cu, the SLG layers will present different grains with different orientations [1, 15, 19, 87, 93, 96].

The CVD growth technique also brings an extra component of versatility: it is possible to synthesize carbon structures that present in their structures both carbon 12 (^{12}C) and carbon 13 (^{13}C), which are carbon isotopes. The electronic properties of these isotopes are the same, but their unified atomic masses are different: ^{12}C has an unified atomic mass equals 12 and ^{13}C has an unified atomic mass equals 13. Consequently, their vibrational properties (and any other property which is mass dependent) will be different. Moreover, this isotope labeling of CVD carbon layers may also be used as a characterization technique [14, 88–95, 97–100]. Li et al. were pioneers on using ^{12}C and ^{13}C to study the dynamics of SLG and bilayer graphene (BLG) on bulk Cu surface and bulk Ni surface [90]. In their work, the different masses presented by the carbon isotopes are used to identify aspects of the spatial distribution of graphene domains over the catalyst substrates and also to identify the mechanisms ruling the growth in each substrate [90]. In the case of growth in bulk Ni, since the solubility of carbon in this catalyst is very high, by introducing $^{12}CH_4$ and $^{13}CH_4$ in the CVD chamber in a specific sequence, the ^{12}C and ^{13}C dissociated from the $^{12}CH_4$ and $^{13}CH_4$ molecules will diffuse into the bulk Ni followed by segregation and precipitation of those atoms at the bulk Ni surface. However, this mechanism produces a random allocation of carbon species at the

surface. Therefore, the resultant carbon layer will contain a random mixing of ^{12}C and ^{13}C atoms, and such randomness should be independent of which is introduced first in the CVD chamber: $^{12}CH_4$ or $^{13}CH_4$ [90]. On the other hand, since in Cu the solubility of carbon is not high, the growth of carbon structures will rely upon the adsorption of carbon atoms at the bulk Cu surface. In this case, the order with which the $^{12}CH_4$ and $^{13}CH_4$ are introduced into the CVD chamber should matter because the carbon structure will have its formation started with whatever carbon atoms (^{12}C or ^{13}C) that are initially available [90]. Indeed, as shown in Fig. 13.9, the isotopic labeling technique works well. Figures 13.9a–c show the G-band images of a SLG deposited on SiO_2 substrate, and Figs 13.9d–f show the D-band images for the same SLG. The G-band can be described as in plane vibrations in which the two carbon atoms of the graphene unit cell vibrate out of phase. The D-band is a defect activated feature and will show up every time the translational symmetry in the graphene layer is lost. Figures 13.9a–d show the G-band and the D-band, respectively, for the image containing contributions from areas with only ^{12}C, areas with only ^{13}C, and areas with a mixture of both altogether. Figures 13.9b, c show (see the bright areas), respectively, areas with only ^{13}C and areas with only ^{12}C in an experiment in which $^{13}CH_4$ was introduced first into the CVD chamber. Figures 13.9e, f show, respectively, the D-band areas with only ^{13}C and areas with only ^{12}C, and these images give insights on where the grain boundaries are located [90].

In a publication from another group, Li et al. demonstrated that the isotopic labeling technique could help to understand how the growth of BLG via the CVD technique happens [94]. The growth of BLG via CVD was already being studied by several groups [14, 88–96] using both Cu and Cu–Ni alloys as catalyst substrates. However, several questions were still without answer, as for example, which layer would grow first, the top layer or the bottom layer [14, 88–96]. In their work, Li and collaborators were able to identify that the adlayer graphenes composed of ^{13}C, which were synthesized on a ^{12}C graphene film previously grown, produced isotopically distinct regions and they also shown that the ^{13}C atoms would use the same nucleation centers established for growing the ^{12}C graphene layer [94]. Since the experiment revealed that the carbon layers comprise either only ^{12}C or only ^{13}C, the authors attacked the BLG samples with O_2 plasma and demonstrated that the adlayer was indeed the bottommost layer (see Fig. 13.10). Wu and collaborators also used the isotopic labeling technique to understand the growth mechanisms of SLG and BLG in Cu–Ni alloys [93]. These alloys, depending on the concentration of its constituents, may observe properties similar to bulk Cu, properties similar to bulk Ni, or hybrid properties (properties observed in bulk Cu and bulk Ni). They studied Cu–Ni foils, which are commercially available and whose weight percent of its constituents is 88.00% Cu and 9.90% Ni. With such substrate, one would expect the formation of carbon layers to happen through adsorption of carbon atoms at the bulk surface as it happens when Cu is used as the catalyst substrate [93]. However, they demonstrate that even at this lower concentration of Ni relative to Cu, in the Cu–Ni foils, the dominant growth mechanisms are diffusion into the bulk, segregation, and

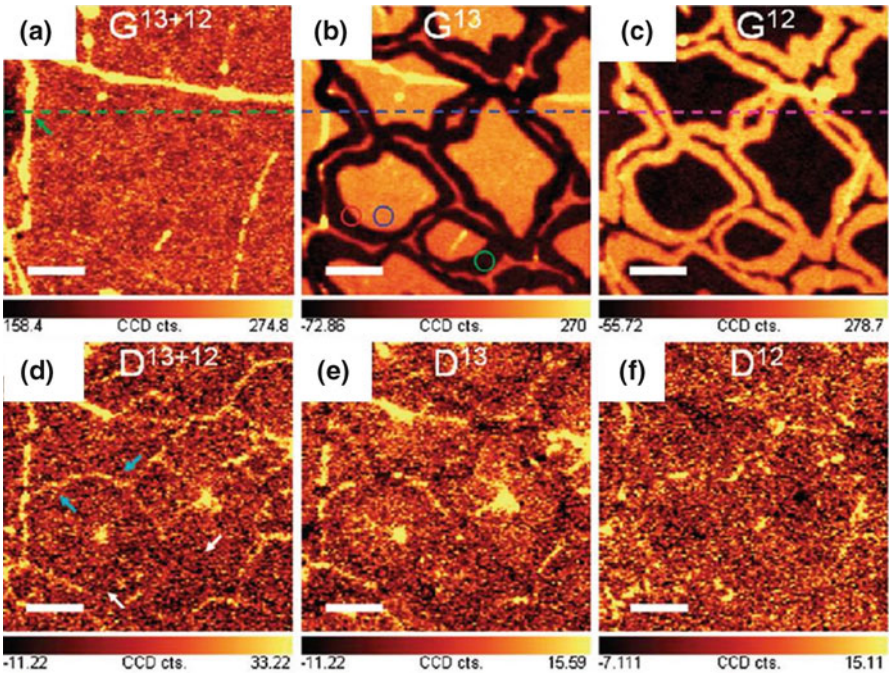

Fig. 13.9 (**a**) shows the G-band for the image containing contributions from areas with only ^{12}C, areas with only ^{13}C, and areas with a mixture of both altogether. (**b**, **c**) show (see the *bright areas*), respectively, areas with only ^{13}C and areas with only ^{12}C in an experiment in which $^{13}CH^4$ was introduced first into the CVD chamber. (**d**) shows the D-band for the image containing contributions from areas with only ^{12}C, areas with only ^{13}C, and areas with a mixture of both altogether. (**e**, **f**) The D-band areas with only ^{13}C and areas with only ^{12}C, and these images give insights on where the grain boundaries are located. As expected, the distribution of ^{13}C and ^{12}C is not random (Figure adapted from Ref. [90]. Reproduced with permission from American Chemical Society Copyright © 2009)

precipitation [93]. These growth mechanisms explain, as mentioned earlier in the text, the growth of carbon structures in bulk Ni, in which the carbon solubility is high. Wu et al. also showed that the diffusion of ^{12}C atoms is about 4% higher than the diffusion of ^{13}C atoms [93].

Later, Fang and collaborators used a combination of Raman spectroscopy and isotopic labeling technique to implement a fast route to identify if the BLG grown in a Cu substrate via the CVD method is turbostratic or AB stacked (also known as Bernal stacking) [91]. As shown in Fig. 13.11, Raman spectroscopy provides unique signatures related to the top and bottom layers of an isotopically labeled turbostratic BLG system ($^{12}C/^{13}C$ t-BLG) and isotopically labeled AB-stacked BLG ($^{12}C/^{13}C$ AB-BLG) [91]. In their experiments, Fang et al. used Cu enclosures to grow the BLG systems. First, through the admission of $^{12}CH_4$ into the CVD chamber, ^{12}C

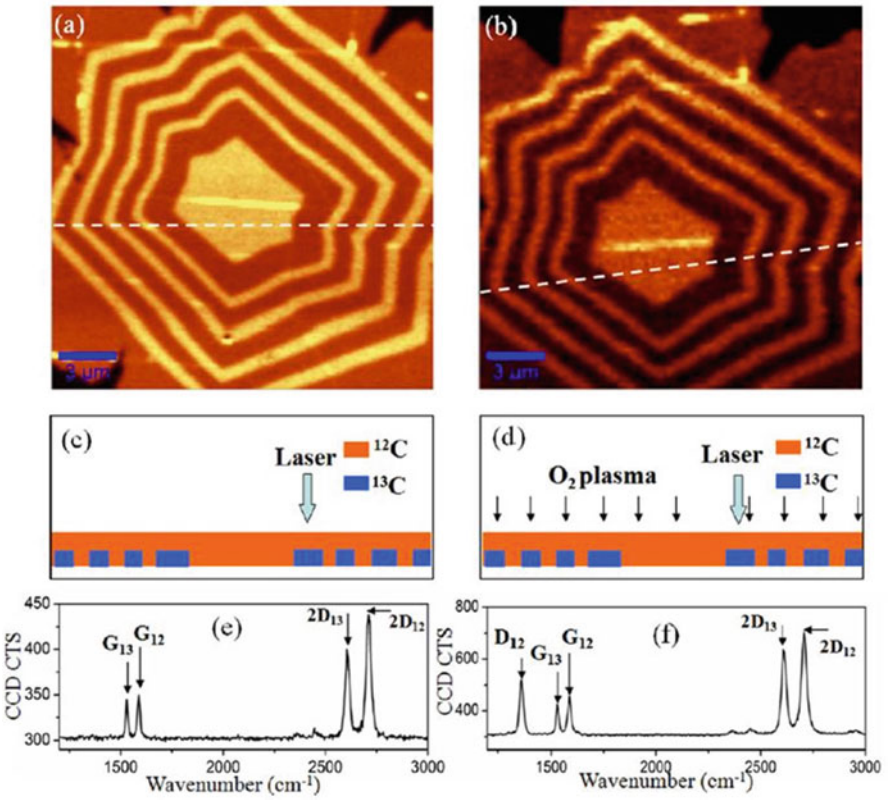

Fig. 13.10 (**a**) shows the G-band image for the ^{12}C SLG before the plasma etching, and (**b**) shows the G-band image for the ^{12}C SLG after plasma etching. (**c**, **d**) are schematics that represent the cross sections (*dashed lines* in (**a**) and (**b**)) of the images shown in (**a**) and (**b**). (**e**, **f**) show the Raman spectra for the samples before and after plasma, respectively. G_{12} and G_{13} stand for the G-band originated from the ^{12}C layer and ^{13}C layer, respectively; D_{12} stands for the D-band generated by the ^{12}C layer; $2D_{12}$ and $2D_{13}$ stand for the 2D-band originated from the ^{12}C layer and ^{13}C layer, respectively. After plasma exposure, only the ^{12}C layer presented a D-band, suggesting it is the topmost layer (Figure extracted from Ref. [94]. Reproduced with permission from American Chemical Society Copyright © 2013)

SLG was grown, and, subsequently, through the admission of $^{13}CH_4$ into the CVD chamber, ^{13}C SLG was grown underneath the preexisting ^{12}C SLG, using the same nucleation center established to grow this preexisting SLG [91]. Figure 13.11a shows the BLG systems as transferred to a SiO_2 substrate. The filled circle and filled square represent two different positions in an isotopically labeled AB-BLG in which a Raman spectrum (shown in Fig. 13.11b) was taken in each position. The filled circle is on top of a nucleation center in which $^{12}C/^{12}C$ AB-BLG is expected, while the filled square is on top of a $^{12}C/^{13}C$ AB-BLG. Still in Fig. 13.11a, the open circle and open square represent two different positions in an isotopically

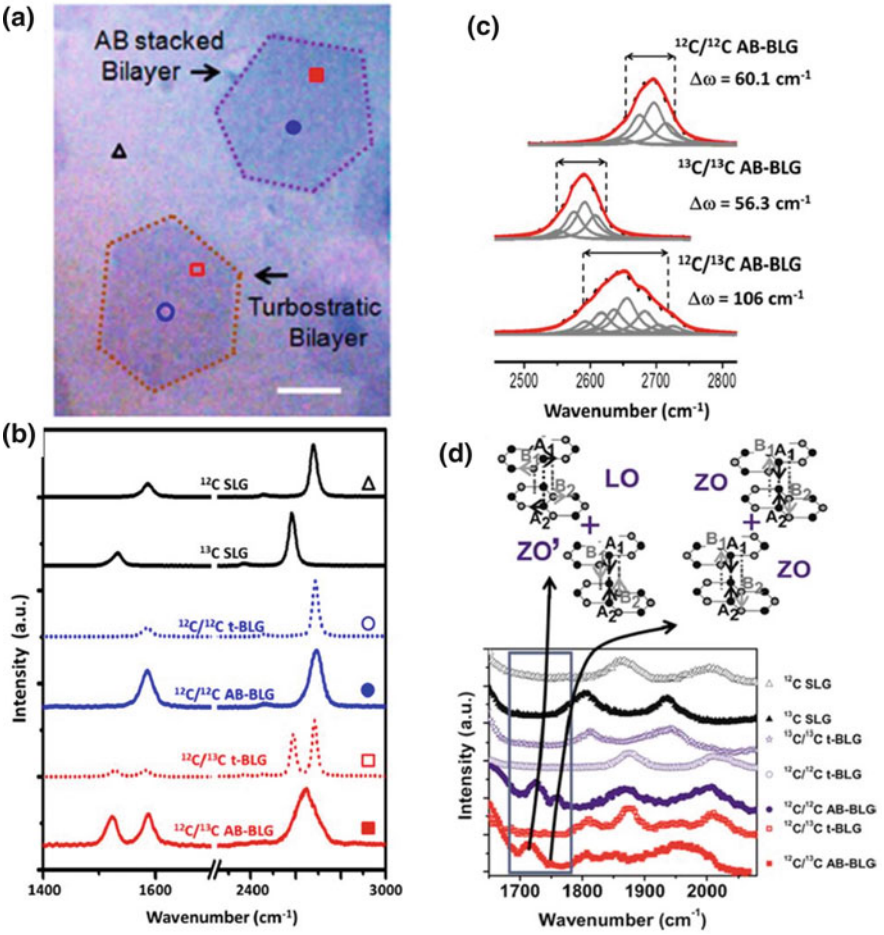

Fig. 13.11 (**a**) Optical image of bilayer graphene transferred on Si/SiO2. Scale bar is 5 μm. (**b**) Raman spectra of a ^{12}C SLG and ^{13}C SLG (*black*), ^{12}C/^{12}C t-BLG (*dotted blue*), ^{12}C/^{12}C AB-BLG (*solid blue*), ^{12}C/^{13}C t-BLG (*dotted red*), and ^{12}C/^{13}C AB-BLG (*solid red*) taken from (**a**). (**c**) Peak fitting of the 2D band for ^{12}C/^{12}C AB-BLG, ^{13}C/^{13}C AB-BLG, and ^{12}C/^{13}C AB-BLG. As expected, the 2D linewidth for the ^{12}C/^{13}C AB-BLG sample is almost twice the linewidth of the ^{12}C/^{12}C AB-BLG and ^{13}C/^{13}C AB-BLG samples. (**d**) The spectral region in the frequency range from 1650 to 1750 cm^{-1} (see the region delimited by the *gray box*) shows the combination of mode LOZO′ and 2ZO, which are only observed in the two AB-BLG systems (Figure adapted from Ref. [91]. Reproduced with permission from American Chemical Society Copyright © 2013)

labeled t-BLG. Again, a Raman spectrum (shown in Fig. 13.11b) was taken in each position. The open circle is on top of a nucleation center in which ^{12}C/^{12}C t-BLG is expected, while the open square is on top of a ^{12}C/^{13}C t-BLG. The open black triangle is in an area in which only ^{12}C SLG graphene is present. Looking at Fig. 13.10, it is clear that the Raman features for each type system are quite unique [91].

Particularly special, the 2D-band carries a clear signature to distinguish between AB-BLG and t-BLG. Figure 13.11c shows the Raman spectra zoomed into the 2D range for a $^{12}C/^{12}C$ AB-BLG (top), for a $^{13}C/^{13}C$ AB-BLG (middle), and for a $^{12}C/^{13}C$ AB-BLG (bottom). The top and middle spectrum lineshapes are similar to that lineshape observed for the scotch-taped AB-BLG, which is typically fitted using 4 Lorentzian peaks and presents a linewidth of 58 cm^{-1} in average, while the bottom lineshape seems to add up the other two. Therefore, the 2D band for the $^{12}C/^{13}C$ AB-BLG is fitted with 8 Lorentzian peaks and presents a linewidth almost twice as broad, averaging about 106 cm^{-1}. Another signature for the $^{12}C/^{13}C$ AB-BLG is observed in the spectral range between 1650 cm-1 and 2100 cm-1. AB-BLG systems have non-negligible interlayer interactions [97, 98]. The vibrations related to these interlayer interactions, which are known as the ZO' (symmetric breathing of the layers) and ZO (antisymmetric vibrations of the layers), are observed around 1700 cm^{-1} and 1800 cm^{-1} as a combination mode (LOZO') and an overtone (2ZO). These spectral features are not present in turbostratic systems.

Another application for this isotopic labeling technique was demonstrated by Chen and collaborators in which the authors synthesize SLG with different concentrations of ^{12}C and ^{13}C carbon atoms [99]. Figure 13.12a shows the Raman spectrum evolutions as the percentage of ^{13}C changes in a ^{12}C SLG. Then, Chen et al. measured the thermal conductivity on the different SLG with different concentrations of ^{12}C and ^{13}C (the layers were suspended). As shown in Fig. 13.12b, the isotopically pure graphene (^{12}C SLG with 0.01% ^{13}C) has the highest thermal conductivity K (4120 ± 1410) WmK^{-1} measured at the temperature $T_m = 320$ K. The thermal conductivity drops almost twice for the ^{12}C SLG with 1.1% ^{13}C in its composition (K (2600 ± 658) WmK^{-1} at $T_m = 330$ K). Note that this percentage of ^{13}C atoms is the percentage found in graphite samples available in nature. The lowest thermal conductivity was observed for the ^{12}C SLG with 50% ^{13}C in its composition (extrapolated K value of K 2192 WmK^{-1} at $T_m = 300$ K), as shown in Fig. 13.12b. This decrease in the thermal conductivity is a mass-related effect [99]. The thermal conductivity is changed mostly due to changes in the phonon–defect interactions originated from the mass differences observed throughout the hybrid samples. This approach shed light to the understanding of how the introduction of impurities with different masses (relative to the host material) and similar electronic properties (also relative to the host material) will change the thermal properties of the host material and also help to understand what are the mechanisms associated with these changes [99]. In their case, the host material is a ^{12}C SLG [99]. It is worth to comment that Pei et al. observed similar effects for the thermal resistance and thermal conductivity of hybrid $^{12}C/^{13}C$ graphene samples [100].

To the best of the authors' knowledge, there are no experimental data available for isotopically labeled GNRs. However, theoretical calculations by Hu et al. [101] have predicted that the thermal conductivity of ^{12}C GNRs decreases with adding ^{13}C atoms in its structure, in agreement to what is observed for SLG systems. Also, in comparison to the ^{12}C GNRs, the pure ^{13}C GNRs present lower thermal conductivity as well, which is understandable as the mass of ^{13}C atoms is bigger than the mass

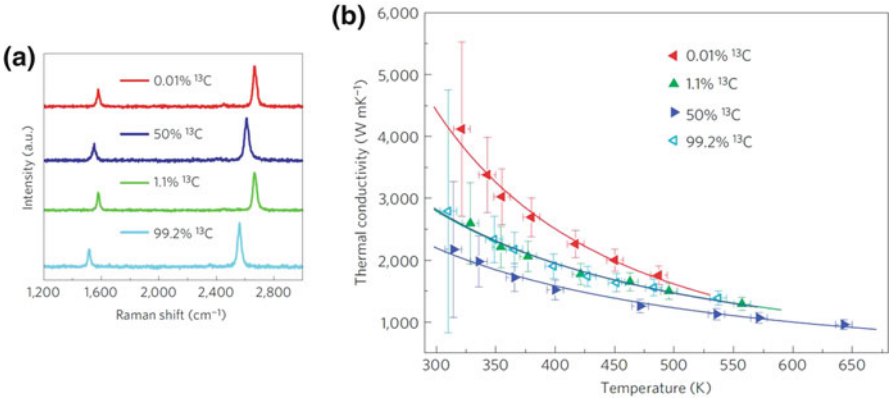

Fig. 13.12 (**a**) shows the evolution of the Raman spectrum for the ^{12}C SLG with different percentages of ^{13}C in its constitution. (**b**) Thermal conductivity measurements for suspended samples of ^{12}C SLG with different concentrations of ^{13}C on its constitution. The extrapolated K values at 300 K are 4419 WmK^{-1}, 2792 WmK^{-1}, 2197 WmK^{-1}, and 2816 WmK^{-1} for 0.01% ^{13}C, 1.1% ^{13}C, 50% ^{13}C, and 99.2% ^{13}C, respectively. The *solid lines* are a guide to the eye only (The figures were adapted from Ref. [99]. Reproduced with permission from Nature Publishing Croup Copyright © 2012)

of ^{12}C atoms [101]. Moreover, the thermal conductivity with a random distribution of ^{13}C in the ^{12}C GNR structure is always higher (regardless the concentration of ^{13}C atoms and ^{12}C atoms) than the thermal conductivity of a superlattice structure. Figure 13.13a shows the thermal conductivity for the ^{12}C GNR with a random distribution of ^{13}C at five different ^{13}C concentrations, while Fig. 13.13b shows the thermal conductivity for the proposed GNR superlattice, which has slabs of ^{13}C atoms and slabs of ^{12}C atoms organized periodically (see the inset in Fig. 13.13b). Still in Fig. 13.13b are results for the thermal conductivity related to superlattices with four different lengths (L) for the ^{13}C slab. Figure 13.13c brings an overview of the thermal conductivities for both the case of random distribution and the case of the superlattice, over a variety of ^{13}C concentrations in the ^{12}C lattice. It is noticeable that only for the case of pure ^{12}C GNR and for the case of pure ^{13}C GNR the thermal conductivities are almost equivalent. For any other ^{13}C concentration, the random distribution case always shows higher conductivities. It is worth mentioning that two other groups [102, 103] made theoretical predictions which are in agreement with the predictions by Hu and collaborators [101].

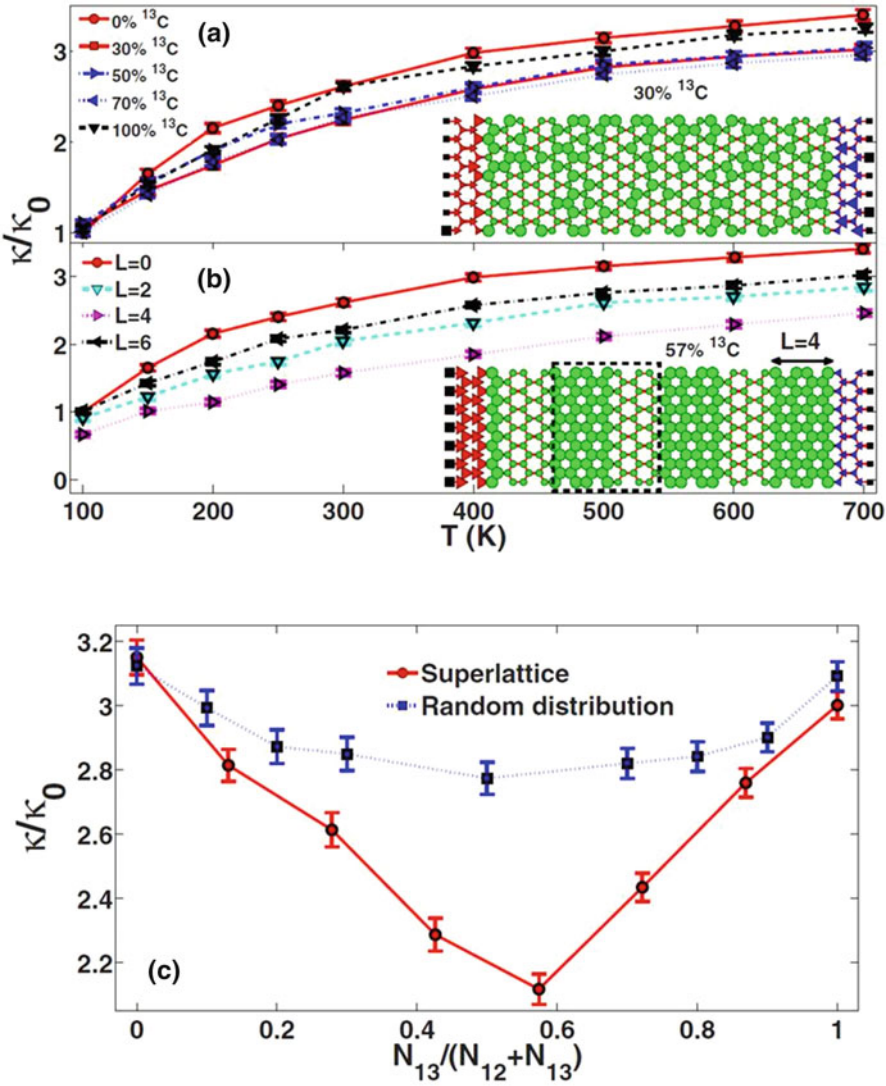

Fig. 13.13 (**a**) shows the temperature-dependent thermal conductivity for five different concentrations of ^{13}C atoms distributed randomly in a ^{12}C GNR structure. (**b**) shows the temperature-dependent thermal conductivity for superlattice structures composed of slabs of ^{12}C atoms and ^{13}C atoms, as illustrated in the inset of the figure. The figure shows the results for four different lengths set for the ^{13}C slabs. (**c**) shows the thermal conductivity as a function of the ^{13}C concentration for both cases: the random distribution case and the superlattice case (This figure is adapted from Ref. [101]. Reproduced with permission from AIP Publishing group Copyright © 2010)

References

1. Geim AK, Novoselov KS (2007) The rise of graphene. Nat Mater 6:183–191
2. Singh V et al (2011) Graphene based materials: past, present and future. Prog Mater Sci 56:1178–1271
3. Cai J et al (2010) Atomically precise bottom-up fabrication of graphene nanoribbons. Nature 466:470–473
4. Biró LP, Nemes-Incze P, Lambin P (2012) Graphene: nanoscale processing and recent applications. Nanoscale 4:1824–1839
5. Cai J et al (2014) Graphene nanoribbon heterojunctions. Nat Nanotechnol 9:896–900
6. Terrones M et al (2010) Graphene and graphite nanoribbons: morphology, properties, synthesis, defects and applications. Nano Today 5:351–372
7. Castro Neto AH, Guinea F, Peres NMR, Novoselov KS, Geim AK (2009) The electronic properties of graphene. Rev Mod Phys 81:109–162
8. Wallace PR (1947) The band theory of graphite. Phys Rev 71:622–634
9. Saito R, Dresselhaus G, Dresselhaus M (1998) Physical properties of carbon nanotubes. Imperial College Press, London
10. Dresselhaus MS, Jorio A, Hofmann M, Dresselhaus G, Saito R (2010) Perspectives on carbon nanotubes and graphene Raman spectroscopy. Nano Lett 10:751–758
11. Avouris P (2010) Graphene: electronic and photonic properties and devices. Nano Lett 10:4285–4294
12. Novoselov KS et al (2004) Electric field effect in atomically thin carbon films. Science 306:666–669
13. Blake P et al (2007) Making graphene visible. Appl Phys Lett 91:63124
14. Seah C-M, Chai S-P, Mohamed AR (2014) Mechanisms of graphene growth by chemical vapour deposition on transition metals. Carbon 70:1–21
15. Mattevi C, Kim H, Chhowalla M (2011) A review of chemical vapour deposition of graphene on copper. J Mater Chem 21:3324–3334
16. Borin Barin G et al (2015) Optimized graphene transfer: influence of polymethylmethacrylate (PMMA) layer concentration and baking time on graphene final performance. Carbon 84:82–90
17. Mafra DL, Ming T, Kong J (2015) Facile graphene transfer directly to target substrates with a reusable metal catalyst. Nanoscale 7:14807–14812
18. Martins LGP et al (2013) Direct transfer of graphene onto flexible substrates. Proc Natl Acad Sci 201306508. doi:10.1073/pnas.1306508110
19. Zhang Y, Zhang L, Zhou C (2013) Review of chemical vapor deposition of graphene and related applications. Acc Chem Res 46:2329–2339
20. Rogers JA (2008) Electronic materials: making graphene for macroelectronics. Nat Nanotechnol 3:254–255
21. Zhou SY et al (2007) Substrate-induced bandgap opening in epitaxial graphene. Nat Mater 6:916–916
22. Balog R et al (2010) Bandgap opening in graphene induced by patterned hydrogen adsorption. Nat Mater 9:315–319
23. Zhang Y et al (2009) Direct observation of a widely tunable bandgap in bilayer graphene. Nature 459:820–823
24. Vo TH et al (2014) Large-scale solution synthesis of narrow graphene nanoribbons. Nat Commun 5, 3189(2014) doi:10.1038/ncomm54189
25. Bennett PB et al (2013) Bottom-up graphene nanoribbon field-effect transistors. Appl Phys Lett 103:253114
26. Zschieschang U et al (2015) Electrical characteristics of field-effect transistors based on chemically synthesized graphene nanoribbons. Adv Electron Mater 1:1400010

27. Liang G, Neophytou N, Nikonov DE, Lundstrom MS (2007) Performance projections for ballistic graphene nanoribbon field-effect transistors. IEEE Trans Electron Devices 54:677–682
28. Han MY, Ozyilmaz B, Zhang Y, Kim P (2007) Energy band-gap engineering of graphene nanoribbons. Phys Rev Lett 98:206805
29. Jiao L, Zhang L, Wang X, Diankov G, Dai H (2009) Narrow graphene nanoribbons from carbon nanotubes. Nature 458:877–880
30. Jiao L, Wang X, Diankov G, Wang H, Dai H (2010) Facile synthesis of high-quality graphene nanoribbons. Nat Nanotechnol 5:321–325
31. Tapasztó L, Dobrik G, Lambin P, Biró LP (2008) Tailoring the atomic structure of graphene nanoribbons by scanning tunnelling microscope lithography. Nat Nanotechnol 3:397–401
32. Yoon Y, Nikonov DE, Salahuddin S (2011) Role of phonon scattering in graphene nanoribbon transistors: nonequilibrium green's function method with real space approach. Appl Phys Lett 98:203503
33. Chen Y-C et al (2013) Tuning the band gap of graphene nanoribbons synthesized from molecular precursors. ACS Nano 7:6123–6128
34. Narita A, Feng X, Müllen K (2015) Bottom-up synthesis of chemically precise graphene nanoribbons. Chem Rec N Y N 15:295–309
35. Campos-Delgado J et al (2008) Bulk production of a new form of sp^2 carbon: crystalline graphene nanoribbons. Nano Lett 8:2773–2778
36. Talirz L et al (2013) Termini of bottom-up fabricated graphene nanoribbons. J Am Chem Soc 135:2060–2063
37. Chen Y-C et al (2015) Molecular bandgap engineering of bottom-up synthesized graphene nanoribbon heterojunctions. Nat Nanotechnol 10:156–160
38. Talirz L, Ruffieux P, Fasel R (2016) On-surface synthesis of atomically precise graphene nanoribbons. Adv Mater 28:6222–6231
39. Bai J, Huang Y (2010) Fabrication and electrical properties of graphene nanoribbons. Mater Sci Eng R Rep 70:341–353
40. Nakada K, Fujita M, Dresselhaus G, Dresselhaus MS (1996) Edge state in graphene ribbons: nanometer size effect and edge shape dependence. Phys Rev B Condens Matter 54:17954–17961
41. Ruffieux P et al (2016) On-surface synthesis of graphene nanoribbons with zigzag edge topology. Nature 531:489–492
42. Wang S et al (2016) Giant edge state splitting at atomically precise graphene zigzag edges. Nat Commun 7:11507
43. Costa Girão E, Liang L, Cruz-Silva E, Souza Filho AG, Meunier V (2011) Emergence of atypical properties in assembled graphene nanoribbons. Phys Rev Lett 107:135501
44. Costa Girão E, Cruz-Silva E, Liang L, Souza Filho AG, Meunier V (2012) Structural and electronic properties of graphitic nanowiggles. Phys Rev B 85:235431
45. Li Y, Zhou Z, Cabrera CR, Chen Z (2013) Preserving the edge magnetism of zigzag graphene nanoribbons by ethylene termination: insight by Clar's rule. Sci Rep 3:2030
46. Llinas JP et al (2016) Short-channel field effect transistors with 9-Atom and 13-Atom wide graphene nanoribbons. ArXiv Prepr. ArXiv160506730
47. Fantuzzi P et al (2016) Fabrication of three terminal devices by ElectroSpray deposition of graphene nanoribbons. Carbon 104:112–118
48. Mak KF, Ju L, Wang F, Heinz TF (2012) Optical spectroscopy of graphene: from the far infrared to the ultraviolet. Solid State Commun 152:1341–1349
49. Nair RR et al (2008) Fine structure constant defines visual transparency of graphene. Science 320:1308
50. Kuzmenko AB, van Heumen E, Carbone F, van der Marel D (2008) Universal optical conductance of graphite. Phys Rev Lett 100:117401
51. Bae S et al (2010) Roll-to-roll production of 30-inch graphene films for transparent electrodes. Nat Nanotechnol 5:574–578

52. Mak KF et al (2008) Measurement of the optical conductivity of graphene. Phys Rev Lett 101:196405
53. Wang F et al (2008) Gate-variable optical transitions in graphene. Science 320:206–209
54. Mak KF, Shan J, Heinz TF (2011) Seeing many-body effects in single- and few-layer graphene: observation of two-dimensional saddle-point excitons. Phys Rev Lett 106:46401
55. Lui CH, Mak KF, Shan J, Heinz TF (2010) Ultrafast photoluminescence from graphene. Phys Rev Lett 105:127404
56. Stöhr RJ, Kolesov R, Pflaum J, Wrachtrup J (2010) Fluorescence of laser-created electron-hole plasma in graphene. Phys Rev B 82:121408
57. Wei W, Qu X (2012) Extraordinary physical properties of functionalized graphene. Small Weinh Bergstr Ger 8:2138–2151
58. Li L et al (2013) Focusing on luminescent graphene quantum dots: current status and future perspectives. Nanoscale 5:4015–4039
59. Loh KP, Bao Q, Eda G, Chhowalla M (2010) Graphene oxide as a chemically tunable platform for optical applications. Nat Chem 2:1015–1024
60. Rienstra-Kiracofe JC, Barden CJ, Brown ST, Schaefer HF (2001) Electron affinities of polycyclic aromatic hydrocarbons. J Phys Chem A 105:524–528
61. Lu G, Yu K, Wen Z, Chen J (2013) Semiconducting graphene: converting graphene from semimetal to semiconductor. Nanoscale 5:1353–1368
62. Yan X, Li B, Li L (2013) Colloidal graphene quantum dots with well-defined structures. Acc Chem Res 46:2254–2262
63. Pan D, Zhang J, Li Z, Wu M (2010) Hydrothermal route for cutting graphene sheets into blue-luminescent graphene quantum dots. Adv Mater 22:734–738
64. Chopra S, Maidich L (2014) Optical properties of pure graphene in various forms: a time dependent density functional theory study. RSC Adv 4:50606–50613
65. Zhao M, Yang F, Xue Y, Xiao D, Guo Y (2014) A time-dependent DFT study of the absorption and fluorescence properties of graphene quantum dots. Chemphyschem Eur J Chem Phys Phys Chem 15:950–957
66. Chopra S (2015) Study of electronic, optical absorption and emission in pure and metal-decorated graphene nanoribbons (C29H14-X; X = Ni, Fe, Ti, Co+, Al+, Cu+): first principles calculations. ChemPhysChem 16:1948–1953
67. Qu D et al (2013) Highly luminescent S, N co-doped graphene quantum dots with broad visible absorption bands for visible light photocatalysts. Nanoscale 5:12272–12277
68. Zhuo S, Shao M, Lee S-T (2012) Upconversion and downconversion fluorescent graphene quantum dots: ultrasonic preparation and photocatalysis. ACS Nano 6:1059–1064
69. Zheng XT, Ananthanarayanan A, Luo KQ, Chen P (2015) Glowing graphene quantum dots and carbon dots: properties, syntheses, and biological applications. Small 11:1620–1636
70. Riesen H, Wiebeler C, Schumacher S (2014) Optical spectroscopy of graphene quantum dots: the case of C132. J Phys Chem A 118:5189–5195
71. Eda G et al (2010) Blue photoluminescence from chemically derived graphene oxide. Adv Mater 22:505–509
72. Zhang R et al (2015) Size and refinement edge-shape effects of graphene quantum dots on UV–visible absorption. J Alloys Compd 623:186–191
73. Pan D et al (2015) Efficient separation of electron–hole pairs in graphene quantum dots by TiO2 heterojunctions for dye degradation. ACS Sustain Chem Eng 3:2405–2413
74. Peng J et al (2012) Graphene quantum dots derived from carbon fibers. Nano Lett 12:844–849
75. Huang K, Lu W, Yu X, Jin C, Yang D (2016) Highly pure and luminescent graphene quantum dots on silicon directly grown by chemical vapor deposition. Part Part Syst Charact 33:8–14
76. Li D, Müller MB, Gilje S, Kaner RB, Wallace GG (2008) Processable aqueous dispersions of graphene nanosheets. Nat Nanotechnol 3:101–105
77. Yang P et al (2014) Facile synthesis and photoluminescence mechanism of graphene quantum dots. J Appl Phys 116:244306

78. Jin SH, Kim DH, Jun GH, Hong SH, Jeon S (2013) Tuning the photoluminescence of graphene quantum dots through the charge transfer effect of functional groups. ACS Nano 7:1239–1245
79. Lingam K, Podila R, Qian H, Serkiz S, Rao AM (2013) Evidence for edge-state photoluminescence in graphene quantum dots. Adv Funct Mater 23:5062–5065
80. Pal SK (2015) Versatile photoluminescence from graphene and its derivatives. Carbon 88:86–112
81. Wang L et al (2014) Common origin of green luminescence in carbon nanodots and graphene quantum dots. ACS Nano 8:2541–2547
82. Zhu S et al (2015) The photoluminescence mechanism in carbon dots (graphene quantum dots, carbon nanodots, and polymer dots): current state and future perspective. Nano Res 8:355–381
83. Zhu S et al (2014) Investigation of photoluminescence mechanism of graphene quantum dots and evaluation of their assembly into polymer dots. Carbon 77:462–472
84. Lin L et al (2014) Luminescent graphene quantum dots as new fluorescent materials for environmental and biological applications. TrAC Trends Anal Chem 54:83–102
85. Cushing SK, Li M, Huang F, Wu N (2014) Origin of strong excitation wavelength dependent fluorescence of graphene oxide. ACS Nano 8:1002–1013
86. Shi W, Fan H, Ai S, Zhu L (2015) Preparation of fluorescent graphene quantum dots from humic acid for bioimaging application. New J Chem 39:7054–7059
87. Muñoz R, Gómez-Aleixandre C (2013) Review of CVD synthesis of graphene. Chem Vap Depos 19:297–322
88. Yan Z, Peng Z, Tour JM (2014) Chemical vapor deposition of graphene single crystals. Acc Chem Res 47:1327–1337
89. Zhou H et al (2013) Chemical vapour deposition growth of large single crystals of monolayer and bilayer graphene. Nat Commun 4:2096
90. Li X, Cai W, Colombo L, Ruoff RS (2009) Evolution of graphene growth on Ni and Cu by carbon isotope labeling. Nano Lett 9:4268–4272
91. Fang W et al (2013) Rapid identification of stacking orientation in isotopically labeled chemical-vapor grown bilayer graphene by Raman spectroscopy. Nano Lett 13:1541–1548
92. Li X et al (2010) Graphene films with large domain size by a two-step chemical vapor deposition process. Nano Lett 10:4328–4334
93. Wu Y et al (2012) Growth mechanism and controlled synthesis of AB-stacked bilayer graphene on Cu–Ni alloy foils. ACS Nano 6:7731–7738
94. Li Q et al (2013) Growth of adlayer graphene on Cu studied by carbon isotope labeling. Nano Lett 13:486–490
95. Li X et al (2011) Large-area graphene single crystals grown by low-pressure chemical vapor deposition of methane on copper. J Am Chem Soc 133:2816–2819
96. Dahal A, Batzill M (2014) Graphene–nickel interfaces: a review. Nanoscale 6:2548–2562
97. Araujo PT et al (2013) Mass-related inversion symmetry breaking and phonon self-energy renormalization in isotopically labeled AB-stacked bilayer graphene. Sci Rep 3:2061
98. Araujo PT et al (2012) Unraveling the interlayer-related phonon self-energy renormalization in bilayer graphene. Sci Rep 2:1017
99. Chen S et al (2012) Thermal conductivity of isotopically modified graphene. Nat Mater 11:203–207
100. Pei Q-X, Zhang Y-W, Sha Z-D, Shenoy VB (2012) Carbon isotope doping induced interfacial thermal resistance and thermal rectification in graphene. Appl Phys Lett 100:101901
101. Hu J, Schiffli S, Vallabhaneni A, Ruan X, Chen YP (2010) Tuning the thermal conductivity of graphene nanoribbons by edge passivation and isotope engineering: a molecular dynamics study. Appl Phys Lett 97:133107
102. Li X, Chen J, Yu C, Zhang G (2013) Comparison of isotope effects on thermal conductivity of graphene nanoribbons and carbon nanotubes. Appl Phys Lett 103:13111
103. Li C, Miao L, Tan X, Han M, Jiang J (2014) Thermal conductivity of graphene nanoribbons with regular isotopic modification. J Comput Theor Nanosci 11:348–352

Chapter 14
The Amazing Chemistry of Metal-Organic Frameworks

Regina C. G. Frem, Guilherme Arroyos, Guilherme N. Lucena, Jader B. da Silva Flor, Marcelo A. Fávaro, Mariana F. Coura, and Renata C. Alves

1 Introduction

The study of metal-organic frameworks (MOFs) is a multidisciplinary field of research that has risen rapidly over recent years, particularly after the iconic work of Omar Yaghi, reported in 1999, about a Zn(II) porous solid of high structural stability, named *MOF-5* [1]. Following that, over more than one hundred review articles [2–12] and some relevant books [13–19] have been published in a short time concerning the design and new synthetic strategies of linkers and MOFs, structural and topological analysis, properties and applications, as well as theoretical and modeling studies. The interest in this kind of the complex material came, in part, from its peculiar properties, such as high crystallinity, microporosity, high surface area [20, 21], low density, and good thermal stability. These interesting properties and the fact that it is possible to functionalize the pores of the material make MOFs highly attractive in frontier research. In fact, several and important applications of MOFs have been recently investigated in different areas, such as gas storage [22, 23] and separation [24], heterogeneous catalysis [25], drug delivery [26], and photonics [27], among others [28–31]. From 2013, the IUPAC Inorganic Chemistry Division has recommended the use of the official definition of MOF as "a coordination network with organic ligands containing potential voids" [32, 33]. In other works, the cavities of MOFs should be empty, or at least it should be theoretically possible to remove what is within them. From the historical point of view, the first publishing about this new class of synthetic inorganic porous material

R.C.G. Frem (✉) • G. Arroyos • G.N. Lucena • J.B. da Silva Flor • M.A. Fávaro
M.F. Coura • R.C. Alves
Institute of Chemistry, São Paulo State University, UNESP, São Paulo, Brazil
e-mail: rcgfrem@iq.unesp.br; guiarroyos@gmail.com; guilherme_nunes7@hotmail.com; jaderinorg@hotmail.com; marcelo.a.favaro@gmail.com; mariana.coura@hotmail.com; renata88_alves@hotmail.com

E. Longo, F.A. La Porta (eds.), *Recent Advances in Complex Functional Materials*,
DOI 10.1007/978-3-319-53898-3_14

was initially reported by Kinoshita et al. in 1959 [34]. This article involved the synthesis of a novel four-connected coordination solid constructed by the covalent interaction between tetrahedral copper(I) ions and adiponitrile ligands. Thirty years later, Hoskins and Robson published the first paper in which it has introduced the concept of porous polymeric structures based on metal-ligand coordinate bonds. By using the nod-and-spacer approach proposed by Wells in 1978 [35], it was possible to obtain a 3D coordination solid consisting mainly of tetrahedral centers linked together by rodlike building units [36]. However, almost another 10 years have passed (1998) before the proof of its permanent porosity for the MOFs was obtained [37]. This same research group led by Professor Omar Yaghi prepared the highly stable zinc(II) coordination compound, Zn(BDC)(DMF)(H_2O) (BDC = 1,4-benzenedicarboxylate, DMF = N,N′-dimethylformamide), named *MOF-5* [1], whose structure is shown in Fig. 14.1.

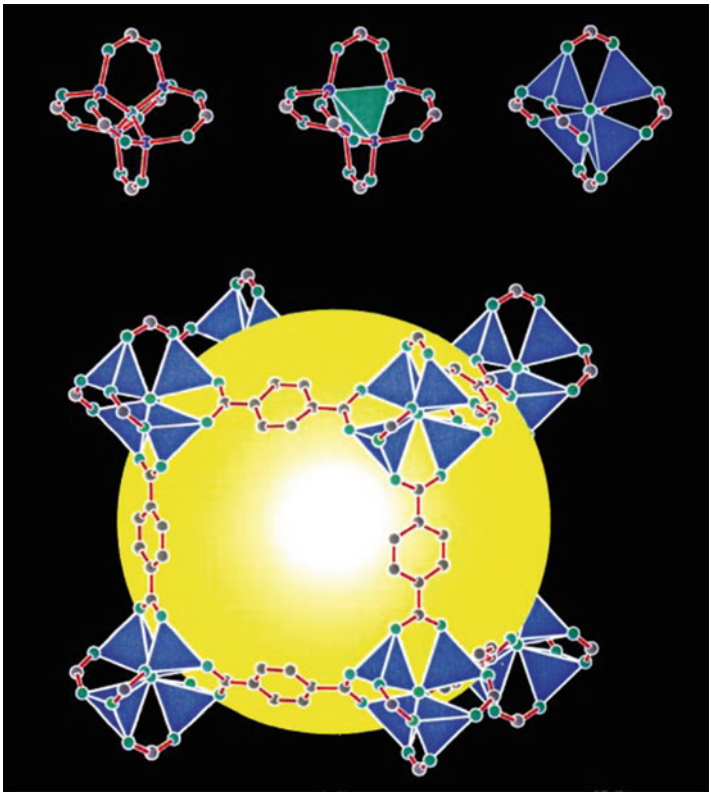

Fig. 14.1 Construction of the *MOF-5* framework. On *top*, the $Zn_4(O)O_{12}C_6$ cluster is shown in different representations. *Left*, as a ball and stick model (Zn, *blue*; O, *green*; C, *gray*). *Middle*, the same with the $Zn_4(O)$ tetrahedron indicated in *green*. *Right*, the same but now with the ZnO_4 tetrahedra indicated in *blue*. On the *bottom*, the *yellow sphere* represents one of the cavities in the $Zn_4(O)(BDC)_3$, *MOF-5*, framework. Eight clusters (only seven visible) constitute a unit cell and enclose a large cavity with a diameter of 18.5 Å in contact with 72 C atoms (*gray*) (Reprinted with permission from [1])

As it can be shown in Fig. 14.1, in *MOF-5* structure, the OZn4 clusters are linked by 1,4-benzenedicarboxylate ligand (BDC) to form a continuous cubic framework of composition $Zn_4O(BDC)_3$ (see the concept of *secondary building units* (*SBUs*) in the next section). In other words, the compound is formed by tetranuclear clusters of the type $Zn_4O(O_2CR)_6$ that share a central oxygen atom. The cluster structure is extended through Zn-O-C bond to the formation of the 3D solid, whose pore is represented as a yellow sphere in Fig. 14.1. Therefore, from 1999, the MOFs became more known, and there has been a spectacular growth and development of this modern chemistry area. Concerning the nomenclature of this kind of inorganic porous material, it is very common that MOFs take the name of the place in which they were discovered, followed by an integer (n) assigned in chronological order, such as *MIL-n* (MIL = Matériaux de l'Institut Lavoisier) [38], *HKUST-n* (HKUST = Hong Kong University of Science and Technology) [39], or *CPO-n* (CPO = Coordination Polymer of Oslo) [40].

2 Design and Topologies

In order to analyze the factors contributing to the assembly of these porous coordination solids from molecular building blocks, Yaghi et al. proposed a strategy, based on the modular chemistry concepts [41], by linking polytopic organic molecules with transition metal ions [42]. In the early 2000s, the authors reported the next stage in the development of MOFs, introducing the concept of SBUs [43] for the construction of robust frameworks with its permanent porosity, i.e., the evacuation of the pores occurs without destruction of the structure. SBUs are then defined as "molecular complexes and cluster entities in which ligand coordination modes and metal coordination environments can in principle be easily utilized in the transformation of these fragments into extended porous networks using polytopic linkers." In 2003, the Yaghi group published a definitive article in which it has established a more comprehensive conceptual approach, named *reticular synthesis*, to the rational construction of this new class of highly porous coordination solids from molecular building units [44]. Reticular chemistry is concerned then with the assembling of predetermined ordered frameworks through rigid molecular building blocks (SBUs) which are repeated and held together by strong covalent metal-ligand bonds. In this paper, the authors redefined the term SBU (originally used to describe fragments of zeolites), referring to the geometry of the units defined by the points of extension. In Fig. 14.2, for instance, some examples of inorganic SBUs are illustrated, where the points of extension correspond to the C atoms (in black) in carboxylate MOFs [45]. In the right side of Fig. 14.2, it can be seen a chemical representation of the same SBUs.

Therefore, from the reticular chemistry point of view, for a specific geometry of molecular building units, rationally designed MOFs can easily be synthesized, because the topological different vertices and the connectivity between them are infinite, as well as the number of possible network structures is, in principle, unlimited. However, the central point of this approach is that, according to geometrical

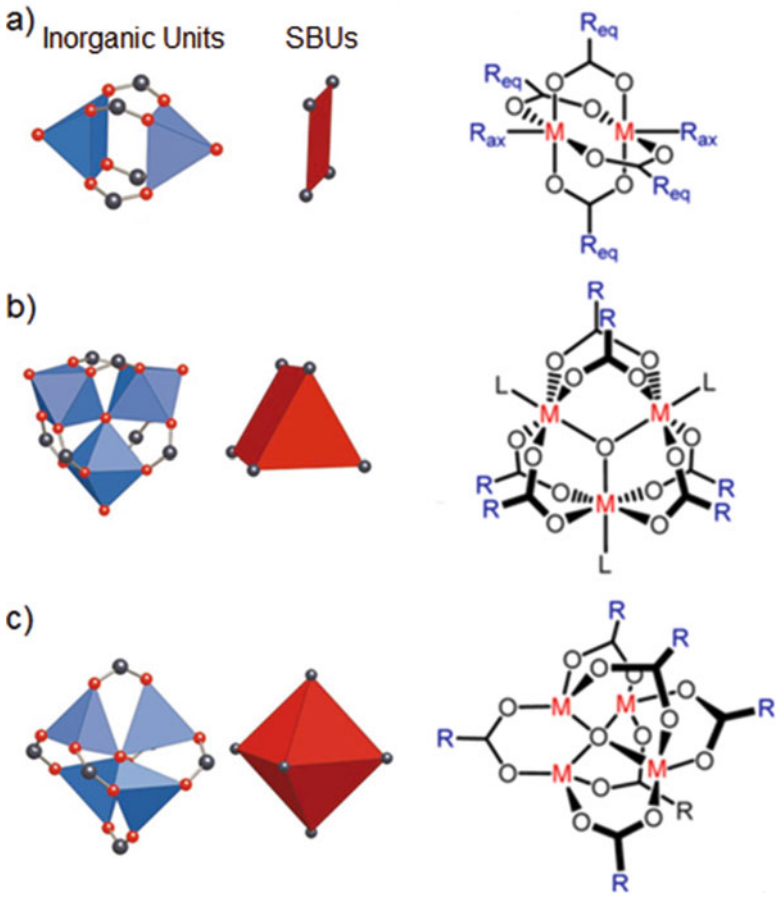

Fig. 14.2 Some common SBUs from carboxylate MOFs. *Left*: O, *red*; C, *black*, metal-oxygen polyhedra are *blue*, and the polygon and polyhedron defined by carboxylate carbon atoms (SBUs) are *red*; *Right*: (**a**) a dinuclear paddle-wheel square SBU of the type $[M_2(O_2CR)_4L_2]$ with four bridging acetates and two axial ligands, (**b**) a trinuclear basic chromium acetate structure with six bridging acetates and three terminal ligands of the type $[M_3O(O_2CR)_6L_3]$, and (**c**) a tetrametallic cluster μ4-oxo hexacarboxylate, $[M_4O(O_2CR)_6]$, prototype to a molecular octahedron (Figures adapted and reprinted with permission from [44] and [45])

design principles, there are a relatively small number of basic topologies (e.g., default nets) that can be expected to form. In other works, depending on the geometry and connectivity of the building blocks, the synthesized MOFs will have simple basic topologies [46, 47]. Based on collected topological data, the more common nets can be identified by the so-called RCSR database [48]. For illustration, an example is given in Fig. 14.3 concerning the copper(II) MOF named *HKUST-1* [39], whose framework is assembled by the linkage between $Cu_2(O_2CR)_4$ square paddle-wheel SBUs (see Fig. 14.2) and three connected nodes (the organic SBU) that consists of BTC (1,3,5-benzenetricarboxylate) ligands. The net describing the

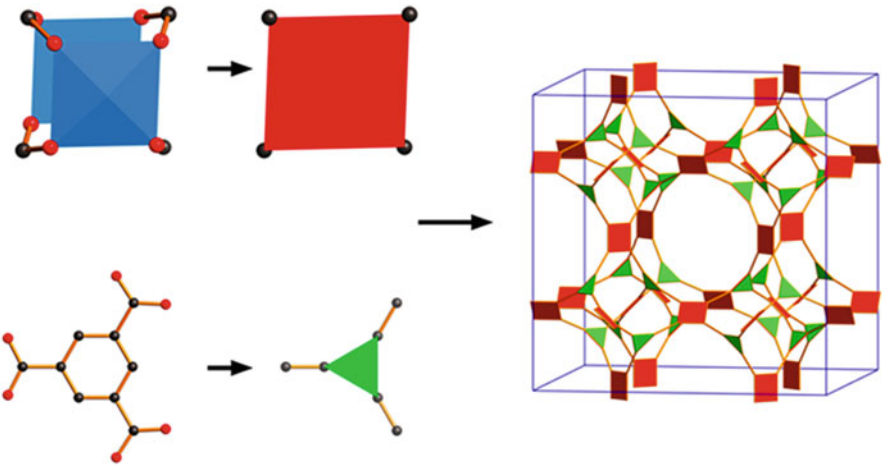

Fig. 14.3 The components of *HKUST-1*, $[Cu_3(BTC)_2(H_2O)_3]_n$ (BTC = 1,3,5-benzenetricarboxylate) [39] showing the $Cu_2(O_2CR)_4$ paddle-wheel SBUs (*square*), the tritopic linker (*triangle*), and their combination to form the *tbo* net (Figure adapted and reprinted with permission from [4])

topology of this highly porous coordination solid, $[Cu_3(BTC)_2(H_2O)_3]_n$, has a three-letter code: *tbo*, derived from twisted boracite. In fact, there are many MOFs with (3,4)-coordinated net (*tbo* topology) in which paddle-wheel SBUs (squares) are linked with tritopic linkers (triangles) [4].

In the moment that this chapter has been written (September 2016), more than 2800 different three-dimensional nets are described in the RCSR database [http://rcsr.anu.edu.au/]. However, most of them have very simple basic topologies for a given choice of shape and connectivity of the molecular building blocks. Table 14.1 lists common default nets with one or two kinds of links and representative-related MOFs [46, 47]. It is worth to mention that the three-letter codes that identify nets describing the topologies of MOFs can be abbreviations of a structure type (*pcu* = primitive cubic), name of mineral (*dia* = diamond), or contracted form of the formula of chemical compounds, like *srs* corresponding to the net of the silicon atoms in $SrSi_2$ [48–50].

In the same period of 2000, when the group of Yaghi and O'Keeffe was performing their studies on MOFs, Kitagawa et al. [57] reported the discovery of the highly porous 3D $[\{CuSiF_6(4,4'\text{-bipyridine})_2\}_n]$, created through analogous building block rational synthetic strategy. It is important to say at this moment that the reticular chemistry approach is only able to predict the structure and net topology of an MOF if its building blocks have a strong tendency to form specific clusters, such as $Zn_4O(COO)_6$ or $Cu_2(COO)_4$, in *MOF-5* and *HKUST-1*, respectively (see above). Reactions involving the same metal ions and organic ligands can otherwise lead to completely different final MOFs, depending on the synthetic route and/or reaction conditions used to obtain the material. On the other hand, it is also very difficult to design a synthesis of an MOF whose structure

Table 14.1 Some common topologies and representative-related MOFs

Coordination number of the vertices	SBU's shape		Net (code)	Example	Refs.	Representation
3	Triangle	Triangle	$SrSi_2$ (*srs*)	*[CuL(DMF)(py)]*[a]	[51]	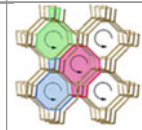
3	Triangle	Triangle	$ThSi_2$ (*ths*)	*[$(ZnI_2)_3(TPT)_2$]*[b]	[52]	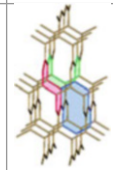
3	Triangle	Triangle	Honeycomb (*hcb*)	*CPO-27-M*	[53]	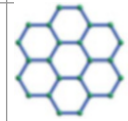
3,4	Triangle	Square	Twisted boracite (*tbo*)	*HKUST-1*	[39]	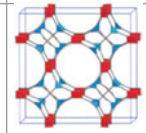
3,4	Triangle	Square	Pt_3O_4 (*pto*)	*MOF-388*	[54]	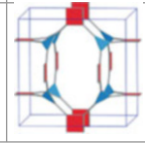

4	Square	Square	Square lattice (*sql*)	*MOF-118*	[55]	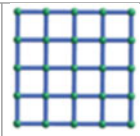
4	Tetrahedron	Tetrahedron	Diamond (*dia*)	$[CuC(C_6H_4.CN)_4]^+$	[36]	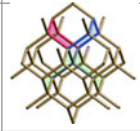
4,4	Square	Tetrahedron	Cooperite (*pts*)	$[Cu_2L'(H_2O)_2]$[c]	[56]	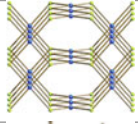
6	Octahedron	Octahedron	Primitive cubic (*pcu*)	*MOF-5*	[44]	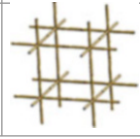

[a]L = 3,5-pyridinedicarboxylate
[b]TPT = 2,4,6-tris(4-pyridil)triazine
[c]L' = tetrakis[4-(carboxyphenyl)oxamethyl]methane

consists of not well-defined shape SBUs, for example. In this context, Yaghi and O'Keeffe published in 2012 a review in which they showed how to reduce structures of high complexity (deconstruction) to an underlying topology [8]. Structurally more complicated MOFs can be designed and constructed using the conceptual *supermolecular building blocks* (SBBs) approach proposed in 2000s by Zaworotko [58–60]. This crystal engineering strategy is mainly based on the use of large-sized and high symmetric metal-organic polyhedra (MOPs) as SBBs, for the construction of a new class of MOFs with a high level of control over the topology and a new level of scale to the resultant framework (several nanometers). Just to give one example, Fig. 14.4 illustrates an extended porous MOF with *pcu* topology, made of discrete MOP of the type $[Cu_6L_8](NO_3)_{12}$ as SBBs [61]. Here, the C_3-symmetric organic compound (N,N′,N″-tris(3-pyridinyl)-1,3,5-benzenetricarboxamide) (see inset of the figure) acts as triangular facial ligands (L), while tetragonally distorted octahedral Cu(II) ions can be regarded as vertex nodes of this structure. The nitrate counterions link these metal vertices, since the axial site of the Cu(II) ion is directed to the exterior of the nanocages, serving as a connecting node for the formation of the three-periodic framework. As can also be seen in Fig. 14.4, two different types of nanocages (e.g., represented by the yellow and green octahedral clusters) are interacting with each other via π . . . π stacking between the central aromatic rings of the ligands. However, the MOF retains the nanosized cavities, which originally belonged to the MOPs.

More recently, Eddaoudi and Lah introduced other design strategy to construct MOFs of high structural complexity based on the concept of *supermolecular building layer* (SBL) [3, 62]. From this approach, it is experimentally possible to construct three-periodic frameworks via pillaring of two-dimensional MOFs using, for example, the neighboring accessible metal/axial sites. Figure 14.5 shows a pillaring scheme of four different 2D MOFs leading to the construction of several topologically different MOFs.

In conclusion, the use of the combination between Crystallography and Coordination Chemistry concepts – symmetry and connectivity of metal ions and organic linkers, experimental conditions of the synthesis (see below), the great variety of available starting materials, and so on – is a great opportunity that can't be missed for the future "designers" of MOF crystals.

3 Synthesis and Characterization

Several synthetic approaches for MOF preparation have been presented and discussed in a few review articles [6, 63, 64]. Most of them are solution-based methods such as direct mixing of soluble metal ions and organic linkers (direct addition or slow diffusion in vertical tube) [65] and solvothermal (using electrical heating) [38], microwave-assisted (also under solvothermal conditions) [66], sonochemical [67], and electrochemical [68, 69] synthesis. Solvothermal synthesis, for example, though very important for growing large and high-quality crystals, needs long reaction

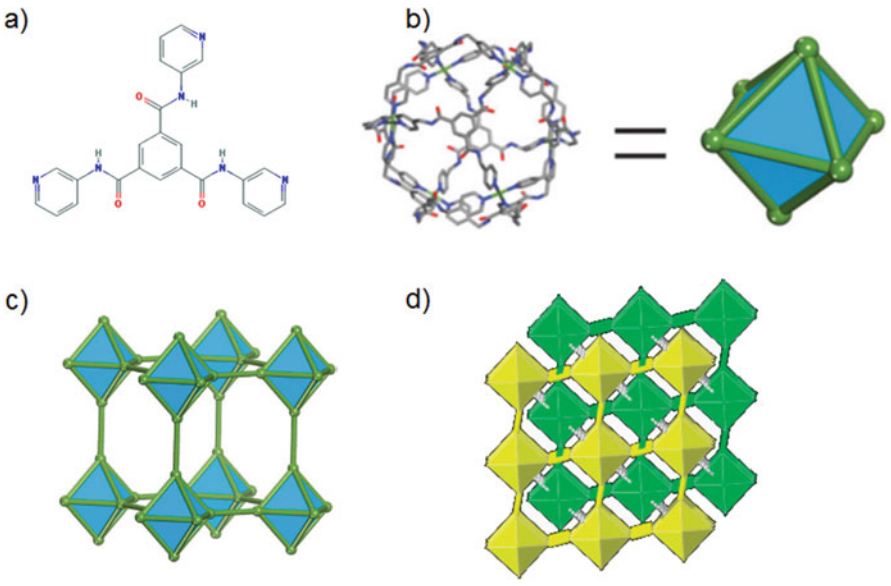

Fig. 14.4 (**a**) N,N′,N″-tris(3-pyridinyl)-1,3,5-benzenetricarboxamide ligand; (**b**) discrete octahedral $[Cu_6L_8]^{12+}$ MOP with blue faces representing C3 ligands and *green* vertices representing Cu^{2+} ions; (**c**) a *pcu*-net obtained by the linkage between the MOPs and nitrate anions; (**d**) schematic packing diagram of the crystal structure showing the ditopic nitrate as *green or yellow* rods and the $\pi \ldots \pi$ intermolecular interaction, as *gray dots* (Figure adapted and reprinted with permission from [61])

times, occurs in relatively high temperature (∼400 K), and requires the use of costly, harmful, and high-boiling-point organic solvents such as dimethylformamide or diethylformamide (which act, in some cases, as templates). Besides that, the formation of impure phases – unreacted or recrystallized organic linker molecules, for example – results in a low product yield when the MOF is prepared by this technique. However, from an environmental point of view, solid-state synthetic approaches are much more adequate to prepare MOF materials. In this context, the mechanochemical method [70, 71] (such as mortar grinding or high-energy ball milling of the metal salt and organic linker) occurs in room temperature; is a very fast, high yield, virtually solvent-free route; and has been widely used to synthesize some MOFs since 2006 [72]. More recently, in order to avoid the use of soluble metal precursors (and the subsequent undesirable formation of acidic by-products), an alternative synthetic strategy starting from cheap solid metal oxide/hydroxide has been proposed [73]. Therefore using this synthetic method, as a result, it is possible to prepare MOFs with water as the only by-product. In this same green synthesis perspective, since 2011, dry gel conversion (DGC) synthesis has been investigated [74–76] to obtain uniform crystalline MOFs in high yield, using a very reduced reaction volume and generating a minimum amount of waste. Finally, another not less important issue to be highlighted is that, independent of the method applied,

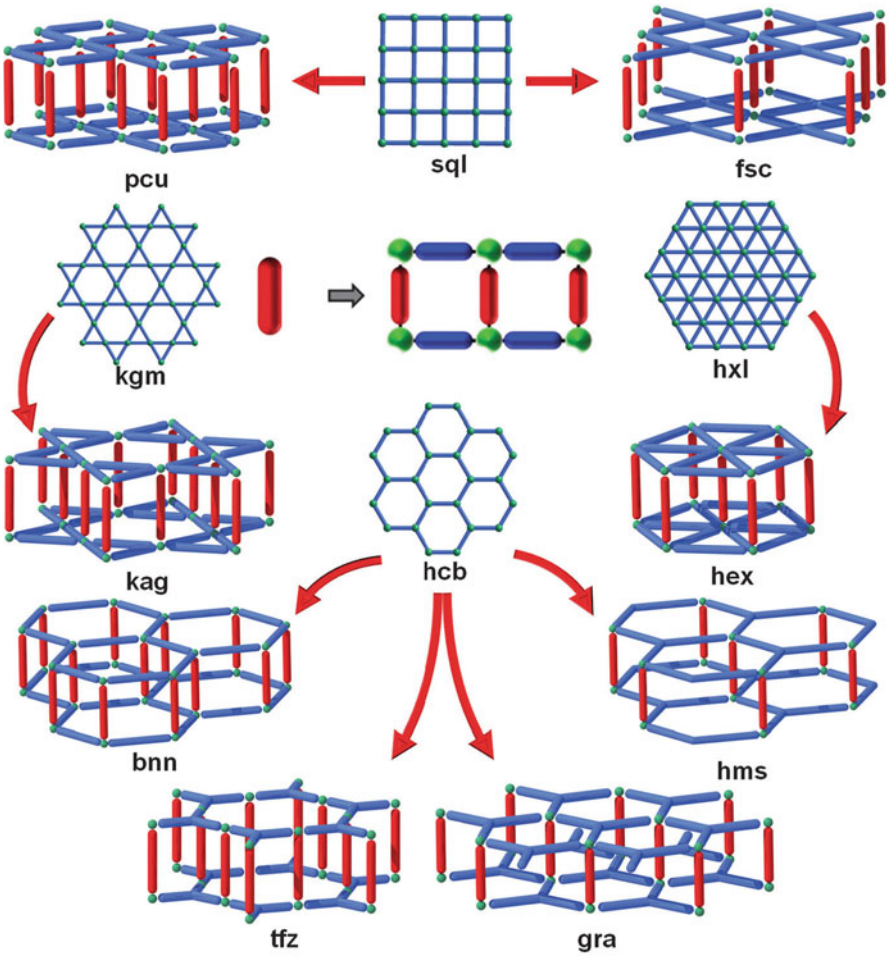

Fig. 14.5 Schematic pillaring of *sql*, *kgm*, *hxl*, and *hcb* 2D layers to form the *pcu*, *fsc*, *kag*, *hex*, *bnn*, *hms*, *gra*, and *tfz* nets. Red rods represent the ditopic ligands (Reprinted with permission from [5])

there are very important reaction parameters that affect the synthesis of MOFs, mainly pH, solvent, metal/ligand molar ratio, the concentration of starting materials, reaction time, and reaction temperature.

Size- and Shape-Controlled Synthesis As expected to most nanoscale materials, nano-MOFs exhibit physical properties distinct from their corresponding bulk crystalline powders [77, 78]. For this reason, depending on the intended application, in particular, it is more appropriate that the MOFs are miniaturized at nanometer scale [26]. Likewise, it is also important that MOFs have nano- and microcrystals whose morphologies are well regulated [79]. Figure 14.6 shows a high-resolution

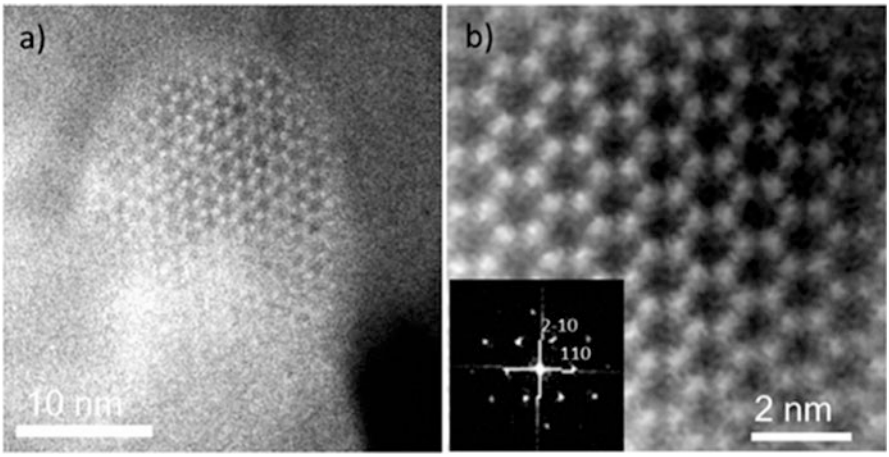

Fig. 14.6 (**a**) Very high-resolution TEM image of a *Zn-MOF-74* nanoparticle (20 nm) oriented along the [001] direction showing a hexagonal arrangement of the pores. (**b**) A closer look at the pores of the particle, where the Zn cluster can be visualized (Reproduced with permission from Sánchez-Sánchez et al. [80])

TEM image of a monodisperse *Zn-MOF-74* nanocrystal [80], where the metal clusters and the hexagonal channels of ∼11 Å of diameter can be observed. According to the authors, this was the first time that high-resolution electron microscopy data allowed the observation of a metal cluster linking the organic phase in an MOF.

Although this MOF has been obtained by the direct mixing method at room temperature and, in principle, the methods used to synthesize conventional micrometer-sized MOF materials [81] can be used to prepare nano-MOFs, there are more specific synthetic approaches to obtain size- and shape-controlled MOF particles [82, 83]. Coordination modulation [84, 85] is one of the most used methods in which monodentate ligands are introduced in a reactional environment in order to directly compete with the linker molecules for the coordination sites at the inorganic building units. Monocarboxylic acids, such as acetic acid or formic acid, for example, can be used as coordination modulators, playing an important role in controlling the nucleation and growth (crystal size and morphology) of the particles. Kitagawa et al. reported an interesting study at the beginning of the 2010s [86], in which it was shown the morphological transition of *HKUST-1* crystals (from octahedron to cube nanoparticles) with an increase in the concentration of the modulators (*n*-dodecanoic or lauric acids, in this case). Alternatively, a large excess of the polydentate linker [87] can also be used for this same purpose. In any case, both mechanisms of modulation often improve the reproducibility of the synthesis and the crystallinity of the obtained MOF nanoparticles. A second strategy well known to modulate the size and the morphology of MOF particles, in part, involves the preparation of reverse micelles by mixing two immiscible liquids in the presence of a surfactant.

In this typical case, the obtained microemulsions act as nanostructured chemical reactors confining the synthesis of MOFs to the nanometric scale [88]. Besides that, by adjusting the concentration of the surfactant, Sun et al. have demonstrated that it is also possible to control the nanoparticle morphology, and, in this way, cubes, truncated cubes, cuboctahedrons, and octahedrons could be obtained [89]. However, it is worth to mention that the microemulsion approach affords poor yields as well as have a low reproducibility, most likely because of a large number of parameters associated with the processes of micelle formation. To avoid some of these problems, Maspoch et al. [90] have proposed the use of spray-drying as a method for creating and heating droplets containing the precursors without the need to add immiscible solvents or surfactants.

Large-Scale Production To produce high quantities of MOFs to the market, some synthetic routes have been investigated. The methods for upscaling manufacture of MOF-based products must fulfill certain requirements such as reproducibility, efficiency (high yields), economy (not expensive raw materials), and environment-friendly (high purity of product and low energy consumption). From 2005, when it was reported by the first time the use of the electrochemical route to prepare *HKUST-1* [91], BASF company has been producing this MOF on a ton scale (Basolite C300, commercialized by Sigma-Aldrich) [64] using this versatile and low-cost method. Continuous MOF production can also be reached using flow reactors [92, 93], solvothermal method [94, 95], spray-drying or aerosol continuous-flow technique [96, 97], or the virtually solvent-free mechanochemical route. From this solid-state methodology, synthesis by extrusion has recently allowed the continuous and large-scale production of some types of MOFs [98]. Some interesting works have also been published in literature concerning the use of different synthetic strategies for scalable batch production of some MOFs [99–102]. Besides the utilization of versatile scale-up methodologies to prepare large quantities of MOFs, typically they are obtained as powders. It is convenient to process and formulate them into specific macroscopic shapes with a view toward application-specific configurations. In fact, from different approaches such as mechanical pressure, the use of extrusion methods, or incorporation of binders, some authors have reached success in shaping MOF powders into mm-sized extrudates [103], spherical pellets [104], spherical beads [96], and monoliths [105], among others. Under this same perspective and envisaging industrial applications [106, 107], MOFs have also been employed in the production of crystalline thin films [108–114], membranes [115–117], and composites [118–123].

Characterization of MOFs To determine the structural and surface properties of MOFs, several experimental techniques are available. Due to their very large unit cells and high structural complexity, single-crystal X-ray diffraction (XRD) is the main method for determining the structure of these coordination solids, and, for this purpose, single crystals are indispensable. However, some MOFs do not yield suitable crystals, and, in these cases, we have to recourse to complementary experimental and computational methods of structural analysis such as solid-state nuclear magnetic resonance [124], powder X-ray diffraction and scattering

measurements [125], and X-ray absorption (EXAFS) spectroscopy [126]. Besides the use of these techniques for structural analysis, it is also important to know other very special properties of the MOFs such as particle size and morphology [127, 128], thermal stability [129], and surface properties. Concerning to this matter and according to Stoddart et al. [130], the applicability of nitrogen adsorption at 77 K as standard method for surface area assessment and micropore size analysis must be made with care, and, for this reason, since 2015, the IUPAC has recommended the use of argon adsorption at 87 K to determine surface properties of microporous materials, including MOFs [131]. Finally, it is also important to mention that in order to understand the complicated nucleation and crystallization processes of MOFs from solutions and to gain more detailed information on the interactions at molecular level [132], some authors have been using time-resolved in situ techniques such as X-ray absorption spectroscopies [126], X-ray diffraction [133], synchrotron diffraction [134], and high-resolution microscopies [135, 136]. In fact, to understand how complex extended networks are self-assembled in solution from simple metal salts and organic ligands is very important, not only to have some control over the reaction conditions, but it can allow the isolation of kinetic phases that may have practical applications as well.

4 Applications

The unique physical and chemical properties of MOFs, such as permanently ordered porosity and tunable functionality, make them very interesting materials for a wide range of technological applications [137, 138]. More specifically, the use of MOFs in drug delivery and photonics will be discussed in detail on this chapter (see later), while review articles in gas storage [23, 57, 139–149], gas separation [150–153], catalysis [25, 154–158], and magnetism [31, 159, 160], among others [29, 161–167], are easily accessed. However, despite the vast literature on this exciting growing research area, we intend here to present available literature about two very important aspects when referring to applications of MOFs: pore size and pore wall surface. In fact, for some applications (especially gas storage/separation and catalysis), the very small micropores (< 2 nm) available in most MOFs can be an issue in mass transport, for example. For this reason, some different strategies have been used to introduce large pores [167, 168] aiming the construction of mesoporous [169–171] MOFs and macroporous [172] materials as well, such as capsules, hollow microspheres, and so on. The use of longer organic linkers [173, 174] was one of the first methods to introduce large pores in MOFs, although in some cases it can lead to interpenetrated structures (catenation) [175–177], reducing the available surface area, pore size, and framework stability as well. Surfactant templating is another approach that can be used, and in this case, the mesopores are present in addition to the micropores [178–180]. Besides the possibility of tailoring pore size, it is also possible to modulate the pore surface by attaching functional groups to organic linkers and, in this way, give MOFs new levels of functionality. In this context,

Yaghi et al. [181, 182] have proposed a method that allows the prediction of gas adsorption properties of the same MOF crystal after the incorporation of different combinations of functional chemical groups. Several different functionalities can also be introduced into one MOF structure, with full retention of its crystallinity and porosity, by covalent post-synthesis modification (PSM) approach, i.e., chemical modification after the synthesis of the MOF [183–185]. The tailoring of the pore wall can occur either by the covalent attachment of functional groups to the organic linkers or the coordinatively unsaturated open metal sites within the backbone of MOFs, among other strategies [186–189]. In addition to the covalent chemistry within the pores, new properties such as acidity/basicity or magnetism can be provided by the encapsulation of inorganic nanoparticles into the pores of the MOFs [28, 190, 191]. This synthesis strategy for tailoring the pore architecture has given to MOFs new performances, mainly in the area of heterogeneous catalysis [192].

MOFs in Drug Delivery MOFs provide different opportunities for applications in the biomedicine area. Most of them, including drug delivery and intracellular imaging, require the use of biologically compatible metal ions and organic linkers (bio-MOFs) [193]. In fact, several MOFs have been carefully designed and synthesized by the judicious selection of specific inorganic bioelements (e.g., zinc, iron, copper) and biomolecules such as amino acids, nucleobases, and sugars, among others. Building blocks based in biomolecules can offer some additional advantages to MOFs as higher structural diversity and framework flexibility, significantly impacting in the properties of the biomaterial obtained. Moreover, the chiral centers of some biomolecules afford the possibility to combine chirality and porosity in a single material, giving it unprecedented selectivity in molecular recognition [194]. Concerning the use of bio-MOFs as drug carriers, these materials exhibit in fact the main desired properties for the application, such as exceptionally high surface areas and large pore sizes (for drug encapsulation), intrinsic biodegradability (as a result of relatively labile metal-ligand bonds), and functionality for covalent post-synthesis grafting of drug molecules [195]. Bio-MOFs also can be scaled down to nanosize in order to allow the entrance of anticancer drugs into the cells [196]. It should be highlighted that when a drug is administered by conventional means, its action may be limited by some factors such as low solubility, high toxicity, very short biological half-lives (e.g., as ibuprofen), and/or in vivo degradation [26, 197]. And, in this context, storage systems and controlled release provide some advantages over conventional methods, including the maintenance of constant drug levels within the organism and the possibility of direct application of the drug to the main action sites [198]. Some factors must be taken into consideration in the development of drug delivery systems, including the chemical nature, the porosity and adsorption capacity of the biomaterial, and the different kinetic mechanisms to control the release, such as erosion or swelling of the matrix and/or diffusion of the drug [199, 200]. Based on this, two general strategies have been developed to use MOFs in drug delivery. As illustrated in Fig. 14.7, in the first one, the organic linker itself has therapeutic activity, while, in the other, the pharmacological species is incorporated within the porous structure of the MOF [201].

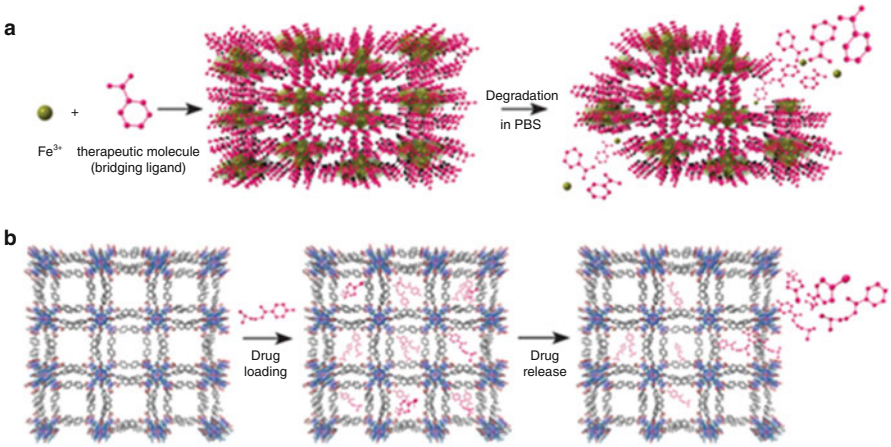

Fig. 14.7 MOFs as drug carriers. (**a**) Drug as an organic linker; (**b**) drug adsorbed into the porous structure of the MOF (Reprinted with permission from Imaz et al. [194])

The use of MOFs with large surface area to high drug loading can be avoided in the first approach [199]. Some bio-MOFs have been constructed using this strategy, such as *bioMIL-5*, based on Zn^{2+} ions and azelaic acid, an antibacterial agent [200], the biocompatible porous Mg-gallate with antioxidant activities [201], and *bioMIL-1*, a biodegradable MOF containing Fe^{3+} ions and vitamin B3 [202] and a zinc MOF with curcumin, a biomolecule with antioxidant and anti-inflammatory activities [203]. On the other hand, when a drug is adsorbed into the porous of bio-MOFs, several factors may influence the drug release kinetics, including exogenous concentrations of ions, pH, and temperature. In fact, it was recently reported that the release of 5-fluorouracil drug from the MOF *UiO-66-*NH_2 is simultaneously controlled by pH and Ca^{2+} concentration on bone tumor cells [204]. Some drug release studies showing the potential application of MOFs as drug carriers are compiled in Table 14.2.

It is also important to mention that this new area of biomedical applications is just in the beginning, and numerous detailed investigations of the MOF usage as drug carriers will be required before clinical use. These actions must involve the evaluation of the bio-MOFs in vivo toxicity, determination of the stability in biological environment, investigation of the mechanisms of degradation in the organism, the modification of MOF surfaces to improve the cellular recognition, and also, undertaking drug metabolism and pharmacokinetic (DMPK) studies [26].

MOFs in Photonics MOFs can exhibit luminescence if they are constructed from certain metals (e.g., lanthanide ions), specific organic ligands, or when they adsorb luminescent guest molecules [27]. The photophysical behavior can come from different sources, such as antenna effect (see below), excitation of fluorophore linkers, or charge transfer mechanisms. These porous materials are usually sensitive to UV excitation, but some of them can also show emission when exposed to

Table 14.2 Some MOFs examples in drug delivery

MOF	Drug	Loading ($g.g^{-1}$)	Release rates	Refs.
$[Zn(NO_2\text{-BDC})(dmbpy)_{0.5}]_n$	Busulfan	0.17	45%, 0 55%, 20	[205]
$[Cu_2(L_2)(H_2O)_2]_n$	5-fluorouracil	0.42	96%, 5 d	[206]
$NH_2(CH_3)_2[Zn_3(L')_2]_n$	5-fluorouracil	0.22	92%, 5 d	[207]
$[Zn_8(O)_2(CDDB)_6(DMF)_4(H_2O)]_n$	5-fluorouracil	0.66	65%, 3 d	[208]
$[Cu(L'')(4,4'\text{-bipy})(H_2O)]_n$	5-fluorouracil	0.27	61%, 4 d	[209]
MOF-74	Ibuprofen	0.21	50%, 4 h	[210]
$[Zn_2(1,4\text{-bdc})_2(dabco)]_n$	Ibuprofen	0.15	80%, 12 d	[211]
MIL-53-Fe	Ibuprofen	0.21	100%, 21 d	[212]
Bio-MOF-1	Procainamide	0.22	100%, 3 d	[213]
MIL-100-Fe	Sodium diclofenac	0.63	63%, 3 d	[209]

NO_2-BDC 5-nitroisophathalate, *dmbpy* 4,4´-dimethyl-2,2´-bipyridine, *L* 2,5-di(3′,5′-dicarboxylphenyl)pyridine), *L'* 1,1′,4′,1″,4″,1‴-quaterphenyl-3,5,3‴,5‴-tetracarboxylic acid 1,3,5-benzenetrisbenzoate, *CDDB* 4,4′-(9-H carbazole-3,6-diyl)dibenzoic acid, *L"* diphenylmethane-4,4′-dicarboxylic acid, *4,4′-bipy* 4,4′-bipyridine, *1,4-bdc* benzene-1,4-dicarboxylic acid, *dabco* 1,4-diazabicyclo[2.2.2] octane

X-rays, through a phenomenon called scintillation [214–216]. The luminescence based on the emission of the fluorophore organic ligand is particularly interesting for biological applications, since the materials can be synthesized using biocompatible metals (bio-MOFs, see above). However, when the metallic ion is also susceptible to excitation, it opens up a range of possibilities for designing new structures through supramolecular chemistry and crystal engineering knowledges [217]. Typically, some lanthanide-based MOFs, named Ln-MOFs, show high luminescence under UV excitation through antenna effect. This phenomenon involves the absorption of UV radiation through the ligand's conjugated bonds and the transfer of this energy to the lanthanide ion, which then proceeds to emit visible light through *f-f* transitions [218]. Ln-MOFs have attracted extensive attention due to their permanent porosity and the unique luminescence properties such as high emission quantum yield, long-lived emission, large Stokes shifts, and characteristically sharp line emissions [219–224]. For these reasons, in the last years, a new set of applications for these multifunctional materials has emerged, and some of them are illustrated in Fig. 14.8. Besides the use of chemical sensors and biological markers (see below for more detail), Ln-MOFs can also be utilized for gas storage, as materials for organic light-emitting diodes (OLEDs) or as magneto-luminescent materials [225–227].

One of the most reported potential applications for Ln-MOFs is as chemical and biological sensor. There are a lot of mechanisms in which the MOF can alter a property producing the sensor signal. Ln-MOFs usually can be changed in their luminescence behavior when a substance enters into their cavities; however, the mechanisms in which this happens are dependent on the system. The pore size can be a factor for selectivity, alongside the particular properties of the lanthanide ion and/or the organic spacer. An Ln-MOF with large pores, for example, can be selective for small molecules if they contain open sites or functional groups

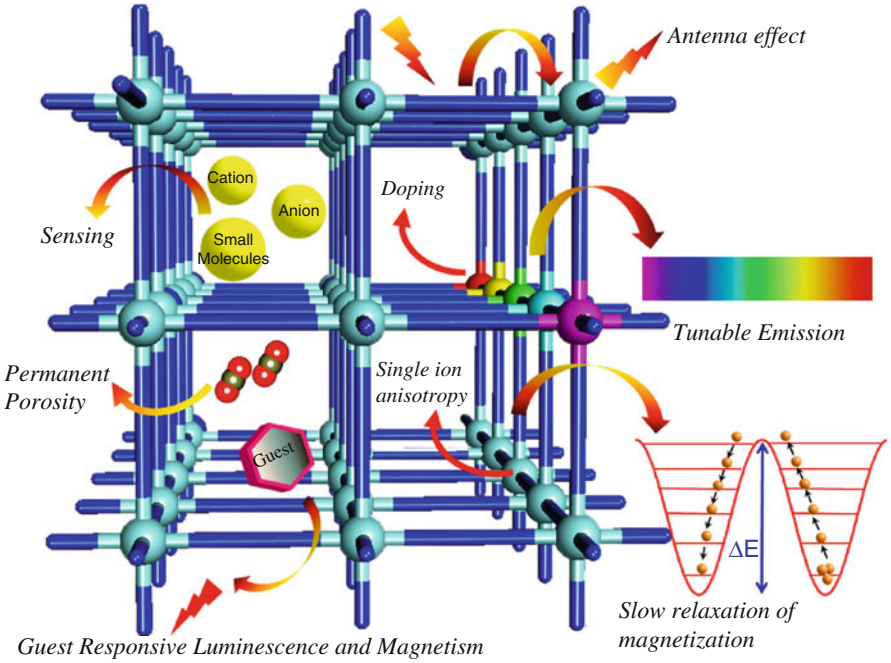

Fig. 14.8 Schematic representation of porous lanthanide-organic frameworks with versatile functionalities (Reprinted with permission from [226])

that the analyte can interact with. On the other hand, although Ln-MOFs with small pores are most selective for small molecules, the permanence of these guests inside the cavities is dependent on the interactions as well [228–232], which can include hydrogen bonding to the structure, covalent bond with the inorganic building block, and/or chirality (for enantiomeric sensing) [233]. Besides that, nanosized synthetized MOFs are ideal for sensing applications since the effective contact area between the analyte and the porous surface is increased, thus intensifying the signal [234, 235]. In this context, there are recent and advanced studies on using Ln-MOFs as molecular thermometers, pH sensors, and imaging agents [236–238], where nanoscale MOFs are important for biological applications of these types of sensors, especially for monitoring small temperature and pH changes in biological environments such as living cells. In fact, under the biomedical point of view, Ln-MOFs exhibit some particular physical properties that make them possible to use in quantitative (biosensor) and qualitative (MRI and optical multimodal imaging contrast agents) sensing [88]. As mentioned above, the use of luminescent nanoMOFs in this area is highly promising, by giving them the capability to enter into cells through the mechanism of endocytosis [239]. One of its first applications was in the detection of dipicolinic acid (DPA), a component of bacterial endospores [232]. After that, several organic compounds – from ascorbic acid, glucose, and dopamine to large biomolecules such as DNA and proteins – and bioelements

(Cu^{2+}, Fe^{3+}) were fast and efficiently detected using Ln-MOF-based sensors [232, 240]. On the other hand, contrast-enhancing agents based on gadolinium MOFs [88] have been used in noninvasive MRI diagnostic technique [219]. The paramagnetic properties of the Gd^{3+} ions increase the proton relaxation rates in tissues, making it possible to reduce substantially the contrast agent dose used during the procedure.

5 Final Considerations

We hope that this chapter is useful for an introduction to the fascinating MOF research area whose importance has been demonstrated by the very large number of publications, growing engagement of researchers from other fields and emerging commercial interest. Nowadays, an MOF picture is on the cover of a highly regarded book of General Chemistry [241], and one of the syntheses has been recently published in the *Journal Chemical Education* [242]. With almost limitless possibilities for the tuning of the metal centers and organic linkers, new MOFs with unimaginable properties are being discovered, but that is only the beginning. With the design and synthesis of new organic linkers [5, 243, 244], usage of ligands other than carboxylate ones [245–248], modification of the chemical components and/or physical forms of MOFs [249], and the possibility of structural transformation under various stimuli [24, 250–253], helped by recent advances on computational screening [254, 255], new frameworks with desirable topologies, architectures, and improved performances will be obtained. And then, the pores of these fascinating materials could be commercially exploited in a range of processes such as carbon dioxide capture [146, 256–258] and transformation [259], hydrogen storage for fuel-cell vehicles [260], natural gas adsorption for green car [261, 262], and so on. In fact, it is not surprising that some renowned researchers of the MOF area, such as Jeffrey R. Long and Omar Farha, have recently created the Mosaic Materials and Nu Mat Technologies start-up companies [263], respectively. Besides that, the MOF field is also taking several new research directions such as the possibility of manufacturing molecular-electronic devices through the incorporation of dynamic interlocked components within MOF crystal lattice [264–267], the X-ray structure determination of natural large biomolecules within MOFs [268, 269], the investigation of framework melting into an amorphous liquid as route for the synthesis of glasses with controllable chemical functionality [270], and the use of MOFs as sacrificial templates for syntheses of materials [271, 272]. As Yaghi has recently said, in a very elegant paper [273], *"the emerging inclusion properties of these materials are examples of the far-reaching implications and significance of translating molecular chemistry into the solid state."*

References

1. Li H et al (1999) Design and synthesis of an exceptionally stable and highly porous metal-organic frameworks. Nature 402(6759):276–279
2. Coudert F-X, Fuchs AH (2016) Computational characterization and prediction of metal–organic framework properties. Coord Chem Rev 307:211–236
3. Kim D, Liu X, Lah MS (2015) Topology analysis of metal–organic frameworks based on metal–organic polyhedra as secondary or tertiary building units. Inorg Chem Front 2: 336–360
4. Li M, Li D, O'Keeffe M, Yaghi OM (2014) Topological analysis of metal ─ organic frameworks with polytopic linkers and/or multiple building units and the minimal transitivity principle. Chem Soc Rev 114:1343–1370
5. Lu W, Wei Z, Gu Z-Y, Liu T-F, Park J, Park J, Tian J, Zhang M, Zhang Q, Gentle T III, Boscha M, Zhou H-C (2014) Tuning the structure and function of metal–organic frameworks via linker design. Chem Soc Rev 43:5561–5593
6. Dey C, Kundu T, Biswal BP, Mallick A, Banerjee R (2014) Crystalline metal-organic frameworks (MOFs): synthesis, structure and function. Acta Cryst B70:3–10
7. Furukawa H, Cordova KE, O'Keeffe M, Yaghi OM (2013) The chemistry and applications of metal-organic frameworks. Science 341:1230444
8. O'Keeffe M, Yaghi OM (2012) Deconstructing the crystal structures of metal organic frameworks and related materials into their underlying nets. Chem Rev 112:675–702
9. Rowsell JLC, Yaghi OM (2004) Metal–organic frameworks: a new class of porous materials. Microporous Mesoporous Mater 73:3–14
10. Kitagawa S, Kitaura R, Noro S-I (2004) Functional porous coordination polymers. Angew Chem Int Ed 43:2334–2375
11. James SL (2003) Metal-organic frameworks. Chem Soc Rev 32:276–288
12. Rosi NL, Eddaoudi M, Kim J, O'Keeffe M, Yaghi OM (2002) Advances in the chemistry of metal–organic frameworks. CrystEngComm 4:401–404
13. Stefan Kaskel (2016) The chemistry of metal-organic frameworks. Synthesis, characterization and applications, vol 1. Wiley, Weinheim, 849p
14. Jiang J (ed) (2015) Metal–organic frameworks materials modeling towards potential engineering applications. Pan Stanford Publishing, Boca Raton
15. MacGillivray LR, Lukehart CM (eds) (2014) Metal-organic framework materials. Wiley, Chichester\West Sussex
16. Farrusseng D (ed) (2011) Metal-organic frameworks. Applications from catalysis to gas storage. Wiley, Weinheim
17. Schröder M (ed) (2010) Functional metal-organic frameworks: gas storage, separation and catalysis. Springer, Berlin
18. Macgillivray LR (ed) (2010) Metal-organic frameworks. Design and application. Wiley, Hoboken
19. Férey G (2008) Hybrid porous solids: past, present, future. Chem Soc Rev 37:191–214
20. Farha OK, Eryazici I, Jeong NC, Hauser BG, Wilmer CE, Sarjeant AA, Snurr RQ, Nguyen ST, Yazaydın AO, Hupp JT (2012) Metal ─ organic framework materials with ultrahigh surface areas: is the sky the limit? J Am Chem Soc 134:15016–15021
21. Furukawa H, Ko N, Go YB, Aratani N, Choi SB, Choi E, Yazaydın AO, Snurr RQ, O'Keeffe M, Kim J, Yaghi OM (2010) Ultrahigh porosity in metal-organic frameworks. Science 329:424–428
22. Song Z, Nambo A, Tate KL, Bao A, Zhu M, Jasinski JB, Zhou SJ, Meyer HS, Carreon MA, Li S, Yu M (2016) Nanovalved Adsorbents for CH4 Storage. Nano Lett 16:3309–3313
23. Férey G, Serre C, Devic T, Maurin G, Jobic H, Llewellyn PL, Weireld GD, Vimont A, Daturif M, Changg J-S (2011) Why hybrid porous solids capture greenhouse gases? Chem Soc Rev 40:550–562

24. Férey G, Serre C (2009) Large breathing effects in three-dimensional porous hybrid matter: facts, analyses, rules and consequences. Chem Soc Rev 38:1380–1399
25. Llabrés i Xamena F, Gascon J (2013) Metal organic frameworks as heterogeneous catalysts, RSC Publishing, Cambridge, 432 p
26. Giménez-Marqués M, Hidalgo T, Serre C, Horcajada P (2016) Nanostructured metal–organic frameworks and their bio-related applications. Coord Chem Rev 307:342–360
27. Metal-organic frameworks for photonics applications (2014) Structure and Bonding 157, Series Editor: D.M.P. Mingos. Springer, Berlin, 189p
28. Zou Z, Wang S, Jia J, Xu F, Long Z, Hou X (2016) Ultrasensitive determination of inorganic arsenic by hydride generation-atomic fluorescence spectrometry using Fe_3O_4@ZIF-8 nanoparticles for preconcentration. Microchem J 124:578–583
29. Choi KM, Jeong HM, Park JH, Zhang Y-B, Kang JK, Yaghi OM (2014) Supercapacitors of Nanocrystalline metal organic frameworks. ACS Nano 8:7451–7457
30. Yamagiwa H, Sato S, Fukawa T, Ikehara T, Maeda R, Mihara T, Kimura M (2014) Detection of volatile organic compounds by weight-detectable sensors coated with metal-organic frameworks. Sci Rep 4:06247
31. Coronado E, Espallargas GM (2013) Dynamic magnetic MOFs. Chem Soc Rev 42: 1525–1539
32. Batten SR, Champness NR, Chen X-M, Garcia-Martinez J, Kitagawa S, Öhrström L, O'Keeffe M, Suhh MP, Reedijki J (2012) Coordination polymers, metal–organic frameworks and the need for terminology guidelines. CrystEngComm 14:3001–3004
33. Batten SR et al (2013) Terminology of metal-organic frameworks and coordination polymers (IUPAC recommendations 2013). Pure Appl Chem 85:1715–1724
34. Kinoshita Y et al (1959) The crystal structure of bis(adiponitrilo)copper(I) nitrate. Bull Chem Soc Jpn 32:1221–1226
35. Weels AF (1978) Three-dimensional nets and polyhedra. Bull Am Math Soc 84:466–470
36. Hoskins BF, Robson R (1989) Infinite polymeric frameworks consisting of three dimensionally linked rod-like segments. J Am Chem Soc 111:5962–5964
37. Li H, Eddaoudi M, Groy TL, Yaghi OM (1998) Establishing microporosity in open metal-organic frameworks: gas sorption isotherms for Zn(BDC) (BDC = 1,4-Benzenedicarboxylate). J Am Chem Soc 120:8571–8572
38. Férey G et al (2005) A chromium terephthalate-based solid with unusually large pore volumes and surface area. Science 309:2040–2042
39. Chui SS-Y, Lo SM-F, Charmant JPH, Orpen AG, Williams ID (1999) A chemically Functionalizable Nanoporous material $[Cu_3(TMA)_2(H_2O)_3]$n. Science 283:1148–1150
40. Dietzel PDC et al (2010) Interaction of hydrogen with accessible metal sites in the metal-organic frameworks M(2)(dhtp) (CPO-27-M; M = Ni, Co, Mg). Chem Commun 46: 4962–4964
41. Michl J (ed) (1995) Modular chemistry. Kluwer Academic Publishers, Dordrecht
42. Yaghi OM, Li H, Davis C, Richardson D, Groy TL (1998) Synthetic strategies, structure patterns, and emerging properties in the chemistry of modular porous solids. Acc Chem Res 31:474–484
43. Eddaoudi M, Moler DB, Li H, Chen B, Reineke TM, O'Keeffe M, Yaghi OM (2001) Modular chemistry: secondary building units as a basis for the design of highly porous and robust metal-organic carboxylate frameworks. Acc Chem Res 34:319–330
44. Yaghi OM, O'Keeffe M, Ockwig NW, Chae HK, Eddaoudi M, Kim J (2003) Reticular synthesis and the design of new materials. Nature 423:705–714
45. Cook TR, Zheng Y-R, Stang PJ (2013) Metal − organic frameworks and self-assembled supramolecular coordination complexes: comparing and contrasting the design, synthesis, and functionality of metal − organic materials. Chem Rev 113:734–777
46. O'Keeffe M, Eddaoudi M, Li H, Reineke TM, Yaghi OM (2000) Frameworks for extended solids: geometrical design principles. J Solid State Chem 152:3–20
47. Ockwig NW, Delgado-Friedrichs O, O'Keeffe M, Yaghi OM (2005) Reticular chemistry: occurrence and taxonomy of nets and grammar for the design of frameworks. Acc Chem Res 38:176–182

48. O'Keeffe M, Peskov MA, Ramsden SJ, Yaghi OM (2008) The Reticular Chemistry Structure Resource (RCSR) database of, and symbols for crystal nets. Acc Chem Res 41:1782–1789
49. Hendon CH, Walsh A (2015) Chemical principles underpinning the performance of the metal–organic framework HKUST-1. Chem Sci 6:3674–3683
50. Öhrström L (2015) Let's talk about MOFs—topology and terminology of metal-organic frameworks and why we need them. Crystals 5:154–162
51. Eubank JF, Walsh RD, Eddaoudi M (2005) Terminal co-ligand directed synthesis of a neutral, non-interpenetrated (10,3)-a metal–organic framework. Chem Commun 16:2095–2097
52. Biradha K, Fujita M (2002) A springlike 3D-coordination network that shrinks or swells in a crystal-to-crystal manner upon guest removal or readsorption. Angew Chem Int Ed 41: 3392–3395
53. Dietzel PDC, Morita Y, Blom R, Fjellvg H (2005) An in situ high-temperature single-crystal investigation of a dehydrated metal–organic framework compound and field-induced magnetization of one-dimensional metal–oxygen chains. Angew Chem 117:6512–6516
54. Furukawa H, Go YB, Ko N, Park YK, Uribe-Romo FJ, Kim J, O'Keeffe M, Yaghi OM (2011) Isoreticular expansion of metal–organic frameworks with triangular and square building units and the lowest calculated density for porous crystals. Inorg Chem 50:9147–9152
55. Furukawa H, Kim J, Ockwig NW, O'Keeffe M, Yaghi OM (2008) Control of vertex geometry, structure dimensionality, functionality, and pore metrics in the reticular synthesis of crystalline metal − organic frameworks and Polyhedra. J Am Chem Soc 130:11650–11661
56. Liang L-L, Zhang J, Ren S-B, Ge G-W, Li Y-Z, Du H-B, You X-Z (2010) Rational synthesis of a microporous metal–organic framework with PtS topology using a semi-rigid tetrahedral linker. CrystEngComm 12:2008–2010
57. Noro S-I, Kitagawa S, Kondo M, Seki K (2000) A new, methane adsorbent, porous coordination polymer $[\{CuSiF_6(4,4'\text{-bipyridine})_2\}_n]$. Angew Chem Int Ed 39:2081–2084
58. Lu J, Mondal A, Moulton B, Zaworotko MJ (2001) Polygons and Faceted Polyhedra and Nanoporous Networks. Angew Chem Int Ed 40:2113–2116
59. Perry JJ IV, Perman JA, Zaworotko MJ (2009) Design and synthesis of metal–organic frameworks using metal–organic polyhedra as supermolecular building blocks. Chem Soc Rev 38:1400–1417
60. Zaworotko MJ (2009) Metal–organic materials: a reversible step forward. Nat Chem 1: 267–268
61. Park J, Hong S, Moon D, Park M, Lee K, Kang S, Zou Y, John RP, Kim GH, Lah MS (2007) Porous Metal − Organic frameworks based on metal − organic Polyhedra with Nanosized cavities as Supramolecular building blocks: two-fold interpenetrating primitive cubic networks of $[Cu_6L_8]^{12+}$ Nanocages. Inorg Chem 46:10208–10213
62. Guillerm V, Kim D, Eubank JF, Luebke R, Liu X, Adil K, Lah MS, Eddaoudi M (2014) A supermolecular building approach for the design and construction of metal–organic frameworks. Chem Soc Rev 43:6141–6172
63. Bhattacharjee S, Chenab C, Ahn W-S (2014) Chromium terephthalate metal–organic framework MIL-101: synthesis, functionalization, and applications for adsorption and catalysis. RSC Adv 4:52500–52525
64. Stock N, Biswas S (2012) Synthesis of metal-organic frameworks (MOFs): routes to various MOF topologies, morphologies, and composites. Chem Rev 112:933–969
65. He M, Yao J, Liu Q, Wang K, Chen F, Wang H (2014) Facile synthesis of zeolitic imidazolate framework-8 from a concentrated aqueous solution. Microporous Mesoporous Mater 184: 55–60
66. Klinowski J, Paz FAA, Silva P, Rocha J (2011) Microwave-assisted synthesis of metal–organic frameworks. Dalton Trans 40:321–330
67. Son W-J, Kim J, Kim J, Ahn W-S (2008) Sonochemical synthesis of MOF-5. Chem Commun 47:6336–6338
68. Joaristi AM et al (2012) Electrochemical synthesis of some archetypical Zn^{2+}, Cu^{2+}, and Al^{3+} metal organic frameworks. Cryst Growth Des 12:3489–3498
69. Stassen I et al (2015) Electrochemical film deposition of the zirconium metal-organic framework UiO-66 and application in a miniaturized sorbent trap. Chem Mater 27: 1801–1807

70. Sakamoto H, Matsuda R, Kitagawa S (2012) Systematic mechanochemical preparation of a series of coordination pillared layer frameworks. Dalton Trans 41:3956–3961
71. Friscic T (2010) New opportunities for materials synthesis using mechanochemistry. J Mater Chem 20:7599–7605
72. Pichon A, Lazuen-Garay A, James SL (2006) Solvent-free synthesis of a microporous metal–organic framework. CrystEngComm 8:211–214
73. Zhan G, Zeng HC (2016) Alternative synthetic approaches for metal–organic frameworks: transformation from solid matters. Chem Commun 53(1):72–81
74. Shi Q, Chen Z, Song Z, Li J, Dong J (2011) Synthesis of ZIF-8 and ZIF-67 by steam-assisted conversion and an investigation of their tribological behaviors. Angew Chem Int Ed 50: 672–675
75. Ahmed I, Jeon J, Khan NA, Jhung SH (2012) Synthesis of a metal − organic framework, iron-Benezenetricarboxylate, from dry gels in the absence of acid and salt. Cryst Growth Des 12:5878–5881
76. Das AK, Vemuri RS, Kutnyakov I, McGrail BP, Motkuri RK (2016) An efficient synthesis strategy for metal-organic frameworks: dry-gel synthesis of MOF-74 framework with high yield and improved performance. Sci Rep 6:28050
77. Carné A, Carbonell C, Imaz I, Maspoch D (2011) Nanoscale metal–organic materials. Chem Soc Rev 40:291–305
78. Sindoro M, Yanai N, Jee A-Y, Granick S (2014) Colloidal-sized metal organic frameworks: synthesis and applications. Acc Chem Res 47:459–469
79. Masoomi MY, Beheshti S, Morsali A (2015) Shape control of Zn(II) Metal − Organic frameworks by modulation synthesis and their morphology-dependent catalytic performance. Cryst Growth Des 15:2533–2538
80. Díaz-García M, Mayoral A, Díaz I, Sánchez-Sánchez M (2014) Nanoscaled M-MOF-74 materials prepared at room temperature. Cryst Growth Des 14:2479–2487
81. Bunzen H, Grzywa M, Hambach M, Spirkl S, Volkmer D (2016) From micro to Nano: a toolbox for tuning crystal size and morphology of Benzotriazolate-based Metal − Organic frameworks. Cryst Growth Des 16:3190–3197
82. Jin L-N, Liu Q, Sun W-Y (2014) An introduction to synthesis and application of nanoscale metal–carboxylate coordination polymers. CrystEngComm 16:3816–3828
83. Flugel EA, Ranft A, Haase F, Lotsch BV (2012) Synthetic routes toward MOF nanomorphologies. J Mater Chem 22:10119–10133
84. Diring S, Furukawa S, Takashima Y, Tsuruoka T, Kitagawa S (2010) Controlled Multiscale synthesis of porous coordination polymer in Nano/micro regimes. Chem Mater 22: 4531–4538
85. Guo H, Zhu Y, Qiu S, Lercher JA, Zhang H (2010) Coordination modulation induced synthesis of Nanoscale $Eu_{1-x}Tb_{x-}$ metal-organic frameworks for luminescent thin films. Adv Mater 22:4190–4192
86. Umemura A, Diring S, Furukawa S, Uehara H, Tsuruoka T, Kitagawa S (2011) Morphology design of porous coordination polymer crystals by coordination modulation. J Am Chem Soc 133:15506–15513
87. Cravillon J, Munzer S, Lohmeier S-J, Feldhoff A, Huber K, Wiebcke M (2009) Rapid room-temperature synthesis and characterization of nanocrystals of a prototypical zeolitic imidazolate framework. Chem Mater 21:1410–1412
88. Rieter WJ, Taylor KML, An H, Lin W, Lin W (2006) Nanoscale metal-organic frameworks as potential multimodal contrast enhancing agents. J Am Chem Soc 128:9024–9025
89. Liu Q, Jin L-N, Sun W-Y (2012) Facile fabrication and adsorption property of a nano/microporous coordination polymer with controllable size and morphology. Chem Commun 48:8814–8816
90. Carné-Sánchez A, Imaz I, Cano-Sarabia M, Maspoch D (2013) A spray-drying strategy for synthesis of nanoscale metal–organic frameworks and their assembly into hollow superstructures. Nat Chem 5:203–211
91. Mueller U, Puetter H, Hesse M, Wessel H (2005) Patent WO 2005/049892

92. Gimeno-Fabra M, Munn AS, Stevens LA, Drage TC, Grant DM, Kashtiban RJ, Sloan J, Lester E, Walton RI (2012) Instant MOFs: continuous synthesis of metal–organic frameworks by rapid solvent mixing. Chem Commun 48:10642–10644
93. Rubio-Martinez M, Batten MP, Polyzos A, Carey K-C, Mardel JI, Lim K-S, Hill MR (2014) Versatile, high quality and scalable continuous flow production of metal-organic frameworks. Sci Rep 4:5443
94. Dunne PW, Munn AS, Starkey CL, Huddle TA, Lester EH (2015) Continuous-flow hydrothermal synthesis for the production of inorganic nanomaterials. Article in Philosophical Transactions of The Royal Society A Mathematical Physical and Engineering Sciences
95. McKinstry C, Cathcart RJ, Cussen EJ, Fletcher AJ, Patwardhan SV, Sefcik J (2016) Scalable continuous solvothermal synthesis of metal organic framework (MOF-5) crystals. Chem Eng J 285:718–725
96. Garzón-Tovar L, Cano-Sarabia M, Carné-Sánchez A, Carbonell C, Imaz I, Maspoch D (2016) A spray-drying continuous-flow method for simultaneous synthesis and shaping of microspherical high nuclearity MOF beads. React Chem Eng 1:533–539
97. Marquez AG, Horcajada P, Grosso D, Ferey G, Serre C, Sanchez C, Boissiere C (2013) Green scalable aerosol synthesis of porous metal–organic frameworks. Chem Commun 49: 3848–3850
98. Crawford D, Casaban J, Haydon R, Giri N, McNally T, James SL (2015) Synthesis by extrusion: continuous, large-scale preparation of MOFs using little or no solvent. Chem Sci 6:1645–1649
99. Reinsch H, Waitschat S, Chavan SM, Lillerud KP, Stock N (2016) A facile "green" route for scalable batch production and continuous synthesis of zirconium MOFs. Eur J Inorg Chem 2016:4490–4498
100. Majano G, Pérez-Ramírez J (2013) Scalable room-temperature conversion of copper(II) hydroxide into HKUST-1 (Cu3(btc)2). Adv Mater 25:1052–1057
101. Huo J, Brightwell M, El Hankari S, Garai A, Bradshaw D (2013) A versatile, industrially relevant, aqueous room temperature synthesis of HKUST-1 with high space-time yield. J Mater Chem A 1:15220–15223
102. Cho H-Y, Kim J, Kim S-N, Ahn W-S (2013) High yield 1-L scale synthesis of ZIF-8 via a sonochemical route. Microporous Mesoporous Mater 169:180–184
103. Ferreira AFP, Santos JC, Plaza MG, Lamia N, Loureiro JM, Rodrigues AE (2011) Suitability of Cu-BTC extrudates for propane–propylene separation by adsorption processes. Chem Eng J 167:1–12
104. Ren J, Musyoka NM, Langmi HW, Swartbooi A, North BC, Mathe M (2015) A more efficient way to shape metal-organic framework (MOF) powder materials for hydrogen storage applications. Int J Hydrog Energy 40:4617–4622
105. Moitra N, Fukumoto S, Reboul J, Sumida K, Zhu Y, Nakanishi K, Furukawa S, Kitagawa S, Kanamori K (2015) Mechanically stable, hierarchically porous Cu3(btc)2 (HKUST-1) monoliths via direct conversion of copper(II) hydroxide-based monoliths. Chem Commun 51:3511–3514
106. Czaja AU, Trukhan N, Muller U (2009) Industrial applications of metal–organic frameworks. Chem Soc Rev 38:1284–1293
107. Silva P, Vilela SMF, Tomé JPC, Paz FAA (2015) Multifunctional metal–organic frameworks: from academic to industrial applications. Chem Soc Rev 44:6774–6803
108. Zacher D, Shekhah O, Wöll C, Fischer RA (2009) Thin films of metal–organic frameworks. Chem Soc Rev 38:1418–1429
109. Shekhah O, Liu J, Fischer RA, Woll C (2011) MOF thin films: existing and future applications. Chem Soc Rev 40:1081–1106
110. Zacher D, Schmid R, Woll C, Fischer RA (2011) Surface chemistry of metal–organic frameworks at the liquid–solid Interface. Angew Chem Int Ed 50:176–199
111. Bradshaw D, Garai A, Huo J (2012) Metal–organic framework growth at functional interfaces: thin films and composites for diverse applications. Chem Soc Rev 41:2344–2381

112. Tsotsalas M, Umemura A, Kim F, Sakata Y, Reboul J, Kitagawa S, Furukawa S (2012) Crystal morphology-directed framework orientation in porous coordination polymer films and freestanding membranes via Langmuir–Blodgettry. J Mater Chem 22:10159–10165
113. Stassen I, Styles M, Grenci G, Gorp HV, Vanderlinden W, De Feyter S, Falcaro P, De Vos D, Vereecken P, Ameloot R (2015) Chemical vapour deposition of zeolitic imidazolate framework thin films. Nat Mat 15:304–310
114. Toyao T, Liang K, Okada K, Ricco R, Styles MJ, Tokudome Y, Horiuchi Y, Hill AJ, Takahashi M, Matsuoka M, Falcaro P (2015) Positioning of the HKUST-1 metal–organic framework ($Cu_3(BTC)_2$) through conversion from insoluble Cu-based precursors. Inorg Chem Front 2:434–441
115. Li Y-S, Bux H, Feldhoff A, Li G-L, Yang W-S, Caro J (2010) Controllable synthesis of metal–organic frameworks: from MOF Nanorods to oriented MOF membranes. Adv Mater 22: 3322–3326
116. Qiu S, Xue M, Zhu G (2014) Metal-organic framework membranes: from synthesis to separation application. Chem Soc Rev 43:6116–6140
117. Kong L, Zhang X, Liu Y, Li S, Liu H, Qiu J, Yeung KL (2014) In situ fabrication of high-permeance ZIF-8 tubular membranes in a continuous flow system. Mater Chem Phys 148: 10–16
118. Aguilera-Sigalat J, Bradshaw D (2016) Synthesis and applications of metal-organic framework-quantum dot (QD@MOF) composites. Coord Chem Rev 307:267–291
119. Liang K, Carbonell C, Styles MJ, Ricco R, Cui J, Richardson JJ, Maspoch D, Caruso F, Falcaro P (2015) Biomimetic replication of microscopic metal–organic framework patterns using printed protein patterns. Adv Mater 27:7293–7298
120. Zhu Q-L, Xu Q (2014) Metal–organic framework composites. Chem Soc Rev 43:5468–5512
121. Ricco R, Malfatti L, Takahashi M, Hillad AJ, Falcaro P (2013) Applications of magnetic metal–organic framework composites. J Mater Chem A 1:13033–13045
122. Ahmed I, Jhung SH (2014) Composites of metal–organic frameworks: preparation and application in adsorption. Mater Today 17:136–146
123. Zornoza B, Tellez C, Coronas J, Gascon J, Kapteijn F (2013) Metal organic framework based mixed matrix membranes: an increasingly important field of research with a large application potential. Microporous Mesoporous Mater 166:67–78
124. Baxter EF, Bennett TD, Mellot-Draznieks C, Gervais C, Blanc F, Cheetham AK (2015) Combined experimental and computational NMR study of crystalline and amorphous zeolitic imidazolate frameworks. Phys Chem Chem Phys 17:25191–25196
125. Mazaj M, Kaucic V, Logar NZ (2016) Chemistry of metal-organic frameworks monitored by advanced X-ray diffraction and scattering techniques. Acta Chim Slov 63:440–458
126. Bordiga S, Bonino F, Lillerud KP, Lamberti C (2010) X-ray absorption spectroscopies: useful tools to understand metallorganic frameworks structure and reactivity. Chem Soc Rev 39:4885–4927
127. Suga M, Asahina S, Sakuda Y, Kazumori H, Nishiyama H, Nokuo T, Alfredsson V, Kjellman T, Stevens SM, Cho HS, Cho M, Han L, Che S, Anderson MW, Schüth F, Deng H, Yaghi OM, Liu Z, Jeong HY, Stein A, Sakamoto K, Ryoo R, Terasaki O (2014) Recent progress in scanning electron microscopy for the characterization of fine structural details of nano materials. Prog Solid State Chem 42:1–21
128. Wiktor C, Turner S, Zacher D, Fischer RA, Tendeloo GV (2012) Imaging of intact MOF-5 nanocrystals by advanced TEM at liquid nitrogen temperature. Microporous and Mesoporous Mater 162:131–135
129. Mu B, Walton KS (2011) Thermal analysis and heat capacity study of metal-organic frameworks. J Phys Chem C 115:22748–22754
130. Wang TC, Bury W, Gómez-Gualdrón DA, Vermeulen NA, Mondloch JE, Deria P, Zhang K, Moghadam PZ, Sarjeant AA, Snurr RQ, Stoddart JF, Hupp JT, Farha OK (2015) Ultrahigh surface area zirconium MOFs and insights into the applicability of the BET theory. J Am Chem Soc 137:3585–3591
131. Thommes M, Kaneko K, Neimark AV, Olivier JP, Rodriguez-Reinoso F, Rouquerol J, Sing KSW (2015) Physisorption of gases, with special reference to the evaluation of surface area and pore size distribution (IUPAC technical report). Pure Appl Chem 87(1-19):1051–1069

132. Singh M, Kumar D, Thomas J, Ramanan A (2010) Crystallization of copper(II) sulfate based minerals and MOF from solution: chemical insights into the supramolecular interactions. J Chem Sci 122:757–769
133. Millange F, Medina MI, Guillou N, Ferey G, Golden KM, Walton RI (2010) Time-resolved in situ diffraction study of the Solvothermal crystallization of some prototypical metal–organic frameworks. Angew Chem Int Ed 49:763–766
134. Zahn G, Zerner P, Lippke J, Kempf FL, Lilienthal S, Schröder CA, Schneider AM, Behrens P (2014) Insight into the mechanism of modulated synthesis: in situ synchrotron diffraction studies on the formation of Zr-fumarate MOF. Cryst Eng Comm 16:9198–9207
135. Shoaee M, Anderson MW, Attfield MP (2008) Crystal growth of the Nanoporous metal–organic framework HKUST-1 revealed by in situ atomic force microscopy. Angew Chem Int Ed 47:8525–8528
136. Patterson JP, Abellan P, Denny MS Jr, Park C, Browning ND, Cohen SM, Evans JE, Gianneschi NC (2015) Observing the growth of metal–organic frameworks by in situ liquid cell transmission electron microscopy. J Am Chem Soc 137:7322–7328
137. Bai Y, Dou Y, Xie L-H, Rutledge W, Li J-R, Zhou H-C (2016) Zr-based metal–organic frameworks: design, synthesis, structure, and applications. Chem Soc Rev 45:2327–2367
138. Kuppler RJ, Timmons DJ, Fang Q-R, Li J-R, Makal TA, Young MD, Yuan D, Zhao D, Zhuang W, Zhou H-C (2009) Potential applications of metal-organic frameworks. Coord Chem Rev 253:3042–3066
139. Rowsell JLC, Spencer EC, Eckert J, Howard JAK, Yaghi OM (2005) Gas adsorption sites in a large-pore metal-organic framework. Science 309:1350–1354
140. Millward AR, Yaghi OM (2005) Metal-organic frameworks with exceptionally high capacity for storage of carbon dioxide at room temperature. J Am Chem Soc 127:17998–17999
141. Dinca M, Long JR (2008) Hydrogen storage in microporous metal–organic frameworks with exposed metal sites. Angew Chem Int Ed 47:6766–6779
142. Yan Y, Blake AJ, Lewis W, Barnett SA, Dailly A, Champness NR, Schroder M (2011) Modifying cage structures in metal–organic polyhedral frameworks for H_2 storage. Chem Eur J 17:11162–11170
143. Schlichtenmayer M, Hirscher M (2012) Nanosponges for hydrogen storage. J Mater Chem 22:10134–10143
144. Liu J, Thallapally PK, McGrail BP, Brown DR, Liu J (2012) Progress in adsorption-based CO_2 capture by metal–organic frameworks. Chem Soc Rev 41:2308–2322
145. Barea E, Montoro C, Navarro JAR (2014) Toxic gas removal – metal–organic frameworks for the capture and degradation of toxic gases and vapours. Chem Soc Rev 43:5419–5430
146. Sabouni R, Kazemian H, Rohani S (2014) Carbon dioxide capturing technologies: a review focusing on metal organic framework materials (MOFs). Environ Sci Pollut Res 21: 5427–5449
147. He Y, Zhou W, Qian G, Chen B (2014) Methane storage in metal–organic frameworks. Chem Soc Rev 43:5657–5678
148. Stoeck U, Senkovska I, Bon V, Krause S, Kaskel S (2015) Assembly of metal–organic polyhedra into highly porous frameworks for ethene delivery. Chem Commun 51:1046–1049
149. Koh HS, Rana MK, Wong-Foy AG, Siegel DJ (2015) Predicting methane storage in open-metal-site Metal ─ Organic frameworks. J Phys Chem C 119:13451–13458
150. Banerjee D, Cairns AJ, Liu J, Motkuri RK, Nune SK, Fernandez CA, Krishna R, Strachan DM, Thallapally PK (2015) Potential of Metal ─ Organic frameworks for separation of xenon and krypton. Acc Chem Res 48:211–219
151. Liu B (2012) Metal–organic framework-based devices: separation and sensors. J Mater Chem 22:10094–10101
152. Lee CY, Bae Y-S, Jeong NC, Farha OK, Sarjeant AA, Stern CL, Nickias P, Snurr RQ, Hupp JT, Nguyen ST (2011) Kinetic separation of propene and propane in metal-organic frameworks: controlling diffusion rates in plate-shaped crystals via tuning of pore apertures and crystallite aspect ratios. J Am Chem Soc 133:5228–5231

153. Chen YF, Lee JY, Babarao R, Li J, Jiang JW (2010) A highly hydrophobic metal-organic framework Zn(BDC)(TED)$_{0.5}$ for adsorption and separation of CH_3OH/H_2O and CO_2/CH_4: an integrated experimental and simulation study. J Phys Chem C 114:6602–6609
154. Liu J, Chen L, Cui H, Zhang J, Zhang L, Su C-Y (2014) Applications of metal–organic frameworks in heterogeneous supramolecular catalysis. Chem Soc Rev 43:6011–6061
155. Valvekens P, Vermoortele F, De Vos D (2013) Metal–organic frameworks as catalysts: the role of metal active sites. Cat Sci Technol 3:1435–1445
156. Dhakshinamoorthy A, Opanasenko M, Cejka J, Garcia H (2013) Metal organic frameworks as heterogeneous catalysts for the production of fine chemicals. Cat Sci Technol 3:2509–2540
157. Ranocchiari M, van Bokhoven JA (2011) Catalysis by metal–organic frameworks: fundamentals and opportunities. Phys Chem Chem Phys 13:6388–6396
158. Corma A, García H, Llabrés i Xamena FX (2010) Engineering metal organic frameworks for heterogeneous catalysis. Chem Rev 110:4606–4655
159. Kurmoo M (2009) Magnetic metal–organic frameworks. Chem Soc Rev 38:1353–1379
160. Ferrando-Soria J, Ruiz-García R, Cano J, Stiriba S-E, Vallejo J, Castro I, Julve M, Lloret F, Amorós P, Pasán J, Ruiz-Pérez C, Journaux Y, Pardo E (2012) Reversible Solvatomagnetic switching in a spongelike manganese(II)–copper(II) 3D open framework with a Pillared Square/octagonal layer architecture. Chem Eur J 18:1608–1617
161. Dhakshinamoorthy A, Asiri AM, García H (2016) Metal–Organic Framework (MOF) compounds: photocatalysts for redox reactions and solar fuel production. Angew Chem Int Ed 55:5414–5445
162. Mondloch JE, Katz MJ, Isley WC III, Ghosh P, Liao P, Bury W, Wagner GW, Hall MG, DeCoste JB, Peterson GW, Snurr RQ, Cramer CJ, Hupp JT, Farha OK (2015) Destruction of chemical warfare agents using metal–organic frameworks. Nat Mater 14:512–516
163. Li N, Zhu Q, Yang Y, Huang J, Dang X, Chen H (2015) A novel dispersive solid-phase extraction method using metal-organic framework MIL-101 as the adsorbent for the analysis of benzophenones in toner. Talanta 132:713–718
164. Ramaswamy P, Wonga NE, Shimizu GKH (2014) MOFs as proton conductors – challenges and opportunities. Chem Soc Rev 43:5913–5932
165. Kreno LE, Leong K, Farha OK, Allendorf M, Duyne RPV, Hupp JT (2012) Metal-organic framework materials as chemical sensors. Chem Rev 112:1105–1125
166. Gu Z-Y, Yang C-X, Chang N, Yan X-Y (2012) Metal-Organic frameworks for analytical chemistry: from sample collection to chromatographic separation. Acc Chem Res 45: 734–745
167. Park JH, Choi KM, Jeon HJ, Choi YJ, Kang JK (2015) In-situ observation for growth of hierarchical metal-organic frameworks and their self sequestering mechanism for gas storage. Sci Rep 5:12045
168. Bradshaw D, El-Hankari S, Lupica-Spagnolo L (2014) Supramolecular templating of hierarchically porous metal–organic frameworks. Chem Soc Rev 43:5431–5443
169. Senkovska I, Kaskel S (2014) Ultrahigh porosity in mesoporous MOFs: promises and limitations. Chem Commun 50:7089–7098
170. Song L, Zhang J, Sun L, Xu F, Li F, Zhang H, Si X, Jiao C, Li Z, Liu S, Liu Y, Zhou H, Sun D, Du Y, Caoh Z, Gabelica Z (2012) Mesoporous metal–organic frameworks: design and applications. Energy Environ Sci 5:7508–7520
171. Xuan W, Zhu C, Liu Y, Cui Y (2012) Mesoporous metal–organic framework materials. Chem Soc Rev 41:1677–1695
172. Ahmed A, Hodgson N, Barrow M, Clowes R, Robertson CM, Steiner A, McKeown P, Bradshaw D, Myersa P, Zhang H (2014) Macroporous metal–organic framework microparticles with improved liquid phase separation. J Mater Chem A 2:9085–9090
173. Li T, Kozlowski MT, Doud EA, Blakely MN, Rosi NL (2013) Stepwise ligand exchange for the preparation of a family of mesoporous MOFs. J Am Chem Soc 135:11688–11691
174. Deng H, Grunder S, Cordova KE, Valente C, Furukawa H, Hmadeh M, Gándara F, Whalley AC, Liu Z, Asahina S, Kazumori H, O'Keeffe M, Terasaki O, Stoddart JF, Yaghi OM (2012) Large-pore apertures in a series of metal-organic frameworks. Science 336:1018–1023

175. Chen B, Eddaoudi M, Hyde ST, O'Keeffe M, Yaghi OM (2001) Interwoven metal-organic framework on a periodic minimal surface with extra-large pores. Science 291:1021–1023
176. Shekhah O, Wang H, Paradinas M, Ocal C, Schüpbach B, Terfort A, Zacher D, Fischer RA, Wöll C (2009) Controlling interpenetration in metal–organic frameworks by liquid-phase epitaxy. Nat Mater 8:481–484
177. Farha OK, Malliakas CD, Kanatzidis MG, Hupp JT (2010) Control over catenation in metal-organic frameworks via rational design of the organic building block. J Am Chem Soc 132:950–952
178. Seoane B, Dikhtiarenko A, Mayoral A, Tellez C, Coronas J, Kapteijna F, Gascon J (2015) Metal organic framework synthesis in the presence of surfactants: towards hierarchical MOFs? CrystEngComm 17:1693–1700
179. Zhao Y, Zhang J, Han B, Song J, Li J, Wang Q (2011) Metal–organic framework Nanospheres with well-ordered mesopores synthesized in an ionic liquid/CO_2/surfactant system. Angew Chem Int Ed 50:636–639
180. Qiu L-G, Xu T, Li Z-Q, Wang W, Wu Y, Jiang X, Tian X-Y, Zhang L-D (2008) Hierarchically micro- and mesoporous metal–organic frameworks with tunable porosity. Angew Chem Int Ed 47:9487–9491
181. Deng H, Doonan CJ, Furukawa H, Ferreira RB, Towne J, Knobler CB, Wang B, Yaghi OM (2010) Multiple functional groups of varying ratios in metal-organic frameworks. Science 327:846–850
182. Kong X, Deng H, Yan F, Kim J, Swisher JA, Smit B, Yaghi OM, Reimer JA (2013) Mapping of functional groups in metal-organic frameworks. Science 341:882–885
183. Cohen SM (2012) Postsynthetic methods for the functionalization of metal–organic frameworks. Chem Rev 112:970–1000
184. Deria P, Mondloch JE, Karagiaridi O, Bury W, Hupp JT, Farha OK (2014) Beyond post-synthesis modification: evolution of metal–organic frameworks via building block replacement. Chem Soc Rev 43:5896–5912
185. Cohen SM (2010) Modifying MOFs: new chemistry, new materials. Chem Sci 1:32–36
186. Karagiaridi O, Bury W, Mondloch JE, Hupp JT, Farha OK (2014) Solvent-assisted linker exchange: an alternative to the de novo synthesis of unattainable metal–organic frameworks. Angew Chem Int Ed 53:4530–4540
187. Evans JD, Sumby CJ, Doonan CJ (2014) Post-synthetic metalation of metal–organic frameworks. Chem Soc Rev 43:5933–5951
188. Brozek CK, Dinca M (2014) Cation exchange at the secondary building units of metal–organic frameworks. Chem Soc Rev 43:5456–5467
189. Han Y, Li J-R, Xie Y, Guo G (2014) Substitution reactions in metal–organic frameworks and metal–organic polyhedra. Chem Soc Rev 43:5952–5981
190. Juan-Alcaniz J, Gascon J, Kapteijn F (2012) Metal–organic frameworks as scaffolds for the encapsulation of active species: state of the art and future perspectives. J Mater Chem 22:10102–10118
191. Esken D, Turner S, Lebedev OI, Van Tendeloo G, Fischer RA (2010) Au@ZIFs: stabilization and encapsulation of cavity-size matching gold clusters inside functionalized zeolite imidazolate frameworks, ZIFs. Chem Mater 22:6393–6401
192. Lu G, Li S, Guo Z, Farha OK, Hauser BG, Qi X, Wang Y, Wang X, Han S, Liu X, DuChene JS, Zhang H, Zhang Q, Chen X, Ma J, Loo SCJ, Wei WD, Yang Y, Hupp JT, Huo F (2012) Imparting functionality to a metal–organic framework material by controlled nanoparticle encapsulation. Nat Chem 4:310–316
193. Horcajada P, Gref R, Baati T, Allan PK, Maurin G, Couvreur P, Férey G, Morris RE, Serre C (2012) Metal-organic frameworks in biomedicine. Chem Rev 112:1232–1268
194. Imaz I, Rubio-Martínez M, An J, Solé-Font I, Rosi NL, Maspoch D (2011) Metal–biomolecule frameworks (MBioFs). Chem Commun 47:7287–7302
195. Lanchas M, Arcediano S, Beobide G, Castillo O, Luque A, Pérez-Yáñez S (2015) Towards multicomponent MOFs via solvent-free synthesis under conventional oven and microwave assisted heating. Inorg Chem Front 2:425–433

196. Rieter WJ, Pott KM, Taylor KML, Lin W (2008) Nanoscale coordination polymers for platinum-based anticancer drug delivery. J Am Chem Soc 130:11584–11585
197. Huxford RC, Rocca JD, Lin W (2010) Metal–organic frameworks as potential drug carriers. Curr Opin Chem Biol 14:262–268
198. Ummadi S, Shravani B, Rao NGR, Reddy MS, Nayak BS (2013) Overview on controlled release dosage form. Int J Pharma Sci 3:258–269
199. Miller SR, Heurtaux D, Baati T, Horcajada P, Grenèche J-M, Serre C (2010) Biodegradable therapeutic MOFs for the delivery of bioactive molecules. Chem Commun 46:3634–3640
200. Tamames-Tabar C, Imbuluzqueta E, Guillou N, Serre C, Miller SR, Elkaïm E, Horcajada P, Blanco-Prieto MJ (2015) A Zn azelate MOF: combining antibacterial effect. Cryst Eng Comm 17:456–462
201. Cooper L, Hidalgo T, Gorman M, Lozano-Fernández T, Simón-Vázquez R, Olivier C, Guillou N, Serre C, Martineau C, Taulelle F, Damasceno-Borges D, Maurin G, González-Fernández A, Horcajada P, Devic T (2015) A biocompatible porous Mg-gallate metal-organic framework as an antioxidant carrier. Chem Commun 51:5848–5851
202. Miller SR, Heurtaux D, Baati T, Horcajada P, Grenèche J-M, Serre S (2010) Biodegradable therapeutic MOFs for the delivery of bioactive molecules. Chem Commun 46:4526–4528
203. Su H, Sun F, Jia J, He H, Wanga A, Zhu G (2015) A highly porous medical metal-organic framework constructed from bioactive curcumin. Chem Commun 51:5774–5777
204. Tan L-L, Song N, Zhang SX-A, Li H, Wang B, Yang Y-W (2016) Ca^{2+}, pH and thermos triple-responsive mechanized Zr-based MOFs for on-command drug release in bone diseases. J Mater Chem B 4:135–140
205. Ma D-Y, Li Z, Xiao J-X, Deng R, Lin P-F, Chen R-Q, Liang Y-Q, Guo H-F, Liu B, Liu J-Q (2015) Hydrostable and Nitryl/methyl-functionalized metal–organic framework for drug delivery and highly selective CO2 adsorption. Inorg Chem 54:6719–6726
206. Liu J-Q, Li X-F, Gu C-Y, Silva JCS, Barros AL, Alves-Jr S, Li B-H, Ren F, Batten SR, Soares TA (2015) A combined experimental and computational study of novel nanocage-based metal–organic frameworks for drug delivery. Dalton Trans 44:19370–19382
207. Li Q-L, Wang J-P, Liu W-C, Zhuang X-Y, Liu J-Q, Fan G-L, Li B-H, Lin W-N, Man J-H (2015) A new (4,8)-connected topological MOF as potential drug delivery. Inorg Chem Commun 55:8–10
208. Bag PP, Wang D, Chen Z, Cao R (2016) Outstanding drug loading capacity by water stable microporous MOF: a potential drug carrier. Chem Commun 52:3669–3672
209. Liu K, Gao Y, Liu J, Wen Y, Zhao Y, Zhang K, Yu G (2016) Photoreactivity of metal − organic frameworks in aqueous solutions: metal dependence of reactive oxygen species production. Environ Sci Technol 50:3634–3640
210. Hu Q, Yu J, Liu M, Liu A, Dou Z, Yang Y (2014) A low cytotoxic cationic metal − organic framework carrier for controllable drug release. J Med Chem 57:5679–5685
211. Motakef-Kazemi N, Shojaosadati SA, Morsali A (2014) In situ synthesis of a drug-loaded MOF at room temperature. Microporous Mesoporous Mater 186:73–79
212. Horcajada P, Serre C, Maurin G, Ramsahye NA, Balas F, Vallet-Regí M, Sebban M, Taulelle F, Férey G (2008) Flexible porous metal-organic frameworks for a controlled drug delivery. J Am Chem Soc 130:6774–6780
213. An J, Geib SJ, Rosi NL (2009) Cation-triggered drug release from a porous zinc-Adeninate metal-organic framework. J Am Chem Soc 131:8376–8377
214. Allendorf MD, Bauer CA, Bhakta RK, Houk RJT (2009) Luminescent metal–organic frameworks. Chem Soc Rev 38:1330–1352
215. Perry JJ IV, Feng PL, Meek ST, Leong K, Doty FP, Allendorf MD (2012) Connecting structure with function in metal–organic frameworks to design. J Mater Chem 22:10235–10248
216. Čejka J (2001) Metal-organic frameworks: applications from catalysis to gas storage. Farrusseng D (ed) Wiley-VCH Verlag GmbH & Co. KGaA, Weinheim
217. Zhang X, Wang W, Hu Z, Wang G, Uvdal K (2015) Coordination polymers for energy transfer: preparations, properties, sensing applications, and perspectives. Coord Chem Rev 284:206–235

218. Alpha B, Ballardini R, Balzani V, Lehn J-M, Perathoner S, Sabbatini N (1990) Antenna effect in luminescent lanthanide cryptates: a photophysical study. Photochem Photobiol 52: 299–306
219. Dang S, Zhang J-H, Sun Z-M (2012) Tunable emission based on lanthanide(III) metal–organic frameworks: an alternative approach to white light. J Mater Chem 22:8868
220. T.de. Lill D, Tareila AM, Cahill CL (2009) Synthesis, structure, and luminescence of a two-dimensional lanthanide(III)-suberate coordination polymer resulting from dimeric secondary building units. Inorg Chem Commun 12:191–194
221. Zhu W-H, Wang Z-M, Gao S (2007) Two 3D porous Lanthanide − Fumarate − Oxalate frameworks exhibiting framework dynamics and luminescent change upon reversible de- and rehydration. Inorg Chem 46:1337–1342
222. Zhang L-Z, Gu W, Li B, Liu X, Liao D-Z (2007) $\{[Nd_4(ox)_4(NO_3)_2(OH)_2(H_2O)_2]\cdot 5H_2O\}_n$: a porous 3D lanthanide-based coordination polymer with a special luminescent property. Inorg Chem 46:622–624
223. Dang S, Zhang JH, Sun ZMH (2012) Luminescent lanthanide metal–organic frameworks with a large SHG response. Chem Commun 48:11139–11141
224. White KA, Chengelis DA, Zeller M, Geib SJ, Szakos J, Petoud S, Rosi NL (2009) Near-infrared emitting ytterbium metal–organic frameworks with tunable excitation properties. Chem Commun 45:4506
225. Hasegawa Y, Nakanishi T (2015) Luminescent lanthanide coordination polymers for photonic applications. RSC Adv 5:338
226. Roy S, Chakraborty A, Maji TK (2014) Lanthanide–organic frameworks for gas storage and as magneto-luminescent materials. Coord Chem Rev 273−274:139–164
227. Cui Y, Chen B, Qian G (2014) Lanthanide metal-organic frameworks for luminescent sensing and light-emitting applications. Coord Chem Rev 273-274:76–86
228. Cui Y, Chen B, Qian G (2013) Lanthanide metal-organic frameworks for luminescent sensing and light emitting applications. Coord Chem Rev 273–274:76–86
229. Zhao D, Cui Y, Yang Y, Qian G (2016) Sensing-functional luminescent metal–organic frameworks. CrystEngComm 18:3746
230. Banerjee D, Hu Z, Li J (2014) Luminescent metal–organic frameworks as explosive sensors. Dalton Trans 43:10668
231. Hu Z, Deibert BJ, Li J (2014) Luminescent metal–organic frameworks for chemical sensing and explosive detection. Chem Soc Rev 43:5815–5840
232. Miller SE, Teplensky MH, Moghadam PZ, Fairen-Jimenez D (2016) Metal-organic frameworks as biosensors for luminescence-based detection and imaging. Interface Focus 6:20160027
233. Liu D, Lu K, Poon C, Lin W (2014) Metal − organic frameworks as sensory materials and imaging agents. Inorg Chem 53:1916–1924
234. Xu H, Liu F, Cui Y, Chen B, Qian G (2011) A luminescent nanoscale metal–organic framework for sensing of nitroaromatic explosives. Chem Commun 47:3153–3155
235. Guan W, Zhou W, Lu J, Lu C (2015) Luminescent films for chemo- and biosensing. Chem Soc Rev 44:6981–7009
236. Shen X, Lu Y, Yan B (2015) Lanthanide complex hybrid system for fluorescent sensing as thermometer. Eur J Inorg Chem 2015:916–919
237. Lu Y, Yan B (2014) A ratiometric fluorescent pH sensor based on nanoscale metal–organic frameworks (MOFs) modified by europium(III) complexes. Chem Commun 50:13323
238. Amoroso AJ, Pope SJA (2015) Using lanthanide ions in molecular bioimaging. Chem Soc Rev 44:4723–4742
239. Foucault-Collet A, Gogick KA, White KA, Villette S, Pallier A, Collet G, Kieda C, Li T, Geib SJ, Rosi NL, Petoud S (2013) Lanthanide near infrared imaging in living cells with Yb^{3+} nano metal organic frameworks. Proc Natl Acad Sci U S A 110:17199–17204
240. Cho W, Lee HJ, Choi S, Kim Y, Oh M (2014) Highly effective heterogeneous chemosensors of luminescent silica@coordination polymer core-shell micro-structures for metal ion sensing. Sci Rep 4:6518

241. Brown TE, LeMay HE, Bursten BE, Murphy C, Woodward P, Stoltzfus ME (2015) Chemistry: the central science, 13th edn. Pearson, Upper Saddle River, 1248p
242. Crane JL, Anderson KE, Conway SG (2015) Hydrothermal synthesis and characterization of a metal–organic framework by Thermogravimetric analysis, powder X-ray diffraction, and infrared spectroscopy: an integrative inorganic chemistry experiment. J Chem Educ 92: 373–377
243. Zhang Z, Nguyen HTH, Miller SA, Cohen SM (2015) polyMOFs: a class of Interconvertible polymer-metal-organic-framework hybrid materials. Angew Chem Int Ed 54:6152–6157
244. Paz FAA, Klinowski J, Vilela SMF, Tomé JPC, Cavaleiro JAS, Rocha J (2012) Ligand design for functional metal–organic frameworks. Chem Soc Rev 41:1088–1110
245. Eddaoudi M, Sava DF, Eubank JF, Adil K, Guillerm V (2015) Zeolite-like metal–organic frameworks (ZMOFs): design, synthesis, and properties. Chem Soc Rev 44:228–249
246. Mah RK, Gelfand BS, Taylor JM, Shimizu GKH (2015) Reconciling order, stability, and porosity in phosphonate metal–organic frameworks via HF-mediated synthesis. Inorg Chem Front 2:273–277
247. Zhang J-P, Zhang Y-B, Lin J-B, Chen X-M (2012) Metal Azolate frameworks: from crystal engineering to functional materials. Chem Rev 112:1001–1033
248. Park KS, Ni Z, Côté AP, Choi JY, Huang R, Uribe-Romo FJ, Chae HK, O'Keeffe M, Yaghi OM (2006) Exceptional chemical and thermal stability of zeolitic imidazolate frameworks. Proc Natl Acad Sci U S A 103:10186–10191
249. Furukawa S, Reboul J, Diring S, Sumida K, Kitagawa S (2014) Structuring of metal–organic frameworks at the mesoscopic/macroscopic scale. Chem Soc Rev 43:5700–5734
250. Bureekaew S, Shimomura S, Kitagawa S (2008) Chemistry and application of flexible porous coordination polymers. Sci Technol Adv Mater 9:014108
251. Schneemann A, Bon V, Schwedler I, Senkovska I, Kaskel S, Fischer RA (2014) Flexible metal–organic frameworks. Chem Soc Rev 43:6062–6096
252. Mendes RF, Paz FAA (2015) Transforming metal–organic frameworks into functional materials. Inorg Chem Front 2:495–509
253. Kolea GK, Vittal JJ (2013) Solid-state reactivity and structural transformations involving coordination polymers. Chem Soc Rev 42:1755–1775
254. First EL, Floudas CA (2013) MOFomics: computational pore characterization of metal–organic frameworks. Microporous Mesoporous Mate 165:32–39
255. Wilmer CE, Leaf M, Lee CY, Farha OK, Hauser BG, Hupp JT, Snurr RQ (2011) Large-scale screening of hypothetical metal–organic frameworks. Nature Chemistry
256. Chen S, Lucier BEG, Boyle PD, Huang Y (2016) Understanding the fascinating origins of CO_2 adsorption and dynamics in MOFs. Chem Mater 28:5829–5846
257. Zhang J, Shreeve JM (2016) 3D nitrogen-rich metal–organic frameworks: opportunities for safer energetics. Dalton Trans 45:2363–2368
258. Zhao P, Lampronti GI, Lloyd GO, Suard E, Redfern SAT (2014) Direct visualisation of carbon dioxide adsorption in gate-opening zeolitic imidazolate framework ZIF-7. J Mater Chem A 2:620–623
259. Beyzavi MH, Stephenson CJ, Liu Y, Karagiaridi O, Hupp JT, Farha OK (2015) Metal–organic framework-based catalysts: chemical fixation of CO_2 with epoxides leading to cyclic organic carbonates. Front Energy Res 2:1–10
260. Schoedel A, Ji Z, Yaghi OM (2016) The role of metal–organic frameworks in a carbon-neutral energy cycle. Nat Energy 1:16034. doi:10.1038/nenergy.2016.34
261. BASF (2014) Metal Organic Frameworks (MOFs): innovative fuel systems for Natural Gas Vehicles (NGVs). Chem Soc Rev. 43:6173–6174
262. Mason JA, Oktawiec J, Taylor MK, Hudson MR, Rodriguez J, Bachman JE, Gonzalez MI, Cervellino A, Guagliardi A, Brown CM, Llewellyn PL, Masciocchi N, Long JR (2015) Methane storage in flexible metal–organic frameworks with intrinsic thermal management. Nature 527:357–361
263. Peplow M (2015) The hole story. Nature 520:148–150
264. Olson MA (2015) Shuttling in the solid state. Nat Chem 7:470–471

265. Vukotic VN, Harris KJ, Zhu K, Schurko RW, Loeb SJ (2012) Metal–organic frameworks with dynamic interlocked components. Nat Chem 4:456–460
266. Deng H, Olson MA, Stoddart JF, Yaghi OM (2010) Robust dynamics. Nat Chem 2:439–443
267. Li Q, Sue C-H, Basu S, Shveyd AK, Zhang W, Barin G, Fang L, Sarjeant AA, Stoddart JF, Yaghi OM (2010) A Catenated strut in a Catenated metal–organic framework. Angew Chem Int Ed 49:6751–6755
268. Lee S, Kapustin EA, Yaghi OM (2016) Coordinative alignment of molecules in chiral metal-organic frameworks. Science 353:808–811
269. Inokuma Y, Yoshioka S, Ariyoshi J, Arai T, Fujita M (2014) Preparation and guest-uptake protocol for a porous complex useful for 'crystal-free' crystallography. Nat Protoc 9: 246–252
270. Bennett TD, Tan J-C, Yue Y, Baxter E, Ducati C, Terrill NJ, Yeung HH-M, Zhou Z, Chen W, Henke S, Cheetham AK, Greaves GN (2015) Hybrid glasses from strong and fragile metal-organic framework liquids. Nature Commun 6:8079. doi:10.1038/ncomms9079
271. Pachfule P, Shinde D, Majumder M, Xu Q (2016) Fabrication of carbon nanorods and graphene nanoribbons from a metal–organic framework. Nat Chem 8(7):718–724
272. Zhang S, Liu H, Sun C, Liu P, Li L, Yang Z, Feng X, Huo F, Lu X (2015) CuO/Cu_2O porous composites: shape and composition controllable fabrication inherited from metal organic frameworks and further application in CO oxidation. J Mater Chem A 3:5294–5298
273. Jiang J, Zhao Y, Yaghi OM (2016) Covalent chemistry beyond molecules. J Am Chem Soc 138:3255–3265

Part III
Computational Perspectives in Complex Functional Materials

Chapter 15
Review on Simulation Models for Materials and Biomolecular Study and Design

Carlton Anthony Taft and Jose Gabriel Solano Canchaya

1 Introduction

From quantum mechanics, we know that a 3N wave function that obeys the Schrodinger equation (SE) can be used to determine the properties of an N-particle system. However, since the number of atoms of a macroscopic material is on the order of 10^{23}, for a realistic system, it is not trivial to solve SE, i.e., approximations/alternatives become necessary. Hartree eliminated the dimensionality problem of electrons yielding single-electron wave functions in a mean-field approximation for electrons. Since the nuclei are more massive than electrons and move faster, the Hamiltonian can be further simplified, i.e., motion of nuclei can be neglected in the Born-Oppenheimer (BO) approximation. Hartree's method depends on a three-dimensional space instead of a 3N-dimensional space. However, electronic correlation is not taken into account. Incorporating antisymmetry of the wave functions yields the Hartree-Fock (HF) method, whereas pairwise electron-electron repulsion is replaced by the interaction of the i^{th} electron with the average electrostatic field, and an exchange term keeps electrons with the same spin apart. The conceptual framework for chemistry as well as the theoretical foundation of methods that model chemical compound's electronic structure is provided by quantum mechanics [1–8].

In this chapter, we review HF, post-HF (CI, MRCI, CC, MCSCF, CASSCF, MBPT, LMP2, CCSD(T)), semiempirical (Hückel, CNDO, INDO, NDDO, MNDO,

C.A. Taft (✉)
Centro Brasileiro de Pesquisas Físicas, Rua Dr. Xavier Sigaud, Urca, 22290-180, Rio de Janeiro, Brazil
e-mail: catff@terra.com.br

J.G.S. Canchaya
Universidade Católica Santa Maria, Urb. San Jose s/n, Umacol, 51-54382038, 040000, Arequipa, Peru

E. Longo, F.A. La Porta (eds.), *Recent Advances in Complex Functional Materials*,
DOI 10.1007/978-3-319-53898-3_15

AM1, OMx, PM7, RM1), density functional theory ((challenges, LDA, GGA, meta-GGA, hyper-GGA, hybrids, range separation, screened, fitting, adiabatic, local, fifth rung) functionals, random phase approximation, thermochemical data sets, prediction of geometries, reaction barriers and kinetics, hydrogen bonding, response functions, performance of DFA, van der Waals forces, frontier eigenvalues and band gaps, time-dependent DFT, vdW-DF, and new trends), basis sets, plane waves and pseudopotentials, projected augmented plane wave method, generalized plane waves, wavelets, discrete variable representations, augmented and mixed basis sets, Wannier functions and real-space grids, quantum Monte Carlo, ab initio molecular dynamics, quantum mechanics/molecular mechanics, coarse-graining, and multi-scaling. An overview of selected application areas for materials and biomolecular structures, including functional materials is also presented, i.e., dielectrics, capacitors, batteries, superconductors, hydrogen storage, photovoltaics, catalysts, nanomaterials, surface adsorption, and functionalization [1–24].

2 Approaches to Solve the SE

At present, there are three approaches to solve the SE. The first is the quantum-chemical ab initio method that yields a convergent path to exact solutions of quantum-mechanical SE. Nonetheless, these methods are expensive, and for correlated/accurate approaches, they are in general restricted to small molecules. The second method is density functional theory (DFT) with a good performance/price ratio, which yields, for medium-sized molecules, sufficiently accurate calculations. Notwithstanding, the first-principle nature of DFT, the method does not yield a systematic path for improvement. The third method is quantum-chemical semiempirical, which involves parametrizations and approximations, but makes them efficient with the possibility of modeling in a realistic manner larger molecules, but with limited accuracy. The models are also divided into those that depend on wave function theory (WFT) and those that depend on DFT.

3 Valence Bond and Molecular Orbitals

Concepts of valence and bonding are central to understand reactivity and molecular structure, whereas the treatment of molecules via quantum mechanics is necessary. Valence bond (VB) and molecular orbital (MO) theories are two alternatives to explain chemical bonding. VB, chemically intuitive, helps understand chemical concepts based on bond/lone pairs. During the second half of twentieth century, with increasing computer power and programs, the attractive orthogonal MO formalism has become very tractable, in particular, for medium-sized molecules. MO theory is an extension to the molecular regime of the atomic structure. They are delocalized over nuclear framework yielding computationally tractable equations. The linear

combination of atomic orbitals (LCAO) is at the heart of the MO approach. Generating MOs from LCAOs helps understand, from an electronic structure view point, the relationship between atoms and molecules. In VB theory, electron correlation is overemphasized, whereas in simple MO theory it is neglected. In polyatomic molecules, directed valence, based on principle of maximum overlap and valence shell electron pair repulsion (VSEPR) theory, has been successful. Improvements in both VB and MO theories can lead to convergence [23].

4 HF and Post-HF

For polyatomic molecules, MO theories can be classified as electron-independent (non-self-consistent field) and electron-dependent SCF methods. The non-SCF has the possibility of modeling in a realistic manner larger molecules. Hückel's theory only includes π basis, whereas extended Hückel theory includes all valence basis. SCF methods iteratively solve many-electron SE equations in matrix form based on HF theory. They are ab initio when the Fock matrix is constructed from first principles and semiempirical when approximation and parameters are used. The HF method treats interaction of one electron with the average field of other electrons but does not consider instantaneous electrostatic interactions, whereas correlated motions of electrons are neglected, yielding higher energies. Correlation energy is the difference between exact and HF energies. Note that the quantum-mechanical exchange term, i.e., two electrons of same spin cannot occupy a single orbital, is included in HF theory [1].

For a good description of properties and structure of molecules, electron correlation is necessary and thus addressed in post-HF methods, i.e., configuration interaction (CI), multireference CI (MRCI), multiconfiguration SCF (MCSCF), coupled cluster (CC), many-body perturbation theory (MBPT), and complete active space self-consistent field method (CASSCF) [3, 13, 14].

MO theory is improved via configuration interaction (CI), whereas excitation of one or more electrons (single, double, and multiply occupied) configurations can be generated. Slater determinants can be used to describe these excited configurations. In CI methods, we note that HF determines energetically the best determinantal trial wave function which could however be improved with more configurations. Excited configurations can be generated promoting electrons from occupied to virtual orbitals. MRCI uses an expansion of Slater determinants (corresponding to excitation of ground state configurations and some excited states).

Dynamic correlation for closed shell ion addresses instant correlation between electrons occupying same spatial electrons, whereas nondynamic correlation describes electrons avoiding each other by occupying different spatial orbitals. Consequently, one Slater determinant cannot describe the ground state, and MCSCF is necessary. In the MCSF, the MOs construct the determinants whereas coefficients are optimized using the variational principle. The optimization is an iterative-like procedure.

In the CASSCF method, the selections of configurations are performed by partitioning the MOs into inactive and active spaces, whereas the active MOs have some of the lowest unoccupied as well as highly occupied MOs from an HF calculation. Other high virtual orbitals and high stable orbitals constitute the inactive orbitals (doubly occupied or completely unoccupied).

In MBPT, the Hamiltonian operator consists of the unperturbed Hamiltonian and the perturbation term, yielding corrections of various orders. As one increases from zero to finite values, the perturbation, the energy, and wave functions change continuously, which can be written as a Taylor expansion (power of perturbation parameter). Perturbation approaches (MP2, MP3, etc.) were quite powerful/popular QM methods which naturally include dispersion effects. However, they show systematic errors causing unbalance to intermolecular interactions contributions, whereas the accuracy at MP2 level is not guaranteed.

A traditional well-established WFT methods yield reliable accurate results. Correlations (electron-electron) are introduced by many-body wave function (WF) expansions, i.e., single (S), doubly (D), triply (T), etc., excited determinants (using reference wave functions). In full configuration interaction (FCI), all excited determinants are included which yields the best variational results (for given basis set). Due to high computational cost with increasing electrons and basis functions, these calculations are only performed on small systems.

The coupled cluster (CC) theory was constructed for interacting particles system using N-particle excitation operators. Once trial wave functions are expressed as determinant of HF orbitals, one obtains coupled nonlinear equations whose amplitudes are solved by some iteration technique in order to compute the CC energy. This approach emerged as very practical reference method. Consequently, CC with singles, doubles, and perturbative triples has been considered a "gold standard" for many applications (medium systems) although accuracy in large systems have not been confirmed. The CCSD(T) approach extrapolated to complete basis set (CBS) limit, i.e., CCSD(T)/CBC, is accurate for intermolecular interaction energies providing results of chemical accuracy (1 kcal/mol). For small systems with dispersive interactions, it may be necessary to use 0.1 kcal/mol subchemical accuracy.

Other approaches include complete active space with second-order perturbation theory (CASPT2) and LMP2 theory where the Hartree-Fock orbitals are localized to lone pairs and bonds from which electrons are correlated, rather than the Hartree-Fock delocalized canonical orbitals. Electronic structure quantum Monte Carlo (QMC) is a set of methods for solving the stationary Schrodinger equations using sampling of wave functions in the space of electron positions and usage of stochastic processes. This approach also indicates basis set-based limitations.

At this point, it is noteworthy that DFT reasonably includes electron correlation at a fractional cost of typical post-HF methods previously discussed.

5 Basis Sets

After selection of methods, it is necessary to represent the orbitals by basis sets, i.e., a linear combination of functions, which can represent exactly any reasonable function (limit of complete base set). Quantum chemists have used Slater-type orbitals (STOs) with a radial part that is exponentially decaying as well as Gaussian-type orbitals (GTOs), which is widely used in software. The coefficients of the linear expansions are fixed, and only the orbital expansion coefficients are optimized. Fixed linear combinations of these primitives can define angular momentum (contracted basis sets). Slater/Gaussian sets are centered at nuclei (atoms) leading to linear combination of atomic orbitals (LCAO). WF methods, unfortunately, have known imitations. The correlation energy converges slowly with size of one-particle atomic basis sets. There are often basis sets superposition and incompleteness errors. For benchmark calculations, large basis sets (augmented with diffuse basis functions) are often necessary [1, 24].

6 Plane Waves and Pseudopotentials

In order to solve the many-body problem SE (with large number of ions and electrons) more simplifications are required for practical purposes. Taking advantage of symmetry and periodicity of solid structures is one route. In addition, core electrons are typically not involved in bonding making it advantageous to write the MO in terms of plane waves with the periodicity of the crystal structure. Plane waves are rooted in solid-state theory, whereas the periodicity of the lattice yields a periodic potential, imposed on the density (Bloch's theorem). Forming a complete and orthonormal set of functions, plane waves can be used to expand orbitals where labeling can be given by vectors in reciprocal space yielding simple forms for total electronic energy and gradients. It is noteworthy that plane waves do not depend on the positions of the nuclei and are delocalized in space not favoring specific atoms or regions. To improve quality of basis set, it is necessary to increase the cutoff energy (largest reciprocal vector included in the finite expansion). Plane waves also have advantages with delocalized electrons. A plane wave basis is a lattice-symmetry-adapted three-dimensional Fourier decomposition of the orbitals. Consequently, ever larger Fourier components are necessary to solve structures in real space with decreasing small distance scales.

Core electrons can be considered inert and thus removed explicitly. Actually, they can also be represented by smooth modeless effective potential (effective core potentials, ECPs), i.e., the pseudopotential which yields pseudo-wave functions representing valence electrons close to the nuclear core region as smoothly as possible. Nonetheless, properties that depend essentially on wave function close to core are not obtained in a straightforward manner. Valence wave functions are highly oscillatory inside core region where many terms are required for their

expansion. This leads to the usage of so-called pseudo-wave functions for valence states (replacing true all-electron wave functions). However, this method is subject to transferability errors and information on the all-electron wave function in the core region is lost [4].

7 Plane Wave Methods

In order to address pseudopotential method drawbacks, powerful techniques were introduced for plane wave calculations, i.e., "soft" norm-conserving ab initio pseudopotentials, ultrasoft pseudopotentials, and the projector augmented wave (PAW) method. The PAW method uses operators to map a smooth auxiliary wave function into the true all-electron single-particle wave function. The wave functions are decomposed into one with rapid oscillations acting only at nucleus and another that is smooth everywhere. Although each part is treated separately, information about the core region is not lost, and the all-electron wave function can at any time be retrieved [4, 25].

The above methods led to important approaches for plane wave/pseudopotential electronic structure calculation using the DFT framework. It is noteworthy, however, that for the plane waves, it may be difficult to put more required basis functions in regions of space where they are needed such as in systems with strong inhomogeneity. For some cases, an enormous cutoff parameter may be needed whereas only a few regions in real space would suffice.

8 Generalized Plane Waves

A generalization of the plane wave concept is obtained by defining them in curved space yielding orthonormal functions that form a complete basis set and used for reciprocal point sampling. As a result, the density of grid points (cutoff energy) is now highest in regions close to nuclei and lowest in vacuum regions. For a given accuracy, a lower number of generalized plane waves are required allowing even all-electron electronic structure calculations where the simple plane wave fails. Other methods consider the distortion of the metric frozen spherically around atoms via deformation functionals leading to nonuniform atom-centered meshes in real-space methods. In such approaches, locally adaptive models based on predefined coordinate transformations are used for Pulay force contributions evaluated explicitly. Freely floating Gaussians can also be used, which are distributed in space forming an originless basis set (not atom fixed/localized) [25].

9 Wavelets and Discrete Variable Representations

Similar to generalized plane waves are powerful multiscale properties of wavelets which allows exploitation of multiple length scales without introducing Pulay forces (handled efficiently by wavelet transformation). They also count on powerful routes to linear scaling. The discrete variable representation (DVR) approach consists of using continuous functions which satisfy properties of eigenfunction positions on an auxiliary grid yielding high localization about the auxiliary grid points. Plane waves are simple but lack the spatial bias of Gaussian basis sets which eliminates the problem of delocalization at the expense of increased complexity. However, DVR can be well localized about points on the grid with basis functions that satisfy orthogonality and completeness relations and constructed for simple basis functions according to boundary conditions [4, 25, 26].

10 Mixed Basis Sets

There are two extremes: plane waves on one hand and localized Gaussian basis function on the other, yielding considerable long-standing efforts to combine/exploit the mutual strengths of these approaches. The projector augmented wave method maps a smooth auxiliary wave function into true all-electron wave function using operators which yields highly oscillatory wave functions into components that contains rapid oscillations smooth and continuous everywhere as well as a contribution with rapid oscillations only in the core region for each atom. For the PAW method, for example, each part can be treated separately. Plane waves could represent delocalized wave functions. Centered radial grids (Gaussians, Bessel functions, polynomials) can be used for localized contributions. One does not lose information about core region, and all-electron wave functions can be retrieved [4, 25].

11 Wannier Functions and Real-Space Grids

For periodic solid-state theory calculations, Wannier functions can be of interest since they are formally obtained from a unitary transformation of Bloch orbitals and can be, under circumstances, localized exponentially and proven useful for electronic structure calculations. The generalized Wannier functions (maximally localized) are periodic analogs of Boys' localized orbitals for isolated systems [27].

A completely different approach consists of using real-space methods in which continuous space is substituted by discrete space whereas the derivative operator and total energy expression are discretized in some way. A number of real-space approaches have been devised including finite difference approximation with equally spaced cubic meshes in real space, nonuniform meshes, multigrid

acceleration, discretization techniques, and finite element methods. In real-space methods, we can exploit the nearsightedness of electronic matter for linear scaling, whereas the multiple length scale problem can be addressed by hierarchically adapting the grid in framework of multigrid methods [28].

12 Intermolecular Interactions

Noncovalent interactions are important in areas such as materials science, chemistry, biology, and drug design. These are weak interactions, i.e., with minimum changes in the electronic structures and geometries of the individual components. Hydrogen bonding and stacking (π-π interactions) are the most studied as they play very important roles in biochemical systems. Other noncovalent interactions identified include sigma-hole interaction, halogen bond, blue-shifting hydrogen bond, and anion-/cation-π interaction. These nonbonding interactions operate at larger (several angstroms) interatomic distances, whereas overlapping is not necessary since the attraction arises from electrical properties of participating molecules. These interactions can be described in terms of dispersion, induction (polarization), electrostatic, and exchange repulsion components. The total intermolecular interaction potential is determined by the balance of the cited interactions. The classical Coulomb interaction of the monomers electron distribution (unperturbed by the interaction) gives the electrostatic interaction. Change of the electrostatic interaction due to polarization of the monomer charge density by the interacting molecules yields the induction. Interaction of the instantaneous fluctuations of electronic density and multipoles induced by fluctuation yields the dispersion term. In other words, for induction terms, charged molecules polarize neighboring species, whereas dispersion interactions arise from the interactions between fluctuating multipoles. The dispersion is a correlation effect requiring a quantum chemical approach. The attractive short-range forces are opposed due to Pauli principle (exchange repulsion). Electrons flow from donor to acceptor in charge transfer (CT) interactions. The van der Waals (vdW) forces often describe repulsion and dispersion contributions, whereas other long-range contributions may also contribute [14, 29, 30].

13 Semi-empirical Methods

The π-electron Hückel method is one of the early semiempirical approaches. This method uses the connectivity matrix of a molecule to generate MOs. For unsaturated molecules, it provides good insight into stability, structure, and spectroscopy. All valence electrons are included in the extended Hückel theory which has been qualitatively applied to organometallic and inorganic compounds [12].

Hückel-type methods are noniterative since they only include one-electron integrals. In semiempirical self-consistent field (SCF) methods, two-electron interactions are explicitly taken into account. The Pariser-Parr-Pople method [31, 32], among the first SCF approach, was restricted to π electrons yielding, for unsaturated molecules, a reliably description. Pople introduced the generalization to valence electrons via integral approximations which satisfied rotational invariance as well as other consistency criteria. These approximations yielded the complete neglect of differential overlap (CNDO), intermediate neglect of differential overlap (INDO), neglect of diatomic differential overlap (NDDO) [31–35].

For organic molecules, Dewar introduced a new parameterization strategy by addressing the realistic description of ground-state potential surfaces via calibration against experimental reference data. This line of work yielded MINDO/3 (INDO-based method) as well as MNDO (NNDO-based method) and AM1. Parameterization of the MNDO model yielded PM3. The choice of empirical core repulsion functions determines the formal difference between MNDO and (AM1, PM3) [12, 34–36].

There are two other developments based on INDO approach before 1990, i.e., in the INDO approach, the orthogonalization corrections to the one-electron integrals by Jug et al. as well as parametrization for ground-state properties (SINDO1) [37]. This was later upgraded to MSINDO [38]. The INDO/S method by Zerner et al. focused on vertical excitation energies, using configuration interaction with single excitations (CIS) [38]. The MNDO model has progressed since the 1990 from an sp basis to an spd basis. The treatment of heavier elements has thus enabled improving results for hypervalent main-group elements. The extension to an spd basis has led to PM6 and PM7 covering the whole periodic table with applications to both solid-state and molecular properties. The usage of pairwise distance directed Gaussians (PDDG) for empirical code repulsions resulted in the PDDG/PM3 and PDDG/MNDO models. Some recent work address hydrogen bonding and dispersion by using special purpose parameterizations. Using a larger reference data set introduces the general-purpose RM1 model [39–41].

By including orthogonalization, corrections in the one-electron terms of Fock matrices yields the OM1, OM2, and OM3 models which go beyond MNDO method since they can account for the effects of Pauli exchange repulsions [42]. OM3 includes corrections to the two-center and one-electron terms of the Fock matrix to account for Pauli exchange repulsion. OM1 and OM2 include them in the one-center electron term.

We note, however, that conceptually, these semiempirical methods can be considered as simplified ab initio MO approaches. Semiempirical tight-binding (TB) versions of DFT methods have also been designed, i.e., DFTB approach, as well as the self-consistent charge (SCC) DFT method. We note that the DFTB method uses extensive integral approximations and parameterizations, especially in medium-/large-sized molecules. MNDO methods were mostly used in the 1980s and 1990s for quantum-chemical computations [43]. At present the MNDO, AM1, and PM3 approaches are still used along with more recent versions such as PM6 and PM7. Although DFT calculations have become dominant, OMx methods appear to

have merit for electronically excited states. INDO/S methods are still useful in many applications. In biochemistry and materials science, DFTB methods are popular. Recently, graphic processing units (GPUs) have been used on hybrid platforms to accelerate numerically the calculations [12].

14 Density Functional Theory

It was recognized in the early 1920s that in a uniform electron gas approximation, the kinetic energy density could lead (via constraints) to the ground-state energy functional minimization. However, only in 1964 did Hohenberg and Kohn show that properties of many-body systems are a function of the ground-state density and could thus be determined. Consider any system of electrons in an external potential. Except for a constant, the latter potential will be determined uniquely, and all the properties of the system as well as the many-body wave function are determined. Another theorem indicates that for all-electron system, a universal functional for the energy of the density could be defined. The global minimum for a given external potential would yield the exact ground-state energy. A new independent electron problem was provided to substitute the many-body problem. The independent electron problem can be solved by requiring the ground-state density and the exact density to be the same. The Kohn-Sham (KS) DFT, in use today, defines equations (self-consistent) to be solved for a set of orbitals whose density is defined to be exactly that of the real system.

DFT, with a better cost/performance than WFT, has become, in electronic structure problems, a very popular tool allowing us to solve the electron correlation problem which is included in the exchange-correlation potential. However, the exact formula is not known which yields different approximations for implementations (B3LYP and PBE are among the popular approximations [2, 9, 15–18, 44–56].

15 Some DFT Challenges

The early basic DFT challenges focused on functionals that could yield a description of dissociation energies and geometries of molecules. Subsequent challenges were to address barrier heights of reactions to determine van der Waals interactions and kinetics of chemical reactions. There is still much debate about the ability of DFT to predict the small van der Waals interactions. Current research still tries to determine whether nonlocal functionals of the density are required for these interactions. Although this is one of the weakest interactions, it is essential for a good understanding of biological processes involved in protein-drug/protein interactions [15, 18, 57].

In DFT, simple systems can indicate intricacies of larger systems such as strong correlations and encompass breakdown of the single-particle picture, based on a

determinant of single-particle Kohn-Sham orbitals. The quantum nature of matter is described by a Hamiltonian which for a Coulombic system is determined by a specified set of nuclei with charges and positions as well as a number of electrons. One needs to minimize the energy over all possible antisymmetric wave functions in order to find the appropriate wave function and thus the ground-state energy. In DFT, the external potential is a ground-state density functional. The observable 3D space density can be used to describe the interactions between electrons. Consequently, everything is determined. DFT is very useful for systems with many electrons. Kohn-Sham theory is formulated as a ground-state energy expression where the kinetic energy, the nucleus electron potential energy, and the classical electron-electron repulsion energy are known. Although an explicit form is not available, much is known about the principal remaining term, the exchange-correlational, which can be expressed via density functionals.

One of the important challenges of DFT is to maintain simplicity. The DFT functionals should not become too complicated. However, the method should not be empirical, and the cost of the simplicity should not be too high. Density functional approximations (DFA) lie in between. DFT was important for accurate description of binding energies and geometries of simple molecules. The solid-state community also widely used DFT since local-density approximation (LDA) was not performing well, overbinding molecules but yielding good geometries. The introduction of generalized gradient approximation followed by exact Hartree-Fock exchange led to B3LYP that has indicated a great performance over numerous systems becoming the most widely used functional serving as a route for improving DFT functionals [15, 18, 57].

Another challenge for DFT is to improve description of dispersion/van der Waals interaction and reaction barriers. One needs to go past equilibrium geometry and better describe transition states and weakly interacting molecules. However, LDA-/GGA-type functions underestimate by several kilocalories/mole the transition state barriers. Basic arguments include the need for a $1/R^6$ decaying attractive part of the energy, when the interaction distance increases. LDA or GGA functional do not show this behavior. Hartree-Fock nonlocal functional indicates repulsive long-range behavior. For weakly bound dimers, for example, popular functionals often yield poor results. There is still thus a challenge in DFT to correctly describe covalent bonding and van der Waals attraction [15, 18, 57].

It is important in developing DFT functional to remember the connection to the exact exchange-correlation functional and understand how the popular approximations yields known properties of the exact functional. For this purpose, the uniform/slowly varying electron gas has been very useful. The use of eigenvalues and orbitals to describe the Kohn and Sham reference system is the basis of most approximations. It is also possible to consider this as a mathematical artifact not effectively linked to density/total energy. Some authors suggest substitution of the electron density by the potential.

Most authors solve single-electron systems using the wave function, whereas DFT considers their total density. Thus, single electrons could unphysically self-interact. However, including full exact Hartree-Fock exchange cancels the Coulomb

term exactly and consequently corrects the self-interaction error. For DFT to remain strong in the future, it is important to understand theoretical/practical inconsistencies. In simple systems, we can still find errors of 100 kcal/mol.

Strongly correlated systems are still a challenge/important frontier for DFT. If we consider infinitely separated protons with different number of electrons, most functionals fail, and the integer nature of electrons is important to better understand correlation. For integer number of electrons, the energy functionals should indicate correctly the discontinuous behavior in order to yield the energy gap and describe correctly strong correlation.

16 Exchange-Correlation Functionals

16.1 LDA

The form of the uniform electron gas exchange (as a functional of density) was known from the time of Dirac in 1930. However, Monte Carlo simulations (not first principles) served to investigate high-/low-density limits. Vosko, Perdew, and others developed popular LDA correlation functionals. The uniform electron gas has played an important role in the development of functionals [58, 59].

16.2 GGA

The uniform electron gas can indicate different density from that of molecular/atomic systems. We note that the gradient of the density at the nucleus tells what the nucleus is and that the Hohenberg-Kohn proof applies to any external potential (including nucleus), yielding some insight regarding the importance of the knowledge of gradient of the density at a fundamental level.

Using the dimensionless reduced gradient for slowly varying uniform electrons gas, the gradient expansion yields major problems when applied directly to molecules and atoms due to the fact that their densities are not varying slowly. This can be attributed not to the well-defined nuclei but to the exponentially decaying atomic tails. This led to development of the generalized gradient approximation (GGA) with the introduction of functionals for exchange. With mathematical derivations as well as solid-state physics/chemistry involved, gradient functionals took some time to be developed. Although many functionals have been developed, LYP and PBE are among the main ones established [59–62].

16.3 Meta-GGA

GGA brought an order of magnitude improvement in binding energies with respect to LDA. There was thus much expectation for inclusion of higher order density derivatives. Perdew and Schmidt introduced the term meta-GGA via the Jacob's ladder of approximation to the exact exchange-correlation functional. The ladder starts with LDA and continues with GGA. Next, meta-GGA is incorporated with local ingredients including the kinetic energy density [63].

16.4 Hyper-GGA

Subsequently, at the fourth ring, nonlocal functional of the occupied orbitals involving functionals with Hartree-Fock exchange terms (hyper-GGA) is introduced. In the ladder, each rung should satisfy some constraints, whereas each step up the ladder should have previous rung functionals (B88C, B95, TPSS, and others) [64–68].

17 Hybrid Functionals

In 1993, an important advance came via inclusion in the functional of some Hartree-Fock exchange using a linear model that mixed correlation type functionals with local DFA exchange yielding BHLYP among others. Subsequently, this model was improved using experimental data (G1 data set of Pople and co-workers) yielding the B3LYP model (implemented in Gaussian package) which is a linear combination of HF, LDA, B88, LYP, and VWN [69–76].

18 Range Separation

Another idea is to separate the electron-electron interaction into short-range and long-range interactions using an error function and different functions for each interaction. The long-range LDA exchange energy can be calculated from the exchange-hole explicit form, and the Hartree-Fock potential can be considered correct in the asymptotic limit. It is thus possible to mix short-range DFA with long-range Hartree-Fock to yield a corrected functional [77–81].

19 Screened Functionals

These solid-state types of functionals use long-range DFA and short-range HF yielding an area with interesting applications in solid-state chemistry with improvements in excitation energies and other properties [82, 83].

20 Fitting

It is difficult to determine an accurate form from first principles. A more accurate exchange correlation functional can be obtained from a fitting approach, which consists of using experimental information to determine/test the functionals using some form of parameterization. Although this model has been successfully used in B3LYP and B97 functionals, it is not clear how many parameters are required. Nonetheless, this model has led to development of numerous functionals including (VS98, τ-HCTH, MO6-L, MO6, MO6-2X, MO6-HF) some of which indicate good improvement over standard B3LYP [66, 67, 76, 84].

21 Adiabatic Functionals

The idea of the adiabatic connection is that the interaction between electrons can vary with a family of Hamiltonians (H_λ) and minimizing wave functions ψ_λ such that $H_\lambda \psi_\lambda = \psi_\lambda$ and $\rho_\lambda(r) = \rho(r)$ for all λ. The exchange-correlation energy can thus be expressed by integral over λ. The path is from the noninteracting Kohn-Sham system ($\lambda = 0$) to the real physical system ($\lambda = 1$). An important advance in the functional development comes from including Hartree-Fock fraction in the hybrid functional based on adiabatic connections. Functionals can be developed from the adiabatic connection integrand, using both linear and nonlinear models, as well as the exact adiabatic connection [65, 85–89].

22 Local Hybrids

Another method consists of using a variable amount of exact exchange at each point in space. This can be done by using a local variant of exact exchange with a local mixing function. The mixing function now plays a key role [90–93].

23 Fifth Rung Functionals

Usage of fifth rung functionals involves unoccupied eigenvalues and orbitals, whereas the MP2 (second-order many-body perturbation theory) functional is the simplest form when the eigenvalues are from Hartree-Fock [94–96].

24 Random Phase Approximation

The difference between the single-particle excitations and the many-body formulation yields the random phase approximation (RPA) correlation energy. RPAX and RPAE differ in choice of eigenvalues and orbitals. Some models combine the coupled cluster formulation with RPA, whereas others connect range-separation and second-order screened exchange (SOSEX) with the RPA method [96–99].

25 Performance with Selected Properties

25.1 Thermochemical Data Sets

An important challenge in DFT is to test the results with experimental data of high quality. Pople and collaborators developed the G1, G2, and G3 sets including large molecules, ionization energies, heats of formation, proton affinities, and electron affinities. Boese and Handy and Truhlar's group as well as Grimme have also developed data sets (including AE6 and BH6) that can be used to test/benchmark DFT performance [100–103].

25.2 Prediction of Geometries

DFT has done well with geometries. Even the early LDA, without a satisfactory energetic performance, yields reasonable geometries. Sometimes, the geometries are better than GGA (with magnitudes of order better formation heats). For many geometric quantities, there is also very good performance from hybrid functionals [18, 104].

25.3 Reaction Barriers and Kinetics

Functionals indicate good performance for atomization energies but yield poor results for barrier heights of reactions even for the simplest reactions. Even hybrid functionals are known to underestimate reaction barriers by 3 kcal/mol. Reaction rates are also not well addressed. Truhlar's group work included modification of exact exchange to yield new functionals (MPW1K, HTBH42, NHTB38) that address reaction barriers and kinetics [105, 106].

26 Hydrogen Bonding, Inorganic Chemistry, and Transition Metals

Hydrogen bonding is much weaker than ionic and covalent bonds and is on the order of 1–10 kcal/mol. They are however much stronger than van der Waals interactions and weak dispersion. There exists a good difference between functionals that perform on hydrogen bonding. Since there are electrostatic interactions between fragments and overlap of electron density, functionals for hydrogen bonding has been a challenge, yielding wide differences [107].

For inorganic chemistry and main periodic group, there appears to be improvements on going from semilocal GGA to meta-GGA and forward to hybrids. When barriers are included, the trend is to include/increase Hartree-Fock exchange. For inorganic/transition metal chemistry, the opposite is suggested, i.e., there is a better performance with smaller percentages of exchange [18, 108].

27 Response Functions

In general, GGAs overestimate for small molecules the polarizability. Hybrid functionals improve the performance. Again for polymer chains, polarizability is overestimated by LDA/GGA and corrected by HF and hybrid functionals. Similarly, range-separated hybrids perform better for long-distance charge transfer excitations. On the other hand, for NMR shielding constants, hybrid functionals make the performance worse [109].

28 Performance of DFA

LDA does well in geometries but not for energetic differences. For energetics, GGA/meta-GGA is superior to LDA. However, the three models overestimate polarizabilities and underestimate reaction barriers. For weak interactions and

hydrogen bonding, there is a wide variance among the methods. For some of the most recent functionals, a much better description is obtained including Hartree-Fock exchange in hybrids and range-separated functionals. Inclusion of theoretical and physically motivated corrections sometimes can yield a worse description of chemistry although they may yield good results in other areas [18].

29 Van Der Waals Forces and Simple Corrections

For the exact theory, dispersion forces are not a problem, but local/semilocal functions cannot capture the asymptotic $1/R^6$ behavior. There may be basic/mathematical flaws in the DFT functional, and thus failure to give correct energy for two fixed densities at long distances has originated simple corrections.

Since LDA and GGA cannot describe van der Waals long-range behavior, the correct $1/R^6$ will be missing. Empirical $1/R^6$ pairwise correction has been thus proposed. These can also be functionals of both the density and the nuclear geometry and extended to higher-order corrections. The coefficients can be calculated from ab initio methods or derived from experimental information. Nonempirical functionals can also be developed from the dipole moment of the exact exchange hole. Pseudopotentials can also be used to capture the dispersion interaction. It is also possible to develop explicit functionals from the density of two separate fragments that are weakly interacting [110–113].

30 New Trends

One of the new trends consists of constructing approximate functionals and minimizing the total energy. One can also allow the interaction between electrons to vary using a family of Hamiltonians and minimizing the wave functions. Another approach would be development of models based on implicit density functionals [15, 18, 57].

Another way to carry out energy minimization with orbital functionals is the optimized effective potential (OEP) method which depends, however, on the choice of balanced potential basis sets and orbitals. The theoretical foundation of potential-centric view was established as potential functional theory (PFT). For nonlocal OEP, one can optimize the ground-state energy, whereas the optimization variables are orbitals. Using functionals such as the exact exchange (E_{xx}) yields the generalized Kohn-Sham (GKS) equations. These are also called Hartree-Fock-Kohn-Sham equations. For a functional such as B3LYP, GKS and OEP methods can yield similar results [114, 115].

Although DFT is reaching success and maturity, it is important to understand the errors which arise from the approximate functionals used in the calculations. Understanding the root of the errors can offer good insight into improving the

physics, chemistry, biology, and engineering involved, i.e., delocalization errors, self-interaction, many-electron self-interaction, and fractional charges errors [116].

Since a system of fractional number of electrons does not supposedly exist, what is the important perspective of fractional charges? Is the purpose to look at the properties of the functional rather than the chemistry? [18]

The initial/simple way to use approximate functionals to calculate fractional charge was to perform calculation on molecules with odd number of electrons. These were then stretched to infinity. However, the stretching can cause technical challenges. Another route involves modifications of code to involve fractional occupation. Generalization to fractional numbers can also be obtained by using fractional numbers for the frontier orbitals.

Another important question regards the correctness of ensemble or factional occupation. We must keep in mind that the importance of really understanding calculations on integer systems is that the density matrix appears to have been separated into fractional pieces. In other words, it is important to understand the role of functionals for calculations with fractionals essentially because of their appearance in real integer calculations [117, 118].

It is known that approximate functionals deviate from linearity condition for fractional charges with a convex behavior. They will thus give low energies for delocalized charge distribution or favor delocalized charge distributions over integer or localized ones yielding delocalization errors. For functionals with concave behavior, for fractional charges, delocalization will raise the energy yielding localization errors. The delocalization error is essentially an example of delocalized densities and can have physical consequences [119].

From a quantum perspective, static correlation and degeneracies are inherently multideterminental. The methods used for these cases are often built upon a multiconfigurational starting point yielding methods such as CASDFT where a deep understanding of the method is required [120].

Formal occupation numbers apply in the case of exact degeneracy. This idea could be extended to near degeneracy or density functional approximation (DFA) where orbital are not exactly degenerate. Degenerate ensemble of states (spatial degeneracies) can yield fractional-spin states. Both charge and fractional-spin errors can produce wrong densities. DFA has been used successfully with fractional spin to describe spin state splitting in open-shell singlet molecules [18, 121].

For the simple case of one and two electrons with a proton, the long-range asymptotic DFA behavior indicates challenges in the construction of functions which raises questions regarding usage of long-range Hartree-Fock exchange. The screening of the long-range electron-electron interactions is important in solid-state systems having different external potentials [122].

Although strongly correlated systems are difficult to describe, the problem in DFT can be focused from the functional perspective, whereas it is necessary to find one functional that works for all systems. Quantum chemistry divides the correlation energy into dynamic or nondynamic correlation, whereas the correlation energy is given by $E_c = E_{exact} - E^{HF}$. DFT dynamic correlation is describable by functionals such as E_c^{LYP} and E_c^{PBE}, i.e., not unlike correlations of uniform electron gas.

Static correlation functionals of DFT appears for cases with multiple determinants associated with degeneracy. It can be considered as the deviation from the constancy condition for fractional spins, whereas we can detect if a DFA describes it correctly [18, 123].

A fundamental understanding of band gap lies in the change in derivative when orbitals change between LUMO and HOMO. In band theory, the eigenvalue picture for the Mott insulators breaks down. The frontier KS and GKS eigenvalues are the chemical potentials when E_{xc} is an explicit and differentiable functional of the noninteracting density matrix or orbital functionals. However, the exact functional cannot be a differentiable and explicit functional of the noninteracting density matrix for all physical densities/matrices. For E_{xc} the functionals can be non-differentiable. For a Mott insulator, with zero eigenvalue difference, the gap can thus be written as $E_{\mathrm{gap}} = I - A =$ $_{\mathrm{XC},}$ which includes the explicit discontinuity of the exchange-correlation term which implies that there is a change in the functional itself (not only a change in the density or orbitals that functional acts on). $_{\mathrm{XC}}$ represents only the explicit discontinuity of the exchange-correlation term, I is the ionization potential, and A is the electron affinity. For a pure Mott insulator, only a change in E_{xc} can yield a gap. This is a new difficult concept [124, 125].

We note that the rapid rise of DFT was supported by the similarity of computation solving KS equations using simple ab initio methods (HF). However, there is a strong philosophical difference between both methods, i.e., wave functional versus exchange functional of density. The actual challenge is concentrated on finding E_{xc},

31 Frontier Eigenvalues and Band Gaps

The fundamental band gap for solids is the difference between the electron affinity and the ionization potential, whereas for molecules, it is the chemical hardness (a one-half factor neglected). For energetics, structure, defects, interfaces, and electron transport as well as electromagnetic responses, the band gap plays a key role. The frontier orbitals are either the highest occupied molecular orbital (HOMO) or the lowest unoccupied molecular orbital (LUMO).

When the exchange functional is an explicit functional of the electron density, (local or nonlocal), the frontier KS or GKS eigenvalues are the chemical potentials. The total energy is a linear interpolation between integer points. For functionals that satisfy exact linearity conditions, those are simple differentiable and depend explicitly on electron density $\varepsilon_{\mathrm{HOMO}} = -I$ (ionization potential) and $\varepsilon_{\mathrm{LUMO}} = -A$ (electron affinity). The functional satisfy linearity conditions will determine how well the frontier KS and GKS determine experiments. Molecules that include long-range Hartree-Fock exchange should improve the description of the frontier eigenvalues [18, 121, 126].

We also note that the fundamental band gap can also be understood from the behavior of E versus N, i.e., as the difference between the electron affinity and the ionization, whereas this can be compared with derivatives with respect to N

(difference between derivative to the right and to the left). For an exact functional, we would observe that the $E_{gap}{}^{integer} = E_{gap}{}^{derivative}$. This may explain some of difficulties of approximate functionals to determine accurate band gaps of solids [124, 127].

32 vdW-DF Method

Even nearly 100 years after van der Waals received the Nobel Prize in Physics, the complex manifestations of the vdW force is still a challenging research area. In physical chemistry, vdW includes a permanent dipole and corresponding induced dipole (Debye force), two permanent dipoles (Keesom force), and London dispersion force (two instantaneously induced dipoles). For the condensed-matter scientist, the latter nonclassical term is the vdW force. The vdW interaction is a true quantum phenomenon which emanates from dynamic electron correlation causing a net attraction between fragments of electrons in many-electron systems. Since it is a correlation effect, vdW interactions are included in exact DFT functional, but in practice, approximate forms are necessary. Analysis of polarizabilities of interacting inert atoms, molecules, and surfaces yield for inert atoms molecules and surfaces the R^{-6} asymptotic form of London force for atomic and molecular dimers, the Z^{-3} law for a neutral molecule on a surface and d^{-2} interaction law for pairs of solids [128].

The vdW has been important to investigate physical and chemical properties of functional materials. Indeed, today's emphasis in computational materials science has shifted from metals and semiconductors to biological materials and nanomaterials due to many low-density vdW regions. The applications of vdW functionals include interaction of atoms, molecules and solids, molecular solids, surfaces, adsorption, graphene, metal, oxides, polymers, nanosystems, adsorbate interactions, clusters, nanotubes, water, and others [15].

Initial vdW-DF work focused on nonlocal correlation. Asymptotic behavior such as R^{-6}, z^{-3}, and d^{-2} offered simple vdW parameters/formulas yielding promising results. Significant improvements for description of vdW-bonded regions originated vdW-DF0 and vdW-DF1 functionals. vdW-DF2 included nonlocal correlation energy and exchange energy update to address overestimation of separation and molecule-molecule interactions. Recently, the focus has been placed on exchange to improve performance, internal inconsistencies, covalent solids, and systems with different binding characteristics yielding energies that now approach chemical accuracy. The vdW-DF-cx functional attempts to use an exchange functional derived from the same plasmon-based model originating nonlocal correlation energy. An ultimate solution would be generalization to a unified treatment with an explicit solution of the electrodynamics to smaller separation. vdW-DF0 attempts to do such a generalization. The vdW-DF method also has a good potential for transferability [15].

Phenomena and processes where flexibility of DFT could be important include molecules on metal surfaces (strongly differing from bulk), charge transfer, and

screening at grain boundaries. Weaknesses of vdW-DF include lack of spin, exchange mechanisms, low accuracy for noble-gas dimers, d and f electron effects, and incorrect asymptotic power laws of low-dimensional structures. Dispersion interactions are ubiquitous and still challenging but are essential not only for typical weakly bound systems but also for materials (where they were traditionally considered negligible). New application areas should include disordered systems, liquids, several length scale systems, biological/competing interactions systems [15].

33 Time-Dependent DFT

Time-dependent density functional theory (TD-DFT) is an extension of ground-state (GS) DFT which allows electronic modeling of excited states (ESs). Runge and Gross in 1984 defined the fundamental equations [129]. Casida provided, 11 years later, linear-response expression for calculation of excitation energies (TD-DFT) [46, 130, 131]. For adiabatic approximation, considering the exchange-correlation independent of the frequency, the so-called memory effect is lost, yielding a pseudo eigenvalue matrix formulation. When the de-excitation matrix is set to zero, one obtains Tamm-Dancoff approximation (TDA), which corresponds to configuration interaction singles (CIS) when HF wave functions are used. The Casida formulation has been successful for a number of approaches since all single-reference theories using TD-DFT is straightforward/accessible. The method can treat photoactive compounds in a realistic environment, i.e., once coupled to environmental models, large compounds can be considered via scaling [54].

Nonetheless, with this formulation, it is difficult to properly investigate excited states (ESs), high-spin states, and multi-reference systems although the method has a good accuracy/computational cost accuracy. Many calculations use the vertical approximation, whereas frozen geometries (ground-state DFT/X-Ray geometries) are used, and vibronic effects (coupling between electronic and nuclear degrees of freedom) are neglected yielding Rydberg, localized, charge-transfer effects, but not a good comparison with experiment (measured optical spectra). The vertical excitation limits have stimulated new research in computing 0-0 energies/vibrationally resolved band shapes. However, this implies on one hand expensive Hessians (second geometrical derivatives of TD-DFT energy) to yield improved potential energy surfaces (PESs). On the other hand, important information can be obtained. Analytical geometrical derivative (at least first two) has been increasingly important in this line of research [46].

TD-DFT approaches that provide data comparable to experiment should become standard. Development of new exchange functionals such as range-separated hybrids should allow more accurate studies including charge-transfer effects. Constricted variational DFT [56], less sensitive than TD-DFT to selected functional, may be better suited for investigating states with double excitation character. The equation of motion coupled-cluster expansion, an alternative single-reference theory, such as CC2, includes contributions for double excitations and can be

consequently more accurate than TD-DFT. With a computational cost three times smaller than CC2 with an equivalent accuracy, we have algebraic diagrammatic construction (ADC). These models can be improved with more correlation effects and high-computational requirements yielding (CCSD, CC3). Another popular alternative from solid-state physics is BSE/GW with enhanced accuracy [132].

Continuous developments of TD-DFT permits calculation of larger/more complex systems whereas the role of nonadiabatic coupling cannot be ignored requiring models such as quantum-dynamical wave packet propagation from multiconfigurational time-dependent Hartree (MCTDH) and its multilayer expansion [133].

34 Force Fields

For large systems with temporal/length scales of ns/hundreds of Á, where QM is clearly limited, a less expensive computational model such as force fields (FF) are required. This method uses inter-site potentials to describe interactions between sites (atomic) requiring a different parameterization (data from QM or experiments) for each system. The number of bonds is fixed in a conventional FF simulation, whereas it is possible to capture dynamics and formation/destruction of covalent bonds in a reactive FF simulation. The classical potential contains bonded and nonbonded contributions. Molecular bonded potentials contain bond stretch as well as bond bending and torsion (3-body and 4-body terms). Harmonic functions can be used to describe stretching and bending, whereas periodic functions can be used for torsional energy. Nonbonding interactions are typically electrostatic (Coulomb), whereas for van der Waals, a simple description is quantum fluctuation of charges whose interaction can be given by the Lennard-Jones (L-J) M model, i.e., a repulsion 12th power term (Pauli repulsion due to overlapping electron orbitals) and an attractive sixth power (dispersion force of neutral atoms) term. It was shown that it was possible to reduce scaled L-J term to a single universal binding energy curve for numerous materials laying the basis for bond-order concept [8, 134, 135].

35 Characterization of PES (MC/MD)

Molecular simulations and computational chemistry have evolved as major techniques to study physics and chemistry of materials, whereas one of the objectives of molecular simulation is characterization of system's potential energy surface (PES) due to the interest in locating minima and saddle point connections on the PES. Approaches based on energy minimization may work well for well-ordered, high symmetry, small systems, whereas for other more complex systems, characterization of the PES requires extensive sampling. There are two traditional classes of techniques for dynamics and sampling, i.e., Monte Carlo (MC) and molecular dynamics (MD).

35.1 Monte Carlo

MC methods employ random number in order to solve a wide range of problems, including simulation of physical processes, solution of integral and linear operator equations, and evaluation of multidimensional integrals. In this method, the PES is characterized using extensive statistical sampling (accessible basins). Random changes are made in the method to an existing configuration so as to generate new configurations. A criterion such as the Metropolis criterion can be used to either accept or reject these configurations [10, 14].

35.2 Quantum Monte Carlo

MC techniques can be applied to problems in quantum mechanics whereas the intersection of MC and QM methods is referred to as quantum Monte Carlo (QMC) methods, which are accurate tools for studying molecular quantum mechanics including thorough treatment of static and dynamic correlation effects and are not constrained by considerations of many-particle expansions and basis set considerations. In QMC, a trial wave function approximates the true/exact Schrodinger wave function, and its parameters can be varied to obtain a more accurate function. The method can be considered as a family of stochastic methods for solving quantum many-body problems such as the stationary Schrodinger equation. Stochastic methodologies offer direct/correct particle correlations, favorable scaling, and a wide range of chemical/physical mechanisms. QMC is a unique approach combining known analytic insights/direct constructions with robustness of stochastic methods to capture many-body effects efficiently. Effective core potentials, periodicity, and noncovalent interactions are addressed in QMC [10, 14].

QMC approach offers new insights of the nature of quantum correlations that are stimulating for WFT methods. A complete basis set is used for stochastic sampling (determined automatically) with explicit inclusion of exact nonanalytical behavior (electron-electron cusps). The smooth, long-range, medium correlations are captured with efficiency. Limitations/challenges include the fundamental Fermion sign problem, better understanding of errors related to QMC procedures, and development of new fast algorithms.

The most common approaches to QMC include variational MC (VMC), fixed-node diffusion MC (FN-DMC), Green's function MC (GFMC), Fermion MC (FMC), self-healing diffusion MC (SH DMC), auxiliary field quantum MC (AFQMC), reputation quantum MC (RQMC), and full-CI Quantum MC (FCI-QMC). These methods rely on random walks in space of electron configurations. Time-dependent quantum Monte Carlo (TDQMC) can be seen as a set of coupled time-dependent Schrodinger equations for the guiding waves in physical space. Although QMC methods are among the most accurate tools for studying molecular quantum mechanics, the computed time for each step of a QMC calculation increases roughly as N^3 where N describes the size/number particles of the system [10, 14].

Important advantages in QMC include accurate description of noncovalent interactions, larger molecular systems than current WFT approaches (due to low-order polynomial scaling) and favorable parallelism of algorithms for supercomputer usage and straightforward treatment of periodicity [136–141].

35.3 Molecular Dynamics

In MD, the PES is sampled, whereas the initial configuration is propagated and explored with time using Newton's equation of motion yielding a trajectory (series of molecular configurations). Classical molecular dynamics, with force fields and predefined potentials are based on independent electronic structure calculations or empirical data. At the heart of this model is the description/approximation of the interatomic interactions mostly determined in advance. The full interaction comprises two-body, long-range/short-range interactions, many-body contributions, electrostatic/non-electrostatic interactions represented by appropriate functional forms. Elaborate methods, including analytic potentials, have been developed. However, despite significant success, there are serious drawbacks due to the need to devise fixed predefined potential, i.e., when the electronic structure/chemical bonding pattern changes qualitatively during simulation or when different atom/molecules yield different interatomic interactions/parameterizations and no suitable set of potentials is already available [4, 19, 142, 144].

35.4 Ab Initio Molecular Dynamics

Despite the success of MD, the necessity to construct a predefined/fixed potential is a drawback in particular for complex systems. Consequently, traditional MD was extended to (AIMD) ab initio MD or Carr-Parinello (CP), first-principles MD (FPMD) on the fly, directed extended Lagrangian MD (ELMD), density functional MD (DFMD), quantum chemical, Fock matrix, Hellmann-Feynman MD, and quantum MD (QMD). How does this theory work? As the molecular dynamics trajectory is generated, the forces acting on the nuclei are determined by "on-the fly" electronic structure calculations. The electronic variables are not represented by fixed interaction potentials and are not integrated out beforehand. Complex system can thus be handled by AIMD. The approximation is shifted from constructing an interaction potential to selecting an approximation for solving Schrodinger equation [4, 19, 142–144].

AIMD joins ab initio electronic structure theory (solving the wave equation numerically for Schrodinger and using HF or KS/LDA) with classical molecular dynamics (for a given interaction Newton's equation of motion is solved numerically). However, the relaxation times and correlation lengths are relatively smaller which is sometimes addressed by increasing computer power. Also, AIMD can yield promising results in terms of the electronic structure and chemical bonding.

36 Quantum Mechanics/Molecular Mechanics

Quantum mechanics/molecular mechanics (QM/MM) is one of the first hybrid models which includes the combination of more accurate QM strength with faster and more efficient MM methods in order to generate a stronger tool for investigating larger more complex systems. In this model, the system is divided into two regions, whereas the outer region is described by a force field and the inner region is treated quantum-mechanically. Often a small region of the system can be modeled by ab initio quantum chemistry, whereas the other can be treated more approximately. The interface between the QM and MM regions is the key issue [3, 145]. A less expensive alternative is the usage of self-consistent reaction field (SCRF) approaches, for the coupling of quantum chemical calculations with continuum models, which has been implemented over the decades in quantum chemical softwares [3, 5, 6].

37 Coarse-Grained and Multiple Scale Models

The traditional approaches using all atoms are still not adequate for appropriately simulating large temporal/spatial scales. In the coarse-grained (CG) model, one neglects some of the atomistic degrees of freedom (DOFs). The CG models can increase over temporal/spatial limitations of all-atom models. The physics of the detailed system may be sensitive to small-scale phenomena, and there is a challenge to develop accurate/transferable force fields, which can be extracted from atomistic simulations or by reproducing key experimental data [8, 20, 22, 146–152].

CG creates lower resolution/simplified model of the system by grouping atoms into CG beads (pseudoatoms) whose number determines the level of coarse-graining (degree depends on number of atoms represented). A lower-resolution model can be obtained by increasing atom-to-bead ratio, whereas total number of degrees of freedom is reduced. CG beads interact with each other via potentials yielding considerable increase in time/space accessibility. The basic idea of simulations with coarse-graining is thus to represent the system with reduced number of degrees of freedom (compared to all-atom representation).

In energy-based CG, interaction potentials of beads are derived/parameterized so that it is possible to reproduce energies of all atom system. In force-matching method, sum of atomistic forces are mapped onto corresponding CG beads. Structure-based CG methods depend on reproducing interactions obtained from atomistic simulations (radial distribution functions). The CG models can relate phenomena such as energy, force and structure molecular dynamics, or experimental results. The aim is to provide most efficient computational model with adequate details. Using coarse-graining, we can achieve a simpler description by reducing the structural details of a complicated system by grouping into fewer interaction sites. Challenges of designing CG models include choice of pseudoatom sites

(represent combined groups of multiple atoms), effective energy function (defines interaction between the pseudoatoms), and effective dynamical equations (necessary for dynamic properties).

One of the popular energy-based approaches CG models is the Martini model which uses a four-to-one mapping scheme (average four heavy atoms are represented by one interaction site or bead). Standard masses of each bead are assigned to yield a more computationally efficient model. Main types of interaction considered are polar, apolar, nonpolar, and charged with subtypes that describe the hydrogen-bonding capabilities whose combination yields different bead types (diversity leads to more accurate description of chemical nature and structure).

CG models can simulate large systems with size ($100 \times 100 \times 100$ nm^3) which contains millions of particles as well as slow micro- to millisecond range processes. High-throughput studies can be done via thousands of parallel runs indicating location/importance of detailed insights regarding fundamental driving forces for novel pathways at a much smaller computation cost than other available models.

It is of interest to link CG simulations with that of detailed models, whereas behavior can be determined at multiple scales (different scales share information regarding interactions). This can be done *bottom-up*, whereas fundamental physical principles at detailed scale parametrize a CG scale model, or *top-down* when larger scale behavior is used to inform more detailed scale interactions.

The CG Boltzmann inversion (BI) method aims to obtain an accurate reproduction of structural details via interaction potentials, based on the idea that for particles to interact with each other via forces that only depend on the scalar distance that separates them, it is necessary a one-to-one correspondence between potential and radial distribution function. The radial distribution function indicates correlations in distribution of particles due to forces exerted on each other from pair potentials. When atomistic simulations yield CG interactions, the BI method is an example of multiscale method.

Another model, the force matching method, is also an example of a multiscale method, whereas the interaction potentials are determined from atomistic simulations (structural information not used).

Another approach is the thermodynamic-based model, whose premise is that if the local thermodynamic properties are correct, dynamics on long time scales will be also correct, whereas analytical potentials are often chosen (Lennard-Jones potentials for nonbonded interactions, harmonic bond stretching/bending potentials as in atomistic simulations).

Physical and mechanical properties for systems including polymeric materials can depend on phenomena at different temporal and spatial scales making it necessary to use multiscale techniques for modeling purposes, whereas it is necessary to establish a link between macroscopic mechanical properties and molecular constituents. Difficulties arise from a wide range of spatial and temporal scales involved.

For covalent bonds, typical vibrations are on the length scale of Á with sub-picosecond time scale. Typical length of a monomer is nanometers (nm with tens of picoseconds relevant dynamics. Polymer chains are $\sim$10–100 nm with single-chain

interactions of 10–1000 nanoseconds (ns). Polymeric networks are on the order of 1–100 μm indicating relaxation times of micro- to milliseconds. Bulk polymeric materials indicate length scales of millimeters to centimeters, whereas aging and relaxation of polymeric materials happen in seconds/hours/years range. These wide ranges of temporal/length scales show clearly that it is necessary to introduce multiscale modeling if one wants to characterize correctly the hierarchy of scales.

Future predictions? Our present limitation is for systems containing 10^7 interacting atoms and 1 μs which can be investigated using particle-based simulations. Even if we could count on doubling yearly computational performance (Moore's law), we could not model with atomistic resolution 10^{14} atoms (complete cell) although a bacterial cell may be feasible in the future. Let us go another step further and consider a typical membrane patch of length L, whereas it is assumed that the computational effort to increase membrane size scales as L^6. Assuming again Moore's law, it would take us 40 years to increase the membrane size by a factor of 10.

38 Simulation of Materials and Biomolecular Structures

The underlying physical laws (encapsulated in the Schrodinger equation) for the mathematical theory of a large part of physics and chemistry are known from the 1920s. The exact solutions of these laws are not tractable for realistic materials. Nonetheless, the application of numerous approximations previously discussed reduces considerable the number of electrons to be simulated. This advancement, coupled with computational advancements allows techniques such as DFT to solve the fundamental laws of SE and predict properties of materials and biomolecular structures.

Inputs of DFT calculations including identities and coordinates of atoms in the material's repeating lattice is often used as well as exchange correlation functional and algorithms for convergence and methods such as pseudopotential approach to treat the core electrons. The choice of the exchange correlation functional can often improve the calculation. DFT codes can tackle periodic unit cells with ∼1000 atoms. Difficulties can arise in modeling weak van der Walls interactions, long period dynamics, and finite temperature excited states. However, there are methods for overcoming these limitations. Linear scaling approaches can be used for larger systems. TD-DFT can address the electronic excitations. Approaches previously discussed can model the van der Walls interactions. In order to screen for materials properties using DFT, the input is given via crystal structure (atomic positions, unit cells) of hypothetical material, as well as "choice" of approximations/convergence parameters yielding total energies, charge densities, band, and crystal structures. Outputs produce descriptors for relevant applications [8, 11, 153–187].

Total energy calculations can yield important properties. The energy difference between a point defect and the perfect crystal can yield the thermodynamic

properties of the defects. The energetics of diffusion barriers can be evaluated as the energy differences along an atom's migration path. Analyzing the resultant force on remaining atoms, after displacing some atoms, it is possible to determine phonon modes (vibrational heat capacity). In the field of catalysis, we can use DFT results as descriptors to be used in scaling relations or heuristics.

Lithium-ion batteries will provide for the next-generation electric vehicles, whereas the expected voltage determines energy stored per unit charge. Using electron localization, it is possible to predict voltage increase in hypothetical doped materials. High-throughput automation virtual screening of materials can be used to predict new cathode and anodes [154–156].

Hydrogen can be generated from hydrocarbons via a steam reforming process, whereas the necessary catalysts can be predicted theoretically and the binding energies related to catalytic behavior. Since hydrogen can be embedded in a solid compound, theoretical methods can be used to identify new compound mixtures for hydrogen storage [16–160].

Traditional superconductors (electron pairing interactions arise from electron-phonon coupling) can in principle be predicted in systems with anomalously high-electron density at the Fermi level. Since many materials exhibit phase transition as a function of pressure, it may be possible to use crystal structure determination to predict high-pressure superconductivity in materials with unknown structures. Theoretical methods are expected to evolve to screen for novel higher T_c compounds [161–164].

Contribution of photovoltaics to the total electricity generation is small. Theoretical screening can be made on a wide range of materials (chalcogenides, organic photovoltaics, copolymers, transparent conducting films, alloys). PVs can be analyzed by looking at the HOMO energy level relative to air and charge-transfer energy offset of LUMO as well as band gaps [165–167].

Thermoelectric materials drive electrical currents via temperature differences. Despite their potential applications (transportation vehicles, power generation), the performance of these materials can be determined by ZT (figure of merit) which is proportional to electronic conductivity, Seebeck coefficient, and electronic conductivity). Due to inherent trade-off among these properties, there is a limit on attainable ZT. In large complex materials, it is not straightforward to obtain, from DFT, accurate band gaps and carrier lifetimes. Despite difficulties, screening of materials with improved ZT is still feasible [168, 169].

Using the polarization of an electric field within a material, the capacitor stores electrostatic energy, i.e., pseudocapacitors, carbon-based supercapacitors, ferroelectrics, dielectric capacitors. A dielectric capacitor should have high breakdown strength, good cycling stability, and high dielectric constant. The electronic component of the dielectric constant depends on the band gap. The dielectric constant can be evaluated as a function of structural and chemical properties. For most materials, it is not necessary to do, in silico, the entire material design, but focus the experimental efforts within a structural and chemical space [153, 170].

Molecular modeling is appropriate for developing quantitative and qualitative knowledge of structure-properties relationships (selective adsorption, catalysis,

separation technology) for a wide range of systems (bulk, interfaces, molecules) yielding important information regarding pore size, temperature, shape, and other variables in selectivity adsorption. Simulation methods are important for computational study/design of synthetic sorbents and catalysts (zeolites, aluminophosphates, aluminosilicates, nano, mesotubes, fullerenes, heterofullerenes, pillared clays, disordered porous solids) as well as surface heterogeneity/equilibrium and kinetics of fluid adsorption, thermal desorption, surface diffusion, and surface reactions. Solid oxide fuel cells can be improved by studying the effects of doping one the ionic conductivity [8, 11]. Future trends should include development/application of widely understood modern techniques to study adsorption experiments in order to design new types of catalysts and adsorbents. Usage of experimental databases, artificial intelligence, and advanced simulation techniques will open new strategic technologies [11, 153].

Nanotechnology with its applications for electronics, batteries, drug/gene delivery, water desalination, and diagnostics has an increasing participation in sustainable technologies that address society needs, i.e., clean water/air/energy supplies. On the other end, the usage of small size/reactive nature of nanomaterials in addition to positive contributions, raise issues regarding potential health, environmental, and safety concerns. There are challenging chemical, biological, and physical issues involving interactions between biological and nanomaterials that span spatial and broad length scales. Nanomaterials may be involved in electron transfer in cells, generation of damaging reactive oxygen species as well as undergo undesired chemical transformations. Theoretical and computational studies are expected to play important roles in elucidating the complexity of nano/bio interfaces. Coarse-grained models (structure and dynamics) may be necessary to access the large length (>100 nm) and time (>μs-ms) scales relevant to behavior and impact of nanomaterials with biological settings. Top-down approaches that depend on semiempirical methods can also provide insights into effects of nanomaterials on biological structures such as lipid membranes.

In modern surface science technology, modeling the reactions and adsorption of organic molecules at metal surfaces has important applications in molecular switches, sensors, photovoltaics, energy devices, and catalysis. The highly tunable properties of organic molecules and the electrical conductivity of metals can result in new functionalities not present in either material. An accurate description of bonding between substrate and adsorbate is essential for control and understanding functionality and design of these types of hybrid systems in which there is a delicate balance between van der Waals (vdW), covalent, hydrogen bond, Pauli repulsion, and charge transfer [144].

Due to nontoxicity, high stability, and abundance, metal oxides such as TiO_2 (nano) materials have been the subject of numerous theoretical investigations regarding chemical and physical fundamental properties. It was challenging for a long time to correctly describe relative stabilities of anatase and rutile bulk phases. Inclusion of dispersion in DFT calculations have been suggested to be important for reproducing the greater stability of rutile. Stable in nanoparticles, anatase indicates higher photocatalytic/photovoltaic activity, whereas the electronic

structure plays an important role in these applications, i.e., positions of valence and conduction band edges relative to the potentials of relevant redox couples determine occurrence of photocatalytic reactions. The optical absorption is determined by the band gap. States near conduction and valence band edges have more influence on chemical reactivity and electrical conductivity. Accurate theoretical description of band gap is important allowing quantitative energetic prediction of trap states, impurity levels, defects as well as influence of doping on optical absorption which is crucial for design of oxides with improved properties. It is also important whether charge carriers (reducing defects, doping, and photoexcitation) are in delocalized band states or coupled to lattice polarization forming localized polaronic states. Choice of electronic structure method is important, and nonstandard DFT methods are sometimes used [171]. Fullerenes, nanotubes, nanowires, and other nano systems have been designed and investigated using semiempirical, ab initio, density functional, and molecular dynamics methods [172–175].

Surface functionalization/modification is used to induce new material's properties (hybrid photovoltaics and dye-sensitized solar cells). Molecular dynamics simulations based on force fields potential allows modeling the sintering of oxide nanoparticles. Photoelectrochemical and photocatalytic processes can be elucidated using modern parallel computers and computational algorithms expanding first-principles electronic structure simulations to better understand realistic oxide nanocrystals of a few nm size. Simulation models are being applied to an ever increasing number of diversified areas including crystal structure, phase stability, mechanical properties, elasticity, theoretical strength, fracture, magnetism, conductivity, phonon frequencies, liquids, amorphous, semiconductor, insulators, metals), surfaces, interfaces, and thin films [144].

The earliest example of CG approach in structural biology was developed in the mid-1970s, i.e., a simplified simulation model of proteins. The field has branched out considerable since then, yielding many variants of protein representation, sampling models, and interaction potentials, whereas the growing number of experimentally solved structures of large biomolecules is too large to be addressed by all-atom simulations. Some of the CG models enable protein structure prediction. Interaction schemes are typically based on mean-force potentials (derived from known protein structures), and the simulation processes can be controlled by the MC method. One of the future trends of CG dynamics lies in design of approaches for efficient/reliable transition between atomic resolution and simplified levels. Using CG approaches, we will be able to send CG scale simulations to detailed all-atomic simulations (vice versa). CG simulation is playing an increasing role in protein mechanostability, folding, unfolding, and understanding mechanisms of virus binding to its host cell. CG simulation of protein-protein interaction dynamics is now in the spotlight of biomedical research since these interaction dynamics can yield essential insight into important biological processes as well as causes of diseases/drug-receptor interactions. Membrane proteins are responsible for molecular transport across lipid bilayers, signaling, maintaining cell structural stability, and control of cell-cell interactions. Nonetheless, 1% of all known 3D protein structures account for membrane proteins. The complexity of these biomolecular structures

makes CG molecular dynamics (CG-MD) simulations a very valuable approach to investigate stability, dynamics, and structure-function relationships. The MARTINI force field is of the most recognized and best performing CG-MD approaches that uses four-to-one atom mapping enabling treatment of more than 500,000 atoms with time scales above 100 μs (far beyond classical all-atom MD) [8, 22, 146–152].

Although thermodynamically stable, protein conformation was treated as responsible for biological functions; it is now known that intrinsically disordered proteins (IDP) can retain their functionality. Conformational studies of protein systems remain highly challenging. Nonetheless, CG approaches have been used to yield insights into the binding mechanisms of these complexes. CG protein simulation thus enables studies of larger protein systems and longer time scales compared with atomistic models.

Processes which are photoinitiated play very important roles in living organisms, whereas photosynthesis is performed via absorption of sunlight by bacteria, algae, and plants. Carbon dioxide and water are converted into oxygen and carbohydrates, yielding basis for Earth life. Using the rhodopsin protein, vision of animals/humans is accomplished in the eye, whereas absorption of a photon performs isomerization of the central retinal chromophore. Phototaxis of plants/bacteria begins with photoexcitation of protein pigment followed by excitation energy transfer, electron transfer isomerization among other reactions. For some of these reactions, the important ultrafast processes occur in very small spatial regions of the protein environment with only a few nuclear degrees of freedom of the pigment. The remaining protein environment has often only negligible influence on relevant excited states of pigment. Consequently, for these systems, DFT can be successfully applied within QM/MM schemes [176].

The properties of polymers depend on numerous time and length scales which are coupled. These systems indicate unique viscoelastic properties arising from atomistic level interactions. There is thus a need to probe polymers across length/time scales in order to capture their behavior making their computational modeling very challenging. With increasing molecular weight, these systems become entangled yielding long-time diffusive regimes (not accessible to atomistic simulations). Coarse-graining the polymer, i.e., increasing the time scale and reducing the degrees of freedom, is one path to overcome the theoretical/computational challenges posed by polymeric systems [8, 150].

Multiscale top-down and bottom-up approaches have been used to investigate complex biological systems, whereas an emerging approach is the middle-out approach which starts with an intermediate biological cell which is gradually expanded to include both smaller and larger spatial scales [22]. 3D multiscale numerical models were used to analyze stress/deformation of cells subject to mechanical loads. There has also been modeling of organ-level bone modeling, physical and coronary artery processes, wounded epithelial cell monolayers, simulation of heart, and immunological interactions. Future trends aim to describe complex bio systems and develop predictive models of human disease. CG representations of the DNA are being developed which should enable extensive simulations that could permit, in a reasonable amount of time, a better comprehension of essential

physical/chemical/biological processes involved [146]. Docking, molecular dynamics, pharmacophore modeling, and ADME/Tox predictions have been used in simulations to propose new drugs for cancer, aids, Alzheimer's, diabetes, and other diseases [177–187].

Although protein folding takes several minutes, their hydrogen bonds and van der Waals interactions occur within picoseconds. Corrosion of metals, in material engineering, destroy or compromise billions of dollars of advance products/process of fundamental importance to society. It takes femtoseconds for a single-electron transfer at metallic surface, minutes for multiple reaction cascades diffusion) and decades/hundreds of years for macroscopic corrosion and decomposition of metallic structures. For both materials and biomolecular systems, the underlying phenomena span a very large hierarchically organized sequence (length and time scales).

Understanding, describing, and predicting these multiscale and multiphysics/chemistry/biology/engineering phenomena with advanced theoretical-computational methods is a very important task to assure the well-being of our society.

Acknowledgments We acknowledge financial assistance from CNPq.

References

1. Helgaker T, Jorgensen P, Olsen J (2000) Molecular electronic structure theory. Wiley, Chichester
2. Geerlings P, De Proft F, Langenaeker W (2003) Conceptual density functional theory. Chem Rev 103:1793
3. Friesner RA (2005) PNAS 102:6648
4. Mark D, Hutter J (2009) Ab initio molecular dynamics, basic theory and advanced methods. Cambridge University Press
5. Taft CA, da Silva CHTP (eds) (2010) New developments in medicinal chemistry, vol 1. U.A.E. Bentham Science, Saif Zone Sharjah
6. Taft CA, da Silva CHTP (eds) (2014) New developments in medicinal chemistry, vol 2. U.A.E. Bentham Science, Saif Zone Sharjah
7. Taft CA, da Silva CHTP (2013) J Biomol Struc Dyn 31:1001. doi:10.1080/07391102.2012.748540
8. Canchaya JGS, Furtado NC, Taft CA (2015) Curr Phys Chem 5:223
9. Jones RO (2015) Rev Mod Phys 87:897
10. Austin BM, Zubarev DY, Lester WA Jr (2012) Chem Rev 112:263
11. Canchaya JGS, Rebaza AVG, Lemelle DS, Taft CA (2014) Curr Phys Chem 4:45
12. Thiel W (2013) Comput Mol Sci doi:10.102/wcms.1161
13. Rezac J, Dubecky M, Jurecka P, Hobza P (2015) Phys Chem Chem Phys 17:19268
14. Dubecky M, Mitas L, Jurecka P (2016) Chem Rev 116:5188
15. Berland K, Cooper VR, Lee K, Schröder E, Thonhauser TT, Hyldgaard P, Lundqvist BI (2015) Prog Phys 78:066501
16. Domingo LR, Gutiérrez MR, Pérez P (2016) Molecules 21:748
17. Becke AD (2014) J Chem Phys 140:18A301
18. Cohen AJ, Sanchez PM, Yang W (2011) Chem Rev 112:289
19. Kuhne TD (2014) WIREs Comput Mol Sci 4:391

20. Kamerlin SCL, Dryga A, Vicatos S, Warshel A (2011) Annu Rev Phys Chem 62:41
21. Voth GA (2008) Coarse-graining of condensed phase and biomolecular systems. CRC Press, New York
22. Noid WG (2013) J Chem Phys 139:90902
23. Chattaraj PK (2009) Chemical reactivity theory, a density functional view. CRC Press (Taylor & Francis Group), Boca Raton
24. Riley KE, Pitonak M, Jurecka P, Hobza P (2010) Chem Rev 110:5023
25. Singh DJ (1994) Planewaves, pseudopotentials and the LAPW method. Kluwer, Dordrecht
26. Goedecker S, Ivanov OV (1998) Comput Phys 12:548
27. Marzari N, Vanderbilt D (1997) Phys Rev B 56
28. Chelikowsky JR, Troullier N, Saad Y (1994) Phys Rev Lett 72:1240
29. Stone A (2002) The theory of intermolecular forces. Calerdon Press, Oxford
30. Hobza P, Dethlefs KM (2010) Non-covalent interactions, RSC theoretical and computational chemistry series. RSC Publishing
31. Pariser R, Parr RG (1953) J Chem Phys 21:466
32. Pople JA (1953) Trans Farad Soc 49:1375
33. Pople JA, Santry DP, Segal GA (1965) J Chem Phys 43:S129
34. Dewar MJS, Thiel W (1977) J Am Chem Soc 99:4907
35. Dewar MJS, Zoebish E, Healy EF, Stewart JP (1985) J Am Chem Soc 107:3902
36. Stewart JJP (1989) J Comput Chem 10:221
37. Jug K, Iffert R, Schulz J (1987) Int J Quant Chem 32:265
38. Ahlswede B, Jug K (1999) J Comput Chem 20:563
39. Bacon AD, Zerner MC (1979) Theor Chim Acta 53:21
40. Tubert-Brohman I, Guimaraes CRW (2004) J Comput Chem 25:138
41. Rocha GB, Freire RO, Simas AM, Stewart JJP (2006) J Comput Chem 27:1101
42. Weber W, Thiel W (2000) Theor Chem Accounts 103:495
43. Korth M, Thiel W (2011) J Chem Theory Comput 7:2929
44. Grimme S, Antony J, Schwabe T, Lichtenfeld CM (2007) Org Biomol Chem 5
45. Yoo S, Zahariev F, Sok S, Gordon MS (2008) J Chem Phys 129:144112
46. Casida ME, Huix-Rotllant M (2011) Annu Rev Phys Chem 63:287
47. Burke K (2012) J Chem Phys 136:150901
48. Mourik T, Bühl M, Gaigeot MP (2012) Phil Trans R Soc A 372:4088
49. Peverati R, Truhlar DG (2014) Philos Trans R Soc A 10:372
50. Kohn W, Sherrill CD (2014) J Chem Phys 140:18A201
51. Maitra NT (2016) J Chem Phys 144:220901
52. Kryachko ES, Ludeña EV (2014) Phys Rep 544:123
53. Pribram-Jones A, Gross DA, Burke K (2015) Annu Rev Phys Chem 66:283
54. Santoro F, Jacquemin D (2016) WIREs Comput Mol Sci. doi:10.1002/wcms.1260
55. Kraisler E, Kronik L (2014) J Chem Phys 140:18A540
56. Ziegler T, Krykunov M, Seidu I, Park Y (2015) Density functional methods for excited states. Springer, Berlin/Heidelberg, pp 1–35
57. Cramer CJ, Truhlar DG (2009) Phys Chem Chem Phys 11:10757
58. Vosko SH, Wilk SHL, Nusair LM (1980) Can J Phys 58:1200
59. Perdew P, Burke K, Ernzerhof M (1996) Phys Rev Lett 77:3865
60. Langreth DC, Perdew JP (1979) Solid State Commun 31:567
61. Gross EKU, Dreizler RMZ (1981) Phys A: Hadrons Nucl 302:103
62. Levy M, Perdew JP (1985) Phys Rev A 32:2010
63. Perdew JP, Schmidt K (2001) Jacob's ladder of density functional approximations for the exchange_correlation energy. In: VanDoren V, VanAlsenoy C, Geerlings P (eds) Density functional theory and its application to materials, vol 577. American Institute of Physics, Melville, New York, pp 1–20
64. Van Voorhis T, Scuseria GE (1998) J Chem Phys 109:400
65. Perdew JP, Kurth S, Seidl M (2001) Int J Mod Phys B 15:1672
66. Boese AD, Handy NC (2002) J Chem Phys 116:9559

67. Zhao Y, Truhlar DG (2006) J Chem Phys 125:194101
68. Perdew JP, Ruzsinszky A, Tao J, Csonka GI, Scuseria GE (2007) Phys Rev A 76:42506
69. Becke AD (1993) J Chem Phys 98:1372
70. Stephens PJ, Devlin FJ, Chabalowski CF, Frisch MJJ (1994) J Phys Chem 98:11623
71. Becke AD (1997) J Chem Phys 107:8554
72. Adamo C, Barone VJ (1999) J Chem Phys 110:6158
73. Lynch BJ, PL Fast, M. Harris, DG Truhlar (2000) J Phys Chem A 104:4811
74. Wilson PJ, Bradley TJ, Tozer DJ (2001) J Chem Phys 115:9233
75. Keal TW, Tozer DJ (2005) J Chem Phys 123:121103
76. Zhao Y, Truhlar DG (2008) Theor Chem Accounts 120:215
77. Yanai T, Tew DP, Handy NC (2004) Chem Phys Lett 51:393
78. Toulouse J, Colonna F, Savin A (2005) J Chem Phys 122:14110
79. Vydrov OA, Heyd J, Krukau AV, Scuseria GE (2006) J Chem Phys 125:074106
80. Cohen AJ, Mori-Sanchez P, Yang WT (2007) J Chem Phys 126:191109; (81) Bylander DM, Kleinman L (1990) Phys Rev B 41:7868
81. Chai JD, Head-Gordon MJ (2008) Chem Phys 128:84106; (82) Heyd J, Scuseria GE, Ernzerhof MJ (2003) Chem Phys 118:8207
82. Heyd J, Scuseria GE, Ernzerhof M (2006) J Chem Phys 124:219906
83. Krukau AV, Vydrov OA, Izmaylov AF, Scuseria GE (2006) J Chem Phys 125:224106
84. Chan GKL, Handy NC (2000) Chem Phys 112:5639
85. Langreth DC, Perdew JP (1977) Phys Rev B 15:2884
86. Mori-Sanchez P, Cohen AJ, Yang WT (2006) J Chem Phys 124:91102
87. Teale AM, Coriani S, Helgaker T (2010) J Chem Phys 133:164112
88. Liu ZF, Burke K (2009) Phys Rev A 79:64503
89. Gori-Giorgi P, Seidl M (2010) Phys Chem Chem Phys 12:14405
90. Jaramillo J, Scuseria GE, Ernzerhof MJ (2003) J Chem Phys 118:1068
91. Becke AD (2005) J Chem Phys 122:064101
92. Becke AD, Johnson ER (2007) J Chem Phys 127:124108
93. Arbuznikov AV, Kaupp M (2007) Chem Phys Lett 440:160
94. Grimme S (2006) J Chem Phys 124:34108
95. Karton A, Tarnopolsky A, Lamere JF, Schatz GC, Martin JML (2008) J Phys Chem A 112:12868
96. Zhang Y, Xu X, Goddard WA (2009) Proc Natl Acad Sci U S A 106:4963
97. Scuseria GE, Henderson TM, Sorensen DC (2008) J Chem Phys 129:231101
98. Toulouse J, Gerber IC, Jansen G, Savin A, Angyan JG (2009) J G Phys Rev Lett 102:96404
99. Gruneis A, Marsman M, Harl J, Schimka L, Kresse G (2009) Chem Phys 131:154115
100. Curtiss LA, Raghavachari K, Redfern PC, Pople JA (2000) J Chem Phys 112:7374
101. Amin EA, Truhlar DG (2008) J Chem Theory Comput 4:75
102. Zhao Y, Truhlar DG (2008) Acc Chem Res 41:157
103. Schultz NE, Zhao Y, Truhlar DG (2005) J Phys Chem A 109:4388
104. Staroverov VN, Scuseria GE, Tao JM, Perdew JP (2003) J Chem Phys 119:12129
105. Zhao Y, Lynch BJ, Truhlar DG (2004) J Phys Chem A 108:2715
106. Zhao Y, Schultz NE, Truhlar DG (2005) J Chem Phys 123:161103
107. Zhao Y, Truhlar DG (2005) J Chem Theory Comput 1:415
108. Schultz NE, Zhao Y, Truhlar DG (2008) J Comput Chem 29:185
109. Hieringer W, Gorling A (2006) Chem Phys Lett 426:234
110. Wu Q, Yang WT (2002) J Chem Phys 116:515
111. Grimme S, Antony J, Ehrlich S, Krieg HJ (2010) J Chem Phys 132:154104
112. Di Labio GA (2008) Chem Phys Lett 455:348
113. Johnson ER, Becke AD (2006) J Chem Phys 124:174104
114. Seidl A, Gorling A, Vogl AP, Majewski JA, Levy M (1996) Phys Rev B 53:3764
115. Yang WT, Ayers PW, Wu Q (2004) Phys Rev Lett 92:146404
116. Vandevondele J, Sprik M (2005) Phys Chem Chem Phys 7:1363
117. Perdew JP (1985) Int J Quantum Chem 28:497

118. Yang WT, Zhang YK, Ayers PW (2000) Phys Rev Lett 84:5172
119. Mori-Sanchez P, Cohen AJ, Yang WT (2008) Phys Rev Lett 100:146401
120. Grafenstein J, Cremer D (2005) Mol Phys 103:279
121. Cohen AJ, Mori-Sanchez P, Yang WT (2008) J Chem Phys 129:121104
122. Janesko BG, Henderson TM, Scuseria GE (2009) Phys Chem Chem Phys 11:443
123. Handy NC, Cohen AJ (2001) Mol Phys 99:403
124. Mori-Sanchez P, Cohen AJ, Yang WT (2009) Phys Rev Lett 102:66403
125. Johnson ER, Contreras-Garcia J (2011) J Chem Phys 135:81103
126. Janak JF (1978) Phys Rev B 18:7165
127. Perdew JP, Levy M (1993) Phys Rev Lett 51:1884
128. Margenau H, Kestner NR (1969) Theory of interatomic, forces, 2nd edn. Pergamon Press, Oxford
129. Runge E, Gross EKU (1984) Phys Rev Lett 52:997
130. Casida ME (1995) In: Chong DP (ed) Time-dependent density-functional response theory for molecules, vol 1, Chap. 5. World Scientific, Singapore, pp 155–192
131. Casida ME, Jacquemin D, Chermette H (2009) J Mol Struct Theochem 914:1
132. Faber C, Boulanger P, Attaccalite C, Cannuccia E, Duchemin I, Deutsch T, Blasé X (2015) Phys Rev B 91:155109
133. Meyer HD, Gatti F, Worth GA (eds) (2009) Multidimensional quantum dynamics: MCTDH theory and applications. Wiley-VCH, Weinheim
134. Hughes ZA, Walsh TR (2015) Nanoscale Rev 7:6883
135. Jorgensen WL, Maxwell D, Tirado-Rives J (1996) J Am Chem Soc 118:11225
136. Azadi S, Foulkes WMC (2015) J Chem Phys 143:102807
137. Shulenburger L, Mattsson TR (2013) Phys Rev B Condens Matter Mater Phys 88:245117
138. Wagner LK, Abbamonte P (2014) Phys Rev B Condens Matter Phys 90:125129
139. Morales MA, McMinis J, Clark BK, Kim J, Scuseria GE (2012) J Chem Theory Comput 8:2181–2188
140. Drummond ND, Monserrat B, Lloyd-Williams JH, López Ríos P, Pickard CJ, Needs RJ (2014) Nat Commun 6:7794
141. Clay R, Morales MA (2015) J Chem Phys 142:234103
142. Tuckerman ME (2002) J Phys Condens Matter 14:1297
143. Kirchner B, di Dio PJ, Hutter J (2012) Top Curr Chem 307:109
144. Liu W, Tkatchenko A, Scheffler M (2014) Top Catal 57:40
145. Menikarachi LC, Gascon JA (2010) Curr Top Med Chem 10:46
146. Potoyan DA, Savelyev A, Papoian GA (2012) WIREs Comput Mol Sci. doi:10.1002/wcms.1114
147. Saunders MG, Voth GA (2013) Annu Rev Biophys. doi:10.1146/annurev-biophys-083012-130348
148. Carbone P, Avendaño C (2014) WIREs Comput Mol Sci 4:62–70. doi:10.1002/wcms.1149
149. Karimi-Varzaneh HA, Muller-Plathe F (2012) Top Curr Chem 307:295
150. Salerno KM, Anupriya A, Perahia D, Grest GS (2016) Phys Rev Lett 116:058302
151. Balaji V, Benson R, Wyman B, Held I (2016) Geosci Model Dev Discuss. doi:10.5194/gmd-2016-114
152. Li Y, Abberton BC, Kroger M, Liu WK (2013) Polymers 5:751
153. Jain A, Shin Y, Persson KA (2016) Nat Rev/Mater 1. doi:10.1038/natrevmats.2015
154. Aydinol M, Kohan A, Ceder G, Cho K, Joannopoulos J (1997) Phys Rev B 56:1354
155. Zhou F, Cococcioni M, Kang K, Ceder G (2004) Electrochem Commun 6:1144
156. Ceder G (2010) MRS Bull 35:693
157. Greeley J, Jaramillo TF, Bonde J, Chorkendorff IB, Nørskov JK (2006) Nat Mater 5:909
158. Alapati SV, Johnson JK, Sholl DS (2006) J Phys Chem B 110:8769
159. Siegel D, Wolverton C, Ozolins V (2007) Phys Rev B 76:134102
160. Persson KA, Waldwick B, Lazic P, Ceder G (2012) Phys Rev B 85:235438
161. Chang KJ, Cohen MML (1984) Phys Rev B 30:5376
162. Pickard CJ, Needs RJ (2006) Phys Rev Lett 97:045504

163. Mazin II (2010) Nature 464:183
164. Li Y, Hao J, Liu JH, Li Y, Ma Y (2014) J Chem Phys 140:174712
165. Yu Y, Zunger A (2012) Phys Rev Lett 108:068701
166. Körzdörfer T, Brédas JL (2014) Chem Res 47:3284
167. Shin Y, Liu J, Quigley JJ, Luo H, Lin X (2014) ACS Nano 8:6089
168. Tritt T, Subramanian M (2006) MRS Bull 31:188
169. Madsen GKH (2006) J Am Chem Soc 128:12140
170. Wang CC, Pilania G, Ramprasad R (2013) Phys Rev B 87:35103
171. De Angelis F, Di Valentin C, Fantacci S, Vittadini A, Selloni A (2014) Chem Rev 114:9708
172. Silva JCF, dos Santos JD, Taft CA, Longo E (2016) Curr Phys Chem 6:805
173. Silva GO, Santos JD, Martins JBL, Taft CA, Longo E (2016) Curr Phys Chem 6:10
174. Costa RJ, Martins JBL, Longo E, Taft CA, Santos JD (2016) Curr Phys Chem 6:60
175. Sodre JM, Longo E, Taft CA, Martins JBL, dos Santos JD Comptes Reundus Chimie. doi:10.1016/j.crci2016.05.023
176. Dreuw A (2006) Chem Phys Chem 7:2259
177. da Silva CHTP, Taft CA (2004) J Biomolec Struc Dyn 22:59
178. da Silva CHTP, Carvalho I, Taft CA (2005) J Comp Aided Molec Des 19:83
179. da Silva CHTP, Taft CA, Carvalho I (2006) J Theor Computat Chem 5:579
180. da Silva VB, Andrioli WJ, Carvalho I, Taft CA, da Silva CHTP (2007) J Theor Comput Chem 6:811
181. da Silva VB, Kawano DF, Gomes AS, Carvalho I, Taft CA, da Silva CHTP (2008) J Phys Chem A 112:8902
182. Hage-Mellin LIS, da Silva CHTP, Semighini EP, Taft CA, Sampaio SV (2009) J Biomolec Struct Dyn 27:27–36; (185) da Silva CHTP, da Silva VB, Resende J, Rodrigues PF, Bononi FC, Benevenuto CG, Taft CA (2010) J Molec Graph Model 28:513
183. da Silva VB, Leopoldino AM, da Silva CHTP, Taft CA (2011) Drug Metab Lett 5:267
184. Ferreira FP, Couto WF, Fontana F, Taft CA, da Silva CHTP (2014) Curr Phys Chem 4:94105
185. Federico LB, de Almeida JR, Taft CA, da Silva CHTP (2015) Curr Phys Chem 3:253; (188) Hage-Melim L, Sampaio S, Taft CA, da Silva CHTP (2013) Mini Rev Med Chem 13:1348
186. de Souza R, Picanço RM, Pinheiro AA, da Silva KR, Taft CA, da Silva CHTP, dos Santos CBR, da Silva LR, Hage-Melim L (2016) Curr Phys Chem 1:40
187. da Silva CHTP, Taft CA (2016) J Biomolec Struct Dyn. doi.org/10.1080/07391102.2016.1237382

Chapter 16
Iron Oxides Applied to Catalysis

Maíra dos Santos Pires, Lívia Clara Tavares Lacerda, Silviana Corrêa, Telles Cardoso Silva, Alexandre Alves de Castro, and Teodorico C. Ramalho

1 Iron Oxides

It is recognized that iron oxides are compounds formed by the chemical elements iron (Fe) and oxygen (O); they occur naturally and are widely distributed in the global sphere. Their abundance, coupled with the ease of synthesis in the laboratory and magnetic, electrical, morphological, physical, and chemical properties, makes them potentially relevant and interesting in many technological applications [72].

Due to the redox chemical behavior, low toxicity, and low cost of the element Fe, its oxides have been extensively used for various applications, mainly related to catalytic reactions. The different physical-chemical characteristics of these oxides can make them more or less favorable to the oxidative reactions. Properties such as specific area, pores size/volume, and crystal structure, in particular, have major effects on their activities [29]. These solid catalysts exhibit powerful degradation potential of recalcitrant pollutants, such as colorants and phenolic compounds. A literature review performed by Oliveira et al. [44] reveals that several studies show the high efficiency of these oxides for the degradation of organic compounds.

The use of iron oxide materials can be explored to Fenton-type heterogeneous reactions for the degradation of phenolic compounds is the focus of many studies, since iron catalyzes the decomposition of hydrogen peroxide (H_2O_2) for the generation of hydroxyl radicals ($OH^{\bullet}$), highly oxidant species, capable of causing organic matter mineralization to carbon dioxide (CO_2), water, and inorganic ions. This process is of great importance, since these pollutants may cause serious damage to the environment and public health [26].

M. dos Santos Pires • L.C.T. Lacerda • S. Corrêa • T.C. Silva • A.A. de Castro • T.C. Ramalho (✉)
Department of Chemistry, Federal University of Lavras, Caixa Postal 37, CEP, 37200-000, Lavras, Minas Gerais, Brazil
e-mail: teo@dqi.ufla.br

E. Longo, F.A. La Porta (eds.), *Recent Advances in Complex Functional Materials*,
DOI 10.1007/978-3-319-53898-3_16

Among the iron oxides and hydroxides, the best known are magnetite (Fe_3O_4), maghemite (γ-Fe_2O_3), hematite (α-Fe_2O_3), goethite (α-FeOOH), and feroxyhyte (δ-FeOOH). In this chapter, we will discuss each of them, addressing their properties, structures, and applications in catalytic reactions.

1.1 Magnetite

Magnetite (Fe_3O_4) is an oxide formed by the mixture of FeO and Fe_2O_3. It presents magnetic, optical, and dielectric properties which have application in various fields, such as catalysis, technology, and medicine, among others. It occurs naturally in igneous and metamorphic rocks and is found in large amounts in beach sand known as mineral sand, ferrous sand, or black sand. Furthermore, it is believed that it, along with its weathering product, the maghemite has a correlation with the natural fertility of tropical soils [58].

This oxide is a ferrimagnetic mineral which contains iron in two oxidation states, Fe^{2+} and Fe^{3+}, having a cubic crystallization system with inverted spinel-type structure belonging to the Fd-3m space group (Fig. 16.1). In a unit cell, the O_2^- ions form a dense packing in the fcc (face-centered cubic); the Fe^{3+} ions are located in tetrahedral sites and the Fe^{2+} and Fe^{3+} ions in octahedral sites [74]. As shown in Fig. 16.1, the inverse spinel structure of Fe_3O_4 materials can be conveniently described, as the tetrahedral [FeO_4] and octahedral [FeO_6] cluster units are connected by vertices, whereas the octahedral [FeO_6] units are connected to each other via edges. As the γ-Fe_3O_4 has an inverted spinel structure, in particular, the Fe^{3+} ions are divided equally between both tetrahedral and octahedral positions; there is no magnetic moment resulting from the presence of these ions. However, all Fe^{2+} species reside in octahedral clusters, being responsible for the saturation magnetization or also for the magnetic behavior of this material [21].

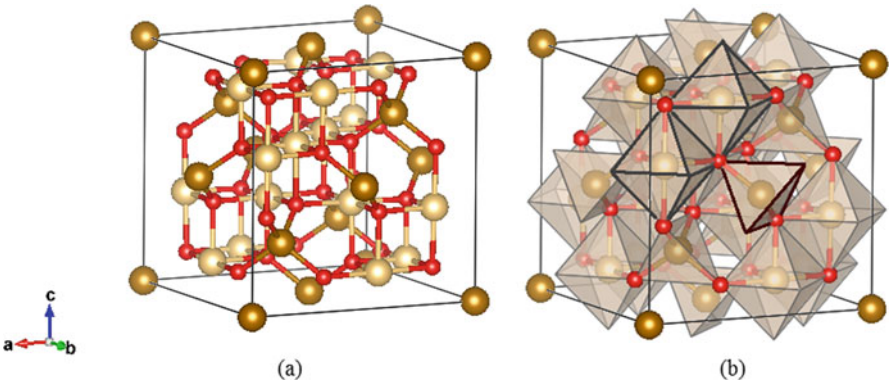

Fig. 16.1 Schematic representation of the unit cell corresponding to the magnetite: (**a**) Stick-and-ball and (**b**) polyhedral

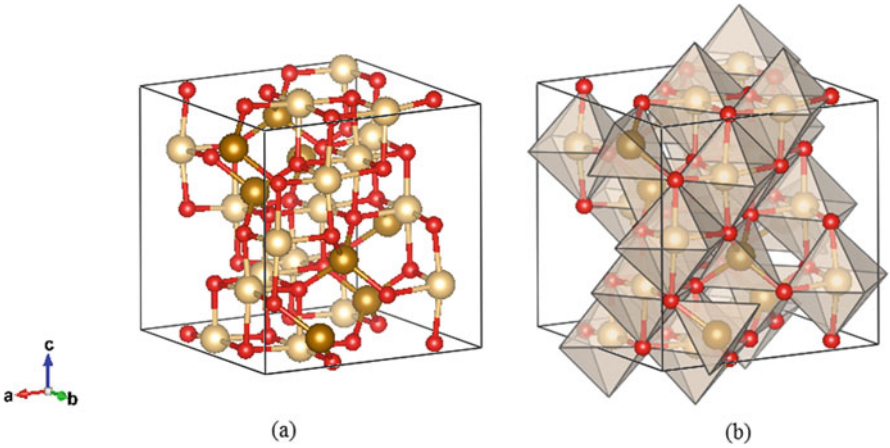

Fig. 16.2 Schematic representation of the unit cell corresponding to the maghemite: (**a**) Stick-and-ball and (**b**) polyhedral

1.2 Maghemite

Maghemite is mainly present in tropical soils derived from basic rocks and can also be found in soils of temperate climate regions [19, 24].

The structure of γ-Fe_2O_3 is very similar to that of magnetite, the main difference being the presence of Fe^{3+} as the only cation in the structure. Each unit cell contains an average of 32 O^{2-} ions, 21.33 Fe^{3+} ions, and 2.66 vacancies, since the cations are distributed in 8 tetrahedral sites and 16 octahedral sites (Fig. 16.2). The vacancies are mainly located in octahedral sites [32]. The maghemite originates from magnetite oxidation; in this case, one Fe^{2+} ion exits the site, leaving a vacancy in the crystal lattice, and another Fe^{2+} ion becomes Fe^{3+}.

The distribution of the cationic vacancies in the octahedral and tetrahedral sites has not yet been fully established and can be distributed randomly on both sites or focus on only one of the sites [60], but according to studies by Lindsley [36], there is a preference for the octahedral site.

Maghemite may exhibit a cubic symmetry ($a = 0.8350$ nm) or tetragonal symmetry ($a = 0.8340$ nm; $c = 2.502$ nm). When the vacancies are located at the tetrahedral site and are arranged, the symmetry is tetragonal, but if they are arranged at random, the cubic symmetry will prevail [8]. It is characterized as ferrimagnetic oxide at room temperature, and its magnetic properties depend on the particle size and surface effects. Particles larger than 10 nm are magnetic at room temperature, while smaller particles are superparamagnetic [44].

The isomorphic substitution of Fe^{3+} ions by other cations (Al, Ti, Co, Zn, Ni, Cu, Mn) is also quite common in maghemite. In the transformation of maghemite to hematite, cations of distinct oxidation states, differently from 3+, are expelled from the structure [59], because otherwise there would be the creation of vacancies, incompatible with the compact hexagonal symmetry of the hematite phase.

1.3 Hematite

As is well known, the hematite is the most abundant of the iron oxides in soils and sediments. It occurs, particularly, in temperate climate regions [64] and is usually found in soils, dispersed in the form of small grains with diameter of less than 2 μm, characteristic of the clay fraction [53]. In nature, there are two varieties of hematite, the red hot, when pure, and brown when hydrated, the latter being more commonly known as goethite [39]. Large Brazilian hematite deposits originated from ancient limonitic segments that have undergone dehydration by the metamorphism effect, crystallizing itself as iron oxide [61].

The hematite crystalline system is trigonal. Its crystalline structure is rhombohedral and can be described as being a compact arrangement of oxygen anions in the direction [001] with the Fe^{3+} ions occupying two third of the octahedral interstices (Fig. 16.3). In this structure, six oxygen atoms surround each iron, with three of these nearer the iron, forming an asymmetric octahedral environment that leads to the formation of a rhombohedral structure [18]. The magnetic behavior of hematite is relatively complex: above the Curie temperature (Tc ∼ 955 K) it is paramagnetic; between Tc and Morin temperature (TM ∼ 260 K), it presents a weakly ferrimagnetic phase; finally, under TM the electron spin orientation occurs, which leads to an antiferrimagnetic phase [64]. The hematite is characterized by a high thermodynamic stability and may have different characteristics, depending on the preparation method, the time, and the calcination temperature [20]. The performance of this iron oxide for the degradation of organic compounds is reported in some works [20, 34], which show its effectiveness when used at pHs near neutrality.

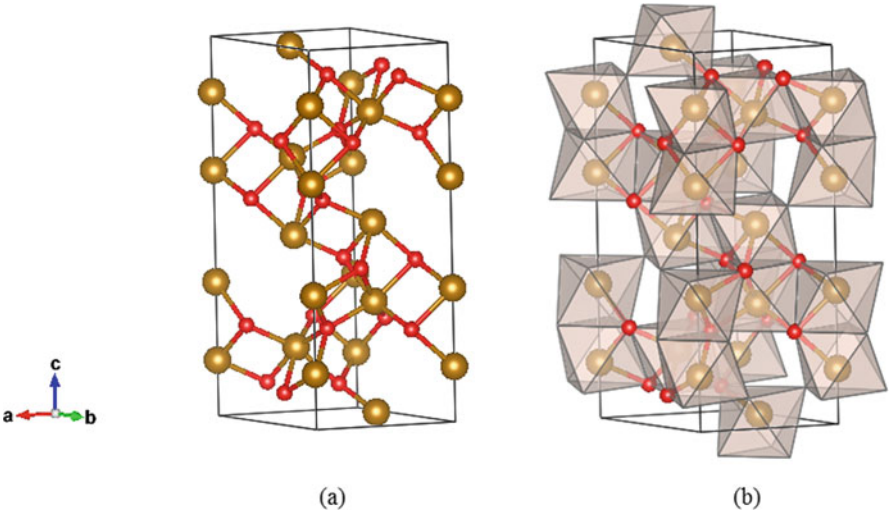

Fig. 16.3 Schematic representation of the unit cell corresponding to the hematite: (**a**) Stick-and-ball and (**b**) polyhedral

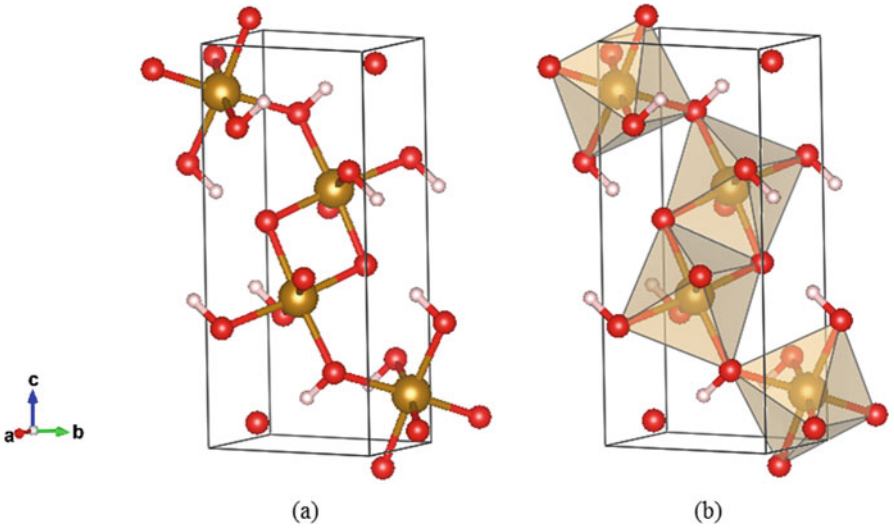

Fig. 16.4 Schematic representation of the unit cell corresponding to the goethite: (**a**) Stick-and-ball and (**b**) polyhedral

1.4 Goethite

Goethite (α-FeOOH) is the most common mineral from the iron oxyhydroxide group, besides having the highest thermodynamic stability among the iron oxides. It is an important component of soil and of many minerals, normally found in nature as small size particles in wet and semiarid regions. Goethite differs from hematite in relation to the mineralogical characteristics, crystallinity degree, size and shape of the mineral, and weathering stage [16].

The unit cell of goethite (Fig. 16.4) presents an orthorhombic crystalline system with $a = 0.4608$, $b = 0.9956$, and $c = 0.3021$ nm, in which Fe^{3+} cations are coordinated to three O^{2-} and three OH^{-}, forming an octahedral. Two octahedra comprise double octahedral clusters chains linked by edges forming parallel planes to the direction [100], whereas these chains are connected with each other through the vertex, and the OH groups are attached to another O atom in a diagonally opposite chain [37].

1.5 Feroxyhyte

Feroxyhyte was introduced by Chukhrov et al. [6] as a mineral with a rather orderly and ferrimagnetic structure. It is a rare iron oxide with little known thermodynamic properties, having specific structural and magnetic properties contrary to all other

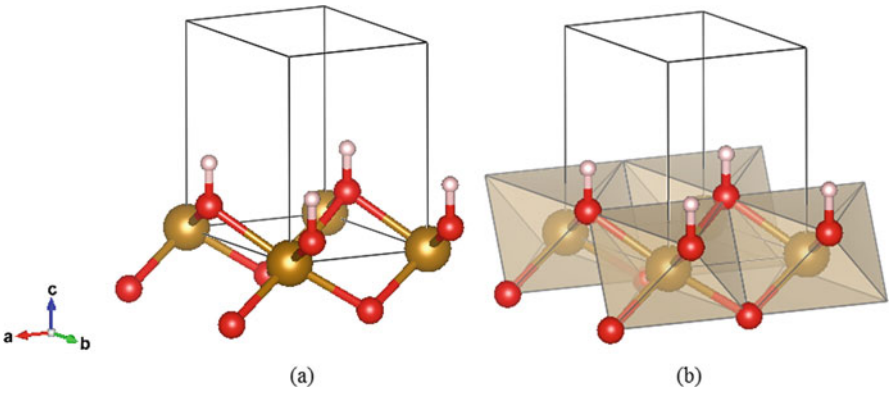

Fig. 16.5 Schematic representation of the unit cell corresponding to the feroxyhyte: (**a**) Stick-and-ball and (**b**) polyhedral

polymorphs of magnetic iron oxyhydroxide at room temperature. In natural occurrences, it is always fine grain; although the samples with larger particle size and better crystallinity can be synthesized in the laboratory, its magnetic properties depend strongly on these aspects [4].

The crystallographic structure of the feroxyhyte is based on a hexagonal closed-packed oxygen lattice, with Fe^{3+} ions occupying half of the octahedral interstice sites (Fig. 16.5). In the literature, the X-ray diffraction (XRD) patterns of the feroxyhyte reported four peaks, corresponding to d (h k l) of values 2.55, 2.23, 1.70, and 1.47 Å [55]. Comparing the feroxyhyte nanocrystals with other iron oxyhydroxides, these Bragg peaks are well defined [7].

The studies of Chen et al. [4] show that the obtained δ-FeOOH ultrathin nanosheets were of high quality; in the XRD pattern, the synthesized sample could be readily indexed to pure hexagonal δ-FeOOH (space group P3m1), $a = b = 2.95$ Å, $c = 4.53$ Å, $\alpha = \beta = 90°$, and $\gamma = 120°$.

The feroxyryte has been used in various applications. One area that has been quite explored is heterogeneous catalysis in the organic contaminant degradation such as cationic polyacrylamide (methylene blue) and anionic dye (indigotin) [49]. Pereira et al. [48] show the application of this oxide as a photocatalyst in the production of hydrogen from water.

Studies from Chagas et al. [3] have reported that δ-FeOOH nanoparticles release a controlled amount of heat when influenced by a magnetic field; this classifies this material as promising for biomedical applications.

Hybrid materials containing polymers and iron oxide have been investigated mainly due to magnetic properties and biocompatibility. Corrêa et al. [11] synthesized hybrid nanocomposites of δ-FeOOH/PMMA, which aim at future biomedical applications.

2 Iron Oxides Applied to Catalysis

The rich chemical and physical properties of catalysts based on iron oxides enable their use in the chemical industry in diverse reactions, such as the synthesis of ammonia, dehydrogenation reaction of ethylbenzene to styrene, and Fischer-Tropsch (FT) synthesis, among others. The wide natural availability, stability, low cost, and high corrosion resistance of these materials have ensured their use as an industrial catalyst in recent years [47]. Their activity and selectivity not only depend on their composition but are also strongly linked to their structure, such as morphology, size and shape of the particles, and surface characteristics.

Iron oxides are used for the synthesis of various organic compounds via oxidation, dehydrogenation, isomerization, and other chemical processes [73]. One of the most important processes is the FT synthesis, a catalytic method for the production of hydrocarbons from synthesis gas, a mixture of CO and H_2. The great emphasis on FT is related to the obtaining of alternative and clean fuels in response to the current global requirements [71]. Iron oxides have been considered promising catalysts in this type of synthesis in much of the discussion on the subject in literature [5, 15, 51, 65]. Tu and co-workers used Fe_3O_4 nanocatalysts applied to FT synthesis, achieving a higher selectivity of heavy hydrocarbons as compared to the traditional Fe catalysts [63].

Besides the synthesis, iron oxides are present in the decomposition and reformation reactions of organic compounds involving several purposes. The production of environmentally clean hydrogen as fuel, for example, takes place from the catalytic reforming of hydrocarbons and alcohols. Recent investigations have focus on the use of iron oxide-based catalysts in these reactions [1, 17]. Yharour et al. [68] studied the catalytic behavior of maghemite and magnetite against the hydrotreating ethanol to produce H_2. The catalysts showed an activity, as well as a satisfactory selectivity for H_2 with a low CO content.

Another hotly debated topic in this context is undoubtedly the environmental issue, especially as regards the effective degradation of several organic pollutants in wastewater. The advanced oxidation processes (AOPs) have been considered as the most promising approach for use in contaminated effluents, mainly leading to the formation of cleaner compounds or even total degradation [23, 56].

AOPs are oxidation processes that produce hydroxyl radicals ($HO^{\bullet}$), highly oxidizing species, in amounts sufficient to cause mineralization of organic matter to carbon dioxide (CO_2), water, and inorganic ions from the heteroatoms. These processes are divided into homogeneous and heterogeneous systems wherein the hydroxyl radicals are generated with or without ultraviolet radiation, and can also involve the use of ozone, hydrogen peroxide, and semiconductors (photocatalysis) [42].

Among AOPs, heterogeneous Fenton-like systems are widely studied using iron oxides as a catalyst [13, 38, 46]. There are numerous works involving the treatment of dyes and/or wastewater from the textile industry by the Fenton process [41, 52]. This interest is mainly due to the effective application of the Fenton reaction in

the dye oxidation, more precisely the reactive dyes, which are quite recalcitrant compounds. Despite its advantages, the application of the Fenton reaction on an industrial scale is still seen with some concern, due to the fact that the process presents a great potential for sludge generation by the precipitation of Fe^{3+} ions as in hydroxide form. The sludge formation takes place mostly because of the excess iron dissolved in the solution. From an environmental standpoint, the sludge generation in the industry is an inconvenience, needing to seek an appropriate end to this waste, so that it does not become an environmental liability. Aiming to reduce this problem, some authors have investigated the use of hydrogen peroxide along with an iron-containing solid in the degradation of organic pollutants, whose process is called heterogeneous Fenton. The main feature of this technology is the use of iron in the form of a solid catalyst, which may be supported on another material or in the form of poorly soluble oxides. The mineral iron oxides have two major advantages that lead to the interest in their application in the heterogeneous Fenton reaction: their abundance, especially in Brazilian soils, and the high iron content in their composition [14].

The use of iron oxides in heterogeneous photocatalysis has been widely studied, mainly for use in environmental decontamination process. The oxides, Fe_2O_3 and Fe_3O_4, for example, are semiconductors of small "bandgap" ($\sim$2.2 eV), low cost, and low toxicity and for these reasons play a great role in photocatalytic reactions [40].

Semiconductors are characterized by valence bands (VB) and conduction bands (CB); the region between the two energy bands is called bandgap. The absorption of photons with energy higher than the bandgap energy results in the promotion of an electron (e^-) from the VB to the CB, with concomitant generation of a gap (h^+) in the valence band; these gaps have sufficiently positive potential to generate $HO^\bullet$ radicals from adsorbed water molecules on the catalyst surface [42]. The possibility of using solar energy makes the process economically viable, in addition to producing low waste after treatment.

To optimize the process with the use of solar radiation, one of the aspects that should be explored further in research on photocatalysis is the expansion of the spectrum of light absorption by the catalyst in the visible region. The synthesis of new complex materials using different oxides and the possibility of incorporating metals to semiconductors have been used for this purpose [12].

In the iron oxides, the conductivity can be increased by adding isomorphic substitution via other elements, a process known as doping. Studies have shown that the doping process significantly improves the catalytic activity of the material. Cui et al. [12], for example, observed that the titanium dioxide doped with iron promoted an improvement in the photocatalytic action of the semiconductor. According to the authors, this improvement in catalytic activity may be due to lower energy values for the formation of the electron/hole pair, i.e., reduced bandgap.

2.1 Modified Iron Oxides

Although pure iron oxides are widely applied in several reactions, changes in their structures have been put into practice, in order to optimize their catalytic activity. According to Guimarães [27], the surface heat treatment of the catalyst under H_2 atmosphere, for example, resulted in the generation of Fe^{2+} sites on the surface of goethite and therefore significantly increased its Fenton reaction efficiency for the degradation of quinoline compounds.

Chelating agents are also an interesting alternative, since they can increase the efficiency of iron minerals to a near neutral pH [66], by means of their positive effects on nonreducing/reductive dissolution rate of iron oxide [75]. Xue et al. [66] have proved the best performance of magnetite for the decomposition of pentachlorophenol when this oxide was worked along with the EDTA chelating agents, carboxymethyl-β-cyclodextrin (CMCD), oxalate, tartrate, citrate, and succinate.

Another interesting modification is the isomorphic substitution of iron species by developing systems involving doping with transition metals, since these can facilitate electronic transfers [73]. There are several challenges regarding the practical implementation of these iron oxides replaced for use as heterogeneous catalysts, because of, among other factors, the need for relatively simple and inexpensive production methods [9, 73]. Thus, attention is increasingly focused on the development of iron oxides doped by elements that are able to further optimize the catalytic properties of the pure oxides. Thus, many transition metals (Ti, Mn, Cr, Co, Nb, Ni, Cu, Zn, Mo, etc.) have been impregnated into the matrix of iron oxides, giving significant improvements in their properties [22, 30, 70].

Studies show that niobium is capable of improving the goethite activity in the H_2O_2 decomposition and oxidation of some dyes, as well as promoting an increase in the surface area by decreasing the particle size [45].

Iron oxides doped with cobalt and manganese have been used as heterogeneous catalysts in fine chemicals, in the aerobic oxidation of various monoterpene alkenes to obtain new products with added values, like epoxides [44]. In addition to this application, the work of Costa et al. [10] showed that the systems created by doping the magnetite with cobalt, manganese, and nickel have high potential for application in advanced oxidation processes based on heterogeneous Fenton systems.

Magnetite was also studied in the presence of copper and aluminum dopants. According to the authors, copper favors the formation of the active phase (magnetite) and its stability. The aluminum acts to increase the specific area (textural promoter), while copper increases the activity of catalytic sites (structural promoter). In the case of copper, this action can be attributed to electronic changes caused by its interaction with iron atoms [2].

The interest in doping iron oxides with Cu is mainly due to the fact that this element acts similarly to Fe in Fenton processes, in so-called cuprous Fenton reactions, in addition to the synergistic properties that it can bring to the material, since previous studies point out the high efficiency of Cu in degradation reactions of diverse organic compounds [62].

2.2 Computational Studies Related to Iron Oxides Applied to Catalysis

The use of computational tools for molecular modeling in recent years has shown great potential in the study of several systems, especially those containing solids such as iron oxides and oxyhydroxides [28].

Solid surfaces have technological importance in different fields, including semiconductor manufacturing, gas separation membranes, and catalysis. Due to the possible applications, it is very important to understand the geometry and the electronic structure of surfaces. Knowing the correlation between the structure of a surface and its catalytic activity, the computational calculations of molecular modeling can be an important alternative for research into catalysis, having the technological improvement and cost reduction in the catalyst production as the main goals. Computational methods, such as density functional theory (DFT), can accurately describe the properties of materials used in catalysis, having an important role in the elucidation of reaction mechanisms in the surface of metal catalysts, zeolites, and oxides, among others [57, 33].

Coupled to the diverse experimental techniques, such as scanning tunneling microscopy (STM), temperature-programmed desorption, and X-ray diffraction, the DFT method has been widely used in the investigation of solid surfaces [57, 31].

Many theoretical studies report the study of the catalytic properties of iron oxides. In the 1980s, calculations based on DFT theory predicted that the Fe_3O_4 structure has ferrimagnetic properties [67]. Moving ahead, the theoretical research evolution on these materials helped to elucidate most of the surface phenomena known today [35, 54, 69]. The bulk structures of iron oxides can also be instigated by these methods; Grau-Crespo et al. [25] studied the stabilities of cubic and tetragonal systems of maghemite based on the distribution of vacancies in their structures, revealing that the tetragonal phase presents homogeneous distribution of cations and vacancies, resulting in a favorable electrostatic contribution.

According to Norskov and co-workers [43], even with all the progress achieved in the electrocatalytic and photocatalytic processes using DFT, some methodological improvements are still necessary to investigate electron transfer processes at interfaces and address the limitations of this method in the treatment of electronic bandgap and excited electronic states.

2.3 Cu-Doped Maghemite for Use as a Catalyst in Heterogeneous Fenton Reactions: A Case Study

A study by Pires et al. [50] reveals that the catalyst doping based on iron oxides with Cu^{2+} ions is a promising alternative in heterogeneous Fenton processes for degrading phenolic compounds present in wastewater. The development of technologies that are satisfactory from a technical and operational point of view

is extremely important, since the presence of these contaminants can cause serious environmental and public health damage, even at concentrations around 1 mg L^{-1}. Several studies show that these pollutants, while in sublethal doses, affect the nervous and circulatory system, reducing blood cell growth in humans. According to the authors, the maghemite (γ-Fe_2O_3), iron oxide characterized by the high catalytic activity and thermodynamic stability, showed significant improvements in phenol degradation reactions (model molecule used) after addition of 2% m/m of Cu^{2+} to its matrix (Cu/γ-Fe_2O_3).

The materials were synthesized by following the procedures of the polymeric precursor method that, besides being economically viable, provided the obtainment of nanostructures with good homogeneity. Scanning electron microscopy (SEM), XRD with Rietveld refinement, energy-dispersive X-ray spectroscopy (EDX), and temperature reduction (TR) have provided support for the investigation of the material characteristics.

The SEM data indicate that Cu doping caused reduction in grain size when compared to the undoped catalyst. EDX spectra show that the copper content in the sample is 1.8% m/m, close to the nominal content of 2% m/m; furthermore, it was observed that the synthesis method provided good Cu atom dispersion in the iron oxide matrix. XRD analyses identified the maghemite and hematite phases in the two catalysts; however, the data refinement revealed that the percentage of maghemite phase increased from 41 to 69.5% m/m after doping, indicating that the Cu^{2+} ions play a significant role in the stability of its structure. The substitution of Fe^{3+} ions by Cu^{2+} occurred only in the maghemite phase, because its tetragonal unit cell was strongly distorted. This behavior was not observed in the hexagonal unit cell of hematite.

Knowing that the Fe^{2+} species are the most active in heterogeneous Fenton process, the use of a catalyst that is more willing to reduce is interesting. The RTP data indicate that the material doped with Cu exhibits a significant decrease in reduction temperature of iron species. Most reducibility of the species in the presence of Cu^{2+} dopant can be attributed to the small size of the iron oxide particles in the modified catalyst and also because this ion is able to increase the mobility of oxygen and hydroxyl groups present. This effect is related to the ability of Cu to dissociate H_2 and provide a source of atomic H which assists in the reduction of Fe_2O_3.

As discussed in Sect. 2 of this chapter, an important step in the degradation of organic pollutants by heterogeneous Fenton-*like* reactions is the decomposition of hydrogen peroxide to the generation of hydroxyl radicals active in the process. Thus, the authors evaluated the catalytic behavior of materials in contact with H_2O_2. The decomposition profiles exhibit a significant improvement in the evolution of O_2 from H_2O_2, for the doped catalyst in comparison with the undoped, indicating that the Cu^{2+} ions play a key role in this type of reaction. Moreover, experiments using phenol as a scavenger of radicals were performed to study the mechanism of H_2O_2 decomposition in the presence of the doped catalyst. The results indicate a reduction in the O_2 evolution of approximately 50% after 50 min of reaction, suggesting that the H_2O_2 decomposition mechanism is accomplished through the

formation of radicals as intermediate species. Thus, once the radical is formed, it can react with a competitive pathway with phenol, thus decreasing the O_2 evolution. In the catalytic tests of phenol molecule degradation, the catalyst Cu/γ-Fe_2O_3 also showed better performance. In the absence of copper, the maghemite's ability to degrade phenol remained at values near 16 and 17%. However, after the addition of this metal, 32% degradation was initially obtained; this value increased to 45% after 30 min of reaction, remaining constant until the end of the process. This suggests a rapid consumption of hydrogen peroxide by the catalyst, which limits the reaction rate over time. To better understand the catalytic behavior of the doped catalyst, several additions of hydrogen peroxide were performed. As expected, the phenol degradation significantly increased to 70% after 2 h of reaction, confirming the high activity of the Cu-doped catalyst for generation of hydroxyl radicals ($OH^{\bullet}$). Thus, the addition of copper makes the iron oxide becomes more efficient and promising in the degradation of organic pollutants.

Allied to the experimental characterization, theoretical studies were explored for the investigation of the properties of the catalysts (γ-Fe_2O_3 and Cu/γ-Fe_2O_3). Computational calculations allow a better understanding of the electronic properties and interatomic bonds of the compounds. Therefore, obtaining experimental and theoretical data in relation to the material characteristics provides greater reliability in its performance in the desired application. The authors used the DFT method along with the PBE (Perdew, Burk, and Ernzerhof) functional and TZP (triple-zeta polarized) basis function, which are recognized in the description of solid systems.

The computational calculations confirmed the order of stability of the crystalline planes already provided by XRD analysis. The ascending energy value order was $E_{311} < E_{220} < E_{440}$.

The improved catalytic activity of the Cu-doped catalyst can be attributed to changes in the electronic structure properties of maghemite. The presence of more reactive catalytic sites, after the insertion of Cu^{2+} atoms, can be understood through the electron density map analysis. The formation of more positive regions (less electron density) near the Cu ions can be seen in Fig. 16.6, inferring that Cu is more susceptible to interact with the hydrogen peroxide molecule than iron ions, which can favor the occurrence of cuprous Fenton reactions.

The work also included the thermodynamic analysis of different routes of the peroxide decomposition mechanism on the surface of the catalysts. The authors suggest that the interaction takes place between the oxygen atoms of the H_2O_2 molecule and the metals on the surfaces, as shown in Fig. 16.7. Thereafter, complexes of the type HO—M—OH, M—O—O—M, M—H_2O_2, and M—OOH are formed.

In all suggested routes, the formed intermediate complexes became more stable in the presence of Cu^{2+} ions. This may be due to the formation of more positive regions around the Cu atoms on the catalyst surface, as previously discussed. Among the evaluated paths, the authors concluded that the generation of $OH^{\bullet}$ radicals takes place preferably by the route shown in Fig. 16.8. This, besides being the most favorable thermodynamically pathway, is also the one that underwent higher influence by the presence of copper, reducing its energy to about 25 kcal mol^{-1} after doping.

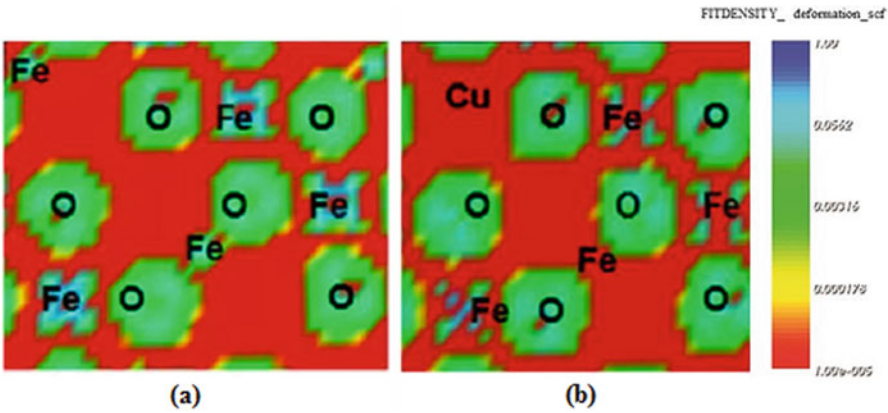

Fig. 16.6 Map of electronic densities of (**a**) γ-Fe_2O_3 and (**b**) Cu/γ-Fe_2O_3.*Red* indicates regions of low density and *green*/*blue* of high electronics

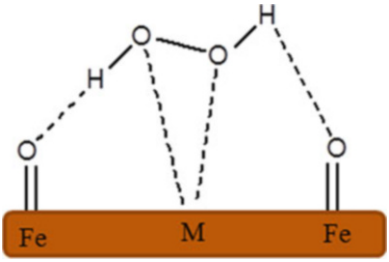

Fig. 16.7 Illustration of the interaction between the H_2O_2 molecule and the catalyst surface, where M = Cu for the Cu-doped catalyst and M = Fe for the undoped catalyst

The results of this study illustrate the successful use of iron oxides as catalysts in Fenton reactions. Moreover, they demonstrate that the modification of the structure in these materials, by insertion of a new metal, leads to significant improvements in their catalytic properties. This is a simple strategy that can be extended to other materials for the production of active heterogeneous catalysts in environmental restoration processes.

3 Conclusion

The iron oxides are configured as an excellent alternative for catalytic application in different reactions. They are present in processes ranging from the obtainment of products of interest to the degradation of compounds highly damaging to living organisms in general. Due to the wide range of application of these materials, an alternative that has been widely explored is the optimization of their properties by doping with other metals. The insertion process of metal ions in the oxide matrix is considered simple, inexpensive, and capable of causing highly interesting synergistic effects on their performance in reactions.

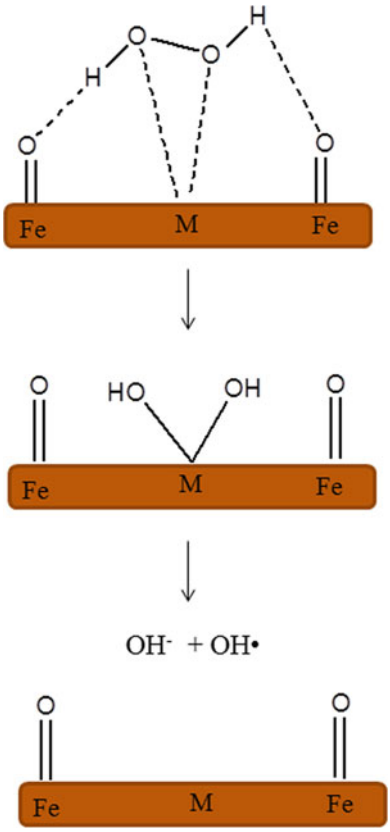

Fig. 16.8 Most favorable route for the generation of $OH^{\bullet}$ radicals by decomposition of H_2O_2 on the catalyst surface

In this chapter, a study about the heterogeneous Fenton catalysts γ-Fe_2O_3 and Cu/γ-Fe_2O_3 was presented as a way to elucidate the advantages that the addition of a second metal, in this case Cu^{2+} ions, can bring to the properties of iron oxides in general. We have seen that the structural and electronic characteristics of the starting material were beneficially affected after the change, which justifies the best performance of Cu/γ-Fe_2O_3 for the degradation of phenol (model molecule used). It is expected, therefore, that this section had been effective for a better understanding of the numerous advantages that the use of iron oxide-based compounds may bring to several reaction systems.

References

1. Acha E, Requies J, Guemez MB et al (2014) Process integration for hydrogen production, purification and storage using iron oxides. Inter J Hydrogen Energ 39:5257–5266
2. Araujo FVF, Yokoyama L, Teixeira LAC (2006) Colour removal of reactive dye solutions by oxidation with H_2O_2/UV. Quim Nova 29(1):11–14

3. Chagas P, Silva AC, Passamani EC et al (2013) δ-FeOOH: a superparamagnetic material for controlled heat release under AC magnetic field. J Nanopart Res 15(4):1544
4. Chen P, Xu K, Li X et al (2014) Ultrathin nanosheets of feroxyhyte: a new two-dimensional material with robust ferromagnetic behavior. Chem Sci 5:2251–2255
5. Cho JM, Jeong MH, Bae JW (2016) Fischer-Tropsch synthesis on potassium-modified Fe3O4 nanoparticles. Res Chem Intermediat 42:335–350
6. Chukhrov FV, Zvyagin BB, Gorshkov AI et al (1977) Feroxyhyte, a new modification of FeOOH. Int Geol Rev 19(8):873–890
7. Cornell RM, Schwertmann U (2003) The iron oxides. Wiley-VCH, Weinheim
8. Costa GM d, De Grave E, Bryan AM et al (1993) Mössbauer studies of nano-sizes aluminium-substituted maghemites. Hyperfine Interact 83:112
9. Costa RCC, Lelis MFF, Oliveira LCA et al (2003) Remarkable effect of Co and Mn on the activity of $Fe_{3-x}M_xO_4$ promoted oxidation of organic contaminants in aqueous medium with H_2O_2. Catal Comm 4(10):525–529
10. Costa RCC, Lelis QFP, Oliveira LCA (2006) Novel active heterogeneous Fenton system based on $Fe_{3-x}M_xO_4$ (Fe, Co, Mn, Ni): the role of M^{2+} species based the reactivity towards H_2O_2 reactions. J Hazard Mat 129(1/3):171–178
11. Corrêa S, Lacerda LCT, Pires M dos S et al (2016) Synthesis, structural characterization, and thermal properties of the poly(methylmethacrylate)/δ-FeOOH hybrid material: an experimental and theoretical study. J Nanomat 2016(2462135):1–7. doi: dx.doi.org/10.1155/2016/2462135
12. Cui L, Wang Y, Niu M et al (2009) Synthesis and visible light photocatalysis of Fe-doped TiO_2 mesoporous layers deposits on hollow glass micro beads. J Solid State Chem 182(10):2785–2790
13. Cruz RM (2000) Reactive Fenton and photo-Fenton high salinity effluent. Dissertation, Federal University of Rio de Janeiro
14. Da Fonseca Araújo FV (2008) Study Fenton heterogeneous process using hematite (Fe2O3) as a catalyst in the reactive dye bleaching solutions. Federal University of Rio de Janeiro
15. De Berti IOP, Bengoa JF, Stewart SJ (2016) Effect of activation atmosphere in the Fischer-Tropsch synthesis using a "quasi-model" catalyst of gamma-Fe2O3 nanoparticles supported on SBA-15. J Catal 335:36–46
16. De Leeuw NH, Cooper TG (2007) Surface simulation studies of the hydration of white rust $Fe(OH)_2$, goethite α-FeO(OH) and hematite α-Fe_2O_3. Geochim Cosmochim Ac 71:1655–1673
17. Dolgykh LY, Stolyarchuk IL, Staraya LA (2015) Steam reforming of ethanol over manganese and iron oxides for hydrogen production. Adsorpt Sci Technol 33:715–721
18. Doriguetto AC, Fernandes NG, Persiano AIC et al (2003) Characterization of a natural magnetite. Phys Chem Miner 30:249–255
19. Fabris JD, De Jesus FMF, Coey JMD et al (1997) Iron-rich spinels from Brazilian soils. Spogli Riviste 110(1):23–32
20. Flores RG (2012) Catalysts and adsorbents produced from the acid drainage from coal mine and application to the treatment of wastewater. Thesis, Federal University of Santa Catarina
21. Ghazanfari M, Yazdani A (2015) Influence of MWCNTs on the formation, structure and magnetic properties of magnetite. Mat Sci in Semicon Proc 40:152–157
22. Glasscock JA, Barnes PRF, Plumb IC, Savvides N (2007) Enhancement of photoelectrochemical hydrogen production from hematite thin films by the introduction of Ti and Si. J Phys Chem C 111:16477–16488
23. Gonçalves M, Guerreiro MC, Oliveira LC et al (2008) Iron oxide based materials for oxidation of compounds present in the effluent of the coffee pulping. Quim Nova 31:1636–1640
24. Goulart AT, De Jesus FMF, Fabris JD et al (1997) Multiple iron-rich spinel phases and hematite in a magnetic soil developing on tuffite. Phys Chem Miner 25(1):63–69
25. Grau-Crespo R, Al-Baitai AY, Saadoune I, De Leeuw NH (2010) Vacancy ordering and electronic structure of gamma-Fe2O3 (maghemite): a theoretical investigation. J of Phys Condens Matter 22:255401

26. Guerra R (2001) Ecotoxicological and chemical evaluation of phenolic compounds in industrial effluents. Chemosphere 44:1737–1747
27. Guimaraes IR (2007) Use of natural and synthetic iron oxides for the oxidation of organic compounds. Dissertation, Federal University of Lavras
28. Guo H, Barnard AS (2011) Modeling the iron oxides and oxyhydroxides for the prediction of environmentally sensitive phase transformations. Phys Rev B 83(9):1–18
29. Huang HH, Lu MC, Chen JN (2001) Catalytic decomposition of hydrogen peroxide and 2-chlorophenol with iron oxides. Water Res 35(9):2291–2299
30. Ingler WB, Baltrus JP, Khan SUM (2004) Photoresponse of p-type zinc-doped iron(III) oxide thin films. J Am Chem Soc 126:10238–10239
31. Jones RO (2015) Density functional theory: its origins, rise to prominence, and future. Rev Mod Phys 87:897–923
32. Karunakaran C, Senthil Velan S (2006) Fe2O3-photocatalysis with sunlight and UV light: oxidation of aniline. Electrochem Commun 8(1):95–101
33. Lejaeghere K, Bihlmayer G, Björkman T et al (2016) Reproducibility in density functional theory calculations of solids. Science 351(6280):1415–1422
34. Li P, Miser DE, Rabiei S et al (2003) The removal of carbon monoxide by iron oxide nanoparticles. Appl Catalysis B-Environmental 43:151–162
35. Liao PL, Carter EA (2010) Ab initio DFT plus U predictions of tensile properties of iron oxides. J Mater Chem 20:6703–6719
36. Lindsley DH (1991) Experimental studies of oxide minerals. In: Lindsley DH (ed) Oxide minerals: petrologic and magnetic significance. Rev Mineral 25:69–106
37. Liu HB, Chen TH, Frost RL (2014) An overview of the role of goethite surfaces in the environment. Chemosphere 103:1–11
38. Martínez NSS, Fernández JF, Segura XF et al (2003) Pre-oxidation of an extremely polluted industrial wastewater by Fenton's reagent. J Hazard Mater B101:315–322
39. Martins F G (2002) Spectrophotometric study of iron (II) system/thiocyanate and its analytical use. Dissertation, Faculty of Philosophy, Sciences and Letters of the University of São Paulo
40. Magalhães F (2008) Synthesis and characterization of iron oxides and composite applications for the redox wastewater treatment watery. Thesis, Federal University of Minas Gerais
41. Neamtu M, Siminiceanu I, Yediler A et al (2002) Kinetics of decolorization and mineralization of reactive azo dyes in aqueous solution by the UV/H_2O_2 oxidation. Dyes Pigments 53:93–99
42. Nogueira RFP, Jardim WF (1998) The heterogeneous photocatalysis and its environmental applications. Quim Nova 21:69–72
43. Norskov JK, Abild-Pederson F, Studt F et al (2011) Density functional theory in surface chemistry and catalysis. P Natl Acad Sci USA 108(3):937–943
44. Oliveira LCA, Fabris JDF, Pereira MC (2013) Iron oxides and their applications in catalytic processes: a review. Quim Nova 36:123–130
45. Oliveira LCA, Gonçalvez M, Oliveira DQL (2007) Synthesis and catalytic properties in goethites oxidation reactions containing niobium. Química Nova 30(4):925–929
46. Pacheco JR, Peralta-Zamora PG (2004) Integration of physical and chemical oxidation processes for advanced remediation leachate landfill (leachate). Eng Sanit Ambient 9(4):306–311
47. Pradhan GK, Parida KM (2012) Dramatic enhancement of catalytic activity over transition metal substituted hematite. J Ind Eng Chem 18:1612–1619
48. Pereira MC, Garcia EM, Silva AC et al (2011) Nanostructured δ-FeOOH: a novel photocatalyst for water splitting. J Mater Chem 21:10280–10282
49. Pinto ISX, Pacheco PHVV, Coelho JV et al (2012) Nanostructured δ-FeOOH: an efficient Fenton-like catalyst for the oxidation of organics in water. Appl Catal B-Environ 119–120:175–182
50. Pires M d S, Nogueira FGE, Torres JA et al (2016) Experimental and theoretical study on the reactivity of maghemite doped with Cu^{2+} in oxidation reactions: structural and thermodynamic properties towards a Fenton catalyst. RSC Adv 6:80830–80839

51. Pour AN, Modaresi SM (2016) Methane formation in Fischer-Tropsch synthesis: role of nanosized catalyst particles. J Nano Res 35:39–54
52. Ramirez JH, Costa CA, Madeira L (2005) Experimental design to optimize the degradation of the synthetic dye Orange II using Fenton's reagent. Catal Today 107-108:68–76
53. Resende M, Allan J, Coey JMD (1986) The magnetic soils of Brazil. Earth Plant Sc Lett 78:322–326
54. Saito M, Roberts CA, Ling C (2015) DFT plus U study of the adsorption and oxidation of an iron oxide cluster on CeO2 support. J Phys Chem C 119:17202–17208
55. Sestu M, Carta D, Casula MF et al (2015) Novel interpretation of the mean structure of feroxyhyte. J Solid State Chem 225:256–260
56. Shanmukhappa DR, Ananda Alwar RP, Srinivasan CS (1998) Water pollution by coffee processing units and its abatement. Indian Coffee 10:3–9
57. Sholl DS, Steckel J (2009) Density functional theory : a practical introduction. Wiley-VCH, Hoboken
58. Silva GA (2013) Study of magnetic oxides in roraima soils. Dissertation, Federal University of Roraima
59. Sidhu PS, Gilkes RJ, Posner AM (1980) The behavior of Co, Ni, Zn, Cu, Mn and Cr in magnetite during alteration to maghemite and hematite. Soil Sci Soc Am J 444:135–138
60. Taylor RM, Schwertmann E (1974) Maghemite in soils and ist origin. I. Properties and observations on soil maghemites. Clay Miner 10:289–297
61. Terra LHSA (1997) Development of spectrophotometric methods for determining nickel II in the absence and presence of iron. Thesis, Federal University of São Paulo
62. Timofeeva MN, Khankhasaeva STS, Talsi EP et al (2009) The effect of Fe/Cu ratio in the synthesis of mixed Fe, Cu, Al-clays used as catalysts in phenol peroxide oxidation. Appl Catal B-Environm 90(3/4):618–627
63. Tu JL, Ding MY, Zhang YL (2015) Synthesis of Fe3O4-nanocatalysts with different morphologies and its promotion on shifting C-5(+) hydrocarbons for Fischer-Tropsch synthesis. Catal Commun 59:211–215
64. Vandenberghe RE, Van San E, De Grave E et al (2001) About the morin transition in hematite in relation with particle size and aluminium substitution. Czechoslov J Phys 51(7):663–675
65. Xu JD, Chang ZY, Zhu KT (2016) Effect of sulfur on alpha-Al2O3-supported iron catalyst for Fischer-Tropsch synthesis. Appl Catal A-Gen 514:103–113
66. Xue X, Hanna K, Despas C et al (2009) Effect of chelating agent on the oxidation rate of PCP in the magnetite/H_2O_2 system at neutral pH. J Mol Catal A-Chem 311(1/2):29–35
67. Yanase A, Siratori K (1984) Band-structure in the high-temperature phase of Fe3O4. J Phys Soc Japan 53:312–317
68. Yharour MFR, Fellenz NA, Alvarez AM (2014) Hydrogen production from ethanol with low carbon monoxide generation in a one-pot reaction with iron oxides as catalysts. Inter J of Hydrogen Energ 39:12563–12571
69. Yin SX, Ma XY, Ellis DE (2007) DFT studies of initial stage water adsorption on iron oxide surfaces: a-Fe2O3 (0001). Abstr Pap Am Chem S 233:74–74
70. Youssef AM, Amin NM (1978) Surface properties of Mn-doped iron-oxide. Surf Technology 7:469–478
71. Zhang YL, Ma LL, Wang TJ (2016) MnO2 coated Fe2O3 spindles designed for production of C5+ hydrocarbons in Fischer-Tropsch synthesis. Fuel 177:197–205
72. Zhao DL, Zeng XW, Xia QS (2009) Preparation and coercivity and saturation magnetization dependence of inductive heating property of Fe3O4 nanoparticles in an alternating current magnetic field for localized hyperthermia. J Alloy Compd 469(1/2):215–218
73. Zhong Y, Liang X, Tan W et al (2013) A comparative study about the effects of isomorphous substitution of transition metals (Ti, Cr, Mn, Co and Ni) on the UV/Fenton catalytic activity of magnetite. J Mol Catal A-Chem 372:29–34
74. Zhu L, Yao KL, Liu ZL (2006) First-principles study of the polar (111) surface of Fe3O4. Phys Rev B 74(3):035409
75. Wang X, Liu C, Li X et al (2008) Photodegradation of 2-mercaptobenzothiazole in the γ-Fe_2O_3/oxalate suspension under UVA light irradiation. J Hazard Mat 153(1/2):426–433

Chapter 17
Bridging Structure and Real-Space Topology: Understanding Complex Molecules and Solid-State Materials

J. Andrés, V. S. Safont, L. Gracia, R. Llusar, and E. Longo

Structural elucidation through experiments (e.g., X-ray diffraction and Rietveld refinements) and quantum chemical computations has seen tremendous progress in the last few decades. In particular, the characterization of crystalline substances at the level of electron density has become possible owing to new X-ray diffraction instrumentation and an increasing number of tools suitable for the description and treatment of the tiny details at the electron density level. However, despite the contemporary high standards for the determination of geometrical parameters, questions about chemical bonding are still highly controversial. The "classical" concepts of bonding analysis and the corresponding chemical reactivity have been seriously challenged in cases of multicenter-bonded systems, or materials subjected to certain special conditions, such as high pressures or irradiation by electron beams.

To overcome these problems, topological partitioning of the electron density has been used to provide an unambiguous definition of chemical structure and reactivity and promises to shed light into the complex modes of bonding in the mentioned systems. This strategy generalizes quantum mechanics to a subsystem by taking note of the topological and geometric properties of the electron density. The most prominent approaches are the quantum theory of atoms in molecules (QTAIM) and

J. Andrés (✉) • V.S. Safont • R. Llusar
Department of Physical and Analytical Chemistry, Universitat Jaume I, Campus Riu Sec, E-12071, Castellón, Spain
e-mail: andres@qfa.uji.es

L. Gracia
Department of Physical and Analytical Chemistry, Universitat Jaume I, Campus Riu Sec, E-12071, Castellón, Spain

Department of Physical Chemistry, Universitat de Valéncia, 46100 Burjassot, Spain

E. Longo
CDMF, INCTMN, Instituto de Química, Universidade Estadual Paulista, Araraquara, 14801-907, Brazil

E. Longo, F.A. La Porta (eds.), *Recent Advances in Complex Functional Materials*,
DOI 10.1007/978-3-319-53898-3_17

the electron localization function (ELF). Through the topological analysis of the three-dimensional electron density and the definition of surfaces of zero electronic flux, QTAIM divides direct space into discrete atomic basins and provides self-consistent atomic properties such as the atomic charge and volume, as well as topological interatomic bond path motifs, which are often assigned to a molecular structure. The ELF performs a topological analysis of the same-spin pair probability density and thus generates basins of localized electron pairs. These procedures are particularly appropriate for this task, because they represent molecular structure and bonding as a consequence of the electron density topology and geometry and give clues about real electrons fluxes. This method grounded solely on the electronic density extracted from a wave function can be generalized to any complex molecule and solid-state material of interest.

This information can be used to explain chemical behavior and thus give rise to the rational design of novel chemical structures and materials with tuned chemical and physical properties. Herein, computational insights based on the density functional theory into the structure, bonding, and energetics of several representative examples from the authors' work are reviewed, and we show how QTAIM and ELF tools can be used to model bonding patterns in complex molecules and the solid state, such as in transition metal clusters or silver chromate. A bright future of interfacing-chemical structure and reactivity in catalysis and solid state waits, where the interplay of theory and experiment is sure to bring unexpected results.

> Measure that which is measurable and make measurable that which is not. Galileo Galilei
>
> In exact sciences, every theory has a philosophical, mathematical and empirical content. All these aspects are equally important; if we neglect one of them, we sooner or later get into difficulties. Hans Primas (H. Primas, In Quantum Dynamics of Molecules: The New Experimental Challenge to Theorists; R. G. Woolley, Ed.; Plenum: New York, 1980)

1 The Road Map: Chemical Bond and Novel Structures

Chemistry is the science of atoms, molecules, matter, and their transformations. Chemists, with the help of sophisticated experimental techniques and accurate first principle calculations, are capable of obtaining a wide range of molecules and determining their structures, even at extraordinary levels of complexity. These types of works are devoted to elucidating how atoms are held together by chemical bonds in order to understand their 3D rearrangement in molecules and materials. In general terms, a molecule possesses one stable structure, with a defined geometry at a given condition, determined by its chemical bond. Therefore, chemical bonding is at the heart of chemistry.

Our understanding of how atoms form favorable nuclei and electron arrangements at the most fundamental level within molecules or materials provides a solid foundation for modern science and technology. The multifarious properties of molecules and materials, such as their structure and reactivity, are intimately related to the very concept of chemical bonds, providing a solid foundation for modern science and technology. The chemical structure and reactivity of molecules are usually

built up from the qualitative application of physical and chemical principles (e.g., electrostatics, polarizability, electronegativity, etc.). In the center of these principles is the concept of the chemical bond [1]. Similar to other fundamental concepts in chemistry, such as valency, bond order, and aromaticity, the chemical bond has not been sharply defined by modern quantum mechanics; it lacks a precise definition, and its quantification is difficult, if not impossible. From the perspective of quantum mechanics, the difficulty stems from the fact that although a proper description of the chemical bond can be rooted on physically observable properties, no quantum mechanical "bond operator" exists that would provide a conventional expectation value. At the heart of the matter is the question: what is the nature of the chemical bond? Unfortunately, the chemical bond cannot be unambiguously assigned to any quantum chemical observable, as the chemical bond is unobservable, and there is also no unique way to theoretically define the chemical bond.

Currently, new chemical understanding has been driven mainly by the experimental discovery of new compounds and their reactivity. This experimental work is expensive and time consuming, but the payoff for discovering new chemical structures and chemical reactions is enormous in terms of both fundamental understanding and practical engineering. In recent years, attention to this field has increased, and new types of chemical bonds have been invoked with a plethora of important new types of molecules discovered. Computational advances have brought quantum chemistry to the stage where it is widely applied for the qualitative interpretation of new experimental findings and increasingly used to construct detailed quantitative descriptions of chemical bonds. We will now present a compilation of current literature about the different types of chemical bonds whose nature still gives rise to debates.

The discussion on the existence (or not) of a sextuple and quadruple bond in Cr_2 in C_2, respectively [2–9], is contrary to what would be normally expected for main group elements because, in principle, they should exhibit at most a triple bond. Furthermore, there is a debate on the nature of hydrogen bonding [10–12], while the unusual bonding arrangements found in highly strained small-ring polycyclic molecules are still a matter of controversy, thereby presenting challenging issues from a theoretical point of view [13]. Very recently, discrete compounds possessing long, multicenter bonds have been reported [14], and an interesting discussion on the nature of the multicenter bonding that arises in the central rectangular C4 component of the ditetracyanoethylene dianion complex $[TCNE]_2^{2-}$ has been presented [15–17].

Wolstenholme [18] provides a detailed account of recent advances in our understanding of homopolar dihydrogen bonding and an appreciation of its effects on the structure and reactivity of hydrogen-rich materials. Hicks et al. [19] have reported examples of a variety of novel compounds containing metal–metal bonds, including at least one Group 12 metal center in the formal 0 or +1 oxidation states, that have been prepared and analyzed by spectroscopic, crystallographic, and computational techniques. In particular, these authors prepared species containing the first Zn–Cd bond in a molecular compound. The stability of all the new compounds can be attributed to the considerable steric protection provided to their metal–metal cores by the extremely bulky amide ligands that coordinate those cores.

Butovskii and Kempe [20] presented recent advances, challenges, and perspectives on rare earth–metal bonding in molecular compounds and highlighted novel aspects of their syntheses, properties, and reactivities.

Very recently, Blake et al. [21] created the unique trimetallic complex $\{(^{Ar'}NacNac)Zn\}_2Hg$**.** At the molecule's heart lies a Zn–Hg–Zn unit, which is the first example of a bond between two different group 12 metals. This metal chain is also the first example of catenation between group 12 elements other than just mercury, and it is also a rare instance of zinc in the +1 oxidation state, and an analysis based on a theoretical study suggests that it is best described as two formally Zn (I) atoms with a Hg(0) atom positioned in between. Cui et al. [22] reported a multicenter-bonded $[Zn^I]_8$ cluster with cubic aromaticity, where quantum chemical studies reveal extensive electron delocalization and stabilization over the cube, with the bonding pattern of the cube being a class of aromatic system that they refer to as cubic aromaticity. On the other hand, an interdisciplinary research team [23] observed and theoretically investigated (with the relativistic density functional theory including spin–orbit coupling effects) the 1-bond ^{199}Hg ^{15}N J-coupling within the Hg II-mediated thymine–thymine base pair (T–Hg II–T). This strikingly large 1 J (^{199}Hg, ^{15}N) is the first one for canonical sp^2-nitrogen atoms, which can be a sensitive structure-probe of N-mercurated compounds, and direct evidence for N-mercuration. Very recently, through comprehensive characterizations, in-depth analysis, and first principle calculations, Qian et al. [24] found that the Ge–Ge bonds formed in Zn_2GeO_4 can act as a light-absorbing chromophore-like structure, which plays a crucial role in enhancing the visible-light adsorption. On the other hand, Liddle et al. synthesized an uranium (IV)–arsenic complex, using the soft donor ligand tri(amido)amine, where the central bond remained stable under ambient conditions. Although the uranium–arsenic bond was polarized and fragile, the bonding remained covalent and one-, two-, or threefold depending on the parent complex synthesized. This discovery may help improve the performance of chemical treatments used to recycle nuclear waste [25].

Bauzá and Frontera [26] proposed the new term of "aerogen bonding" to describe the unprecedented σ-hole interactions between electron-rich entities (anions or lone pair-possessing atoms) and elements belonging to Group 18 (known as the noble gases or aerogens). Aerogen bonds involve low-electron density areas around xenon atoms that are known as σ-holes. These atoms have already been found to mediate non-covalent bonds for every other p-block group and to complement the σ-hole interactions involving group 15, 16, and 17 elements known as pnicogen, chalcogen, and halogen bonding, respectively. The first examples of Xe^{VI}–N bonds were reported by Schrobilgen et al. [27], who synthesized and structurally characterized $F_6XeNCCH_3$ and $F_6Xe(NCCH_3)_2$ compounds by X-ray crystallography, Raman, and NMR spectroscopy, as well as first principle calculations. The geometry of the XeF_6 moiety in $F_6XeNCCH_3$ was nearly identical to the calculated distorted octahedral (C_{3v}) geometry of gas-phase XeF_6. The C_{2v} geometry of the XeF_6 moiety in $F_6Xe(NCCH_3)_2$ resembled the transition state proposed to account for the fluxionality of gas-phase XeF_6.

Frenking et al. [28] reported a combined experimental and theoretical work for the synthesis and spectroscopic characterization of the boron dicarbonyl complex $[B(CO)_2]$. A detailed analysis using state-of-the-art methods of the electronic structure of $B(CO)_2$ suggests that the bonding situation is best described in terms of donor–acceptor interactions. The chemical behavior shows typical features of carbonyl complexes, which are known from transition metal carbonyls. This is further supported by the suggestion that the anion $[B(CO)_2]$ is a boron complex. In addition, the associated neutral boron dicarbonyl complex $[(RB)(CO)_2]$, in which R is a bulky aryl group, has been synthesized and structurally characterized by X-ray crystallography by Braunschweig and coworkers [29, 30]. Chen et al. [31], based on isotope effects and quantum chemical calculations, identified that diborane B_2H_4 possesses two bridging B–H–B bonds. Plenty of controversy on the nature of the central B–B bond in the diboryne compound $B_2(NHCR)_2$, where diatomic B_2 binds two N-heterocyclic carbenes (NHC) that carry bulky R groups in the nitrogen atom, can be found in recent literature [32–39]. Wu et al. [40] reported ultrashort metal−metal distances (1.728–1.866 Å) between two Be atoms in different molecular environments, including a rhombic Be_2X_2 (X = C, N) core, a vertical Be−Be axis in a 3D molecular star, and a horizontal Be − Be axis supported by N-heterocyclic carbene (NHC) ligands, rivaling metal−metal quintuple bonds between the transition metals.

Studies on the nature of the chemical bond in heavier group 14 element (E) alkene analogues, and related multiple-bonded compounds, have been a topic of broad interest [41–43]. Analyzing their results from accurate calculations, Power et al. [44] showed that the interplay between dispersion force attraction, steric repulsion, and element–element bonding stabilizes dimeric structures. Although the E–E distances indicate that E–E bonding is present in the germanium and tin dimers, and possibly the lead dimer, the bonding is weak and represents a relatively small fraction of the binding energy. The results emphasize the importance of including attractive dispersion force interactions in consideration of multiple-bonded heavier main group element species, where sterically encumbering ligands are employed in their stabilization. Based on structural, spectroscopic, and theoretical considerations, Ruschewitz [45] has evidenced the presence of $[Ge = Ge]^{4-}$ dumbbells with unprecedented short Ge−Ge distances in the Zintl phase Li_3NaGe_2.

Based on their analysis of the results obtained from high-angle X-ray diffraction techniques and quantum theory of atoms in molecules, Mitzel et al. [46] shed new light on the nature of the chemical bonds in $Al_2(CH_3)_6$, which was previously described by contradicting interpretations of bonding. In a theoretical work, Ohno et al. [47] reported a new class of carbons called wavy-carbon sheets and tubes, which adopt wavy structures with condensed four-membered rings. The variety of the forms can give a hint into designing novel materials with new mechanical, physical, and/or chemical properties. For example, because of the very high relative energies with respect to graphene, the wavy carbons may behave as energy-reserving materials.

In recent years the importance of non-covalent intermolecular interactions in chemistry, such as hydrogen bonding (H-bonding) and pi-stacking, has been clearly recognized and has risen to the forefront of chemical research [48–50]. Therefore,

adequate computational tools have been developed and applied to understand these type of interactions [51–53]. In this context, Zhao et al. [54] presented a perspective highlighting the importance of unorthodox non-covalent interactions in functional systems, and these authors placed an emphasis on anion and cation interactions, halogen, and chalcogen bonds in catalysis, self-assembly, transport, sensing, and templating processes.

2 Quantum Mechanics and Electron Density

In 2007, a special issue of the *Journal of Computational Chemistry* titled "*90 Years of Chemical Bonding*" was published [55]. In this issue, Frenking and Krapp compared the chemical bond to a "unicorn", seeing it as a "mythical but useful creature which brings law and order [···] in an otherwise chaotic and disordered world" [56], where everyone knows what it looks like, despite nobody ever having seen one [57, 58]. This line of reasoning is similar to Coulson's comment: "Sometimes it seems to me that a bond between two atoms has become so real, so tangible, so friendly, that I can almost see it. Then I awake with a little shock, for a chemical bond is not a real thing. It does not exist. No one has ever seen one. No one ever can. It is a figment of our own imagination" [59]. Even, chemical bonds have been described as "noumenon" rather than as "phenomenon" [60–62].

In chemistry, as in other scientific disciplines, there is no place for ambiguity. The definition of a concept, such as a chemical bond, must be clear and unequivocal, building those definitions is the raison d'être for the existence of the IUPAC body (the "IUPAC Gold Book" can be found under http://goldbook.iupac.org); unfortunately, this is not the case. As other fundamental concepts, the chemical bond lacks a unique and precise definition. As quoted by in the Ritter's paper: [63] "My advice is this," Hoffmann says. "Push the concept to its limits. Be aware of the different experimental and theoretical measures out there. Accept that at the limits a bond will be a bond by some criteria, maybe not others. Respect chemical tradition, relax, and instead of wringing your hands about how terrible it is that this concept cannot be unambiguously defined, have fun with the fuzzy richness of the idea." In science, advanced theories are held by two milestones: (i) a mathematical structure/formalism disclosing the basic entities of the theory and their mathematical relationships and (ii) an "interpretative" recipe of the basic entities of the theory. The latter discloses the qualitative meaning of the basic entities and their relation to other known entities within and beyond the theory. It is important to recognize that the connection between the mathematical formalism of a theory and its interpretation is always subtle. This problem can be traced back to the lack of a clear and unambiguous definition of a bond in quantum mechanics, and a plethora of interpretations have been introduced with various "meanings" of the "mathematical symbols/entities" of the theory [64].

In regard to this quandary, two opposite attitudes can be envisaged. The first on is the the old and negative statement of the French mathematician R. Thom, who stated, "Il me faut cependant avouer que la chimie proprement dite ne m'a

jamais beaucoup intéressée. Pourquoi? Peut-être parce que des notions telles que celles de valence, de liaisons chimique etc., ont toujours semblées peu claires du point de vue conceptuel." (I should admit that chemistry never really interested me. Why? Perhaps because notions such as that of valence, chemical bond, etc., always appeared unclear from the conceptual point of view.) The second one is the more actual and pragmatic comment by Alvarez et al. who said, "Chemistry has done more than well in a universe of structure and function on the molecular level with just this imperfectly defined concept of a chemical bond. Or maybe it has done so well precisely because the concept is flexible and fuzzy" [65]. However, it is important to note that scientific arguments, debates, and controversy are at the heart of chemistry. This situation has been clearly stated in the very recent paper entitled "*The Nature of the Fourth Bond in the Ground State of C2: The Quadruple Bond Conundrum*" by Danovich et al. [66], in which these authors recognize that they are in front of a "Rashomon effect" (see en.wikipedia.org/wiki/Rashomon effect), in which the bonding picture risks are becoming too fuzzy to be constructive anymore.

For decades, from an experimental point of view, the possibility to manipulate the bond-breaking process in a polyatomic molecule has been acknowledged as a crucial ability in both science and technology. The nuclear motion involved in the breaking of a chemical bond in a molecule typically proceeds on time scales from several femtoseconds to picoseconds. These dynamics are driven by the derivatives of the potential formed by the electron distribution, which can restructure on much faster, attosecond, time scales. A suitable perturbation of the equilibrium bound electronic distribution, for example, induced by ultrashort intense laser pulses, can therefore initiate nuclear motion toward a desired bond-breaking event. A relatively slow molecular fragmentation can thus be predetermined on the much faster electronic time scale. This has been demonstrated for fragmentation reactions resulting in two moieties using the carrier-envelope offset phase of few-cycle laser pulses as the control parameter [67–73]. Very recently, Xie et al. demonstrated how to control decomposition reactions by the selective removal of electrons from either the inner or outer valence orbitals based on their different shapes [74] or their different sensitivity to laser intensity and/or pulse duration [75]. In particular, this research group showed experimentally and by quantum simulations that the outcome of complex fragmentation reactions of an ethylene trication, which involves the breakage of more than one chemical bond, sensitively depends on the duration of the inducing intense, nonresonant, ultrashort laser pulse. Specifically, they demonstrated that the yield ratio for fragmentation into three versus two fragment ions can be determined using the duration of the laser pulses as a parameter [76].

Almost all of quantum chemistry are based on the solution of the many-body Schrodinger equation. This solution consists of the eigenvalues (the energies typically obtained from ab initio calculations) and eigenfunctions (the wave function, where $\Psi(r).\Psi^*(r) = \rho(r)$ and is a quantum mechanical observable). It is important to include the eigenfunctions, as they contain a plethora of information which would otherwise be lost, particularly considering that the charge density $\rho(r)$ is an experimentally observable—and thus a directly comparable—parameter. Therefore, a quantum mechanics-based theory should be able to provide the framework to

make sense of and predict future experimental findings, as empirical techniques improve beyond current expectations. To this end, there is growing interest in explaining chemical phenomena arising from the structure of the electron density. In this context, Heisenberg expresses this necessity to establish quantum mechanics in the introductory sentence to his 1926 seminal manuscript: "The present paper seeks to establish a basis for theoretical quantum mechanics founded exclusively on relationships between quantities which are in principle observable" [77, 78].

One branch of this developing discipline is the conceptual density functional theory [79], which has provided rigorous definitions for various chemical concepts such as electronegativity [79] and hardness [80], as well as relating changes within the density to frontier orbital concepts through the Fukui function [81]. Electron density is the best choice because it is a local function defined within the exact many-body theory, and it is also an experimentally accessible scalar field. Its paramount role in the description of many-body problems is supported by the Hohenberg–Kohn theorem [82]. The density functional theory [82, 83] asserts that the single particle density $\rho(r)$ contains all the information of a system, and the total energy attains the minimum value for the true density. In Kohn − Sham DFT (KS-DFT) calculations [83], the unknown piece of the energy, the exchange-correlation energy, $E_{XC}[\rho]$, is approximated, $E_{XC}{}^{app}[\rho]$. The self-consistent solution of the KS equations then yields the density that minimizes the total energy, $\rho^{app}(r)$, and the calculated approximate total energy is $E^{app}[\rho^{app}]$.

Considering the solid foundations and remarkable success of the density functional theory, today there is very little doubt that electron density contains all the useful information about the electronic structure of molecular systems. The electron density, $\rho(r)$, of a molecular system can represent all information hidden in the wave function of such systems.

The electron density distribution of a molecule or a crystalline material can be obtained from high-resolution X-ray diffraction experiments or first principle calculations. These physical–chemical methods provide detailed information about the nature of intra- and intermolecular charge interactions in these systems. Presently, the current electronic structure theory of molecules, i.e., quantum chemistry, can provide accurate snapshots of the electronic distribution associated with geometrical changes of very large molecules, which can provide us with a picture resembling the total electron density distribution coming from X-ray diffraction but, arguably, significantly richer in information about the nature of chemical bonds. Although the Hohenberg–Kohn theorem guarantees that all the molecular information is encoded in the electron density, the physical description of chemical systems requires additional postulates for extracting observable information in terms of atomic contributions. Stalke [84] provides a short introduction to the basics of electron density investigations to demonstrate how charge density analyses can shed light on aspects of chemical bonding and reactivity resulting from the determined bonding situation. Very recently, Karadakov and Horner [85] analyzed the possibility to describe chemical bonds using detailed computed isotropic shielding isosurfaces and contour plots, providing an unexpectedly clear picture of chemical bonding, which is much more detailed than the traditional description in terms of the total electron density.

Alternatively, the nature of the chemical bond can be investigated using concepts from quantum information theory [86–92]. Information-theoretical quantities such as Shannon entropy [93], Fisher information [94], Ghosh-Berkowitz-Parr entropy [95, 96], and information gain [97] are functionals of the electron density and its associated quantities (e.g., density gradient and Laplacian, etc.), and so they should be natural descriptors of chemical reactivity. This approach allows to interpret chemical structures and phenomena through the information content of the electron densities in conjugated spaces (position and momentum) [98]. Esquivel [99] and Dehesa et al. [100] have studied the quantum information features of selected elementary chemical reactions, and very recently, these authors gained a deeper understanding about the role played by entanglement on molecular systems and chemical processes, particularly in the water molecule, and the hydrogenic abstraction reaction, showing that the entanglement phenomenon could be associated with the chemical reactivity of the process [101].

3 Topological Analysis

Quantum mechanics constitutes the fundamental framework behind the theoretical study of chemical structures, reactivity molecular systems, and chemical reactions. The quantum mechanical approach to chemical phenomena usually deals with very complex numerical algorithms for the approximate solution of the many-body Schrödinger equation. Within this context, the direct analysis of the wave function, as an eigenstate of an electronic Hamiltonian, provides complete information on the electronic structure of the system. Unfortunately, the wave function is an extremely complex object that depends on the positions and spins of all the electrons; therefore, analyzing details or comparing many-electron wave functions is virtually impossible owing to various practical difficulties. Furthermore, the indistinguishability of electrons means that any property extracted for a given electron (treated as distinguishable) from a properly antisymmetrized wave function must be identical to what would be obtained from any other electron. To overcome this difficulty, two approaches are used. The first involves analyzing molecular orbitals as a set of one-particle wave functions. This way, the properties of a single electron, identified as a core, a lone pair, or a bonding electron, for instance, can be extracted. These orbitals are functions of just three dimensions and are easier to interpret, either as density plots or isosurfaces. However, orbitals are nonunique, and a given wave function may not even be dominated by a single configuration. The second revolves around condensing the relevant information into a single three-dimensional function of space: a molecular scalar field. Therefore, the attempts made so far to extract the flow and electron transfer processes along the reaction pathway associated to a chemical reaction from quantum chemical calculations are wave function-based or orbital-based methods. These methods generate orbital representations of the wave functions and the derived based energy properties, which in turn assist the qualitative interpretation of the chemical structure and reactivity

of molecules, and provide predictive capabilities. In this sense, molecular orbitals allow one to define the chemical bond as a pair of electrons shared by two or more nuclei, as put forward by Lewis [102]. Furthermore, the valence bond theory developed by Pauling [103–106], in which the superposition of resonating Lewis structures represents the chemical bonds of the molecule by localized electron pairs, provides interpretations on the very nature of bonds, the structure of the molecules, and even their reactivity [107, 108].

On the other hand, methods based on the analysis of the wave function or electron density form, the so-called quantum chemical topology (QCT) [109–112], such as the quantum theory of atoms in molecules [113] and the electron localization function (ELF) [114, 115], have provided concepts arising from topological properties of the electron density, and several fields derived from it to obtain chemically relevant information. Topological analysis is a useful tool to characterize intra- and intermolecular interactions, and different classes of bonding analysis methods are based on the topology of scalar fields [116, 117], with different applications of these already published in the literature [118–128].

Scalar and vector fields, such as the gradient of the electron density ($\nabla\rho$), the electron localization function (ELF) and its gradient, the localized orbital locator, the region of slow electrons, the reduced density gradient, the localized electrons detector, information entropy, molecular electrostatic potential, and the kinetic energy densities K and G, among others, can be evaluated on zero, one, two, and three-dimensional grids. These latter methods have the advantage of being based on the analysis and response of the electron density, i.e., a quantum mechanical observable. The topology of these fields associated with the electron density distribution is, in principle, independent of the approximations made to calculate the approximate wave function. Recently, different authors answered the following questions: what is the significance of a topological approach? Can new chemical concepts be found by a topological approach? What is the status of a chemical concept within a topological approach? Should topological approaches provide measurable quantities? Is it possible to predict the outcome of a topological approach without performing calculations on a computer? And what are the new domains for which topological approaches would be useful? [129].

The name QTC [110, 130] has been introduced to embrace all topological investigations of three-dimensional scalar fields [113, 114, 131–136], to rationalize the chemical bond, and to further understand chemical reactivity [137–145]. A number of excellent works in the subject have been published to highlight the importance of charge density analysis applied to chemical and biological systems and solids [84, 111, 113, 146–152]. Recently, Pendás and Hernández-Trujillo [153] found that the topology of a vector field, i.e., the Ehrenfest force density that corresponds to the force density, is the electrostatic force acting on any point in the electron density due to all the other particles in the molecule, while Dillen [154] analyzed the topology of the Ehrenfest force density using basis sets based on Slater-type orbitals.

In this context, the best-known approaches include the “atoms in molecules” theory (QTAIM), which relies on the properties of the empirically observable

electron density $\rho(r)$ [113, 148, 151, 155], and the electron localization function (ELF) method [156]. The QTAIM has been widely used to study molecules [157, 158], solids [159–161], complexes [162–165], and chemical reactions [166–168]. QTAIM uses the electron density to study well-defined localized parts of a system, instead of dealing with the whole molecule. The electron density can be obtained from ab initio calculations and directly from X-ray diffraction experiments. Moreover, QTAIM allows the classification of interactions within a molecule with the molecular graph (i.e., the set of bond paths and its critical points that define its molecular structure).

Using the topology of the electron density, the atoms inside a molecule are defined by regions in space called atomic basins, which are bounded by zero-flux surfaces. Atomic properties (e.g., electron population and atomic volume) are calculated using the volume integral of the appropriate variable over the atomic basin. Bader's approach provides an excellent tool for the interpretation of both X-ray determined and theoretical charge densities. An analysis of the charge density is based upon the topological properties of the density $\rho(r)$, which is based upon the bond critical points where the gradient of the density vanishes. The properties evaluated at such points characterize the bonding interactions that are present and have been widely used to study intermolecular interactions. The application of this approach allows for the establishment of a network of intermolecular contacts, and it permits an estimation of their energy through the correlation between the energy and the electron density at the bond critical point [113].

The electron localization function (ELF) was introduced by Becke and Edgecombe [156] for the Hartree–Fock theory, and it was extended to the Kohn–Sham density functional theory (DFT) via an alternative interpretation by Savin and Silvi [114]. This function has enjoyed enormous success as a tool for understanding and visualizing chemical bonds. The ELF analysis is based on the topology of the electron localization function $\eta(r)$ [156, 169, 170], which measures the Pauli repulsion between electrons due to the exclusion principle [171], and is widely used to characterize localized electrons. ELF performs a topological analysis of the same-spin pair probability density and thus generates basins of localized electron pairs. Each ELF basin is related to pairs or groups of electrons, such as core and valence basins. Lone pairs and bonds involving hydrogen atoms are associated with monosynaptic basins, whereas covalent and polar bonds usually exhibit disynaptic basins [172, 173]. The electron population and shape of the ELF basins are commonly used to feature bond interactions [114, 115]. A topological analysis allows for an evaluation of the relationship between the nature of the bond and the chemical reactivity of the molecule. The quantification of the electron density and the associated energetics in both intra- and intermolecular space in solids is thus of extreme interest.

As it was mentioned below, the chemical bond is a chemical concept and not an observable in the quantum mechanical sense; therefore, it does not appear in the Hamiltonian. In other words, no quantum mechanical "bond operator" exists that would provide the desired answer, for example, as a conventional expectation value. As Fleming Crim of the University of Wisconsin–Madison puts it, cited by P. Ball

[174], "A bond is an entity described by quantum mechanics but not a fixed "entity" in that it will behave differently depending on how we perturb and interrogate it," but our intuitive perception of molecular phenomena in the three-dimensional space demands such a representation. Thus, interpretative tools are necessary to recover the chemical structure and reactivity, and more specifically to understand the process of bond formation and breaking during reactions. With a similar perspective, Lewis conceived the idea of electron pairs [102]. The description of electron pairs is at the heart of understanding the chemistry of a given compound because the reorganization of electron pairs drives any chemical reaction, and it is based on the seminal work of Lewis, who identified chemical bonds as electron pairs shared between the bonded atoms [175].

The theoretical background of the quantum chemical methodologies and details of the quantum chemical calculations we have used for this study are included in the ESI.‡. Their brief description is given here.

In summary, the electron density $\rho(r)$ contains the complete information about a molecular system. It may be obtained using several methods of quantum chemistry, ranging from the very state function by contraction of density matrices [176], to the Kohn–Sham density functional theory [177]. Further progress has been achieved with the advent of topological theories of the electron density and its related functions [148, 178], and computational tools have enabled a more detailed description of the electron distribution. Overall, a more precise understanding of the interactions between atoms has led to the detection of the onset of complex patterns of chemical bonding. This subject is under consideration here, and this chapter constitutes a natural scenario for the application of these techniques to complex systems such as transition metal clusters or silver chromate.

4 Transition Metal Clusters

Transition metal clusters can act as selective catalysts in several cases. For instance, diphosphino, aminophosphino, and diamino Mo_3S_4 cuboidal clusters are efficient catalysts or pre-catalysts for the hydrogenation of aromatic nitro derivatives [179, 180]. The core of these trimetallic clusters is chiral, and the terms *P* and *M* are used depending on the stereospecific arrangement of the substituents around the Mo_3S_4 core. In addition, depending on the nature of the ligands, additional sources of stereogenicity can be provided.

In particular, the synthesis of $Mo_3S_4Cl_3$ clusters bearing (*R*)- and (*S*)-2-[(diphenylphosphino)methyl]pyrrolidine ligands, which are aminophosphine ligands derived from (*R*) and (*S*) proline, could afford several diastereoisomers depending on how the ligand binds to the molybdenum centers, on the substituents' arrangement around the core of the cluster, and on the atomic arrangement around the chiral carbon atom of the ligands, and also around its chiral nitrogen atom. In Scheme 17.1, the *P* and *M* dispositions around the cluster core are depicted in the upper row, where two different binding modes of the ligands to the molybdenum

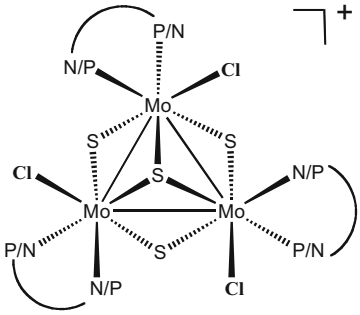

P arrangement around the cluster core

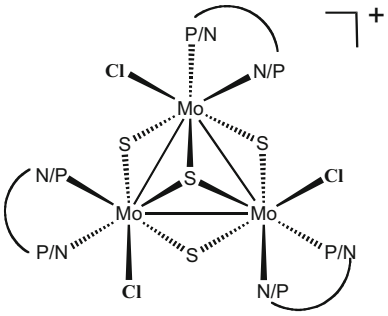

M arrangement around the cluster core

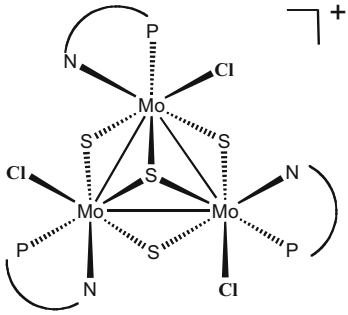

Ligand coordination with P atoms trans to the capping sulphur

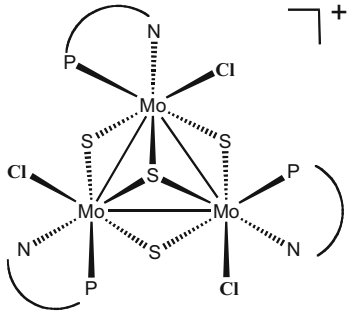

Ligand coordination with N atoms trans to the capping sulphur

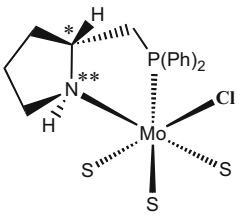

* *R* arrangement around the chiral C atom and
** *S* arrangement around the N atom

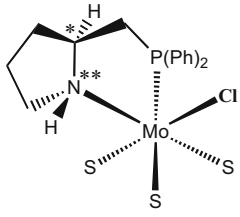

* *S* arrangement around the chiral C atom and
** *R* arrangement around the N atom

Scheme 17.1 Different sources of stereogenicity in Mo_3S_4 aminophosphino clusters

centers are schematized for a *P* arrangement in the middle row; and two examples of arrangements around the chiral atomic centers of the coordinated ligands are offered in the bottom row.

It has been established that, among all possible diastereomers, only those with phosphorus atoms on the ligands placed *trans* to the capping sulfur of the cluster core can be obtained and also that the stereochemistry around the N atom of the ligands is always *S*. In this way, only four diastereomers with *S* arrangement around the N atoms (S_N), with an *R* or *S* distribution around the chiral C atoms of the ligands (R_C or S_C), and with a (*P*)- or (*M*)- distribution around the cluster core remain as possible products of the synthesis. We use the following notation for these diastereomers: *(P)-[Mo-(S_N,R_C)]*$^+$, *(M)-[Mo-(S_N,R_C)]*$^+$, *(P)-[Mo-(S_N,S_C)]*$^+$, and *(M)-[Mo-(S_N,S_C)]*$^+$. At variance with the results observed with similar diphosphine clusters, in which (*R*,*R*) diphosphine invariably led to *P* clusters, while (*S*,*S*) diphosphines afforded only *M* clusters [181–183], in the present case only the (*P*)-diastereomers could be experimentally detected within the synthetic outcome [184]. To rationalize this unexpected result, a theoretical study including the topological aspects was conducted. All geometrical optimizations and NBO calculations were performed with the Gaussian09 program suite [185]. The density functional theory was applied with the Becke hybrid B3LYP functional [186–188]. The double-ξ pseudo-orbital basis set LanL2DZ, in which all atoms are represented by the relativistic core LanL2 potential of Los Alamos, was used. Geometry optimizations were performed in the gas phase without any symmetry constraint, followed by analytical frequency calculations to confirm that a minimum had been reached. The ELF analysis was performed by means of the TopMod package, [131] considering a cubical grid of stepsize smaller than 0.05 Bohr, on the wave function obtained at the B3LYP/3-21G//B3LYP/LanL2DZ theoretical level.

The four aforementioned diastereoisomers, *(P)-[Mo-(S_N,R_C)]*$^+$, *(M)-[Mo-(S_N,R_C)]*$^+$, *(P)-[Mo-(S_N,S_C)]*$^+$, and *(M)-[Mo-(S_N,S_C)]*$^+$, were taken as cluster models for the B3LYP calculations. The initial structural parameters of the *(P)-[Mo-(S_N,R_C)]*$^+$ and *(P)-[Mo-(S_N,S_C)]*$^+$ cations were extracted from crystallographic data, whereas the (*M*)-isomers were built by changing the chlorine and aminophosphine orientation while preserving the configuration of the stereogenic centers. The optimized bond distances and dihedral angles, as well as the calculated relative energies, are listed in Table 17.1. The experimentally isolated *(P)-[Mo-(S_N,R_C)]*$^+$ and *(P)-[Mo-(S_N,S_C)]*$^+$ stereoisomers were the most stable compounds and the highest stability calculated for *(P)-[Mo-(S_N,S_C)]*$^+$ agreed with the expected stabilization attributed to the vicinal Cl···HN interaction observed in the crystal structure and also to the ligand configuration. In contrast, *(P)-[Mo-(S_N,R_C)]*$^+$ turned out to be 15.4 kcal/mol more stable than its corresponding *M* diastereoisomer; the *(P)-[Mo-(S_N,S_C)]*$^+$ isomer was 20.0 kcal/mol less energetic than the *(M)-[Mo-(S_N,S_C)]*$^+$ cation. These differences suggest a thermodynamic preference to the formation of *P* isomers.

The calculated bond distances listed in Table 17.1 show good agreement with the experimental data for the *(P)*-clusters [184], whereas the longer Mo–Mo and Mo-(μ_3-S) distances for *(M)-[Mo-(S_N,R_C)]*$^+$ and *(M)-[Mo-(S_N,S_C)]*$^+$ suggest a slight distortion of the Mo_3S_4 cluster core for these theoretically calculated species. The calculated values for the dihedral angles that describe the conformation of the bicyclic system in the ligand are also in good agreement with the experimental data,

Table 17.1 Theoretical averaged bond distances, dihedral angles, and relative energies for compounds *(P)-[Mo-(S_N,R_C)]*$^+$, *(P)-[Mo-(S_N,S_C)]*$^+$, *(M)-[Mo-(S_N,R_C)]*$^+$, and *(M)-[Mo-(S_N,S_C)]*$^+$

Distances (Å)	*(P)*-[Mo-(S_N,R_C)]$^+$	*(P)*-[Mo-(S_N,S_C)]$^+$	*(M)*-[Mo-(S_N,R_C)]$^+$	*(M)*-[Mo-(S_N,S_C)]$^+$
Mo–Mo	2.807	2.805	2.834	2.845
Mo-(μ_3-S)	2.438	2.443	2.461	2.449
Mo-(μ-S)[a]	2.380	2.387	2.376	2.376
Mo-(μ-S)[b]	2.379	2.367	2.356	2.371
Mo–P	2.661	2.631	2.673	2.633
Mo–N	2.289	2.291	2.297	2.362
Mo–Cl	2.550	2.570	2.600	2.544
Dihedral C_5-N-C_2-C_1	8.770°	95.723°	24.866°	81.800°
Dihedral C_3-C_2-N-Mo	179.573°	14.052°	6.480°	4.885°
Energies (kcal/mol)[c]	4.8	0.0	20.2	20.0

[a]Distance *trans* to the Mo–N bond
[b]Distance *trans* to the Mo–Cl bond
[c]Relative to *(P)-[Mo-(S_N,S_C)]*$^+$

with differences ranging less than three degrees. Therefore, both the experimental and the theoretical studies establish that the *(P)-[Mo-(S_N,S_C)]*$^+$ complex exhibits a *cis*-fused conformation of the bicyclic system, which confers additional stabilization to the system. In addition, the stabilizing effect of the vicinal Cl···HN interaction can also be observed in the *(P)-[Mo-(S_N,S_C)]*$^+$ calculated structure, which showed an interatomic Cl···H distance of only ca. 2.32 Å. A similar Cl···HN interaction was also noticed in the calculated *(M)-[Mo-(S_N,R_C)]*$^+$ species, with a Cl···H distance of 2.255 Å, although in this case the interaction took place between the NH and Cl belonging to the coordination sphere of the same metal center as the cluster unit.

In order to gain a deeper insight into the nature of such Cl···HN interactions, we performed natural bond order (NBO) and a topological electron localization function (ELF) analyses. The bonding character of the shortest Cl···HN interactions for *(M)-[Mo-(S_N,R_C)]*$^+$ and *(P)-[Mo-(S_N,S_C)]*$^+$ were confirmed by their higher bond orders (0.043 and 0.052, respectively; see Table 17.2) in comparison to those calculated for geminal and vicinal Cl···HN interactions found for the respective *(P)-[Mo-(S_N,R_C)]*$^+$ and *(M)-[Mo-(S_N,S_C)]*$^+$ isomers (bond orders of ca. 0.003). The Cl–H bond order calculated for the *(M)-[Mo-(S_N,R_C)]*$^+$ species was ca. 17% lower than the bond order calculated for the *(P)-[Mo-(S_N,S_C)]*$^+$ species, which qualitatively agrees with the calculated stabilities, i.e., the *(P)-[Mo-(S_N,S_C)]*$^+$ species has a higher bond order and is more stable than the *(M)-[Mo-(S_N,R_C)]*$^+$ cation.

On the other hand, the ELF analysis of the Cl···HN molecule fragment shows the disynaptic V(N–H) basin accounting for the covalent N–H bond and two monosynaptic V(Cl) basins, one roughly oriented to the hydrogen atom and the other to the molybdenum atom, as can be seen in Fig. 17.1.

There was no disynaptic V(Cl–H) basin, as was expected due to the ionic character of this Cl···H interaction. The population of the V(Cl) basin pointing to

Table 17.2 Wiberg bond indexes (B) obtained at the B3LYP/3-21G//B3LYP/LanL2DZ theoretical level

Bond	*B* averaged	Bond	*B* averaged
(M)-[Mo-(S_N,R_C)]$^+$		*(M)-[Mo-(S_N,S_C)]*$^+$	
Cl–Mo	0.655	Cl–Mo	0.740
N–Mo	0.489	N–Mo	0.447
Mo–Mo	0.743	Mo–Mo	0.736
NH	0.747	N–H	0.782
Cl···H (geminal)	0.043	Cl···H (geminal)	0.005
		Cl···H (vicinal)	0.002
(P)-[Mo-(S_N,R_C)]$^+$		*(P)-[Mo-(S_N,S_C)]*$^+$	
Cl–Mo	0.726	Cl–Mo	0.686
N–Mo	0.476	N–Mo	0.478
Mo–Mo	0.751	Mo–Mo	0.751
N–H	0.767	N–H	0.729
Cl···H (vicinal)	0.013	Cl···H (vicinal)	0.052

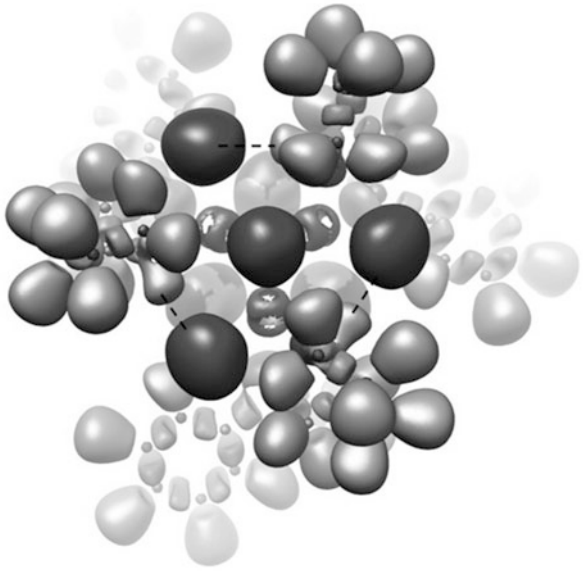

Fig. 17.1 ELF isosurfaces ($\eta = 0{,}75$) for the *(P)-[Mo-(S_N,S_C)]*$^+$ structure. *Dashed yellow lines* indicate the vicinal interaction between the disynaptic V(N–H) basins (*blue*) accounting for the covalent N–H bond and the monosynaptic V(Cl) basins (*red*). Purple basins represent core basins, while green basins indicate disynaptic (covalent bond) basins

the H atom and therefore involved in the Cl···HN interaction was higher for the *(P)-[Mo-(S_N,S_C)]*$^+$ structure (3.91 e^-) than the one found in the *(M)-[Mo-(S_N,R_C)]*$^+$ structure (3.77 e^-). This indicates a more electronic contribution of the V(Cl) to the vicinal Cl···HN interaction in *(P)-[Mo-(S_N,S_C)]*$^+$, as compared with the geminal Cl···HN in *(M)-[Mo-(S_N,R_C)]*$^+$, which supports the higher stabilizing effect of such interactions observed for the *(P)-[Mo-(S_N,S_C)]*$^+$ structure from a topological point of view.

Therefore, in spite of the similar Cl···HN distance calculated for the vicinal interaction in *(P)-[Mo-(S_N,S_C)]*$^+$ as well as for the geminal interaction in *(M)-[Mo-(S_N,R_C)]*$^+$, both the NBO and the ELF analysis suggest a stronger interaction in the vicinal case, thus contributing to its higher stability.

5 Silver Chromate, Ag_2CrO_4

Silver chromate, Ag_2CrO_4, belongs to the important chromate family of Ag-containing compounds with the formula Ag_2MO_4 (M = Cr, Mo, W) [189]. Ag_2CrO_4-based materials have been the subject of extensive research because of their excellent applications in different branches of science and technology, such as IN cathodes for lithium cells and catalysts [190–193].

The motivation for this investigation essentially arises from the discovery of an unwanted real-time in situ nucleation and growth of Ag filaments on Ag_2WO_4, Ag_2MoO_4, Ag_3PO_4, and $AgVO_3$ crystals, which was driven by the accelerated electron beam from an electronic microscope under high vacuum [194–200].

The electron-irradiation-induced formation of Ag nanoparticles on Ag_2CrO_4, synthesized by the coprecipitation method, was observed for the first time [201]. Figure 17.2 shows the TEM images and EDS characterization of Ag_2CrO_4 and the composition of Ag, Cr, and O in the sample, proving that Ag nanoparticles grew on the material's surface. Point 1, which is located in the Ag filament, has a Ag content of 100%. Point 2, which is located in the vicinity of the interface, is composed of 83.92% Ag, 14.64% O, and 1.42% Cr. However, points 3 and 4, which are located in the internal region of the Ag_2CrO_4, are composed of 78.25% Ag, 6.76% O, and 14.98% Cr and 78.42% Ag, 6.01% O, and 15.57% Cr, respectively. The formation of Ag^0 promotes Ag–nanoparticle growth on the surface of the

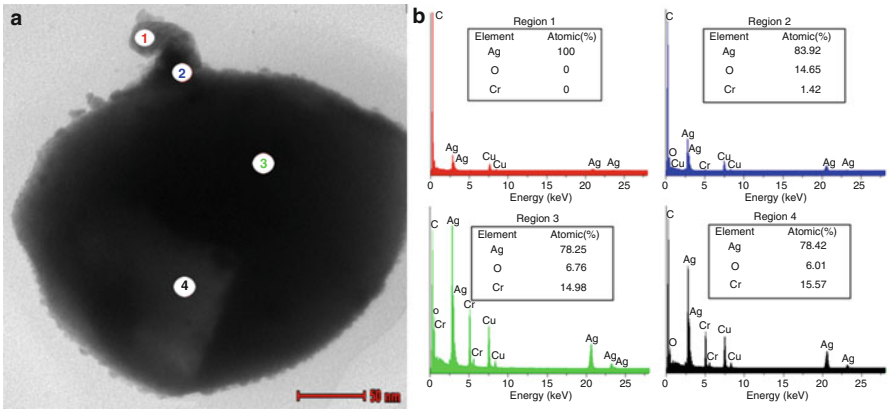

Fig. 17.2 (**a**) TEM image of the Ag_2CrO_4 and (**b**) EDS spectra controlled for four regions

Ag_2CrO_4 microcrystal. Electron irradiation of the material induces the formation of Ag vacancies and thereby transforms the specific region to a p-type semiconductor. In fact, the size of the Ag nanoparticles increases with increasing concentration of Ag vacancies. The material is therefore transformed from an n-type semiconductor to an n-type semiconductor with p-type semiconductors in specific regions, owing to the electron-induced formation of internal defects. The formation and corresponding structural modifications of the $[AgO_6]$ and $[AgO_4]$ clusters were confirmed via theoretical analysis.

To rationalize the experimental measurements (X-ray diffraction with Rietveld analysis, field-emission scanning electron microscopy, transmission electron microscopy with energy-dispersive spectroscopy, micro-Raman spectroscopy, and ultraviolet-visible diffuse reflectance spectroscopy), the QTAIM methodology was used in order to obtain a mechanism capable of explaining the electron redistribution induced by the excess electrons in the bulk and surface of Ag_2CrO_4. In addition, this theory was used to determine the relationship between the structural and electronic changes in both Ag–O and Cr–O bonds of the $[AgO_6]$, $[AgO_4]$, and $[CrO_4]$ constituent clusters, which are shown in Fig. 17.3.

First-principles total-energy calculations were carried out within the periodic DFT framework using the VASP program [202, 203]. In the calculations, electrons were introduced one by one up to four in the orthorhombic unit cell of Ag_2CrO_4, and the distribution of these extra electrons took place by means of simultaneous geometry optimization on the lattice parameters and the atomic positions. The Kohn–Sham equations were solved by means of the Perdew, Burke, and Ernzerhof exchange–correlation functional and by the electron–ion interaction described by the projector-augmented-wave pseudopotentials [204, 205]. The plane–wave expansion was truncated at a cut-off energy of 400 eV, and the Brillouin zones were

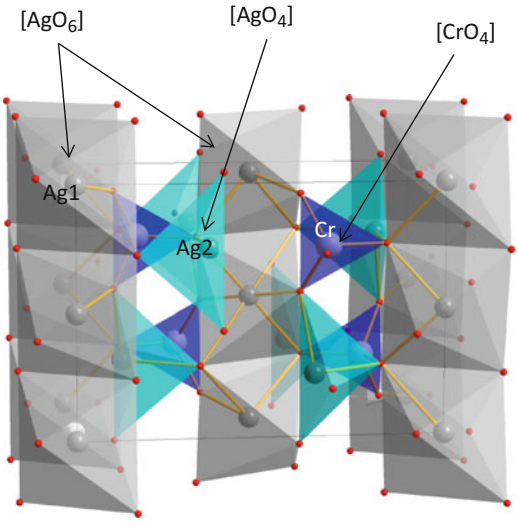

Fig. 17.3 Theoretical representation of the Ag_2CrO_4 orthorhombic structure

Table 17.3 Lattice parameter and bond length as a function of the number of electrons (N) added

	Cell parameters (Å)			Bond lengths (Å)		
N	a	b	c	Ag1–O in [AgO_6]	Ag2–O in [AgO_4]	Ag1–Ag2
0	10.176	7.011	5.618	2.32, 2.40, 2.67	2.31, 2.39, 2.45	3.59
1	10.405	7.079	5.676	2.35, 2.45, 2.73	2.33, 2.41, 2.49	3.62
2	10.751	7.172	5.747	2.27, 2.63, 2.89	2.36, 2.38, 2.48	3.60
3	11.131	7.282	5.933	2.16, 2.94, –	2.40, 2.35, 2.40	3.55
4	11.297	7.463	6.104	2.27	2.37, 2.55, 2.48	3.28
5	11.457	7.644	6.116	2.30	2.44, 2.95, 2.60	2.92
6	11.696	7.533	6.354	2.75	2.51, – , 2.50	2.78
7	13.538	7.612	7.247	2.88	2.71, – , 2.64	2.75

Three different sets of values are shown for the bond lengths: two sets of equal values for the Ag1–O distance and one for the Ag2–O distance

sampled through Monkhorst–Pack special k-point grids that assured geometrical and energetic convergence for the Ag_2CrO_4 structure. Bader atomic charges were calculated using integrations of the charge density (n) within the atomic basins, Ω, and subtracting the nuclear charge, Z, of the corresponding atom.

$$q(\Omega) = Z_\Omega - n(\Omega) \text{ with } n(\Omega) = \int_\Omega \rho(\Omega)\, dr$$

The theoretically estimated values of the lattice parameters and bond lengths as a function of the number of electrons (N) are shown in Table 17.3. As the table shows, the lattice parameters and the lengths of the Ag1–O and Ag2–O bonds increased significantly with an increasing number of electrons. However, the opposite trend was observed in the case of the Ag1–Ag2 bond.

For $N = 3$, [AgO_6] transformed to [AgO_4]´, and [AgO_4] was maintained. When one more electron was added, ($N = 4$), [AgO_4]´ transformed into [AgO_2], and Ag1 was coordinated to two O atoms at 2.27 Å. On the other hand, Ag2, which formed [AgO_4] clusters, maintained its coordination with three equal distances at 2.50 Å, until $N = 6$. When the addition of five electrons was taken into account in the calculations, the Ag1–Ag2 distance decreased from more than 3 Å to 2.92 Å, 2.78 Å, and 2.75 Å at $N = 5$, $N = 6$, and $N = 7$, respectively.

The four Cr–O bond lengths remain practically constant as the number of electrons increased. Hence, the theoretical analyses indicate that the incorporation of electrons is responsible for the structural modification and formation of defects on the [AgO_6] and [AgO_4] clusters, generating the ideal conditions for the growth of Ag nanoparticles.

The Bader charge density of Ag, Cr, and O centers as a function of N is presented in Fig. 17.4. The theoretical calculations indicated that the Ag atoms of [AgO_6] and [AgO_4] had a higher tendency to be reduced, in comparison to the Cr atoms.

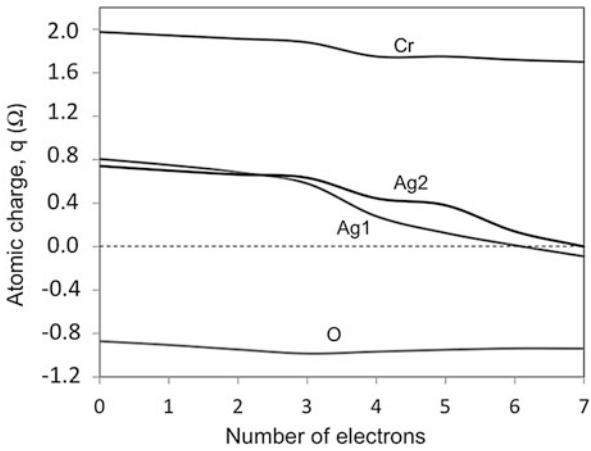

Fig. 17.4 The Bader charge density of Ag, Cr, and O centers as a function of N

Particularly at $N = 6$, Ag1 and Ag2 atoms were practically reduced (from 0.81e to 0.01e), and almost reduced (from 0.74e to 0.14e), whereas for the Cr atoms, a constant value of the electron density was maintained (slight decrease of 0.25 units at $N = 7$).

An analysis of the results presented in Table 17.3 and Fig. 17.4 reveals that the electron density distribution was enhanced between Ag1–Ag2, at the same time that the Ag1–Ag2 contact distance was significantly shortened when the number of added electrons was up to 4. In addition, there was an increase in the electronic charge density in the vicinity of Ag1 from $N = 4$, since Ag1 was coordinated to only two O atoms, and therefore it was more prone to reduction than the Ag2 atoms. At $N = 6$, the Ag1 atoms were practically reduced, whereas the Ag2 atoms required 7 electrons to reach the same state. This behavior implies the existence of two different paths to obtain metallic Ag, which are associated with $[AgO_2]$ (coming from $[AgO_6]$) and $[AgO_4]$ clusters.

Two-dimensional charge density maps associated with the interaction of $[AgO_6]$ clusters and $[AgO_6]-[AgO_4]$ clusters are presented in Fig. 17.5a and b, respectively. Figure 17.5a shows charge density maps associated with four Ag1–O bonds of $[AgO_6]$ clusters, considering a neutral state ($N = 0$) and addition of three ($N = 3$) and six ($N = 6$) electrons, respectively. The zones with high- and low-charge densities are specified by the concentration of charge lines around the atoms, revealing a decrease in the electronic charge density between Ag and O atoms for N from 0 to 6. Thus, the Ag − O bond lengths were enlarged because of the perturbation caused in the system with the incorporation of electrons ($N = 6$). In addition, the charge density maps presented in Fig. 17.5b indicate that the interactions of $[AgO_6]$ and $[AgO_4]$ clusters became weaker when N was increased from 0 to 6, in good agreement with the shortening of $Ag1-Ag2$ distances presented in Table 17.3. Hence, both behaviors theoretically obtained in Figs. 17.5a and 17.5b can be associated with the growth of metallic Ag nanoparticles.

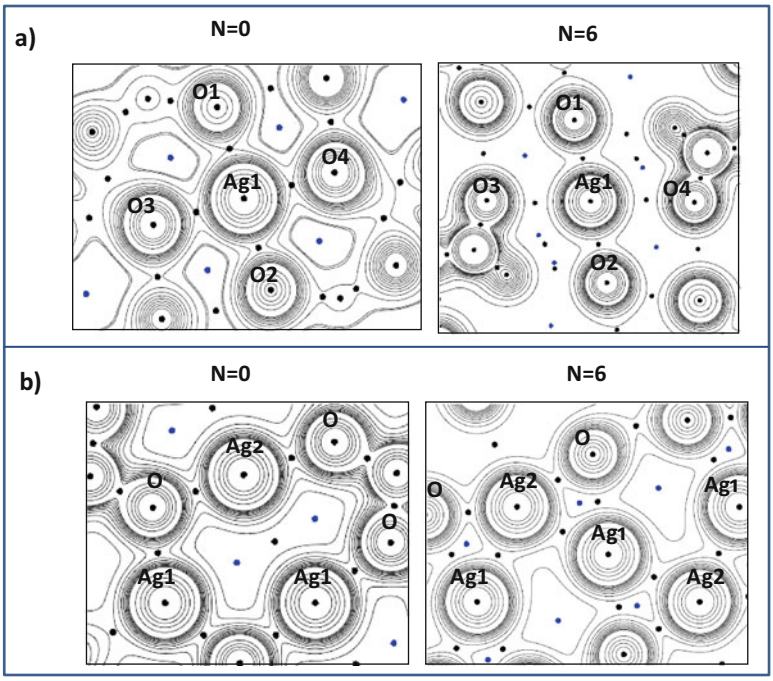

Fig. 17.5 Charge density maps associated with the interaction of (**a**) $[AgO_6]$ clusters and (**b**) $[AgO_6]$ and $[AgO_4]$ clusters

Consequently, the electron excess imposed in the material was transferred from one cluster to another through the Ag_2CrO_4 lattice, so that the formation and growth processes of Ag involved adjacent $[AgO_6]$ and $[AgO_4]$ clusters.

6 Conclusions

One of the most fundamental concepts within chemistry, i.e., the chemical bond, is still a matter of lively debate among chemists and physicists. The nature of the chemical bond is not unambiguous; it lacks a unique and precise definition, and there are disputes about what a bond is and what it is not, about different types of bonds, and how we should define bonds.

In the above context, new and more robust models of chemical bonds (structure) and chemical reactivity are necessary to further our understanding of chemical phenomena. Probing the electron density distribution during a chemical reaction can provide important insights, making it possible to understand and control chemical reactions. Rationalizing the chemical structure and reactivity patterns in terms of the electron density distribution, and their changes along the reaction pathway,

represents the key goal in all branches of chemistry, because the electron density distribution is an observable and therefore can also be determined experimentally [147]. This representation can be considered as a further step with respect to the interpretation based on the concept of molecular orbitals (MOs) [206] or the valence bond theory (VB) [207]. The current electronic structure theory of molecules, i.e., quantum chemistry, can provide accurate snapshots of the electronic distribution associated with geometrical changes of very large molecules. Although the Hohenberg–Kohn theorem guarantees that all the molecular information is encoded in the electron density, the physical description of chemical systems requires additional postulates for extracting observable information in terms of atomic contributions.

In the present study, we used QTAIM, ELF, and CT to analyze and monitor the structure of transition metal clusters and silver chromate. Taking into account this theoretical background, our results are capable of clarifying the nature of chemical bonds on physical grounds and showing how we can directly afford fresh and richer insights and a more correct description of the electronic properties in intuitive terms and unprecedented detail.

The authors apologize to the readers for the often intentional and unintentional simplification of the presentation. The task in this work is to demonstrate to the reader the need to allow a degree of chemical complexity to enter into the rigorous world of structure and chemical reactivity. We believe that these kinds of studies may serve to provide more specific information as to nourish chemical structure theories.

In summary, we tried to study chemical structures from the strict viewpoint of quantum mechanics and, by extension, of quantum chemistry. Such a situation is clearly defined by using QTAIM and ELF. We hope that these examples demonstrate the power of relatively simple ideas applied for the understanding of chemical structures. As Sunko [208] wrote: “By choosing appropriate examples, links between theory and observable phenomena should be established keeping always in mind the fact that theories are not absolute truths but rather our inventions developed in order to account for the observable facts. They are based on models but these models are subject to changes as new facts are discovered.” In the end, we would like to use an ancient Chinese poem about Mountain Lu written by Su Shi: “It’s a range viewed in face and peaks from the side. Assuming different shapes viewed from far and wide. Of the Mountain Lu we cannot make out the true face. For we are lost in the heart of the very place.” We have shown that the shape and scenery of Mountain Lu are different from different perspectives (this sentence is extracted from the paper of Su et al. [6]) on VB and MO theories to describe the C_2 bond. Similarly, our study conquers the shortcomings of traditional schemes to describe chemical structures.

References

1. Atkins P, de Paula J (2006) Atkins' physical chemistry, 8th ed, vol 2. WH Freeman and Company. New York
2. Shaik S, Rzepa HS, Hoffmann R (2013) Angew Chem Int Ed Engl 52:3020
3. Frenking G, Hermann M (2013) Angew Chem Int Ed Engl 52:5922
4. Danovich D, Shaik S, Rzepa HS, Hoffmann R (2013) Angew Chem-Int Ed 52:5926
5. Zou W, Cremer D (2015) Chem Eur J 21:1
6. Zhong RL, Zhang M, Xu HL, Su ZM (2016) Chem Sci 7:1028
7. Piris M, López X, Ugalde JM (2016) Chem Eur J 22:4109
8. Zou WL, Cremer D (2016) Chem Eur J 22:4087
9. Oliveira de Sousa DW, Chaer Nascimento MAJ (2016) Chem Theor Comput 12:2234
10. Weinhold F, Klein RA (2014) Angew Chem-Int Ed 53:11214
11. Frenking G, Caramori GF (2015) Angew Chem Int Ed 54:2596
12. Frenking G, Krapp A (2007) J Comput Chem 28:15
13. Bremer M, Untenecker H, Gunchenko PA, Fokin AA, Schreiner PR (2015) J Org Chem 80:6520
14. Graham AG, Mota F, Shurdha E, Rheingold AL, Novoa JJ, Miller JS (2015) Chem Eur J 21:13240
15. Harcourt RD, Chem J (2015) Theor Comput 11:1979
16. Braida B, Hendrickx K, Domin D, Dinnocenzo JP, Hiberty PC (2013) J Chem Theor Comput 9:2276
17. Capdevila Cortada M, Ribas-Ariño J, Chaumont A, Wipff G, Novoa JJ (2016) Chem Eur J 22:1
18. Wolstenholme DJ, Dobson JL, McGrady GS (2015) Dalton Trans 44:9718
19. Hicks J, Underhill EJ, Kefalidis CE, Maron L, Jones C (2015) Angew Chem Int Ed 54:1
20. Butovskii MV, Kempe R (2015) New J Chem 39:7544
21. Blake MP, Kaltsoyannis N, Mountford P (2015) Chem Commun 51:5743
22. Cui P, Hu H-S, Zhao B, Miller JT, Cheng P, Li J (2015) Nat Commun 6:6331
23. Dairaku T, Furuita K, Sato H, Sêbera J, Yamanaka D, Otaki H, Kikkawa S, Kondo Y, Katahira R, Bickelhaupt FM, Fonseca Guerra C, Ono A, Sychrovsky V, Kojima C, Tanaka Y (2015) Chem Commun 51:8488
24. Qian L, Chen JF, Li YH, Wu L, Wang HF, Chen AP, Hu P, Zheng LR, Yang HG (2015) Angew Chem 127:1
25. Gardner BM, Balázs G, Scheer M, Tuna F, McInnes EJ, McMaster J, Lewis W, Blake AJ, Liddle ST (2015) Nat Chem 7:582
26. Bauzá A, Frontera A (2015) Angew Chem Int Ed 54:1
27. Matsumoto K, Haner J, Mercier HPA, Schrobilgen GJ (2015) Angew Chem Int Ed 54:1
28. Zhang Q, Li W-L, Xu C-Q, Chen M, Zhou M, Li J, Andrada DM, Frenking G (2015) Angew Chem Int Ed 54:1
29. Braunschweig H, Dewhurst RD, Hupp F, Nutz M, Radacki K, Tate CW, Vargas A, Ye Y (2015) Nature 522:327
30. Frenking G (2015) Nature 522:297
31. Chou S-L, Lo J-I, Peng Y-C, Lin M-Y, Lu H-C, Cheng B-M, Ogilvie JF (2015) Chem Sci 6:6872
32. Braunschweig H, Dewhurst RD, Hammond K, Mies J, Radacki K, Vargas A (2012) Science 336:1420
33. Pyykkö P, Riedel S, Patzschke M (2005) Chem Eur J 11:3511
34. Holzmann N, Stasch A, Jones C, Frenking G (2011) Chem Eur J 17:13517
35. Holzmann N, Stasch A, Jones C, Frenking G (2013) Chem Eur J 19:6467
36. Köppe R, Schnöckel H (2015) Chem Sci 6:1199
37. Frenking G, Holzmann N (2012) Science 336:1394

38. Mondal KC, Roesky HW, Schwarzer MC, Frenking G, Tkach I, Wolf H, Kratzert D, Herbst-Irmer R, Niepötter B, Stalke D (2013) Angew Chem Int Ed 52:1801
39. Holzmann N, Hermann M, Frenking G (2015) Chem Sci 6:4089
40. Yuan C, Zhao X-F, Wu YB, Wang X (2016) Angew chem Int Ed 55:15651
41. Lee VY, Sekiguchi A (2010) Organometallic compounds of low coordinate Si, Ge, Sn and Pb. Wiley, Chichester
42. Fischer RC, Power PP (2010) Chem Rev 110:3877
43. Frenking G, Tonner R, Klein S, Takagi N, Shimizu T, Krapp A, Pandey KK, Parameswaran P (2014) Chem Soc Rev 43:5106
44. Guo J-D, Liptrot DJ, Nagase S, Power PP (2015) Chem Sci 6:6235
45. Ruschewitz U (2016) Angew Chem Int Ed 55:3264
46. Stammler H-G, Blomeyer S, Berger RJF, Mitzel NW (2015) Angew Chem Int Ed 54:1
47. Ohno K, Satoh H, Iwamoto T, Tokoyama H, Yamakado H (2015) Chem Phys Lett 639:178
48. Knowles RR, Jacobsen EN (2010) Proc Natl Acad Sci U S A 107:20678
49. Riley KE, Hobza P (2011) Wiley Interdiscip Rev-Comput Mol Sci 1:3
50. Wagner JP, Schreiner PR (2015) Angew Chem Int Ed 54:12274
51. Grimme S (2011) Wiley Interdiscip Rev-Comput Mol Sci 1:211
52. Ehrlich S, Moellmann J, Grimme S (2013) Acc Chem Res 46:916
53. Zhao Y, Truhlar DG (2008) Acc Chem Res 41:157
54. Zhao Y, Cotelle Y, Sakai N, Matile S (2016) J Am Chem Soc 138:4270
55. Woolley RG (1991) Theochem-J Mol Struct 76:17
56. Woolley RG (1998) J Mater Chem 23:3
57. Fetter AL, Walecka JD (2003) Quantum theory of many-particle systems; 1st Dover (ed). Dover Publications, Mineola
58. Mattuck RD (1992) A guide to Feynman diagrams in the many-body problem, 2nd edn. Dover Publications, New York
59. Lowdin PO (1991) Theochem 76:1
60. Schleyer PV (2005) Chem Rev 105:3433
61. Popelier PLA (2007) Faraday Discuss 135:3
62. Alabugin IV, Gilmore KM, Peterson PW (2011) Wiley Interdiscip Rev-Comput Mol Sci 1:109
63. Ritter SK (2013) Chem Eng News 91:28
64. Kutzelnigg W (1990) In: Maksic ZB (ed) Theoretical models of chemical bonding: part 2. Springer, The physical origin of the chemical bond, Berlin, p 1
65. Ruedenberg K (1962) Rev Mod Phys 34:326
66. Danovich D, Hiberty PC, Wu W, Rzepa HS, Shaik S (2014) Chem Eur J 20:6220
67. Kling MF, von den Hoff P, Znakovskaya I, de Vivie-Riedle R (2013) Phys Chem Chem Phys 15:9448
68. Kling MF, Siedschlag C, Verhoef AJ, Khan JI, Schultze M, Uphues T, Ni Y, Uiberacker M, Drescher M, Krausz F, Vrakking MJJ (2006) Science 312:246
69. Xie X, Doblhoff-Dier K, Roither S, Schöffler MS, Kartashov D, Xu H, Rathje T, Paulus GG, Baltuska A, Gräfe S, Kitzler M (2012) Phys Rev Lett 109:243001
70. Liu Y, Liu X, Deng Y, Wu C, Jiang H, Gong Q (2011) Phys Rev Lett 106:073004
71. Znakovskaya I, von den Hoff P, Marcus G, Zherebtsov S, Bergues B, Gu X, Deng Y, Vrakking MJJ, Kienberger R, Krausz F, de Vivie-Riedle R, Kling MF (2012) Phys Rev Lett 108:063002
72. Xu H, Xu T-Y, He F, Kielpinski D, Sang RT, Litvinyuk IV (2014) Phys Rev A 89:041403
73. Alnaser AS, Kübel M, Siemering R, Bergues B, Kling NG, Betsch KJ, Deng Y, Schmidt J, Alahmed ZA, Azzeer AM, Ullrich J, Ben-Itzhak I, Moshammer R, Kleineberg U, Krausz F, de Vivie-Riedle R, Kling MF (2014) Nat Commun 5:3800
74. Xie X, Doblhoff-Dier K, Xu H, Roither S, Schöffler MS, Kartashov D, Erattupuzha S, Rathje T, Paulus GG, Yamanouchi K, Baltuska A, Gräfe S, Kitzler M (2014) Phys Rev Lett 112:163003
75. Xie X, Roither S, Schöffler MS, Lötstedt E, Kartashov D, Zhang L, Paulus GG, Iwasaki A, Baltuska A, Yamanouchi K, Kitzler M (2014) Phys Rev X 4:021005

76. Xie X, Lötstedt E, Roither S, Schöffler MS, Kartashov D, Midorikawa K, Baltuska A, Yamanouchi K, Kitzler M (2015) Sci Rep 5:12877
77. Heisenberg W (1926) Z f Phys 38:411
78. Farmelo G (2009) The strangest man: he hidden life of Paul Dirac, mystic of the atom. Basic Books, New York
79. Parr RG, Yang WT (1995) Annu Rev Phys Chem 46:701
80. Parr RG, Pearson RG (1983) J Am Chem Soc 105:7512
81. Parr RG, Yang WT (1984) J Am Chem Soc 106:4049
82. Hohenberg PC, Kohn W (1964) Phys Ther Rev 136:B864
83. Kohn W, Sham LJ (1965) Phys Ther Rev 140:A1133
84. Stalke D (2011) Chem Eur J 17:9264
85. Karadakov PB, Horner KE (2016) J Chem Theor Comput 12:558
86. Nalewajski RF (2000) J Phys Chem A 104:11940
87. Nalewajski RF (2004) Mol Phys 102:531
88. Nalewajski RF (2009) J Mater Chem 47:692
89. Nalewajski RF, Gurdek P (2012) Struct Chem 23:1383
90. Boguslawski K, Tecmer P, Legeza O, Reiher M (2012) J Phys Chem Lett 3:3129
91. Boguslawski K, Tecmer P, Barcza G, Legeza O, Reiher M (2013) J Chem Theor Comput 9:2959
92. Mottet M, Tecmer P, Boguslawski K, Legeza O, Reiher M (2014) Phys Chem Chem Phys 16:8872
93. Shannon CE (1948) Bell Syst Tech J 27:623
94. Fisher RA (1925) Proc Camb Philos Soc 22:700
95. Ghosh SK, Berkowitz M, Parr RG (1984) Proc Natl Acad Sci U S A 81:8028
96. Rong CY, Lu T, Chattaraj PK, Liu SB, Indian J (2014) Chem A 53:970
97. Kullback S (1997) Information theory and statistics. Dover, Mineola
98. Esquivel RO, Angulo JC, Dehesa JS, Antolín J, López-Rosa SL, Flores-Gallegos N, Molina-Espíritu M, Iuga C (2012) In: Deloumeaux P, Gorzalka JD (eds) Recent advances toward the nascent science of quantum information chemistry in information theory: new research. Nova Science Publishers, Hauppage, p 297
99. Esquivel RO, Flores-Gallegos N, Iuga C, Carrera EM, Angulo JC, Antolín J (2009) Theor Chem Accounts 124:445
100. Esquivel RO, Molina-Espíritu M, Plastino AR, Dehesa JS (2015) Int J Quantum Chem 115:1417
101. Molina-Espíritu M, Esquivel RO, López-Rosa SL, Dehesa JS (2015) J Chem Theor Comput 11:5144
102. Lewis GN (1916) J Am Chem Soc 38:762
103. Pauling L (1931) J Am Chem Soc 53:1367
104. Pauling L (1931) J Am Chem Soc 53:3225
105. Pauling L (1932) J Am Chem Soc 54:988
106. Pauling L (1948) The nature of the chemical bond. Cornell University Press, Ithaca
107. Shaik SS, Shurki A (1999) Angew Chem Int Ed 38:586
108. Shurki A, Derat E, Barrozo A, Kamerlin SCL (2015) Chem Soc Rev 44:1037
109. Popelier PLA (2005) In: Wales DJ (ed) Structure and bonding: intermolecular forces and clusters I, Quantum chemical topology: on bonds and potentials, vol 115. Springer, Heidelberg
110. Popelier PLA, Bremond EAG (2009) Int J Quantum Chem 109:2542
111. Gatti C, Macchi P (2012) Modern charge density analysis. Springer, New York
112. Popelier PLA (2014) In: Frenking G, Shaik S (eds) The chemical bond: fundamental aspects of chemical bonding. Wiley, VCH, p 271
113. Bader RFW (1990) Atoms in molecules: a quantum theory. Oxford University Press, Oxford
114. Silvi B, Savin A (1994) Nature 371:683
115. Silvi B (2004) Phys Chem Chem Phys 6:256
116. Vieira FS, Fantuzzi F, Cardozo TM, Chaer Nascimento MA (2013) J Phys Chem A 117:4025

117. Kumar A, Shridhar RG (2016) J Chem Theor Comput. 12:1705
118. Bader RFW, Henneker WH (1965) J Am Chem Soc 87:3063
119. Sini G, Maitre P, Hiberty PC, Shaik SS (1991) Theochem-J Mol Struct 75:163
120. Chesnut DB (2008) J Chem Theory Comput 4:1637
121. Shaik S, Danovich D, Wu W, Hiberty PC (2009) Nat Chem 1:443
122. Gamez JA, Yáñez M (2013) J Chem Theory Comput 9:5211
123. Goddard WA, III, Harding LB (1978) The description of chemical bonding from ab initio calculations. Ann Rev Phys Chem 29:363
124. Kovacs A, Esterhuysen C, Frenking G (2005) Chem Eur J 11:1813
125. Gadre SR, Shrivastava IH (1991) J Chem Phys 94:4384
126. Kumar A, Gadre SR, Chenxia X, Tianlv X, Kirk SR, Jenkins S (2015) Phys Chem Chem Phys 17:15258
127. Leboeuf M, Köster AM, Jug K, R. SD (1999) J Chem Phys 111:4893
128. Roy D, Balanarayan P, Gadre SR (2008) J Chem Phys 129:174103
129. Ayers PL, Boyd RJ, Bultink P, Caffarel M, Carbó-Dorca R, Causá M, Cioslowski J, Contreras-García J, Cooper DL, Coppens P, Gatti C, Grabowsky S, Lazzaretti P, Macchi P, Martín-Pendás A, Popelier PLA, Ruedenberg K, Rzepa H, Savin A, Sax A, Schwarz WHE, Shahbazian S, Silvi B, Solà M, Tsirelson V (2015) Comput Theor Chem 1053:2
130. Popelier PLA (2005) In: Wales DJ (ed) Structure and bonding, Intermolecular forces and clusters-quantum chemical topology: on bonds and potentials, vol 115. Springer, Berlin, p 1
131. Noury S, Krokidis X, Fuster F, Silvi B (1999) Comput Chem 23:597
132. Popelier PLA (1996) Comput Phys Commun 93:212
133. Kohout M, Wagner FR, Grin Y (2002) Theor Chem Accounts 108:150
134. Biegler-Konig F, Schonbohm J, Bayles D (2001) J Comput Chem 22:545
135. Otero-de-la-Roza A, Blanco MA, Pendas AM, Luana V (2009) Comput Phys Commun 180:157
136. Gillespie RJ, Popelier PLA (2001) Chemical bonding and molecular geometry: from Lewis to electron densities. Oxford University Press, New York
137. de Courcy B, Pedersen LG, Parisel O, Gresh N, Silvi B, Pilme J, Piquemal JP (2010) J Chem Theory Comput 6:1048
138. Pilme J, Berthoumieux H, Robert V, Fleurat-Lessard P (2007) Chem Eur J 13:5388
139. de la Lande A, Maddaluno J, Parisel O, Darden TA, Piquemal JP (2010) Interdiscip Sci-Comput Life Sci 2:3
140. Berski S, Andrés J, Silvi B, Domingo LR (2006) J Phys Chem A 110:13939
141. Poater J, Duran M, Sola M, Silvi B (2005) Chem Rev 105:3911
142. Pauzat F, Pilme J, Toulouse J, Ellinger Y (2010) J Chem Phys 133:054301
143. Rivera-Fuentes P, Aonso-Gomez JL, Petrovic AG, Seiler P, Santoro F, Harada N, Berova N, Rzepa HS, Diederich F (2010) Chem Eur J 16:9796
144. Kozlowski D, Pilmé J (2011) J Comput Chem 32:3207
145. Jenkins S (2013) Int J Quantum Chem 113:1603
146. Koritsanszky TS, Coppens P (2001) Chem Rev 101:1583
147. Coppens P (1997) X-ray charge densities and chemical bonding. Oxford University Press, Oxford
148. Popelier PL (2000) Atoms in molecules: an introduction. Pearson Education, Harlow
149. Tsirelson VG, Ozerov RP (1996) Electron density and bonding in crystals. Institute of physics publishing, Bristol
150. Jeffrey GA, Piniella JF (1991) The applications of charge density research to chemistry and drug design. Springer, New York
151. Matta CF, Boyd RJ (2007) The quantum theory of atoms in molecules: from solid state to DNA and drug design. Wiley-VCH, Weinheim
152. Chopra D (2012) J Phys Chem A 116:9791
153. Pendás AM, Hernández-Trujillo J (2012) J Chem Phys 137:134101
154. Dillen J (2015) J Comput Chem 36:883
155. Bader RFW (1994) Phys Rev B 49:13348

156. Becke AD, Edgecombe KE (1990) J Chem Phys 92:5397
157. Firme CL, Barreiro NBP, Esteves PM, Correa RJ (2008) J Phys Chem A 112:686
158. Rzepa H (2011) J Chem Theor Comput 7:97
159. Otero de la Roza A, Luaña V (2010) J Chem Theor Comput 6:3761
160. Otero de la Roza A, Luaña V (2011) J Phys Chem A 115:12953
161. Vidal I, Sánchez Navas A (2014) J Mol Model 20:2425
162. Grabowsky SJ, Phys J (2012) Chem A 116:1838
163. Jenkins S, Rong C, Kirk SR, Yin D, Liu S (2011) J Phys Chem A 115:12503
164. Mierzwicki K, Berski S, Latajka Z (2011) Chem Phys Lett 507:29
165. Syzgantseva OA, Tognetti V, Loubert L (2013) J Phys Chem A 117:8969
166. Andrés J, Gracia L, Gonzalez-Navarrete P, Safont VS (2015) Comput Theor Chem 1053:17
167. García-Revilla M, Popelier PLA, Francisco E, Martín-Pendás A (2011) J Chem Theor Comput 7:1704
168. Heverly-Coulson GS, Boyd RJ (2012) J Chem Theor Comput 8:5052
169. Savin A, Jepsen O, Flad J, Andersen OK, Preuss H, Schnering HG v (1992) Angew Chem Int Ed Engl 31:187
170. Savin A, Nesper R, Wengert S, Fässler TF (1997) Angew Chem Int Ed Engl 36:1808
171. Chesnut DB (2000) J Phys Chem A 104:11644
172. Fuentealba P, Chamorro E, Santos JC (2007) Theor Comp Chem 19:57
173. Silvi B, Fourre I, Alikhani ME (2005) Monatshefte Fur Chemie 136:855
174. Ball P (2011) Nature 469:26
175. Shaik S (2006) J Comput Chem 28:51
176. Coleman AJ, Yukalov VI (2000) Reduced density matrices: coulson's challenge. Springer, New York
177. Parr RG, Yang W (1989) Density-functional theory of atoms and molecules. Oxford University Press, New York
178. Bader RFW (1994) Atoms in molecules: a quantum theory. Clarendon Press, Oxford
179. Sorribes I, Wienhofer G, Vicent C, Junge K, LLusar R, Beller M (2102) Angew Chem Int Ed 51:7794
180. Pedrajas E, Sorribes I, Junge K, Beller M, Llusar R (2015) ChemCatChem 7:2675
181. Feliz M, Guillamon E, Llusar R, Vicent C, Stiriba SE, Perez-Prieto J, Barberis M (2006) Chem Eur J 12:1486
182. Guillamon E, Llusar R, Pérez-Prieto J, Stiriba SE (2008) J Organomet Chem 693:1723
183. Guillamon E, Blasco M, Llusar R (2010) Inorg Chim Acta 424:5935
184. Alfonso C, Feliz M, Safont VS, Llusar R (2016) Dalton Trans 45:7829
185. Frisch MJ, Trucks GW, Schlegel HB, Scuseria GE, Robb MA, Cheeseman JR, Scalmani G, Barone V, Mennucci B, Petersson GA, Nakatsuji H, Caricato M, Li X, Hratchian HP, Izmaylov AF, Bloino J, Zheng G, Sonnenberg JL, Hada M, Ehara M, Toyota K, Fukuda R, Hasegawa J, Ishida M, Nakajima T, Honda Y, Kitao O, Nakai H, Vreven T, Montgomery JA Jr, Peralta JE, Ogliaro F, Bearpark M, Heyd JJ, Brothers E, Kudin KN, Staroverov VN, Kobayashi R, Normand J, Raghavachari K, Rendell A, Burant JC, Iyengar SS, Tomasi J, Cossi M, Rega N, Millam NJ, Klene M, Knox JE, Cross JB, Bakken V, Adamo C, Jaramillo J, Gomperts R, Stratmann RE, Yazyev O, Austin AJ, Cammi R, Pomelli C, Ochterski JW, Martin RL, Morokuma K, Zakrzewski VG, Voth GA, Salvador P, Dannenberg JJ, Dapprich S, Daniels AD, Farkas O, Foresman JB, Ortiz JV, Cioslowski J, Fox DJ (2010) Revision B.01 ed. Gaussian Inc, Wallingford
186. Becke AD (1988) Phys Rev A 38:3098
187. Becke AD (1993) J Chem Phys 98:5648
188. Lee C, Yang W, Parr RG (1988) Phys Rev B 37:785
189. Xu DF, Cheng B, Zhang JF, Wang WK, Yu JG, Ho WK (2015) J Mater Chem A 3:20153
190. Liu Y, Yu HB, Cai M, Sun JW (2012) Cat Com 26:63
191. Soofivand F, Mohandes F, Salavati-Niasari M (2013) Mater Res Bull 48:2084
192. Xu DF, Cheng B, Cao SW, Yu JG (2015) Appl Catal B-Environ 164:380
193. Xu DF, Cao SW, Zhang JF, Cheng B, Yu JG (2014) Beilstein J Nanotechnol 5:658

194. Andres J, Gracia L, Gonzalez-Navarrete P, Longo VM, Avansi W Jr, Volanti DP, Ferrer MM, Lemos PS, La Porta FA, Hernandes AC, Longo E (2014) Sci Rep 4:5391
195. Pereira WdS, Andres J, Gracia L, San-Miguel MA, da Silva EZ, Longo E, Longo VM (2015) Phys Chem Chem Phys 17:5352
196. Andrés J, Ferrer MM, Gracia L, Beltran A, Longo VM, Cruvinel GH, Tranquilin RL, Longo E (2015) Part Part Syst Charact 32:646
197. Longo E, Cavalcante LS, Volanti DP, Gouveia AF, Longo VM, Varela JA, Orlandi MO, Andres J (2013) Sci Rep 3:1676
198. Botelho G, Sczancoski JC, Andres J, Gracia L, Longo E (2015) J Phys Chem C 119:6293
199. Roca RA, Gouveia AF, Lemos PS, Gracia L, Andrés J, Longo E (2016) Inorg Chem 55:8661
200. Oliveira RC d, Assis M, Mondego M, Penha M, Li MS, Andres J, Gracia L, Longo E (2016) J Phys Chem C 120:12254
201. Fabbro MT, Gracia L, Silva GS, Santos LPS, Andrés J, Cordoncillo E, Longo E (2016) J Solid State Chem 239:220
202. Kresse G, Furthmuller J (1996) Comput Mater Sci 6:15
203. Kresse G, Hafner J (1994) Phys Rev B 49:14251
204. Kresse G, Joubert D (1999) Phys Rev B 59:1758
205. Perdew JP, Burke K, Ernzerhof M (1996) Phys Rev Lett 77:3865
206. Mulliken RS (1928) Phys Rev 32:186
207. Heitler W, London F (1927) Z Physiother 44:455
208. Sunko DE (1983) Pure Appl Chem 55:375